



UNIVERSITÀ
DEGLI STUDI
FIRENZE

PhD in
Chemical Sciences (curriculum Science for the
Conservation of Cultural Heritage)

CYCLE XXXVI

COORDINATOR Prof. Anna Maria Papini

Development of an innovative chemical methodology for the
treatment of cellulose triacetate motion picture films affected by
the "vinegar syndrome"

Academic Discipline (SSD) CHIM/12

Doctoral Candidate

Dr. Francesca Porpora

Supervisor

Prof. Emiliano Carretti

Co-Supervisor

Prof. Luigi Dei

Coordinator

Prof. Anna Maria Papini



UNIVERSITÀ
DEGLI STUDI
FIRENZE

PhD
Chemical Sciences

The consultation of the thesis is free. Unless a specific authorization is obtained from the author, the thesis can be, however, downloaded and printed only for strictly personal purposes related to study, research and teaching, with the explicit exclusion of any use that has – even indirectly – a commercial nature.

Dedicated to my family

Summary

The present work was focused on the setup of innovative, cheap, easy-to-produce and handle and possibly reusable chemical inhibitors for the so-called “*vinegar syndrome*” that affects motion picture films whose support is made by cellulose acetate (CA). We proposed and characterized several systems based on two strategies: the use of sponge-like systems (1) made of polyethyleneimine (PEI) and/or (2) uploaded with zinc oxide nanoparticles. The intent was to use free amino groups, in the first case, and inorganic nanoparticles, in the second case, to convert acetic acid into ammonium carboxylate and zinc acetate, respectively, through an acid/base reaction.

In order to evaluate the performance of our systems, an innovative degradation method to artificially induce the deacetylation reaction on motion picture films based on the exposition to a high acidity saturated atmosphere has been successfully set up. Another fundamental novelty of this work was the development of a multi-analytical protocol able to monitor the chemical alterations of the base supports connected with the occurrence and the evolution of the “*vinegar syndrome*”. This is a key point of this project, being that this degradation phenomenon, at today, has been mostly investigated by using single techniques that often do not give exhaustive information about all the aspects involved in the progress of the deacetylation process. In particular, its evolution has been monitored by focusing the attention on the trend of the acetyl content, the free acidity and the ratios between the intensities of some FTIR-ATR diagnostic peaks. In addition, TGA analysis and tensile tests gave precious informations about collateral degradation pathways that are promoted by deacetylation (i.e. variation in the molecular weight of CA chains and loss of plasticizers).

Then, the evaluation of the efficacy of the above-mentioned systems in inhibiting the vinegar syndrome was performed both on real motion picture films on which the deacetylation process has been artificially induced with our degradation protocol and

on films naturally affected by the “*vinegar syndrome*”. The different behaviors of untreated and treated films have been evaluated through the above-mentioned multi-analytical protocol. The results clearly indicate that the chemical approach based on the use of sponge-like systems made by polyethyleneimine and/or soaked with metal oxide nanoparticles set up in the frame of this work is a highly effective and promising tool for the inhibition of the “*vinegar syndrome*”. If properly developed and applied, in collaboration with motion picture film conservators, it can potentially represent a valid alternative to the procedures that at today are still commonly used for this purpose and that are mainly focused on the slowdown of the kinetic of the process.

Index

I. Introduction	1
CHAPTER II	7
Materials of cinema: motion picture films and their degradation	
2.1 Historically evolution of cinematography from its beginnings to the Lumière Brothers	7
2.2 The film-making industry	10
2.3 Motion picture film: the structure	15
2.4 The emulsion layer and the photographic process	17
2.5 The supports	22
2.5.1 Cellulose	24
2.5.2 The first option: celluloid	25
2.5.2.1 History	25
2.5.2.2 Synthesis and properties	25
2.5.2.3 Degradation Processes	27
2.5.2.4 Observable signs of degradation	29
2.5.3. The safer option: cellulose acetate	30
2.5.3.1 History	30
2.5.3.2 Synthesis and properties	32
2.5.3.3 Degradation processes: the “vinegar syndrome”	34
2.5.3.4 Observable signs of degradation	37
2.5.3.5 Monitoring and taking care of the syndrome: state of the art	39
2.5.3.5.1 Monitoring the evolution of the syndrome	40
2.5.3.5.1 Taking care of the vinegar syndrome	44
2.5.4 The final option: polyesters	48
2.5.4.1. History	48
2.5.3.2 Synthesis and properties	49
2.5.4.3 Degradation processes	50
<i>References</i>	<i>51</i>
CHAPTER III	59
Set up of a method for the artificial induction of the deacetylation	

process and of a multi-analytical protocol for its monitoring	
3.1 Materials and Methods	60
3.1.1 Chemicals and materials	60
3.1.2 The artificial induction of the deacetylation process	62
3.1.2.1 The high acidity induction method (HC15M)	64
3.1.2.2 The high acidity induction method (ATM2.X)	66
3.1.3 A multi-analytical protocol to monitor the evolution of the degradation process	68
3.2 Results and Discussion	75
3.2.1 The high acidity induction method (HC15M)	75
3.2.1.1 CTA-based films (FX_HC15M)	75
3.2.1.2 Real motion picture films (PX_HC15M)	85
3.2.2 The high acidity induction method (ATM2.X)	97
3.2.2.1 CTA-based films (ATM2.3)	97
3.2.2.2 Real motion picture films (ATM2.9)	103
3.3. The validation of the multi-analytical method	109
3.4. Comparison of the degradation protocols	113
3.5. Conclusions	115
<i>References</i>	<i>117</i>
CHAPTER IV	120
Proposal of inhibitors for the “vinegar syndrome” made of polyethyleneimine	
4.1 Polyethyleneimine (PEI) surfaces	121
4.2 PVA-PEI-based systems	123
4.2.1 PVA-PEI cryogels	123
4.2.2 PVF-PEI sponge-like systems	124
4.2.3 Chemicals	126
4.2.4 Syntheses of the systems	127
4.2.4.1 PVA-PEI cryogels	127
4.2.4.2 PVF sponge	127
4.2.4.3 PVA/PVF-PEI sponge-like systems	128
4.2.5 Characterization of the systems	132
4.2.6 Results and discussion	136
4.3. Polyethyleneimine-based sponge systems (SPEI)	153
4.3.1 Chemicals	155
4.3.2 Synthesis of the systems	155

4.3.3	Characterization of the systems	156
4.3.4	Results and discussion	158
4.4.	Conclusions	175
	<i>References</i>	176
<i>Appendix of Chapter IV</i>		182
CHAPTER V		184
Proposal of inhibitors for the “vinegar syndrome” based on inorganic nanoparticles		
5.1	Inorganic nanoparticles for acetic acid absorption	184
5.2	Material and methods	190
5.2.1	Chemicals	191
5.2.2	Synthesis of the sponges	192
5.2.3	Acetic acid absorption-desorption tests on nanoparticles	192
5.2.4	Characterization of the sponges	195
5.3.	Results and discussion	196
5.3.1	Pure nanoparticles	196
5.3.2	Whatman paper with nanoparticles	205
5.3.3	Inorganic nanoparticles uploaded on PVF and SPEI sponges	207
5.4	Conclusions	216
	<i>References</i>	218
CHAPTER VI		223
Evaluation of the efficacy of our systems in the inhibition of the “vinegar syndrome”		
6.1	Material and Methods	223
6.1.1	Chemicals and samples	223
6.1.2	The inhibition of the artificially-induced deacetylation process	225
6.1.2.1	The protocol to artificially induce the deacetylation process	225
6.1.2.2	Treatments and their applications	226
6.1.3	The inhibition of the naturally induced deacetylation process	229
6.1.4	The multi-analytical method to monitor the degradation process	231

6.2 Results and discussion	232
6.2.1 Ca(OH) ₂ , Mg(OH) ₂ and ZnO nanoparticles uploaded on Whatman® Paper	232
6.2.2 SPEI and PVF	238
6.2.3 SPEI and PVF uploaded with ZnO nanoparticles (SPEI+ZnO, PVF+ZnO)	244
6.2.4 Comparison between various treatments	250
6.2.5 Evaluation of the efficacy of SPEI on real motion picture films naturally affected by the vinegar syndrome	255
6.3 Conclusions	261
<i>References</i>	263
VII. Conclusions	264
<i>Acknowledgments</i>	270
PAPER I	272
“Performance of innovative nanomaterials for bone remains consolidation and effect on ¹⁴C dating and on palaeogenetic analysis”	
<i>Supporting Information</i>	284
PAPER II	296
“Nanostructured fluids confined into Highly Viscous Polymeric Dispersions as cleaning tools for artifacts: A rheological, SAXS, DSC and TOF-SIMS study”	
<i>Supporting Information</i>	307
PAPER III	347
“Non-Aqueous Poly(dimethylsiloxane) Organogel Sponges for Controlled Solvent Release: Synthesis, Characterization, and Application in the Cleaning of Artworks”	
<i>Supporting Information</i>	366

I. Introduction

The birth of cinema in the late XIX century and the evolution of the motion picture film industry in the following century are a milestone in the history of humanity. The evolution of this technology as a medium of expression and diffusion of information radically and deeply changed the habits and the possibilities of men during the past century in every aspect of life. On these bases, motion picture films are precious proofs of this technological, scientific, social and humanistic evolution. The history of the materials used for the manufacture of motion picture films is a very interesting topic, and their choice and stability problems have sometimes spurred and sometimes followed the technological developments of the XIX and XX centuries. This point will be discussed in more detail in Chapter II.

In particular, this thesis is focused on the study of motion picture films made of cellulose acetate (CA), a material widely used as support since the beginning of the XX century, chosen as a safer substitute for the more unstable and dangerous cellulose nitrate.

Unfortunately, also this material soon showed instability issues due to its characteristic degradation process, traditionally called "*vinegar syndrome*". This phenomenon concerns the side chain scission through ester hydrolysis induced by moisture and high temperatures, with the formation of hydroxyl groups and the release of acetic acid. This reaction is strictly influenced by temperature, moisture and acidity: the released acetic acid acts as a catalyst for the deacetylation and induces an autocatalytic process. A secondary effect induced by the deacetylation is the hydrolysis of the glycosidic bonds between the glycosidic units constituting the backbone of CTA. In addition to the smell, the deformation and the embrittlement of the support and the detachment of the emulsion layer are macroscopic symptoms of the vinegar syndrome and can strictly compromise the usability of the films.

Therefore, controlling the temperature, reducing environmental moisture and removing alteration by-products from the storing environment is mandatory to limit this phenomenon.

To this day, the most used method by conservators and archivists, proposed in the “Storage Guide for Acetate Film” of the Image Permanence Institute (IPI), suggests acting on the macroenvironment conditions, properly setting temperature and humidity, based on the conservation status of the film. For example, for films in very serious degradation conditions, the suggestion is to store them at low temperature (down to -18 °C) and at RH of around 20% (it is important to limit the moisture that can promote hydrolysis reactions but also to store films in a not-too-dry environment that could have detrimental effects on the conservation of the emulsion). However, this solution can only act on the kinetics of the process, slowing down the rate of acetic acid production, and strictly limits the use and the handle of the films. Apart from this protocol, activated silica gel and/or molecular sieves are also used to reduce the moisture and to adsorb the acetic acid formed. However, also these solutions can only slow down the process and, for example, the presence of molecular sieves for extended periods increases the risk of excessive desiccation and consequent stiffening of the emulsion layer. The last studies on this purpose suggest the use of Molecular Organic Frameworks (MOFs): these systems are very performing and have been successfully tested for the conservation of motion picture films but have high manufacturing costs and a huge amount of time is needed for their synthesis. For these reasons, the use of these systems on a large scale is unlikely. In addition, all the systems reported above are not reusable.

On these bases, the main goals of this project could be schematized as follows:

- 1) the development of a proper degradation protocol to artificially induce the “*vinegar syndrome*”;
- 2) the definition of an innovative multi-analytical protocol to monitor the evolution of the “*vinegar syndrome*” that, at today has been mostly investigated by using single

techniques that often do not give exhaustive information about all the aspects involved in the progress of the deacetylation process.

These two first steps of the work are functional to the third and main goal of the whole project which is:

3) the set up of some innovative materials effective as inhibitors of the “*vinegar syndrome*”, which typically affects CA motion picture films, based on a chemical approach. In particular, the efficacy of the proposed systems will be tested through the analytical approach indicated in point 2.

Concerning point (3), the idea is to set up cheap, easy-to-handle and possibly reusable systems able to neutralize the acetic acid in order to inhibit and/or block the deacetylation reaction and the other correlated degradation processes.

The research strategy was based on three different directions:

- the set-up and the application of sponges or gel-like systems based on polyethyleneimine (PEI) and/or polyvinylalcohol (PVA). The aim was to incorporate PEI in a stable and porous structure and to use its free amino groups to convert acetic acid into ammonium carboxylate through an acid/base reaction (the discussion of these systems is reported in Chapter IV). Part of this topic was the subject of the work I did at the Chemistry Department of Georgetown University (Washington D.C.) where I spent five months of my PhD under the supervision of Prof. Richard G. Weiss.
- the use of inorganic nanoparticles uploaded on different substrates, such as paper or sponges. The intent was to create an easy-to-handle composite system based on a porous support on which oxide or hydroxide nanoparticles are uploaded. Nanoparticles convert the acetic acid into the corresponding acetate salt through an acid/base reaction (the discussion of these systems is reported in Chapter V).

The physico-chemical characterization of these systems was conducted by multiple techniques, based on the nature of the product (Fourier Transform Infrared Spectroscopy, FTIR, Elemental analysis, EA, Thermogravimetric analysis, TGA, for all the systems and X-ray diffraction, XRD, for inorganic nanoparticles). Their morphology was investigated through Scanning Electron Microscopy (SEM) and X-ray microtomography (TOM) and their rheological behavior was studied, too. In addition, preliminary tests to evaluate their capacity in the absorption of gaseous glacial acetic acid were conducted.

Then, their efficacy in the inhibition of the vinegar syndrome on real motion picture films was tested. For this purpose, the development of a proper method to artificially induce the deacetylation process in motion picture films has been an essential step in performing this evaluation (point 2). The ideal degradation protocol for our purposes may be reproducible and able to induce the deacetylation process in a controlled way, with proper timelines to appreciate the evolution of the process in a lab context and it does not excessively alter the performance of the inhibitor whose efficacy we want to test. As it was mentioned above, the deacetylation process could be induced and favored by high values of temperature, moisture and acidity in the storage environment. For this reason, several degradation methods were proposed and evaluated based on the exposition of the films to one (or two) of the above-mentioned parameters (high temperature, moisture and/or acidity).

In order to monitor the evolution of the deacetylation in motion picture films during the degradation protocol and to evaluate the efficacy of our inhibitors, another fundamental step of this work was the definition and the optimization of a multi-analytical protocol (point 3). The idea was to monitor the chemical alterations of all the samples in terms of acetyl content (amount of acetic acid esterified onto the cellulose backbone of the polymer) and free acidity (non-esterified acetic acid adsorbed on the film). For this purpose, an ASTM normative (ASTM D 871 – 96), on which protocols for the calculation of both the acetyl content and free acidity for pure CA are reported, has been properly adapted to the analysis of CA-based motion

picture films. In addition, a non-invasive and non-destructive method based on the use of the Fourier Transform Infrared – Attenuated Total Reflectance (FTIR-ATR) Spectroscopy was also proposed. These analyses were also correlated with optical microscopy evaluations, gravimetry and solubility tests. All the above-mentioned parameters are directly associated with deacetylation, which in turn causes depolymerization and loss of plasticizers that induce the alteration of both thermal and mechanical properties. To evaluate these latest points TGA and tensile tests have been performed. The studies on both the evaluation of the best artificial degradation protocol and the set-up of the multi-analytical protocol are reported in Chapter III. In this way, it was possible to evaluate the theoretical efficacy of our inhibitors by comparing the characteristics (in terms of acetyl content, free acidity, thermal and mechanical properties) of untreated and treated films subjected to the same artificial degradation protocol (Chapter VI).

The last step of this thesis concerned the evaluation of the performance of the best of our systems in the inhibition of the vinegar syndrome on a film naturally affected by this disease (Chapter VI).

The additional three papers, attached to this manuscript, concern three other side projects on which I worked before and during my PhD period, based on the application of nanotechnology to the conservation of Cultural Heritage:

- in “Performance of innovative nanomaterials for bone remains consolidation and effect on ^{14}C dating and on palaeogenetic analysis”, the results of my Master's degree thesis regarding the development of a consolidation protocol of ancient bone remains based on the use of nanometric hydroxyapatite (HAP) are reported.

-In “Nanostructured fluids confined into Highly Viscous Polymeric Dispersions as cleaning tools for artifacts: A rheological, SAXS, DSC and TOF-SIMS study”, the development and the structural and mechanical characterization of a new complex system composed by an oil-in-water microemulsion (μE) embedded in an aqueous

3D Highly Viscous Polymeric Dispersion (HVPD) of poly (vinyl alcohol) (PVA) cross-linked by borax, is presented together with its possible implications in paintings conservation.

- In “Non-Aqueous Poly(dimethylsiloxane) Organogel Sponges for Controlled Solvent Release: Synthesis, Characterization, and Application in the Cleaning of Artworks” I had the opportunity, working in collaboration with Georgetown University and the National Gallery of Art (Washington D.C.) during my stage in the US, to evaluate the possibility of using polydimethylsiloxane (PDMS) organogel sponges as potential innovative support for controlled and selective cleaning of works of art surfaces.

Chapter II

Materials of cinema: motion picture films and their degradation

In this Chapter, a summary of the history of the evolution of cinematography is reported. Traditionally, the birth of cinematography is dated December 28th, 1895, the date of the first projection of a motion picture film by the Lumière Brothers.

Subsequently, the attention will be focused on the products of the analogic film-making industry, the motion picture films, in particular on their manufacturing processes, structure and materials.

Finally, a focus on different materials used for producing motion picture films is reported, examining their composition, characteristics and degradation problems. A detailed study has been dedicated to cellulose acetate-based media, which are the main subject of this thesis: further in-depth analysis has been conducted to examine the literature regarding degradation processes and conservation methods currently proposed for these objects.

2.1 Historically evolution of cinematography from its beginnings to the Lumière Brothers

Cinematography, intended as the projection of images through which the appearance of movement is induced (the word “cinema” itself derives from the ancient Greek κίνημα, -τος: "movement "), has origins as old as human beings. The hunting scenes painted on the walls of the Altamira Caves (Spain) or Chauvet (France), in which the "actors," prey and predators, were reproduced several times giving the impression of movement, could be ascribed as examples of cinema *ante litteram* [1]. Other examples of primordial cinematography come from the Far and Middle East, with the Chinese *shadow puppet theater* (2nd century B.C.) [1]–[3], and from Europe, in Plato’s famous Myth of Cave (4th century B.C.) [4][5], with the shadows cast by

prisoners on the wall, or the bas-reliefs of the Trajan Column (2nd century A.D.), in which the events of war are narrated chronologically sequence by sequence, "frame by frame".

To reach the current conception of cinematography, technical and scientific knowledge led to the creation of optical specific devices for the projection of images was needed.

One of the first of these devices was the *camera obscura*, designed by Leonardo da Vinci, who described its principle of operation in the Codex Atlanticus (1515): inside the chamber, the image from the outside was reproduced upside down, and this image was used as a draft to copy buildings and landscapes "live" and "in detail" [1]. This method was largely used by Venetian Vedutist painters in the 18th century. The step forward is achieved thanks to the *magic lantern* [3], dating back to the XVII century, whose invention is attributed to Athanasius Kircher and Christiaan Huygens [1], [6]; unlike the *camera obscura*, thanks to a light source, the magic lantern allows to project onto a screen or a wall, images painted on glass plates, magnified through a lens. Projections evolved from being visible only within a small chamber, intended for the eyes of only one viewer at a time, to being piped outward onto large surfaces for collective enjoyment and educational purposes. Understanding the great potential of this medium for public entertainment, it became indispensable and a real challenge for XIX-century scientists to devise methods and tools not only to project but also to move images on the screen.

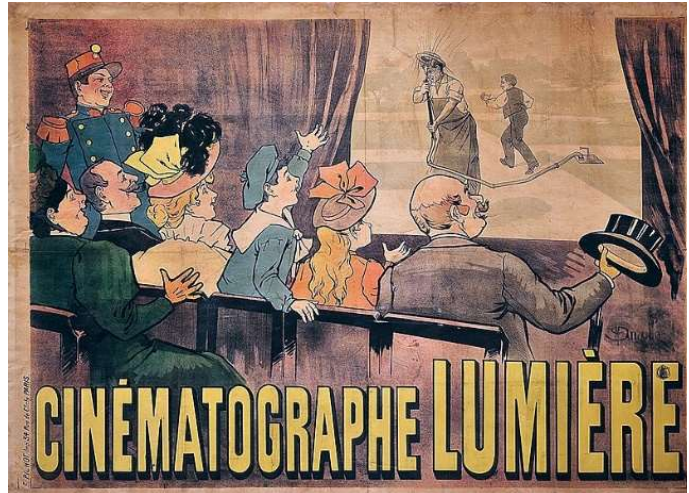
Underlying these new inventions, there was the discovery of a physiological phenomenon called *persistence of vision* or "*retina lag*", whereby vision is not a continuous but an intermittent process due to the time lapse between the acquisition of an image by the retina and its processing by the nervous system [7]. Meanwhile, no other image can be registered by our eyes. Because of this phenomenon, the brain is not able to process more than 10 to 12 images in one second and this is exactly the reason why, if slightly different images occur in very rapid succession, as is the case in film projectors, these images blend, giving the eye the sensation of motion [6].

Many instruments were developed as a result of this discovery, such as the *thaumatrope* (1824), Joseph Plateau's *phenakhtoscope* (1832), William George Horner's *zootrope* (1834), and Émile Reynaud's *optical theatre with praxinoscope* (1876), the latter is the only one among these instruments that allowed the projection of moving images (in this specific case of paintings made by Reynaud himself on glass plates) onto a screen, according to the same physical principle as the magic lantern [1], [6]. Reynaud's optical theater, however, did not have a long life because of the birth of photography. The evolution of photography, indeed, is inextricably linked to the development of cinematography due, first of all, to the rapidity in image acquisition and development and, secondly, to the transition to new media for negatives, no longer rigid like metal, paper or glass but transparent and flexible like plastic film, which could easily slide into a projection machine [6]. Indeed, it was the introduction of the celluloid film roll in 1889 by George Eastman that led to the experimentation of cameras and projectors and the creation of the Lumière brothers' cinematograph [6], [8]. Some mention should be made to Eadward Muybridge with his *zoopraxinoscope* (1878), Étienne-Jules Marey and his *photographic gun* (1882) capable of capturing 12 frames per second and to whom we owe the earliest motion picture in the history of cinema (*La Vague*, 1891). In 1891 Thomas A. Edison and his collaborator W.K. L. Dickson developed a film camera, the *kinetograph*, and a projector, the *kinetoscope*, inside which spectators, by inserting a coin, turning a crank and resting their eye on the top of the instrument, could enjoy the projection of a short movie imprinted on a 35 mm wide (the standard size still in use today) celluloid film perforated at the edges [6]–[8] (Fig. 1A). However, Edison's kinetoscope had an important limitation: its viewing system can be used by only one viewer at a time. For this reason, it was surpassed by brothers Auguste and Louis Lumière's celebrated *cinematograph*, an extremely practical and lightweight apparatus compared to the kinetoscope that worked both as a camera and as a projector on a wide screen. After shooting some of their most historic films, the Lumière brothers were finally ready to show them to the public, at the price of one

franc per person, on December 28th, 1895 in the Salon Indien of the Grand Café in Boulevard des Capucines, in Paris. This date, now historic, is generally considered as the birth of cinema [6], [8] (Fig.1B).



A



B

Figure 1(A). Publicity photograph of man using Edison Kinetophone, ca. 1895. One of the first billboards for cinématographe Lumière; a scene from *L'Arroseur arrosé* is projected on the screen; Imprimerie Pichot, Paris, 1896.

2.2 The film-making industry

The success of the Lumière Brothers laid the foundation of the motion picture film industry which fundamentals as they were both then and now, are [7]:

1. Motion picture films were made on two film stocks, the original negative film and the print film (for release to the cinemas).
2. The picture is composed of a series of consecutive frames (i.e. photographs) capturing different stages of the movement.
3. The film is made of a transparent plastic base and a photographic emulsion of natural gelatines and light-sensitive silver salts adhered to it.
4. The film moves through both the camera and projector intermittently, transported by means of teeth (called sprockets) on wheels or rollers. The sprockets engage with

holes called “perforations” in the film base. These sprockets and perforations define the synchronism between the frame, the camera shutter, the printer gate and the projector shutter throughout the entire shooting, laboratory processing and projection sequence.

The shape, size, and spacing between perforations and the size of frames are standardized.

Motion picture films are cataloged in different “formats” based on their width, measured from side to side and expressed in millimeters. The most common formats are 35 mm, 16 mm, 8 mm and Super 8 mm (Fig. 2), but many more have been produced. Each of these formats has its specific use; for example, smaller formats such as 16 mm and 8 mm, which often have perforations only on one side and are cheaper, are used for educational and amateur purposes (documentaries and home movies); 35 mm was the first format used and in 1908 has been recognized as the standard format for cinema and television: the larger the format (and thus the larger the frame size), the more defined the image is.

In the beginning, movies were silent and the sound was integrated “live” during every show by the accompaniment of an orchestra or by actors. Only since 1920, many attempts have been made to include sound into motion picture films, by registering it simultaneously with pictures. After various preliminary systems (in the very first phonograph invented by Edison and used by a just-born Warner Bros Studio, the sound was registered on a synchronized disc to the shooting and the projection), two methodologies caught on: first, the optical soundtrack and, then, the magnetic soundtrack [7] (Fig.2).

Optical sound recording (by the 1920s) is a system in which an optical recorder, or sound camera, transfers sound to an optical image, by recording the variations of the sound as variations of density or area in a photographic image. Then the photographic (optical) soundtrack on a film is scanned by a horizontal slit beam of

light that modulates a photoelectric cell. The voltages generated by the cell produce audio signals that are properly amplified.

For magnetic sound recording (since 1953), the sound waves are picked up by a microphone that creates a modulation (proportional in intensity and frequency of the original sound) of an electrical signal. By powering an electromagnet, a magnetically neutral emulsion is impressed onto the film: the changes in the electrical magnet orientate the metallic particles of the emulsion, obtaining a magnetic representation of the intensities of the original sound modulation. In order to reproduce the signal, the magnetic track is run (at the same speed as the recording speed) and “read” by an electromagnet. The fluctuations in the magnetic field create electrical fields in the electromagnet; then, the resulting current is amplified, and the signal is routed to the speakers to reproduce the sounds.

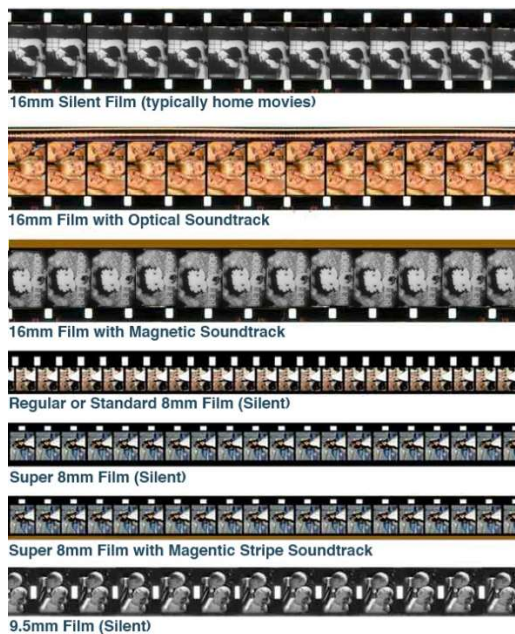


Fig.2 Common formats of motion picture films with different types of soundtracks (optical and magnetic).

Motion pictures originated in monochrome (black and white, Fig. 3A), but inventors continually attempted to introduce “natural” color. The very first methods involved:

1. *hand-coloring*, using brush and water-based or alcohol-based artificial organic dyes on each frame;
2. *stenciling*, by a stencil cut out in the shape of the area to be colored and used as a guide;
3. *tinting*, entirely coloring the emulsion with a monochromatic tone by hand-brushing the film or by immersing it into water-based acid dyes or by factory-dyeing the film base before coating with the emulsion (1920s);
4. *toning processes* (Fig. 3B), replacing the silver by metallic salts (metallic toning) or organic synthetic dyes (mordant dye toning) [7].

Moreover, other methods have been developed, based on *additive synthesis* by the use of colored filters on both the camera and the projector (es. Kinecolor, 1906; Dufeycolor), or *subtractive synthesis* (Fig. 3C), using film with two or three layers of emulsion, selectively sensitive to a certain range of wavelengths (Kodachrome, 1910; Prizma, 1916; Technicolor, 1915-21; the multilayer monopack by Kodachrome, 1935) [7]. Today a typical color negative film purchased by Eastman©, Kodak© and Fujifilm© is made up of three layers: the blue record, green record, and red record. Each layer is made of two separate layers containing silver halide crystals and dye-couplers. In addition, there is an UV filter on top to shade the silver-halide crystals from the non-visible ultraviolet radiation.

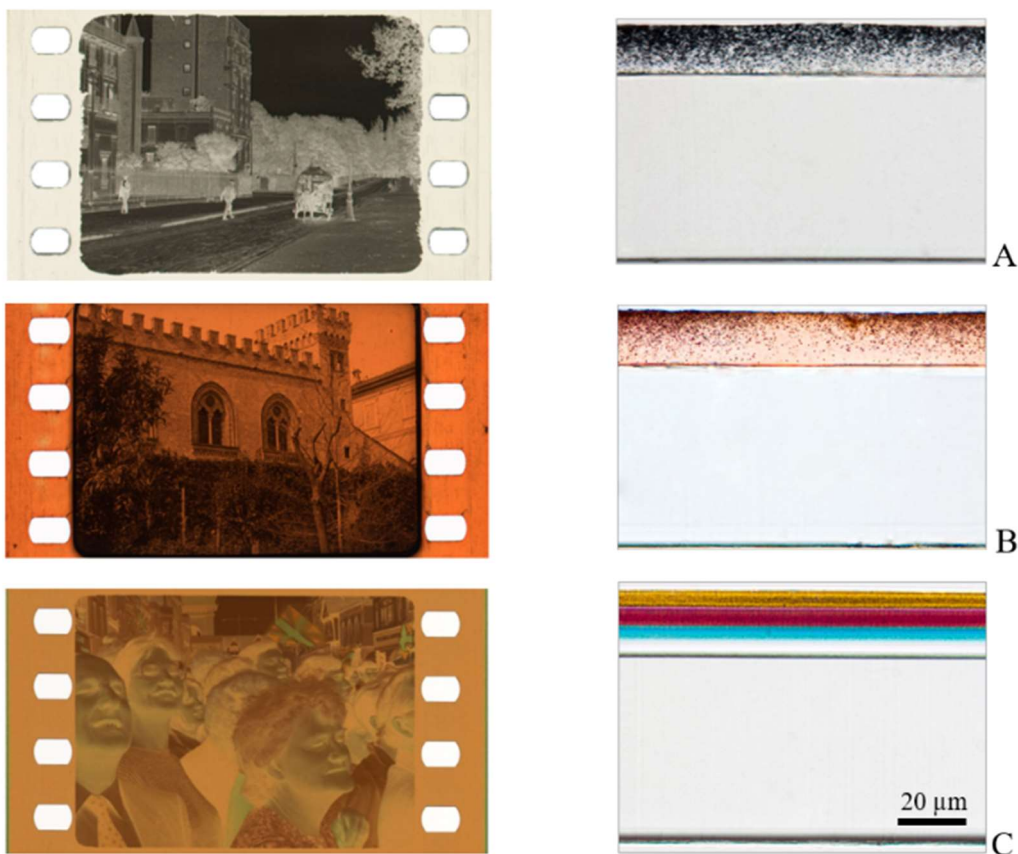


Fig. 3 The evolution of the color in motion picture films: (A) 35mm black and white negative on cellulose nitrate support and the corresponding cross-section in which is possible to see the silver particles suspended in the gelatin binder layer on the plastic support; (B) 35 tinted negative on cellulose nitrate support and the corresponding cross-section in which is possible to see aniline dyes absorbed in the gelatine layer; (C) a 35 mm chromogenic negative on a cellulose acetate support and the corresponding cross-section in which is possible to see the yellow, magenta and cyan layers [9].

Moreover, on the edges of motion picture films are reported some precious informations, regarding the material used for the base, the producer and the manufacturing date and place (Fig. 4). This practice began with the Eastman Kodak Company that, in 1913 printed the word "EASTMAN" on the films. Since 1916, the company introduced a codified system to indicate the date of manufacture of the film, which consists of a combination of four symbols corresponding to a certain year and the place of production. In older films, there may also be small cuts on the

edges, called “notch codes”. In addition, the word "SAFETY" printed on some cellulose acetate and polyester films was used to identify them as safe materials and to distinguish them from celluloid (instable and flammable), sometimes labeled as "NITRATE" [7], [10], [11].

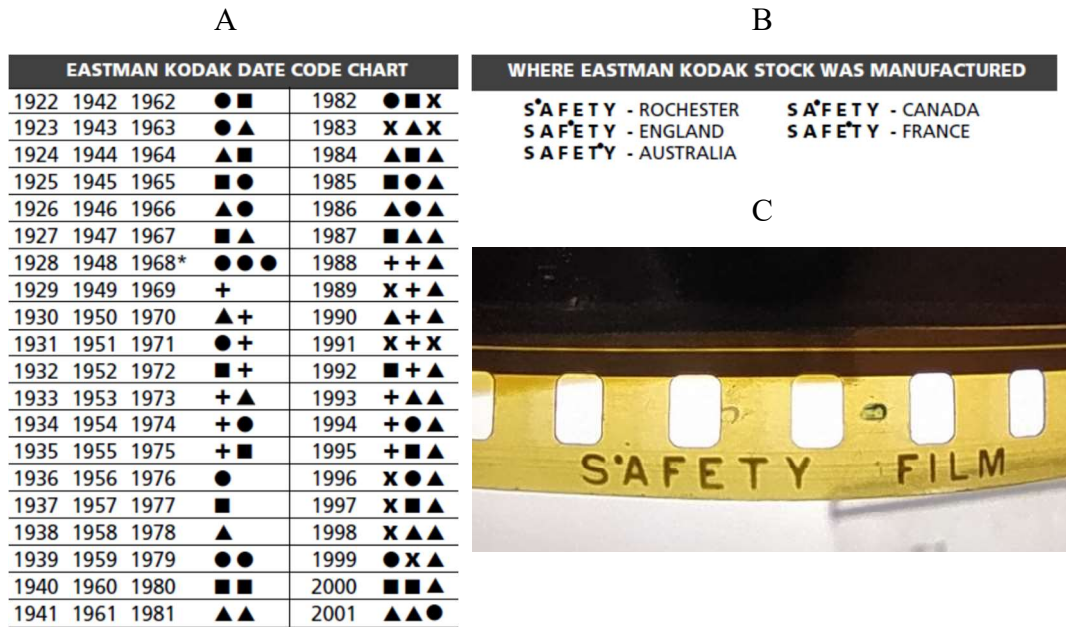


Fig.4. (A) Symbols used by Eastman Kodak to indicate the manufacture date of a negative [12]; (B) the position of the dot within the word SAFETY indicates the place of production of an Eastman Kodak film negative [12]; (C) The inscription "SAFETY FILM" is printed on a cellulose triacetate film.

2.3 Motion picture film: the structure

All film-based negatives and motion picture films are composed of different layers, each with a different function (Fig. 5). The number and thickness of the layers may differ according to the type of film; moreover, the overall thickness of the film may vary usually between 120 to 145 microns [7].

Typically a motion picture film is composed of five main layers [10], [13], [14]:

- Protective varnish: when it is present, it is a very thin layer that is applied after the development as an anti-scratch. It consists of a layer of shellac, dammar varnishes, or gelatin. The protective varnish layer is often omitted.
- Emulsion: the image is impressed on this layer, which consists of a binder made of gelatin in which small salt crystals, photosensitive silver halides, are dispersed. Black-and-white negatives contain only one layer of emulsion while color negatives have three, each of which is sensitive to a certain portion of the electromagnetic spectrum (red, green and blue). About 3-10% of the entire film thickness is occupied by the emulsion[7].
- Adhesive layer: promotes the adhesion between the emulsion (hydrophilic) and the underlying substrate (hydrophobic); usually it is made up of a very thin layer of nitrocellulose.
- Support or base: it is the thickest layer (about 90-97% of the total thickness [7]) of the whole film because it supports all other layers; it must have several properties, such as transparency, flexibility and resistance, both chemical and mechanical. It is made of polymeric materials, mainly cellulose esters such as nitrocellulose and cellulose acetate, and polyesters.
- Anti-curling and anti-alone layer: this is an additional layer of gelatin placed on the back side of the support, added since 1903 to compensate for the tension induced by the emulsion layer (continually subject to shrinkage and swelling depending on environmental thermohygrometric conditions) and to ensure dimensional stability; early nitrocellulose negatives did not possess this layer and one of their typical degradation phenomena is the rolling up on itself. The anti-curling layer also contains anti-halo dyes, that prevent exposure of silver salts to the light reflected by the support.

In parallel to the evolution of technologies associated with the acquisition and projection of images, the development of new materials played an important role in the birth of cinema. In the next paragraph, the attention will be focused on the

materials used to manufacture the two most important layers of a motion picture film (and a photograph): the emulsion and the support.

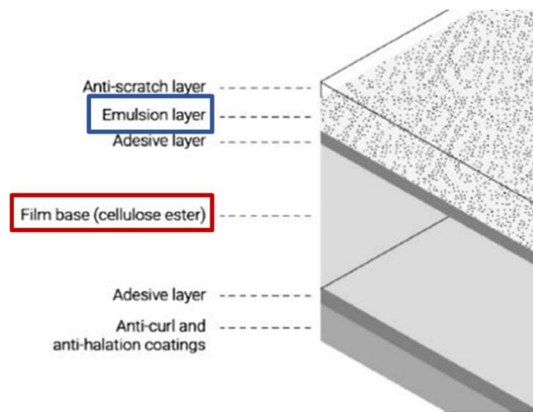


Fig. 5. Layers of a motion picture film [15].

2.4 The emulsion layer and the photographic process

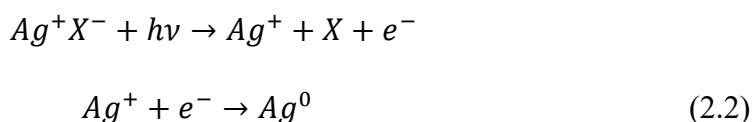
The emulsion is the layer of a film in which the image is captured.

The emulsion of a black-and-white film consists of two components: the silver salts and the binder in which they are embedded and dispersed. It would be more accurate to talk about “dispersion” rather than “emulsion”, in which the dispersed phase consists of micrometer- or submicrometer-sized crystals, “grains”, and a continuous phase[11].

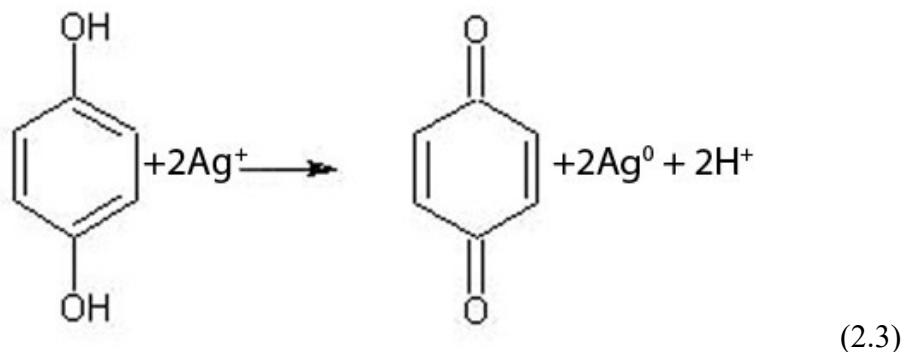
The first type of emulsions used for photographic negatives was made of albumen (1848), soon replaced by the so-called “collodion” or nitrocellulose (1851), obtained by modifying cellulose with nitric acid (nitration) and dissolved in alcohol and ether. The major drawback of these systems was the necessity to impress and develop the negative when the collodion was still wet, so immediately after the preparation [10]. In 1871, Richard Leach Maddox solved this problem by proposing gelatin as a binder. Gelatin is a protein-based product, manufactured by the partial hydrolysis of collagen extracted from connective tissues and skin of animals [10], [13]. Thanks to its sol-gel properties and hygroscopicity, it can form a medium sufficiently viscous

to hold salt crystals in a stable suspension, allowing the fabrication of ready-to-use films with a long shelf life and the development of the image much later. This type of emulsion is used for motion picture films.

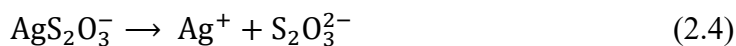
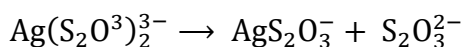
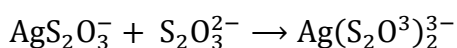
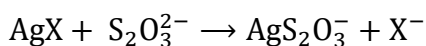
The other components of the emulsion are the silver salts. AgX silver halides (where X stands for the corresponding halogen) commonly used in film emulsions are AgBr (silver bromide), AgCl (silver chloride) and AgI (silver iodide) and are all photosensitive compounds: when the electromagnetic radiation ($h\nu$) hits a silver halide crystal, the X^- anion ($X = \text{Br}, \text{Cl}, \text{I}$) is oxidized to X^0 ; the electron is captured by the Ag^+ cation, which is reduced to metallic silver Ag^0 [13], [16].



Depending on how long the emulsion is exposed to light (exposure time), the amount of silver ions that are transformed into metallic silver varies: for very short exposure times, only very few silver atoms are formed, which are not visible to the naked eye; the so-formed image is therefore called a latent image. It becomes visible only if these small silver atoms grow to micrometer size, appearing black in color. Sensitizers, complexes of gold and sulfur such as gold thiocyanate, are added to the emulsion in order to increase the light sensitivity of AgX crystals [17]. The growth of the nuclei constituting the latent image is induced during the first step of the photographic process, the development [16]. In this step, the film is immersed in a basic aqueous solution containing some reducing agents (usually aromatic organic compounds, such as hydroquinone). These reduce the silver ions not reduced by light radiation [11].



The longer the emulsion is kept soaking within this solution, the more the image blackens; having reached the desired blackening point, the film is immersed in another solution, the stop bath, an acidic aqueous solution (usually acetic acid) that stops the reduction process. After this process, the image is now perfectly visible but is in negative: points hit by light, that are white in reality, are black on the film, while the black parts are white. To prevent further reaction of not-reacted halide crystals when exposed to light again, they are solubilized in a solution of sodium thiosulfate ($\text{Na}_2\text{S}_2\text{O}_3 \cdot 5\text{H}_2\text{O}$), traditionally called *hypo* (fixing step) [16].



In addition to sodium thiosulfate, other agents are added to the fixing bath: acetic acid, which removes any residual developing agent, a preservative (sodium sulfite, Na_2SO_3), which restores sodium thiosulfate that has been reduced to sulfur by the presence of acetic acid, a hardener (usually potassium alum, $\text{KAl}(\text{SO}_4)_2 \cdot 12\text{H}_2\text{O}$),

which prevents excessive swelling of the gelatin, softened during the development [16].

Finally, the last steps of the photographic process consist of washing the film with water to remove any residual chemical compounds and drying [16].

As mentioned above, color negatives have a three-layer emulsion and, for this reason, they require a different process of image formation and development. The three layers contain, in addition to silver halides, different chromogenic dyes such as cyan, magenta and yellow, each of which is sensitive to a certain range of visible wavelengths. At the end of the photographic process, each layer presents the same image in a different color. The optical merging of the three images forms a single colored negative picture. To obtain the final image, silver grains are totally removed during the bleaching process, leaving in place only the dyes [10].

Dyes dispersed in the emulsion are organic molecules generated by the interaction between a developing agent and a copulant [18]. The process involves the reduction of the activated halide by the developing agent, usually a p-phenyldiamine, which subsequently interacts with a copulant agent and leads to the formation of the dye. It is important to remember that yellow, magenta and cyan dyes absorb blue, green and red light, respectively, and consequently, reflect or transmit the other two primary colors.

Copulants for yellow dye formation contain a methylene group that is usually part of an acyclic portion. The most important class consists of molecules of the types α -pivaloylacetanilide and α -benzoylacetanilide.

Substituent R^1 , in Figure 6, represents a group capable of causing a change in the shade of the dye. The ballast is generally made up of a long aliphatic chain or a combination of an aliphatic and aromatic group. Its function is to anchor the copulant in the appropriate layer and prevent the dye from leaking into adjacent layers.

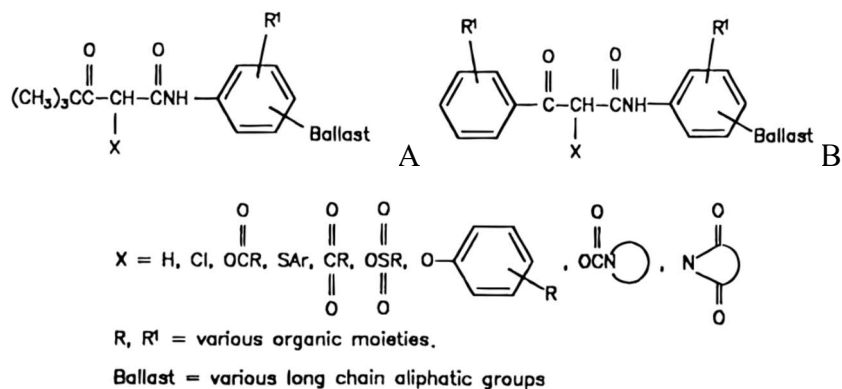


Fig. 6 α -pivaloylacetyl (A) and α -benzoylacetyl (B) [18].

Magenta dye-forming copulants have a methylene group within a heterocyclic ring. The main compounds are pyrazolinone derivatives, especially arylamino- and acylamino-substituted (Figure 7).

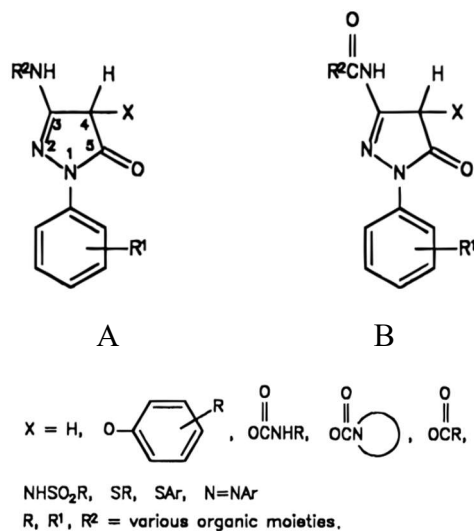


Fig. 7 Pyrazolinone derivatives arylamino- (A) and acylamino- (B) substituted [18].

Cyan dye-forming copulants are characterized by the presence of a methine group. They are phenol and naphthol substituted type (Figure 8).

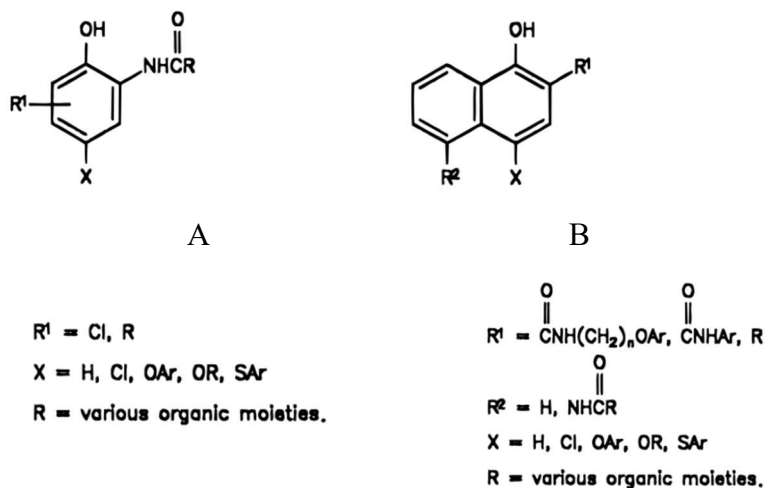


Fig. 8 Phenol- (A) and naphthol- (B) substituted [18].

2.5 The supports

Unlike photography, for which a wide variety of media were used as a support for the emulsion layer, such as metal, paper and glass, in motion picture films, considering the special mechanical properties required for a film, only polymeric materials were used, in particular cellulose esters or polyesters. The perfect motion picture film, indeed, has to be transparent, optically homogeneous, colorless, flexible, strong, with high tensile strength, chemically stable and resistant to chemicals used during the photographic processes and compatible with the emulsion layer.

Materials typically used for this purpose are [10], [19]:

- Cellulose nitrate, CN, or celluloid (from about 1889 to 1950);
- Cellulose acetates, CA (cellulose diacetate, CDA, and triacetate, CTA) (from about 1925 to the present);
- Polyesters, PE (from 1955 to the present).

Each of these three categories of materials gradually replaced the other because of their stability issues. In further paragraphs, a deep look at the history and characteristics of these materials will be reported.

Cellulose esters are semisynthetic polymers obtained by esterification of cellulose: the hydroxyl groups (-OH) in cellulose are replaced by nucleophilic groups in the presence of mineral acids or organic acids (or their anhydrides) and a catalyst [20]. The esterification process may occur by fully or partially replacing OH groups with nitro or acetyl group substituents. Replacing OH groups with ester groups, strong intermolecular forces in cellulose due to hydrogen bonds (40 kJ energy per mole of repeating unit) decrease and resulting polymers are more soluble and less crystalline [21].

To quantify the number of substitutions, it is possible to talk about acetyl or nitro content or degree of substitution (DS).

The acetyl or nitro content is the measure of the amount of the mass percentage of acetyl or nitro groups esterified onto the cellulose backbone; it can range from 0% (cellulose) to above 45% (fully substituted cellulose).

The degree of substitution (DS) of a polymer is the average number of substituent groups attached per monomeric unit; it may range from 0 (cellulose itself) to 3 (fully substituted cellulose).

The amount of substitution of acetate ester has a very strong effect on the polymer's solubility and physical properties.

Polyesters are synthetic polymers obtained from polycondensation between a diol, ethylene glycol, and a diacid, specifically terephthalic acid in the case of polyethylene terephthalate (PET) and naphthalene-2,6-carboxylate in the case of polyethylene naphthalate (PEN), which are the products typically used for motion picture films. Polyesters replaced cellulose acetate because of their better chemical and mechanical-physical stability.

2.5.1 Cellulose

Cellulose esters are both semisynthetic polymers obtained from cellulose (Fig. 9). Cellulose is a natural organic compound synthesized by plants; the purest ($\geq 98\%$) is extracted from cotton linters (the hair adhering to the seeds of the plant). In general, textile fibers, including flax and hemp, contain much more cellulose than wood, in which is found in combination with hemicelluloses, lignin and other extractives [22][21].

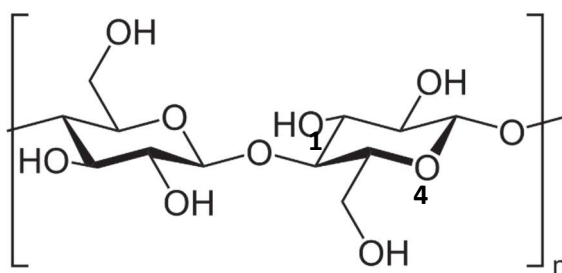


Fig.9 Molecular structure of the repeating unit of cellulose.

Cellulose is a linear polysaccharide, obtained by condensation between monomeric units of D-glucose ($C_6H_{12}O_6$) and the formation of β 1,4-glycosidic bonds between the -OH group of C1 of one molecule and the -OH group of C4 of the other. The other three groups not involved in the glycosidic bond can form both intramolecular and intermolecular hydrogen bonds: the first cause the folding of the chains and are responsible for its rigidity and crystallization; the latter are formed between different chains that arrange themselves into superior microfibrillar structures [22]. The -OH groups also make cellulose highly hygroscopic: although it can absorb large amounts of water, it is completely insoluble in water and most organic solvents. Finally, the -OH groups are also responsible for the reactivity of cellulose since under appropriate conditions they can give condensation, for example, with both organic and inorganic acids and form esters just like cellulose acetate and cellulose nitrate [20].

2.5.2 The first option: celluloid

2.5.2.1 History

The mass diffusion of photography and the birth of cinematography were only possible with the introduction of a lightweight and flexible material to replace the previous rigid supports (i.e. glass, metal panels etc.). Cellulose nitrate or nitrocellulose, the polymer obtained by treating cellulose with a mixture of nitric and sulfuric acid, had already been synthesized for the first time in the 1840s by C.F. Schönbein and it had been used in its highly nitrated and flammable form as an explosive named *gun cotton*. In the 1850s, A. Parks and D. Spill suggested the use of a flexible medium consisting of many overlapping layers of *collodion*, a solution of pyroxylin (low nitrated nitrocellulose with a nitrogen content of 11-14%) in alcohol and ethyl ether (40/60). But only thanks to the intuition of camphor as a plasticizer (1873) by the Hyatt brothers, the material commonly known as *celluloid* was born [10], [23]. J. Carbutt became the first to produce plastic film negative using celluloid sheets by applying a gelatin emulsion layer on one of its faces (1887) and, later, Goodwin submitted a patent application to create rolls (1889). In the same year, the Eastman Kodak Company proposed its celluloid film supports. In 1890 Eastman and Dickson (Edison's pupil) collaborated on the development of the motion picture film used in Edison's kinematograph. Almost all 35 mm films produced from 1896 until 1950 were supported by a cellulose nitrate film (the major manufacturing companies were the Eastman Kodak Company, Ansco, Dupont and Agfa). Eastman Kodak produced its last celluloid film in 1951 because cellulose nitrate was replaced by the safer and more stable cellulose triacetate in most parts of the world, except for China and the USSR where it was used until the 1960s [10].

2.5.2.2 Synthesis and properties

Cellulose nitrate (Fig. 10A) is a cellulose ester obtained by the condensation between the -OH groups of cellulose and nitric acid (HNO_3) that produces water as a by-

product (nitration); an increase in the amount of water reduces the percentage of nitrogen in the final product. This problem can be solved by adding sulfuric acid (H_2SO_4), which acts as a dehydrating agent [24], [25] (Fig. 10C). The hydrolysis of the esterified nitro groups is a competitive reaction to condensation and can easily lead to denitration of the product; in fact, this is one of the main causes related to the degradation of celluloid.

High-nitrated cellulose nitrate (higher than 12.5%), called *gun cotton*, *gunpowder* and *smokeless powdergun*, is highly flammable and is mainly used as an explosive [25]–[27]; cellulose nitrate containing between 10.5 to 12.5% of nitrogen is called *pyroxylin* [28]. Cellulose nitrate in this form was used to manufacture *celluloid*, the material for the production of motion picture films. It is a mixture of a solution of pyroxylin in alcohol, ether, acetone, amyl acetate ($\text{CH}_3\text{COO}(\text{CH}_2)_4\text{CH}_3$) and camphor, a monoterpene monocyclic ketone (Fig. 10B) extracted by distillation from the roots of *Cinnamomum camphora*[27][25]. Camphor, added in amounts of 10–15%, works as a plasticizer, lowering the glass transition temperature (T_g) of the cellulose nitrate [27].

Celluloid has excellent optical and mechanical properties: it is transparent, flexible, possesses high tensile strength and does not absorb moisture. Because of all these characteristics, it was the optimal material for the manufacture of motion picture films for a long time, providing images of extraordinary definition. However, cellulose nitrate is an unstable and unsafe polymer due to its high flammability. This was the main reason why, for safety reasons, it was replaced with cellulose acetate at the beginning of the last century [10].

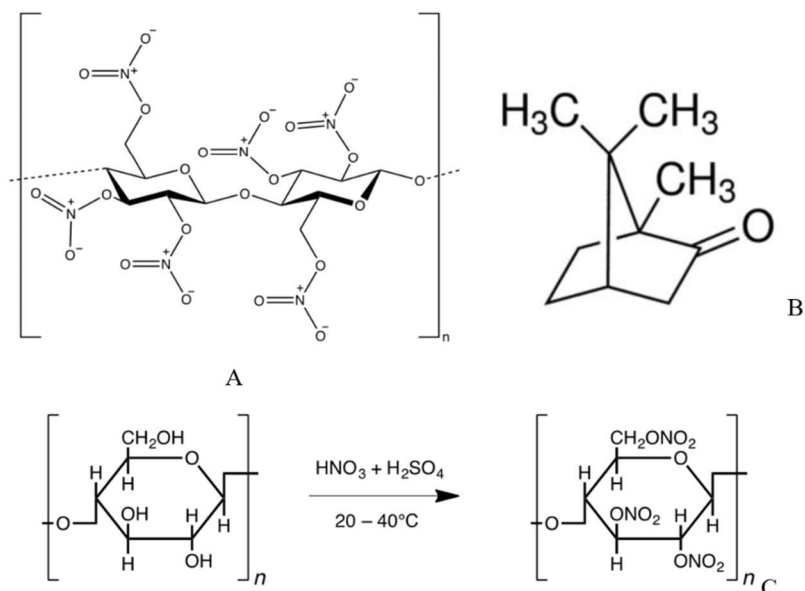


Fig.10 (A) Chemical structure of the repeating unit of cellulose nitrate; (B) chemical structure of camphor; (C) esterification of cellulose to cellulose nitrate [25].

2.5.2.3 Degradation Processes

Cellulose nitrate is a very unstable material: nitration is a reversible process because the hydrolysis of the nitrogroups is a competitive reaction to their condensation on the backbone. The hydrolytical decomposition of cellulose nitrate is a spontaneous process catalyzed by external factors such as heat and moisture; the result of hydrolysis is the release of NO₂⁻ nitro groups, resulting in the formation of very dangerous, strongly acidic and oxidizing agents [23], [29], [30].

The instability of cellulose nitrate should be attributed mainly to its thermal sensitivity: the low energy of the N-O bond (163 kJ mol⁻¹) makes it easily breakable causing the formation of nitrogen oxides (Fig. 11). If these by-products are not removed, they can induce secondary reactions in both the celluloid support and the emulsion layer, including oxidation, nitration, nitrosation, hydrolysis of other ester groups, and even hydrolytic cleavage of the cellulose glycosidic bond. In addition to heat, moisture also plays a key role, further accelerating most of the above processes and in particular, the hydrolysis reaction [31].

When N-O bonds are broken, they produce nitrogen dioxide (NO₂), that, in the presence of environmental moisture, reacts to form nitric or nitrous acid, promoting hydrolysis of other N-O bonds. The decomposition reaction is thus autocatalytic: if the NO₂ is not removed from the environment, it acts as a catalyst and accelerates the process. Moreover, the reaction is exothermic and the heat produced contributes to a further cleavage of other N-O bonds. The process is, unfortunately, irreversible: hydrolysis can go ahead until the material is reduced to dust [23], [29], [30].

Furthermore, NO₂ is also deleterious for the other components of the film: released acids attack the emulsion, which became soft and steaky, and bleach the silver image or the color. The aggressiveness of the degradation products is so high that even the metal containers in which the films are stored corrode and rust.

One of the main drawbacks typical of cellulose nitrate-based motion picture films is the highly flammability of this support. Cellulose nitrate in good conservation condition does not burn below 130°C, but highly degraded cellulose nitrate can spontaneously combust at temperatures close to 40°C, a threshold not so difficult to reach in cinemas or archives: for example, a film running inside a projector may get hot enough to trigger the combustion reaction; or a large number of degraded nitrate films stored together, producing heat during their degradation process, may raise the temperature of the room to the burning point [10].

The burning of nitrate produces toxic gases such as carbon monoxide and nitrogen peroxide, but also oxygen. Oxygen production means that, once a film has begun to burn, it is impossible to extinguish the flames since the combustion reaction is completed. Then, a nitrate film can burn even under water or covered by sand. The flammability of nitrates has destroyed multiple movie theaters and archives, as well as a very large part of motion picture films and other objects made in cellulose nitrate [7].

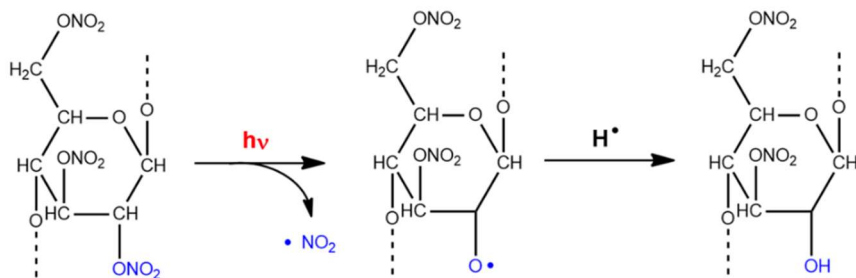


Fig. 11 Degradation reaction of cellulose nitrate [32].

2.5.2.4 Observable signs of degradation

Unfortunately, the degradation process described above is irreversible and unstoppable, but it can be slowed down by controlling the environmental parameters: storing the films at very low-temperature (below 2 °C) and relative humidity (RH, 20-30%) [23], [33].

Cellulose nitrate decomposition can go on for a long time without any outwardly visible signs of degradation. Only at the final stages, a few months before the complete self-destruction of the film, visible changes appear in this order:

1. The substrate turns yellow and the image shows the first signs of silver mirror formation (Fig. 12A); the silver mirror is a typical degradation phenomenon of cellulose nitrate films and consists of the formation of reflective and iridescent surfaces. Gases released from the substrate, moisture and pollutants oxidize the silver particles and form ions; the silver ions migrate within the gelatin and diffuse to the surface, where they react with sulfur compounds in the atmosphere to form silver sulfide Ag_2S crystals, which reflect light and locally create the effect of a mirror [34].
2. The emulsion becomes sticky and the film releases a strong smell of nitric acid.

3. The emulsion partially softens and a yellowish foam appears on the surface (*honey formation*, visible in Fig.12B), the odor of nitric acid gets more intense and the released vapors may attack adjacent films;
4. The film compacts into a solid mass, adhering to adjacent negatives and cases; from this point on, it is impossible to unroll it without damaging it;
5. The film is reduced to a brown powder (Fig. 12C).

The film and in particular the emulsion with the image are considered savable up to the second stage of degradation; from the third stage onward the image is already lost and destruction of the film is strongly recommended due to its high flammability [35].

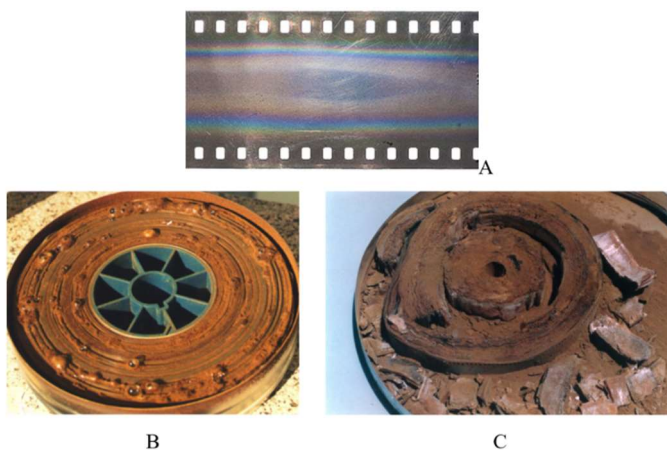


Fig. 12 (A) Cellulose nitrate-based motion picture film with silver mirror formation[9]; (B) Cellulose nitrate-based motion picture film at the third stadium of degradation with typical bubble formation on the surface due to the melting of the emulsion, the so-called “honey-formation”; (C) Cellulose nitrate-based motion picture film at the fifth stadium of degradation.

2.5.3 The safer option: cellulose acetate

2.5.3.1 History

Because of the instability and flammability of cellulose nitrate, the film industry started to look for a safer alternative with similar physicochemical properties, such

as good mechanical strength, limited moisture absorption capacity and the capability to provide high image definition [10].

Cellulose acetate was synthesized for the first time by Schützenber in 1865 by heating a mixture of cellulose and acetic anhydride in a sealed test tube. In 1879, Franchimont discovered that by using sulfuric acid as a catalyst, cellulose acetate could also be produced at room temperature. In 1894 Cross & Bevan submitted a patent for the manufacture of cellulose acetate, considered more stable and less hazardous than cellulose nitrate. Initially, cellulose acetate was produced in its highly substituted form (cellulose triacetate), which is soluble only in chlorinated solvents (dichloromethane or chloroform): the difficulties in finding low-cost media to cast it caused a delay in the commercial production of cellulose triacetate [25]. In 1904, an alternative was found by performing partial hydrolysis of cellulose triacetate adding water during synthesis and obtaining a polymer with a lower substitution degree (cellulose diacetate) [25], [36], [37]. The synthesis can be carried out at lower temperatures obtaining a product soluble in cheaper solvents, such as acetone, allowing a decrease in manufacturing costs [38]. These properties led the plastic industry as well as the photography industry to recognize the commercial opportunity to produce objects and film-based photographic negatives with cellulose acetate instead of the more hazardous cellulose nitrate [25]. The first cellulose diacetate was produced by Bayer & Co. under the name *Cellit*. *Cellit* was used as a film support for the first time in 1912 and, thanks to its safer nature, allowed the introduction of motion picture film for amateur use in 1923 (the Kodak 16mm). Other companies that produced cellulose diacetate films between 1935 and 1955 were Agfa/Ansco® and Dupont® [10]. The optical and mechanical properties of cellulose diacetate were good, comparable to those of nitrate, but diacetate, because of its unsubstituted -OH groups, is very hydrophilic and therefore can absorb much more moisture than nitrate. Adsorbed water promoted chemical degradation phenomena that macroscopically resulted in the characteristic vinegar odor and the physical instability of the film (e.m. shrinkage and embrittlement). To solve this

problem, Eastman Kodak began to produce mixed cellulose esters such as acetate butyrate and acetate propionate. These media were used for X-rays, photographic film and home movies, but their quality (i.e. resolution of the images) was not good enough for their use in motion picture films [10].

Thanks to the cheaper availability of the dichloromethane (CH_2Cl_2) needed to solubilize cellulose triacetate and to the optimization of the manufacturing process (Dreyfus, 1939), during the 1950s this polymer was proposed as a substitute for celluloid for making motion picture films. Cellulose triacetate is the most stable of the acetates, it exhibits similar physical properties and good dimensional stability and it possesses a very high flash point compared to nitrate: $430\text{ }^\circ\text{C}$ versus $4.4\text{ }^\circ\text{C}$ [7], [14]. Thanks to its less flammability, motion picture films made of cellulose acetate are called *Safety Films*. Nevertheless, if compared to nitrate, it has a moisture absorption index that is two to three times higher.

Unfortunately, also cellulose triacetate showed very important degradation issues and, during the 1960s and 1970s, more stable polyesters gradually replaced acetate supports [39].

2.5.3.2 Synthesis and properties

Cellulose acetate is an ester that is obtained by a reaction between the hydroxyl groups of cellulose and acetic anhydride $(\text{CH}_3\text{CO})_2\text{O}$, in the presence of acetic acid (CH_3COOH). The acetylation reaction consists of a replacement of hydroxyl groups of cellulose by acetyl groups (CH_3CO). Depending on how many of the three hydroxyl groups in a monomeric unit are subjected to acetylation, three different types of acetate are distinguished: monoacetate (CMA), diacetate (CDA) and triacetate (CTA) [25].

Cellulose acetate is produced industrially on a large scale, by combining cellulose with anhydrous acetic acid as solvent, acetic anhydride, from which the acetyl groups are derived, and concentrated sulfuric acid, as catalyzer [22][36]. Direct acetylation

produces cellulose triacetate (Fig.13A), which has a degree of substitution (DS) between 2.8 and 3.

By hydrolyzing cellulose triacetate with water, is possible to obtain an acetate with a lower DS such as diacetate [36]. The relationship between the degree of substitution (DS) and the acetyl content (%) is shown in the following Equation [40]:

$$DS = \frac{(3.86 \times \%acetyl)}{(102.4 - \%acetyl)} \quad (2.1)$$

The degree of substitution of cellulose acetate influences many of its properties, such as solubility profile (Tab.1) [22], [36].

Both cellulose diacetate and triacetate can be doped with proper plasticizers to reduce their flash and melting points and improve their mechanical properties in terms of elasticity and flexibility. Another important function of plasticizers is the reduction of the dimensional instability of the film caused by solvent evaporation and volume changes related to temperature and humidity fluctuations [33]. The most widely used plasticizers (which concentration ranges up to 20-30 wt%) since 1929 have been triphenyl phosphate, TPP (Fig.12B), phthalates (dimethyl and diethyl phthalate, Fig. 9C), and other phosphates (tricresyl phosphate) [36].

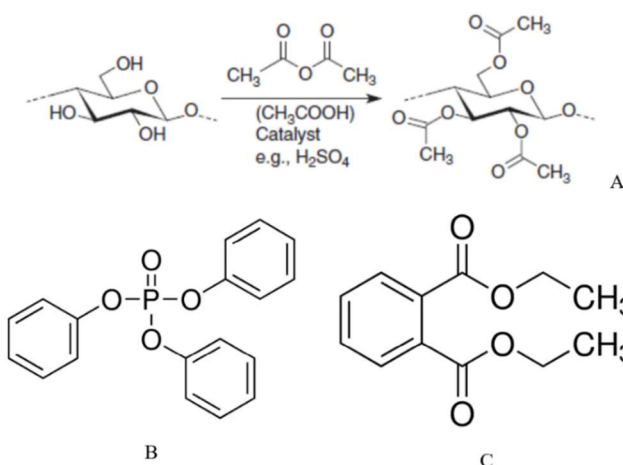


Fig. 12 (A) Acetylation reaction of cellulose to cellulose triacetate catalyzed by sulfuric acid [36]; Plasticizers commonly used in cellulose triacetate-based films: (B) triphenyl phosphate; (C) diethyl phthalate.

Tab.1 Variation in solubility with the degree of substitution [41].

Degree Of Substitution	Acetyl content (%)	Type of cellulose acetate	Common Solvent
0,6-0,9	13,0-18,6	«zeroacetate»	water
1,2-1,8	22,2-32,2	monoacetate	2-methoxy-ethanol
2,2-2,7	36,5-42,2	diacetate	acetone
2,8-3	43,0-44,8	triacetate	chloroform

2.5.3.3 Degradation processes: the “vinegar syndrome”

Even if the degradation mechanisms of cellulose acetate do not have hazardous effects such as the ones previously described for cellulose nitrate, also these materials show irreversible instability issues. Most chemical mechanisms of deterioration that affected cellulose acetate could be ascribed to a phenomenon commonly known as “vinegar syndrome”. The major chemical degradation reaction of cellulose triacetate concerns the cleavage of the ester bonds between the acetate group (CH_3COO) and the cellulose backbone through ester hydrolysis (deacetylation), with the formation of hydroxyl groups and the release of acetic acid (Fig.13A) [25], [36]. The “vinegar syndrome” gets this name because of the characteristic smell emitted by degraded cellulose triacetate films. The very first investigations about cellulose ester films and their degradation mechanisms were launched initially by manufacturers, such as Eastman Kodak Company and Agfa-Gevaert Inc. [42], [43], and later by some research units of different centers such as the Centre for Polymer Stability at Manchester Polytechnic in the United Kingdom, the Centre de Recherche sur la Conservation des Collections in France and the Image Permanence Institute (IPI) in the United States of America [44]–[46]. Starting from the 1980s and 1990s, analyzing the behavior of both naturally and artificially aged motion picture films [31], [45], [47]–[52], a model for the evolution of the vinegar syndrome was proposed by the Image Permanence Institute: it was found that deacetylation is strictly influenced by temperature, humidity and pH (acid or alkaline)[33]. Researchers analyzed various factors, such as moisture retention, UV absorption, and

degree of insolubilization and assumed free acidity (i.e. the total amount of the free acetic acid absorbed in the film, determined by the volume of 0.1 N NaOH required to neutralize 1g of film [45]) as the most sensitive indicator for degradation in cellulose triacetate films. In Fig.13B, free acidity is reported as a function of time: accelerated aging experiments revealed that in the early stage (the “induction period”) the reaction rate is driven mainly by heat and humidity and its duration depends strongly on the environmental conditions at which films are stored. When the acetic acid concentration increases up to the so-called “autocatalytic point” (that corresponds to a value of free acidity equal to 0.5), the acetic acid formed acts as a catalyst for the deacetylation reaction and induces an autocatalytic process [33]. Later studies pointed out that the scientific data provided to explain why a free acidity value of 0.5 has been chosen as the autocatalytic point were not strong enough. Knight (2014), for example, affirms that could be more correct to describe the deacetylation process as autocatalytic process occurring at all concentrations of acid [53]. Mohtar et al. (2021) recently proposed a deep investigation of the reaction mechanism of hydrolysis using electronic density functional theory calculations and transition-state theory: the presence of acetic acid decreases significantly the activation energy of the first step of the reaction (about 20 kcal/mol) and this reduction justifies the higher rate of the acid-catalyzed reaction path [54], [55].

Using nuclear magnetic resonance Derham et al. have shown that the loss of acetate groups occurs with a certain order in carbons on the glucose ring: C2 -> C6 -> C1. Despite C2 and C3 are both secondary alcohols while C6 is primary, this behavior has been attributed to the mechanism of the acetylation reaction of cellulose (the hydroxyl groups bond to C2 and C6 are the first that are acetylated) [56]. The presence of more hydroxyl groups makes the polymer more hygroscopic and susceptible to the absorption of additional moisture, which can further promote hydrolysis [57].

Another hydrolysis process takes place during the degradation pathway and involves depolymerization due to cleavage of the glycosidic bonds of the cellulose triacetate

backbone [36], [57]. Deacetylation occurs first due to the lower value of its activation energy [42] and also because deacetylation by-products can favor glycosidic cleavage. Moreover, the chain scission can be triggered by ultraviolet or visible light by the generation of radical species [37]. Depolymerization results in a decrease in the molecular weight and an increase in solubility. In the most severe stage of degradation, also the lactose ring can undergo an acid-catalyzed opening [37]. Furthermore, oxygen can react with the acetate pendant groups and the glycosidic ring structure leading to the production of small molecules, such as formic acid, oxalic acid, carbon dioxide and various aldehydes [57] and the formation of chromophores carbonyl groups with consequent yellowing of the film [42]. In addition, degraded polymeric networks are not able to retain plasticizers, which are insoluble in the deacetylated polymer and they migrate to the surface [37]. Loss of plasticizers leads to embrittlement and consequent cracking of the material [57]. Other factors that may contribute to the chemical instability of these supports are some residual products, used during both the manufacturing and the photographic process, in particular sulfuric acid [40], [46]. They can alter the pH and act as catalyzers for the hydrolysis, or promote an oxidative degradation route, considering the redox nature of many constituents. Also, some metal ions such as iron and chromium, present in the magnetic audio tracks and/or released from enclosures in which CA-based films are typically stored, can act as promoters of redox processes [50]. This effect could be inhibited by the presence of plasticizers, which can complex metal ions carrying out the function of antioxidants [58], [59]. On the other hand, acid hydrolysis of some plasticizers, such as triphenyl phosphate, can lead to the formation of acids, which can further catalyze the deacetylation of cellulose acetate [59]. Emulsion, depending on its thickness, can act as a protective barrier against acetic acid and oxygen and slow down the degradation processes [58], [59]. Cellulose diacetate is less stable than cellulose triacetate, because is more hygroscopic, having more hydroxyl groups available.

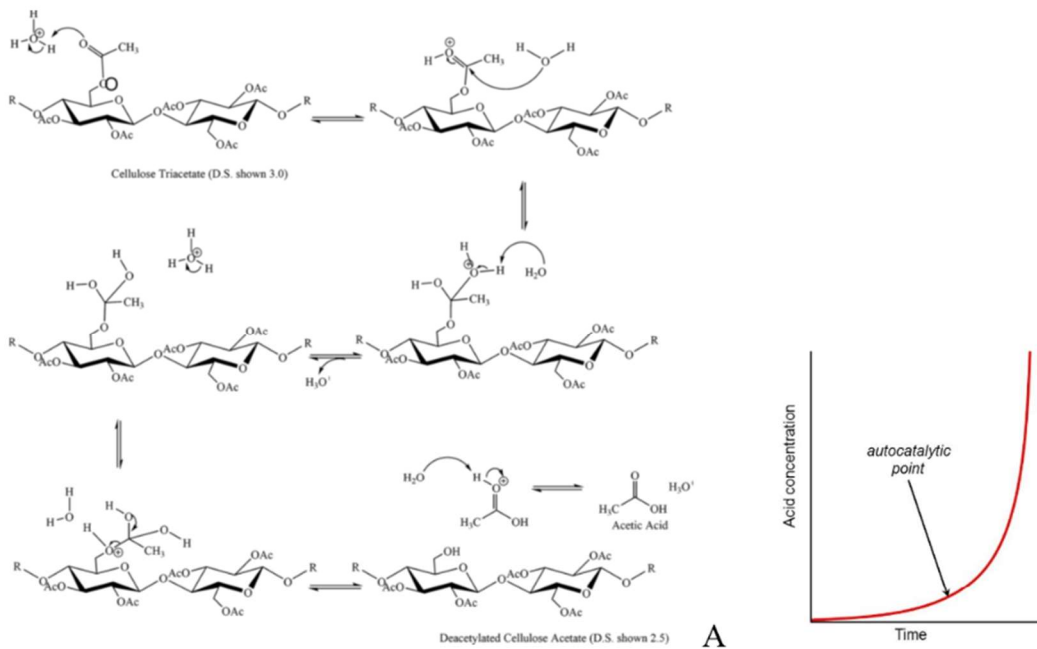


Fig. 13(A) Acid-catalyzed deacetylation of cellulose triacetate[36]; (B) Free acidity curve vs time for cellulose triacetate films[33].

2.5.3.4 Observable signs of degradation

In addition to the characteristic smell of vinegar, other macroscopic symptoms reveal the ongoing vinegar syndrome[33]:

- Embrittlement: the material, initially tough and flexible, breaks easily, even at the slightest bending (Fig.14A). This is a consequence of the hydrolysis of the glycosidic bonds of the cellulose chains, induced by the acetic acid, and of the loss of plasticizer.
- The depolymerization process causes the shrinkage of the support (Fig.14B): a reduction of the size even just 1%, causes very serious damage. While the support shrinks, the emulsion frequently does not: the result is the detachment of the emulsion in some places and the creation of a pattern that experts call *channeling* (Fig.14C).
- Formation of crystals or bubbles on the surface: the appearance of crystalline deposits or liquid-filled bubbles is due to the exudation of plasticizers from the

degraded polymeric network (Fig.14D). Exudation of plasticizers is typical of films in an advanced state of degradation.

- Blue or pink color: this is due to the alteration of the antihalation dyes contained in the anticurling layer.

- Yellowing of the film because of the formation of chromophore carbonyl, ketone and aldehyde groups mainly due to thermal oxidation.

In general, as for nitrate ones, the degradation process of cellulose acetate films can be summarized in five stages:

1. The film releases an acetic acid odor, begins to shrink and become brittle;
2. The film begins to curl because the base thins out unevenly;
3. The film deforms and loses flexibility;
4. White crystalline deposits or bubbles appear on the surface of the film;
5. The emulsion exhibits channeling on both sides of the film; the film becomes rigid, crystallized, and breaks easily [33].

The conservation of the image depends on the degradation level of the emulsion, that in cellulose triacetate films is always less severe than in nitrate films. In most cases, the image is still readable up to the third stage, while from the fourth the readability may be compromised [33].

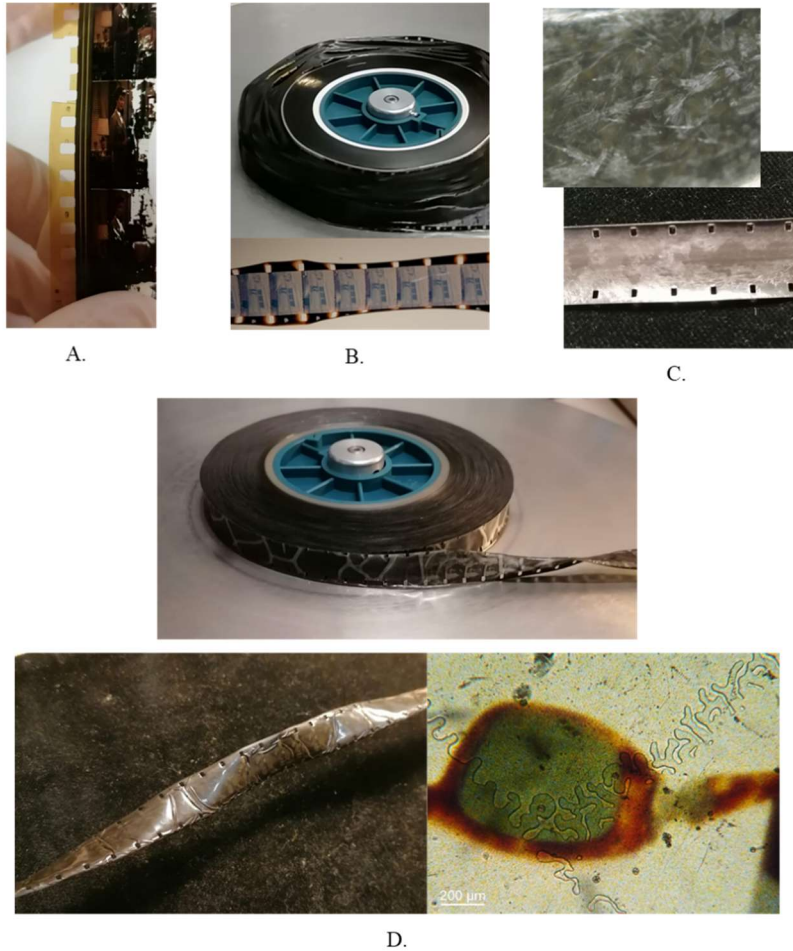


Fig.14 Macroscopic symptoms of the “vinegar syndrome”: (A) embrittlement; (B) deformation and shrinkage; (C) exudation of plasticizers; (D) channeling.

2.5.3.5 Monitoring and taking care of the syndrome: state of the art

In parallel with the study of the processes involved in the vinegar syndrome, researchers focused on the definition of preservation strategies for film collections and active conservation methodologies that were progressively tested and implemented.

Indeed, another hot topic of the previously mentioned studies is the development of a method to evaluate the conservation status of the film, before planning any preservation strategy, and to detect as early as possible the insurgence of decay processes of cellulose acetate film negatives and motion picture film [48], [60].

In the further paragraph, an overview concerning methods to monitor the evolution of the vinegar syndrome and protocols to inhibit degradation processes will be reported.

2.5.3.5.1 Monitoring the evolution of the syndrome

From several studies conducted between the eighties and nineties [45], [48], [60], [61], it was found that the best way to define the conservation status of a cellulose acetate-based media was to quantify the amount of acetic acid produced, the so-called free acidity.

The first method, called the water-leach free acidity test, proposed by the IPI [62], is sensitive but experimentally complex, invasive and destructive, and consists of an acid-base titration, based on a standardized procedure (ANSI Standard IT9.1 - 1996[63]) and then reported in the ISO 18901:2010 [64]. The acidity is measured in terms of milliliters of 0.1N NaOH solution required to neutralize the acetic acid produced by 1g of cellulose triacetate. A similar procedure is reported also in the ASTM D871-96(2019) [65]. This method was traditionally preferred to pH tests, which tend to underestimate the acidity of the samples: due to the low value of K_a of acetic acid, only a fraction of the total acidity is reflected in the hydrogen ion concentration revealed by means of pH measurement. This reduces the sensitivity of the pH test as a measure of film deterioration; a second important factor is that pH is a logarithmic parameter and that decreases the sensitivity still further [62].

The second way involves the use of paper strips containing an acid-base indicator, the bromocresol green, implemented and commercialized by the IPI as the A-D Strips (Acid-Detecting strips)[33]. A small strip is put inside the sealed case, in contact with the film, over a period that varies based on T and RH conditions (from one day to a few weeks). At the end of the exposure, the color obtained is compared with the five reference levels (Fig.15); Table 2 shows the levels of the A-D strips related to the free acidity content in the acetate film, the conditions of the film, and the recommended actions for the best storage [33], [66] The A-D Strips method,

therefore, unlike titration, is an indirect measurement because it is based on the detection of the acidity in the atmosphere surrounding the film. However, although less precise, it is easier, cheaper, not invasive and faster than titration and, for this reason, it is the most widely used method by conservators and archivists. Only after learning the condition of the film by its acidity, it is possible to plan the most suitable storage plan.

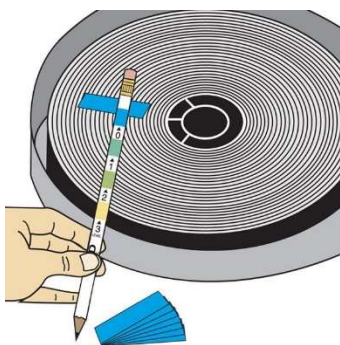


Fig.15 Use of A-D strips: comparing the color of the strips in contact with the film with reference levels[33].

Tab. 2 Different levels of A-D strips compared to the amount of free acidity in cellulose acetate films, conservation status and recommended actions for the storage[67].

Level	Free acidity (ml 0,1 NaOH/g)	Film condition	Recommended Actions
0	0 - 0,1	Good – No deterioration	Cool/cold storage
1	0,2	Fair to good – Deterioration starting	Cold storage Monitor closely
1,5	0,5	Rapid degradation starting – point of autocatalytic decay	Cold storage or freeze
2	1	Poor – Actively degrading	Freeze Copying advisable
3	≥2	Critical – Shrinkage and warping imminent; possible handling hazard	Freeze immediately Copy

Another approach has been proposed by Ballany and Littlejohn (2001, 2012), who developed a route to detect different ions from cellulose acetate artifacts by ion chromatography: they investigated the presence of acetate, formate, chloride, nitrate, sulfate and oxalate. They assess that an increase in acetate levels indicates that deacetylation is occurring, oxalate is related to chain scission and formate is produced by oxidative degradation. Chloride and sulfate are residual chemicals from the manufacturing process and the presence of nitrate indicates the use of an acetate-nitrate cellulose mixture [37], [57]. They proposed two different routes for sampling: a destructive procedure, which involved the removal of 50 mg of material for the extraction of ions in distilled water and a non-destructive procedure, which involved the use of a cotton wool swab moistened with distilled water and wiped twenty times over a 2 cm² area of the artifact. This method seems to give a good evaluation of the state of the syndrome in both naturally and artificially aged samples of motion picture films. Despite the non-destructive method, the analysis is limited to the surface, the overall trends observed for both the destructive and the non-destructive procedures are in agreement. Only relative evaluations could be done with this method.

A similar approach was developed by Curran et al., using a Solid Phase Micro Extraction – Gas Chromatography/ Mass Spectrometry (SPME-GC/MS) method for the analysis of VOC emissions in the headspace above historic plastic and rubber materials [68]–[71]. They mainly used this method to define the object composition by the detection of their degradation products and also the risk of cross-infections for nearby objects in a non-destructive way. Regarding CA, they observed different amounts of emitted acetic acid in objects of different ages and different conservation statuses (defined by macroscopic symptoms) but no quantitative evaluations by the use of a calibrated setup, are provided.

Another approach to defining the conservation status of cellulose acetate media is based on the definition of the acetyl content, that is the amount of the mass percentage of acetyl groups esterified present onto the cellulose backbone.

Allen et al. initially proposed a UV-vis spectrophotometric procedure based on the measurement of the n-n* acetate carbonyl absorption at 210 nm as a direct measure of the degree of deacetylation [46]. Measurements were carried out on solutions of acetate films dissolved in a methylene chloride/methanol mixture (9:1 v/v) at 5% w/v. Moreover, Casarano et al. (2011) set up a method based on the same technique through the evaluation of the dependence of the maximum absorption wavelength λ_{\max} due to the intra-molecular charge-transfer bands of polarity probes adsorbed on DS of the ester films (solvatochromism) [72]. The measurements are usually carried out by solubilizing the samples in DMSO.

The weak point of these methods that require the use of liquid analytes, is the dependence of the solubility of cellulose acetate from the degree of substitution: in particular, cellulose acetate with a very low degree of substitution is not soluble in the abovementioned solvents anymore.

Another approach, as mentioned above, is based on Nuclear Magnetic Resonance (NMR) that allows the determination of the ^1H and ^{13}C NMR chemical shifts of the eight anhydroglucose units (AGU) that contain CA. A comparative analysis of the chemical shift data can reveal the substituent effect of acetyl groups at the 2,3,6 position on the ^1H and ^{13}C nuclei in the same AGU and also provide structural information [32], [56], [73]. In a recent study, Da Ros et al. (2020) provide a method to quantify simultaneously the average DS and the plasticizer (diethyl phthalate) content with high-resolution ^1H -NMR [71]. Nevertheless, also in this case, the critical aspect of the technique is associated with the solubilization of cellulose acetate with a low degree of substitution [74].

Another method reported in the literature concerns the derivation of cellulose acetate through aminolysis using pyrrolidine to convert acetyl groups in acetylpiperidine that is quantified via GC/MS [40].

All the abovementioned methods are invasive and/or destructive techniques.

Infrared Spectroscopy, in particular ATR or μ -FTIR, has been used to define the degree of substitution of cellulose acetate by means of a non-invasive or micro-

destructive protocol [32], [74]. The ratio between a probe peak, capable of monitoring the degradation of cellulose acetate, and a reference peak, which does not suffer relevant changes during degradation, is calculated [32], [50], [74]. Typically, the peak associated with the C-O-C stretching mode of the cellulose backbone was chosen as the reference peak, while peaks associated with the acetyl groups were used as probes (the C-O and the C=O stretching) [74]. In real motion picture films, recently Nunes et al. (2020) proposed a method based on the monitoring of the OH stretching signal because the presence of plasticizers can affect the absorption of the abovementioned peaks [32]. It is important to point out that the moisture content in cellulose acetate samples is strictly influenced by the degree of substitution [46], [47] and it could alter the results of this test.

Other methods for the characterization of cellulose acetate-based motion picture films are focused on the quantification of the plasticizer content, considering the plasticizer loss a consequence (but also a cause) of the degradation [75]–[77].

2.5.3.5.1 Taking care of the vinegar syndrome

Particular attention was focused on the relationship between the onset and the progress of the *vinegar syndrome* and the storage conditions of the film (temperature, humidity and acidity). Thus naturally and artificially aged films were analyzed to estimate the lifetime of such objects under different storage conditions [31], [45], [47]–[52]. Another crucial aspect was to determine the autocatalytic point from which this process passes from the induction period to the irreversible and unstoppable degradation of the film [66]. Therefore, to ensure good preservation, first studies proposed methods in order to not reach this value.

Based on the aforementioned studies, still today, the most diffuse way to prevent the trigger of the vinegar syndrome and try to inhibit it is to act on parameters that determine the rate of its progress: humidity, temperature, and acidity. The control of these parameters is carried out by following two different approaches: in the first, the environmental conditions of the storage room are kept under control [33], while

in the second, the goal is to create an optimal microclimate inside the different cases (closed, open or ventilated) [78]–[80]. From the studies of the Image Permanence Institute (IPI), the *Storage Guide for Acetate Film* [33] was born as one of the reference manuals. The Guide consists of a series of predictions about how long it will take a film to reach the vinegar syndrome trigger point in association with a particular combination of temperature and humidity. A “wheel” is provided with the guide in order to have an easy-to-use tool to calculate these predictions; it is a two-sided disk (Fig. 16). Side 1 shows the number of years needed by a fresh film to reach the threshold level of free acidity equal to 0.5 at various storage conditions, while side 2 shows the approximate number of years that an already partially degraded film will take to reach the 1.0 free acidity level at various temperature and humidity conditions. According to the wheel, at room temperature (22°C) and relative humidity (RH) of 40%, it takes 50 years to trigger the vinegar syndrome; on the other hand, by lowering the temperature as much as possible (down to -18°C to freeze the acid), and storing the film at RH 20% (it is important to store films in a not too dry environment that could have detrimental effects on the conservation of the emulsion), life expectancy increases up to hundreds years.

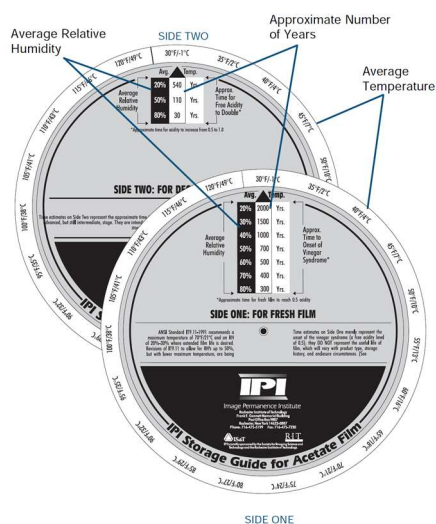


Fig. 16 The IPI Wheel for the monitoring of the vinegar syndrome in cellulose triacetate-based motion picture films: the Media Storage Summary is on Side 1 of the Wheel. The Media Support Chronology is on Side 2.

On these bases, a good storage environment, therefore, must be very cold and not very humid but also well-ventilated to facilitate the removal of the degradation by-products that catalyze the deacetylation reaction. In addition, it is fundamental to separate films affected by the syndrome from others stored nearby, to not risk “infecting” them.

In recent studies [53], [55], [81], more efficient models to predict degradation pathways of cellulose acetate films have been proposed, pointing out that the model used by IPI to calculate the deacetylation rate and CTA-based films life expectancy in their Guide does not account for the autocatalytic effect of acetic acid on the deacetylation reaction. In particular, Ahmad et al. (2020) [81] presented a different mathematical model for predicting the onset of the vinegar syndrome and validating it using a set of previously published experimental data of cellulose triacetate films aged in different conditions. The results indicate not only that film permanence may be overestimated by the Guide, but also that cold storage may be less effective than previously thought, in inhibiting the *vinegar syndrome*.

On these bases, the interest of research has turned toward the control of humidity and of the acidity inside of the cases. Films are often kept in sealed containers, which protect them from pollutants, dust, and abrasive particulate matter [16]. But being enclosed in such a confined space accelerates degradation processes due to fast increment in the concentration of acetic acid [33]. Ventilated enclosures [82] have also been developed for this purpose, but they have not led to relevant improvement [83].

Two different strategies have been tried to solve the moisture problem. The first has been developed by the Swedish Film Institute and consists of preconditioning the film to a fixed humidity value (RH 25%) before sealing it inside the case; this procedure is carried out through the Fi.C.A (Film Conditioning Apparatus) machine [84]. The second, on the other hand, consists in using desiccants such as silica gel to reduce moisture [7], [25]. Although it cannot absorb pollutant gases as well, the stabilization or reduction of moisture conducted through silica gel prevents mold

growth and slows down the hydrolysis processes [16]. In particular, molds, and in general parasitic microorganisms, predominantly afflict gelatin emulsion but sometimes, can affect also the support [7], [10], [33]. Silica gel can also absorb a small amount of acetic acid, but there are more efficient materials for this purpose. The issue of subtracting acetic acid from the environment has been approached along two lines: absorb it or neutralize it.

For the absorption of acetic acid, Kodak recommends the use of molecular sieves [42], [85]–[87] added inside the case in proportion to 5% by weight of the film. Also called acid scavengers, they consist of zeolites, aluminosilicates with a lattice structure made of three-dimensional polyhedra formed by the assembly of SiO_4 and AlO_4 tetrahedric units. They are porous compounds that are called molecular sieves because they can trap molecules of the same size as their micropores; for acetic acid, 4Å zeolites are commonly used [16].

Activated carbons are used as an alternative to zeolites [16], [25]. The use of dryers and molecular sieves is not a permanent solution strategy and requires systematic renewal, since sooner or later their adsorption capability is exhausted, due to pore saturation. In addition, it has been shown that in some cases their use can also bring damage to the film; excessive absorption of moisture and other volatiles, such as traces of residual solvent within the film, can cause the shrinking of the base or the emulsion layer [16], [79].

On the other hand, concerning the neutralization of acetic acid, some experimentations have been carried out on paper wrappers added with calcium carbonate (CaCO_3), used as a neutralizing agent, or on calcium carbonate mixed with zeolites and/or activated carbon, to combine desiccant and neutralizing action. The results obtained on both naturally and artificially aged films, however, seem to be not very promising [16], [79], [80], [83]: concerning the use of paper loaded with calcium carbonate, even if a lowering in the acidity is observed for motion picture films aged in presence of these treatments, they do not seem to be able to protect films stored nearby ones already infected [83].

Yamamoto et al. (2019) recently proposed the use of a combination of sodium carbonate and sodium polyacrylate for the removal of acetic acid and a dehumidification agent, respectively [88]. Sodium carbonate seems to have a good performance with a durability of its action of several months. Meanwhile, sodium polyacrylate controls humidity at around 40% RH, which is a good value to promote the preservation of motion picture films.

Another option is offered by Dedecker et al. (2018, 2021), which used water-stable metal-organic frameworks (MOFs) [89]–[91]. They found that the best candidates to accomplish a selective absorption of acetic acid were MOFs with appropriate pore size to favor a high degree of confinement and with organic spacers that enhance the van de Waals interactions with the acetic acid. In addition, MOFs with apolar groups in the inorganic node or with lipophilic but polar groups functionalized to the organic linkers, are preferred because the selective absorption of acetic acid is not affected by the competitive absorption of air moisture. These systems are very performing and have been successfully tested for the conservation of motion picture films as part of the project NEMOSINE. The main drawbacks are the high costs and the huge amount of time needed for the synthesis of these products.

In the most dangerous cases, when the image runs the risk of no longer being readable, conservators typically resort to duplication and digitization, sacrificing the original materials [7], [10], [12], [16], [33].

2.5.4 The final option: polyesters

2.5.4.1 History

Issues with the instability of cellulose acetate encouraged researchers to find an alternative and more durable base material. For this purpose, in the 1960s, the first films based on polyester, a fully synthetic polymer much more stable than both nitrate and triacetate cellulose, were introduced and purchased as Estar® and

Cronar®. The first polyester, polyethylene terephthalate (PET) was synthesized for the first time in the 40s, but it had no fortune as a film base due to its low transparency and the difficulty of sticking the emulsion on its surface [7]. In 1996, Kodak introduced polyethylene naphthalate (PEN) under the name of Advantix® [10].

2.5.4.2 Synthesis and properties

Polyesters are thermoplastic heteropolymers that are obtained by the polycondensation process between a diol, the ethylene glycol, and a diacid, specifically terephthalic acid in the case of polyethylene terephthalate (Fig. 13A) and naphthalene-2,6-carboxylate in the case of polyethylene naphthalate (Fig.13B)[10], [25].

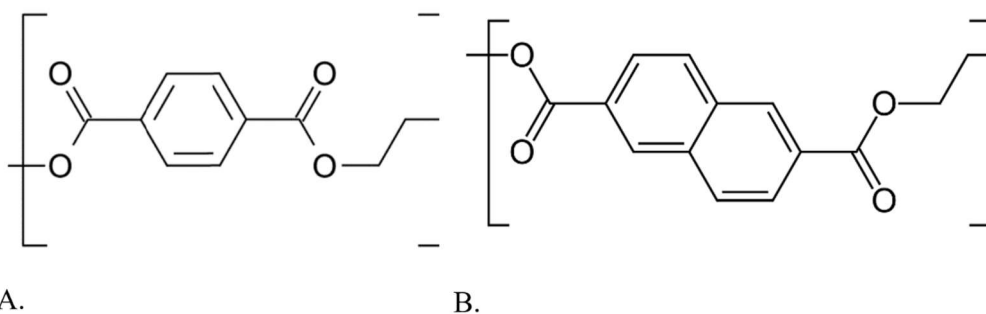


Fig.13. Molecular structure of the repeating unit of polyethylene terephthalate (A) and polyethylene naphthalate (B).

PET is insoluble in common solvents, so film production is not achieved by casting a solution, but by melting the polymer and stretching it while cooling. It does not require the addition of plasticizers [7], [10], [25]. Compared to cellulose nitrate, polyesters-based films are less flammable (for this reason are marked "SAFETY" or simply "S" as cellulose acetate ones). It is possible to distinguish them from cellulose triacetate films by checking the date of manufacture (a film is probably CTA-based if it was made before the 1960s) or performing the polarization test: when a polyester-based film is put between two polarizing filters, shows birefringence, while cellulose triacetate does not [7], [10], [19] PET is also chemically very stable, less

sensitive to shrinkage, and has the highest hardness and tensile strength compared to all other base materials [10].

1.5.5.3 Degradation processes

Polyester is the most stable of substrates. As an ester, may be subjected to hydrolysis, but at room temperature and in accelerated aging tests, degradation phenomena take place after a much longer time than with acetate and nitrate cellulose. Currently, no cases of chemical degradation of polyesters have yet been reported in the archives, but degradation occurs just as embrittlement and loss of tensile properties. Tests showed that degradation of polyester depends on temperature and humidity, therefore, storage in cool, dry places is always recommended [33]. As it contains neither solvents nor plasticizers that can exude, it is also not affected by further shrinkage [10].

References

- [1] S. Bernardi, *L'avventura del cinematografo: storia di un'arte e di un linguaggio*, Marsilio E. Venezia, 2020.
- [2] S. Herbert, *A History of Pre-Cinema, Volume I*, Routledge. 2000.
- [3] N. P. Durata Presenti Campagnoni, *Museo Nazionale del Cinema di Torino, Catalogo*, Silvana Ed. Milano, 2016.
- [4] Plato, *The Republic, Vol. II*, Laterza. Bari, 1867.
- [5] Carlo Alberto Minici Zotti, *Magiche visioni prima del Cinema. La Collezione Minici Zotti*, Il Poligra. 2001.
- [6] D. B. Kristin Thompson, *Film history. An introduction; Second edition. Chapter 1: The invention and early years of the Cinema, 18802-1904*, McGraw-Hil. 2002.
- [7] M.-P. M. Paul Read, *Restoration of Motion Picture Film*, Butterwort. Oxford, 2000.
- [8] C. Montanaro, *Dall'Argento al Pixel*, Linea ediz. Padova, 2019.
- [9] Image Permanence Institute (IPI)., "No Title." <https://filmcare.org/index>.
- [10] M. Valverde, "Photographic negatives: nature and evolution of processes," pp. 9–18, 2005, [Online]. Available: <http://www.bcinc.ca/Interface/openbcin.cgi?submit=submit&Chinkey=235796>.
- [11] M. R. V. Sahyun, "Mechanism in Photographic Chemistry," *J. Chem. Educ.*, vol. 51, no. 2, 1974.
- [12] N. Film, P. Foundation, and S. Francisco, *The Film Preservation Guide. The Basics for Archives, Libraries, and Museums*, vol. 58, no. 3. 2005.
- [13] E. Ciliberto, P. Gemmellaro, V. Iannuso, S. La Delfa, R. G. Urso, and E. Viscuso, "Characterization and Weathering of Motion-picture Films with Support of Cellulose Nitrate, Cellulose Acetate and Polyester," *Procedia Chem.*, vol. 8, pp. 175–184, 2013, doi: 10.1016/j.proche.2013.03.023.
- [14] É. C. T. C. Roldão, "A contribution for the preservation of cellulose esters black and white negatives," 2018.
- [15] A. Adams, *The negative*, 2015th ed. Boston: New York Graphic Society, 1982.
- [16] B. Lavédrine, *A Guide to the Preventive Conservation of Photograph Collections*, Getty Publ. Los Angeles, 2003.

- [17] L. Residori, *Chimica e biologia applicate alla conservazione degli archivi. Le fotografie. V. 4*, Union Prin. Roma, 2002.
- [18] R. D. Theys and G. Sosnovsky, "Chemistry and processes of color photography," *Chem. Rev.*, vol. 97, no. 1, pp. 83–132, 1997, doi: 10.1021/cr941191p.
- [19] and A. R. Fischer, Monique C., "Guidelines for Care & Identification of Film-Base Photographic Materials," *Top. Photogr. Preserv.*, vol. 5, pp. 117–122, 1993.
- [20] K. L. B. Alser *et al.*, "Cellulose Esters," 2012, doi: 10.1002/14356007.a05.
- [21] Abbas Hamrang, *Degradation and Stabilisation of Cellulose Based Plastics & Artifacts*. Manchester Metropolitan University, 1994.
- [22] T. Heinze and T. Liebert, *Celluloses and Polyoses/Hemicelluloses*, vol. 10. Elsevier B.V., 2012.
- [23] H. Heckman, "Burn After Viewing, or, Fire in the Vaults: Nitrate Decomposition and Combustibility," *Am. Arch.*, vol. 73, no. 2, pp. 483–506, 2010.
- [24] C. W. Saunders and L. T. Taylor, "A review of the synthesis, chemistry and analysis of nitrocellulose," *J. Energ. Mater.*, vol. 8, no. 3, pp. 149–203, 1990, doi: 10.1080/07370659008012572.
- [25] Y. Shashoua, *Conservation of Plastics: materials science, degradation and preservation*. Oxford: Elsevier Ltd, 2008.
- [26] E. C. Worden, *Nitrocellulose Industry: A Compendium of the History, Chemistry, Manufacture, Commercial Application and Analysis of Nitrates, Acetates and Xanthates of Cellulose as Applied to the Peaceful Arts - Volume II*. Constable and Company LDT, 1991.
- [27] J. A. Reilly, "Celluloid objects: Their chemistry and preservation," *J. Am. Inst. Conserv.*, vol. 30, no. 2, pp. 145–162, 1991, doi: 10.1179/019713691806066700.
- [28] W. D. Field, "Pyroxylin, Its Manufacture and Applications," *J. Am. Chem. Soc.*, vol. 15, no. 3, pp. 140–144, 1893.
- [29] L. S. Sirkis, *The History, Deterioration and Conservation of Cellulose Nitrate and Other Early Plastic Objects*. London: Institute of Archeology, 1982.
- [30] R. Stewart, *Analytical Studies of the Degradation of Cellulose Nitrate Artefacts*. University of Strathclyde, 1997.
- [31] M. Edge, N. S. Allen, M. Hayes, P. N. K. Riley, C. V. Horie, and J. Luc-Gardette, "Mechanisms of deterioration in cellulose nitrate base archival cinematograph film,"

- Eur. Polym. J.*, vol. 26, no. 6, pp. 623–630, 1990, doi: 10.1016/0014-3057(90)90218-S.
- [32] S. Nunes *et al.*, “A diagnostic tool for assessing the conservation condition of cellulose nitrate and acetate in heritage collections: quantifying the degree of substitution by infrared spectroscopy,” *Herit. Sci.*, pp. 1–14, 2020, doi: 10.1186/s40494-020-00373-4.
- [33] P. Krause, P. Kraus, J. P. Reilly, and J. M. Reilly, “IPI Storage Guide for Acetate Film,” *J. Am. Inst. Conserv.*, vol. 33, no. 3, p. 321, 1994, doi: 10.2307/3179643.
- [34] G. Di Pietro, *A local microscopic model for the formation of silver mirroring on black and white photographs. Proceedings of metal*. National Museum of Australia, 2004.
- [35] E. B. J. Kuiper, Ed., *A Handbook or Film Archives*. Brussels: FIAF Secretariat, 1980.
- [36] M. McGath, S. Jordan-Mowery, M. Pollei, S. Heslip, and J. Baty, “Cellulose Acetate Lamination: A Literature Review and Survey of Paper-Based Collections in the United States,” *Restaurator*, vol. 36, no. 4, pp. 333–365, 2015, doi: 10.1515/res-2015-0015.
- [37] J. Ballany, D. Littlejohn, R. A. Pethrick, and A. Quye, “Probing the factors that control degradation in museum collections of cellulose acetate artefacts,” *ACS Symp. Ser.*, vol. 779, pp. 145–165, 2001, doi: 10.1021/bk-2001-0779.ch012.
- [38] E. C. Worden, *Technology of Cellulose Esters*. New York, 1916.
- [39] Y. Shashoua and K. B. Johansen, “Investigation of ATR-FTIR spectroscopy as an alternative to the Water-Leach free acidity test for cellulose acetate-based film,” *14th Trienn. Meet. ICOM-CC*, no. Koenig 1999, pp. 548–555, 2005.
- [40] M. T. Giachet *et al.*, “Assessment of the composition and condition of animation cels made from cellulose acetate,” *Polym. Degrad. Stab.*, vol. 107, pp. 223–230, 2014, doi: 10.1016/j.polymdegradstab.2014.03.009.
- [41] G. Fengel, D. Wegener, *Wood—Chemistry, Ultrastructure, Reactions. 2nd Edition*. Berlin: Walter de Gruyter, 1989.
- [42] A. T. Ram, “Archival Preservation of Photographic Films-A Perspective,” *Polym. Degrad. Stab.*, vol. 29, no. 1, pp. 3–29, 1990, doi: 10.1016/0141-3910(90)90019-4.
- [43] K. A. H. Brems, “The Archival Quality of Film Bases,” *SMPTE J.*, vol. 97, pp. 991–993, 1988.
- [44] J. M. Reilly, *Preserving Photograph Collections in Research Libraries: A*

- Perspective.*” In *Issues in the Conservation of Photographs*, First edit. Los Angeles: Getty Conservation Institute, 2010.
- [45] and C. J. E. P. Z. Adelstein, J. M. Reilly, D. W. Nishimura, “Stability of Cellulose Ester Base Photographic Film: Part I Laboratory Testing Procedures,” *SMPTE J.*, 1992.
- [46] N. S. Allen, M. Edge, J. H. Appleyard, T. S. Jewitt, C. V. Horie, and D. Francis, “Degradation of historic cellulose triacetate cinematographic film: The vinegar syndrome,” *Polym. Degrad. Stab.*, vol. 19, no. 4, pp. 379–387, 1987, doi: 10.1016/0141-3910(87)90038-3.
- [47] M. Edge, N. S. Allen, T. S. Jewitt, J. H. Appleyard, and C. V. Rorie, “The Deterioration Characteristics of Archival Cellulose Triacetate Base Cinematograph Film,” *J. Photogr. Sci.*, vol. 36, no. 6, pp. 199–203, 1988, doi: 10.1080/00223638.1988.11737000.
- [48] M. Edge, N. S. Allen, D. A. R. Williams, F. Thompson, and V. Horie, “Methods for predictive stability testing of archival polymers: A preliminary assessment of cellulose triacetate based motion picture film,” *Polym. Degrad. Stab.*, vol. 35, no. 2, pp. 147–155, 1992, doi: 10.1016/0141-3910(92)90106-F.
- [49] P. Z. Adelstein, J. M. Reilly, D. W. Nishimura, C. J. Erbland, and J. L. Bigourdan, “Stability of Cellulose Ester Base Photographic Film: Part V-Recent Findings Studies of Incubation Techniques Long-Term Incubations of Polyester Base Film Properties of Naturally Aged Films on Acetate Base Infectious Behavior in Acetate Base Film,” no. July, pp. 439–447, 1995.
- [50] M. Edge, N. S. Allen, T. S. Jewitt, and C. V. Horie, “Fundamental aspects of the degradation of cellulose triacetate base cinematograph film,” *Polym. Degrad. Stab.*, vol. 25, no. 2–4, pp. 345–362, 1989, doi: 10.1016/S0141-3910(89)81016-X.
- [51] and C. C. B. Lee, By William E, “The Stability Film Bases of Kodak Professional Motion-Picture.,” *Soc. Motion Pict. Telev. Eng.*, pp. 911–14, 1988.
- [52] J. L. Bigourdan, “Stability of acetate film base: Accelerated-aging data revisited,” *J. Imaging Sci. Technol.*, vol. 50, no. 5, pp. 494–501, 2006, doi: 10.2352/J.ImagingSci.Technol.(2006)50:5(494).
- [53] B. Knight, “Lack of evidence for an autocatalytic point in the degradation of cellulose acetate,” *Polym. Degrad. Stab.*, vol. 107, pp. 219–222, 2014, doi:

- 10.1016/j.polymdegradstab.2013.12.002.
- [54] A. Al Mohtar, S. Nunes, J. Silva, A. M. Ramos, J. Lopes, and M. L. Pinto, “First-Principles Model to Evaluate Quantitatively the Long-Life Behavior of Cellulose Acetate Polymers,” *ACS Omega*, vol. 6, no. 12, pp. 8028–8037, 2021, doi: 10.1021/acsomega.0c05438.
- [55] A. Al Mohtar *et al.*, “Decision making based on hybrid modeling approach applied to cellulose acetate based historical films conservation,” *Sci. Rep.*, vol. 11, no. 1, pp. 1–13, 2021, doi: 10.1038/s41598-021-95373-0.
- [56] and D. M. W. Derham, M., M. Edge, D.A.R. Williams, “The Degradation of Cellulose Triacetate Studied by Nuclear Magnetic Resonance Spectroscopy and Molecular Modelling,” in *Polymers in Conservation Conference*, C. V. N.S. Allen, M. Edge, Horie, Ed. Manchester: Royal Society of Chemistry, 1992.
- [57] D. Littlejohn, R. A. Pethrick, A. Quye, and J. M. Ballany, “Investigation of the degradation of cellulose acetate museum artefacts,” *Polym. Degrad. Stab.*, vol. 98, no. 1, pp. 416–424, 2013, doi: 10.1016/j.polymdegradstab.2012.08.023.
- [58] N. S. Allen, M. Edge, J. H. Appleyard, T. S. Jewitt, C. V. Horie, and D. Francis, “Acid-catalysed degradation of historic cellulose triacetate, cinematographic film: Influence of various film parameters,” *Eur. Polym. J.*, vol. 24, no. 8, pp. 707–712, 1988, doi: 10.1016/0014-3057(88)90002-X.
- [59] N. S. Allen, M. Edge, T. S. Jewitt, and C. V. Horie, “Initiation of the Degradation of Cellulose Triacetate Base Motion Picture Film,” *J. Photogr. Sci.*, vol. 38, no. 2, pp. 54–59, 1989, doi: 10.1080/00223638.1989.11737073.
- [60] M. C. Fischer and J. M. Reilly, “Article: USE OF PASSIVE MONITORS IN FILM COLLECTIONS Author(s): Monique C. Fischer and James M. Reilly,” vol. 6, pp. 11–40, 1995.
- [61] J. C. Harthan, M. Edge, N. S. Allen, and H. Schou, “The development and evaluation of a sensory system to detect degradation in cellulose triacetate photographic film. Part I: The detection of acetic acid evolved from degrading cellulose triacetate photographic film,” *Imaging Sci. J.*, vol. 45, no. 2, pp. 77–80, 1997, doi: 10.1080/13682199.1997.11736379.
- [62] C. J. P. Z. Adelstein, J. M. Reilly, D. W. Nishimura, Erbland, “Stability of Cellulose Ester Base Photographic Film: Part III - Measurement of Film Degradation,” *SMPTE*

- J., 1995.
- [63] “Imaging Materials - Processed Silver-Gelatin Type Black-and White Film - Specifications for Stability,” IT9.1-1996, 1996.
- [64] “Imagin materials - Processed silver gelatin-type black-and-white films - Specifications for stability,” 18901:2010(E), 2010.
- [65] “Standard Test Methods of Testing Cellulose Acetate,” D87-96, 2019.
- [66] P. Z. Adelstein, “IPI Media Storage Quick Reference: Negatives, Prints, Tapes, CDs, DVDs,” *Image Permanence Inst.*, pp. 1–9, 2009, [Online]. Available: https://www.imagepermanenceinstitute.org/webfm_send/301.
- [67] I. P. Institute, *User’s Guide for A-D Strips*. Seventh Edition 1/22, 2022.
- [68] K. Curran, A. Možir, M. Underhill, L. T. Gibson, T. Fearn, and M. Strlič, “Cross-infection effect of polymers of historic and heritage significance on the degradation of a cellulose reference test material,” *Polym. Degrad. Stab.*, vol. 107, no. 2, pp. 294–306, 2014, doi: 10.1016/j.polymdegradstab.2013.12.019.
- [69] K. Curran and M. Strlič, “Polymers and volatiles: Using VOC analysis for the conservation of plastic and rubber objects,” *Stud. Conserv.*, vol. 60, no. 1, pp. 1–14, 2015, doi: 10.1179/2047058413Y.0000000125.
- [70] K. Curran, M. Underhill, L. T. Gibson, and M. Strlic, “The development of a SPME-GC/MS method for the analysis of VOC emissions from historic plastic and rubber materials,” *Microchem. J.*, vol. 124, pp. 909–918, 2016, doi: 10.1016/j.microc.2015.08.027.
- [71] S. Da Ros *et al.*, “Characterising plasticised cellulose acetate-based historic artefacts by NMR spectroscopy: A new approach for quantifying the degree of substitution and diethyl phthalate contents,” *Polym. Degrad. Stab.*, vol. 183, 2021, doi: 10.1016/j.polymdegradstab.2020.109420.
- [72] R. Casarano, L. C. Fidale, C. M. Lucheti, T. Heinze, and O. A. El, “Expedient , accurate methods for the determination of the degree of substitution of cellulose carboxylic esters : Application of UV – vis spectroscopy (dye solvatochromism) and FTIR,” *Carbohydr. Polym.*, vol. 83, no. 3, pp. 1285–1292, 2011, doi: 10.1016/j.carbpol.2010.09.035.
- [73] H. Kono, H. Hashimoto, and Y. Shimizu, “NMR characterization of cellulose acetate: Chemical shift assignments , substituent effects , and chemical shift

- additivity,” *Carbohydr. Polym.*, vol. 118, pp. 91–100, 2015, doi: 10.1016/j.carbpol.2014.11.004.
- [74] P. Fei, L. Liao, B. Cheng, and J. Song, “Quantitative analysis of cellulose acetate with a high degree of substitution by FTIR and its application,” *Anal. Methods*, vol. 9, no. 43, pp. 6194–6201, 2017, doi: 10.1039/c7ay02165h.
- [75] E. Richardson, M. Truffa Giachet, M. Schilling, and T. Learner, “Assessing the physical stability of archival cellulose acetate films by monitoring plasticizer loss,” *Polym. Degrad. Stab.*, vol. 107, pp. 231–236, 2014, doi: 10.1016/j.polymdegradstab.2013.12.001.
- [76] L. Liu, D. Gong, L. Bratasz, Z. Zhu, and C. Wang, “Degradation markers and plasticizer loss of cellulose acetate films during ageing,” *Polym. Degrad. Stab.*, vol. 168, p. 108952, 2019, doi: 10.1016/j.polymdegradstab.2019.108952.
- [77] S. Da Ros *et al.*, “Characterising plasticised cellulose acetate-based historic artefacts by NMR spectroscopy: A new approach for quantifying the degree of substitution and diethyl phthalate contents,” *Polym. Degrad. Stab.*, vol. 183, p. 109420, Jan. 2021, doi: 10.1016/J.POLYMDEGRADSTAB.2020.109420.
- [78] J. Bigourdan and J. M. Reilly, “Effectiveness of Storage Conditions in Controlling the Vinegar Syndrome: Preservation Strategies for Acetate Base Motion-Picture Film Collections,” *Image Sound Arch. Access Challenges 3rd Millenium, Proc. Jt. Tech. Symp.*, pp. 14–34, 2000.
- [79] A. M. News *et al.*, “Strategies for the Storage of Cellulose Acetate Film,” vol. 40, no. 6, pp. 6–7, 2016.
- [80] J. L. Bigourdan, P. Z. Adelstein, and J. M. Reilly, “Use of microenvironments for the preservation of cellulose triacetate photographic film,” *J. Imaging Sci. Technol.*, vol. 42, no. 2, pp. 155–162, 1998.
- [81] I. R. Ahmad, D. Cane, J. H. Townsend, C. Triana, L. Mazzei, and K. Curran, “Are we overestimating the permanence of cellulose triacetate cinematographic films? A mathematical model for the vinegar syndrome,” *Polym. Degrad. Stab.*, vol. 172, p. 109050, 2020, doi: 10.1016/j.polymdegradstab.2019.109050.
- [82] M. Newnham, “Ventilated Film Cans--Their Effect on the Diffusion of Decomposition By-products from Motion Picture Film,” *SMPTE J.*, vol. 111, no. 1, pp. 29–33, 2002, doi: 10.5594/J16413.

- [83] J.-L. Bigourdan, P. Z. Adelstein, and J. M. Reilly, "Article: EFFECT OF PAPER ALKALINE RESERVE ON THE CHEMICAL STABILITY OF ACETATE BASE SHEET FILM EFFECT OF PAPER ALKALINE RESERVE ON THE CHEMICAL STABILITY OF ACETATE BASE SHEET FILM," vol. 7, no. 7, pp. 43–54, 2000, [Online]. Available: http://resources.conservation-us.org/pmgtopics/1997-volume-seven/07_07_Bigourdan.pdf.
- [84] R. H.-E. B. Gooes, "An Inexpensive Method for Preservation and Long-Term Storage of Color Film," *SMPTE J.*, 1983.
- [85] E. Kodak, "Molecular Sieve Acid Scavenger." <https://www.kodak.com/en/motion/page/molecular-sieve-acid-scavenger>.
- [86] A. J. Cruz, J. Pires, A. P. Carvalho, and M. Brotas de Carvalho, "Comparison of adsorbent materials for acetic acid removal in showcases," *J. Cult. Herit.*, vol. 9, no. 3, pp. 244–252, 2008, doi: 10.1016/j.culher.2008.03.001.
- [87] A. João Cruz, J. Pires, A. P. Carvalho, and M. Brotas de Carvalho, "Adsorption of Acetic Acid by Activated Carbons, Zeolites, and Other Adsorbent Materials Related with the Preventive Conservation of Lead Objects in Museum Showcases," *J. Chem. & Eng. Data*, vol. 49, no. 3, pp. 725–731, Apr. 2004, doi: 10.1021/je034273w.
- [88] D. Yamamoto, T. Ishii, A. Hashimoto, and K. Matsui, "Use of sodium carbonate and sodium polyacrylate for the prevention of vinegar syndrome," *Imaging Sci. J.*, vol. 67, no. 3, pp. 171–178, 2019, doi: 10.1080/13682199.2019.1577594.
- [89] K. Dedecker *et al.*, "Metal-Organic Frameworks for Cultural Heritage Preservation : The Case of Acetic Acid Removal," 2018, doi: 10.1021/acsami.8b02930.
- [90] K. Dedecker *et al.*, "Metal-Organic Frameworks for Cultural Heritage Preservation : The Case of Acetic Acid Removal To cite this version : HAL Id : hal-01791096," 2021.
- [91] A. Al Mohtar *et al.*, "Iron(III) based Metal-Organic Frameworks in cellulose acetate film preservation: Fundamental aspects and first application," *J. Cult. Herit.*, vol. 66, pp. 236–243, 2024, doi: 10.1016/j.culher.2023.11.013.

Chapter III

Set up of a method for the artificial induction of the deacetylation process and of a multi-analytical protocol for its monitoring

As reported in Chapter II, the main degradation phenomenon that affects motion picture films with a support made of cellulose acetates is the so-called “*vinegar syndrome*”, which concerns the deacetylation of the polymer due to the cleavage of the ester bonds between the acetate group (CH_3COO) and the cellulose chain through ester hydrolysis, with the formation of hydroxyl groups and the release of acetic acid (CH_3COOH) (Chapter II, Fig. 13A). Another hydrolysis process activated by the acetic acid emission is the cleavage of the glycosidic bonds of the cellulose triacetate backbone, with consequent depolymerization [1], [2].

The main goal of this thesis is the proposal of a remediation for this disease based on a chemical approach. On these bases, two preliminary steps are essential to evaluate the performances of the proposed inhibitor systems and they will be described in the next chapter:

- to develop a method to artificially induce the deacetylation process in motion picture films (i.e. the “*vinegar syndrome*”) in a controlled and reproducible way. To set up the protocol, the first experiments were carried out on pure cellulose triacetate films properly prepared (see paragraph 3.1.1);
- to set up an analytical protocol able to monitor the evolution of the deacetylation process.

In this chapter, both these aspects will be discussed.

3.1 Materials and Methods

3.1.1 Chemicals and materials

Cellulose triacetate (CTA, 43.3-45 wt.% acetyl content), cellulose diacetate (CDA, 39.8 wt.% acetyl content), dichloromethane (DCM, purity $\geq 99.8\%$) were purchased from Sigma Aldrich.

Sodium Hydroxide ($\geq 98.5\%$ pellets, anhydrous) was purchased by Acros Organics. Chloridric acid (37 wt%), chloroform, acetone, 2-methoxy ethanol and ethanol anhydrous denatured were purchased from Carlo Erba Reagents. Phenolphthalein was purchased from Merk reagents. All the products were used without further purification.

Water used for all the procedures was purified by a Millipore MilliQ Direct-Q® & Direct-Q UV water purification system (Water Resistivity: 18.2 M Ω at 25°C).

CTA-based films were obtained by dissolving CTA pellets in DCM under stirring in order to obtain a 3wt% solution. 20 mL of solution was poured into glass Petri dishes (with a diameter of 9 cm) and left for 24 hours under hood (25 ± 1 °C, $50 \pm 2\%$ RH) until the solvent was completely evaporated. Transparent films with a thickness of 130 ± 20 μm (similar to the one of the support in real motion picture films which was of about 140 μm [3]) were obtained (Fig. 1).

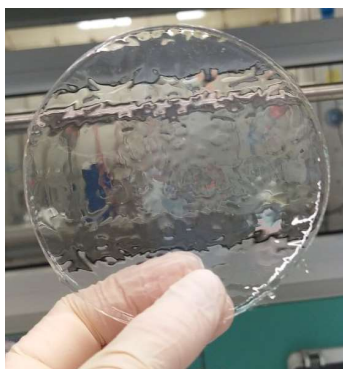


Fig. 1. lab-made CTA-based film

Real motion picture films used in the following experiments came from a reel called “Vita di una Pianta”, an educational documentary of the “Sezione Cinescolastica Paravia” (Fig. 2A, 2B AND 2C). Paravia was born in 1956 and diffused these short movies between the ‘60s and the ‘70s. The motion picture film (support and emulsion) was produced by Ferrania (Savona, Italy, Fig. 2D) and is made by cellulose acetate, as demonstrated by the polarization test (Fig. 2E) [4], the typical edge code “SAFETY” (Fig. 2F)[5], [6], and the FTIR-ATR analysis reported below (Paragraph 3.2.2). This reel was provided by the “Istituto Agrario ITAGR” (Florence, Italy) which is gratefully acknowledged.

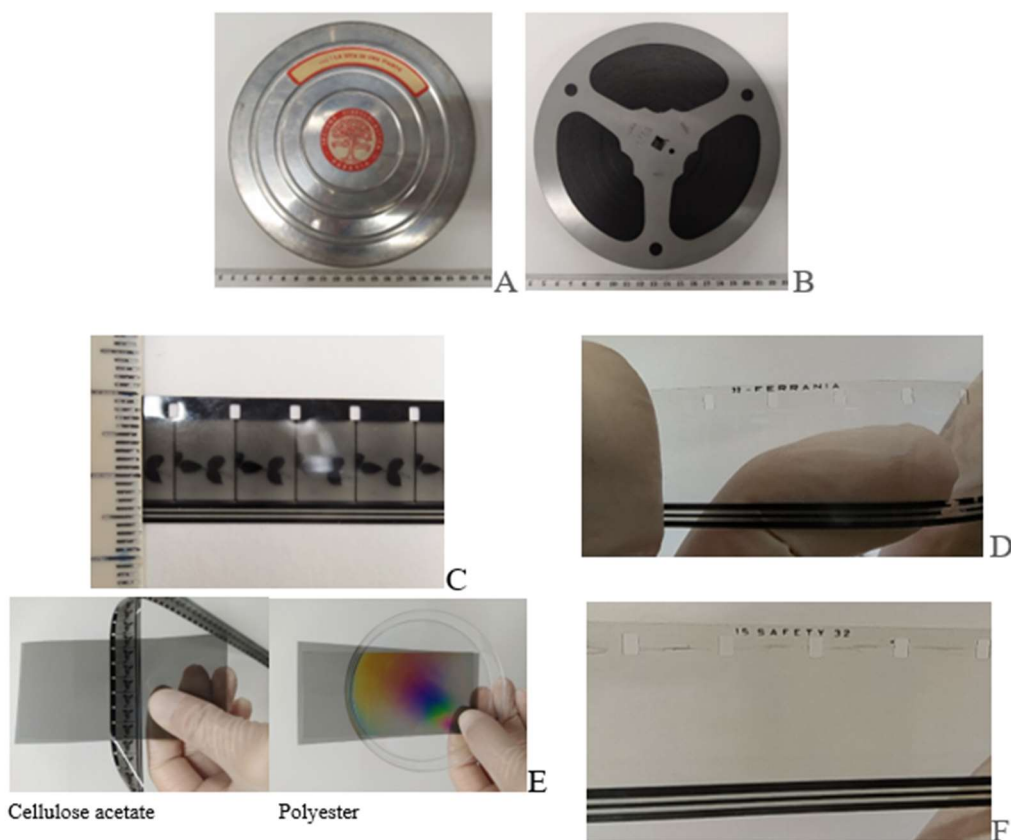


Fig 2. (A, B, C) Real motion picture film “Vita di una Pianta”; (D) edge code with the name of the manufacturer “FERRANIA”; (E) polarization test: CTA-based motion picture film does not show birefringence, which is evident in PE-based objects, instead; (F) edge codes indicating the material (“SAFETY”).

3.1.2 The artificial induction of the deacetylation process

Being the main aim of this project the evaluation of the performance of some systems properly set up as inhibitors for the “*vinegar syndrome*” in real motion picture films, in the first phase of this study, it was considered useful to develop a method to artificially induce the deacetylation process in a controlled and reproducible way, first on lab-made CTA-based films and then in real motion picture films. We decided to work also on CTA-based films to analyze the effects of this alteration method on pure CTA, avoiding the possible side effects due to plasticizers and the emulsion layer.

The characteristics of the perfect degradation protocol for our purposes must be the following:

- the method must be reproducible and able to induce the deacetylation process in a controlled way;
- the method must induce the deacetylation process on real motion picture films and the progress of this process must be followed in a reasonable time, with a not-too-fast kinetics (in order to be able to appreciate and study its evolution) but also not too slow (to be compatible with lab timelines);
- the method must not excessively alter the performance of the inhibitor whose efficacy we want to test.

By artificially inducing the deacetylation reaction and all the associated degradation processes, it could be possible both to define and optimize the multi-analytical protocol to monitor the evolution of the vinegar syndrome and to rigorously evaluate the performance of the inhibitors properly set up. In the latter case, we compared the evolution of the alteration processes in both treated and untreated samples subjected to the same, controlled and reproducible, degradation protocol (Chapter VI). After this preliminary step, we tested our inhibitors on samples on which the vinegar syndrome naturally occurred (Chapter VI).

As it was mentioned in Chapter II, the deacetylation process could be induced and favored by high values of temperature, moisture and acidity in the storage environment[1], [6].

As indicated in the literature, one of the methods commonly used to artificially induce the vinegar syndrome in real motion picture films has been proposed by the Image Permanence Institute [9], [10] and subsequently reported in the ISO 18901:2010 [11]. This method involves the storage of a certain amount of motion picture films, previously conditioned for 15 h at 23 ± 1 °C and 50 ± 2 % RH, in a sealed metal-foil bag (15x20x0.22 cm) internally coated with a layer of polyethylene (Fig. 3). Then the samples are heated up for 72 h at 100 ± 2 °C. A high ratio of film-to-air volume must be ensured by squeezing out excess air before heat-sealing. Processed films should show an increase in free acidity and a loss in tensile properties and emulsion.

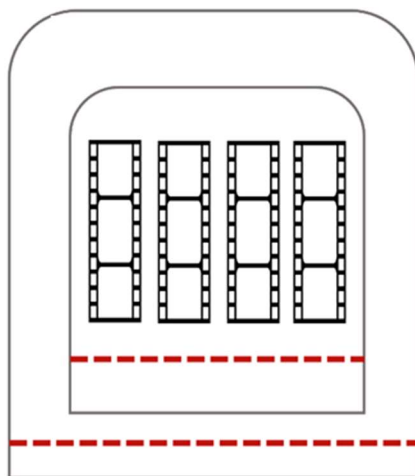


Fig. 3 Motion picture films inside a metal-foil double bag for the TA and the first step of the TA+RH degradation protocols.

Bearing in mind the main purpose of this study (the evaluation of the performance of our inhibitor systems for deacetylation), it is mandatory to remember that most of the products we proposed are not able to withstand such high temperatures for so long.

For this reason, as a first attempt, we tested a degradation protocol based on two steps: during the first step, fragments of films were subjected to the procedure reported in the ISO 18901:2010 and exposed to high temperature for 5 days (Fig. 3); then, during the second step, they were transferred in a 130 mL hermetic jar, hung at the top of the chamber with a Teflon wire and spaced out with glass marbles with a diameter of about 2 mm in order to prevent mutual contact during the experiment (Fig. 4). They were stored at 25 ± 3 °C and $100 \pm 2\%$ RH for 35 days. The environmental conditions (temperature and relative humidity) were monitored with a data logger by acquiring one registration per hour (Elitech GSP-6G Temperature and Humidity Data Logger).

Using these two steps-method, the idea was to induce the deacetylation process during the first step, add the treatment at the end of the first step and then study how the deacetylation process evolves (favored by the acetic acid produced during the first step and the high RH inside the chamber) with and without the treatment.

Unfortunately, even if the activation of the deacetylation process was verified after the first step (by applying the multi-analytical protocol that will be reported below), in the untreated samples no significant variations in the conservation status were appreciated during the second step, showing that the storage at high relative humidity for 35 days was not enough to promote the further evolution of the “*vinegar syndrome*”.

For this reason, an innovative induction method based on high acidity was proposed in this work.

3.1.2.1. The high acidity induction method (HCl5M)

It is well known that the deterioration of CA films by deacetylation could be induced by acid and basic catalytic [7], [8]. We evaluated the effects of the exposure to hydrochloric acid (HCl)-saturated atmospheres on both CTA-based films and real motion picture films.

The samples (both CTA-based films and real motion picture films) were exposed to a saturated atmosphere of HCl 5M in hermetic chambers (volume ca. 130 mL) for different periods of time at room temperature (25 ± 3 °C). The motion picture films and CTA-based films were cut into fragments of 50x16 mm (total amount for each chamber: 1 g) and hung at the top of the chamber with a Teflon wire, spaced out with glass marbles with a diameter of about 2 mm to avoid their mutual contact during the experiment. A vial with 8 mL of HCl 5M was placed at the bottom of the chamber (Fig. 4). CTA-based films were exposed to this HCl atmosphere for up to 16 days (with a sampling every two days), while for real motion picture films, the degradation period lasted for 30 days (with a sampling every 3, 6, 9, 12, 15, 20, 25, 30 days). In both cases, each sampling corresponds to a different hermetic chamber; it means that for these experiments the number of chambers that have been prepared corresponds to the number of samplings that have been done. The samples degraded with this protocol will be labeled as “P/FY_HCl5M”, where “P” means “real motion picture films” and “F” means “CTA-based films”; “Y” is the duration (days) of the exposition to the HCl 5M atmosphere.

The environmental conditions (temperature and relative humidity) were monitored with a data logger by acquiring one registration per hour (Elitech GSP-6G Temperature and Humidity Data Logger).

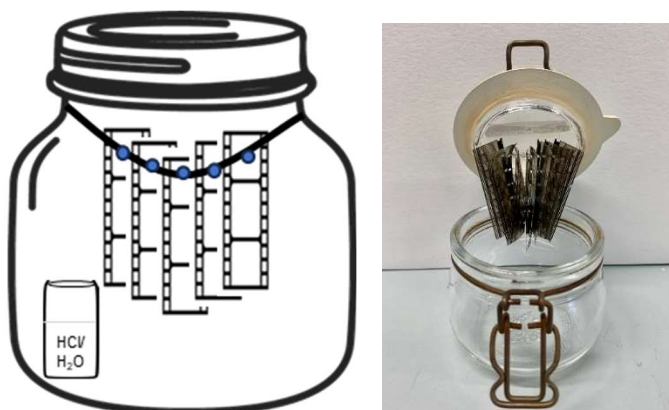


Fig. 4 Assets for the degradation protocols: motion picture films hung to a Teflon wire inside a hermetic jar for the HCl5M and the ATM2.X degradation protocol.

This method was set up to get a first idea of the evolution of the degradation process induced by an acid catalyst and to obtain samples with different acetyl content in order to test the efficacy of our multi-analytical method.

All the samples degraded with protocol HCl5M are resumed in Tab. 1.

Tab. 1 Samples of both lab-CTA-based (F) and real motion picture films (P) degraded with HCl5M degradation protocol (exposition to a saturated atmosphere of HCl 5M for a certain period of time).

Sample	Material of the sample	Duration of the degradation protocol (days)	Degradation protocol
F0 (CTA)	CTA*	0	/
F2 HCl5M	CTA	2	Exposition to a saturated atmosphere of HCl 5M
F4 HCl5M	CTA	4	
F6 HCl5M	CTA	6	
F8 HCl5M	CTA	8	
F10 HCl5M	CTA	10	
F12 HCl5M	CTA	12	
F14 HCl5M	CTA	14	
F16 HCl5M	CTA	16	
P0	RMPF**	0	/
P3 HCl5M	RMPF	3	Exposition to a saturated atmosphere of HCl 5M
P6 HCl5M	RMPF	6	
P9 HCl5M	RMPF	9	
P12 HCl5M	RMPF	12	
P15 HCl5M	RMPF	15	
P20 HCl5M	RMPF	20	
P25 HCl5M	RMPF	25	
P30 HCl5M	RMPF	30	

*CTA: lab-made CTA-based motion picture film

**RMPF: real motion picture film

3.1.2.2 The high-acidity induction method (ATM2.X)

This method was set up in order to have a proper way to evaluate the performance of our inhibitors on samples on which the deacetylation process was artificially induced. It is possible to schematize this protocol in three steps.

First step. We choose a proper time of exposition to HCl 5M (based on tests reported in Paragraph 3.1.2.1) in order to only induce the syndrome, but not to push it too far forward (Fig. 4).

Second step. Then, the samples were put out of the chamber and left for 24 h under hood at 50% relative humidity (RH%) and room temperature (25 ± 3 °C).

Third step. Finally, the samples were stored again in hermetic chambers at 100 RH% and 25 ± 3 °C for 12, 24, 36, 48 days to monitor the further evolution of the deacetylation process under the effect of moisture and acetic acid formed as a by-product of deacetylation (and residual chloride acid adsorbed on the film) during the first step (Fig. 4).

This induction method will be labeled as “P/FY_ATM2.X” where “X” is the duration of the first step of exposition at the HCl 5M atmosphere and “Y” is the duration of the third step of exposition at 100% RH; the acronym “ATM2” means that the samples were subjected to two different atmospheres (HCl 5M and 100% RH).

Samples subjected to the ATM2.X degradation protocol are resumed in Tab. 2

The environmental conditions (temperature and relative humidity) were monitored with a data logger by acquiring one registration per hour (Elitech GSP-6G Temperature and Humidity Data Logger).

Tab. 2 Samples of both lab-CTA-based (F) and real motion picture films (P) degraded with the first, the second and/or the third steps of the ATM2.X degradation protocol.

Sample	Material of the sample	First step	Duration of the first step (days)	Second step	Duration of the second step (hours)	Third step	Duration of the third step (days)
F0 (CTA)	CTA*	/	/	/	/	/	/
F3 HCl5M	CTA	Exposition to a saturated atmosphere of HCl 5M	3	Exposition under hood at 50% relative humidity (RH%) and room temperature (25 ± 3 °C)	24	/	/
F12 ATM2.3	CTA					12	
F24 ATM2.3	CTA					24	
F36 ATM2.3	CTA					36	
F48 ATM2.3	CTA					48	
F60_ATM2.3	CTA					60	
P0	RMPF**	/	/	/	/	/	/
P9 HCl5M	RMPF	Exposition to a saturated atmosphere of HCl 5M	9	Exposition under hood at 50% relative humidity (RH%) and room temperature (25 ± 3 °C)	24	/	/
P12 ATM2.9	RMPF					12	
P24 ATM2.9	RMPF					24	
P36 ATM2.9	RMPF					36	
P48_ATM2.9	RMPF					48	

*CTA: lab-made CTA-based film **RMPF: real motion picture film.

3.1.3 A multi-analytical protocol to monitor the evolution of the degradation process

In order to monitor the evolution of the deacetylation on both CTA-based film and real motion picture films, another fundamental step of this work was the definition and the optimization of a multi-analytical protocol. The idea is to monitor the chemical alterations of all the samples in terms of acetyl content (amount of acetic acid esterified onto the cellulose backbone of the polymer), free acidity (non-esterified acetic acid adsorbed on the film) and solubility of the support. All these parameters are directly associated with deacetylation, which in turn causes depolymerization and loss of plasticizers that induce the alteration of both thermal and mechanical properties (i.e. tensile strength). From the analytical standpoint, it is an innovative and systematic approach for the monitoring of the “*vinegar syndrome*” being that, at today, it is mostly investigated by using single techniques that often do not give exhaustive information about all the aspects involved in the progress of the deacetylation process. Moreover, a comparison between the information obtained by all the techniques used is presented, in order to validate the approach purposed. The experimental protocols are described below.

Optical microscopy. Optical microscopy analyses were performed in transmission mode with a Reichert optical microscope (Austria) coupled with a Nikon Digital-Sight DS-U3 camera; images were acquired at two different magnifications with the epi 5.5 (20x) and epi 11 (40x) lenses and were digitized with the NIS-Elements software.

Solubility tests. A first, rough evaluation of the variation in the acetyl content during the degradation method was carried out through solubility tests. It is known that the solubility of CA varies with the acetyl content as reported in Tab. 3 [1], [12], [13] For FY_HCl5M samples, solubility tests are performed in chloroform, acetone, 2-methoxyethanol and water. 60 mg of sample was cut into little fragments in the order

of a few mm² and dispersed in 3 mL of the chosen solvent. The extent of solubilization was assessed qualitatively after 48 hours.

Tab. 3 Solubility of Cellulose Acetate in different solvents by varying its degree of substitution (DS) and acetyl content.

Cellulose Acetate	DS	Acetyl content %	Solvent
Cellulose Triacetate	2.8-3.0	43.0-44.8	Chloroform
Cellulose Diacetate	2.2-2.7	36.5-42.2	Acetone
Cellulose Monoacetate	1.2-1.8	22.2-32.2	2-methoxy ethanol
Cellulose "0.-acetate"	0.6-0.9	13.0-18.6	Water

Gravimetry test. We investigated if the variation in weight during the degradation procedures could be associated with the deacetylation process. Weight loss has been calculated as follows:

$$\text{Weight Loss (\%)} = \frac{W_t - W_0}{W_0} \times 100 \quad (3.1)$$

Where W_0 is the initial weight of the sample (g) and W_t is the weight of the sample after the degradation procedure. W_t was measured after the end of the degradation process and after 24 hours of equilibration under the hood at 25 ± 3 °C and 50 ± 5 RH%. The reported results are the average value calculated between three samples and its corresponding standard deviation.

Free acidity. To estimate the Free Acidity (that corresponds to the free acetic acid that is adsorbed onto the support, i.e. the unesterified organic acid in the ester) a method reported on the ASTM D 871-96 normative [14] was used with some modifications. 150 mg of each sample were cut into pieces of 1x1 mm ca. (for real motion picture films, the emulsion layer was previously removed with a swab imbibed with water), dried at 60 °C for 2.5 h and cooled in a desiccator for 30

minutes. 4.5 mL of Milli-Q-water were added to the sample and allowed to stand for 72 h. The fragments were filtered and washed. Then, the filtrated solution and the washing water were titrated with 0.01N NaOH, using phenolphthalein as an indicator. Two blanks of Milli-Q water were carried through the complete procedure. The percentage of acidity as free acetic acid has been calculated as follows:

$$\text{Free acidity (\%)} = [(A - B)N \times 0.06 \times 100]/W \quad (3.2)$$

where:

A = NaOH solution used to titrate the sample (mL).

B = NaOH solution used to titrate the blank (mL).

N = normality of the NaOH solution. and

W = sample used (g).

For real motion picture films, the emulsion layer has been removed with a swab imbibed with water.

The reported results are the average value calculated between three samples and its corresponding standard deviation.

Combined acetyl or acetic acid content calculation through Heterogeneous Saponification Method (HSM). This is a method based on Heterogeneous Saponification and reported on the ASTM D 871-96 normative [14] was used with some modifications useful to optimize the method for this kind of support. This procedure allows to measure the total amount of acetyls bound to the cellulose backbone and the free acetic acid (the so-called “free acidity”, see the previous paragraph) adsorbed by the polymeric backbone, but it does not allow the discrimination of these two contributions.

150 mg of each sample were cut into pieces of 1x1 mm ca. (for real motion picture films, the emulsion layer was previously removed with a swab imbibed with water), dried at 60 °C for 2.5 h and cooled in a desiccator for 30 minutes. 6 mL of ethyl alcohol (75 w/w% in water) were added to each sample and kept for 30 min at 55 0

$\pm 5^{\circ}\text{C}$. Then, 6 mL of 0.5 N NaOH solution was added to each sample and heated at $55 \pm 5^{\circ}\text{C}$ for 15 min. The samples were maintained at room temperature for 72 hours. Then, the excess NaOH was titrated with 0.5 N HCl and phenolphthalein as indicator. An excess of about 150 μL of 0.5 N HCl was added and the sample was left at room temperature overnight. This step is useful to neutralize the residual NaOH eventually adsorbed onto the support and/or the emulsion. The small excess of HCl was titrated with 0.5N NaOH. For each sample, three duplicates were analyzed and two blanks of Whatman paper (Cat No. 1001-055) and two standard samples with known acetyl content % (CDA and CTA) were carried through the complete procedure as controls. The percentage of combined acetyl or acetic acid content was calculated as follows:

$$\text{Acetyl or acetic acid (\%)} = [(D - C)N_a + (A - B)N_b + P] \times (F/W) \quad (3.3)$$

where:

A = NaOH solution required for titration of the sample (mL).

B = NaOH solution required for titration of the blank (mL).

N_b = normality of the NaOH solution.

C = HCl required for titration of the sample (mL).

D = HCl required for titration of the blank (mL).

N_a = normality of the HCl solution.

F = 4.305 for acetyl.

W = sample used (g).

The reported results are the average value calculated between three samples and its corresponding standard deviation.

To facilitate understanding of the discussion of the results in the next sections, in Tab. 4 the relationship between the degree of substitution (DS) and the acetyl content (%) based on the following Equation [15] has been calculated.

$$DS = \frac{(3.86 \times \%acetyl)}{(102.4 - \%acetyl)} \quad (3.4)$$

Tab. 4 Relationship between the degree of substitution (DS) and the acetyl content (%) based on Eq. 4 for cellulose acetate.

Cellulose Acetate	DS	Acetyl content (%)
Cellulose Triacetate	$3.0 \leq DS \leq 2.8$	44.8-43.0
Cellulose Diacetate	$2.8 < DS \leq 1.9$	42.9-34.9
Cellulose Monoacetate	$1.9 < DS \leq 1$	34.9-21.1
Cellulose "0.-acetate"	$0.9 < DS \leq 0$	≤ 21.1

Acetyl content with FTIR-ATR Spectroscopy. To evaluate the decrease in the acetyl content on real motion picture films in a non-invasive and non-destructive way we performed FTIR-ATR Spectroscopy before and after the deacetylation induction. The FTIR spectra were collected with an IRAffinity-1S Fourier Transform Infrared Spectrometer (Shimadzu) by using the MIRacle Single Reflection Horizontal ATR Accessory equipped with a Diamond/ZnSe Performance flat tip Crystal Plate. The resolution was 2 cm^{-1} , the number of scans was 64 and the range $4000\text{-}600 \text{ cm}^{-1}$. For comparison, the spectra were adjusted to the same baseline and normalized on the peak at 1030 cm^{-1} [16]–[18]. For each sample of CTA-based film and real motion picture films, five acquisitions were carried out in different areas; the average value and the standard deviation are reported.

We calculated the following ratio:

$$\frac{\text{Intensity of a probe peak}}{\text{Intensity of } 1030 \text{ cm}^{-1} \text{ peak}} \quad (3.5)$$

The peak at 1030 cm^{-1} was chosen as the reference peak: it is assigned to the C-O-C stretching vibration of the anhydroglucose ring and was assumed that it does not vary during the degradation protocol [16], [18]. As probes, able to monitor the evolution of deacetylation, we evaluated various peaks whose intensity is assumed to vary during the deacetylation process (Fig. 5):

- the peak at 1220 cm^{-1} associated with the C-O stretching of the acetyl group;
- the peak at 1730 cm^{-1} associated with the C=O stretching of the acetyl group;
- the peak at 3330 cm^{-1} associated with the O-H stretching.

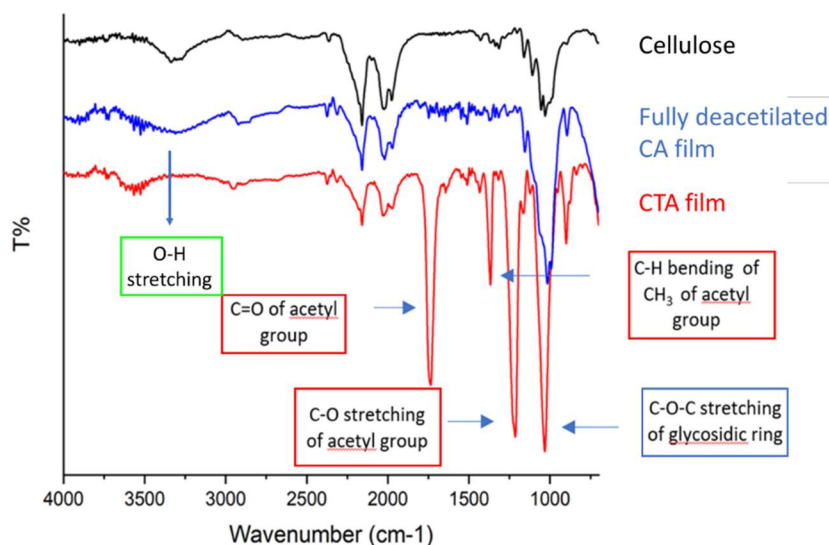


Fig. 5 FTIR-ATR spectra of pure cellulose (Whatman Paper), a fully deacetylated CA film and a CTA film are compared. In red, probe peaks associated with the acetyl group, in green, the probe peak associated with the hydroxyl group and, in blue, the reference peak ascribed to the C-O-C stretching mode of the glycosidic ring.

Thermogravimetric Analysis (TGA). Thermogravimetric Analysis was carried out to test the variation in thermal stability on samples before and after the induced deacetylation process. Tests were performed in a nitrogen atmosphere at a heating rate of $10\text{ }^{\circ}\text{C}/\text{min}$ over a temperature range of $25\text{-}500\text{ }^{\circ}\text{C}$, with an initial sample weight of approximately 5 mg using an SDT 650 thermal analyzer (TA).

Tensile test. Tensile tests have been performed on motion picture film ($5\times 1\text{ cm}$) before and after the induced degradation process to evaluate how mechanical properties vary during this test. Measurements were carried out using a Discovery HR-3 rheometer (TA Instruments) in a tension fixture mode, setting a loading gap of

2 cm and applying an axial force of 40 N. The loading gap corresponds to the space between the two clamps of the instrument and is equivalent to L_0 ; the step termination corresponds to the final distance between the two clamps and depends on the maximum stress to which the samples were subjected (L). The specimens fixed at the two clamps were subjected to tensile stress on the long side at a rate of 94 $\mu\text{m/s}$. From each measurement, a graph of the gap between the two clamps (μm) vs the applied axial force (N) is obtained.

The Young's Modulus (E) is calculated as follows:

$$E = \frac{\sigma}{\varepsilon} \quad (3.6)$$

Where σ is the applied stress given by the F/A ratio where F is the applied tensile stress (in N) and A is the cross-section of the film (in m^2) and ε is the strain.

In particular, σ is the applied axial force per unit area (Pa: N/m^2). The measurements were carried out on fragments of the motion picture film (with a length of 5 cm) having a thickness of 125 μm and a width of 16 mm.

ε is defined as:

$$\varepsilon = \frac{L-L_0}{L_0} \times 100 \quad (3.7)$$

Where L is the final gap between the two clamps (μm) and L_0 is the initial loading gap (μm).

Therefore Young's Modulus is obtained through the linear fitting of the portion of the σ/ε graphs corresponding to the range in which the material manifests elastic behavior: E corresponds to the slope a of the obtained $y = ax + b$ straight lines (Fig. 6).

Five measurements were performed for each sample and the average value with its standard deviation is reported.

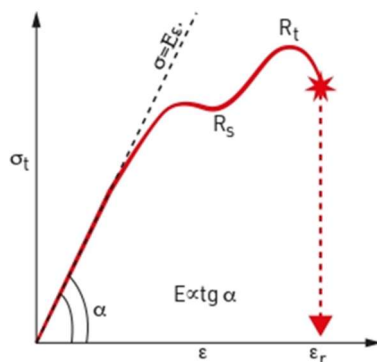


Fig. 6 Calculation of Young's Modulus (E) as the slope of the elastic region in the graphs stress (σ) vs strain (ϵ) obtained from the tensile test.

3.2 Results and Discussion

3.2.1 The high acidity induction method (HCl5M)

Samples subjected to this degradation protocol were first exposed to a saturated atmosphere of HCl 5M for 2, 4, 8, 10, 12, 14, 16 days for the CTA-based films and for 3, 6, 9, 12, 15, 2, 25, 30 for the real motion picture films.

3.2.1.1 CTA-based films (FX_HCl5M)

Analyses of CTA-based films are performed in order to understand the behavior associated only with the CTA support, without emulsion and plasticizers. The samples are labeled as *FX_HCl5M* where "X" is a number indicating the duration of the exposition of the fragments of films to the high acidity conditions (in days).

Solubility tests. In Tab. 5, the results of the solubility tests were reported. The solubility of cellulose acetates is strongly dependent on the average degree of substitution [19]: cellulose acetate with the highest degree of substitution is soluble in chlorinated solvents such as chloroform and dichloromethane; as the weight percentage of acetyls decreases, it becomes progressively soluble in other solvents such as acetone, 2-methoxyethanol and water; in each of these solvents, cellulose acetate is soluble in a very narrow range of values of acetyl content as reported in

Table 3. The solubility of cellulose acetates in these solvents, however, depends not only on the average DS, but also on the position of the substituents within the glucose ring and the chain length of the polymer. The substitution on the C6 of the ring, for example, strongly determines the solubility of the polymer: solubility in water was observed only for cellulose acetates of DS<0.8 in samples with few acetyls [20]. . The extent of solubilization was assessed qualitatively after 48 hours, indicating with the color green the full solubilization, with yellow the swelling of the sample/the partial solubility and with red insolubility..

Tab. 5 Solubility tests on artificially degraded CTA-based films with the degradation protocol HCl5M for 2, 4, 6, 8, 10, 12, 14, 16 days.

Solvent	Sample								
	F0	F2	F4	F6	F8	F10	F12	F14	F16
Chloroform	●	●	●	●	●	●	●	●	●
Acetone	●	●	●	●	●	●	●	●	●
2-methoxy-ethanol	●	●	●	●	●	●	●	●	●
Water	●	●	●	●	●	●	●	●	●

●: SOLUBLE ●: PARTIALLY SOLUBLE/SWELLED ●: INSOLUBLE.

From this first, preliminary and qualitative test, a progressive change in the solubility of the material subjected to HCl atmosphere exposition was evident:

- F0 (the unaged CTA film with an acetyl content between 43.0-44.8%) is soluble in chloroform;
- F2_HCl5M solubilizes in chloroform and swells in acetone and exhibits a behavior similar to F0, but maybe with some traces of deacetylation;
- F4 and F6_HCl5M are no longer soluble in chloroform (only F4_HCl5M swells in it) and are partially soluble in acetone, showing a behavior more similar to pure CDA (acetyl content: 36.5-42.2%) than to CTA;

- F8 and F10_HCl5M are partially soluble in 2-methoxy-ethanol (after 48 hours fragments appear swelled, rounded and opaque), a behavior ascribable to a cellulose monoacetate (CMA, acetyl content: 22.2-32.2%);
- F12 and F14_HCl5M are partially soluble in water, showing a behavior typical of cellulose acetate with a degree of substitution between 0.6 and 0.9 (“0-CA” acetyl content 13.0-18.6%);
- F16_HCl5M is insoluble in every solvent probably because is almost completely deacetylated as cellulose (acetyl content < 13.0%).

This trend could be considered a first, qualitative indicator of the occurrence of the progressive deacetylation process during the test. The incomplete solubilization of some samples and the capacity of solubilization/partial solubilization of these samples in more than one solvent could be ascribed to the inhomogeneity of the deacetylation process during the experiment or to the fact that CA is insoluble in any solvent at some DSs.

Gravimetry test. Gravimetry data reported in Fig. 7A indicate a progressive weight loss of the samples during the test. For the first six days of exposition to HCl 5M atmosphere, the decrease in weight is low (2.97 ± 0.01 wt% for F6_HCl5M) and started to increase more rapidly after the sixth day (9.1 ± 0.4 wt% is measured for F8_HCl5M) up to a loss of 32 ± 2 wt% after sixteen days (sample F16_HCl5).

Free acidity. It is possible to appreciate an increase of the free acidity (Fig. 7B) from 0.06 ± 0.01 % (F0) to 3.2 ± 0.2 % (F16_HCl5M). It is an opposite but coherent trend with both the weight loss (Fig. 7A) and the acetyl content (Fig. 7C). Unlike other data, the rate of the increase of free acidity does not show a variation after the 6th day, but it is quite homogeneous for the whole period.

Acetyl content via HSM. To measure the amount of acetyl content (%) for each sample we based on a protocol reported in ASTM D 871-96 (which was developed

for pure CTA and we adapted for motion picture films). This procedure cannot discriminate between the acetyl content (the acetic acid esterified onto the cellulose backbone of the polymer) and the free acidity (the unesterified acetic acid absorbed in the film). Therefore, to better evaluate the actual acetyl content, the free acidity value was calculated and then subtracted from the acetyl content value obtained via HSM. To calculate the free acidity we use the protocol described in the previous paragraph. In Fig. 7C, acetyl content with (red line) and without (black line) the subtraction of the free acidity is reported: it is evident that the correction is more important for samples exposed to the HCl atmosphere for longer periods, because of the increase in free acidity.

It is very interesting to note that the acetyl content change has the same trend of the weight loss: the acetyl content decreased very slowly from $45\pm 1\%$ (F0) to $37.5\pm 0.3\%$ for F6_HCl5M and more rapidly after the sixth day, until $4.9\pm 0.5\%$ for F16_HCl5M.

Comparing the correct acetyl content obtained with the HSM to values reported in Tab. 4, it is possible to make the following considerations:

- F0 (acetyl content $45\pm 1\%$) is ascribable to a CTA (range of acetyl content 44.8-43.0%);
- F2_HCl5M ($41.4\pm 0.2\%$), F4_HCl5M ($37.84\pm 0.03\%$) and F6_HCl5M ($37.5\pm 0.3\%$) are classifiable as CDA (range of acetyl content 42.9-34.9%);
- F8_HCl5M ($29.8\pm 0.7\%$) and F10_HCl5M ($23\pm 2\%$) are ascribable to CMA (range of acetyl content 34.9-21.1%);
- F12_HCl5M ($13.1\pm 0.2\%$), F14_HCl5M ($11.2\pm 0.4\%$) and F16_HCl5M ($4.9\pm 0.5\%$) are classifiable as "0.-CA" (acetyl content $\leq 21.1\%$).

Moreover, the solubility trend of the samples (Table 5) is coherent with the correct acetyl content calculated via HSM: F0 is soluble in chloroform and has an acetyl content ($45\pm 1\%$) typical of cellulose triacetate (solubility in chloroform in the acetyl

content range of 43.0-44.8%, Tab. 3); F2_HCl5M (41.4±0.2%) is soluble in chloroform and swells in acetone probably because it is a CDA with a high acetyl content (solubility in acetone in the acetyl content range of 36.5-42.2%, Tab. 3); F4_HCl5M and F6_HCl5M, that are partially soluble in acetone, could be considered as CDA according to the acetyl content (37.84±0.03% and 37.5±0.3% respectively); F8_HCl5M (29.8±0.7%) and F10_HCl5M (23±2%) are CMA and are partially soluble in 2-methoxy-ethanol (solubility in 2-methoxy-ethanol in the acetyl content range of 22.3-32.2%, Tab. 3); F12_HCl5M (13.1±0.2%) and F14_HCl5M (11.2±0.4%) could be labeled as “0”-acetate and are partially soluble in water (solubility in water in the acetyl content range of 13.0-18.6%, Tab. 3); finally F16_HCl5M has an acetyl content of 4.9±0.5%, consequently, it is insoluble in any of the solvents because it is almost completely deacetylated.

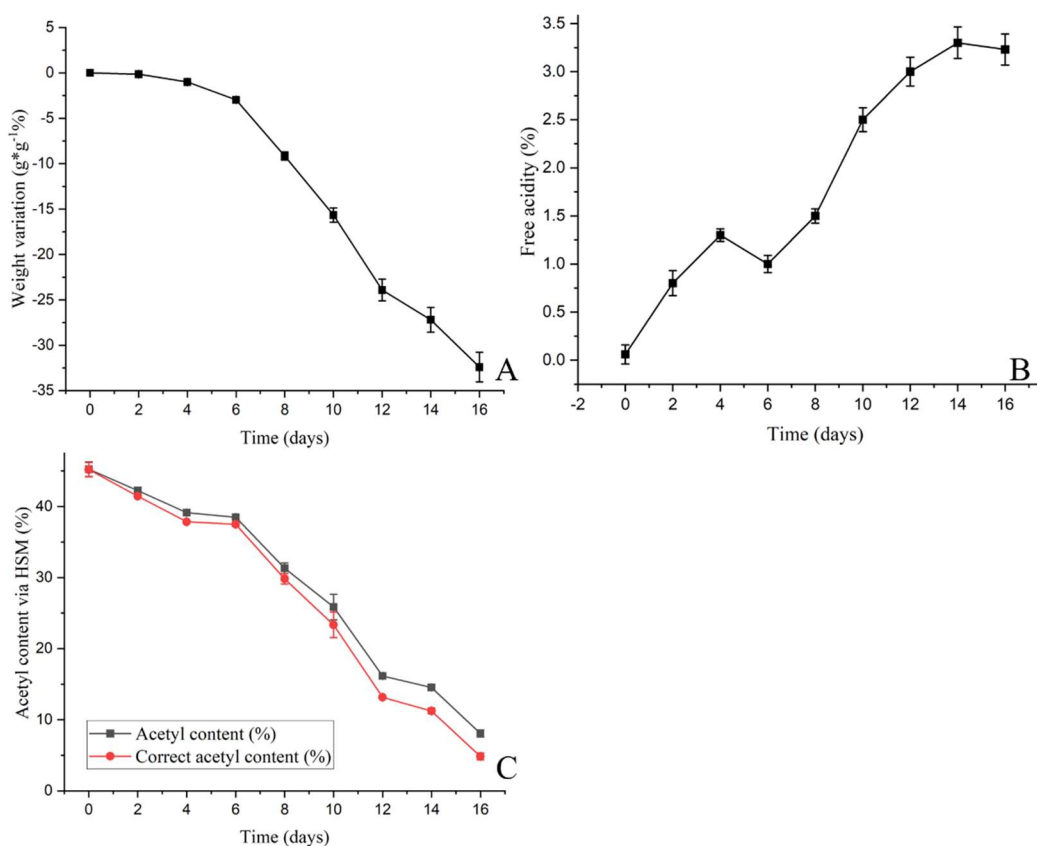


Fig. 7 (A) Weight loss (%), (B) free acidity (%) and (C) acetyl content measured via HSM (%) with (red) and without (black) the correction through free registered for CTA-

based film by varying the time of exposition to HCl 5M saturated atmosphere (F0, F2_HCl5M, F4_HCl5M, F6_HCl5M, F8_HCl5M, F10_HCl5M, F12_HCl5M, F14_HCl5M and F16_HCl5M). The results of each measurement are expressed as the average value and the corresponding standard deviation calculated for three fragments of the same film subjected to the same degradation protocol.

ATR-FTIR Spectroscopy. In Fig. 8A the spectra of all the CTA-based films subjected to the high acidity degradation protocol (HCl5M) are reported.

The intensity of all the peaks associated with the acetyl content (the peak at 1220, 1340 and 1730 cm^{-1} attributed to the C-O stretching, the C-H bending of the CH_3 and the C=O stretching, respectively[7], [16] tends to decrease by increasing the exposition to HCl atmosphere (Fig. 8B). Furthermore the broad peak associated with the OH stretching at 3330 cm^{-1} tends to increase with the duration of the test (Fig. 8C). These data are coherent with the ones obtained from the previous analyses being the intensity of these peaks strictly related to the amount of acetyls bound to the cellulose backbone. Moreover, a variation also in the peak at 1030 cm^{-1} , associated with C-O-C stretching of the glycosidic ring [7], [16], is observed: in F16_HCl5M, it broadens and moves to lower wave numbers (1018 cm^{-1}). Shoulders associated with the glycosidic bonds are observed at 1064 and 1108 cm^{-1} [21].

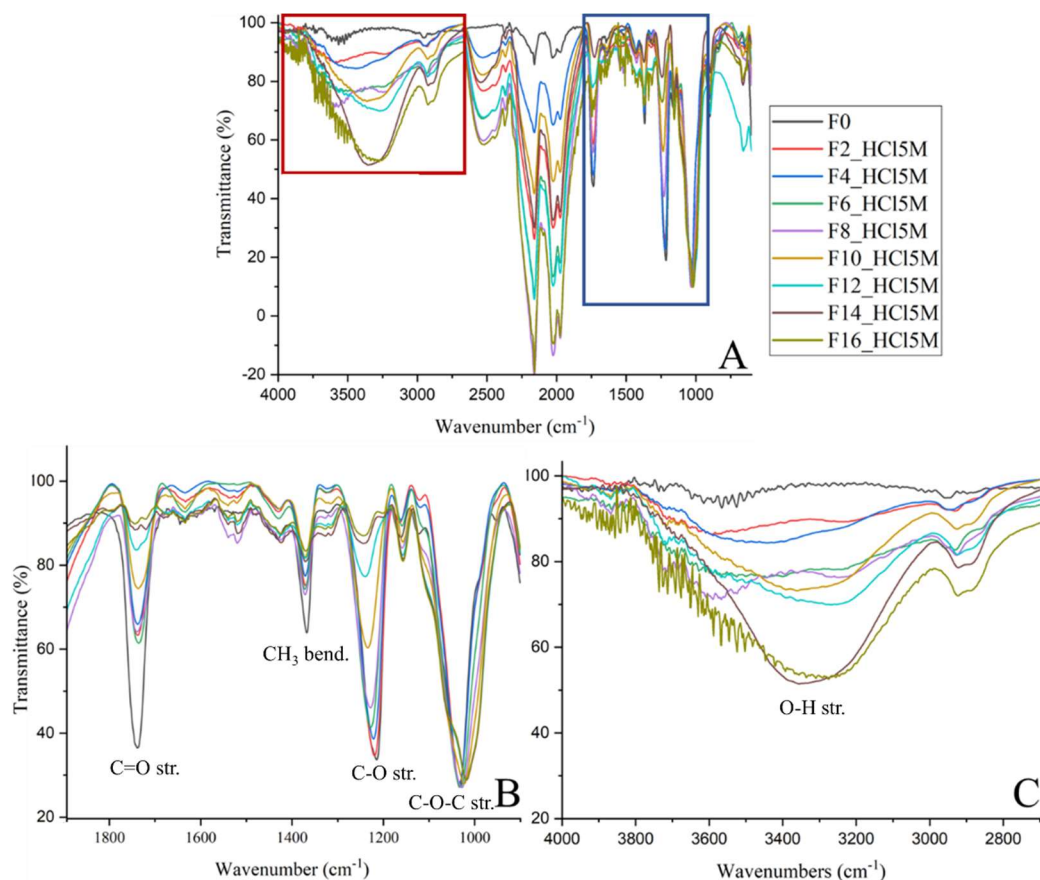


Fig. 8 FTIR-ATR spectra acquired for F0, F2_HCl5M, F4_HCl5M, F6_HCl5M, F8_HCl5M, F10_HCl5M, F12_HCl5M, F14_HCl5M, F16_HCl5M in the range (A) 4000-600, (B) 1800-600, (C) 4000-2700 cm^{-1} .

The spectra of F0, F16_HCl5M and the one of pure cellulose (acquired from a filter of Whatman Paper) are compared in Fig. 9A: while the F0 spectrum shows all the peaks associated with the acetyl group, the disappearance of these peaks in F16_HCl5M, due to deacetylation, makes this sample very similar to pure cellulose. However, the profile of the Whatman paper spectrum in the region between 1200 and 900 cm^{-1} shows some differences from the one of F16_HCl5M. The diversity between the two spectra lies in the degree of crystallinity and polymorphism [22] (Fig. 9B): while the spectrum of the Whatman paper is very similar to the one of the highly crystalline cellulose (I polymorph), the spectrum of F16_HCl5M is much more similar to the spectrum of amorphous cellulose [22]. This result is easily

explicable: the regeneration of -OH groups on the cellulose backbone of CTA is caused by deacetylation and occurs on the already formed and solid CTA films. The regenerated cellulose chains, locked in their position, are not free to generate new hydrogen bonds, consequently, the formation of crystallites is inhibited and an amorphous material is obtained.

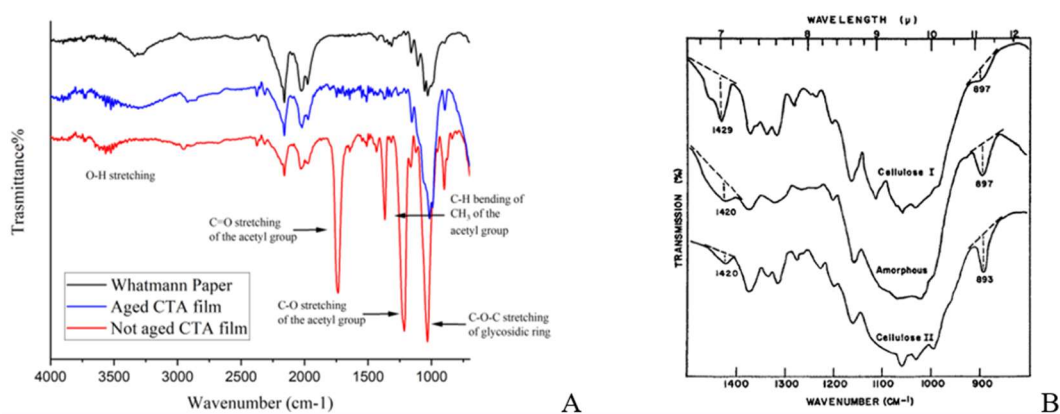


Fig. 9 (A) F0 (red), F16_HCl5M (blue) and pure cellulose (Whatman paper, black) FTIR-ATR spectra; (B) FTIR spectra of cellulose I, amorphous cellulose and cellulose II[22].

In Fig. 10A the ratios I_{1120}/I_{1030} , I_{1750}/I_{1030} and I_{3330}/I_{1030} are reported as a function of time. Considering the variation in the rate of intensity I_{1120}/I_{1030} , a decrease is observed from 0.94 ± 0.04 (F0) to 0.13 ± 0.04 (F16_HCl5M) due to the decrease in the intensity of the peak at 1120 cm^{-1} . Also the ratio I_{1750}/I_{1030} has been calculated and a decrease from 0.83 ± 0.05 (F0) to 0.13 ± 0.09 (F16_HCl5M) is observed. As expected, an opposite trend is observed for the ratio I_{3330}/I_{1030} , which switches from a value of 0.04 ± 0.01 (F0) to 0.44 ± 0.04 (F16_HCl5M). While the variation in the two first ratios could be ascribed to the deacetylation process, it is reasonable to assume that the trend of I_{3330}/I_{1030} ratio could be altered by the high RH of the environment (i.e. the hermetic chambers where the degradation test is carried out), being the peak at 3330 cm^{-1} associated with the stretching of the O-H group. In addition to this, the increase in the polarity of the system with the progress of deacetylation makes it more affine

to environmental moisture, causing an increase in the hydroxyl content as the degradation test progresses.

The trends of the two ratios associated with the acetyl group are quite coherent but the one associated with I_{1120}/I_{1030} seems to be more linear and sensitive to the acetyl content variation than I_{1750}/I_{1030} ratio, in particular in the first period of the experiment (0-6 days). To verify this point, we registered a spectrum on a film cast from a CDA powder (with an acetyl content of 39.8% provided by the manufacturer, Fig. 10B) and we obtained the following ratios: 0.88 ± 0.04 for I_{1120}/I_{1030} , 0.76 ± 0.05 for I_{1750}/I_{1030} and 0.06 ± 0.01 for I_{3330}/I_{1030} . The I_{1120}/I_{1030} ratio is coherent with the one obtained from F2, F4 and F6_HCl15, which are the ones ascribable to CDA according to the acetyl content and the solubility test. On the contrary, I_{1750}/I_{1030} ratios calculated for F2 and F4_HCl15M (0.52 ± 0.05 and 0.48 ± 0.06 , respectively) are sensibly lower than the one obtained from the CDA film. The value associated with the I_{3330}/I_{1030} ratio, instead, is lower for the CDA-based film because the ratio in our degraded sample is probably contaminated by environmental moisture.

The slopes of the linear fittings of normalized data calculated for the three intensity ratios are reported in Tab. 6.

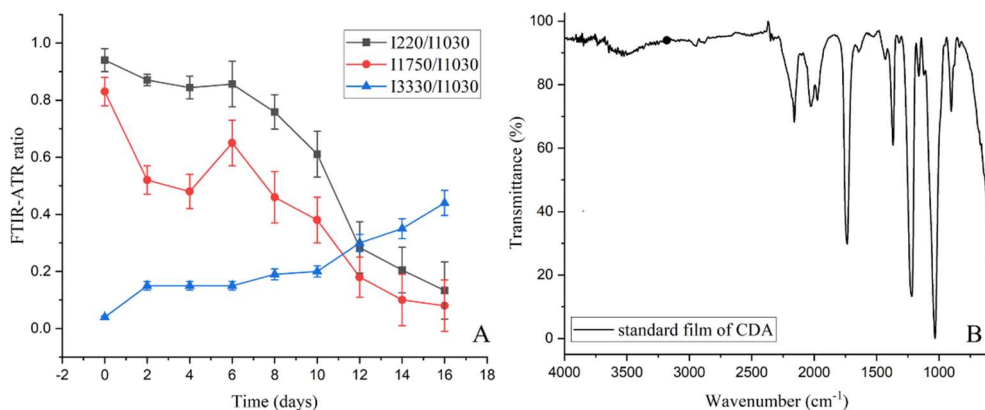


Fig. 10 (A) I_{1220}/I_{1030} (black), I_{1750}/I_{1030} (red), I_{3330}/I_{1030} (blue) ratios obtained through FTIR-ATR spectra of F0, F2_HCl15M, F4_HCl15M, F6_HCl15M, F8_HCl15M, F10_HCl15M, F12_HCl15M, F14_HCl15M, F16_HCl15M; the results of each measurement are expressed as the average value and the corresponding standard deviation calculated from five spectra acquired in different area of the film subjected to the same degradation protocol; (B) ATR-FTIR spectrum of a CDA standard film.

Tab. 6 Slopes of the linear fitting curves associated with the ATR-FTIR ratios.

ATR-FTIR ratio	0-6 days	6-16 days	0-16 days
I ₁₂₂₀ /I ₁₀₃₀	-1.7 (R ² 0.54)	-9.9 (R ² 0.94)	-7.0 (R ² 0.87)
I ₁₇₃₀ /I ₁₀₃₀			-5.7 (R ² 0.83)
I ₃₃₃₀ /I ₁₀₃₀			5.3 (R ² 0.89)

In Tab. 7, all the data associated with the samples degraded with the HCl5M methods are resumed.

Tab. 7 Resume of the data associated with samples subjected to the F_HCl5M degradation protocol.

Sample	Weight Loss (%)	Solubility Test	Correct Acetyl Content (%)	Free acidity (%)	ATR-FTIR Ratio I ₁₂₂₀ / I ₁₀₃₀	ATR-FTIR Ratio I ₁₇₃₀ / I ₁₀₃₀	ATR-FTIR Ratio I ₃₃₃₀ / I ₁₀₃₀	Degree of substitution
CDA Sigma Aldrich	0	Acetone	39.8	0.01	0.88±0.04	0.76±0.05	0.06±0.01	CDA
F0 (CTA)	0	Chloroform	45±1	0.06±0.01	0.94±0.04	0.83±0.05	0.04±0.01	CTA
F2_HCl5M	-0.15±0.01	Chloroform Acetone	41.4±0.2	0.8±0.1	0.87±0.04	0.52±0.05	0.15±0.02	CDA
F4_HCl5M	-1.01±0.01	Chloroform Acetone	37.84±0.03	1.31±0.06	0.84±0.04	0.48±0.06	0.15±0.02	CDA
F6_HCl5M	-2.97±0.01	Acetone	37.5±0.3	1.03±0.09	0.86±0.04	0.65±0.08	0.15±0.02	CDA
F8_HCl5M	-9.15±0.45	2-met.	29.8±0.7	1.56±0.07	0.76±0.04	0.46±0.09	0.19±0.019	CMA
F10_HCl5M	-15.7±0.8	2-met.	23±2	2.5±0.1	0.61±0.04	0.38±0.08	0.23±0.03	CMA
F12_HCl5M	-23±1	Water	13.1±0.2	3.04±0.15	0.28±0.04	0.28±0.07	0.37±0.06	"0"-CA
F14_HCl5M	-27±1	Water	11.2±0.4	3.3±0.2	0.21±0.04	0.20±0.09	0.35±0.04	"0"-CA
F16_HCl5M	-32±2	Unsoluble	4.9±0.5	3.2±0.2	0.13±0.04	0.013±0.09	0.44±0.04	"0"-CA/ cellulose

Thermogravimetric analysis. In Fig. 11, TGA (A) and DTG (B) profiles of F0 and the degraded samples are reported. In F0, an important weight loss is registered between 310 and 400 °C and it is associated with the pyrolysis temperature of the polymer [23]. With the extent of the time of exposition at the HCl atmosphere, this weight loss moves to lower temperatures and the range of temperatures of this transition becomes wider. In particular, from sample F8_HCl5M a shoulder is observed between 320-330 °C, which could be ascribed to the loss of the acetyl

groups. The decrease in the pyrolysis temperature starts to be relevant from sample F12_HCl5M onwards (220-330 °C). This reduction is probably due to the cleavage of the glycosidic bonds between the glycosidic units of the cellulose chain and to the consequent depolymerization, which typically occurs in an acidic environment (induced by both HCl and the acetic acid emitted during the degradation process)[12]. In F12_HCl5M, F14_HCl5M and F16_HCl5M, another weight loss is registered between 120 and 200 °C, which could be ascribed to the moisture absorbed by the films. As we previously noted examining the data of the I₃₃₃₀/I₁₀₃₀ FTIR-ATR ratio, with the extent of the deacetylation reaction and the increase in the number of the hydroxyl groups bonded to the glycosidic unit, also the affinity with water increases and consequently the capacity to absorb the environmental moisture.

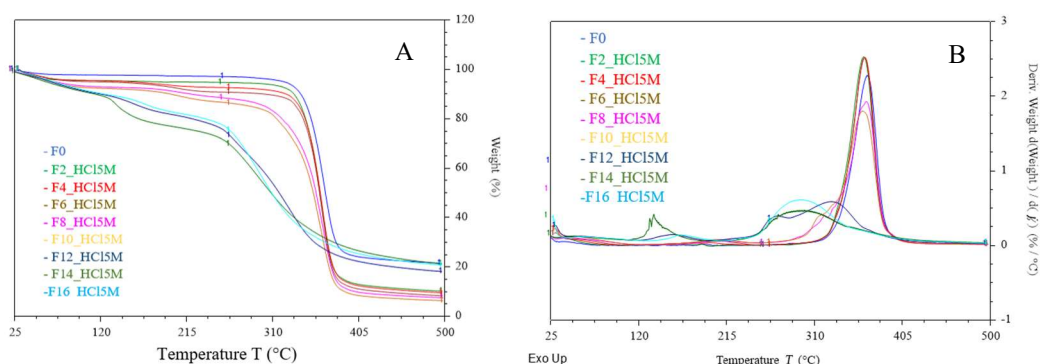


Fig. 11 (A) TGA and DTG (B) profiles registered for F0, F2_HCl5M, F4_HCl5M, F6_HCl5M, F8_HCl5M, F10_HCl5M, F12_HCl5M, F14_HCl5M, F16_HCl5M.

3.2.1.2 Real motion picture films (PX_HCl5M)

The high acidity degradation protocol has been applied also to real motion picture films. The samples are labeled as *PX_HCl5M* where “X” is a number indicating the duration of the exposition of the fragments of films to the high acidity conditions (in days).

At the end of the degradation process, samples appear as in Fig. 12. No alteration is visible up to 9 days of degradation, for whom the emulsion is sticky. Starting from

day 12 (P12_HCl5M), the first macroscopic signs of degradation are evident: the film starts to deform and curl because of the reduction in the size of the cellulose acetate support (the so-called “channeling” phenomenon)[24][6]; moreover, it loses elasticity, becoming progressively more rigid and brittle. At the same time, the emulsion starts to be very sticky and detaches easily from the support [25], as it is possible to appreciate from the micrograph reported in Fig. 13A and B.

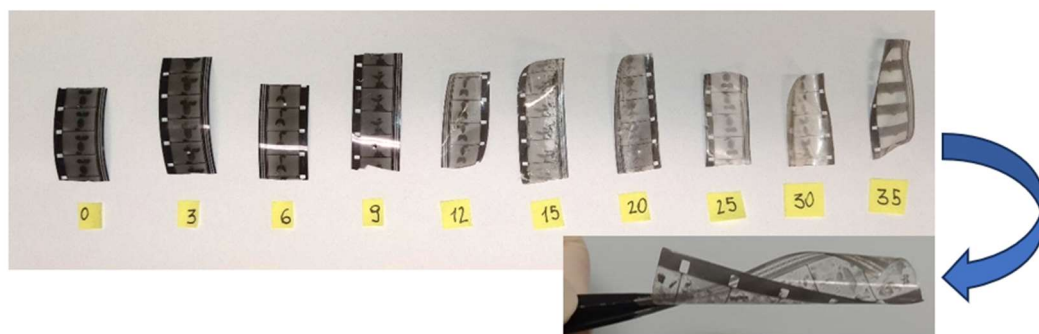


Fig. 12 Real motion picture films subjected to the high acidity degradation process (HCl5M) for 3, 6, 9, 12, 15, 20, 25, 30 days.

Micrographs reported in Figures 13C, 13D and 13E collected from the surfaces of samples P15_HCl5M, P25_HCl5M and P30_HCl5M show the presence of needle-shaped crystals and microbubbles, probably due to the exudation of plasticizers [26]. In particular, the needle-shaped crystals could be associated with triphenyl phosphate, while the microbubbles with phthalates [26], [27].

For this set of samples, the results of the solubility tests are not reported because motion picture films were found to be insoluble in any of the above-reported solvents. This is probably due to the presence of plasticizers, which increase the stability of the support.

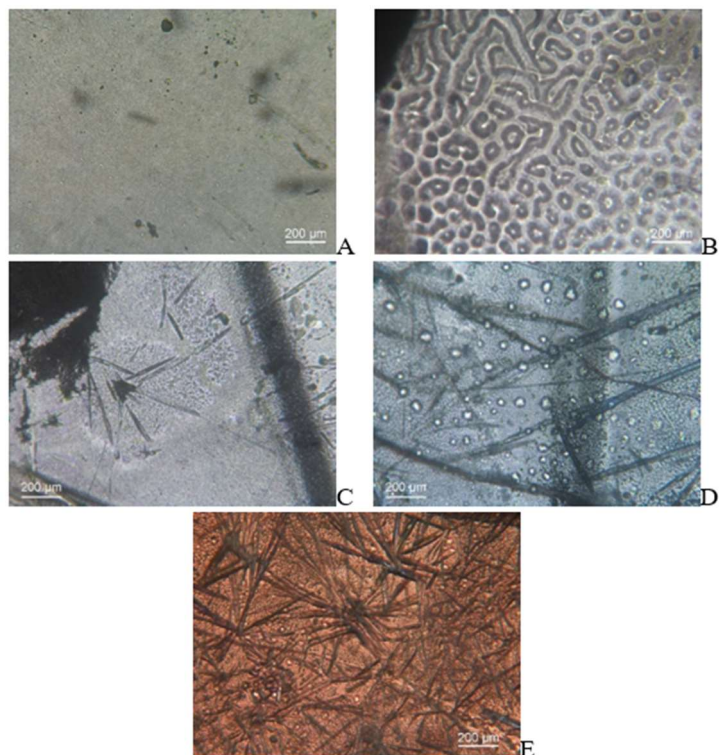


Fig. 13 micrographs of F0 (A) and P9_HCl5M (B) to show the dewetting of the emulsion layer; micrographs of P15_HCl5M (C), P20_HCl5M (D) and P30_HCl5M (E) in which the exudation of plasticizers is evident.

Gravimetry test. The weight loss during the degradation process has also been monitored and results are shown in Fig. 14A. The decrease in weight is not visible for the first 12 days of exposition to the HCl atmosphere (i.e. for P12_HCl5M the decrease in weight is $0.86 \pm 0.04\%$), while in the following 18 days the weight decreases up to the $25 \pm 1\%$.

So, comparing the results of the gravimetry tests for CTA-based films and real motion picture films, it is evident that the weight loss is both lower and slower for the latest ones. These differences may be attributable to three different reasons:

- the emulsion is strongly hygroscopic and it is able to absorb moisture; for this reason, it is reasonable to assume that a large part of the weight recorded post-

exposition, especially for the more degraded samples, is attributable to the presence of retained water in the residues of the emulsion layer;

- the emulsion, acting as a protective, makes the diffusion of acid within the cellulose triacetate support less rapid, slowing its degradation processes;
- the plasticizers increase the stability of the support.

Free acidity. Free acidity (Fig. 14B) increases during the degradation protocol, starting from a value of 0.02 ± 0.01 for P0 to a value of 3.25 ± 0.2 for P30_HCl5M. This value is equal to the one reported for F16_HCl5M ($3.23 \pm 0.2\%$, see Figure 7B), showing that the amount of free acidity emitted by CTA-based film is equal to the one emitted by real motion picture films after being exposed to the same conditions twice as long. This is probably due to the stabilization effect of both the emulsion layer and plasticizers.

Also in the case of free acidity, a variation in the rate of emission of acetic acid is detected on the 9th day of the experiment.

Acetyl content via HSM. In Fig. 14C, the acetyl content calculated through the HSM and corrected as mentioned above (i.e. by subtracting free acidity values) is reported: the original P0 is a cellulose diacetate with an acetyl content of $41.7 \pm 0.7\%$. A very slow variation in the acetyl content is observed in the first 9 days (the acetyl content decreases only up to $39.2 \pm 0.4\%$ for P9_HCl5M, while a more rapid decrease is detected from 9 to 30 days of exposition to the HCl atmosphere (the acetyl content decreases up to $7.0 \pm 0.8\%$ for P30_HCl5M).

By comparing the data in Figure 14A (weight loss) and acetyl content (Figure 14C) it is possible to note that the increase in the rate of weight loss and deacetylation is observed after 12 and 9 days, respectively.

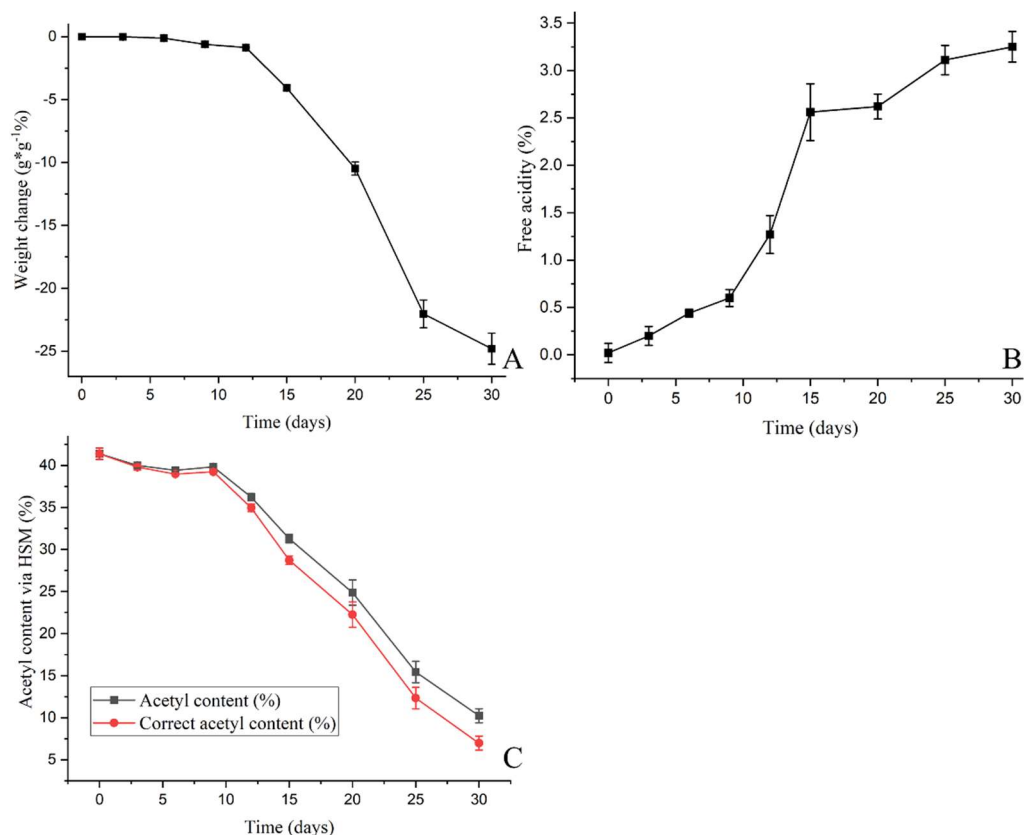


Fig. 14 (A) Weight loss, (B) free acidity and (C) acetyl content with (red) and without (black) the correction with the free acidity calculated via HSM for the HCl5M samples: P3, P6, P9, P12, P15, P20, P25, P30. The results of each measurement are expressed as the average value and the corresponding standard deviation calculated for three fragments of the same film subjected to the same degradation protocol.

FTIR-ATR Spectroscopy. Examining the FTIR-ATR spectrum of P0, a further confirmation of the nature of the support (cellulose acetate) has been obtained. In Fig. 15, the spectra of P0 registered on both the support and the emulsion layer are reported. From the spectrum registered on the emulsion layer, characteristic peaks ascribed to proteic materials (collagen) are detected [28]: peaks at 1018 and 1064 cm^{-1} are due to the CO and COC stretching; absorption at 1234 cm^{-1} is ascribable to the amide III (CN stretching and NH bonding); peaks at 1331 and 1446 cm^{-1} , are attributable to the CH₂ and CH₃ bending; peak at 1527 cm^{-1} is due to amide II (CN stretching and NH bending) and the one at 1620 cm^{-1} to the amide I (C=O stretching); peaks at 2874 and 2930 cm^{-1} are assigned to aliphatics (CH stretching and CH₃

stretching); the broad band between 3500–3300 cm^{-1} is related to NH and OH stretching. On the support side, peaks correspond to the ones of cellulose acetate (Fig. 10).

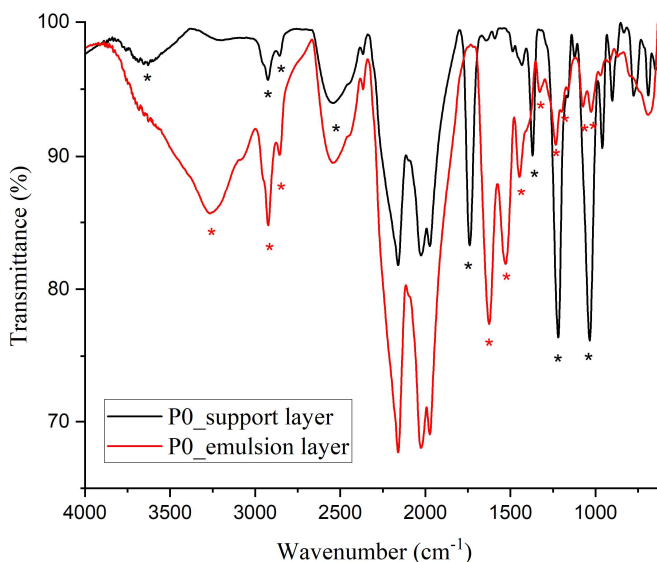


Fig. 15 ATR-FTIR spectrum of P0 acquired on the side of the support layer (black) and the emulsion layer (red). Characteristics peaks of collagen are labeled with a red “*”, the ones of CA with a black “*”.

The following evaluations have been formulated on spectra acquired on the support side.

In Fig. 16A spectra of P0, P3_HCl5M, P6_HCl5M, P9_HCl5M, P12_HCl5M, P15_HCl5M, P20_HCl5M, P25_HCl5M, P30_HCl5M are shown. Also in this case, as observed for the ATR-FTIR spectra collected from CTA films (Figure 8) it is possible to appreciate a decrease in the intensity of the peaks associated with the acetyl group (16B) and an increase in the ones ascribable to the OH stretching (16C) by increasing the degradation period.

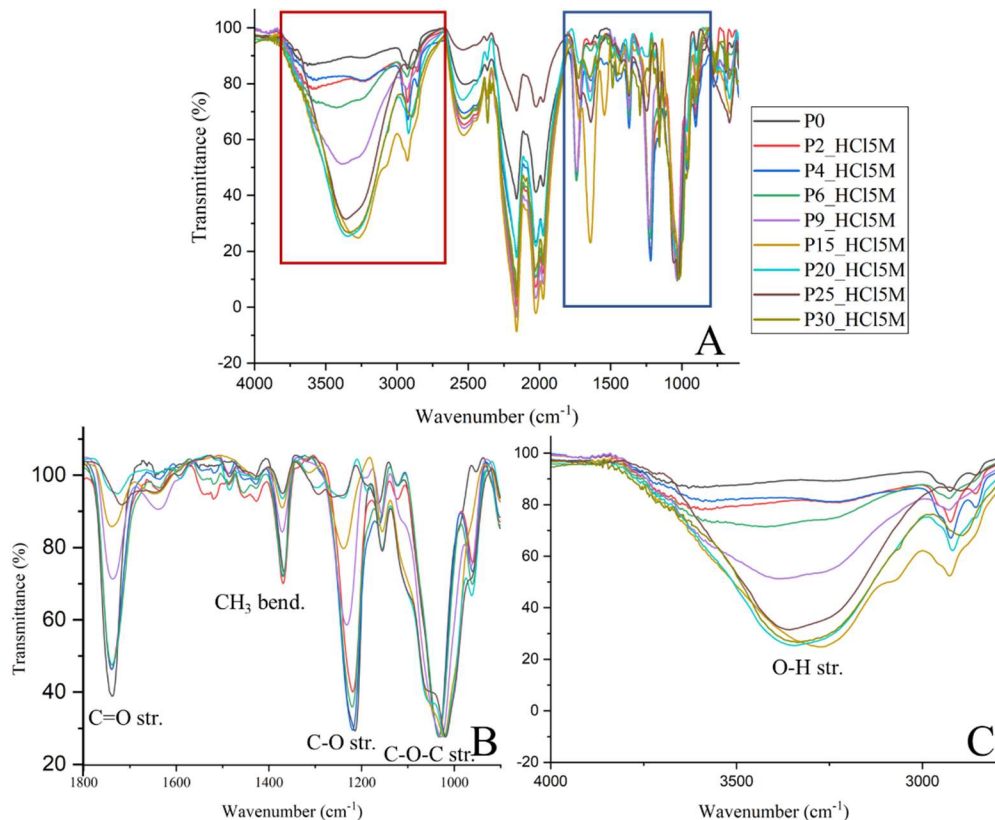


Fig. 16_HCl5M, P6_HCl5M, P9_HCl5M, P15_HCl5M, P20_HCl5M, P25_HCl5M, P30_HCl5M in the range 4000-600 cm^{-1} (A), 1800-600 cm^{-1} (B) and 4000-2800 cm^{-1} (C).

Consequently, a decrease in the ratios I_{1220}/I_{1030} and I_{1730}/I_{1030} is observed (from $0.91 \pm 0.04/0.86 \pm 0.04$ for P0 to $0.15 \pm 0.01/0.13 \pm 0.03$ for P30_HCl5M), while an increase is detected for I_{3330}/I_{1030} (from 0.13 ± 0.04 for P0 to 0.8 ± 0.1 for P30_HCl5M), (Fig. 17). All the ratios, show the same trend observed for the acetyl content via HSM indicating an important change in the rate of deacetylation/hydrolyzation after the 9th day of the text as also confirmed by the slopes of the curves in the time ranges 0-9 and 9-30 days reported in Tab. 8.

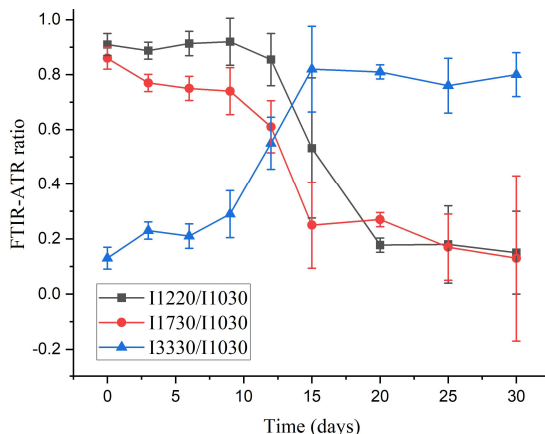


Fig. 17 FTIR-ATR ratios I_{1220}/I_{1030} (black), I_{1730}/I_{1030} (red), I_{3330}/I_{1030} (blue); the results of each measurement are expressed as the average value and the corresponding standard deviation calculated from five spectra acquired in different areas of the film subjected to the same degradation protocol.

Tab. 8 Slopes of the linear fitting curves associated with the ATR-FTIR ratios.

ATR-FTIR ratio	0-9 days	9-30 days	0-30 days
I_{1220}/I_{1030}	-0.9 (R^2 0.28)	-9.27 (R^2 0.96)	-4.0 (R^2 0.87)
I_{1730}/I_{1030}	-1.7 (R^2 0.80)	-11.1 (R^2 0.93)	-3.9 (R^2 0.88)
I_{3330}/I_{1030}	2.2 (R^2 0.80)	12.8 (R^2 0.99)	3.8 (R^2 0.80)

The calculation of the acetyl content using peaks associated with the acetyl groups (in particular the C-O stretching at 1220 cm^{-1}) as probes peaks was proposed by Fei et al. (2017) [16] for the study of pure CTA, while Nunes et al. (2020) [18] suggest the use of the OH stretching (at 3330 cm^{-1}). Indeed plasticizers typically added to motion picture films (such as diethyl phthalate (DEP) and triphenyl phosphate (TPP)) could affect the area of the spectrum where the acetyl group peaks appear. To characterize plasticizers present inside the support of our samples, we extracted them following the procedure proposed by Kemper and Lichtblau (2019) [29] and analyzed their FTIR spectra: typical peaks associated with both DEP and TPP are detected (Fig. 18). In particular, it was possible to see how the peak at 1195 cm^{-1} ,

ascribable to the P=O stretching (DEP) and the ester groups of phthalates (TTP), appears in the proximity of the C-O stretching of the acetyl group at 1220 cm^{-1} , but do not overlap with it. On the contrary, the peak associated with the C=O stretching in DEP at 1730 cm^{-1} overlaps with the one of CA.

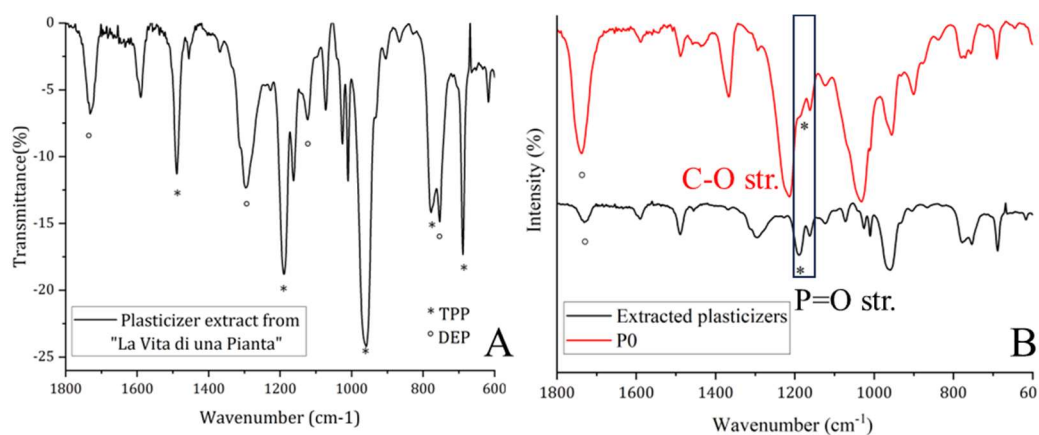


Fig. 18 (A) FTIR-ATR of the extracted plasticizers from P0 and peaks assigned to TPP (“*”) and DEP (“o”); (B) comparison between the spectra of P0 (red) and the extracted plasticizers (black).

In addition, the intensity of the OH stretching could likely be altered by the high environmental moisture present in the degradation chamber as in CTA-based films. The I_{3330}/I_{1030} could be compromised, consequently.

Therefore, for our purpose, the C-O stretching of the acetyl group (1220 cm^{-1}) has been chosen as the most accurate probe peak for motion picture films. In fact, as it is possible to appreciate from Tab. 9, the correspondence between the acetyl content and ATR-FTIR ratios, according also to previous tests conducted on CTA-based films, is better for the ratio I_{1220}/I_{1030} .

A good agreement between these data, the corresponding acetyl content (Tab. 9) and the results obtained for CTA-based films (Tab. 7) is observed. Then the following considerations can be made for the investigated samples:

- the values of the acetyl content measured for samples P0 (41.7±0.7%), P3_HCl5M (39.8±0.4%), P6_HCl5M (30.0±0.1%) and P9_HCl5M (39.2±0.4%) indicate that the support is CDA (range of acetyl content 42.9-34.9%, Tab. 4) as also confirmed by ATR-FTIR. Indeed, the I_{1220}/I_{1030} ratios (respectively 0.91±0.04, 0.89±0.03, 0.91±0.04, 0.92±0.08) are all similar to the one of standard CDA-based films (0.88±0.04).

-P12_HCl5M (34.9±0.5%) has a substitution degree between a CDA and a CMA (range of the acetyl content 34.9-21.1%, Tab. 4) and shows an ATR-FTIR ratio of 0.85±0.09.

-for P15_HCl5M the acetyl content (28.7±0.5%) could be ascribed to a CMA shows an ATR-FTIR ratio of 0.5±0.2.

-for P20_HCl5M the acetyl content (22±1.5%) could be ascribed to a cellulose acetate with an acetylation degree that is between CMA and a 0-CA (acetyl content ≤ 21.1%, Tab. 4) and shows an ATR-FTIR ratio of 0.18±0.02.

-P25_HCl5M could be considered a 0-CA (acetyl content 12±1%) and shows an ATR-FTIR ratio of 0.2±0.1.

-P30_HCl5M is almost completely deacetylated (acetyl content 7.0±0.8%) and shows an ATR-FTIR ratio of 0.1±0.3.

Tab. 9 Resume of data associated with the samples subjected to the P_HCl5M degradation protocol.

Sample	Weight Loss (%)	Acetyl Content (%)	Free acidity (%)	ATR-FTIR	ATR-FTIR	ATR-FTIR	Degree of substitution
				Ratio I_{1220}/I_{1030}	Ratio I_{1730}/I_{1030}	Ratio I_{3330}/I_{1030}	
CDA	0	39.8	0.01	0.88±0.04	0.76±0.05	0.06±0.01	CDA
F0 (CTA)	0	45±1	0.06±0.01	0.94±0.04	0.83±0.05	0.04±0.01	CTA
P0	0	41.7±0.7	0.02±0.1	0.91±0.04	0.86±0.04	0.13±0.04	CDA
P3_HCl5M	-0.006±0.001	39.8±0.4	0.2±0.1	0.89±0.04	0.77±0.04	0.23±0.03	CDA
P6_HCl5M	-0.11±0.01	39.0±0.1	0.44±0.04	0.91±0.04	0.75±0.04	0.21±0.4	CDA
P9_HCl5M	-0.60±0.03	39.2±0.4	0.6±0.09	0.92±0.08	0.74±0.08	0.29±0.08	CDA
P12_HCl5M	-0.86±0.04	34.9±0.5	1.3±0.2	0.85±0.2	0.61±0.09	0.55±0.09	CDA/CMA
P15_HCl5M	-4.1±0.2	28.7±0.5	2.6±0.3	0.53±0.25	0.25±0.1	0.8±0.2	CMA
P20_HCl5M	-10.5±0.5	22.0±1.5	2.6±0.1	0.18±0.02	0.3±0.2	0.81±0.03	CMA/"0"-CA
P25_HCl5M	-22±-1	12.0±1.3	3.1±0.1	0.2±0.1	0.2±0.1	0.8±0.1	"0"-CA
P30_HCl5M	-25±1	7.0±0.8	3.2±0.2	0.15±0.01	0.1±0.3	0.8±0.1	"0"-CA/ cellulose

Thermogravimetric analysis. In Fig. 19 TGA (A) and DTG (B) profiles of the samples before and after the degradation protocol are reported. P0 profile is similar to the one of F0 (pure CTA): until the 20th day of exposition to HCl atmosphere, the profiles of the samples do not significantly vary and a unique weight loss between 310 and 400 °C, ascribable to the degradation of the polymer, is observed. From the sample P20_HCl5M onwards, a shift to lower temperatures and a widening of the range of temperatures associated with the reaction are evident (from 150 to 400 °C for P20_HCl5M and from 100 to 400 °C for P25_HCl5M). This phenomenon is probably due to the depolymerization of the sample and a consequent increase of the polydispersity of the molecular weights, promoted by the onset of the deacetylation process.

Signals present at lower temperatures (between 100 and 150 °C) could be associated with absorbed moisture.

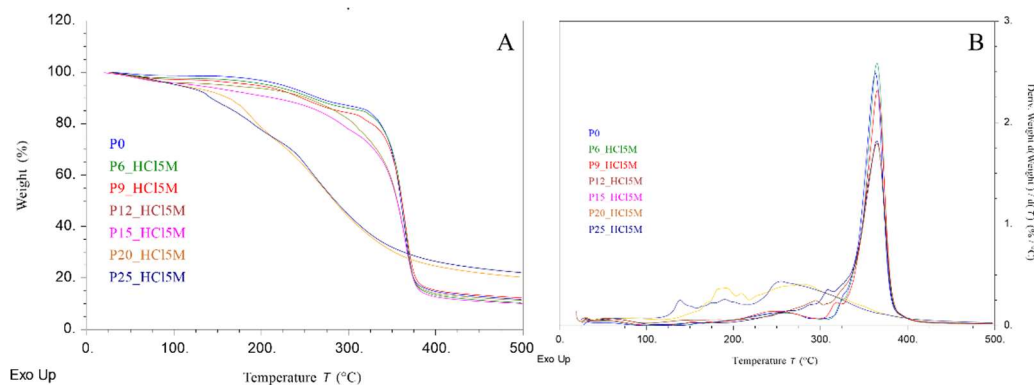


Fig. 19 TGA (A) and DTG (B) profiles of P0 and HCl5M samples: P3, P6, P9, P12, P15, P20, P25, P30.

Tensile test. In real motion picture film, we evaluate also the variation in the tensile strength induced by the degradation protocol. In Fig. 20A and B, the trend of the Axial Force vs Strain and the Young's Modulus (E) vs time (in days) of exposition to HCl are plotted. A well-defined trend is evident: as the exposition time increases, the slope of the curve Axial force vs Strain decreases and, consequently, also the value of E (from a E of 15 ± 1.5 MPa for P0 up to 9.8 ± 0.8 MPa for P25_HCl5M); this

means that samples subjected to the same stress undergo greater deformation as the degradation process goes ahead. Further confirmation of the loss in tensile strength is the fact that sample P15_HCl5M undergoes permanent plastic deformation at 40 N, while specimens P20_HCl5M and P25_HCl5M break at about 39 N and 36 N, respectively. This point confirms that, after 20 days of exposition to HCl atmosphere, the films reach an advanced state of degradation, with a consequent strong reduction of the tensile strength. The decrease in mechanical resistance could be due to both the alteration and the partial loss of the plasticizers and to the deacetylation. In fact, the formed acetic acid (but also the HCl) probably induced the hydrolysis of glycosidic bonds between the glycosidic units of the polymeric chain with a consequent lowering in the average molecular weight. Moreover, depolymerization probably promotes also the partial loss of plasticizers, (see micrographs in Fig. 13C, 13D and 13E), which also plays an important role in the reduction of the tensile strength.

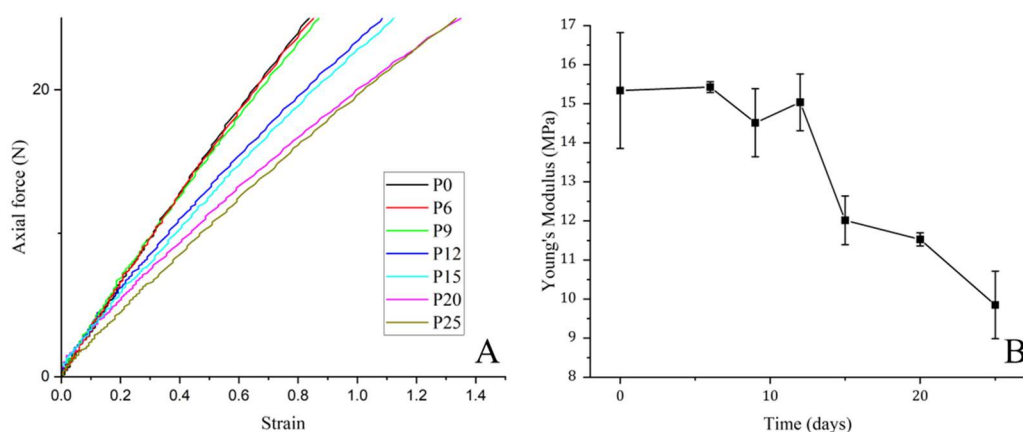


Fig. 20 (A) Axial Force (N) vs Strain graph and (B) Young's Modulus (E) vs Days of Exposition to the HCl atmosphere for P0 and HCl5M samples: P3, P6, P9, P12, P15, P20, P25, P30_HCl5M. The results of each measurement are expressed as the average value and the corresponding standard deviation calculated for five fragments of the same film subjected to the same degradation protocol.

3.2.2 The high acidity induction method (ATM2.X)

Another method that was developed to artificially induce the deacetylation process to monitor its evolution with and without the inhibitors of the “*vinegar syndrome*” is presented in this paragraph. This protocol indicated as ATM2.X involves a first step that induces the deacetylation process thanks to the exposition at an acid atmosphere, using HCl as a catalyst. Afterward, in the second step, the samples are maintained for 24 hours under hood to promote the removal of the HCl absorbed into the film; then, the third step involves the storage of the samples in sealed cells at 100% RH and their monitoring at fixed times. For CTA-based films, the third step has a duration of 12, 24, 36, 48 and 60 days, for real motion picture films of 12, 24, 36, 48 days. The idea is to evaluate the performance of the inhibitor, monitoring, in this last step, the evolution of the deacetylation process promoted by the formed acetic acid, the residual HCl and the moisture.

3.2.2.1 CTA-based films (ATM2.3)

The samples subjected to this degradation protocol will be labeled as “FY_ATM2.X” where “X” is the duration of the first step of exposition at the HCl 5M atmosphere and “Y” is the duration of the third step of exposition at 100% RH; the acronym “ATM2” means that the samples were subjected to two different atmospheres (HCl 5M and 100% RH).

For CTA-based films the duration of the first step of the protocol (exposition to the HCl 5M atmosphere to induce the deacetylation process using the HCl vapors as a catalyst of the deacetylation process) has been set to three days (ATM2.3), based on the results reported in Paragraph 3.2.1.1: between two and four days of exposition to the HCl 5M atmosphere, we registered an increase in the rate of both weight loss and deacetylation. Then, the samples are stored for 24 hours under hood, to promote the removal of most of the HCl adsorbed on the film.

The induction of the deacetylation process during the first step has been confirmed, not only with the methods reported in the previous paragraphs, but also with through

chromatography (IC): fragments of the sample F0 not exposed to HCl 5M atmosphere were maintained in water under stirring for 24 h at 38°C, and then 2.53 and 0.98 mg/L of chloride and acetate ions are detected by IC, respectively; they are probably present because of casting solvent and unreacted polymers residues. After the first step of degradation, both chloride and acetate ions were monitored again through IC; the results indicate a concentration of 24.79 mg/L of Cl⁻ and 291.78 mg/L of acetate. The following equilibration of the CTA films under hood seems to favor the removal of HCl more than acetic acid as confirmed by a further IC test: the concentration of the two species decreases to 11.32 mg/L and 220.10 mg/L, respectively. This trend can be attributed to the higher vapor pressure of the HCl that is more than 2700 times higher than acetic acid (i.e. 4200 kPa vs 1.54 kPa at 21 °C). In the third step, samples are put in hermetic chambers with an RH of 100% for different periods (12, 24, 36, 48, 60 days) to further carry on the deacetylation thanks to the acetic acid formed during the first step (and the residual HCl), which acts as a catalyst for the reaction.

In the following figures, results associated with the third step of the protocol are resumed. The time 0 of this third step is the sample F3_HCl5M.

Gravimetry test. In Fig. 21A, the weight loss for the samples after 12, 24, 36, 48 and 60 days of the third step of the degradation protocol are shown: we registered a weight loss of 38 ± 3 % after 60 days (F60_ATM2.3). Also in this case, the rate of deacetylation seems to increase after a first 24 days-long, slow phase.

Free acidity. The free acidity (Fig. 21B), as expected, increases during the third step from 1.31 ± 0.06 % (F3_HCl5M, assumed as time zero) to 2.71 ± 0.04 % (F60_ATM2.3), with an opposite but consistent trend as compared to the gravimetry (Figure 21A) and the acetyl content measurements (Figure 21C).

Acetyl content via HSM. As we can see from the acetyl content obtained via HSM and corrected with free acidity data (Fig. 21C), a decrease is observed from $42.0 \pm 0.5\%$ (F3_HCl15M, assumed as time zero) to $27 \pm 1\%$ (F60_ATM2.4).

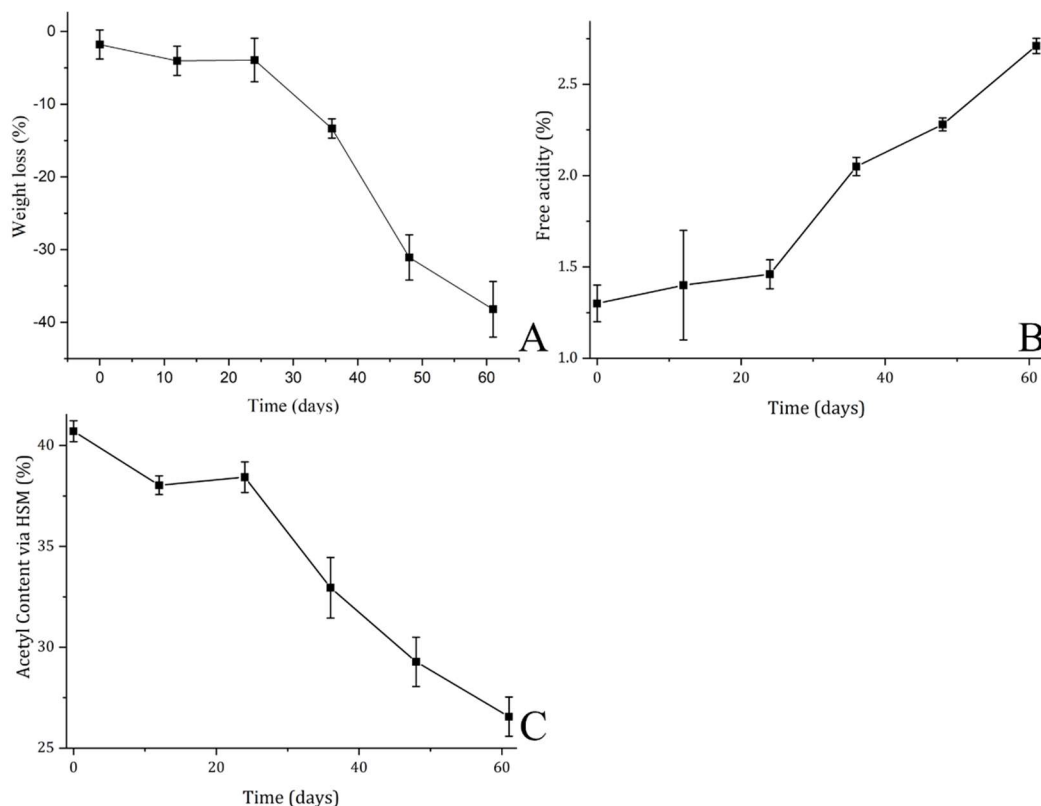


Fig. 21 (A) Weight loss, (B) free acidity and (C) correct acetyl content calculated via HSM reported for F3_HCl15M (Time 0), F12_ATM2.3, F24_ATM2.3, F36_ATM2.3, F48_ATM2.3, F60_ATM2.3. The results of each measurement are expressed as the average value and the corresponding standard deviation calculated for three fragments of the same film subjected to the same degradation protocol.

FTIR-ATR Spectroscopy. In Fig. 22 the FTIR-ATR spectra of sample F3_HCl15M (time 0), F12, F24, F36, F48, F60_ATM2.3 are reported. The intensity of peaks associated with the acetyl group (Fig. 22B), at 1220 and 1730 cm^{-1} , decreases during the third step (12-60 days, when the film fragments are hermetically maintained at 100% RH) while the intensity of the OH stretching increases (Fig. 22C).

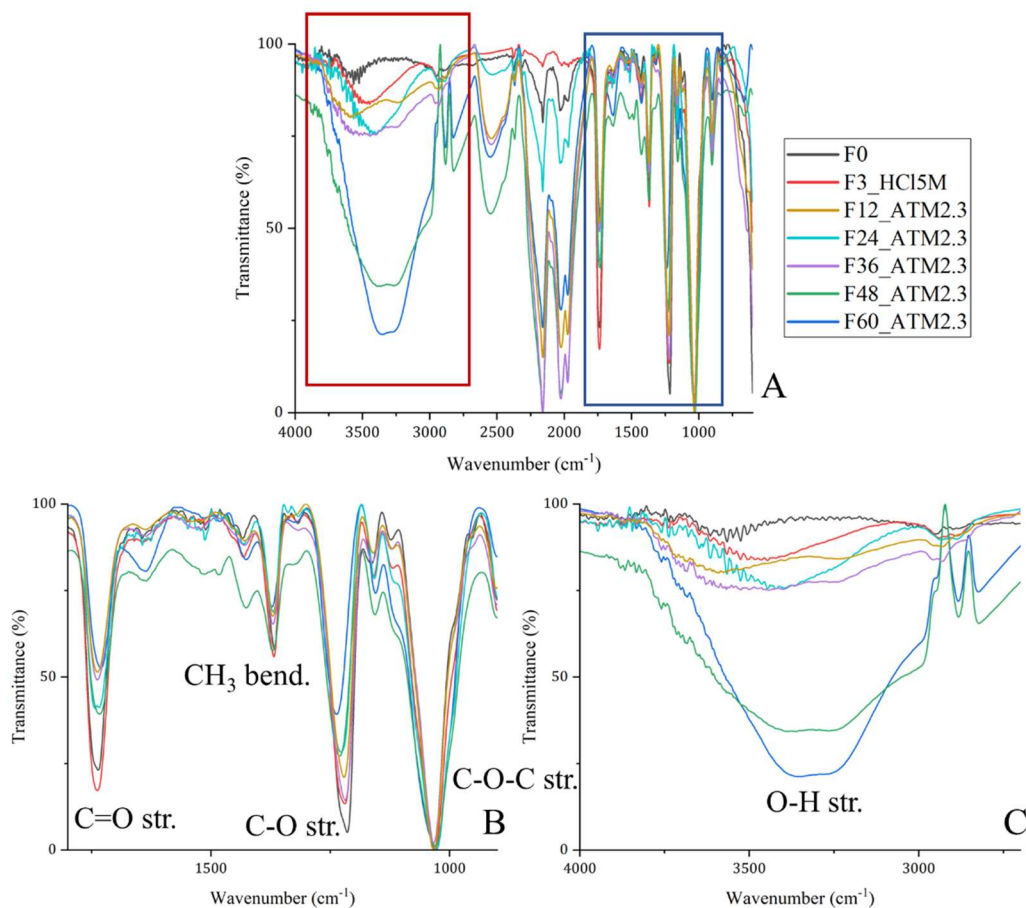


Fig. 22 (A) FTIR-ATR spectra of F0 and F3_HCl5M (time 0), F12_ATM2.3, F24_ATM2.3, F36_ATM2.3, F48_ATM2.3 and F60_ATM2.3 in the range 4000-600 (A), 1800-600 (B), 4000-2800 cm^{-1} (C).

The plots of the ratios $I_{1220/1030}$, $I_{1730/1030}$ and $I_{3330/1030}$ are reported in Figure 23. These data confirm the trend that has already been observed both for gravimetric and HSM analyses with an increase in the rate of the deacetylation process occurring after an induction period of almost 24 days.

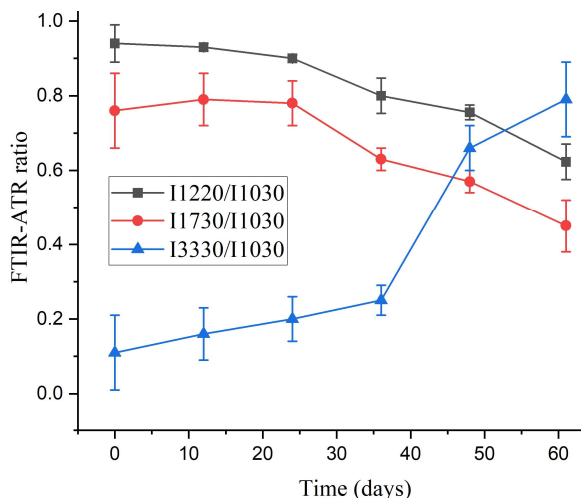


Fig. 23 FTIR-ATR ratios I₁₂₂₀/I₁₀₃₀ (black), I₁₇₃₀/I₁₀₃₀ (red), I₃₃₃₀/I₁₀₃₀ (blue). The results of each measurement are expressed as the average value and the corresponding standard deviation calculated from five spectra acquired in different areas of the film subjected to the same degradation protocol.

The slopes obtained from linear fittings of the experimental data (0-24 and 24-60 days) that are reported in Tab. 10 confirm this datum.

Tab. 10 Slopes of the linear fitting curves associated with the ATR-FTIR ratios.

ATR-FTIR ratio	0-24 days	24-48 days	0-48 days
I ₁₂₂₀ /I ₁₀₃₀	-0.5 (R ² 0.92)	-2.2 (R ² 0.97)	-1.6 (R ² 0.92)
I ₁₇₃₀ /I ₁₀₃₀	/	-2.5 (R ² 0.98)	-1.6 (R ² 0.85)
I ₃₃₃₀ /I ₁₀₃₀	0.6 (R ² 0.99)	3.1 (R ² 0.90)	1.7 (R ² 0.84)

The deacetylation process is slower than in the HCl 5M method because the film is not exposed to the catalyst for the entire duration of the degradation protocol, but the previously formed acetic acid, the residual HCl adsorbed by the film and the high RH promote the further deacetylation of the CTA film during the third step.

According to both the acetyl content and the ATR-FTIR ratios, a decrease in the degree of substitution is evident, from a CTA/CDA sample (F3_HCl5M) to a CMA (F60_ATM2.3) as reported in Tab. 11.

Tab.11 Resume of the data associated with the samples subjected to the F_ATM2.3 degradation protocol.

Sample	Weight Loss (%)	Correct Acetyl Content (%)	Free acidity (%)	ATR-FTIR Ratio I ₁₂₂₀ / I ₁₀₃₀	ATR-FTIR Ratio I ₁₇₃₀ / I ₁₀₃₀	ATR-FTIR Ratio I ₃₃₃₀ / I ₁₀₃₀	Degree of substitution
CDA Sigma Aldrich	0	39.8	0.01	0.88±0.04	0.76±0.05	0.06±0.01	CDA
F0 (CTA)	0	45±1	0.06±0.01	0.94±0.04	0.83±0.05	0.04±0.01	CTA
F3_HCl5M	-1.8±0.9	42.0±0.5	1.31±0.06	0.91±0.05	0.8±0.1	0.1±0.1	CDA
F12_ATM2.3	-4±2	38.03±0.35	1.4±0.3	0.93±0.05	0.79±0.07	0.16±0.07	CDA
F24_ATM2.3	-4±1	38.4±0.7	1.46±0.08	0.90±0.06	0.78±0.06	0.19±0.06	CDA
F36_ATM2.3	-13±1	33±1.5	2.05±0.05	0.81±0.05	0.63±0.03	0.25±0.04	CMA
F48_ATM2.3	-31±2	29±1	2.28±0.03	0.76±0.02	0.57±0.03	0.66±0.06	CMA
F60_ATM2.3	-38±3	27±1	2.71±0.04	0.62±0.05	0.45±0.07	0.8±0.1	CMA

Thermogravimetric analysis. In Fig. 24 TGA (A) and DTG (B) profiles of F0, F3_HCl5M and F60_ATM2.3 are reported. The pyrolysis temperature is identical for F0 and F3_HCl5M (between 310 and 400 °C) while a shift is registered for F60_ATM2.3: for this sample, the weight loss associated with the degradation of the polymer shifts to lower temperatures and the range of the process became wider (250-390 °C) due to the increase in the polydispersity of the molecular weights. The total shift of temperature pyrolysis is less pronounced for this method (ATM2.3) than for the HCl5M degradation protocol.

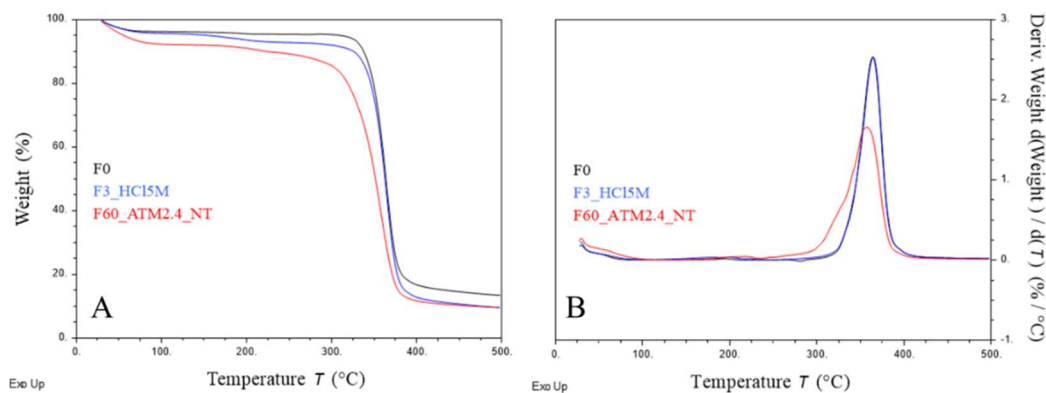


Fig.24 TGA (A) and DTG (B) profiles for F0, F3_HCl5M and F60_ATM2.4.

3.2.2.2 Real motion picture films(ATM2.9)

The samples subjected to this degradation protocol will be labeled as “PY_ATM2.X” where “X” is the duration of the first step of exposition at the HCl 5M atmosphere and “Y” is the duration of the third step of exposition at 100% RH; the acronym “ATM2” means that the samples were subjected to two different atmospheres (HCl 5M and 100% RH).

For real motion picture films we decided to set the duration of the first step to nine days (ATM2.9), based on the results reported in Paragraph 3.2.1.2: after the ninth day of exposition to HCl 5M atmosphere, an important decrease in terms of weight loss and acetyl content is registered.

Also in this case, the amount of chlorides and acetates on samples P0, P9_HCl5M was measured by means of IC by following the procedure described in Paragraph 3.2.2.1_before and after the equilibration under hood: the chloride and the acetate ions concentration in P0 were 9.32 and 12.88 mg/L, respectively, probably due to manufacture residues (chlorides) and some early degradation processes (acetate); in P9_HCl5M the content of chlorides rises until 71.49 mg/L while the content of acetates reaches the 306.57 mg/L; after the equilibration period under hood, the concentration of both chlorides and acetates decreases to 25.78 mg/L and 252.88 mg/L, respectively. By comparing the IC data obtained for these samples (i.e. real motion picture films) with the ones of CTA-based films (Paragraph 3.2.2.1) it is possible to observe that, in this case, the concentration of chlorides and acetates is higher, probably because of the presence of the emulsion layer that acts as an adsorber for both acid chloride and formed acetic acid.

In the third step, samples are put in hermetic chambers with an RH of 100% for different periods (12, 24, 36, 48 days) to further carry on the deacetylation thanks to the acetic acid formed during the first step (and the residual HCl), which acts as a catalyst for the reaction.

In the following figures, results associated with the third step of the protocol are resumed. The time 0 of this third step is the sample P9_HCl5M.

In Fig. 25, P0, P9_HCl5M and samples subjected to the degradation protocol ATM2.9 for 12, 24, 36, 48 days are shown: macroscopic symptoms of alterations are appreciable such as the partial loss of the emulsion layer, probably due to the high RH, and the matting and the curling of the support.



Fig. 25 Real motion picture films before the degradation protocol (P0), after a 9 days-long exposition to HCl 5M atmosphere (P9_HCl5M) and after ATM2.9 protocol (P12, P24, P36, P49_ATM2.9).

Gravimetry test. The total weight loss (Fig. 26A) registered after 48 days of the degradation protocol is $-11\pm 1\%$, quite lower than the weight loss measured for the HCl5M after only 30 days of exposition ($-25\pm 1\%$, Figure 7A). It is worth remembering that the calculated weight loss in real motion picture films is affected by multiple factors not only by the deacetylation, such as the partial loss of the emulsion layer and plasticizers or the absorption of moisture by the emulsion layer itself.

Free acidity. Free acidity values (Fig. 26B) have an opposite but coherent trend with the acetyl content: from a value of $0.61\pm 0.09\%$ (P9_HCl5M) to $0.81\pm 0.02\%$ (P24_ATM2.9) in the range 0-24 days and to a value of $1.85\pm 0.09\%$ for P48_ATM2.9. Also for the free acidity, the amount of the calculated unesterified acetic acid is slower for this degradation protocol than for the HCl5M (Fig. 7B).

Acetyl content via HSM. In Fig. 26C the acetyl content calculated via HSM and corrected with free acidity are reported. The registered decrease in the third step of the ATM2.9 degradation protocol rises from $39.2\pm 0.4\%$ for the sample P9_HCl5M

up to $30.5 \pm 0.4\%$ for sample P48_ATM2.9, with a total decrease of -22% (for the motion picture films subjected to HCl5M degradation protocol was -31% after only 30 days of exposition, Fig. 7C). Unlike gravimetry data, for the acetyl content, the two ranges with two different rates of decrease are visible between 0-24 days and 24-48 days. Also in this case, the rate of decrease in the acetyl content is slower than the one registered for the HCl5M degradation protocol.

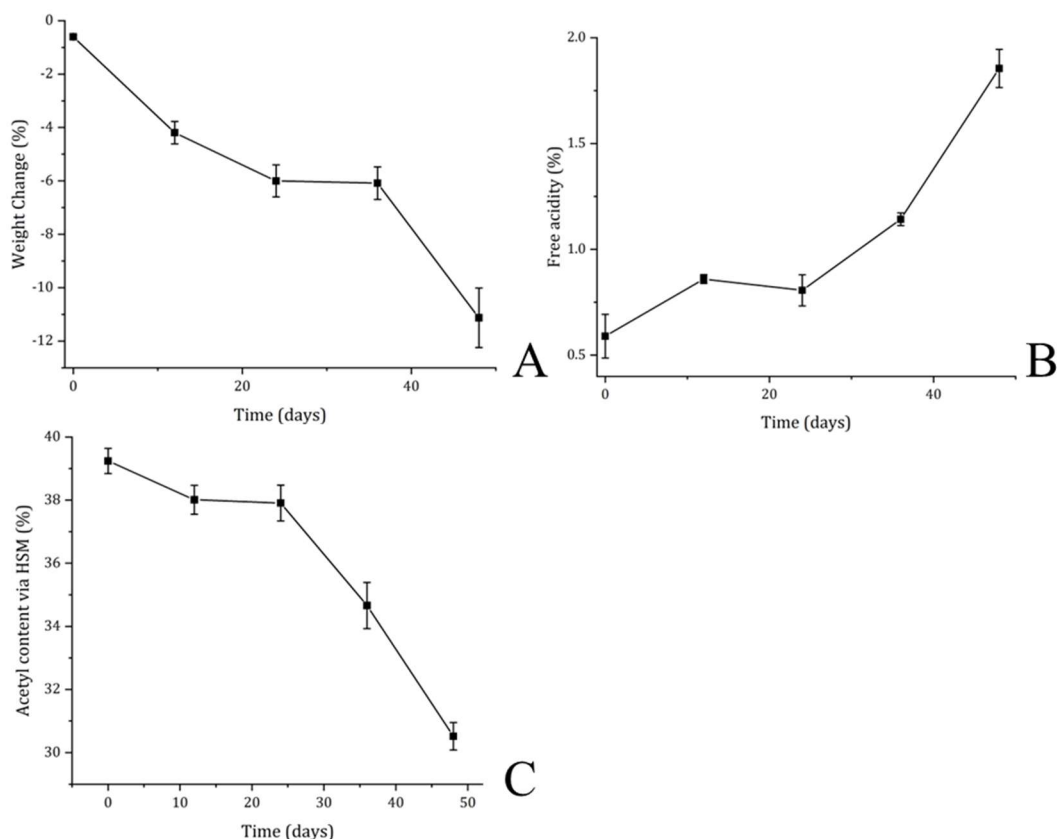


Fig. 26 (A) Weight Loss, (B) Free acidity and (C) Acetyl content calculated via HSM and corrected with free acidity values for P9_HCl5M (0 time), P12_ATM2.9, P24_ATM2.9, P36_ATM2.9, P48_ATM2.9. The results of each measurement are expressed as the average value and the corresponding standard deviation calculated for three fragments of the same film subjected to the same degradation protocol.

FTIR-ATR Spectroscopy. In Fig. 27A the spectra of P0, P9_HCl5M and P12_ATM2.9, P24_ATM2.9, P36_ATM2.9 and P48_ATM2.9 are reported. Also in

this case, the intensity of the peaks associated with the acetyl content decreases with the duration of the degradation protocol (Fig. 27B). Therefore the ratios I_{1220}/I_{1030} and I_{1730}/I_{1030} range from $0.92\pm 0.08/0.74\pm 0.08$ for P9_HCl5M to $0.45\pm 0.04/0.29\pm 0.09$ for P48_ATM2.9, respectively (Fig. 28). On the other hand, the intensity of the peak ascribable to the OH stretching increase (Fig. 27C) and, consequently, the ratio I_{3330}/I_{1030} ranges from 0.29 ± 0.08 for P9_HCl5M to 0.9 ± 0.2 for P48_ATM2.9 (Fig. 28).

The slopes of the linear fitting curves are reported in Tab. 12. Only for I_{1220}/I_{1030} the two steps of kinetics are evident (the first one is slower than the second one).

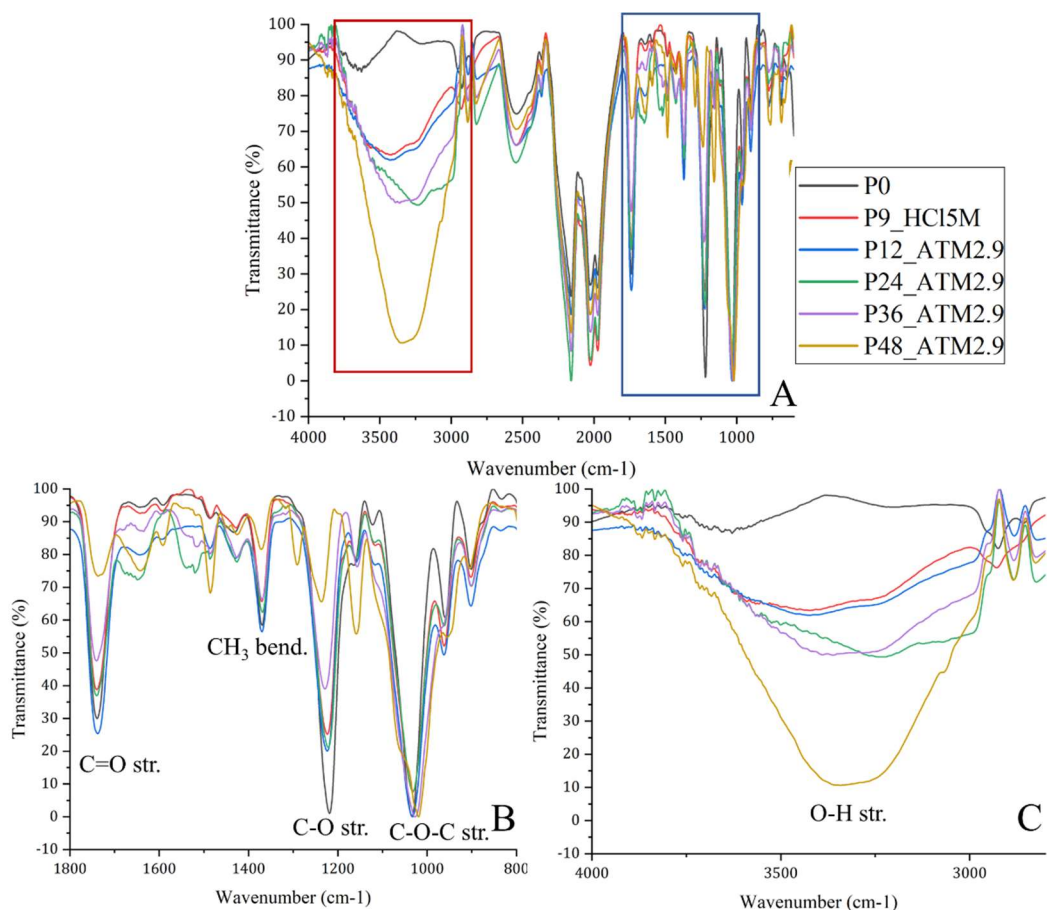


Fig. 27 (A) FTIR-ATR spectra of P0 and P9_HCl5M, P12_ATM2.9, P24_ATM2.9, P36_ATM2.9, P48_ATM2.9 in the range 4000-600 cm^{-1} (A), 1800-600 cm^{-1} (B), 4000-2800 cm^{-1} (C).

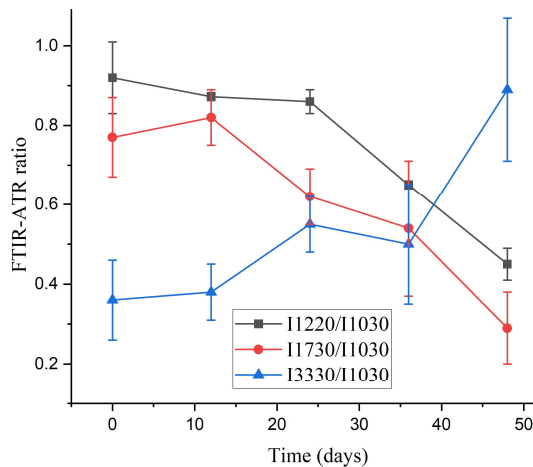


Fig. 28 FTIR-ATR ratios I_{1220}/I_{1030} (black), I_{1730}/I_{1030} (red), I_{3330}/I_{1030} (blue). The results of each measurement are expressed as the average value and the corresponding standard deviation calculated from five spectra acquired in different areas of the film subjected to the same degradation protocol.

Tab. 12 Slopes of the linear fitting curves associated with the ATR-FTIR ratios.

ATR-FTIR ratio	0-24 days	24-48 days	0-48 days
I_{1220}/I_{1030}	-0.5 (R^2 0.90)	-3.6 (R^2 0.99)	-2.1 (R^2 0.87)
I_{1730}/I_{1030}	/	/	-1.9 (R^2 0.87)
I_{3330}/I_{1030}	/	/	1.8 (R^2 0.76)

In Tab. 13 all the results associated with samples subjected to the ATM2.9 degradation protocol are resumed.

Tab. 13 Resume of the data associated with the P_ATM2.9 degradation protocol.

Sample	Weight Loss (%)	Correct Acetyl Content (%)	Free acidity (%)	ATR-FTIR Ratio I ₁₂₂₀ / I ₁₀₃₀	ATR-FTIR Ratio I ₁₇₃₀ / I ₁₀₃₀	ATR-FTIR Ratio I ₃₃₃₀ / I ₁₀₃₀	Degree of substitution
CDA Sigma Aldrich	0	39.8	0.01	0.88±0.04	0.76±0.05	0.06±0.01	CDA
F0 (CTA)	0	45±1	0.0±0.01	0.94±0.04	0.83±0.05	0.04±0.01	CTA
P0	0	41.7±0.7	0.02±0.1	0.91±0.04	0.86±0.04	0.13±0.04	CDA
P9_HCl5M	-0.60±0.03	39.2±0.4	0.6±0.09	0.92±0.08	0.74±0.08	0.29±0.08	CDA
P12_ATM2.9	-4.2±4	38.0±0.4	0.86±0.02	0.87±0.01	0.82±0.07	0.38±0.07	CDA
P24_ATM2.9	-6.0±0.6	37.9±0.6	0.81±0.07	0.86±0.03	0.62±0.07	0.55±0.07	CDA
P36_ATM2.9	-6.0±0.6	35±1	1.14±0.03	0.65±0.01	0.5±0.2	0.5±0.15	CDA-CMA
P48_ATM2.9	-11±1	30.5±0.4	1.85±0.09	0.45±0.04	0.29±0.09	0.9±0.2	CMA

Thermogravimetric analysis. As in the case of CTA-based films, the shift in the pyrolysis temperature registered via TGA (Fig. 29) is less important for this degradation method than for the HCl5M method: the pyrolysis temperature for P48_ATM2.9 shifts from a range of 310-400 °C (P0 and P9_HCl5M) to a range of 200-390 °C due to the depolymerization and the molecular weight dispersion of the CA support.

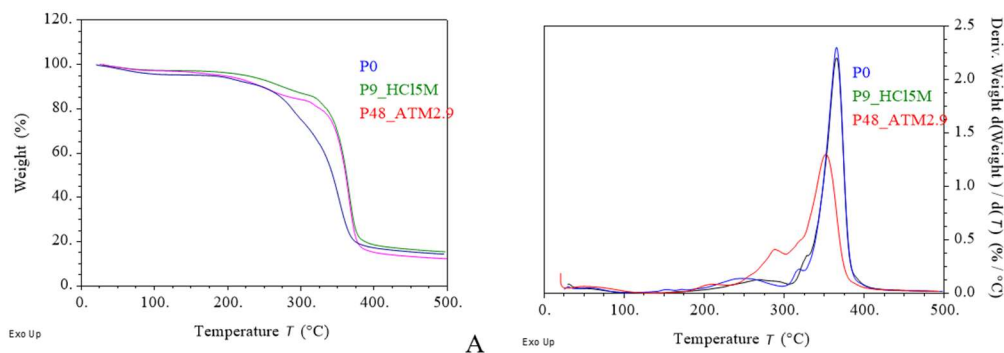


Fig. 29 TGA (A) and DTG (B) profiles for P0, P9_HCl5M and P48_ATM2.9.

Tensile test. Variation in tensile strength during the ATM2.9 degradation protocol has been investigated in Fig. 30. Also in this case, a variation in the tensile strength

is observed: a halving in the Young's Modulus is registered between P9_HCl5M (time 0 of Fig. 22B, 14 ± 1 MPa) and P48_ATM2.9 (7.3 ± 0.2 MPa),(Fig. 33B).

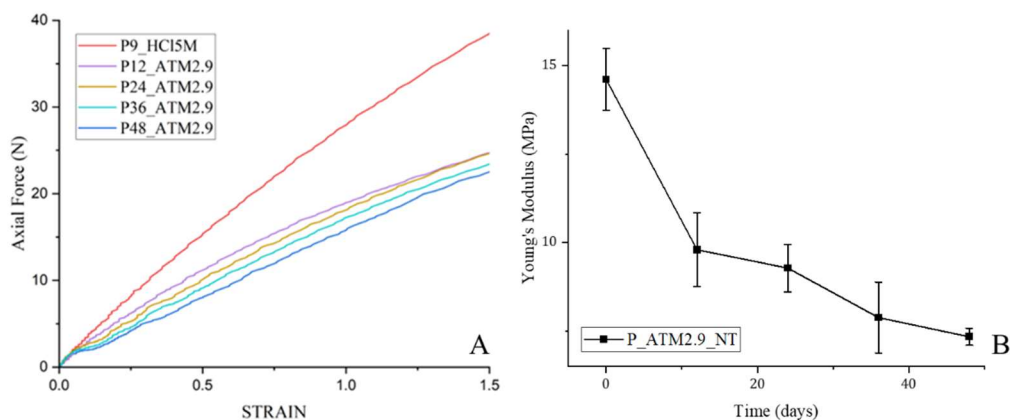


Fig. 30 (A) Axial force vs Strain graph and (B) Young's Modulus vs duration of the third step of the ATM2.9 degradation protocol for P9_HCl5M (time 0), P12, P24, P36, P48_ATM2.9. The results of each measurement are expressed as the average value and the corresponding standard deviation calculated for five fragments of the same film subjected to the same degradation protocol.

3.3 The validation of the multi-analytical method

To validate the multi-analytical protocol, the kinetics data describing the progress of the “vinegar syndrome” obtained through different analytical approaches with the procedures described in Paragraphs 3.2.1 and 3.2.2 of this chapter (weight loss, acetyl content via HSM, free acidity and ATR-FTIR ratio), were normalized between 0 and 100 according to Eq. 8 and compared.

$$Normalized\ value = \frac{(x-x_{min})}{(x_{max}-x_{min})} \times 100 \quad (8)$$

The attention was particularly focused on the trend of the weight loss, the correct acetyl content and the ATR-FTIR ratio because, while all these parameters decrease with time (so the corresponding curves have a negative slope), the free acidity instead, increases and the corresponding curve has a positive slope.

The normalized curves of the weight loss, correct acetyl content, ATR-FTIR ratios and of the free acidity data reported in Fig. 31, relative to CTA-based films (Fig. 31A) and to motion picture films (Fig. 31B) subjected to HCl5M degradation procedure (paragraph 3.2.1) are in perfect agreement with each other. In particular, both the duration of the induction period of the deacetylation process, equal to approximately 6 days for CTA films subjected to the degradation protocol HCl5M (fig. 31A) and 9 days for real motion picture films subjected to the degradation protocol HCl5M (fig. 31B), and the slope of the subsequent segment (6-16 days range for CTA films and in the 9-30 days range for motion picture films) of the curves describing the trend of the weight loss, the correct acetyl content and the ATR-FTIR ratio are very similar for each class of samples (between -8.2 and -9.9 ca. for CTA films and between -4.5 and -5.6 for motion picture films) as indicated in tables 14 and 15 respectively.

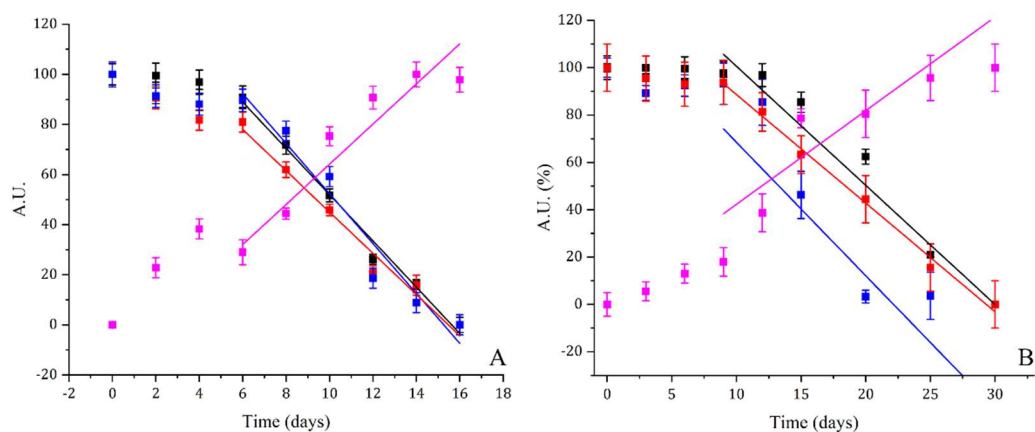


Fig. 31 Normalized (Eq. 8) weight loss (black), correct acetyl content (red), ATR-FTIR ratios (blue) and free acidity (pink) data for (A) CTA-based films subjected to the HCl5M degradation protocol and (B) real motion picture films subjected to the HCl5M degradation protocol.

Tab. 14 Linear fitting parameters of normalized (Eq. 8) weight loss, correct acetyl content, ATR-FTIR ratios and free acidity data for CTA-based films subjected to the HCl5M degradation protocol (paragraph 3.2.1).

Analysis	Range (days)	Linear fitting	R ²
Weight loss (%)	6-16	$y = -9.2x + 144.4$	0.99
Correct acetyl content (%)	6-16	$y = -8.2x + 127.4$	0.97
ATR-FTIR ratio (%)	6-16	$y = -9.9x + 152.2$	0.95
Free acidity (%)	6-16	$y = 8.0x - 16.0$	0.90

Tab. 15 Linear fitting parameters of normalized (Eq. 8) weight loss, correct acetyl content, ATR-FTIR ratios and free acidity data for motion picture films subjected to the HCl5M degradation protocol (paragraph 3.2.1).

Analysis	Range (days)	Linear fitting	R ²
Weight loss (%)	9-30	$y = -5.0x + 151$	0.98
Correct acetyl content (%)	9-30	$y = -4.6x + 134.6$	0.99
ATR-FTIR ratio (%)	9-30	$y = -5.6x + 124.9$	0.71
Free acidity (%)	9-30	$y = 3.9x - 2.7$	0.67

In Figure 32 the normalized curves of the weight loss, correct acetyl content, ATR-FTIR ratios and free acidity data relative to CTA-based films and motion picture films subjected respectively to ATM2.3 (paragraph 3.2.2.1) and to ATM2.9 (paragraph 3.2.2.2) degradation procedures are reported. The graphs in Fig 32A show that the data for CTA-based films are in perfect agreement with each other. Conversely, for motion picture films (Fig. 32B), the normalized gravimetry data are not superimposable to the ones relative to acetyl content and to the ATR-FTIR ratio. This behavior can be ascribed to the presence of the emulsion layer (that is not present in CTA-based films) that, during the third step of the degradation protocol (conditioning at a relative humidity of 100%) adsorbs part of the environmental moisture. Nevertheless, apart from this datum, the duration of the induction period of the deacetylation process measured is always equal to 24 days for both CTA and

motion picture films. Furthermore the slope of the subsequent segment (24-60 days) of all the curves (except for free acidity which, contrary to the other measured parameters increases over time) are all equal to -2.4 for CTA films (Tab. 16) and range between -3.6 (ATR-FTIR ratio), -3.7 (correct acetyl content) and -2.1 (weight loss) for motion picture films (Tab. 17).

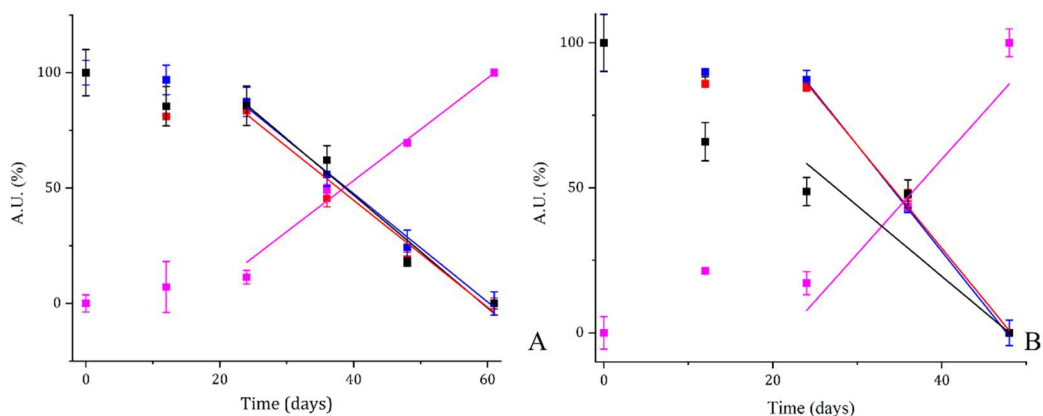


Figure 32. Normalized (Eq. 8) weight loss (black), correct acetyl content (red), ATR-FTIR ratios (blue) and free acidity (pink) data for (A) CTA-based films and subjected to the FX_ATM2.3 degradation protocol and (B) real motion picture films subjected to the PX_ATM2.9 degradation protocol.

Tab. 16 Linear fitting parameters of normalized (Eq. 8) weight loss, correct acetyl content, ATR-FTIR ratios and free acidity data for motion picture films subjected to the FX_ATM2.3 degradation protocol.

Analysis	Range (days)	Linear fitting	R ²
Weight loss (%)	24-60	$y = -2.4x + 116.8$	0.97
Correct acetyl content (%)	24-60	$y = -2.4x + 140.0$	0.99
ATR-FTIR ratio (%)	24-60	$y = -2.4x + 143.6$	0.99
Free acidity (%)	24-60	$y = 2.3x - 38.1$	0.98

Tab. 17 Linear fitting parameters of normalized (Eq. 8) weight loss, correct acetyl content, ATR-FTIR ratios and free acidity data for motion picture films subjected to the PX_ATM2.9 degradation protocol.

Analysis	Range (days)	Linear fitting	R ²
Weight loss (%)	0-48	$y = -2.1x + 101.8$	0.94
Correct acetyl content (%)	24-60	$y = -3.7x + 171.2$	0.99
ATR-FTIR ratio (%)	24-60	$y = -3.6x + 174.3$	0.99
Free acidity (%)	24-60	$y = 3.2x - 70.4$	0.80

On these bases, it is possible to affirm that all the techniques used to monitor the evolution of the deacetylation process of both CTA films and real motion picture films give similar and coherent results. It is interesting to observe that, while some of the used techniques such as free acidity and correct acetyl content measurements, need the collection of samples (and for real analysis of films the weight change is not entirely indicative), the procedure based on ATR-FTIR is not invasive, low cost and can be applied without problems and/or limits in the number of the analyses.

3.4 Comparison of the degradation protocols

Finally, in Fig. 33 and Tab. 18, the trends of the correct acetyl content measured for both CTA films and motion picture films subjected to the different degradation protocols to artificially induce the deacetylation process are reported for comparison. For all the protocols where the degradation of the polymeric support is induced through an exposition of the materials to an atmosphere generated by a solution of HCl5M (HCl5M, ATM2.X) it is possible to observe that the process is characterized by an initial “induction period” followed by a faster phase where the slope of the curve increases.

Fig. 33 A and B show that the faster deacetylation process was registered for CTA-based samples subjected to the HCl5M degradation protocol, while the same protocol applied on real motion picture films induces slower deacetylation, as indicated by the slopes of the curves in the ranges 6-16 days and 9-30 days respectively that are

equal to -3.5 (R^2 0.96) and -1.6, (R^2 0.99, see Tab. 18). This difference is probably due to the presence of both the emulsion layer and plasticizers, that act as stabilizers. Moreover, probably for the same reason, the induction period is longer for real motion picture films than for CTA-based films (9 days vs 6 days).

Concerning the ATM2.3 and ATM2.9 degradation protocols, Fig. 33C and 33D, and the data reported in Tab. 18, indicated that in both these cases the deacetylation of CTA and the support of the motion picture films occurs at a lower rate than for CTA and motion picture films subjected to the HCl5M degradation protocol because the exposition to the acid catalyst is limited to the first phase of the test. This is confirmed by the slope of the curves in the range 24-60 days for CTA-based films and in the range 24-48 days for real motion picture films, which, in both cases is -0.3 (Tab. 18).

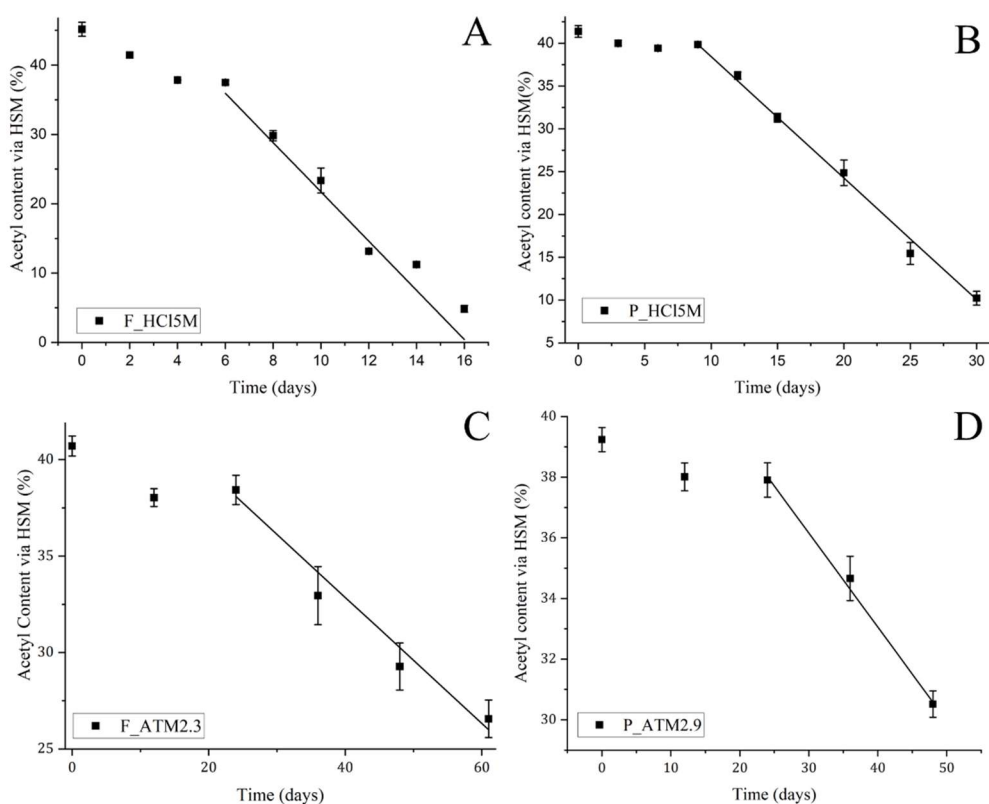


Fig. 33 Linear fitting calculated on the curves associated with the decrease in the correct acetyl content for the following degradation protocols: (A) F_HCl5M, (B) P_HCl5M, (C) F_ATM2.3, (D) P_ATM2.9.

Tab. 18 Linear fitting curves calculated from the data obtained to samples subjected to different degradation protocols.

Degradation protocol	Material	Range (days)	Linear fitting	R ²
HCI5M	CTA-based film	6-16	$y = -3.5x + 57.2$	0.96
HCI5M	Real motion picture film	9-30	$y = -1.6x + 53.5$	0.99
ATM2.3	CTA-based film	24-60	$y = -0.3x + 46.1$	0.98
ATM2.9	Real motion picture film	24-48	$y = -0.3x + 45.4$	0.99

3.5 Conclusions

Based on the results reported above, we can make the following conclusions:

- the multi-analytical method based on the calculation of the acetyl content through HSM (corrected with free acidity) and through the calculation of the ratios between the intensities of some ATR-FTIR diagnostic peaks (in particular the I_{1220/11030} ratio) and on the free acidity could be considered useful to follow the evolution of artificially induced deacetylation processes that simulate the “*vinegar syndrome*” on both CTA-based films and real motion picture films. In fact, comparing the linear fittings calculated on the normalized data, the equations of the curves that describe the correct acetyl content, the ATR-FTIR ratio and the free acidity are coherent. The possible use of ATR-FTIR spectroscopy could be a great alternative to HSM because it is a non-invasive and non-destructive technique [17], [18] that allows to collect a large number of spectra onto a film sample. Otherwise, we will keep performing both HSM and ATR-FTIR spectroscopy measurements, in order to improve the accuracy of our results.
- TGA and tensile tests gave precious informations about collateral degradation pathways which are promoted by deacetylation (i.e. variation in the molecular weight of CA chains).
- As reported in the literature [8], [30], the emulsion layer and plasticizers have a stabilization effect on the film and partially inhibit the degradation processes due to deacetylation of the support.

- To evaluate the performances of our inhibitors on real motion picture films, the ATM2.X has been chosen as the most promising degradation protocol because, at the same time, it was able to artificially induce the deacetylation process and showed proper kinetics to be studied, compatible with laboratory timelines. In addition, no relevant physico-chemical alterations are expected on inhibitors subjected to this degradation protocol as will be discussed in detail in the next chapters.

References

- [1] M. McGath, S. Jordan-Mowery, M. Pollei, S. Heslip, and J. Baty, “Cellulose Acetate Lamination: A Literature Review and Survey of Paper-Based Collections in the United States,” *Restaurator*, vol. 36, no. 4, pp. 333–365, 2015, doi: 10.1515/res-2015-0015.
- [2] D. Littlejohn, R. A. Pethrick, A. Quye, and J. M. Ballany, “Investigation of the degradation of cellulose acetate museum artefacts,” *Polym. Degrad. Stab.*, vol. 98, no. 1, pp. 416–424, 2013, doi: 10.1016/j.polymdegradstab.2012.08.023.
- [3] É. C. T. C. Roldão, “A contribution for the preservation of cellulose esters black and white negatives,” 2018.
- [4] and A. R. Fischer, Monique C., “Guidelines for Care & Identification of Film-Base Photographic Materials,” *Top. Photogr. Preserv.*, vol. 5, pp. 117–122, 1993.
- [5] M.-P. M. Paul Read, *Restoration of Motion Picture Film*, Butterwort. Oxford, 2000.
- [6] P. Krause, P. Kraus, J. P. Reilly, and J. M. Reilly, “IPI Storage Guide for Acetate Film,” *J. Am. Inst. Conserv.*, vol. 33, no. 3, p. 321, 1994, doi: 10.2307/3179643.
- [7] Y. Yamashita and T. Endo, “Deterioration behavior of cellulose acetate films in acidic or basic aqueous solutions,” *J. Appl. Polym. Sci.*, vol. 91, no. 5, pp. 3354–3361, 2004, doi: 10.1002/app.13547.
- [8] N. S. Allen, M. Edge, J. H. Appleyard, T. S. Jewitt, C. V. Horie, and D. Francis, “Acid-catalysed degradation of historic cellulose triacetate, cinematographic film: Influence of various film parameters,” *Eur. Polym. J.*, vol. 24, no. 8, pp. 707–712, 1988, doi: 10.1016/0014-3057(88)90002-X.
- [9] and C. J. E. P. Z. Adelstein, J. M. Reilly, D. W. Nishimura, “Stability of Cellulose Ester Base Photographic Film: Part I Laboratory Testing Procedures,” *SMPTE J.*, 1992.
- [10] J. L. Bigourdan, “Stability of acetate film base: Accelerated-aging data revisited,” *J. Imaging Sci. Technol.*, vol. 50, no. 5, pp. 494–501, 2006, doi: 10.2352/J.ImagingSci.Technol.(2006)50:5(494).
- [11] “Imagin materials - Processed silver gelatin-type black-and-white films - Specifications for stability,” 18901:2010(E), 2010.

- [12] T. Heinze and T. Liebert, *Celluloses and Polyoses/Hemicelluloses*, vol. 10. Elsevier B.V., 2012.
- [13] U. Siemann, “Solvent cast technology - A versatile tool for thin film production,” *Prog. Colloid Polym. Sci.*, vol. 130, no. June, pp. 1–14, 2005, doi: 10.1007/b107336.
- [14] “Standard Test Methods of Testing Cellulose Acetate,” D87-96, 2019.
- [15] M. T. Giachet *et al.*, “Assessment of the composition and condition of animation cels made from cellulose acetate,” *Polym. Degrad. Stab.*, vol. 107, pp. 223–230, 2014, doi: 10.1016/j.polymdegradstab.2014.03.009.
- [16] P. Fei, L. Liao, B. Cheng, and J. Song, “Quantitative analysis of cellulose acetate with a high degree of substitution by FTIR and its application,” *Anal. Methods*, vol. 9, no. 43, pp. 6194–6201, 2017, doi: 10.1039/c7ay02165h.
- [17] Y. Shashoua and K. B. Johansen, “Investigation of ATR-FTIR spectroscopy as an alternative to the Water-Leach free acidity test for cellulose acetate-based film,” *14th Trienn. Meet. ICOM-CC*, no. Koenig 1999, pp. 548–555, 2005.
- [18] S. Nunes *et al.*, “A diagnostic tool for assessing the conservation condition of cellulose nitrate and acetate in heritage collections: quantifying the degree of substitution by infrared spectroscopy,” *Herit. Sci.*, pp. 1–14, 2020, doi: 10.1186/s40494-020-00373-4.
- [19] G. Fengel, D. Wegener, *Wood—Chemistry, Ultrastructure, Reactions. 2nd Edition*. Berlin: Walter de Gruyter, 1989.
- [20] A. Chemical, I. Co, and D. S. C. I. T. G. I. X. D. I, “Kenji KAMIDE and Masatoshi SAITO,” vol. 17, no. 8, pp. 919–928, 1985.
- [21] N. Atykyan, V. Revin, and V. Shutova, “Raman and FT-IR Spectroscopy investigation the cellulose structural differences from bacteria *Gluconacetobacter sucrofermentans* during the different regimes of cultivation on a molasses media,” doi: 10.1186/s13568-020-01020-8.
- [22] M. L. Nelson, “Relation of Certain Infrared Bands to Cellulose Crystallinity and Crystal Lattice Type. Part 11. A New Infrared Ratio for Estimation of Crystallinity in Celluloses I and 11*,” *J. Appl. Polym. Sci.*, vol. 8, pp. 1325–1341, 1964.
- [23] M. R. Huang and X. G. Li, “Thermal degradation of cellulose and cellulose esters,” *J. Appl. Polym. Sci.*, vol. 68, no. 2, pp. 293–304, 1998, doi: 10.1002/(SICI)1097-4628(19980411)68:2<293::AID-APP11>3.0.CO;2-Z.

- [24] M. Valverde, "Photographic negatives: nature and evolution of processes," pp. 9–18, 2005, [Online]. Available: <http://www.bcin.ca/Interface/openbcin.cgi?submit=submit&Chinkey=235796>.
- [25] E. Carretti, M. Milano, L. Dei, and P. Baglioni, "Noninvasive physicochemical characterization of two 19th century English ferrotypes," *J. Cult. Herit.*, vol. 10, no. 4, pp. 501–508, 2009, doi: 10.1016/j.culher.2009.02.002.
- [26] Image Permanence Institute (IPI), "No Title." <https://filmcare.org/index>.
- [27] Z. Jia *et al.*, "Study on microbubble of cellulose acetate microfilm of the Republic of China (AD 1912–1949) collected in the Second Historical Archives of China," *Herit. Sci.*, vol. 8, no. 1, pp. 1–10, 2020, doi: 10.1186/s40494-020-00374-3.
- [28] A. M. Cortizas and O. López-Costas, "Linking structural and compositional changes in archaeological human bone collagen: an FTIR-ATR approach," *Sci. Reports* |, vol. 10, p. 17888, 2020, doi: 10.1038/s41598-020-74993-y.
- [29] B. Kemper and D. Andreas, "Extraction of plasticizers : An entire and reproducible quantification method for historical cellulose acetate material," *Polym. Test.*, vol. 80, no. August, p. 106096, 2019, doi: 10.1016/j.polymertesting.2019.106096.
- [30] N. S. Allen, M. Edge, T. S. Jewitt, and C. V. Horie, "Initiation of the Degradation of Cellulose Triacetate Base Motion Picture Film," *J. Photogr. Sci.*, vol. 38, no. 2, pp. 54–59, 1989, doi: 10.1080/00223638.1989.11737073.

Chapter IV

Proposal of inhibitors for the “vinegar syndrome” made of polyethyleneimine

One of the main aims of this thesis is the set-up and the evaluation of the performances of inhibitors for the “*vinegar syndrome*”, which typically affects CA-based motion picture films.

As reported in Chapter II, the deacetylation of the CA, which is the main cause of the “*vinegar syndrome*”, is favored by the thermohygrometric conditions (i.e. high temperature, moisture and acidity) of the microenvironment where the films are stored. In particular, the most important problem associated with the “*vinegar syndrome*” is the emission of acetic acid, which can promote the hydrolysis of the cellulose backbone, catalyze the deacetylation reaction itself and induce further degradation in objects stored nearby (see Paragraph 2.5.3). On these bases, controlling the temperature, reducing environmental moisture and removing alteration by-products from the storing environment is mandatory to limit this phenomenon.

Then, the goal of this part of the research project is to develop systems with the following characteristics:

- they should be able to neutralize the acetic acid in order to inhibit and/or block the deacetylation reaction and other correlated degradation processes;
- they should help to maintain the environmental moisture in the values recommended for the optimal conservation of motion picture films (RH between 20-50%, to not favor the hydrolysis of the acetyl groups and/or of the glycosidic bonds between the units of the polymeric chains and/or the mold grow, but also to not excessively dry -and alter- the gelatin of the emulsion layer[1]);

- they should be chemically and physically stable and not alter motion picture films;
- they should be able to be placed inside the containers in which motion picture films are stored;
- they should be cheap and easy to handle for conservators to consent the periodic replacements on a large scale (i.g. in archives);
- possibly they should be regenerable and reusable.

The research strategy was based on three different directions:

- the setup and the application of sponges or gel-like systems based on polyethyleneimine and/or polyvinylalcohol compounds (the discussion of these systems is reported in this Chapter).
- the use of inorganic nanoparticles uploaded on different substrates, such as paper or sponges (the discussion of these systems is reported in Chapter V).

In this Chapter, the synthesis procedures and the characterizations of sponge- and gel-like systems based on the use of polyethyleneimine will be discussed.

4.1 Polyethyleneimine (PEI)

Polyethylenimine (PEI) is a polymer with repeating units containing amine functions. It is possible to distinguish linear polyethyleneimine, which contains only secondary amine groups (Fig. 1A), and branched polyethyleneimine, which is composed of primary, secondary and tertiary amine groups [2] (Fig. 1B).

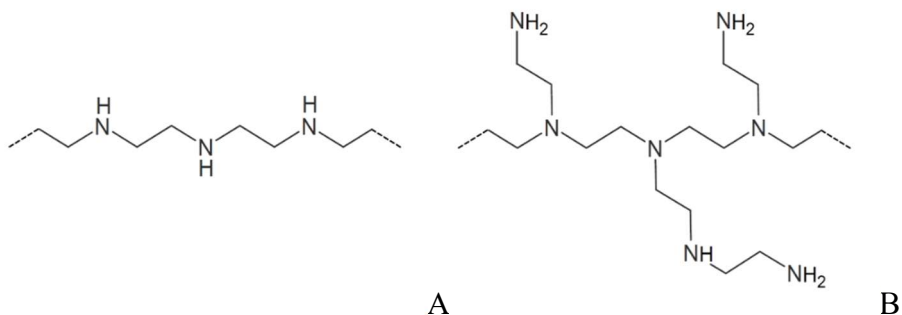


Fig. 1 (A) Linear PEI and (B) Branched PEI.

PEI is traditionally used as polymeric nucleic acid delivery vectors due to its biocompatibility [2]. Moreover, the basic character of the amine groups gives PEI a strong ability to absorb many chemical species having acidic properties, particularly organic acids [3].

The use of PEI for the absorption of VOC is described in various studies. For example, multiple systems, such as nanoparticles of poly(D,L-lactic acid)-poly(ethylene glycol)-poly(ethyleneimine) (PDLLA-PEG-PEI) [4], [5] and poly(ethyleneimine)-modified cellulose nanocrystals (PEI-f-CNC) [6] have been synthesized to adsorb volatile organic compounds, specifically aldehydes and carboxylic acids, including acetic acid [7], associated with odors and to chemically degrade common pesticides from water [8]. Yang and Runge published an interesting study about the absorption capacity of crosslinked PEI as a reactive and reversible adsorbent for lignocellulose-derived organic acids (specifically acetic acid) and aldehydes from their sugar precursors and byproducts [9]. In all these studies, the target is the conversion of acetic acid into ammonium carboxylate upon interaction with the amine groups of polyethyleneimine through an acid/base reaction [9] (Fig. 2).



Fig. 2 Acid/base reaction scheme between PEI and acetic acid [9].

To have a stable system, able to not disperse in the cases where the artifacts are stored and easy to handle for conservators, could be a fundamental aspect. On these bases, we tried to include PEI into different types of systems:

- PolyVinyl Alcohol (PVA)-PEI-based systems and, in particular:
 - a cryogel obtained by mixing PVA and PEI (PVA-PEI-CG);
 - a PVA network crosslinked with formaldehyde (PVF) in which PEI is incorporated in order to obtain a sponge-like system (PVF-PEI and PVF-PEI-GA);
- a sponge-like system obtained through the chemical crosslinking of PEI with 1,4-butanedioldyglycidyl ether (BDDE), (SPEI).

4.2. PVA-PEI-based systems

4.2.1 PVA-PEI cryogels

PVA is a hydrophilic and biocompatible polymer synthesized through hydrolysis of polyvinyl acetate, which is obtained via free radical polymerization of vinyl acetate. The alcohol groups are available for hydrogen bonding and, therefore, PVA dissolved in an aqueous solution is able to crosslink with various compounds and produce

hydrogels. When PVA is physically crosslinked using a freeze-thaw (FT) cycling process, the obtained cryogel (PVA-CG) possesses unique mechanical and diffusion properties [10]. The synthesis protocol includes several steps. First, the gel is brought down to a temperature between -5 and -20°C [11], [12], during which the water phase freezes. This creates amorphous regions of low polymer concentration, occupied by ice crystals, as well as regions of high polymer concentration, where crystallites are locally formed [13]. The solution is then thawed back to room temperature leading to the formation of a solid gel PVA-CG in which the tie points of the network are the crystallites of polymer and the pores are the amorphous regions after the ice melting [10].

By varying some synthesis parameters, such as the concentration of PVA and the conditions of the FT cycles (number, thawing rate, upper and lower temperature limits), it is possible to tune the structure and the properties of the polymeric matrix, such as the extension of the network [11], [12], [14]. Thanks to this possibility, PVA-CGs have a lot of applications, in particular in the biomedical field [10] but also as cleaning systems in art conservation [15]–[17].

Recently cryogels made of a mixture of PVA and PEI have been proposed by Wang et al. (2020) as “*stretchable, mechanically robust, biosafe and antibacterial elastomers*” to use as piezoresistive sensors able to monitor facial expressions and vocal signals with high accuracy and sensitivity [18] (Fig. 3). In this case, the polymer-rich phase, which is the network of the gel, is occupied by both PVA and PEI, which is able to form hydrogen bonds through its amino groups.

We decided to exploit this approach to try to obtain a system useful for our purposes (easy to handle and with PEI inside).

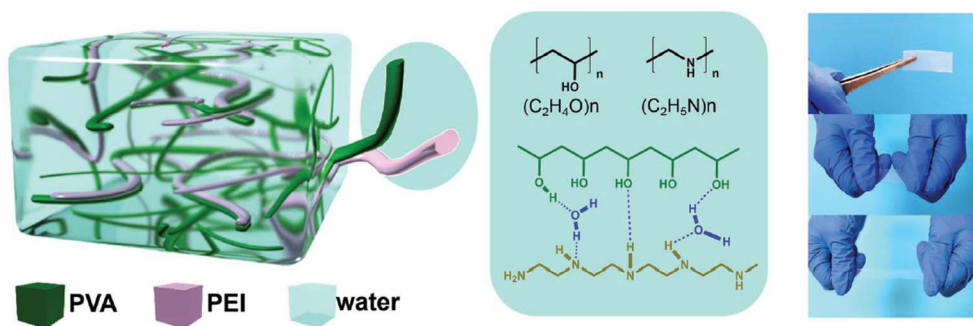


Figure 3. Conceptual illustration and mechanical properties of the elastomer based on the PVA/PEI cryogel [18].

4.2.2 PVF-PEI sponge-like systems

A sponge is a compressible porous material characterized by low bulk density and having a high interphase surface area that imparts excellent adsorption capacity. These characteristics mean that sponge materials can be used for a variety of applications, for example, for surface cleaning, as filtration aids and for adsorption and absorption purposes [19].

We chose also to incorporate PEI in a sponge-like system, in particular inside a polyvinylalcohol formaldehyde (PVF) sponge (Fig. 4). It is obtained through the crosslinking of PVA with formaldehyde at low pH, in the presence of a surfactant (Fig. 4A). During the reaction, the bubbles generated by a surfactant by stirring the system act as porogen of the final sponge-like structure [19]–[23]. The chemical structure of the resulting polymer is characterized by the presence of several hydroxyl groups, which, if properly functionalized, offer the possibility to modify surface properties, giving it a high degree of versatility [20].

These systems have been chosen as support for PEI because of their high hygroscopicity and good mechanical properties. They present a 3D open-cell structure in which is possible to modulate the porosity by varying the ratio between polyvinyl alcohol (PVA) and formaldehyde [22], [23].

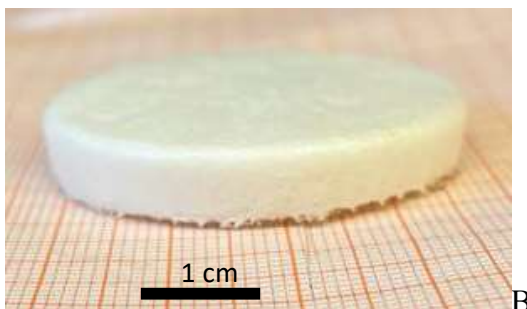
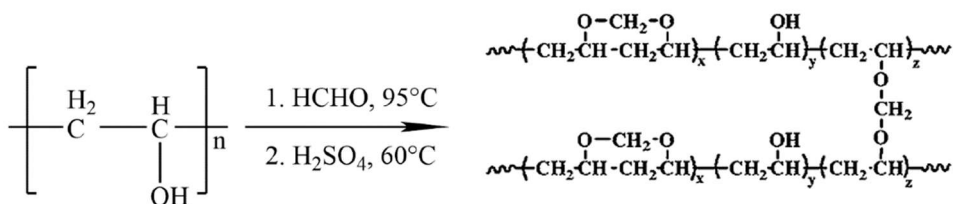


Fig. 4 (A) Preparation of PVF from PVA [24]; (B) PVF sponge.

To include PEI inside the PVF structures, three different strategies have been tested:

- 1) to involve PEI in the crosslinking with formaldehyde during the synthesis of the PVF sponge (PVF-PEI1);
- 2) to promote the ionic interaction between the amine groups of PEI and the residual hydroxyl groups on the pre-formed PVF (PVF-PEI2);
- 3) to induce the crosslinking of PEI and the pre-formed PVF through the formation of imine and acetal bonds between glutaraldehyde (GA) and GA and PVF, respectively (PVF-PEI-GA).

4.2.3 Chemicals

Polyvinyl alcohol was purchased from Kuraray (Kuraray Poval 10-98). Formaldehyde, Triton X100, polyethyleneimine (solution in water 50wt%, Mw 750,000), glutaraldehyde (solution in water 50wt%), hydrochloric acid 37%, 2-propanol, glacial acetic acid were purchased from Sigma Aldrich. Sodium Hydroxide ($\geq 98.5\%$ pellets, anhydrous) was purchased by Acros Organics. Sulfuric acid 96%

was purchased from Carlo Erba Reagents. All the chemicals have been used without further purification.

4.2.4 Syntheses of the systems

4.2.4.1 PVA-PEI cryogels

PVA-PEI cryogels were synthesized by mixing at 95 °C for 1 h 1 g PVA (Poval Kuraray 10:98) and 1 g PEI (Mw 750,000, 50wt%) with 8 mL of water in a 1:2 w/w ratio until all the polymers had been solubilized and a homogenous mixture was obtained. The solution was poured into a glass mold and kept at -30 °C for 24 h, then equilibrated at room temperature. In this way, the physical crosslinking was induced using a freeze-thaw cycling method through a water-polymer phase separation. PVA and PEI chains accumulate in the polymer-rich phase, while ice crystals form in the water-rich phase; owing to the pressure exerted by freezing water, polymer crystallites form and act as tie points in the gel structure, while ice crystals act as porogen [18], [25]. This system is labeled as PVA-PEI-CG.

4.2.4.2 PVF sponge

PVF sponges have been synthesized following the procedures described in the patents US2,668,153 [26] and US2,609,347 [27] and papers [19]–[23] with some modifications in the formulation in order to improve the porosity of the system.

The synthesis procedure could be summarized as follows: 0.5 g of TritonX-100 were added to 20g of a solution of PVA 10 wt% in water, then the system was heated at 95 °C under vigorous stirring for 30 min. Then the proper amount of a formaldehyde solution in water was added dropwise to the mixture, keeping to heat and stirring for at least 5 min, until the foam reached the maximum volume. The solution was left to cool to 60 °C under stirring, then 10 mL of 50% aqueous H₂SO₄ was added. The solution was poured into a mold and cured in an oven at 60°C for 5 h. Then, the

sample is washed with water at least five times to remove the residual solvents and unreacted products. The sponges were dried in an oven at 55-60 °C.

Compared with syntheses traditionally reported in the literature, we decrease the concentration of formaldehyde (see below) in order to increase the porosity of the system and to leave more free hydroxyl groups able to react with PEI [22].

4.2.4.3 PVA/PVF-PEI sponge-like systems

Concerning the *PVA/PVF-PEI sponge-like systems*, three different synthesis strategies have been tested:

1. PEI was added during the synthesis of the PVF sponge, before the addition of formaldehyde (PVAOH_{monomer}/formaldehyde molar ratio = 2.2 instead of ~1 as reported in the literature): to the water solution of PVA (10 wt%, 5g) 0.25g of Mw 750,000 PEI was added (weight ratio of PVF:PEI=2:1). Then the synthesis was carried on as reported above for the PVF sponge. This system is labeled as PVF-PEI1.
2. PEI was loaded by immersing a preformed PVF sponge (obtained with the procedure reported in Paragraph 4.2.4.2) in a water solution of PEI and putting the system under vacuum (-30 in.Hg) to promote the penetration of PEI in the sponge network. Then the PVF-PEI sponge was immersed in an aqueous HCl solution and then in an ultrasonic bath (60 W) [28]–[30]. Finally, the system was washed with water several times and dried. The idea was to promote the ionic interaction between the amine groups of PEI and the residual hydroxyl groups of PVF (Fig. 5A). We carried out several syntheses changing one variable at a time in order to optimize the final product in terms of porosity. In particular, attention has been focused on the weight ratio between PEI and PVF, the amount of hydrochloric acid, the duration of the ultrasonic treatment and the temperature of the ultrasonic

bath. We also changed the synthetic procedure for PVF in order to increase the number of free OH groups, varying the PVA OH/formaldehyde molar ratio. This class of systems is labeled as PVF-PEI2.X (with X varying between 1 and 17). All the syntheses carried out by following protocol 2 are reported in Tab. 1.

3. In a pre-formed PVF sponge, PEI was added under vacuum and the PVF-PEI sponge was crosslinked with glutaraldehyde (GA)[28]–[30]. 0.1 g of PVF sponge ($\text{PVAOH}_{\text{monomer}}/\text{formaldehyde molar ratio} = 2.2$) was soaked with 2 g of 10wt% PEI (750,000 Mw) and left for 2 hours under vacuum to promote the absorption of PEI inside the sponge. The thus obtained PVF-PEI3 sponge was left under hood for 24 hours to promote the evaporation of the water and dried in an oven under vacuum at 50 °C for 6 hours (no washings were performed). Then, the PVF-PEI3 sponge was soaked for 1.5 h in a bath containing 9 mL 2-propanol, 1 mL water, 0.1 mL HCl (37%), and 0.5 mL glutaraldehyde, GA (5wt%). Finally, the sponge was immersed in distilled water for 24 hours to wash it. The idea is to induce the formation of ionic interactions between the amine groups of PEI and the residual hydroxyl groups of PVF (Fig.5A) and, then, the crosslinking of PEI and PVF through the formation of imine and acetal bonds between GA and PEI and GA and PVF, respectively (Fig.5B). This system is labeled as PVF-PEI-GA (Fig. 5C).

Tab. 1 Resume of syntheses of PVF-PEI2.X sponges.

Sample name	molar ratio PVA OH _{monomer} /formaldehyde	PEI			HCl (37wt%)(mL)	Ultrasound procedure		Examined variable
		Mw	Concentration of the initial solution(wt%)	weight ratio PEI:PVF		Time (min)	Temperature (°C)	
PVF-PEI2.1	2.2	800	5	1:6	0.8	5	60	time in the ultrasound bath
PVF-PEI2.2	2.2	800	5	1:6	0.8	10	60	
PVF-PEI2.3	2.2	800	5	1:6	0.8	15	60	
PVF-PEI2.4	2.2	800	10	1:3	1.6	5	60	weight ratio PEI:PVF
PVF-PEI2.5	2.2	800	10	1:3	1.6	10	60	
PVF-PEI2.6	2.2	800	10	1:3	1.6	15	60	
PVF-PEI2.7	2.2	800	10	1:3	0.8	15	60	HCl volume
PVF-PEI2.8	2.2	800	10	1:3	0.02	15	60	
PVF-PEI2.9	2.2	800	10	1:3	0	15	60	
PVF-PEI2.10.1	2.2	750,000	10	1:3	0.8	15	60	PEI Mw
PVF-PEI2.10.2	2.2	750,000	10	1:1	0.02	15	60	
PVF-PEI2.10.3	2.2	750,000	10	1:1	0	15	60	
PVF-PEI2.11.1*	2.2	800	10	1:3	0.8	/	/	Temperature
PVF-PEI2.11.2*	2.2	750,000	10	1:3	0.8	/	/	
PVF-PEI2.11.3	2.2	750,000	10	1:1	0.8	15	25	
PVF-PEI2.12.1	3	800	10	1:1	0.8	15	60	molar ratio PVA OH/formaldehyde
PVF-PEI2.12.2	3	750,000	10	1:1	0.8	15	60	
PVF-PEI2.13	3	750,000	10	1:1	0.02	15	60	
PVF-PEI2.14.1	3	800	50	2.5:1	0.8	15	60	
PVF-PEI2.14.2	3	800	50	2.5:1	0.02	15	60	
PVF-PEI2.15.1	3	800	50	2.5:1	0	15	60	
PVF-PEI2.15.2	4	800	10	1:1	0.8	15	60	
PVF-PEI2.16	4	750,000	10	1:1	0.8	15	60	
PVF-PEI2.17	2.2	750,000	10	1:1	0.8	/	/	without ultrasound

*these two syntheses have been performed at a higher temperature (80°C) through magnetic stirring.

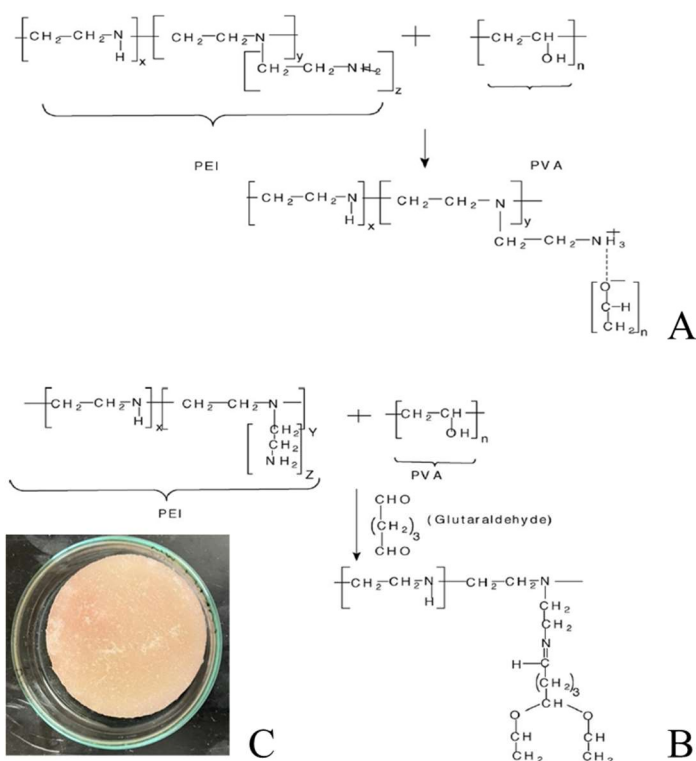
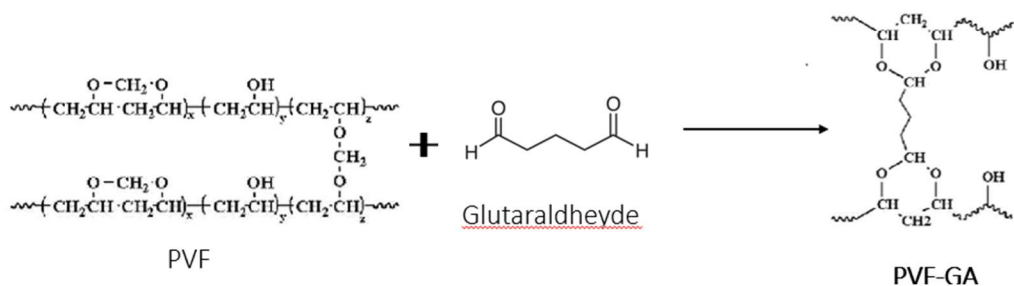
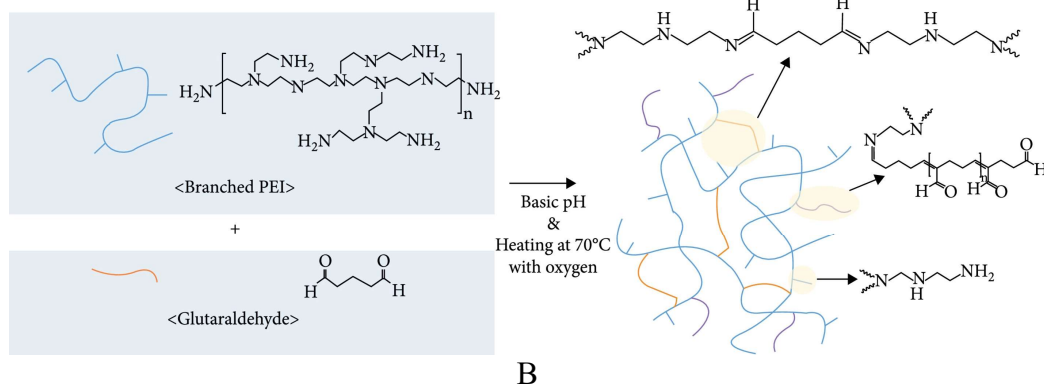


Fig. 5. (A) Formation of polyion complex of PVA and PEI; (B) Crosslinked PEI and PVA with glutaraldehyde [31]; (C) PVF-PEI-GA sponge.

Other reactions may compete with this one, for example, the further crosslinking of PVF (Fig.6A)[20] and PEI (Fig.6B)[32]. Nevertheless, these reactions are useful because they theoretically may help to thicken the sponge network and promote the incorporation of the PEI.



A



B

Fig. 6 (A) Crosslinking of PVF with GA[20]; (B) Crosslinking of branched PEI with GA[30].

4.2.5 Characterization of the systems

The sponges were characterized by the following methods and techniques:

Fourier Transform Infrared Spectroscopy Measurements (FTIR-ATR). Fourier Transform Infrared – Attenuated Total Reflected (FTIR-ATR) spectra were collected using a PerkinElmer FT-IR Spectrometer equipped with an ATR accessory (UATR Two) in the range of $4000\text{--}600\text{ cm}^{-1}$ with a 4 cm^{-1} resolution by taking 32 scans for each sample.

Elemental Analysis. The quantitative elemental analysis on C and N have been performed with a ThermoScientific FlashSmart Elemental Analyzer CHNS/O (accuracy $\pm 0.1\%$), calibrated with the following standards: cystine, methionine,

sulfanilamide. The percentage of each element is expressed as the percentage in weight of the total weight of the sample. With these data, the C/N ratios for the unreacted PEI and all the sponges were calculated.

Thermogravimetric analysis (TGA). TGA was carried out in a nitrogen atmosphere at a heating rate of 10 °C/min over a temperature range of 25-500 °C, with an initial sample weight of approximately 5 mg using a TGA Q500 thermal analyzer (TA).

Scanning Electron Microscopy (SEM). The SEM micrographs were collected using a Hitachi SU3800 instrument, operating in high vacuum mode with an acceleration potential of 15 kV. The metallization was made by using gold vapor under vacuum.

X-ray microtomography (TOM). X-ray microtomography measurements were carried out with a Skyscan 1172 high-resolution MicoCT system at CRIST Centre, University of Florence (Italy) on a sample of ~ 1x0.5x0.25 cm. The X-rays tube equipped with a tungsten anode was operated at 100 kV and 100 µA. Placing the sample between the X-ray source and the CCD detector, 2D X-ray images were captured over a 180-degree rotating sample with a slice-to-slice rotation angle of 0.3. The spatial resolution of the image was kept in a range of 4 µm in terms of pixel size. The 3D image was reconstructed from the projections using the Nrecon software (Bruker µ-CT 1.6.10.2). After reconstruction, the image was analyzed to obtain information on the sponge structure, such as the pore size distribution, through the CTAnalyser software (Bruker µ-CT 1.18.8.0). A 3D representation in false-colour was realized by the CTVox software (Bruker µ-CT 3.3.0).

Rheology. The rheology measurements were carried out on water-saturated samples by the TA Discovery HR-3 hybrid rheometer according to the following procedure. Frequency sweep measurements were performed to monitor the behavior of the two parameters G' (elastic modulus) and G'' (viscous modulus) as a function of the oscillation frequency at constant oscillation amplitude. The check of this range was

determined through amplitude sweep measurements of G' and G'' at constant frequency sweep (1 Hz) as a function of the oscillation amplitude. The normal force was set equal to 0.5 N for all the measurements.

Acetic Acid Absorption-Desorption Tests. To evaluate the capacity of the sponges to absorb gaseous acetic acid, they were dried and weighed (W_{dry}) and put in sealed jars with a vial containing 8 mL of glacial acetic for six days (until saturation). Then, they were weighed (W_{ab}), left to equilibrate for six more days at controlled temperature and humidity (20 °C – RH 50%) and weighed again (W_{eq}).

The amount of absorbed acetic acid after the absorption test ($AcOH_{ab}\%$) and after the equilibration period ($AcOH_{eq}\%$) was evaluated through gravimetric analysis, using the following equations:

$$AcOH_{ab}\% = \left(\frac{W_{ab} - W_{dry}}{W_{dry}} \right) \cdot 100 \quad (4.1)$$

$$AcOH_{eq}\% = \left(\frac{W_{eq} - W_{dry}}{W_{dry}} \right) \cdot 100 \quad (4.2)$$

Where W_{dry} = weight of the dried sample, W_{ab} = weight (g) of the sample after the absorption test and W_{eq} = weight (g) of the sample after the equilibration period. The acetic acid amount after the equilibration period obtained through gravimetric analysis and expressed as follows:

$$AcOH_{eq}\%_2 = \left(\frac{W_{eq} - W_{dry}}{W_{eq}} \right) \cdot 100 \quad (4.3)$$

has been compared with TGA data, calculating the acetic acid amount considering the weight loss in the range 25-200 °C of the thermogravimetric profile of the sponges, acquired after the equilibration period (WL_{eq}), and subtracting the weight loss in the same range measured for the dry sponge (WL_{dry}):

$$AcOH_{eq}\%_{TGA} = WL_{eq} - WL_{dry} \quad (4.4)$$

To obtain further information about the nature of the interaction between the sponges and the acetic acid, desorption tests were performed [33]. Moreover, samples previously subjected to absorption tests and equilibrated at room temperature for 6 days, have been maintained at low pressure (ca. 15 mbar) until they reach a stable weight value. To evaluate the amount of strongly-bounded acetic acid ($AcOH_{sb}\%$) after this further treatment, the following equation was used:

$$AcOH_{sb}\% = \left(\frac{W_{des} - W_{dry}}{W_{dry}} \right) \cdot 100 \quad (4.5)$$

Where W = weight (g) of the dried sample, W_{des} = weight (g) of the sample after the desorption test.

The weakly-bonded acetic acid ($AcOH_{wb}\%$) after the equilibration period, was calculated as:

$$AcOH_{wb}\% = AcOH_{eq}\% - AcOH_{sb}\% \quad (4.6)$$

Three measurements have been performed for each sample and the average values and the corresponding standard deviations are reported. FTIR-ATR spectra were collected before and after the absorption tests and after the desorption test.

Regeneration and reuse tests. To regenerate the material in view of its reuse, sponges previously subjected to acetic acid absorption tests were immersed in a 1M NaOH solution for 10 minutes [9], then it was washed three times for 20 min with water and then dried at 50 °C. To evaluate the possibility of reusing these systems, two cycles of absorption-regeneration were carried out. The performance of the sponges after each absorption test was evaluated through gravimetric analysis as reported in the previous paragraph. Three measurements have been performed for each sample and the average values and the corresponding standard deviations are reported.

4.2.6 Results and discussion

FTIR-ATR Spectroscopy. In Fig.7, the FTIR-ATR spectrum of PVA-PEI-CG (see paragraph 4.2.4.1) is reported. The presence of characteristic peaks of PEI (N-H bending at 1563 cm^{-1} , C-H bending at 1483 cm^{-1}) and PVA (CH bending at 1420 and 1328 cm^{-1} and the C-O stretching at 1087 cm^{-1}) is clear. Then, all the peaks typical of PEI are still present also in the spectrum of the final product. This represents an important feature because, in the view of an application of this system as remediation for the “vinegar syndrome”, the FTIR spectrum indicates that the NH_2 groups are still available for the neutralization of acetic acid.

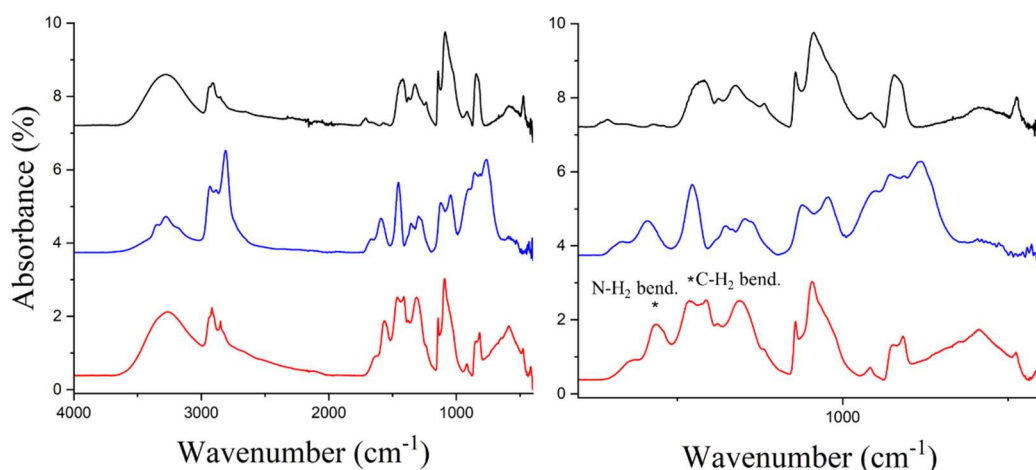


Figure 7. FTIR-ATR spectra of PVA (black), PEI (blue) and PVA-PEI cryogel (red) acquired between $4000\text{-}400\text{ cm}^{-1}$ (A) and $2000\text{-}400\text{ cm}^{-1}$ (B), characteristic peaks of PEI in PVA-PEI-CG are indicated with “*”.

On the other hand, in the spectra for all the products obtained from syntheses PVF-PEI1 (protocol 1) and PVF-PEI2.X (protocol 2), peaks associated with PEI could not be detected; on that basis, it is possible to affirm that, in the limits of the sensitivity of FTIR-ATR, the spectra indicate that the attempt to load PEI into the PVF network through the procedures 1 and 2 described into the paragraph 4.2.4.3 seems to be unsuccessful. Then, being that the idea was to exploit the alkaline character and the NH_2 groups of PEI to adsorb the acetic acid formed by motion picture films, this

class of sponges does not seem to be promising for this purpose. In Fig. 8 the spectra associated with two products of synthesis 1 (PVF-PEI1) and 2 (PVF-PEI2) are compared with those of pure PEI and PVF. None of the products obtained from synthesis 2 reported in Tab. 1 gave good results so only one spectrum is reported as an example (PVF-PEI2.16). As it is possible to see, peaks ascribed with PEI are absent in both spectra.

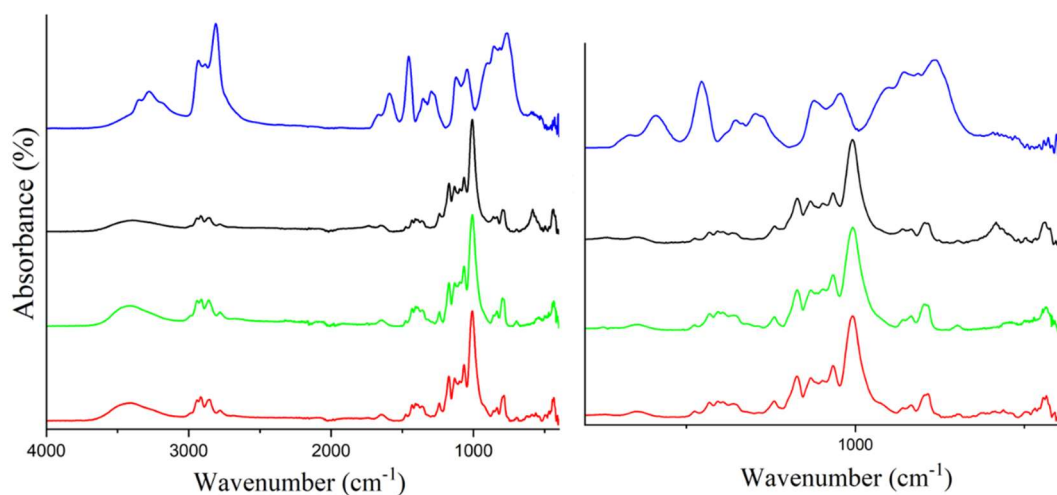


Figure 8. FTIR-ATR spectra of PVF (black), PEI (blue), PVF-PEI1 (synthesis 1, red), PVF-PEI2.16 (synthesis 2, green) in the range 4000-400 cm^{-1} (A) and 1800-400 cm^{-1} (B).

The spectrum of the final product of synthesis 3 (PVF-PEI-GA in Fig. 9), did show peaks associated with PEI (peaks corresponding to N-H bending at 1575 cm^{-1} , to C-H bending at 1473 and 1301 cm^{-1} ; the other PEI characteristic peaks overlap with those of PVF). In addition, the appearance of a weak peak at 1540 cm^{-1} associated with C=N [32], [34]–[36], could be ascribed to the formation of an imine linkage between PEI and GA [28] (Figure 9B). Further tests are needed for more compelling evidence of this point.

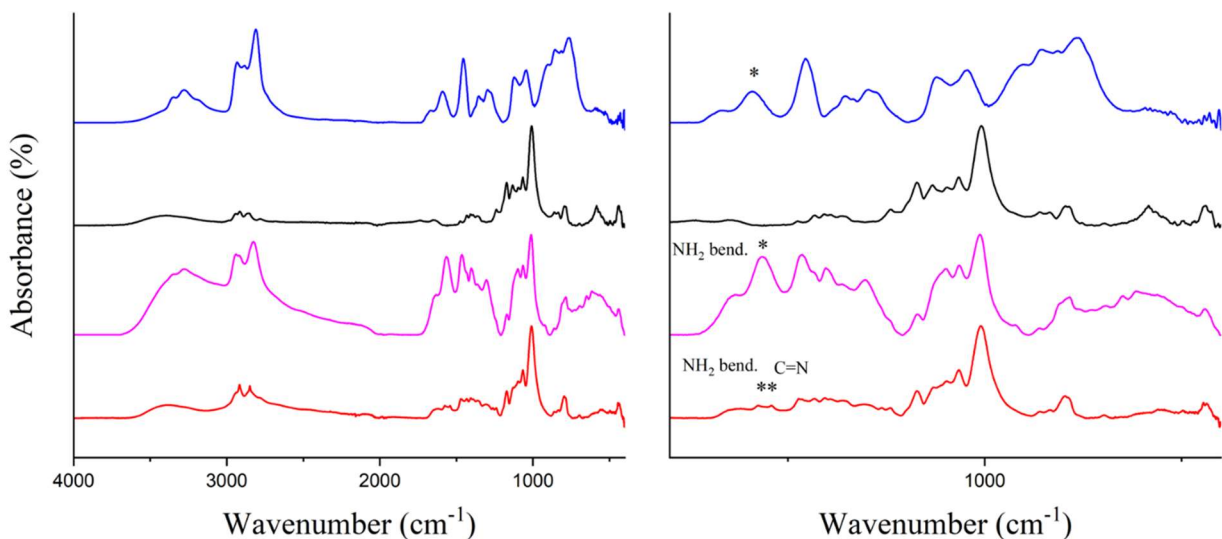


Figure 9. FTIR-ATR spectra of PVF (black), PEI (blue), PVF-PEI3 (intermediate product of synthesis 3, before the crosslinking with GA, pink) and PVF-PEI-GA (final product of synthesis 3, after the crosslinking of GA, red) acquired in the range 4000-400 cm^{-1} (A) and 2000-400 cm^{-1} (B).

Thermogravimetric analysis. Further evidence for the presence of PEI in the final products of PVF-PEI-GA (synthesis 3) and PVA-PEI-CG was provided by TGA and DTG profiles. These profiles have been compared with the ones of PVF, PVA and PEI. Concerning the cryogel PVA-PEI-CG (Fig. 10), the first weight loss between 50°C and 200 °C (Fig. 10A) is due to water evaporation. This temperature is much higher than the boiling temperature of pure water, probably due to the different populations of water molecules differently bound to the polymeric chains of the system [18]. In addition, as indicated in the DTG graph (Fig. 10B), two further thermal events are observed: the first one between 200 °C and 275 °C and the second one between 280 and 470 °C, which could be ascribed to the pyrolysis of PVA and PEI, respectively. On these bases, these data are in agreement with the FTIR analysis (Fig. 7) being that they confirm the presence of PEI inside the PVA-based network.

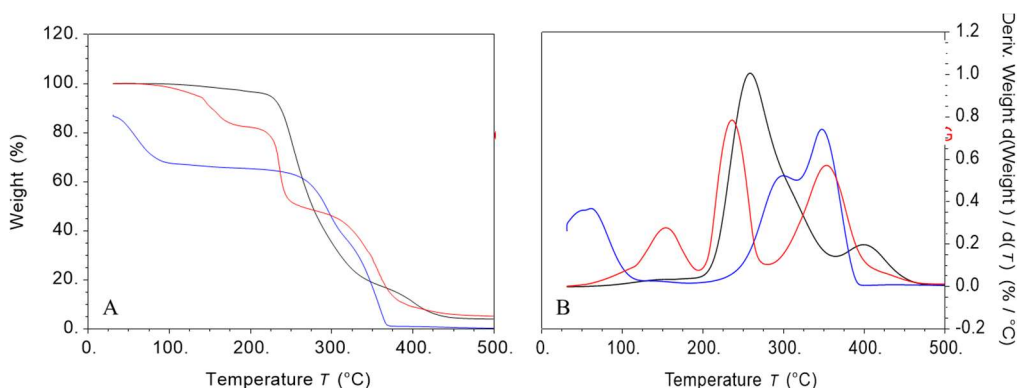


Fig. 10 TGA (A) and DTG (B) profiles of pure PVA (black), pure PEI (blue) and PVA-PEI-CG (red).

The PVF-PEI-GA profile (Fig.11) shows a first weight loss between 30 and 160 °C due to water evaporation (Fig. 11A). In addition, as indicated by the DTG curves (Fig. 11B), two further stages of degradation are detected, the first, in the range between 180 and 350 °C, due to PEI pyrolysis, and the second one resulting from PVF decomposition that occurs in the range of 350-475 °C. The endpoint of the latter is higher than the one of pure PVF (350-420 °C), probably due to the further crosslinking of PVF induced by GA.

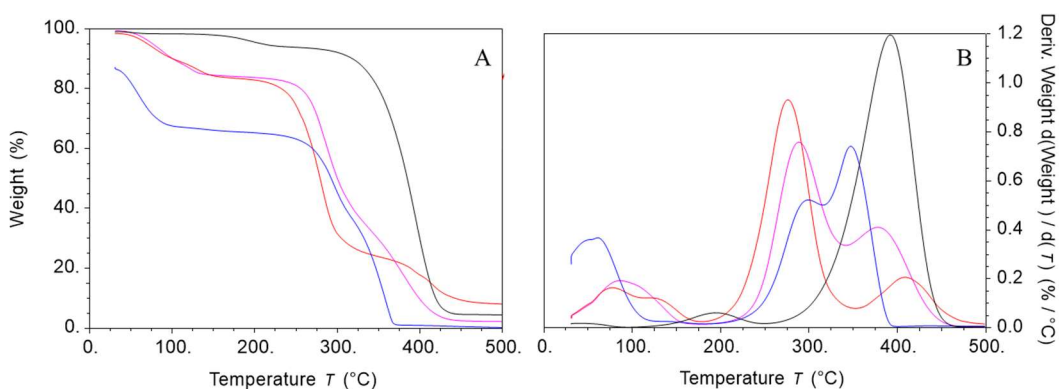


Fig. 11 TGA (A) and DTG (B) of PVF (black), PEI (blue), PVF-PEI3 before the crosslinking with GA (pink) and PVF-PEI-GA after the crosslinking with GA (red).

Elemental Analysis. Elemental analysis has been performed on pure PEI, PVF-PEI1, PVF-PEI-GA and PVA-PEI-CG in order to provide further proof of the presence of nitrogen (that is a marker of PEI, the only component of the system that contains N). The C/N ratio has been calculated (Tab. 2). As it is possible to appreciate, the amount of N is very low (0.65%, C/N 47.7) for PVF-PEI1, while is higher for both the PVA-PEI-CG (9.87%, C/N 4.7) and the PVF-PEI-GA (11.7%, C/N 3.1), demonstrating the presence of only minimal traces of PEI inside the PVF-PEI1 and higher contents inside the latest two systems (more in PVA-PEI-CG than in PVF-PEI-GA). Those data are in perfect agreement with the FTIR analysis. All the systems show a lower N(%) and a higher C/N than in pure PEI (16.5%, C/N 1.8) for the presence of PVA/PVF as a source of C.

Tab. 2 Results of the elemental analysis performed on pure PEI, PVF-PEI1, PVF-PEI-GA and PVA-PEI-CG. The accuracy of the measurement is $\pm 0.1\%$.

Sample	Weight (g)	N (%)	C (%)	C/N
PEI	1.8	16.3	28.8	1.8
PVA-PEI-CG	2.4	9.9	46.75	4.7
PVF-PEI1	1.9	0.65	31.0	47.7
PVF-PEI-GA	1.2	11.7	36.6	3.1

Scanning Electron Microscopy (SEM). From a morphological standpoint, the cryogel (Fig. 12A-B) appears more compact and homogenous than the sponges, as expected. On the other hand, both PVF (Fig. 12C-D) and PVF-PEI-GA (Fig. 12E-F) show an important porosity with different sizes (with diameters from 2 μm to more than 300 μm).

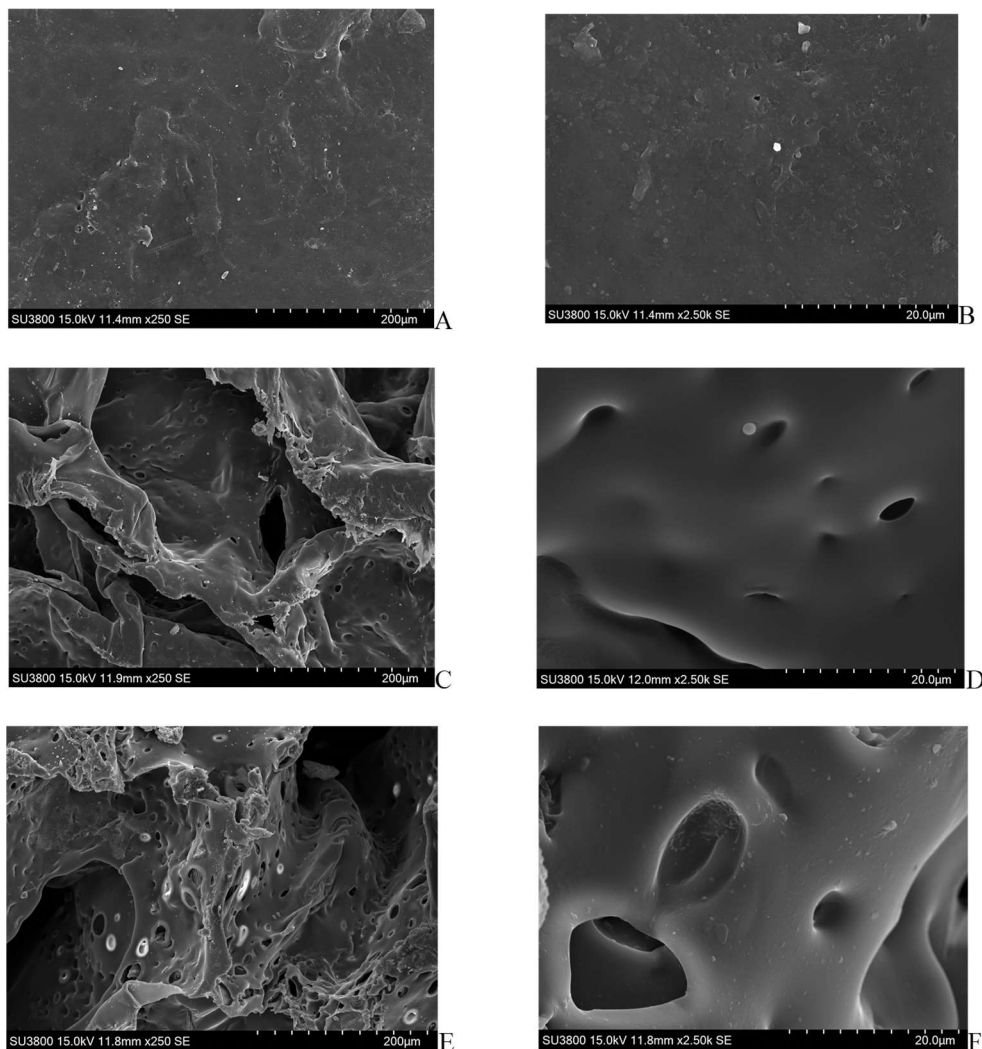


Fig. 12 SEM micrographs acquired with a magnification of 250x (on the left) and 2.5kx (on the right) of PVA-PEI-CG (A-B), PVF (C-D) and PVF-PEI-GA (E-F).

X-ray microtomography (TOM). By comparing micro-tomographies of PVF (13A-C, paragraph 4.2.4.2) and PVF-PEI-GA (13B-D, paragraph 4.2.4.3) it is possible to better understand the variation in density and porosity after the addition of PEI: in PVF-PEI-GA a density gradient from the surface to the bulk of the sponge is evident if compared to pure PVF. This is probably ascribable to the incorporation method of PEI via under-vacuum adsorption which does not guarantee a homogeneous penetration of this polymer into the bulk of the system.

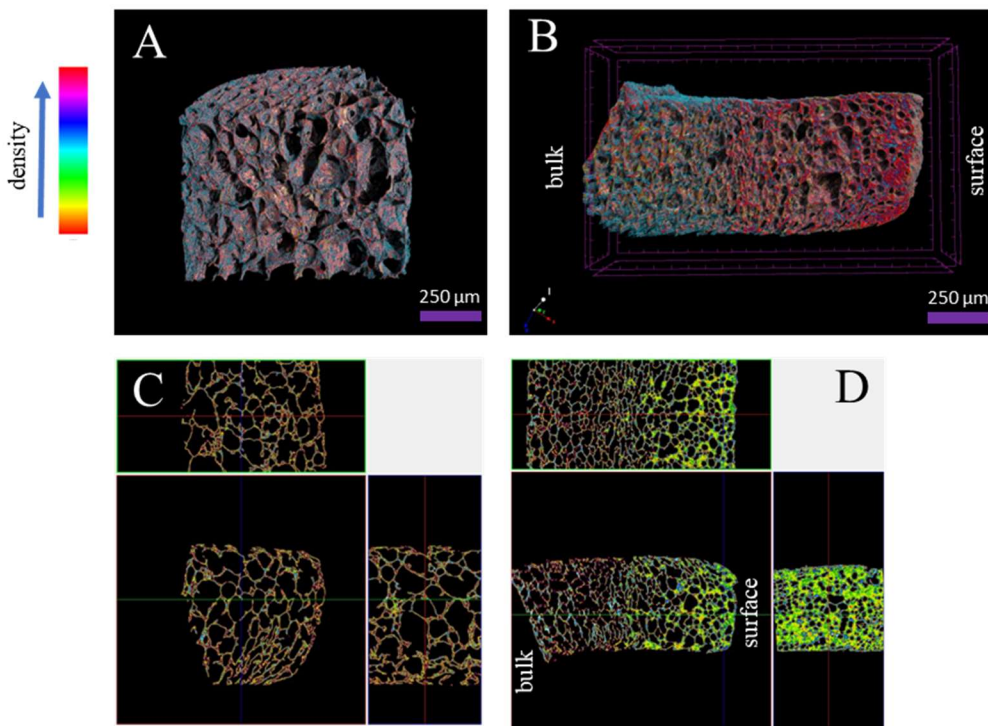


Fig. 13 Micro-tomographies of PVF (A-C) and PVF-PEI-GA (B-D) in false-colors to point out the density variation.

The data reported in Tab. 3 indicate that the total porosity (percentage in volume) in PVF is completely made by open, and then accessible, pores. A decrease in total porosity is observed from 81.45% in PVF to 55.26% in PVF-PEI-GA due to the inclusion of PEI chains in the network. But it is interesting to note that, even if the fraction of closed pores slightly increases (the total porosity rises from 0.01% in PVF to 1.56% in PVF-PEI-GA), the percentage of open pores in PVF-PEI-GA is still high (98.7% in PVF-PEI-GA vs 99.9% in PVF). It is possible to assume that PEI is probably absorbed on the walls of bigger open pores (decreasing their dimensions) without closing them or that completely fills smaller pores. In fact, in the size range investigated by μ -TOM (the spatial resolution is 5 μ m), the PVF dimensions of pores range from a few microns to 400 μ m with a maximum at about 220 μ m (Fig. 14A);

on the other hand, the dimension of pores in PVF-PEI-GA in the superficial area ranges from few microns to 260 μm with a maximum at 140 μm .

Tab. 3 Closed, open and total porosity percentage in volume for PVF and PVF-PEI-GA calculated from micro-tomographies. The error is about 5% of the measurement.

	PVF	PVF-PEI-GA
Closed Porosity (%)	0.01	1.56
Open Porosity (%)	81.44	54.56
Total Porosity (%)	81.45	56.12

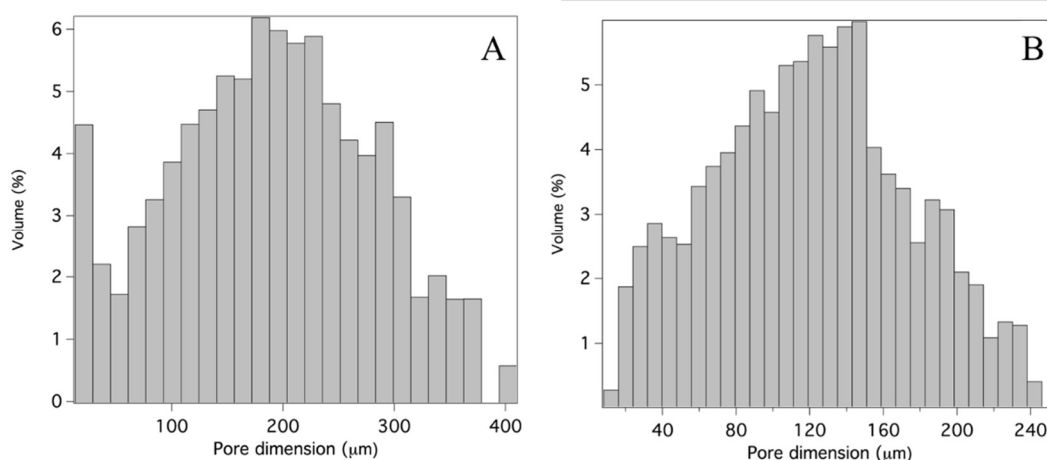


Fig. 14 Percent volume in size range (%) of porous in PVF (A) and PVF-PEI-GA sponge calculated from micro-tomography data.

Rheology. Rheology measurements have been performed on the PVF sponge (Fig. 15). In the linear range identified by the amplitude sweep measurement, PVF shows a solid-like behavior during the frequency sweep measurement because the storage modulus (G') > the loss modulus (G''), (Fig. 14A).

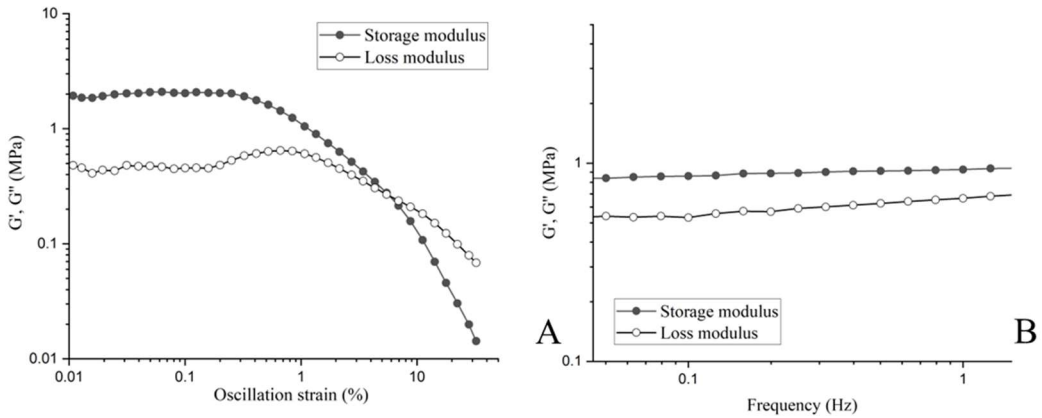


Fig. 15 Graphs associated with (A) the amplitude sweep and the (B) frequency sweep measurements on PVF.

Acetic acid absorption tests. In this paragraph, the capacity of PEI, PVA-PEI-CG, PVF, PVF-PEI3 (i.e. the first step of PVF-PEI-GA synthesis) and PVF-PEI-GA to absorb gaseous glacial acetic acid will be discussed.

In Fig. 16, it is possible to macroscopically appreciate the effects on both the dimensions and the color of the sample after the absorption test. Except for PVF, which appears slightly deformed, no meaningful dimensional alterations are visible in the samples.

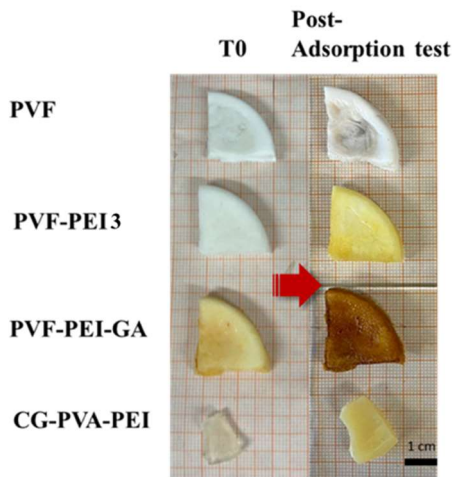


Fig. 16 Image of PVF, PVF-PEI3, PVF-PEI-GA, PVA-PEI-CG before and after the absorption test.

Figure 17 shows the FTIR-ATR spectra of pure PEI (Fig. 17A) and of the samples described in Figure 16 before and after the absorption of acetic acid and after the desorption tests. The experimental procedure is the one described in the paragraph 4.2.5. The spectra in Figure 17 are labeled as follows (Tab. 4):

Tab.4 Legend of the spectra reported in Fig. 17.

Spectrum	Color	Figure
PEI	black	
PEI_AcOH _{ab}	red	17A
PEI_AcOH _{des}	pink	
PVA-PEI-CG	black	
PVA-PEI-CG_AcOH _{ab}	red	17B
PVA-PEI-CG_AcOH _{des}	pink	
PVF	black	
PVF_AcOH _{ab}	red	17C
PVF_AcOH _{des}	pink	
PVF-PEI3	black	
PVF-PEI3_AcOH _{ab}	red	17D
PVF-PEI3_AcOH _{des}	pink	
PVF-PEI-GA	black	
PVF-PEI-GA_AcOH _{ab}	red	17E
PVF-PEI-GA_AcOH _{des}	pink	

In Figure 17A the spectrum of PEI collected immediately after the absorption test (PEI_AcOH_{ab}, red line) shows a peak at 1700 cm⁻¹ associated with the asymmetric stretching of C=O of acetic acid that partially is physically adsorbed and partially forms ammonium acetate groups. In PEI_AcOH_{des} part of the weakly bonded adsorbed is lost, as indicated by the decrease of the intensity of the peak at 1700 cm⁻¹ after the desorption step (Figure 17A, PEI_AcOH_{des}, pink line). Moreover, in the spectrum of PEI, a peak at 1454 cm⁻¹ ascribed to the CH₂ scissoring is present, while, in PEI_AcOH_{ab} and PEI_AcOH_{des} spectra, a shift of this peak at 1391 cm⁻¹ is observed, which is a possible overlap with the complex band due to the combination

of C-O and O-H vibrations that is usually around 1400 cm^{-1} . A further shift of the peaks at 1104 and 1047 cm^{-1} , ascribable to the C-N stretching in pure PEI, is registered in PEI_AcOH_{ab} and PEI_AcOH_{des} (1035 and 1004 cm^{-1}) probably due to the effect of the acetate groups bound to the NH₂.

In PVA-PEI-CG spectra (Fig. 17B) similar trend as the ones reported for PEI (Fig.17A) is observed: the appearance of two new peaks at 1717 , 1254 , 1009 cm^{-1} (asymmetric stretching C=O, CH bending and C-O stretching, respectively) and the shift of the band at 1403 - 1360 cm^{-1} . Also in this case, the intensity and the shift of the peaks are more pronounced in the AcOH_{ab} spectrum than in the AcOH_{des}, probably for the presence of weakly bound acetic acid in the first one.

In PVF spectra (Fig. 17C), only a new peak is detectable in the PVF_AcOH_{ab} at 1723 cm^{-1} , associated with the asymmetric stretching of C=O; the disappearance of this peak in the PVF_AcOH_{des} suggests that probably all the acetic acid was weakly adsorbed and then it was completely lost during the desorption process.

In both PVF-PEI3 and PVF-PEI-GA spectra (Fig. 17D-E), the new peaks at 1701 and 1245 cm^{-1} are visible only in the AcOH_{ab} spectra, while the shift of the peak at 1404 cm^{-1} is detected in both AcOH_{ab} and AcOH_{des}. The shift ascribed to the C-O stretching is not significative in these spectra because the C-O group is present also in the initial PVF.

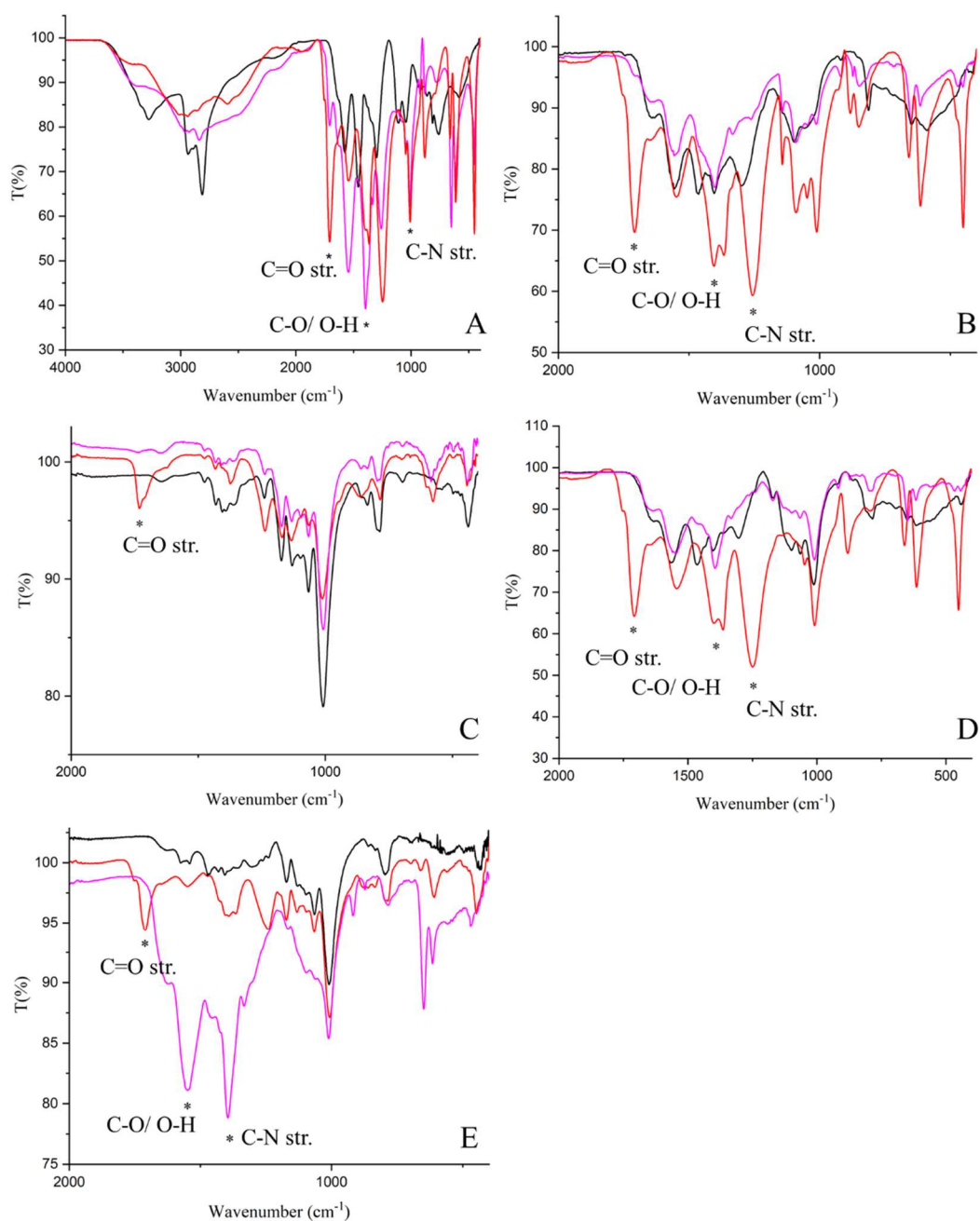


Fig 17 FTIR-ATR spectra of PEI (A), PVA-PEI-CG (B), PVF (C), PVF-PEI3 (D), PVA-PEI-GA (E) in the range 400-2000 cm^{-1} , before the absorption test (black), after the absorption test in glacial acetic acid (red) and after the desorption test (pink). The peak associated with the presence of acetic acid are marked with a “*”,

Data from gravimetry tests are reported in Table 5 and Fig.18.

Tab.5 Gravimetry data of absorption-desorption- tests in acetic acid for PEI, PVA-PEI-CG, PVF, PVF-PEI3, PVF-PEI-GA. Three measurements have been performed for each sample and the average values and the corresponding standard deviations are reported.

Sample	AcOH _{ab} % [°]	AcOH _{eq} % ^{°°}	AcOH _{sb} % [#]	AcOH _{wb} % ^{##}	AcOH _{sb-norm} % [*]	AcOH _{wb-norm} % ^{**}
PEI	119±5	111±2	61±1	50±1	54.9	45.0
PVA-PEI-CG	157±3	35±1	17±1	18±1	11.3	10.8
PVF	114±2	17±1	6±1	11±1	9.9	5.6
PVF-PEI3	126±4	55±2	17±1	38±1	30.3	13.2
PVF-PEI-GA	137±3	52±1	9±1	43±1	31.2	6.5

[°]calculated with Eq. 4.1 ^{°°}calculated with Eq. 4.2
[#]calculated with Eq. 4.5 ^{##}calculated with Eq. 4.6
^{*} calculated as $AcOH_{sb-norm}\% = (AcOH_{sb} * 100) / AcOH_{eq}$
^{**}calculated as $AcOH_{wb-norm}\% = (AcOH_{wb} * 100) / AcOH_{eq}$

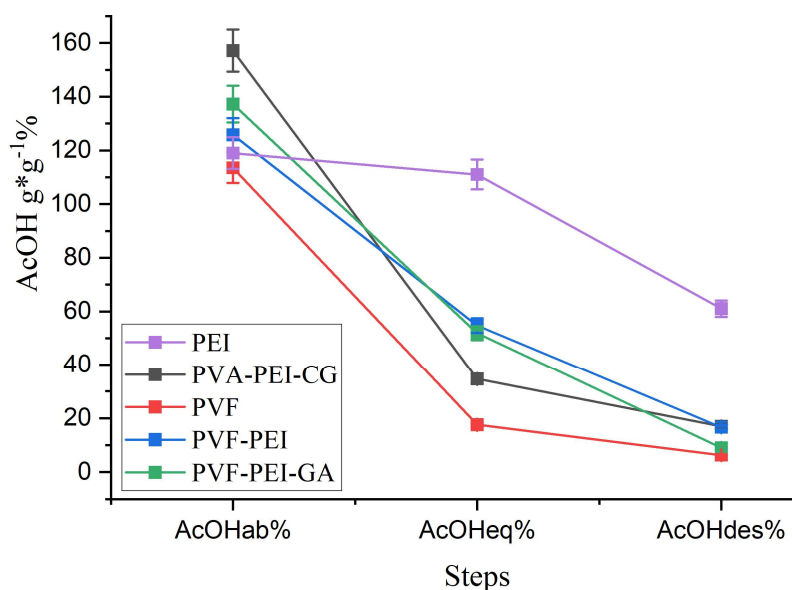


Fig. 18 Percentage in weight of the acetic acid absorbed by PEI (purple), PVA-PEI-CG (black), PVF (red), PVF-PEI3 (blue), PVF-PEI-GA (green) after the absorption test (AcOH_{ab}%), after the equilibration period (AcOHeq%) and after the desorption test (AcOH_{des}%) measured through gravimetric analysis.

In the first column the increase (in weight %) after six days in a glacial acetic acid-saturated environment is reported (AcOH_{ab}%, Eq. 4.1), while in the second column

is registered the value after six days of equilibration at room temperature and RH until a constant weight is reached ($\text{AcOH}_{\text{eq}}\%$, Eq. 4.2). Immediately after the absorption test, PVA-PEI-CG ($160\pm 1\%$) shows the highest weight increase followed by PVF-PEI-GA sponge ($137\pm 3\%$), PVF-PEI3 sponge ($126\pm 4\%$), PEI ($119\pm 5\%$) and PVF ($114\pm 2\%$). After 6 days of equilibration, apart from PEI, all the other systems show a decrease in the amount of adsorbed acetic acid. This trend is probably due to the desorption of a fraction of acetic acid (i.e. a population of molecules of acetic acid) that does not form either ion pairs with the $-\text{NH}_2$ groups of PEI, or direct H bonds with the polymer chains of the network (i.e. does not appertain to the first solvation spheres). Moreover, if compared with the pure systems (i.e. before the exposition to glacial acetic acid vapors), PEI shows a higher weight increase ($111\pm 2\%$), followed by PVF-PEI3 ($55\pm 2\%$), PVF-PEI-GA sponge ($52\pm 1\%$), PVA-PEI-CG ($35\pm 1\%$) and PVF ($17\pm 1\%$). The initial major absorption of PEI-based gel-like and sponge-like systems (i.e. PVA-PEI-CG, PVF-PEI-GA and PVF-PEI3) compared to pure PEI could be explained by the presence of free hydroxyl groups in their networks, which are able to form hydrogen bonds with acetic acid and physisorb it. In fact, after the equilibration period at room temperature and pressure, PEI shows the highest amount of adsorbed acetic acid, probably because sponge-like and gel-like systems loose part of the weakly-bound acetic acid. On the contrary, in PEI, acetic acid is mainly bonded via stronger ionic interaction with the amino groups and it is consequently more stable. The difference between cryogel (PVA-PEI-CG) and the sponges (PVF-PEI-GA and PVF-PEI3) could be ascribed to the different morphology of the samples (sponges are more porous than cryogel) and to the quantity of PEI (not present in PVF), that influences the retention capacity of physisorbed acetic acid.

To validate the data obtained by gravimetric analysis, TGA measurements have been carried out: the thermograms are reported in Figure 19 and the data are resumed in Tab. 6. The weight loss (%) from 25 to 200 °C for sponge-like systems and from 25 to 250 °C for cryogel was measured for the initial, dry sample (WL_{dry} , second column

in Tab. 5), to evaluate the amount of moisture present in the initial sample, and the acetic acid adsorbed after the equilibration period (WL_{eq} , third column in Tab. 5). Then the difference between WL_{eq} and WL_{dry} corresponds to the acetic acid adsorbed after the equilibration period ($AcOH_{eq}\%TGA$, Eq. 4.4, see paragraph 4.2.5). This value has been compared with the amount of acetic acid adsorbed during the equilibration period obtained through gravimetric analysis $AcOH_{eq}\%_2$ (Eq. 4.3, see paragraph 4.2.5). Most of the TGA are coherent with the results obtained via gravimetric analysis (Tab. 5). Only for PVA-PEI-CG there is an important discrepancy ($AcOH_{eq}\%TGA$: 14% vs $AcOH_{eq}\%_2$: $26\pm 4\%$), probably because the cryogel is more affected by oscillation in water content than the others systems.

Tab. 6 Amount of glacial acetic acid absorbed after the equilibration period calculated through gravimetry and TGA measurements in PVF-PEI-GA, PVF-PEI3, PVF, PVA-PEI-CG and PEI.

Sample	$AcOH_{eq}\%_2^*$ (gravimetry)	WL_{dry}	WL_{eq}	$AcOH_{eq}\%TGA^\circ$
PVA-PEI-CG	26 ± 4	18 ± 5	32 ± 5	14
PVF	16 ± 5	6 ± 5	28 ± 5	22
PVF-PEI3	35 ± 4	16 ± 5	50 ± 5	34
PVF-PEI-GA	34 ± 3	15 ± 5	49 ± 5	34
PEI	40 ± 3	21 ± 5	70 ± 5	49

*calculated with Eq. 4.3 $^\circ$ calculated with Eq. 4.4

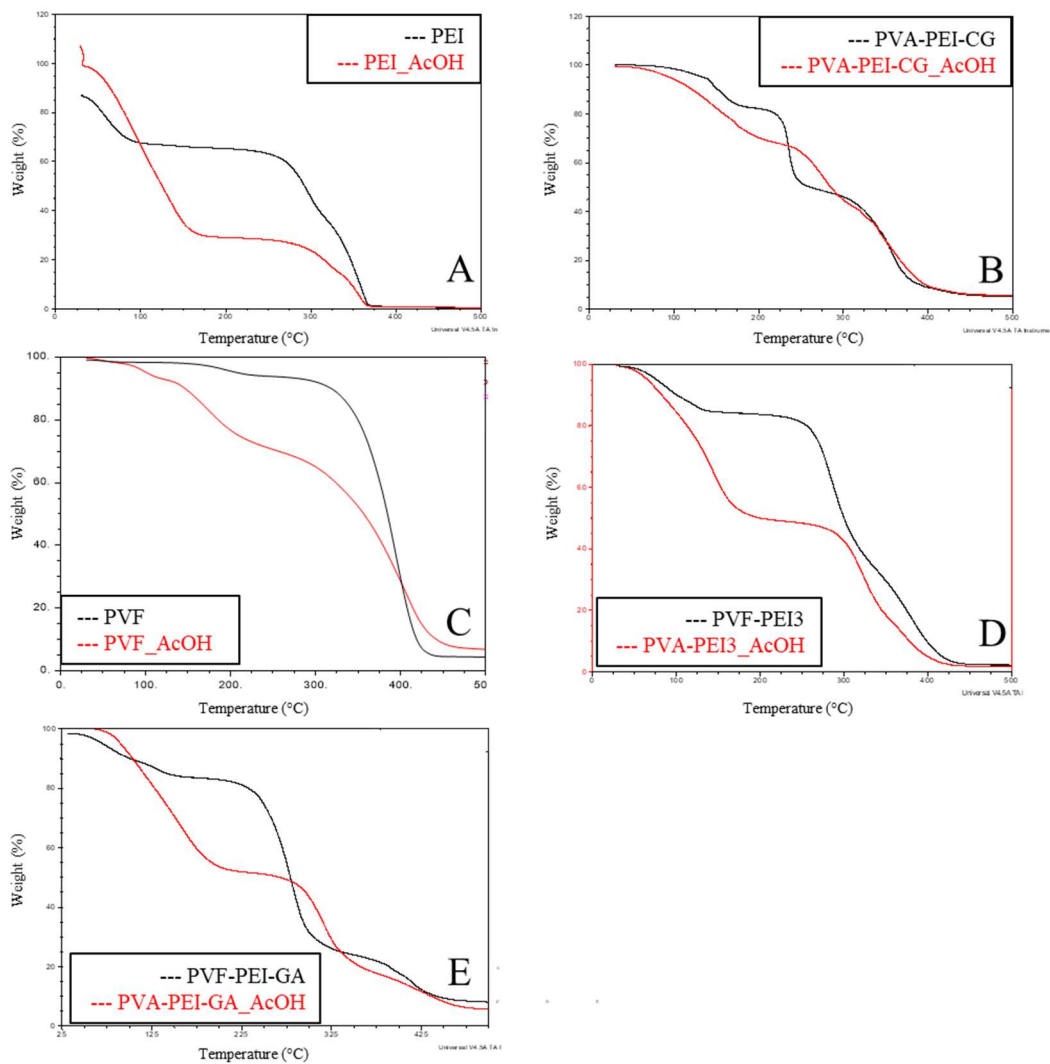


Fig. 19 TGA profiles of PEI (A), PVA-PEI-CG (B), PVF (C), PVF-PEI3 (D) and PVF-PEI-GA (E) before (black) and after (red) the absorption test.

Moreover, desorption tests have been performed to explore the nature of the interaction between the sponge and the acetic acid by curing the sponge under vacuum to a constant value (almost 56 h, Fig. 20, $AcOH_{des}\%$). This weight decrease could be ascribed to the removal of the residual weakly bonded acetic acid ($AcOH_{wb}\%$, Eq. 4.6, see paragraph 4.2.5) that interacts with the polymer chains of the network but that has not been removed during the equilibration at room pressure and temperature. The achievement of a constant weight, higher than the initial one,

could be associated with the presence of residual acetic acid, which it is possible to hypothesize remains more strongly bound to the system or as ammonium acetate [33] or through H bonds ($\text{AcOH}_{\text{sb}}\%$, Eq. 4.5, paragraph 4.2.5). As is possible to see from the data reported in the third and fourth columns of Tab.5, PEI still shows the highest content of $\text{AcOH}_{\text{sb}}\%$ ($61\pm 1\%$), confirming the hypothesis discussed above. Concerning the other systems, PVA-PEI-CG and PVF-PEI3 are the ones that show the major content of $\text{AcOH}_{\text{sb}}\%$ ($17\pm 1\%$), followed by the PVF-PEI-GA ($9\pm 1\%$). As expected, PVF shows a slower amount of $\text{AcOH}_{\text{sb}}\%$ ($6\pm 1\%$) because of the absence of PEI.

Regeneration and Reuse tests. An important goal of this research project has been the evaluation of the possibility of regenerating and reusing the proposed systems. Once PVF-PEI-GA, PVF-PEI3 and PVA-PEI-CG have strongly absorbed gaseous acetic acid as described in the previous paragraph, leading to the formation of ammonium acetate adducts, in order to restore the materials to their initial conditions, they were subjected to an alkaline treatment [9] (i.e. immersion in aqueous NaOH 1M). Then their performance as acetic acid adsorbers was evaluated again.

After the treatment with NaOH (Tab. 7), an important decrease in weight is observed for both PVF-PEI-GA ($-40\pm 2\%$) and PVF-PEI3 ($-55\pm 5\%$), preliminarily ascribable to the partial loss of the uncrosslinked PEI fraction. On the other hand, no variation compared to the initial weight has been detected for PVA-PEI-CG.

After the second absorption cycle in acetic acid, a decrease in both $\text{AcOH}_{2\text{ab}}\%$ and $\text{AcOH}_{2\text{eq}}\%$ was observed for all the systems, for PVF-PEI3 ($\text{AcOH}_{2\text{ab}}\%$: $-26\pm 5\%$ and $\text{AcOH}_{2\text{eq}}\%$: $-40\pm 2\%$). Regarding PVF-PEI-GA the decrease is evident compared to the first cycle, after the equilibration period ($\text{AcOH}_{2\text{ab}}\%$: $23\pm 4\%$; $\text{AcOH}_{2\text{eq}}\%$: $5\pm 2\%$), but it is less pronounced than PVF-PEI3. It is important to point out that these data are normalized by the initial W_{dry} , and, for this reason, values are particularly low for sponge-like systems, which have lost a lot of material during the regeneration process in NaOH. For these systems, indeed, the loss of PEI may

decrease their capacity to absorb acetic acid (and the loss of PEI is more important for PVF-PEI3 than PVF-PEI-GA, where PEI is crosslinked to the PVF network). However, further tests will be necessary to try to improve crosslinking reaction efficiency between PVF and PEI through GA.

Even if a decrease in the yield of acetic acid absorbed is evident also in this case, PVA-PEI-CG gave the best results after the second absorption cycle ($\text{AcOH}_{2\text{ab}}\%$: $45\pm 6\%$; $\text{AcOH}_{2\text{eq}}\%$: $26\pm 3\%$). The observed decrease is probably due to the rearrangement of the polymeric network during the regeneration process. Further tests are needed to clarify this point, too.

Tab. 7 Gravimetry data of absorption-regeneration-absorption tests in acetic acid for PVF-PEI-GA, PVF-PEI and PVA-PEI-CG.

SAMPLE	$\text{ACO}_{\text{H}_{\text{ab}}}\%$	$\text{ACO}_{\text{H}_{\text{eq}}}\%$	$\text{ACO}_{\text{H}_{\text{regenerated}}}\%$	$\text{ACO}_{\text{H}_{2\text{ab}}}\%$	$\text{ACO}_{\text{H}_{2\text{eq}}}\%$
PVA-PEI-CG	157±3	35±1	0±5	45±6	26±3
PVF-PEI3	126±4	55±2	-55±5	-26±5	-40±2
PVF-PEI-GA	137±3	52±1	-40±2	23±4	5±2

4.3 Polyethyleneimine-based sponge systems (SPEI)

The following step of the research was focused on the setup of a further system that should merge three needs at the same time:

- to have a sponge-like system;
- to use PEI as the adsorber improving the adsorption performances with respect to the systems described above;
- to have a more easily regenerable system.

Polyethyleneimine sponges (SPEI) (Fig. 20A) were synthesized through a nucleophilic reaction between PEI and the epoxy groups of 1,4-butanedioldyglycidyl ether (BDDE), used as cross-linking agent. In particular, the reaction occurs through the ring-opening of the epoxy groups. From the literature [37]–[40] is known that,

depending on the amine structure and by varying synthesis conditions (molar ratio of PEI:BDDE, PEI concentration, reaction temperature), two pathways of the addition reaction occur in parallel: cross-linking (both the oxirane rings of the BDDE react with the amino groups of PEI) and grafting reaction (only one oxirane ring reacts with PEI) (Fig. 20B). The predominance of one of these two reactions can influence the physico-chemical properties of the systems, such as the pH and the morphology of the sponges, as we will show in the next paragraphs.

At present, the most eco-friendly and easier method to obtain highly porous structures from PEI is through cryogelation [3], [37], [41], [42]: PEI has been crosslinked with BDDE at a temperature of -20°C in an aqueous environment and ice crystals act as porogen templates that can be easily removable in the thawing step. On these bases, two important conditions about the kinetics of the reaction have been realized to obtain sponge-like systems: the cross-linker has to be chosen in order to be highly reactive at low temperatures; the cross-linking reaction shall be carried out only after the complete and homogeneous freezing of the solution [37]. According to these constrains and to the literature data [3], [37] BDDE has been chosen as the best cross-linking agent for our purpose.

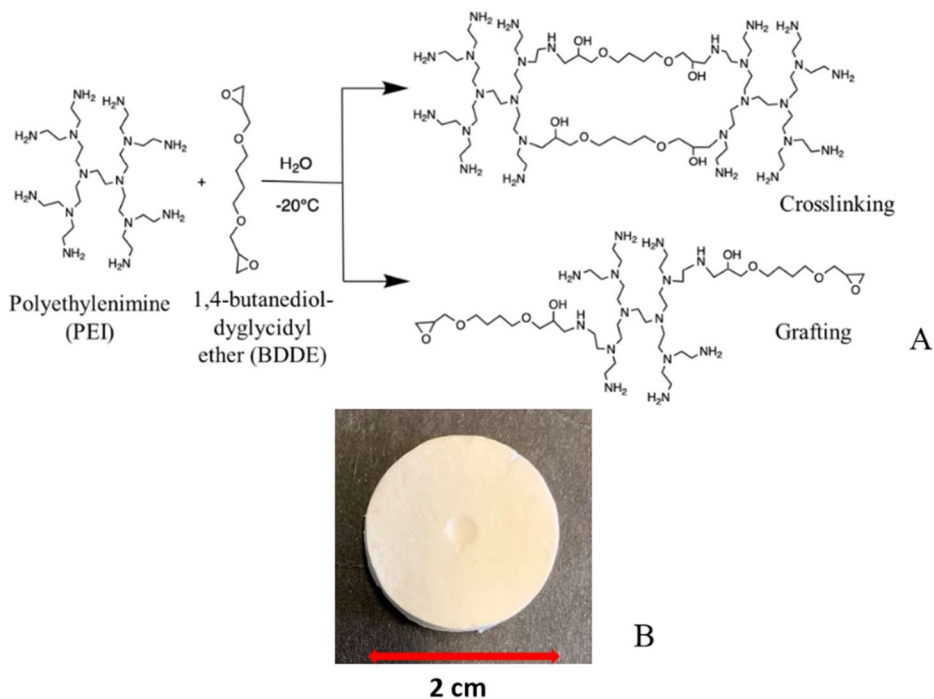


Fig. 20 (A) Scheme of PEI-cross-linking/grafting via epoxy-amine reaction; (B) a polyethyleneimine-based sponge.

4.3.1 Chemicals

Branched polyethyleneimine (PEI) with an average molecular weight of 750 kDa at 50% solution in water, 1,4-butanedioldyglycidyl ether (BDDE), and glacial acetic acid (AcOH, $\geq 99.7\%$) were purchased from Sigma Aldrich. Sodium Hydroxide ($\geq 98.5\%$ pellets, anhydrous) was purchased by Acros Organics.

Water used for all the procedures was purified by a Millipore MilliQ Direct-Q® & Direct-Q UV water purification system (Water Resistivity: 18,2 M Ω at 25°C).

4.3.2 Synthesis of the systems

Polyethyleneimine sponges (SPEI) have been synthesized via epoxy-amine reaction, using BDDE as a cross-linking agent [3], [37], [42].

Syntheses have been carried out by solubilizing PEI in water under stirring and then adding the BDDE. The solution was vortexed for a few seconds, poured into a mold and stored at -20°C for 24 hours. Then, the system was thawed and washed with water five times, in order to remove unreacted reagents. Finally, the sponge was dried at 50 °C. Several syntheses were performed varying the concentration of PEI (4, 6, 8 w/w%) and the PEI:BDDE molar ratio (1:1, 2:1, 3:1) as reported in Tab. 8.

Tab. 8 Scheme of the syntheses performed varying PEI concentration and PEI:BDDE molar ratio.

Sample	PEI concentration (wt%)	PEI:BDDE
SPEI 1	4	1:1
SPEI 2	4	2:1
SPEI 3	4	3:1
SPEI 4	6	3:1
SPEI 5	8	3:1

4.3.3 Characterization of the systems

Fourier Transform Infrared Spectroscopy Measurements (FTIR-ATR). The FTIR spectra were collected by means of a Shimadzu, IRAffinity-1S Fourier Transform Infrared Spectrometer by using the MIRacle Single Reflection Horizontal ATR Accessory equipped with a Diamond/ZnSe Performance flat tip Crystal Plate. The resolution was 2 cm⁻¹, the number of scans was 64 and the range 4000-600 cm⁻¹. All the spectra were reported as Transmittance (%) as a function of wavenumber (cm⁻¹).

Thermogravimetric analysis (TGA). Tests were performed in a nitrogen atmosphere at a heating rate of 10 °C/min over a temperature range of 25-500 °C, with an initial sample weight of approximately 5 mg using a SDT 650 thermal analyzer (TA).

Elemental Analysis. Elemental Analysis has been performed according to the procedure reported in Paragraph 4.2.5.

pH measurements. pH measurements have been carried out on the sponges with a WTW™ ProfiLine™ pH 3310, calibrated with NIST/DIN standard pH 6,865 e pH 9,180. Samples were saturated with water and the head of the pH-meter was put in contact with them for a few seconds. Five measurements were performed for each sample on different points of the surface. The average values and the corresponding standard deviation are reported.

Swelling tests. Swelling tests were performed on sponges in water and the kinetics of the absorption were monitored by the weight increase as a function of time according to the following procedure: the samples were put in a dryer to reach their dried weight (W_{dry}), then immersed in 10 mL of water in a capped vial. At defined time intervals, the sample was taken away from the vial, softly and rapidly dabbed on a Whatman filter paper and immediately weighed (W_{wet}). The value of Weight Increase in percent was calculated according to the following equation:

$$(WI\%)_{\text{time} = t_i} = \frac{W_{\text{wet}}(\text{time} = t_i) - W_{\text{dry}}(\text{time} = 0)}{W_{\text{dry}}(\text{time} = 0)} \cdot 100\% \quad (4.7)$$

This WI% was plotted as a function of time to obtain the kinetics curve of water absorption and the maximum amounts of the absorbed solvents were calculated from the asymptotic values of the curves reported. The results are expressed as the average value and the corresponding standard deviation calculated from the data obtained from three replicas of the same system.

Scanning Electron Microscopy (SEM). The SEM micrographs were collected as reported in Paragraph 4.2.5.

X-ray microtomography (TOM). X-ray microtomography measurements were carried out as reported in Paragraph 4.2.5.

Rheology. The rheology measurements were carried out as reported in Paragraph 4.2.5.

Acetic Acid Absorption-Desorption Tests. To evaluate the capacity of the sponges to absorb gaseous acetic acid, absorption-desorption tests have been performed as reported in Paragraph 4.2.5.

Regeneration and reuse tests. To regenerate the material in view of its reuse, sponges previously subjected to acetic acid absorption tests were subjected to a regeneration process as reported in Paragraph 4.2.5. To evaluate the possibility of reusing them, 3 cycles of absorption-regeneration have been conducted.

4.3.4 Results and discussion

Polyethyleneimine sponges (SPEI) have been synthesized according to the procedure described in the paragraph 4.3.2. In the following sections, the results of the physico-chemical and mechanical characterization of the five systems reported in Table 8 obtained by varying the molar ratio of PEI:BDDE and PEI concentration will be described.

FTIR-ATR Spectroscopy. The chemical composition of the polyethyleneimine sponges has been investigated by means of FTIR-ATR spectroscopy. In Fig. 21A the spectra of the five SPEI and the one of unreacted branched PEI are reported. The characteristics peaks of PEI [43], [44] are visible in all the spectra of the sponges: the out-of-plane wagging at 940 cm^{-1} , the C-NH₂ stretching at 1044 cm^{-1} , the C-N-C stretching at 1110 cm^{-1} , the C-H bending at 1463 cm^{-1} , the NH bending of primary amine at 1600 cm^{-1} , the C-H stretching at 2948 and 2845 cm^{-1} and the N-H stretching between 3100 - 3600 cm^{-1} . Comparing the spectra of the sponges (for the chemical composition, see Table 8) with the one of PEI, the increase in the intensity of the peak at 1105 cm^{-1} (ascribable to both the C-N-C and the C-O stretching) is

appreciable (Figure 21B). This trend can be ascribed to the opening of the epoxy ring and the following crosslinking reaction that gives the formation of new C-N-C bonds [3], [42]. In all the SPEI spectra two further peaks at 1280 cm^{-1} and 1330 cm^{-1} are visible: the first one could be ascribed to the stretching of the C-O of the epoxy ring and its presence could be associated with the BDDE molecules grafted to PEI that still maintain one epoxy ring unreacted; the second one could be associated with the O-H bending of the BDDE chain [42]. In the spectra of the sponges, a peak at 1555 cm^{-1} is present, probably ascribable to the NH bending of secondary amines, which increased its intensity after the epoxy-amine reaction [45].

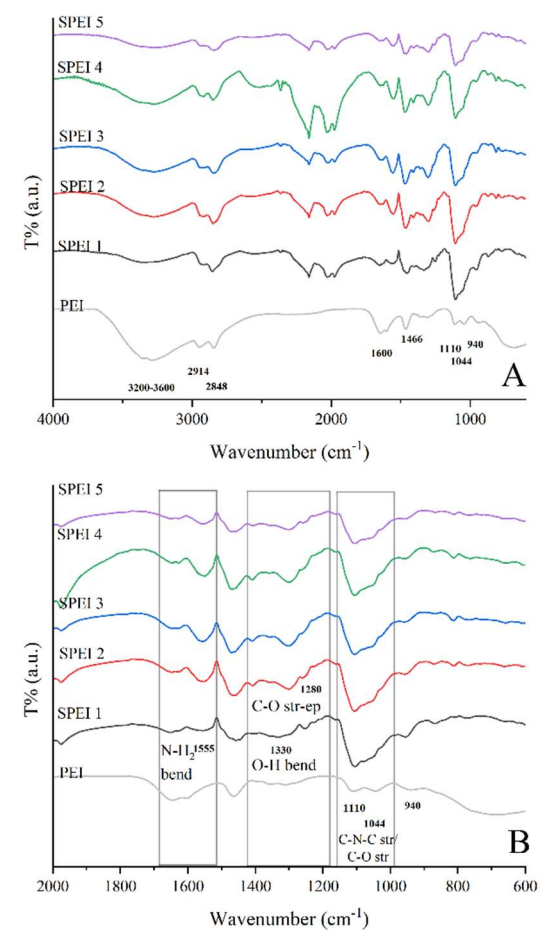


Fig. 21 (A) FTIR-ATR spectra of unreacted branched polyethileneimine (gray) and of SPEI 1 (black), SPEI 2 (red), SPEI 3 (blue), SPEI 4 (green), SPEI 5 (purple); (B) magnification of the spectra in the 2000-600 cm^{-1} range.

Thermogravimetric analysis. In Fig. 22 the TGA (Fig. 22A) and the DTG (Fig. 22B) curves of pure PEI and of the SPEI4 system are reported. All the TGA and DTG curves of the other SPEI sponges (see Tab. 8) have a similar trend to that of SPEI4 which is reported in Fig. 22 as an example. Comparing the thermogravimetric profile of the unreacted PEI and all the sponges, a shift of the pyrolysis temperature [4] is observed (from 250-400 °C for PEI, to 290-390 °C). This datum is an indication of the increase in the average molecular weight of the PEI network and can be read as an indication of the success of the crosslinking reaction between the BDDE and PEI.

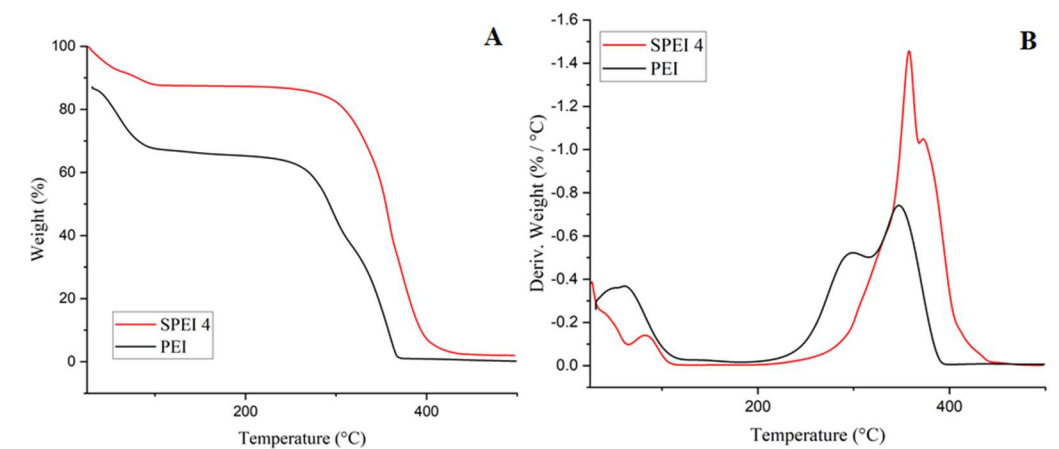


Fig. 22 TGA (A) and DTG (B) curves of PEI (black) and SPEI 4 (red).

Elemental Analysis. Carrying out elemental analysis on both unreacted PEI and sponges, it was possible to calculate the C/N ratio as shown in Fig. 23A-B: the C/N ratio of the unreacted PEI (1.8, the “0” point in Fig. 23) is lower than the one of all the sponges (between 4.5 and 3.4). This trend can be due to the BDDE molecules (that are a “source” of C atoms) crosslinked and/or grafted to PEI. As a consequence, as expected, by decreasing the amount of BDDE added (by maintaining the same PEI concentration), the C/N ratio decreases (4.5 for SPEI 1, 4.3 for SPEI 2 and 3.4 for SPEI 3, Fig. 23A). On the other hand, the increase in PEI concentration by maintaining constant the PEI:BDDE ratio, seems not to affect the C/N ratio that is

3.4 for SPEI 3, 3.65 for SPEI 4 and 3.4 for SPEI 5 (Fig. 23B). The results of the elemental analysis are reported in the Appendix of Chapter IV (Tab. A1).

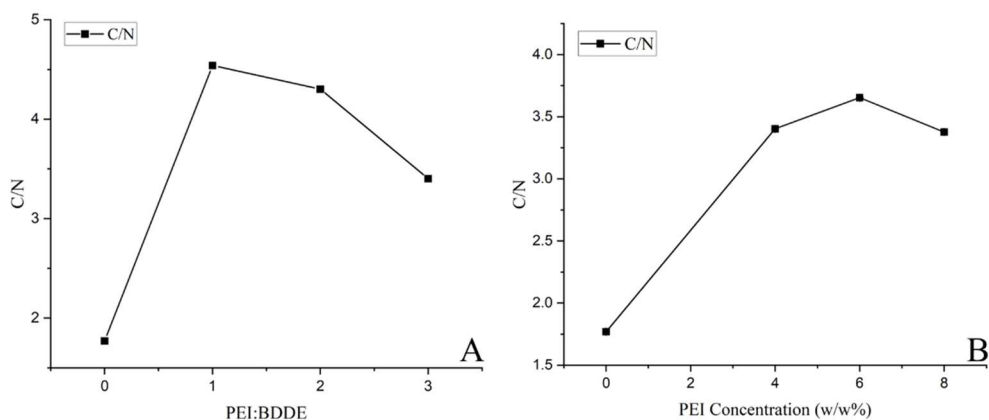


Fig. 23 C/N data in function of PEI:BDDE ratio (A) and PEI concentration (w/w%) (B). The first point is ascribed to pure PEI in both graphs.

pH measurements. pH measurements (Fig. 24A-B) have been carried out to obtain information about the amount of free -NH_2 groups, that determine the alkaline character of the sponges, and also the capability to neutralize the acetic acid produced by motion picture films affected by the “vinegar syndrome”. The pH of pure PEI is about 12.5, while the pH of all the SPEI sponges is still alkaline but its value ranges between 8 and 9. This lowering of the pH can be read as a further confirmation of the occurrence of the epoxy-amine reaction that causes a decrease of the free -NH_2 groups. By comparing the various systems, it is possible to affirm that the pH data are coherent with the results of the elemental analysis: the pH increases with the PEI:BDDE ratio (pH 8.7 ± 0.1 for SPEI 1, 9 ± 0.1 for SPEI 2 and 9.5 ± 0.1 for SPEI 3, Fig. 24A) due to the lower extent of the reaction and so to the higher amount of free amino groups. Consistently with the trend of the C/N ratio, even the pH seems to be almost independent from PEI concentration if the PEI:BDDE ratio is maintained constant (pH 9.5 ± 0.1 for SPEI 3, 9.7 ± 0.1 for SPEI 4 and 9.4 ± 0.2 for SPEI 5, Tab. 8 and Fig. 24B).

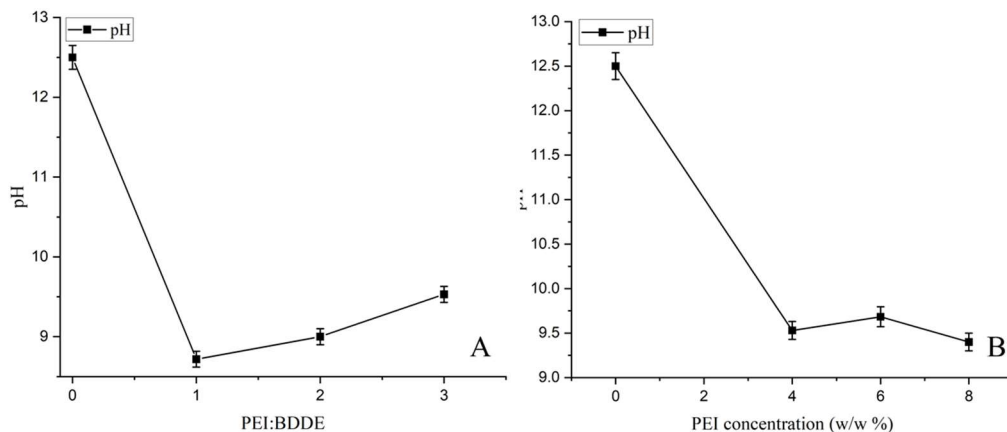


Fig. 24 pH data in function of PEI:BDDE ratio (A) and PEI concentration (w/w%) (B). The first point is ascribed to pure PEI in both graphs.

Swelling tests. Swelling tests in water (Fig. 25) were performed in order to obtain more informations about SPEI structure by comparing these data with C/N results. A more detailed explanation of this point will be reported below. It can be seen that all samples exhibit the same swelling kinetics and that the equilibrium state is reached 120 minutes after immersion in water. The maximum swelling in water (Eq. 4.7, Fig. 25 and 26 A-B) ranges between 771% and 1700%, confirming the high hydrophilic character of polyethyleneimine-based systems.

Upon increasing the PEI:BDDE ratio, the total amount of adsorbed water increases too (775 ± 9 w/w% for SPEI 1, 1046 ± 9 w/w% for SPEI 2, 1700 ± 10 w/w% for SPEI 3, Fig. 26A). On the contrary, the increase of the PEI concentration, causes a decrease of the total amount of water adsorbed (1700 ± 10 w/w% for SPEI 3, 1030 ± 16 w/w% for SPEI 4, 771 ± 9 w/w% for SPEI 5, Fig. 26B), probably due to the increase of the spatial density of the polymer network to which corresponds a decrease of the volume available for water adsorption.

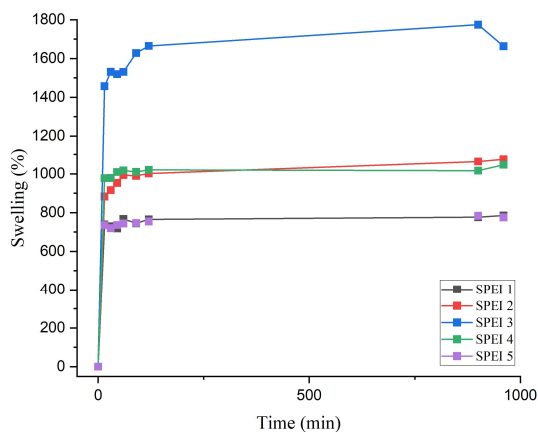


Fig. 25 Swelling behavior of SPEI 1 (black), 2 (red), 3 (blue), 4 (green), 5 (purple) in water.

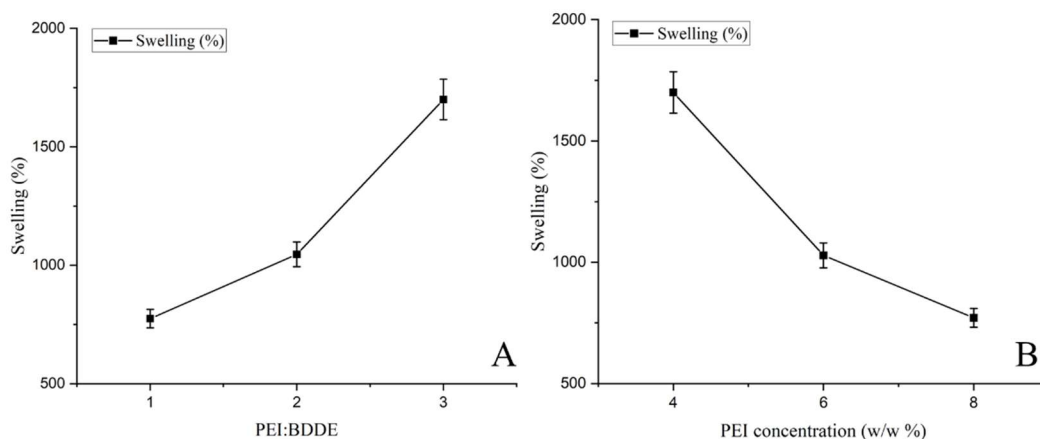


Fig. 26 Swelling capacity in function of PEI:BDDE ratio (A) and PEI concentration (w/w%) (B).

As reported in the literature [37], comparing the swelling capacity of our systems with the C/N ratios could be useful to obtain information about the reaction process, in particular about the pathways that occurred during the syntheses. High swelling values associated with high C/N ratios suggest that the predominant reaction occurring between PEI and BDDE is the grafting of the cross-linker as a side chain rather than the formation of cross-linkings between PEI molecules due to the reaction of both the epoxy groups of the BDDE with the free -NH₂ groups of PEI. By

analyzing the data of the sponges obtained by varying the PEI concentration (SPEI 3, SPEI 4 and SPEI 5, Fig. 23B and Tab. 8), they show the same, high C/N ratio (compared to the one of the unreacted PEI). But, while it is possible to assume that in SPEI 3 and SPEI 4 the grafting reaction was favored due to their higher swelling capacity, for SPEI 5, it is reasonable to affirm that the crosslinking reaction was favored, as indicated by his lower swelling capacity (Fig. 26B). For SPEI 1, which shows the highest C/N ratio (Fig. 23A) but also a low swelling capacity (Fig. 26A), we can assume that the crosslinking reaction was favored. These data indicate that in the formulations characterized by high PEI/BDDE ratios, the use of small amounts of BDDE not only limits the extent of the epoxy-amine reaction but also favors the grafting reaction pathway; on the other hand, the increase in PEI concentration, while maintaining constant this parameter, seems to not sensibly influence the occurrence of the epoxy-amine reaction but favors the cross-linking pathway.

Scanning Electron Microscopy. These hypotheses seem to find a match with the informations obtained from SEM analysis. The micrographs shown in Fig. 27 indicate that by increasing the PEI:BDDE ratio from 1:1 (SPEI 1, Fig. 27A) to 1:3 (SPEI 3, Fig. 27B), the porosity of the sponge increases, too. This behavior can be ascribed to a decrease in the spatial density of the crosslinking between PEI chains formed by BDDE molecules. On the other hand, by increasing the PEI concentration from 6% (SPEI 4, Fig. 27C) to 8% (SPEI 5, Fig. 27D), the structure of the sponge appears more compact and characterized by the presence of lamellar patterns. To confirm these hypotheses and also to obtain information about the structure at a nanometric scale, further investigations will be performed through Small-Angle X-Ray-Scattering (SAXS) on samples reported in Tab. 8.

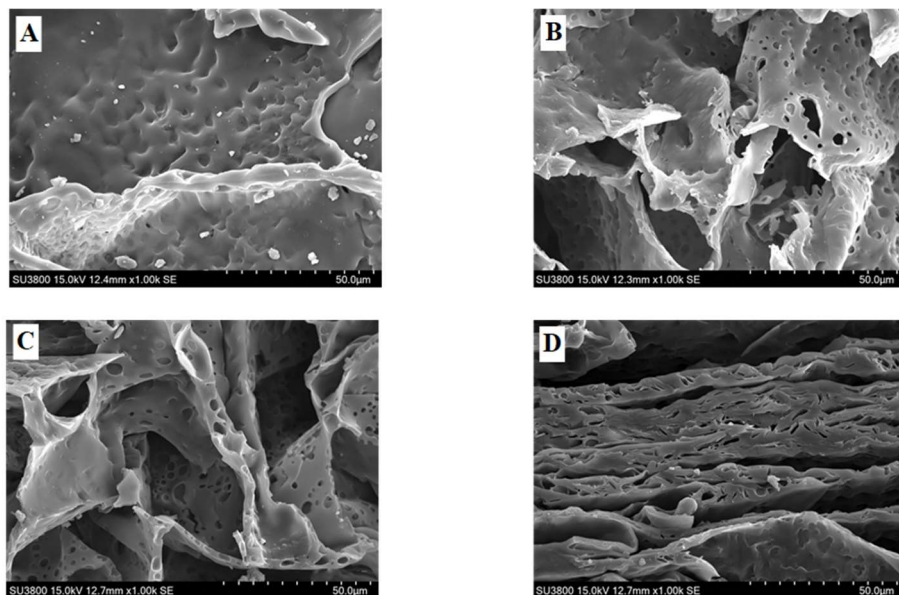


Fig. 27 SEM micrographs performed with 1.00kx magnitude of (A) SPEI 1, (B) SPEI 3 (C) SPEI 4 (D) SPEI 5.

X-ray micro-tomography. For SPEI 4 a further investigation of the pore size distribution (Fig. 28A and B) has been carried out through μ -TOM. It is possible to appreciate a different structure of the network if compared with PVF (see Fig. 13 and 14) in terms of pore dimension, with a higher number of micropores with sizes around $22\text{-}85\ \mu\text{m}^3$ and a peak at $45\ \mu\text{m}^3$. On the other hand, the percentage of total porosity on the total volume of the sample is similar to the one of PVF (for SPEI 4 is 78.29% for PVF 81.45%, see Tab. 3) with a higher percentage of open porosity than closed one (78.29% vs 0.02%) as observed also for PVF (81.44% vs 0.01%).

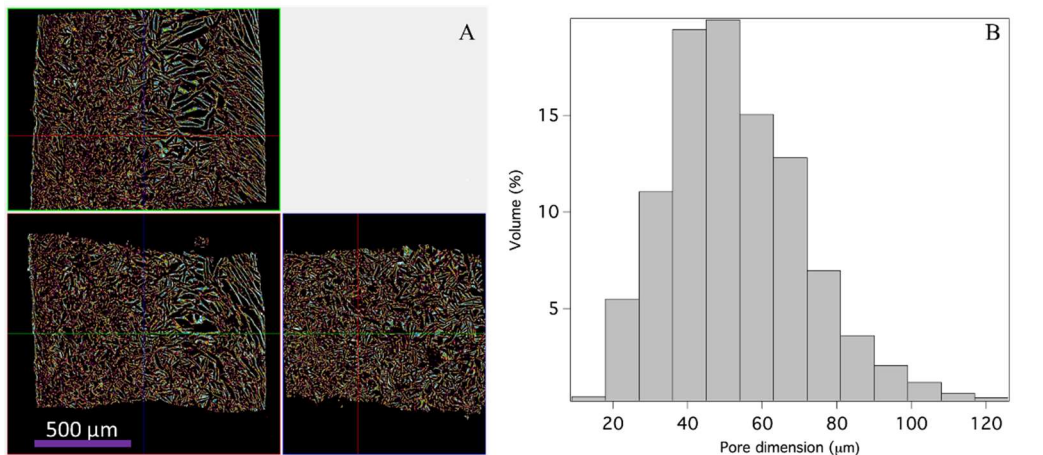


Fig. 28 (A) μ -TOM 3D reconstruction of SPEI4 with sections; (B) pore size distribution of SPEI 4 calculated from the μ -TOM images (the error on the measurements is about 5%).

Rheology. Oscillating rheological measurements have been carried out to obtain information about the effects of the chemical composition of the systems (in particular the amounts of both PEI and BDDE) on their mechanical properties and on the density of the crosslinkings. All the frequency sweeps (i.e. the test where the trend of the moduli G' and G'' is studied as a function of the frequency of the applied shear stress) have been done in the linear viscoelastic range previously determined for each sample through amplitude sweep test [46]. In Figure 29 the amplitude sweep of the SPEI 4 sponge is shown as an example, the amplitude sweep graphs of other samples (SPEI 1, SPEI 2, SPEI 3 and SPEI 5) are reported in the Appendix of Chapter IV (Fig. A1).

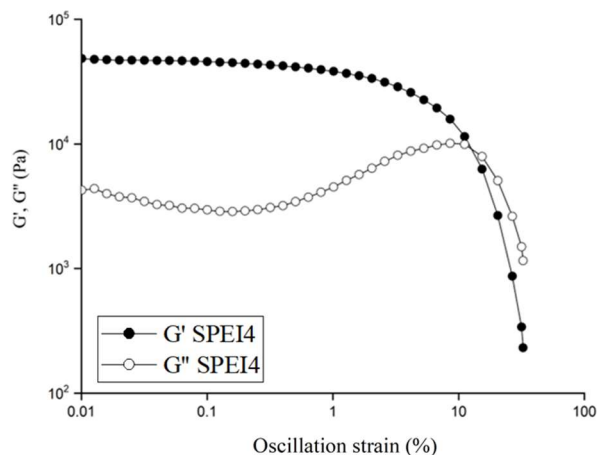


Fig. 29 Amplitude Sweep test performed on SPEI 4.

All the investigated samples (Fig. 30A and B) show a solid-like behavior typical of gels, as indicated by the value of the elastic modulus G' that is always higher than the loss modulus G'' all over the investigated frequency range [47]. In particular, considering the trend of G' , it is possible to obtain informations about the relative mechanical strength of the different systems and about the density of the crosslinking into the PEI/BDDE network that is directly proportional to the G' value. Figure 30A shows the frequency sweep curves of three different sponges (i.e. SPEI1, SPEI2 and SPEI3) in which the PEI:BDDE ratio increases from 1:1 for SPEI1 up to 1:3 for SPEI3. It is possible to observe that G' decreases upon increasing the PEI:BDDE ratio, indicating a decrease in the spatial density of the crosslinking. This datum confirms what was already discussed in the previous paragraphs: a decrease in the amount of BDDE favors the grafting reaction resulting in a decrease in the amount of crosslinking. Moreover, Figure 30B shows the frequency sweeps of SPEI3, SPEI4 and SPEI5 where the PEI concentration is increased while maintaining an equal PEI:BDDE ratio (3:1). The increase of the mechanical strength observed upon increasing the content of PEI and BDDE, as indicated by the growth of G' value, can be attributed, as indicated by the SEM micrographs, to an increase of the compactness and of the density of the system.

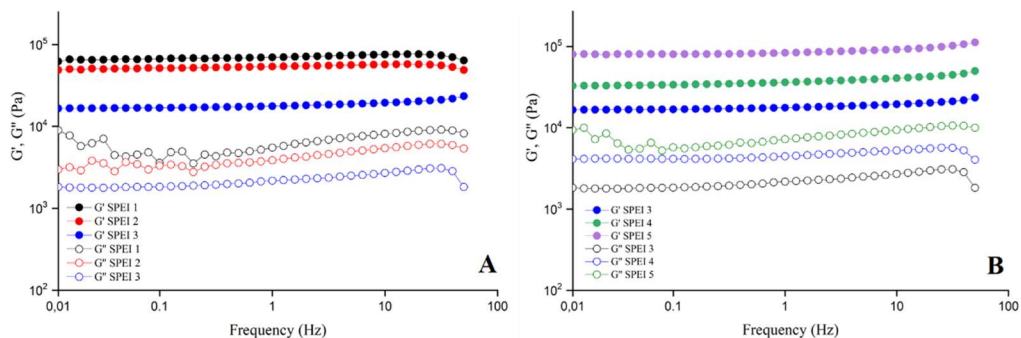


Fig. 30 Graphs associated with (A) the frequency sweep measurements of SPEI 1 (black), SPEI 2 (blue), SPEI 3 (green) to evaluate the variation of G' and G'' with PEI:BDDE ratio; (B) the frequency sweep measurements of SPEI 3 (black), SPEI 4 (blue), SPEI 5 (green), to examine the variation of G' and G'' with PEI concentration (w/w%).

Acetic acid Absorption tests. Finally, acetic acid absorption tests [33] were carried out to evaluate the performances in terms of absorption of gaseous acetic acid by the various samples. The presence of acetic acid inside the sponge was monitored by means of FTIR-ATR spectroscopy and the amount of acetic acid absorbed was evaluated via gravimetric analysis both immediately after the conclusion of the absorption test ($AcOH_{ab}\%$, Eq. 4.1) and after an equilibration period at 20 °C and RH 50% of 6 days ($AcOH_{eq}\%$, Eq. 4.2). TGA was used to validate the gravimetric results: the amount of acetic acid absorbed calculated from gravimetric data using Eq. 4.3 was compared to the weight loss calculated in the range 25-200 °C from the TGA profile of each sample (Eq. 4.4).

Macroscopically, immediately after the acetic acid absorption, all the SPEI appear yellowed (Fig. 31).

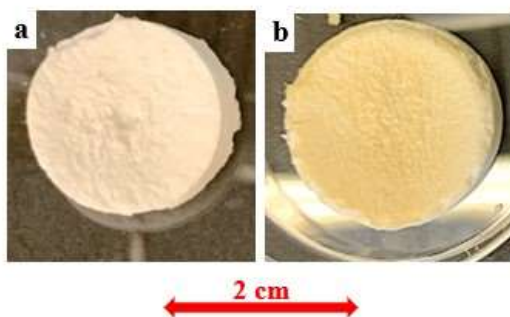


Fig. 31 SPEI 4 before (A) and after (B) the absorption test with glacial acetic acid.

In Fig. 32 the spectra collected on SPEI 4 before and after the absorption tests were reported as an example and compared to the one of the gaseous acetic acid. In the FTIR-ATR spectra collected on the sponges after the absorption test (green line in Fig. 32), peaks associated with acetic acid were detected: the C=O stretching at 1700 cm^{-1} , the C-H bending at 1407 cm^{-1} and the C-O stretching at 1286 cm^{-1} .

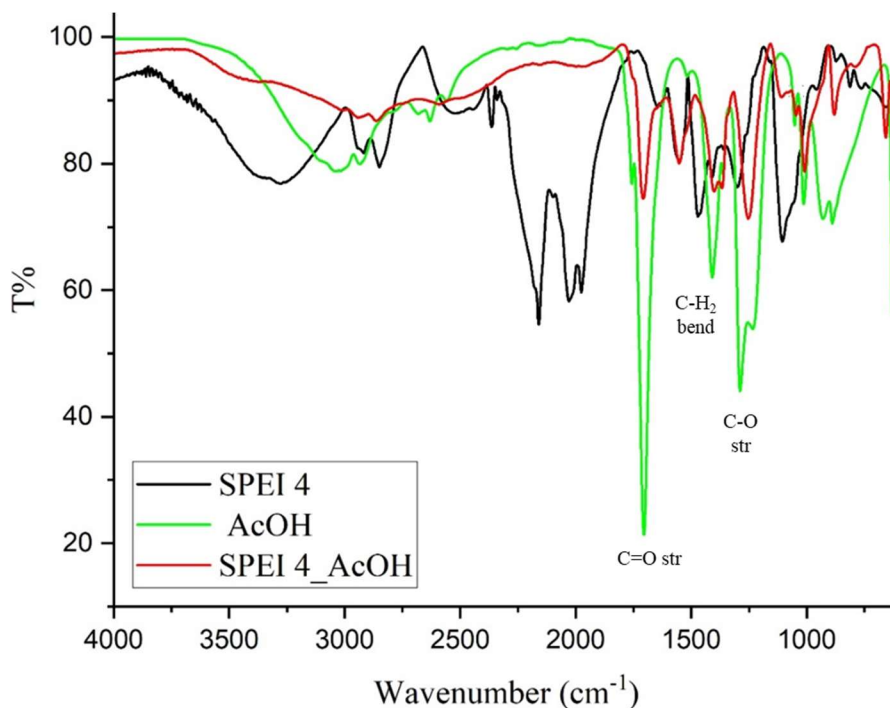


Fig. 32 FTIR-ATR spectra of pure acetic acid (green), SPEI 4 before (black) and after (red) the absorption test of gaseous acetic acid.

The values of $\text{AcOH}_{\text{ab}}\%$ and $\text{AcOH}_{\text{eq}}\%$ are resumed in Tab.9

Tab. 9 Amount of total acetic acid absorbed by SPEI 1-5 immediately after the absorption test ($\text{AcOH}_{\text{ab}}\%$) and after the equilibration period ($\text{AcOH}_{\text{eq}}\%$) and the corresponding weakly ($\text{AcOH}_{\text{wb}}\%$) and strongly ($\text{AcOH}_{\text{sb}}\%$) bonded acetic acid.

Sample	$\text{AcOH}_{\text{ab}}\%$ °	$\text{AcOH}_{\text{eq}}\%$ °°	$\text{AcOH}_{\text{wb}}\%$ #	$\text{AcOH}_{\text{wb-norm}}\%$ *	$\text{AcOH}_{\text{sb}}\%$ ##	$\text{AcOH}_{\text{sb-norm}}\%$ **
PEI	119±5	111±2	50±1	45	61±1	55
SPEI 1	115±7	23±4	16±1	14	7±1	6
SPEI 2	160±8	54±6	37±3	23	17±2	10
SPEI 3	280±9	76±5	42±3	15	34±3	12
SPEI 4	258±9	76±2	44±4	17	32±3	12
SPEI 5	215±7	76±4	49±2	23	27±2	13

°calculated with Eq. 4.1 °°calculated with Eq. 4.2 #calculated with Eq. 4.6 ##calculated with Eq. 4.5

*calculated as $\text{AcOH}_{\text{wb-norm}}\% = (\text{AcOH}_{\text{wb}} * 100) / \text{AcOH}_{\text{ab}}$

** calculated as $\text{AcOH}_{\text{sb-norm}}\% = (\text{AcOH}_{\text{sb}} * 100) / \text{AcOH}_{\text{ab}}$

From Tab. 9 all the samples, except SPEI 1, show higher $\text{AcOH}_{\text{ab}}\%$ but lower $\text{AcOH}_{\text{eq}}\%$ and $\text{AcOH}_{\text{sb}}\%$ (the fraction of strongly-bounded acetic acid), than pure PEI (AcOH_{ab} : 119±5%, AcOH_{eq} :111±2%, AcOH_{sb} :61±1%). This behavior is probably due to the porous structure of the SPEI systems that favors the initial absorption of acetic acid but part of the NH_2 is involved in the epoxy bonds with BDDE and is not available to neutralize it. Comparing the samples obtained varying the PEI:BDDE ratio, the amount of the acetic acid absorbed $\text{AcOH}_{\text{ab}}\%$ sensibly increases with the PEI:BDDE ratio (115±7% for SPEI 1, 160±8% for SPEI 2, 280±9% for SPEI 3, immediately after the absorption tests, Fig. 33A, squares). After the equilibration period, the amount of absorbed acetic acid is lower but the trend is the same (23±4% for SPEI 1, 54±6% for SPEI 2, 76±5% for SPEI 3, Fig. 33A, triangles).

For samples made with different PEI concentrations while maintaining constant the BDDE:PEI ratio, the absorbed acetic acid amount seems to not sensibly vary even if a slight decrease is observed with the increase of PEI concentration (280±9% for SPEI 3, 258±9% for SPEI 4, 215±7% for SPEI 5, Fig. 33B, squares); this is probably

due to the increase of the compactness of the system. After six days of equilibration, no relevant differences are detectable between the three samples ($76\pm 5\%$ for SPEI 3, $76\pm 2\%$ for SPEI 4, $76\pm 4\%$ for SPEI 5, Fig. 33B, triangles), probably because the initial discrepancy was due to weakly-absorbed acetic acid.

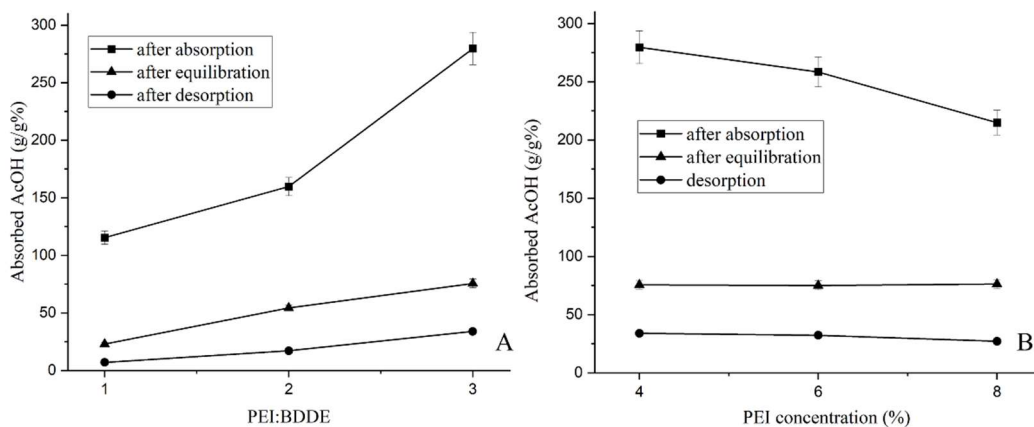


Fig. 33 Percentage of absorbed acetic acid immediately after the six days of absorption test (square), after six days of equilibration (triangle) and after the desorption test (circles) for samples SPEI 1,2,3 as they change PEI:BDDE ratio (A) and SPEI 3,4,6 as they change PEI concentration (w/w%) (B).

In Fig. 34 the thermogravimetric profiles of all the dry systems (solid lines) and of the systems after the equilibration period (dashed lines) are reported. Through thermogravimetric measurements, we validated the data obtained via gravimetric analysis (Tab. 10). Gravimetry data calculated with Eq. 4.3 ($AcOH_{eq}\%$, second column of Tab. 10) are ascribed to acetic acid absorbed on samples after the equilibration period. These data were compared to TGA results obtained with Eq. 4.4 ($AcOH_{eq}\%TGA$, fifth column of Tab. 10): these are obtained by subtracting the weight loss between 25 and 200 °C of the thermogravimetric profile of the dry sponge (WL_{dry} , second line of the column of Tab. 10) to the weight loss associated with the sponge measured after the equilibration period (WL_{eq} , third column of Tab. 9). WL_{dry} provide information about the amount of water absorbed by the systems, WL_{eq} about the acetic acid absorbed on the sponge after the equilibration period.

Subtracting WL_{dry} to WL_{eq} makes it possible to obtain the amount of acetic acid absorbed and corrected by the moisture content, i.e. $AcOH_{eq}\%TGA$, which was compared with $AcOH_{eq}\%_2$. These two data are coherent for most of the samples. Only for SPEI 5, the discrepancy between these two values is quite higher ($AcOH_{eq}\%_2$: $40 \pm 2\%$ vs $AcOH_{eq}\%TGA$: 35%). It may be ascribable to the errors in the experimental procedures. From TGA profiles, it is also possible to appreciate how the pyrolysis temperature of the systems does not vary after the absorption test, indicating that the integrity of the network was not altered by the absorption of gaseous glacial acetic acid.

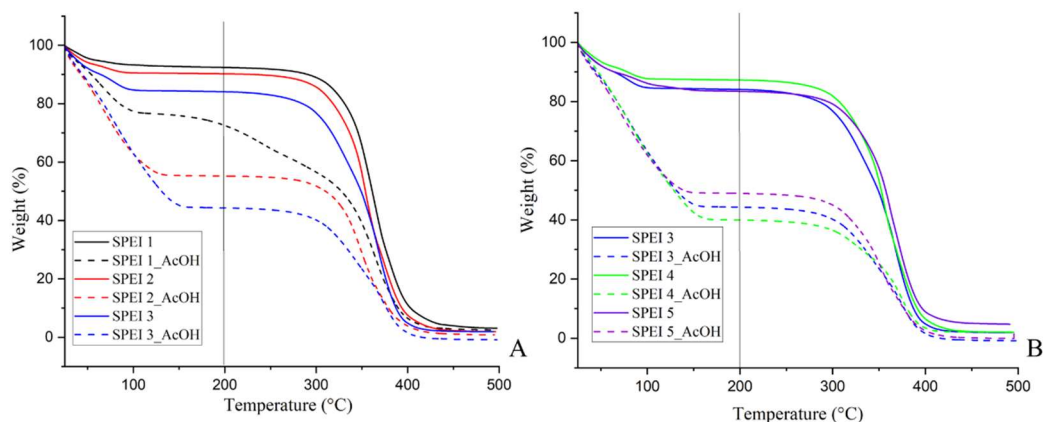


Fig. 34 TGA measurements of (A) SPEI 1,2,3 (as they change PEI:BDDE ratio) and (B) SPEI 3,4,6 (as they change PEI concentration) before (solid line) and after the glacial acetic acid absorption test + equilibration period (dashed line).

Tab. 10 Amount of glacial acetic acid absorbed after the equilibration period calculated through gravimetry and TGA measurements.

Sample	$AcOH_{eq}\%_2$ (gravimetry) *	WL_{dry}	WL_{eq}	$AcOH_{eq}\%TGA^\circ$
SPEI 1	19 ± 3	7 ± 5	26 ± 5	19
SPEI 2	35 ± 4	10 ± 5	46 ± 5	36
SPEI 3	43 ± 2	16 ± 5	55 ± 5	39
SPEI 4	42 ± 3	13 ± 5	59 ± 5	46
SPEI 5	40 ± 2	16 ± 5	51 ± 5	35

* calculated with Eq. 4.3

$^\circ$ calculated with Eq. 4.4

Desorption tests at low pressure have been performed to explore the nature of the interaction between the sponge and the acetic acid: putting the sponge under vacuum, a decrease in weight is measured until it reaches a constant value after 36 h (Tab. 9, AcOH_{sb}% column). The achievement of a constant weight, higher than the one of the initial systems (i.e. their weight before the interaction with acetic acid), could be associated with the presence of residual acetic acid, which remains more strongly bonded to the sponge, probably as ammonium acetate [33].

Considering the sponges in which the ratio PEI:BDDE was varied, the same trend observed after the absorption test (AcOH_{ab}) is evident (the AcOH_{sb}, calculated with Eq. 4.5, is 7±1% for SPEI 1, 17±2% for SPEI 2, 34±3% for SPEI 3, Fig. 33A, circles; the AcOH_{wb}, calculated with Eq. 4.6, is 16±1% for SPEI 1, 37±3% for SPEI 2, 42±3% for SPEI 3). For the SPEI in which the variation in PEI concentration was examined, no relevant differences between the three samples are reported except for a not very pronounced decrease in AcOH_{sb} at the increase of PEI concentration (AcOH_{sb} is 34±3% for SPEI 3, 32±3% for SPEI 4, 27±2% for SPEI 5, Fig. 33B, circles; the AcOH_{wb} is 42±3% for SPEI 3, 44±4% for SPEI 4, 49±4% for SPEI 5). Normalizing the percentage of the weakly and strongly absorbed acetic acid on the total amount of absorbed acetic acid for each sponge (AcOH_{wb-norm}% and AcOH_{sb-norm}%, fifth and seventh column in Tab. 9, respectively), the abovementioned trends are even more evident: the percentage of AcOH_{sb-norm}±% increases with the increase of PEI:BDDE ratio while it is practically unaffected by the concentration of PEI.

Regeneration and Reuse test. An important point of the study has been to evaluate the possibility of regenerating and reusing the proposed systems. Once they had absorbed gaseous acetic acid through an acid-base reaction, leading to the probable formation of ammonium acetate adducts as reported in the literature[33], to restore the material to its initial condition, it was subjected to a strongly alkaline treatment performed by immersing the sample in a 1M NaOH solution [9].

For this reason, SPEI 4 has been subjected to three cycles of absorption-regeneration, in order to evaluate any change in the absorption yield. As it is possible to appreciate in Fig. 35, the amount of acetic acid calculated through gravimetry after three cycles of absorption-regeneration is quite the same, suggesting the advantageous chance of reusing these systems at least 3 times. After the first regeneration [9], an increase in the absorbed AcOH is observed. This increase can be explained by considering the activating action of NaOH toward the amine groups of PEI. Polyethylenimine is in its neutral form at $\text{pH} > 10$ [48]. Initially, the synthesis of the absorbers is conducted in an aqueous environment ($\text{pH} < 10$), and thus a percentage of the amine groups of PEI is protonated upon first exposure to the acetic acid atmosphere [9]. During the regeneration process, the 1M NaOH treatment carried out after the first adsorption cycle is able not only to remove the acetic acid that has interacted with the polymer, but also to neutralize the charged amine groups of PEI, making it more efficient in the next adsorption cycles.

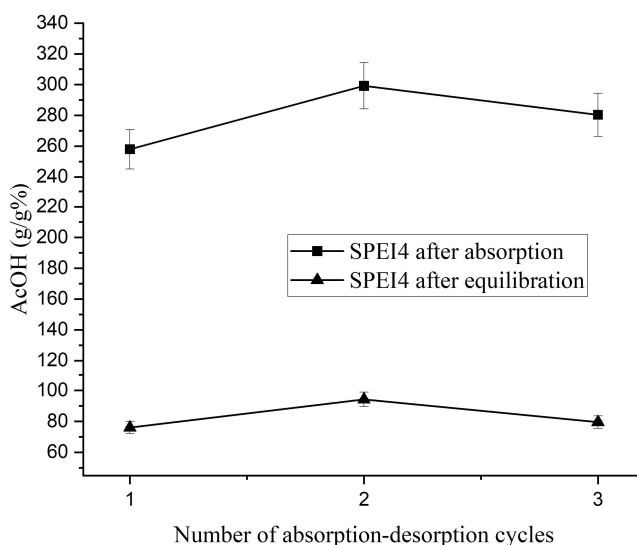


Fig. 35 Reusability test: the amount of acetic acid absorbed after three absorption-washing cycles. The amount of acetic acid right after the absorption test (square) and after 6 days of equilibration (triangle) is reported.

4.4 Conclusions

Sponge-like and gel-like systems based on the use of PEI for the absorption and neutralization of acetic acid have been developed.

All the systems proposed are cheap, easy to synthesize (in particular SPEI and PVA-PEI-CG) and handle and their shape is easy to adjust by simply varying the mold. They showed good physical-chemical stability, in particular PVF.

SPEI sponges seem to have a higher absorption capacity in comparison to PVF-PEI-GA and PVA-PEI-CG, both in terms of weakly ($\text{AcOH}_{\text{wb}}\%$, SPEI4: $258\pm 9\%$, PVF-PEI-GA: $137\pm 3\%$; PVA-PEI-CG: $157\pm 3\%$) and strongly ($\text{AcOH}_{\text{sb}}\%$, SPEI4: $32\pm 2\%$, PVF-PEI-GA: $9\pm 1\%$, PVA-PEI-CG: $17\pm 1\%$) bonded acetic acid. In addition, SPEI systems appear reusable (at least 3 times) because of the possibility to easily regenerate them with a basic bath in 1M NaOH. On the contrary, the efficacy of both PVF-PEI-GA and PVA-PEI-CG drastically drops after the regeneration treatment probably due to the loss of PEI and the rearrangement of the cryogel network, respectively.

Concerning SPEI sponges, the systems with a higher amount of free amino groups (SPEI 3,4,5 with high PEI:BDDE ratio) can absorb a higher amount of both total acetic acid ($\text{AcOH}_{\text{sb}} + \text{AcOH}_{\text{wb}}$) and AcOH_{sb} . Although these three systems show very similar behavior, SPEI 3 and 4 are the ones able to absorb the higher amount of $\text{AcOH}_{\text{sb}}\%$ ($34\pm 3\%$ and $32\pm 2\%$, respectively). In addition, comparing SPEI 3 and 4, SPEI 4 is the one with a higher value of G' (Fig. 30) and so with higher elasticity. On these bases, we choose to use SPEI 4 to carry on the next tests.

References

- [1] J. M. Reilly, "IPI Storage Guide for Acetate Film," *J. Am. Inst. Conserv.*, vol. 33, no. 3, p. 321, 1994, doi: 10.2307/3179643.
- [2] S. G. Spain, G. Yaşayan, M. Soliman, F. Heath, A. O. Saeed, and C. Alexander, "Nanoparticles for Nucleic Acid Delivery," *Compr. Biomater.*, vol. 4, pp. 389–410, Jan. 2011, doi: 10.1016/B978-0-08-055294-1.00133-1.
- [3] Z. Ahmad, Y. Li, C. Huang, X. Gou, Y. Fan, and J. Chen, "Underwater suspended bifunctionalized polyethyleneimine-based sponge for selective removal of anionic pollutants from aqueous solution," *J. Hazard. Mater.*, vol. 412, no. December 2020, p. 125284, 2021, doi: 10.1016/j.jhazmat.2021.125284.
- [4] M. L. Campbell, F. D. Guerra, J. Dhulekar, F. Alexis, and D. C. Whitehead, "Target-Specific Capture of Environmentally Relevant Gaseous Aldehydes and Carboxylic Acids with Functional Nanoparticles," *Chem. - A Eur. J.*, vol. 21, no. 42, pp. 14834–14842, 2015, doi: 10.1002/chem.201502021.
- [5] F. D. Guerra, M. L. Campbell, D. C. Whitehead, and F. Alexis, "Tunable Properties of Functional Nanoparticles for Efficient Capture of VOCs," *ChemistrySelect*, vol. 2, no. 31, pp. 9889–9894, 2017, doi: 10.1002/slct.201701736.
- [6] F. D. Guerra, M. L. Campbell, M. F. Attia, D. C. Whitehead, and F. Alexis, "Capture of Aldehyde VOCs Using a Series of Amine-Functionalized Cellulose Nanocrystals," *ChemistrySelect*, vol. 3, no. 20, pp. 5495–5501, 2018, doi: 10.1002/slct.201703149.
- [7] B. R. Brummel *et al.*, "Scaled Synthesis of Polyamine-Modified Cellulose Nanocrystals from Bulk Cotton and Their Use for Capturing Volatile Organic Compounds," 2021, doi: 10.3390/polym13183060.
- [8] M. I. Swasy *et al.*, "Degradation of pesticides using amine-functionalized cellulose nanocrystals †," 2020, doi: 10.1039/d0ra08308a.
- [9] Q. Yang and T. Runge, "Cross-Linked Polyethylenimine for Selective Adsorption and Effective Recovery of Lignocellulose-Derived Organic Acids and Aldehydes," *ACS Sustain. Chem. Eng.*, vol. 7, no. 1, pp. 933–943, 2019, doi: 10.1021/acssuschemeng.8b04540.
- [10] O. Okay, *Polymeric cryogels macroporous gels with remarkable properties*, vol.

263. 2014.
- [11] W. K. Wan, G. Campbell, Z. F. Zhang, A. J. Hui, and D. R. Boughner, "Optimizing the tensile properties of polyvinyl alcohol hydrogel for the construction of a bioprosthetic heart valve stent," *J. Biomed. Mater. Res.*, vol. 63, no. 6, pp. 854–861, 2002, doi: 10.1002/jbm.10333.
- [12] T. Kanaya, M. Ohkura, K. Kaji, M. Furusaka, and M. Misawa, "Structure of Poly(vinyl alcohol) Gels Studied by Wide- and Small-Angle Neutron Scattering," *Macromolecules*, vol. 27, no. 20, pp. 5609–5615, May 2002, doi: 10.1021/ma00098a014.
- [13] E. Yokoyama, I. Masada, K. Shimamura, T. Ikawa, and K. Monobe, "Morphology and structure of highly elastic poly(vinyl alcohol) hydrogel prepared by repeated freezing-and-melting."
- [14] T. Kanaya *et al.*, "Gelation Process of Poly(vinyl alcohol) As Studied by Small-Angle Neutron and Light Scattering," *Macromolecules*, vol. 28, no. 9, pp. 3168–3174, May 2002, doi: 10.1021/ma00113a019.
- [15] R. Mastrangelo *et al.*, "Twin-chain polymer hydrogels based on poly(vinyl alcohol) as new advanced tool for the cleaning of modern and contemporary art," *Proc. Natl. Acad. Sci. U. S. A.*, vol. 117, no. 13, pp. 7011–7020, 2020, doi: 10.1073/pnas.1911811117.
- [16] R. Mastrangelo, C. Montis, N. Bonelli, P. Tempesti, and P. Baglioni, "Surface cleaning of artworks: Structure and dynamics of nanostructured fluids confined in polymeric hydrogel networks," *Phys. Chem. Chem. Phys.*, vol. 19, no. 35, pp. 23762–23772, 2017, doi: 10.1039/c7cp02662e.
- [17] R. Mastrangelo, C. Resta, E. Carretti, E. Fratini, and P. Baglioni, "Sponge-like Cryogels from Liquid-Liquid Phase Separation: Structure, Porosity, and Diffusional Gel Properties," *ACS Appl. Mater. Interfaces*, 2023, doi: 10.1021/acsami.3c03239.
- [18] C. Wang *et al.*, "Customization of Conductive Elastomer Based on PVA/PEI for Stretchable Sensors," *Small*, vol. 16, no. 7, 2020, doi: 10.1002/smll.201904758.
- [19] N. Minju, S. Ananthakumar, and S. Savithri, "Superswelling Hybrid Sponge from Water Glass for Selective Absorption of Crude Oil and Organic Solvents," *ACS Omega*, vol. 4, no. 19, pp. 17990–18001, 2019, doi: 10.1021/acsomega.9b01655.
- [20] Y. Pan, W. Wang, C. Peng, K. Shi, Y. Luo, and X. Ji, "Novel hydrophobic

- polyvinyl alcohol-formaldehyde foams for organic solvents absorption and effective separation,” *RSC Adv.*, vol. 4, no. 2, pp. 660–669, 2014, doi: 10.1039/c3ra43907k.
- [21] Y. Pan, K. Shi, Z. Liu, W. Wang, C. Peng, and X. Ji, “Synthesis of a new kind of macroporous polyvinyl-alcohol formaldehyde based sponge and its water superabsorption performance,” *RSC Adv.*, vol. 5, no. 96, pp. 78780–78789, 2015, doi: 10.1039/c5ra11958h.
- [22] B. Xue, J. Deng, and J. Zhang, “Multiporous open-cell poly(vinyl formal) foams for sound absorption,” *RSC Adv.*, vol. 6, no. 9, pp. 7653–7660, 2016, doi: 10.1039/c5ra23285f.
- [23] Y. Li, J. Deng, and J. Zhang, “Porous poly(vinyl formal) foam prepared using poly(vinyl alcohol) of low degree of polymerization,” *Polym. Int.*, vol. 67, no. 10, pp. 1438–1444, 2018, doi: 10.1002/pi.5666.
- [24] A. Fahmy, B. Anis, P. Szymoniak, K. Altmann, and A. Schönhals, “Graphene Oxide/Polyvinyl Alcohol-Formaldehyde Composite Loaded by Pb Ions: Structure and Electrochemical Performance,” 2022, doi: 10.3390/polym14112303.
- [25] M. M. Blum and T. C. Ovaert, “A novel polyvinyl alcohol hydrogel functionalized with organic boundary lubricant for use as low-friction cartilage substitute: Synthesis, physical/chemical, mechanical, and friction characterization,” *J. Biomed. Mater. Res. - Part B Appl. Biomater.*, vol. 100 B, no. 7, pp. 1755–1763, 2012, doi: 10.1002/jbm.b.32742.
- [26] H. G. Hammon, “United States Patent Office: METHOD OF MAKING A SPONGE MATERIAL AND THE PRODUCT RESULTING THEREFROM,” 2,668,153, 1994.
- [27] C. L. Wilson, “United States Patent Office: METHOD OF MAKING EXPANDED POLY VINYL ALCOHOL-FORMALDEHYDE REACTION PRODUCT AND PRODUCT RESULTING THEREFROM,” 2,609,347, 1994.
- [28] P. Srinivasa Rao, B. Smitha, S. Sridhar, and A. Krishnaiah, “Preparation and performance of poly(vinyl alcohol)/polyethyleneimine blend membranes for the dehydration of 1,4-dioxane by pervaporation: Comparison with glutaraldehyde cross-linked membranes,” *Sep. Purif. Technol.*, vol. 48, no. 3, pp. 244–254, 2006, doi: 10.1016/j.seppur.2005.07.031.

- [29] S. K. Mani and R. Bhandari, "Microwave-assisted synthesis of self-assembled network of Graphene oxide-Polyethylenimine-Polyvinyl alcohol hydrogel beads for removal of cationic and anionic dyes from wastewater," *J. Mol. Liq.*, vol. 345, p. 117809, 2022, doi: 10.1016/j.molliq.2021.117809.
- [30] L. Shao *et al.*, "PVA/polyethylenimine-functionalized graphene composites with optimized properties," *Mater. Des.*, vol. 99, pp. 235–242, 2016, doi: 10.1016/j.matdes.2016.03.039.
- [31] C. L. Wilson, "United States Patent Office: METHOD OF MAKING AN ABRASIVE SPONGE. MATERIAL AND THE PRODUCT RESULTING THEREFROM," 2,636,013, 1912.
- [32] H. S. Lim *et al.*, "Crosslinked Polyethylenimine Gel Polymer Interface to Improve Cycling Stability of RFBs," *Energy Mater. Adv.*, vol. 2022, 2022, doi: 10.34133/2022/9863679.
- [33] A. Zuliani, D. Bandelli, D. Chelazzi, R. Giorgi, and P. Baglioni, "Environmentally friendly ZnO/Castor oil polyurethane composites for the gas-phase adsorption of acetic acid," *J. Colloid Interface Sci.*, vol. 614, pp. 451–459, 2022, doi: 10.1016/j.jcis.2022.01.123.
- [34] D. J. Merline, S. Vukusic, and A. A. Abdala, "Melamine formaldehyde: Curing studies and reaction mechanism," *Polym. J.*, vol. 45, no. 4, pp. 413–419, 2013, doi: 10.1038/pj.2012.162.
- [35] L. Zhang, D. Dong, L. Shao, Y. Xia, T. Zeng, and Y. Wang, "Cost-effective one-pot surface modified method to engineer a green superhydrophobic sponge for efficient oil/water mixtures as well as emulsions separation," *Colloids Surfaces A Physicochem. Eng. Asp.*, vol. 576, no. March, pp. 43–54, 2019, doi: 10.1016/j.colsurfa.2019.05.022.
- [36] R. K. Brundavanam, G. Eddy, J. Poinern, and D. Fawcett, "Modelling the Crystal Structure of a 30 nm Sized Particle based Hydroxyapatite Powder Synthesised under the Influence of Ultrasound Irradiation from X-ray powder Diffraction Data," *Am. J. Materials Sci.*, vol. 3, no. 4, pp. 84–90, 2013, doi: 10.5923/j.materials.20130304.04.
- [37] Y. Privar *et al.*, "Polyethylenimine cryogels for metal ions sorption," *Chem. Eng. J.*, vol. 334, no. November 2017, pp. 1392–1398, 2018, doi:

- 10.1016/j.cej.2017.11.097.
- [38] B. F. Smith *et al.*, “Boric Acid Recovery Using Polymer Filtration: Studies with Alkyl Monool, Diol, and Triol Containing Polyethylenimines,” 2005, doi: 10.1002/app.21857.
- [39] D. V Nesterov, L. S. Molochnikov, O. V Korjakova, M. I. Kodess, M. A. Ezhikova, and A. V Pestov, “Synthesis of polyaminostyrene-based and polyallylamine-based sorbents for boron removal,” *J. Appl. Polym. Sci.*, p. 43939, 2016, doi: 10.1002/app.43939.
- [40] H. J. Flammersheim, “Kinetics and mechanism of the epoxide–amine polyaddition,” *Thermochim. Acta*, vol. 310, no. 1–2, pp. 153–159, Feb. 1998, doi: 10.1016/S0040-6031(97)00225-6.
- [41] Y. Hwang, C. Zhang, and S. Varghese, “Poly(ethylene glycol) cryogels as potential cell scaffolds: Effect of polymerization conditions on cryogel microstructure and properties,” *J. Mater. Chem.*, vol. 20, no. 2, pp. 345–351, 2010, doi: 10.1039/b917142h.
- [42] N. Sahiner and S. Demirci, “Poly ionic liquid cryogel of polyethyleneimine: Synthesis, characterization, and testing in absorption studies,” *J. Appl. Polym. Sci.*, vol. 133, no. 22, pp. 1–13, 2016, doi: 10.1002/app.43478.
- [43] S. Demirci and N. Sahiner, “Urease-Immobilized PEI Cryogels for the Enzymatic Hydrolysis of Urea and Carbon Dioxide Uptake,” *Ind. Eng. Chem. Res.*, vol. 61, no. 7, pp. 2771–2782, 2022, doi: 10.1021/acs.iecr.1c05087.
- [44] H. A. Zaaeri, F.; Khoobi, M.; Rouini, M.; Javar, “pH-responsive polymer in a core–shell magnetic structure as an efficient carrier for delivery of doxorubicin to tumor cells,” *Int. J. Polym. Mater. Polym. Biomater.*, vol. 67, no. 16, pp. 967–977, 2018.
- [45] A. M. Sajjan, H. G. Premakshi, and M. Y. Kariduraganavar, “Synthesis and characterization of GTMAC grafted chitosan membranes for the dehydration of low water content isopropanol by pervaporation,” *J. Ind. Eng. Chem.*, vol. 25, pp. 151–161, May 2015, doi: 10.1016/J.JIEC.2014.10.027.
- [46] R. W. Goodwin, J.W. and HUGHES, *Rheology for chemists: an introduction*. Cambridge: The Royal Society of Chemistry, 2001.
- [47] K. Almdal, J. Dyre, S. Hvidt, and O. Kramer, “Towards a phenomenological definition of the term ‘gel,’” *Polym. Gels Networks*, vol. 1, no. 1, pp. 5–17, Jan.

1993, doi: 10.1016/0966-7822(93)90020-I.

- [48] R. Mészai, I. Varga, and T. Gilá, “Adsorption of Poly(ethyleneimine) on Silica Surfaces: Effect of pH on the Reversibility of Adsorption,” 2004, doi: 10.1021/la049611l.

Appendix of Chapter IV

Tab. A1 Results of the elemental analysis for SPEI 1, 2, 3, 4 and 5. The accuracy of the measurements is 0.1%.

Sample	Weight (g)	N (%)	C (%)	C/N
PEI	1.8	16.5	28.8	1.8
SPEI 1	1.5	11.6	52.5	4.5
SPEI 2	1.9	12.45	53.55	4.3
SPEI 3	1.6	14.5	49.3	3.4
SPEI 4	1.7	13.6	49.65	3.65
SPEI 5	1.8	14.85	50.15	3.4

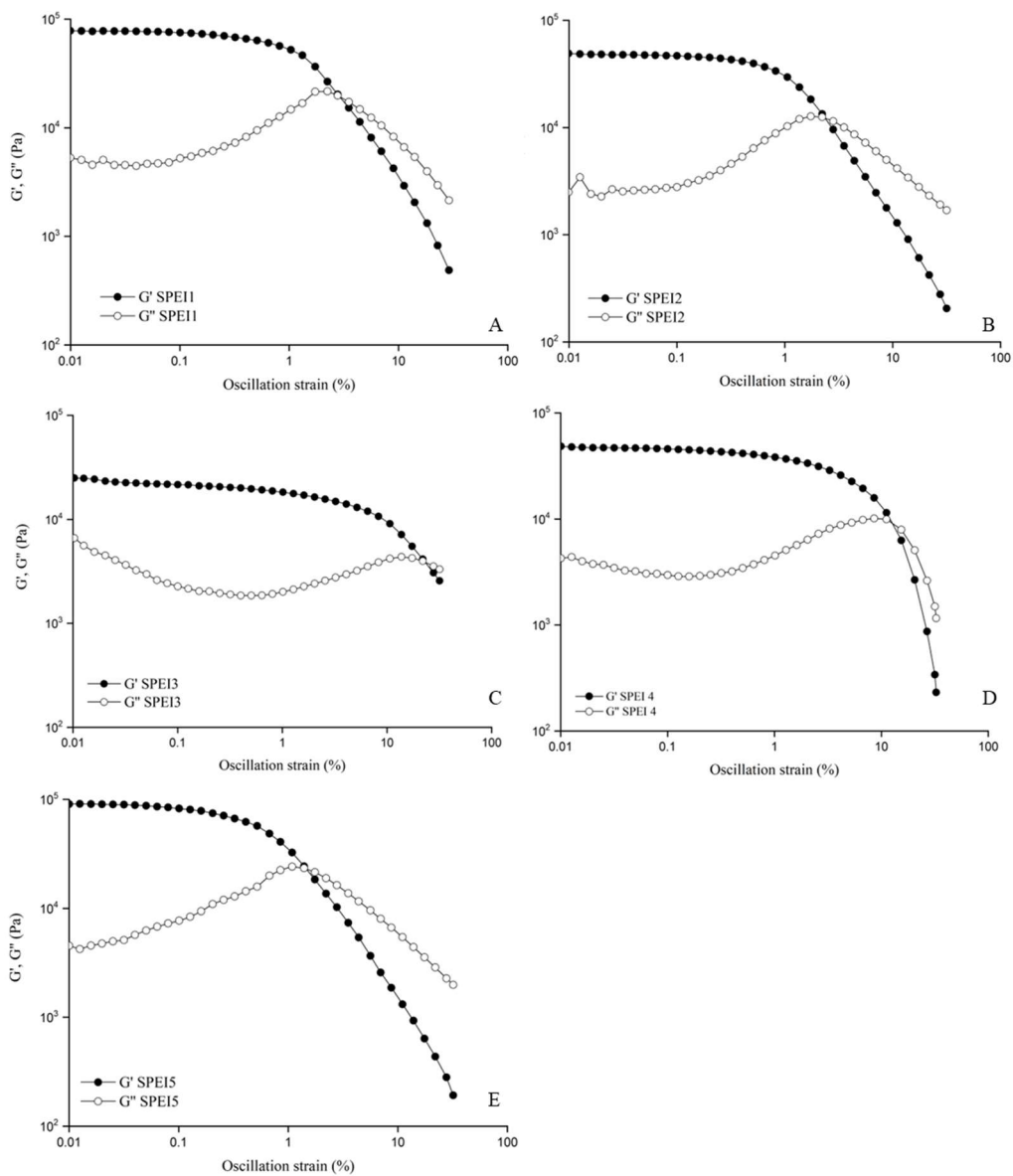


Fig. A1 Amplitude Sweep tests performed on SPEI 1 (A), SPEI 2 (B), SPEI 3 (C), SPEI 4 (D), SPEI 5 (E).

Chapter V

Proposal of inhibitors for the “vinegar syndrome” based on inorganic nanoparticles

In this chapter, a short review of the use of nanoparticles that have been tested for the absorption of acetic acid will be reported. The attention has been focused on different kinds of nanoparticles such as $\text{Ca}(\text{OH})_2$, $\text{Mg}(\text{OH})_2$, CaCO_3 , ZnO , TiO_2 and Al_2O_3 that have been uploaded on various supports (Whatman Paper, PVF and SPEI sponges).

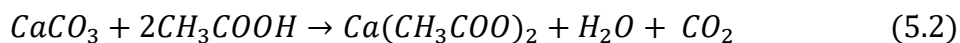
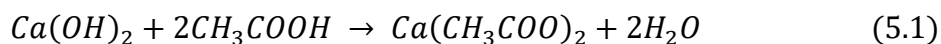
5.1 Inorganic nanoparticles for acetic acid absorption

Nanoparticles offer a lot of advantages over the use of massive materials: the decrease in size corresponds to a decrease in the number of atoms that form the particles. Moreover, the smaller the particles, the greater the number of surface atoms, with a consequent improvement in chemical reactivity, catalytic activity, solubility, and mechanical properties (such as hardness and flexibility)[1].

In the field of Cultural Heritage, inorganic nanoparticles have been extensively used for the consolidation of stones, frescos and, recently, archeological bones, but also for the deacidification of cellulose-based materials [1], [2]. The great results obtained with these systems are due to their high physico-chemical compatibility with the typical constituents of works of art, which consent to minimizing or completely avoiding any alteration of the original physical and chemical properties of the artistic/historical substrates and interfaces.

In particular, dispersions of nanoparticles of alkaline earth metal hydroxides (such as calcium and magnesium hydroxides, $\text{Ca}(\text{OH})_2$ and $\text{Mg}(\text{OH})_2$) in short-chain alcohols have been extensively used for the deacidification of paper, canvas and archeological water-logged wood with excellent results. Part of the hydroxides are consumed for the neutralization of the acidity of cellulose, while the remaining particles react with

CO₂, turning into CaCO₃ (Eq. 5.1) that can act as a buffer against further acidity (Eq. 5.2). Calcium hydroxide nanoparticles have been tested also for the absorption of gaseous acetic acid emitted by the wood of a church organ obtaining very promising results [3].



Stable dispersions of calcium and magnesium hydroxide nanoparticles in short-chain alcohols have been obtained through different synthetic processes [2], [4]–[9]. In particular, procedures based on aqueous homogeneous phase precipitation [4], [8] and solvothermal reaction [9] have been used to synthesize both calcium and magnesium hydroxide nanoparticles for the deacetylation of cellulose-based artifacts. To improve the stability of particles in organic solvents, no additives and surfactants are used to stabilize the systems, which indeed, are usually subjected to ultrasonic treatments. Dispersions are easily applicable on paper by brushing, spraying, dripping or immersion [10]. The reduced size of nanoparticles and consequently their high surface area, contribute to improving the neutralization performance of the treatment and avoiding the formation of white veils on the surface [11]. The effectiveness of treatments based on Mg(OH)₂ nanoparticles on inked papers has been extensively studied [7]: the capacity to stabilize the pH of the treated paper around 7-8 allows to preserve the paper from the degradation induced both by acids (mainly sulphuric acid) and oxidative agents (iron and copper ions). At a molecular level, this was because the amount of cellulose glycosidic bonds scissored by degradation processes was kept low by the treatment with alkaline particles throughout aging [1].

Moreover, the choice of short-chain alcohols used as dispersing media for the nanoparticles is a low environmental impact option and consents also to extend this application to paper containing modern inks [7].

Good results obtained with paper promoted the application of nanoparticle-based deacidification treatments on other cellulose-based substrates with similar problems, such as wood and canvas.

Applying a dispersion of alkaline nanoparticles by spraying on the backside of the painting provides an efficient and feasible deacidification method that does not affect the stratigraphy of the paint.

For what concerns wood artifacts, acidity could be emitted by the wood itself (as acetic or formic acid) or the object can be exposed to an atmosphere containing acidic Volatile Organic Compounds (VOC). To limit these effects, in the past decade, the most common procedure adopted was based on the application of polymeric coatings such as the poly(vinyl acetate)-based ones but it is known that some of these materials, could emit acidic VOC as alteration by-products [12]. Putting an alkaline buffer inside the environment to neutralize acidic emissions directly in situ could be an effective alternative without using potentially hazardous coatings [3].

For the removal and/or mitigation of VOC (Volatile Organic Compounds) in general, nanomaterials have been extensively used in the last decades [13]: noble metal-based nanostructures for VOC catalytic oxidation (i.g. platinum, palladium, gold and silver supported on transition-metal oxides, such as silicon, aluminum and titanium oxides substrates); graphene and graphene oxide (GO) compounds have also attracted much interest as a proficient matrix for gaseous pollutants adsorption, due to the possibility to obtain systems with high surface area, proper pore size distribution, high both chemical and thermal stability. Other interesting systems are silica-based compounds such as mesoporous organosilica nanoparticles (MO SiNPs) and tetraethoxysilane (TEOS) and vinyltriethoxysilane (VTES). Moreover, metal oxides such as TiO_2 , have been used for this purpose due to their photocatalytic activity that promotes the decomposition of VOCs by means of UV light irradiation and also for their low toxicity, high chemical stability and low cost [14], [15].

On these bases, TiO_2 is potentially very interesting for our purposes because the adsorbed acetic acid can be decomposed through photoinduced decomposition (PID) and the nanoparticles can be regenerated and reused, reducing in that way the environmental impact in terms of waste produced.

Concerning the PID of VOC by titanium oxide, TiO_2 , since the early work of Fujishima and Honda in the 1970s [16], there has been an increasing interest in this field, with applications ranging from solar hydrogen production, air and water purification, wet solar cells, and biomedical applications [17], [18].

The three polymorphs of TiO_2 , anatase, brookite and rutile, show different behaviors in terms of adsorption and PID activity: anatase is commonly known to be the most active phase in terms of photocatalytic activity [19], [20], but also brookite [21], [22] and mixtures of the three polymorphs [23], [24] exhibit interesting photocatalytic properties. In particular, Berson et al. (1978) studied the mechanisms involved in the adsorption and PID of acetic acid [25], [26]. On TiO_2 surfaces acetic acid could be adsorbed via hydrogen bonding or Lewis acid-base interaction or converted into acetate groups, through bidentate coordination (Fig. 1A) [27]. Mattsson and Österlund (2010) [28] reported a study about the different behaviors of nanoparticles of polymorphs of TiO_2 in the absorption and PID of acetic acid (Fig. 1B): analysis of chemical shifts in FTIR spectra [29] indicates that acetic acid binds more weakly to brookite than to rutile but more strongly than to anatase. On the contrary, the quantum yield for the PID of coordinated acetate is slightly lower on brookite if compared to anatase, while rutile shows no photoactivity at all. These different behaviors are mainly due to the different binding energy between acetic acid and the three TiO_2 polymorphs that is very high for rutile and progressively lower for brookite and anatase. Then, as indicated in Fig. 1B, in the case of rutile, being the acetic acid strongly bound to TiO_2 , no photoinduced decomposition is observed (Fig. 1B, R20). On the contrary, for brookite and anatase (for whom the binding energy progressively decreases in this order), after irradiation, the energy of the absorption bands associated with acetic acid rapidly decreases. Then, as a consequence, acetic

acid bound to brookite, upon UV irradiation, easily decompose by forming CO₂ and H₂O (Fig. 1B, B12). On the contrary, anatase, for which the binding energy with acetic acid is the lowest, promotes the formation of formate as reaction intermediate (Fig. 1B, A25 and A40) with its following photodecomposition into carbon dioxide and water [28].

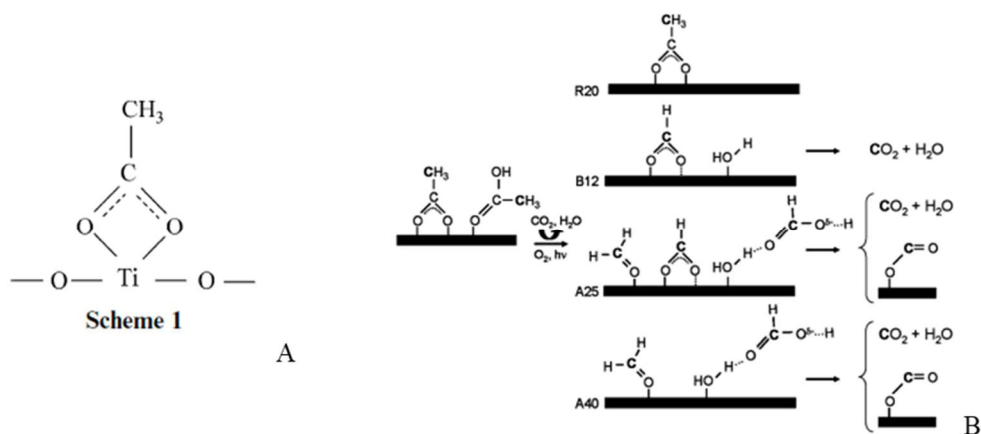


Fig. 1 (A) Acetate group bonded by a chelating bidentate configuration on TiO₂ surface [27]; (B) schematic drawing of the reaction pathways for photoinduced decomposition of acetic acid on anatase (A25 and A40, 25 and 40 are the particle size determined through TEM and XRD (nm)), brookite (B12), and rutile (R20). Acetic acid and acetate coexist on the surface before illumination. The bidentate coordination of formate is tentative and is drawn as a weakly bonded μ -coordinated species (dashed lines). Bold and normal font styles for carbon denote α -carbon (C) and R-carbon (C), respectively [28].

Zinc oxide, ZnO, nanoparticles (and its compounds) are also very promising candidates for removing most VOC due to their wide bandgap (3.37 eV), low cost, and good physical and chemical properties [15], [30].

Recently, a very interesting study has been conducted on the use of ZnO nanoparticles downloaded in castor-oil polyurethane sponges and used for the absorption of acetic acid [31], [32] (Fig. 2): the sponge is easy to handle, with no risk of dispersing particulate into the cases near the work of art (as in the case of gel silica or activated charcoal, for example). In addition, polyurethane acts as a vehicle for the gas through physisorption, and acetic acid can reach the surface of ZnO particles. ZnO is converted into zinc acetate, neutralizing the acetic acid (Eq. 5.3). It has been

shown how the sizes of nanoparticles play an important role in the absorption capacity of the system: decreasing the size of nanoparticles, the amount of the absorbed acetic acid increases, even if aggregation phenomena of the particles during the synthesis procedures can affect their performance. Nevertheless, today there is no literature regarding the PID of these systems on adsorbed VOCs. In addition, while these systems can be used for the adsorption of acetic acid on large museum display cases, they seem not to be suitable for the adsorption of acetic acid in restricted volumes where they could be in direct contact with motion picture films. In fact, being those systems composed of biobased chemicals, due to the thermohygroscopic conditions of the microenvironment that is formed into the motion picture films cases, they can promote the development of biological contamination.

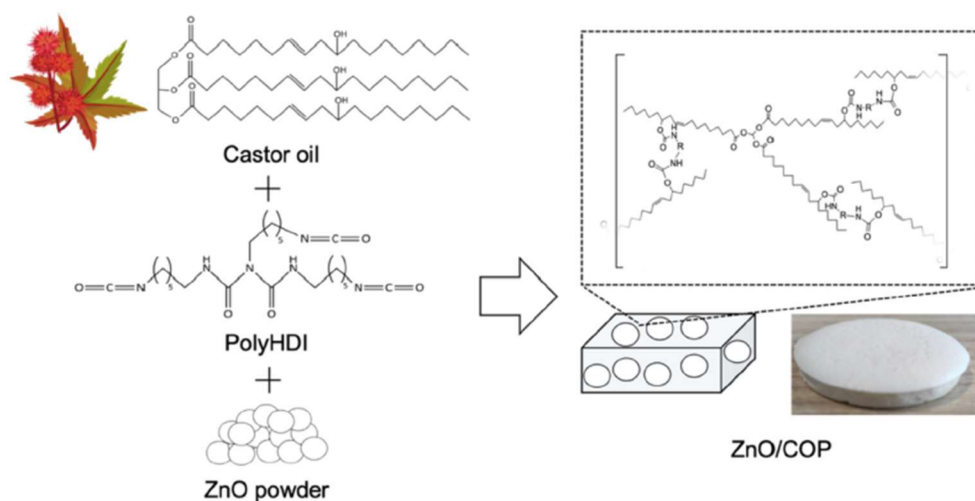
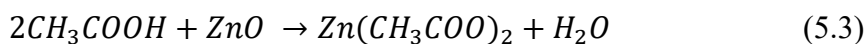
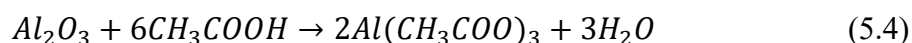


Fig. 2 Scheme of the preparation of ZnO/Castor Oil polyurethane hybrids (ZnO/COPs) [31].

Also Al_2O_3 , nanoparticles have been studied in terms of acetic acid adsorption ability (Eq. 5.4) [33], [34]. In particular, Tang et al. (2016) [34] compared the heterogeneous uptake of gaseous acetic acid on different oxides including $\gamma\text{-Al}_2\text{O}_3$, SiO_2 , and CaO . It has been observed that, at very low relative humidity, while on $\gamma\text{-Al}_2\text{O}_3$ and CaO the uptake of acetic acid leads to the formation of both acetate and molecularly adsorbed acetic acid, only molecularly adsorbed acetic acid has been detected on SiO_2 . In addition, the kinetic analysis shows that for SiO_2 nanoparticles, acetic acid and water are found to compete for surface adsorption. On the other hand, the reaction rate of acetic acid increases by a factor between 3 and 5 for $\gamma\text{-Al}_2\text{O}_3$ when relative humidity increases from 0% to 15%.



Thus far, the use of nanoparticles as a possible solution for the vinegar syndrome on CA-based motion picture films has not been proposed and investigated yet.

5.2 Material and methods

First of all, we decided to perform several tests to investigate the capacity of different types of nanopowders ($\text{Ca}(\text{OH})_2$, $\text{Mg}(\text{OH})_2$, CaCO_3 , ZnO , TiO_2 , Al_2O_3) to absorb glacial acetic acid. Some of these systems have been analyzed as they are but also uploaded on different substrates, such as Whatman Paper (WP), polyvinyl formaldehyde (PVF) and polyethyleneimine (SPEI) sponges. The scope was to identify the most efficient nanoparticles in terms of acetic acid absorption and to evaluate their capacity to absorb acetic acid, once uploaded inside a support such as the ones described in Chapter IV.

We chose to evaluate the performance of both PVF and SPEI systems in which ZnO nanoparticles have been uploaded. PVF has been already used as the base to obtain the PVF-PEI-GA sponges and also the efficacy of pure SPEI sponges in the absorption of glacial acetic acid has been already discussed in Chapter IV. In the case

of SPEI, we will evaluate if the addition of nanoparticles could further increase their performance. We chose to add ZnO nanoparticles to these sponge systems because they showed better performance in terms of glacial acetic acid absorption as we will see below.

5.2.1. Chemicals

Nanorestore Plus® of calcium hydroxide, $\text{Ca}(\text{OH})_2$, nanoparticles dispersed in ethanol (10 g/L) has been kindly provided by the CSGI consortium; magnesium hydroxide, $\text{Mg}(\text{OH})_2$, nanopowder (<100 nm, particle size (laser PSA), 99.8%), zinc oxide, ZnO, nanopowder (<100 nm particle size), aluminum oxide, Al_2O_3 , nanowires (diam. x L 2-6 nm x 200-400 nm), titanium oxide, TiO_2 , nanopowder (<100 nm particle size, 99.99% trace metals basis, mixture of rutile and anatase), calcium carbonate (CaCO_3) (ACS reagent, $\geq 99.0\%$ powder), glacial acetic acid were purchased from Sigma Aldrich.

To obtain $\text{Ca}(\text{OH})_2$ nanoparticles, the Nanorestore Plus® dispersion has been fluxed with nitrogen for 24 hours in order to promote the evaporation of ethanol.

To obtain CaCO_3 nanoparticles $\text{Ca}(\text{OH})_2$ dispersion has been left for 7 days under hood to promote the carbonation process.

Ethanol anhydrous denatured was purchased from Carlo Erba Reagents.

Some of these systems have been applied onto WP sheets (55 mm Ø, Cat. No. 1001-055).

For PVF and SPEI synthesis, the chemicals used are the ones indicated in Paragraphs 4.2.3 and 4.3.1 (Capitolo IV).

All the chemicals have been used without further purification.

Water used for all the procedures was purified by a Millipore MilliQ Direct-Q® & Direct-Q UV water purification system (Water Resistivity: 18,2 MΩ at 25°C).

5.2.2 Synthesis of the sponges

PVF+ZnO sponges were obtained by immersing the PVF sponge in a 10 g/L dispersion of ZnO nanoparticles in ethanol for 2 hours under vacuum (15 mbar). The complete drying of the sponge has been conducted by extracting the sponge from the dispersion and leaving it under vacuum for a further 2 hours (W_{dry}). In order to maximize the surface contact between the PVF sponge and the ZnO nps dispersion, the sponge was suspended inside the dispersion through a Teflon wire and a glass stick so that it would not touch the bottom of the beaker. The amount of downloaded nanoparticles in the sponge has been evaluated by weight and it is about $9.2 \pm 0.9 \%$ of the initial weight of the sponge.

For *SPEI+ZnO sponges*, The incorporation of nanoparticles has been performed during the synthesis reported in Paragraph 4.3.2, as follows. Water dispersion of ZnO nanoparticles has been previously sonicated in an ultrasonic bath (Elmasonic S 30H, Elma) with a power of 80 W for 30 minutes and then added to the PEI solution (we selected SPEI 4, PEI concentration: 6wt% and PEI:BDDE 3:1). Then the system was vortexed for 2 minutes in order to homogenize the blend and the BDDE was added. The system was vortexed again for a few seconds, poured into a mold and stored at -20°C for 24 hours.

Subsequently, the system was thawed and washed with water only once, in order to guarantee the removal of the unreacted chemicals (mainly BDDE and PEI) and minimize the loss of nanoparticles. Finally, the sponge was dried at 50°C (W_{dry}). The amount of downloaded nanoparticles is $10 \pm 1\%$ of the amount (g) of PEI used for the synthesis of the sponge.

5.2.3 Acetic acid absorption-desorption tests on nanoparticles

To evaluate the capacity of the systems to absorb gaseous acetic acid some absorption-desorption tests have been performed on different types of nanoparticles ($\text{Ca}(\text{OH})_2$, CaCO_3 , MgCO_3 , ZnO, TiO_2 , Al_2O_3) exposed to a saturated glacial acetic

acid atmosphere. Nanopowders with similar dimensions (<100 nm) have been chosen in order to minimize the possible variables that could affect the results. While all the nanoparticles are almost spherical, Al₂O₃, are nanowires (size: 2-6 nm x 200-400 nm). For comparison also macropowder of CaCO₃ (grain size in the order of microns) have been considered. Some of these nanoparticles (Ca(OH)₂, Mg(OH)₂ and ZnO) have been also applied onto sheets of WP. To obtain this latter system a WP disk was immersed in a homogeneous dispersion of 5 g/L in ethanol of the nanoparticles previously sonicated for 30 min in an ultrasonic bath (Elmasonic S 30H, Elma) with a power of 80 W. Then the system was left to dry for 24 hours (a nitrogen atmosphere was used for Ca(OH)₂ and Mg(OH)₂) to promote the complete evaporation of the solvent.

All the systems were dried and weight was registered (W_{dry} , weight of a WP disk plus the nanoparticles, 0.3 g for each sample) and put in sealed jars (130 mL) with a vial containing 8 mL of glacial acetic for six days (until saturation). Then, they were weighed (W_{ab}), left to equilibrate for six more days at controlled temperature and humidity (20 °C – RH 50%) and weighed again (W_{eq}).

The amount of absorbed acetic acid after the absorption test ($AcOH_{ab}\%$) and after the equilibration period ($AcOH_{eq}\%$) was evaluated through gravimetric analysis, using the following equations:

$$AcOH_{ab}\% = \left(\frac{W_{ab} - W_{dry}}{W_{dry}} \right) \cdot 100 \quad (5.5)$$

$$AcOH_{eq}\% = \left(\frac{W_{eq} - W_{dry}}{W_{dry}} \right) \cdot 100 \quad (5.6)$$

Where W_{dry} = weight of the dried sample, W_{ab} = weight (g) of the sample after the absorption test and W_{eq} = weight (g) of the sample after the equilibration period.

To obtain further information about the nature of the interaction between the nanoparticles and the acetic acid, desorption tests were performed. Samples previously subjected to absorption tests have been pressured (15 mbar) until they

reach a stable weight value. To evaluate the amount of strongly-bound acetic acid ($AcOH_{sb}\%$) after the equilibration period, the following equation was used:

$$AcOH_{sb}\% = \left(\frac{W_{des} - W_{dry}}{W_{dry}} \right) \cdot 100 \quad (5.7)$$

Where W_{dry} = weight (g) of the dried sample, W_{des} = weight (g) of the sample after the desorption test.

The weakly-bonded acetic acid ($AcOH_{wb}\%$) after the equilibration period, was calculated as:

$$AcOH_{wb}\% = AcOH_{eq}\% - AcOH_{sb}\% \quad (5.8)$$

For each test, three samples were prepared and the average values and the corresponding standard deviation will be reported below.

For pure nanoparticles, FTIR spectra, XRD diffractograms and TGA profiles were acquired before and after the absorption test with the following methodologies.

Fourier Transform Infrared (FTIR) Spectroscopy. FTIR measurements were performed using a BioRad FTS-40 spectrometer in the range 4000–400 cm^{-1} . Spectra were averages of 64 scans recorded in transmittance mode with 2 cm^{-1} resolution. KBr pellets were prepared by finely grinding and mixing a few milligrams of sample and 200 mg of pure KBr.

X-ray diffraction (XRD). Powder X-ray diffraction (XRD) analyses were carried out at the CRIST Centre of the University of Florence (Italy). A Bruker D8 Advance diffractometer equipped with a Cu $K\alpha$ radiation and a Lynx Eye detector was used operating in θ -2 θ Bragg–Brentano geometry at 40 kV and 40 mA, in the range of 4–55° with a step size of 0.04° and a count time of 1 s.

Thermogravimetric analysis (TGA). Tests were performed in nitrogen atmosphere at a heating rate of 10 °C/min over a temperature range of 25-500 °C, with an initial sample weight of approximately 5 mg using a SDT 650 thermal analyzer (TA).

5.2.4 Characterization of the sponges

Fourier Transform Infrared Spectroscopy Measurements (FTIR-ATR). The FTIR spectra were collected as reported in Paragraph 4.2.5.

Thermogravimetric analysis (TGA). Tests were performed as reported in Paragraph 4.2.5.

Field-Emission Scanning Electron Microscopy (FE-SEM). SEM micrographs were collected by means of a Zeiss Sigma FE-SEM instrument, operating in high vacuum mode with an acceleration potential of 2 kV. It was equipped with a GEMINI column and In-Lens detector, capable of providing high-resolution images on non-conductive samples. In addition, through the INCA X-ray Detection System (Oxford Instruments), element distribution maps were collected (acceleration potential of 5 kV).

Acetic Acid Absorption-Desorption Tests. Acetic acid absorption-desorption tests have been performed as reported in Paragraph 5.2.3. FTIR-ATR spectra and TGA profiles were collected before and after the absorption tests as reported in Paragraph 5.2.3.

5.3 Results and discussion

5.3.1 Pure Nanoparticles

To evaluate the absorption capacity of the selected nanoparticles (Ca(OH)_2 , CaCO_3 , Mg(OH)_2 , ZnO , TiO_2 , Al_2O_3) we performed an absorption test in glacial acetic acid. From gravimetry tests (Tab 1 and Fig. 3), two patterns are visible. After six days of absorption test, the best performances in terms of $\text{AcOH}_{\text{ab}}\%$ (Eq. 5.5) are the ones of Mg(OH)_2 ($125 \pm 9\%$), ZnO ($122 \pm 6\%$), Ca(OH)_2 ($116 \pm 3\%$) and CaCO_3 ($98 \pm 2\%$), while the amount of acetic acid adsorbed $\text{AcOH}_{\text{ab}}\%$ by Al_2O_3 and TiO_2 is 33 ± 6 and $25 \pm 1\%$ respectively (Tab 1 and Fig. 3).

It is also interesting to note that after six days of equilibration, the amount of absorbed acetic acid ($\text{AcOH}_{\text{eq}}\%$, Eq. 5.6) is quite unaffected for the first four systems (Mg(OH)_2 ($127 \pm 4\%$), ZnO ($121 \pm 3\%$), Ca(OH)_2 ($113 \pm 1\%$) and CaCO_3 ($94 \pm 2\%$)), while it sensibly decreases for Al_2O_3 ($16 \pm 2\%$) and TiO_2 ($1.5 \pm 0.5\%$), (Fig. 3). This could be probably due to the fact that, for Mg(OH)_2 , ZnO , Ca(OH)_2 and CaCO_3 , the acetic acid is strongly adsorbed with the formation of the corresponding acetate salts. This hypothesis is confirmed by examining results obtained after the desorption tests (Fig. 3): no significant variations have been detected in $\text{AcOH}_{\text{sb}}\%$ (Eq. 5.7) for Mg(OH)_2 ($110 \pm 8\%$), ZnO ($120 \pm 6\%$), Ca(OH)_2 ($111 \pm 4\%$) and CaCO_3 nps ($92 \pm 10\%$); on the contrary, for Al_2O_3 and TiO_2 $\text{AcOH}_{\text{sb}}\%$ decreases up to $10 \pm 0.2\%$ and $0.01 \pm 0.005\%$ respectively. The $\text{AcOH}_{\text{wb}}\%$ (Eq. 5.8) is high for Al_2O_3 ($6 \pm 2\%$) and TiO_2 ($1.49 \pm 0.1\%$) if compared to the initial $\text{AcOH}_{\text{eq}}\%$, as expected. $\text{AcOH}_{\text{wb}}\%$ is unexpectedly high also for Mg(OH)_2 ($17 \pm 4\%$), while for ZnO ($1 \pm 2\%$), Ca(OH)_2 ($2 \pm 3\%$) and CaCO_3 nps ($1 \pm 2\%$) is low and comparable to the standard deviation of the $\text{AcOH}_{\text{eq}}\%$.

Tab. 1 Acetic acid absorbed values calculated after the absorption test ($AcOH_{ab}\%$), after the equilibration period ($AcOH_{eq}\%$) and after the desorption test ($AcOH_{sb}\%$: strongly bonded acetic acid; $AcOH_{wb}\%$: weakly bonded acetic acid) for $Ca(OH)_2$, $Mg(OH)_2$, $CaCO_3$, ZnO , Al_2O_3 , TiO_2 nanoparticles and $CaCO_3$ macropowder.

Sample	$AcOH_{ab}\%$ *	$AcOH_{eq}\%$ #	$AcOH_{sb}\%$ °	$AcOH_{wb}\%$ §	$AcOH_T\%$ @
$Ca(OH)_2$	116 ± 3	113 ± 1	111 ± 4	2 ± 3	113.47
$Mg(OH)_2$	125 ± 9	127 ± 4	110 ± 8	17 ± 4	144.16
$CaCO_3$ nps	98 ± 9	94 ± 2	92 ± 10	2 ± 5	58.03
ZnO	122 ± 6	121 ± 3	120 ± 6	1 ± 2	125.46
Al_2O_3	33 ± 6	16 ± 2	10 ± 0.2	6 ± 2	100.19
TiO_2	25 ± 1	1.5 ± 0.5	0.01 ± 0.005	1.49 ± 0.1	255.65
$CaCO_3$ macro	15 ± 2	10 ± 1	9 ± 1	1 ± 2	58.03

$$*Eq. 5.5: AcOH_{ab}\% = \left(\frac{W_{ab} - W_{dry}}{W_{dry}}\right) \cdot 100 \quad \#Eq. 5.6: AcOH_{eq}\% = \left(\frac{W_{eq} - W_{dry}}{W_{dry}}\right) \cdot 100$$

$$°Eq. 5.7: AcOH_{sb}\% = \left(\frac{W_{des} - W_{dry}}{W_{dry}}\right) \cdot 100 \quad §Eq. 5.8: AcOH_{wb}\% = AcOH_{eq}\% - AcOH_{sb}\%$$

$$@Eq. 5.9: AcOH_T\% = \frac{MW_{Ac\ salt} - MW_0}{MW_0} \cdot 100$$

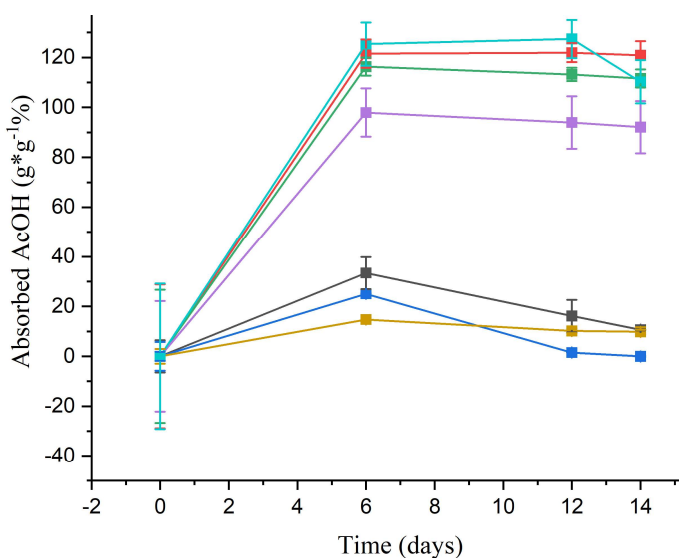


Fig. 3 (A) Absorbed AcOH (%) after the absorption test (6 days); after the equilibration test (after a further 6 days) and after the desorption test (2 days under vacuum) for nanoparticles of Al_2O_3 (black), ZnO (red), TiO_2 (blue), $Ca(OH)_2$ (green), $CaCO_3$ nps (purple) and $Mg(OH)_2$ (cyan), and $CaCO_3$ macropowder (yellow).

It was predictable that $\text{Ca}(\text{OH})_2$ would show greater absorption than CaCO_3 due to the higher reactivity of the first one. No sensible differences have been detected in the performances of $\text{Mg}(\text{OH})_2$ and $\text{Ca}(\text{OH})_2$ nanoparticles.

Concerning TiO_2 nanoparticles, a very low absorption value is measured. This could be because we used a mixture of rutile and anatase, as it will be confirmed by XRD diffractograms reported below: it is known from the literature that the binding energy between acetic acid and TiO_2 is much weaker for anatase than rutile. As a consequence, anatase shows a high yield of PID under solar light [15], [28] and absorption tests have been carried out in transparent vials and jars under solar light. Then, in order to evaluate correctly the real yield in terms of the amount of acetic acid adsorbed, for TiO_2 , the experiments should be repeated or away from the light or by quantitatively monitoring both the acetic acid and the carbon dioxide inside the chamber to verify and deepen this point. Moreover, it has also to be taken into account that usually the amount of acetic acid released by a CTA-based motion picture film is very low (in the order of tens of ppm) and, as a consequence, the possibility to exploit the advantages given by the use of TiO_2 polymorphs should be taken into account. Dedicated and specific experiments will be necessary in this sense. For Al_2O_3 nanoparticles, the very low absorption values are probably due to the fact that these particles have a bigger size than the other ones. In fact, by analyzing the results obtained with CaCO_3 macropowder ($15 \pm 2\%$), also, in this case, the $\text{AcOH}_{\text{ab}}\%$ is sensibly lower than the corresponding nanosized CaCO_3 , $98 \pm 2\%$. $\text{AcOH}_{\text{sb}}\%$ (Eq. 5.7) has been compared also to the theoretical increase in weight expected from the conversion of the starting nanoparticles to the corresponding acetate salt, calculated as follows:

$$\text{AcOH}_T\% = \frac{Mw_{\text{Ac salt}} - Mw_0}{Mw_0} * 100 \quad (5.9)$$

in which, Mw_0 is the molecular weight of the initial compound and the $Mw_{\text{Ac salt}}$ is the molecular weight of the corresponding acetate salt (Tab. 1): experimental results are coherent with the theoretical calculations for ZnO ($\text{AcOH}_T\%$: 125.46% vs

AcOH_{sb}%:120±6%) and Ca(OH)₂ (113.47% vs 111±4%). For Mg(OH)₂ the experimental increase in weight (110±8%) is slightly lower than the theoretical one (144.16%), probably due to the partial carbonation of the hydroxide; on the other hand, concerning CaCO₃, AcOH_{sb}% (92±9%) results higher than AcOH_T% (58±3%): this could be due to residues of hydroxide in the original powder. This hypothesis will be discussed below examining FTIR spectra and TGA profiles. For both TiO₂ and Al₂O₃, the experimental AcOH_{sb}% is significantly lower than the theoretical values (10±0.2% vs 100.19% and 0.01±0.005% vs 255.65%, respectively), for the reasons discussed above (i.e. the PID activity of anatase and rutile and the dimensions of the Al₂O₃ particles).

FTIR spectra of the best four systems (Ca(OH)₂, Mg(OH)₂, CaCO₃ and ZnO) before and after the absorption test have been collected.

For both the FTIR spectra of Ca(OH)₂ and Mg(OH)₂ (Fig. 4A and 4B), the peak associated with the stretching of the O-H bond of the hydroxides at 3646 and 3696 cm⁻¹ are present. Moreover, the peaks due to the stretching modes of the C-O bond at 1470 and 1540 cm⁻¹ and at 870 cm⁻¹ (out of plane bending of the O-C-O bond of the CO₃²⁻ anion) for Ca(OH)₂ and at 1485 and 1399 and cm⁻¹ for Mg(OH)₂ are probably due to partial carbonation of both the hydroxides.

For Ca(OH)₂, in the spectrum registered after the absorption test there are some signals that can be attributed to the presence of acetate [35], [36] (Fig. 4A):

1. the peaks in the region between 3000 and 2850 cm⁻¹ due to the CH₃ stretching are ascribable to calcium acetate;
2. the strong band at 1540 cm⁻¹ is due to C-O antisymmetric stretching vibrations, and the one at 1443 cm⁻¹ may be attributed to the symmetric stretching vibration of the C-O bond;
3. the out-of-plane stretching vibration of the methyl group that is split into two peaks at 1057 and 1022 cm⁻¹;

- the peak at 946 cm^{-1} attributable to the $\nu(\text{C-C})$ stretching vibration of the acetate anion ;
- two peaks at 636 and 616 cm^{-1} were due to out-of-plane stretching vibration of the O-C-O fragment of the acetate anion.

In the $\text{Mg}(\text{OH})_2$ spectrum acquired after the absorption test (Fig. 4B) the peaks ascribable to the acetate salt are the one at 1561 (associated with the asymmetric stretching of the CO) and at 1440 (the symmetric stretching of the CO) and two peaks at 1054 and 1022 cm^{-1} associated with the out-of-plane and in-plane CH_3 rocking, respectively [37].

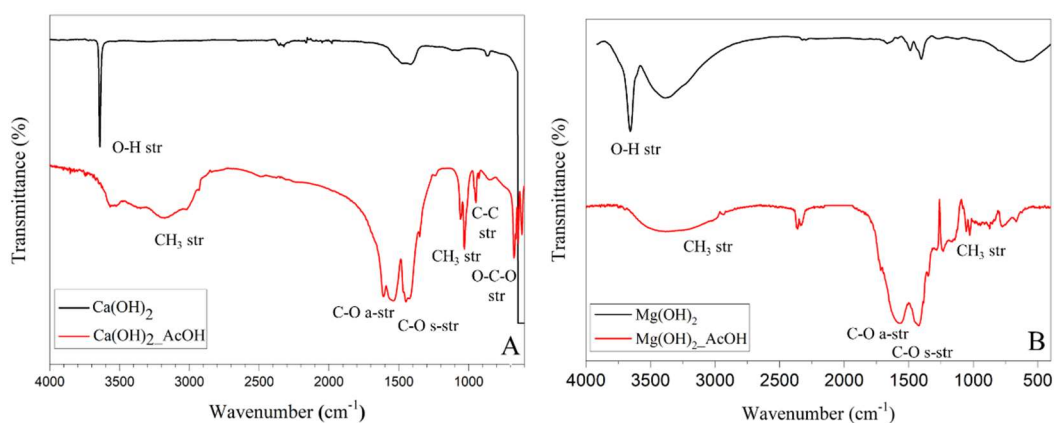


Fig. 4 FTIR spectra of (A) $\text{Ca}(\text{OH})_2$ and $\text{Mg}(\text{OH})_2$ (B) before (black) and after (red) the absorption test.

Also for ZnO (Fig. 5A), it is evident its partial conversion to zinc acetate as indicated by [31], [38]:

- the peaks associated with the COO^- asymmetric and symmetric stretching vibrations modes at 1540 and 1431 cm^{-1} respectively;
- the minor peak at 1380 cm^{-1} is related to the symmetric stretching mode of the CH_3 group.

CaCO₃ spectrum after the absorption test (Fig. 5B) shows promising results, too. Also in this case, peaks associated with the formation of the acetate salt are present [39]: the characteristic peaks at 1529 and 1440 cm⁻¹, at 1354 cm⁻¹ and two peaks at 1054 and 1022 cm⁻¹ are visible.

From all these spectra is possible to confirm that the increase in weight monitored through gravimetry tests is actually due to the conversion of the initial hydroxide/oxide/carbonate into its corresponding acetate salt. However, it is not possible to exclude that also partial carbonatation and moisture retention influenced this increase.

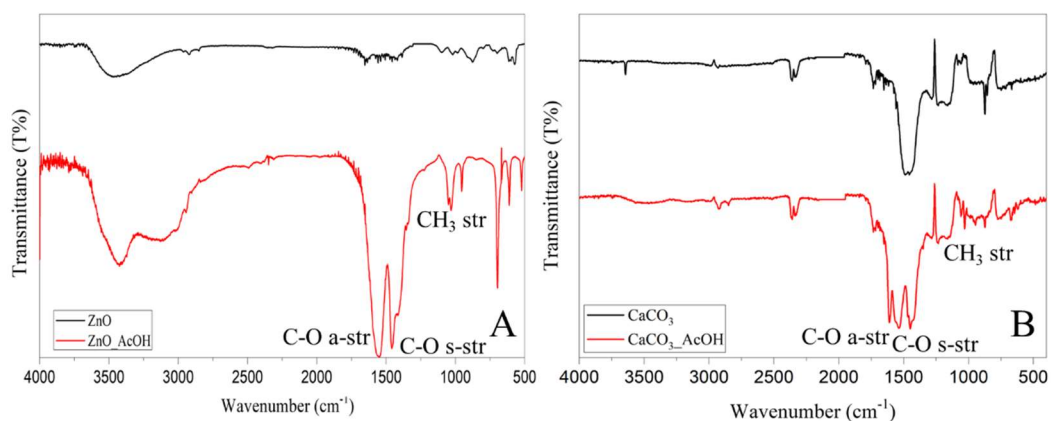


Fig. 5 FTIR spectra of (A) CaCO₃ and (B) ZnO before (black) and after (red) the absorption test.

XRD data, further confirm the formation of Zn acetate from ZnO nanoparticles (Fig. 6): by comparing the diffractograms of pure ZnO (PDF®04-020-0364) with the Powder Diffraction Files (PDF) database of the International Centre for Diffraction Data (ICDD), before and after the acetic acid absorption test, the formation of zinc acetate is evident in Fig. 6A (PDF®02-064-1515).

In addition, from the diffractogram of pure TiO₂, the prevalence of the peaks associated with anatase (PDF® 01-073-1764) compared to the ones of rutile

(PDF®00-021-1276) is shown in Fig. 6B. This point further confirms the hypothesis expressed above about the absence of titanium acetate due to the high photoreactivity of the anatase/acetic acid adduct (see Paragraph 5.1).

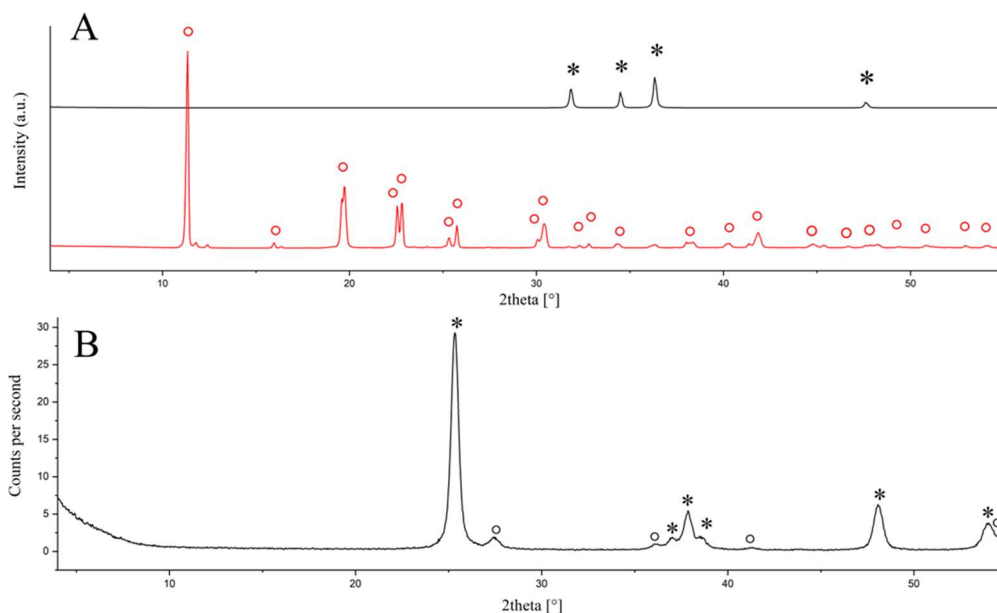


Fig. 6 (A) Diffractograms of ZnO (black) and ZnO_AcOH (red) with characteristics peaks of ZnO (PDF 04-020-0364) labeled with “*” and characteristics peaks of Zn(CH₃COO)₂ labeled with “o”; (B) Diffractogram of TiO₂ with characteristics peaks of anatase (PDF 01-073-1764) labeled with “*” and characteristics peaks of rutile (PDF 00-021-1276) labeled with “o”.

From TGA and DTG profiles, further informations on the nature of our systems and the reaction that occurred during the acetic acid absorption test have been acquired (Fig. 7-8). In particular, weight losses associated with decomposition reactions have been compared to the theoretical weight losses calculated for those transitions in terms of variation in the molecular weights of the involved compounds.

For Ca(OH)₂ (Fig. 7A), a weight loss of 19% is observed between 350 and 420 °C (peak in DTG at 407 °C) corresponding to the decomposition temperature of the calcium hydroxide into CaO, mainly due to water release (theoretical weight loss: 23%) [36], [40]. In the profile of Ca(OH)₂_AcOH, collected after the equilibration period, a first weight loss of 6% is observed between 100 and 230 °C (peak at 208

°C) and a second weight loss of 33% between 400 and 480 °C (peak at 435 °C). The first one could be ascribed to an initial mass loss of water molecules, while the second one to the dehydrated calcium acetate breakdown to acetone and calcium carbonate (theoretical weight loss: 37%). The peak observed at 455 °C is likely to be attributable to the eventual loss of acetone. The further decomposition of calcium carbonate is not seen in this profile because occurs at higher temperatures. The lower weight loss compared to the theoretical one is probably due to the partial carbonation of starting calcium hydroxide into calcium carbonate.

Concerning $\text{Mg}(\text{OH})_2$ TGA and DTG profiles (Fig. 7B), a weight loss of 38% is registered between 300 and 400 °C. It is higher than the theoretical weight loss associated with the dehydroxylation of magnesium hydroxide into MgO (31%) probably because of the presence of magnesium carbonate (due to the partial carbonation of the $\text{Mg}(\text{OH})_2$) and moisture [40]. For $\text{Mg}(\text{OH})_2 \cdot \text{AcOH}$, a first weight loss of 34% is observed between 25 and 200 °C (peak at 79 °C) due to the loss of water molecules from the tetrahydrated magnesium acetate (theoretical weight loss: 34%) [41]; a second weight loss of 44% is registered between 300 and 500 °C and it is associated with the thermal decomposition of magnesium acetate, which occurs in three steps: a first conversion into magnesium oxalate, a second one, immediately after, into magnesium carbonate and finally into magnesium oxide [42]. The residual mass percentage at the end of this process is 21% (theoretical residual mass percentage: 19%).

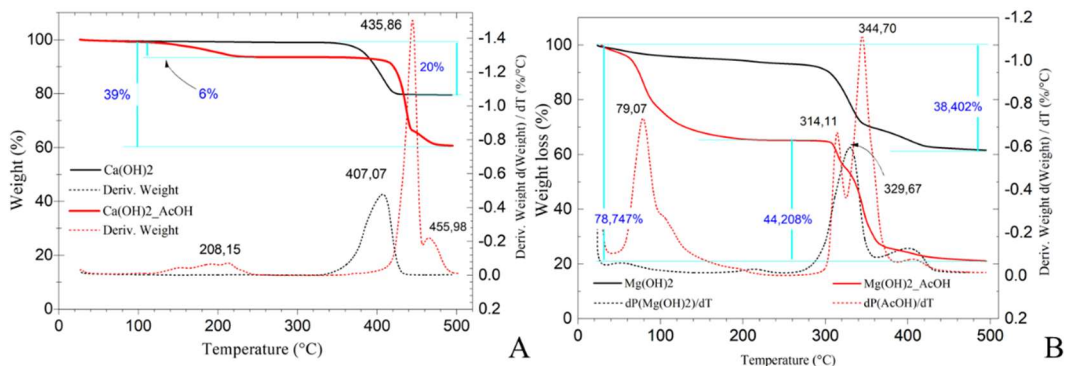


Fig. 7 TGA and DTG profiles of (A) $\text{Ca}(\text{OH})_2$ nps and (B) $\text{Mg}(\text{OH})_2$ nps before (black) and after (red) the absorption test in glacial acetic acid.

In the TGA ZnO profile (Fig. 8A), no weight loss is detected, as expected, because the thermal degradation of zinc oxide occurs at temperatures above $500\text{ }^\circ\text{C}$.

In the ZnO_AcOH profile, a total weight loss of 91% between 160 and $330\text{ }^\circ\text{C}$ is observed and corresponds, in the first range (160 - $250\text{ }^\circ\text{C}$, $\sim 28\%$) to the loss of molecular water and adsorbed acetic acid, and in the second range (250 - $330\text{ }^\circ\text{C}$) to the thermal degradation of zinc acetate into zinc oxide ($\sim 46\%$), the sublimation of zinc acetate species or the formation of other volatile zinc organic composition such as $\text{Zn}_4\text{O}(\text{CH}_3\text{CO}_2)_6$ (residual $\sim 17\%$)[43], [44].

In the CaCO_3 TGA profile (Fig. 8B), a weight loss of 13% is visible between 340 and $420\text{ }^\circ\text{C}$ (peak at $395\text{ }^\circ\text{C}$), probably due to residual calcium hydroxide in the starting sample.

CaCO_3_AcOH TGA profile shows two weight losses of 12% between 100 and $222\text{ }^\circ\text{C}$ (peak at $190\text{ }^\circ\text{C}$) due to the removal of water molecules and 31% between 391 and $460\text{ }^\circ\text{C}$ (peak at $437\text{ }^\circ\text{C}$) due to the thermal degradation of calcium acetate into calcium carbonate (theoretical weight loss: 37%)[36].

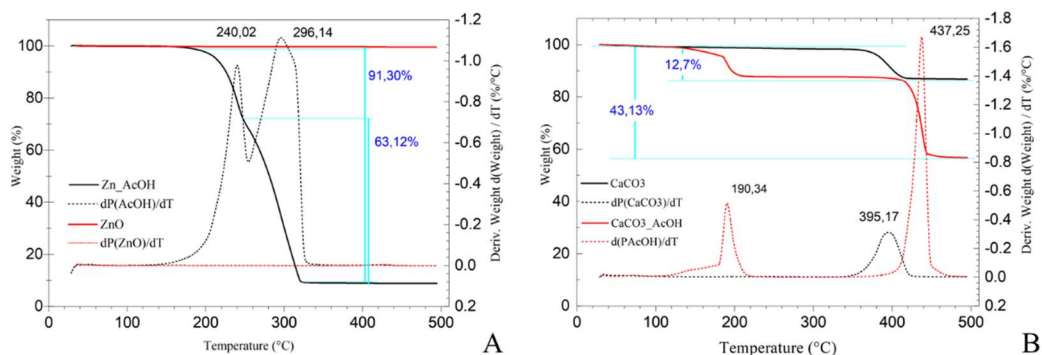


Fig. 8 TGA and DTG profiles of (A) ZnO nps and (B) CaCO₃ nps before (black) and after (red) the absorption test in glacial acetic acid.

5.3.2 Whatman paper with nanoparticles

We performed the acetic acid absorption test also on a Whatman paper sheet soaked with dispersions of several nanoparticles (ZnO, Ca(OH)₂ and Mg(OH)₂) in ethanol (5 g/L). The total amount of nanoparticles absorbed on the sheet was evaluated by comparing the weight of the dried Whatman paper sheet uploaded with nanoparticles and the original weight of the sheet (Tab. 2).

From the gravimetric analysis (Tab. 2), the AcOH_{ab}% (Eq. 5.5) after six days of absorption is 17±1% for ZnO, 13±2% for Ca(OH)₂, 11±2% for Mg(OH)₂ and only 8.7±0.5% for pure Whatman Paper. These values remain unchanged after the equilibration period (AcOH_{eq}%, Eq. 5.6) and slightly decrease after the desorption tests (AcOH_{sb}%, Eq. 5.7) for all the samples, except for the pure Whatman paper (WP), for which the residual absorbed acetic acid is very low (3.5±0.4%). The weight loss detected after the desorption test (AcOH_{wb}%, Eq. 5.8) in all the samples is probably due to the acetic acid physisorbed on the paper.

The overall trend observed is similar to the one reported in Paragraph 5.3.1 but the AcOH_{ab}% for nanoparticles inside WP is sensibly lower than for pure nanoparticles. This is probably because nanoparticles tend to aggregate during the absorption/drying procedure.

Tab. 2 Acetic acid absorbed values calculated after the absorption test ($\text{AcOH}_{\text{ab}}\%$), after the equilibration period ($\text{AcOH}_{\text{eq}}\%$) and after the desorption test ($\text{AcOH}_{\text{sb}}\%$: strongly bonded acetic acid; $\text{AcOH}_{\text{wb}}\%$: weakly bonded acetic acid) for a sample of pure Whatman Paper (WP) and samples of WP uploaded with $\text{Ca}(\text{OH})_2$, $\text{Mg}(\text{OH})_2$ and ZnO nanoparticles.

Sample	Nps (mg/cm^2)	$\text{AcOH}_{\text{ab}}\%^*$	$\text{AcOH}_{\text{eq}}\%^\#$	$\text{AcOH}_{\text{sb}}\%^\circ$	$\text{AcOH}_{\text{wb}}\%^\S$
WP $\text{Ca}(\text{OH})_2$	1.1±0.3	13±2	13±1	10±1	3±1
WP $\text{Mg}(\text{OH})_2$	0.9±0.3	11±2	10±2	9.1±0.4	0.9±0.5
WP ZnO	1.05±0.3	17±1	17±1	14±1	3±1
WP	/	8.7±0.5	6.7±0.7	3.5±0.4	3.2±0.5

$$*\text{Eq. 5.5: } \text{AcOH}_{\text{ab}}\% = \left(\frac{W_{\text{ab}} - W_{\text{dry}}}{W_{\text{dry}}}\right) \cdot 100 \quad \# \text{Eq. 5.6: } \text{AcOH}_{\text{eq}}\% = \left(\frac{W_{\text{eq}} - W_{\text{dry}}}{W_{\text{dry}}}\right) \cdot 100$$

$$^\circ \text{Eq. 5.7: } \text{AcOH}_{\text{sb}}\% = \left(\frac{W_{\text{des}} - W_{\text{dry}}}{W_{\text{dry}}}\right) \cdot 100 \quad \S \text{Eq. 5.8: } \text{AcOH}_{\text{wb}}\% = \text{AcOH}_{\text{eq}}\% - \text{AcOH}_{\text{sb}}\%$$

In Fig. 9, FTIR-ATR spectra of pure WP, WP uploaded with $\text{Ca}(\text{OH})_2$, $\text{Mg}(\text{OH})_2$ and ZnO nanoparticles before and after the absorption test with glacial acetic acid are reported. In this last spectrum, it is possible to appreciate peaks ascribable to the acetate salts: C-O asymmetric and symmetric stretching vibrations modes are detected at about 1550 and 1435 cm^{-1} , respectively [31], [38]. In addition, a peak at about 1700 cm^{-1} is detected, ascribable to the asymmetric stretching of C=O group.

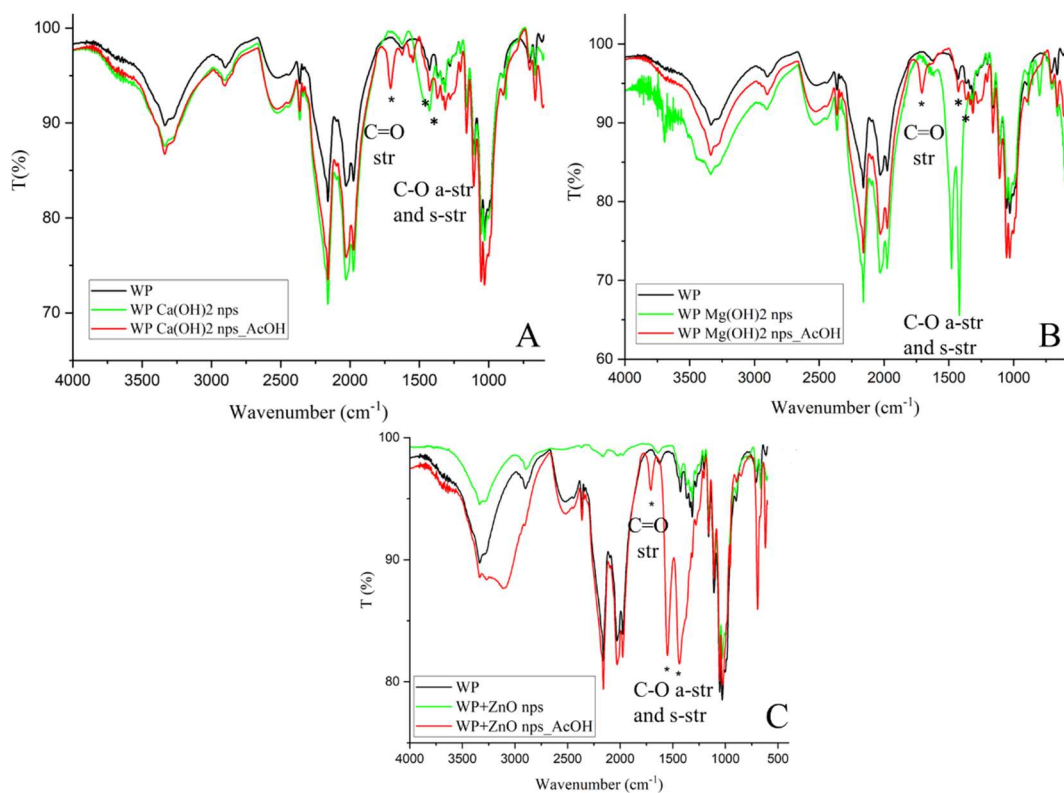


Fig. 9 FTIR-ATR spectra registered on pure WP (black), WP uploaded with Ca(OH)₂ (A), Mg(OH)₂ (B) and ZnO (C) nps before (green) and after (red) the absorption test with glacial acetic acid. Peaks associated with the acetate group are labeled with “*”.

5.3.3 Inorganic nanoparticles uploaded on PVF and SPEI sponges

FE-SEM. Before analyzing the absorption capacity of gaseous glacial acetic acid of these systems, their structure was analyzed through FE-SEM.

In Fig. 10, the presence of nanoparticles on the surface of a PVF sponge is clear: while the sample of pure PVF has a clean surface only interrupted by its porosities (Fig. 10A), in the PVF+ZnO sponge, ZnO nanoparticles are visible (Fig. 10B and 10C). It is possible to see both the presence of isolated nanoparticles, which have preserved their size and structure, but also of bigger aggregates of several microns.

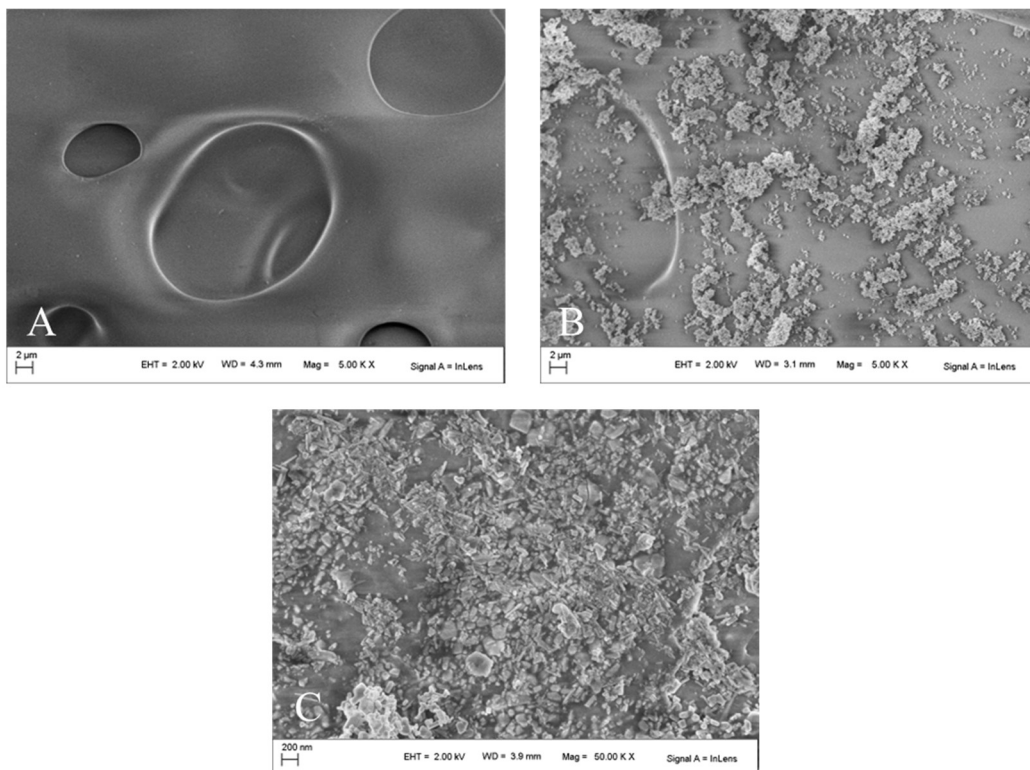


Fig. 10. FE-SEM micrographs acquired on pure PVF sponge (A) and PVF+ZnO sponge (B) with 5.00kx magnitude and (C) on PVF+ZnO sponge with 50.00kx magnitude.

In Fig. 11, the surface of a pure SPEI sponge (Fig. 11A) is compared to the one of a SPEI+ZnO sponge (Fig. 11B): also in this case, the samples of pure SPEI appears clean and smooth, while, in the sponge with nanoparticles, surface and also pore edges appear more irregular and rough. Fewer aggregates are visible compared to PVF (Fig. 11C). Nanoparticles do not lean on the surface of the sponge, as in PVF, but seem to be covered by a thin veil, as if they are incorporated in the sponge itself. This difference between the two systems is probably due to the different uploading methods of nanoparticles inside the two sponges: while for PVF, nanoparticles have been uploaded after the synthesis of the sponge, for SPEI, nanoparticles have been incorporated during the synthesis of the sponge itself.

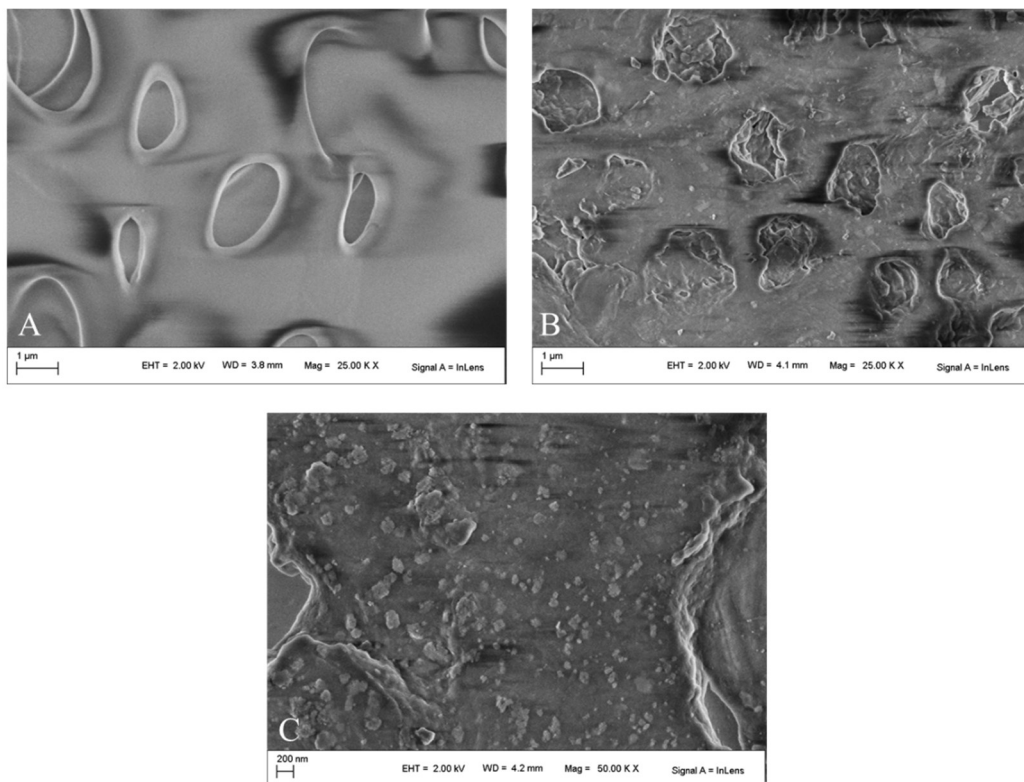


Fig. 11. FE-SEM micrographs acquired on pure SPEI sponge (A) and SPEI+ZnO sponge (B) with 5.00kx magnitude and (C) on SPEI+ZnO sponge with 50.00kx magnitude.

The presence of ZnO nanoparticles inside the two sponges was further confirmed by EDX as it is possible to see from the spectra in Fig. 12: in PVF spectrum (Fig. 12A) C and O are detected and in SPEI spectrum (Fig. 12B) C, O and N, as expected. In PVF+ZnO (Fig. 12C) and SPEI+ZnO (Fig. 12D) also the presence of Zn is evident.

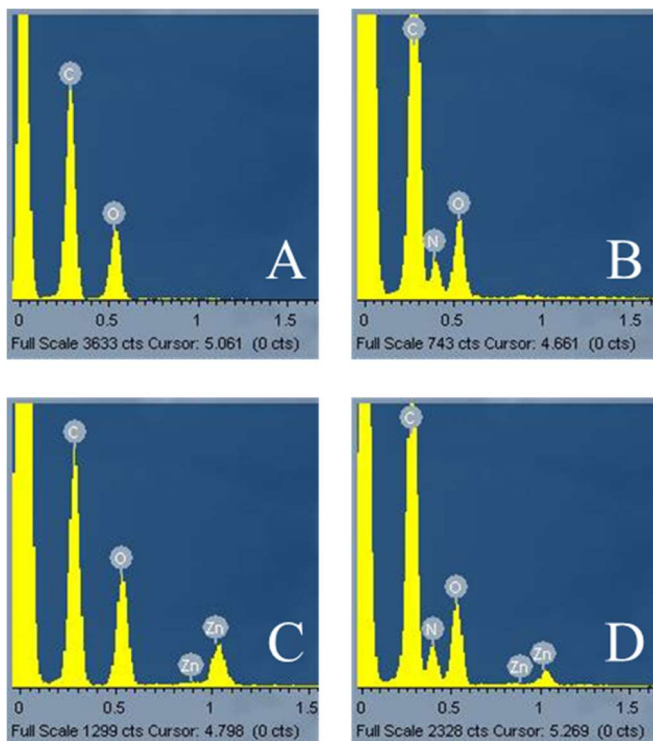


Fig. 12 EDX spectra of pure PVF (A), pure SPEI (B), PVF+ZnO (C) and SPEI+ZnO (D).

Acetic acid absorption tests. The absorption capacity of gaseous glacial acetic acid has been evaluated also for PVF and SPEI sponges uploaded with ZnO nanoparticles (Tab. 3) that were chosen because, as indicated in the previous paragraphs (i.e. 5.3.1 and 5.3.2), give the best performances in terms of adsorbed acetic acid within the explored nanomaterials.

For the PVF-based systems, the presence of ZnO nanoparticles increases the absorption capacity of the pure PVF (Paragraph 4.2.6), in particular in terms of $\text{AcOH}_{\text{sb}}\%$ (Eq. 5.7, PVF: $6\pm 1\%$, PVF+ZnO: $20\pm 2\%$). An increase is observed also comparing this system with WP+ZnO ($\text{AcOH}_{\text{sb}}\%$ of WP+ZnO: $14\pm 1\%$). Nevertheless, an important decrease is observed, if PVF+ZnO is compared with pure ZnO nanoparticles ($\text{AcOH}_{\text{sb}}\%$ of ZnO: $120\pm 3\%$). As discussed in Chapter IV, the PVF sponge is able only to establish weak interaction with the acetic acid; however, its porous structure probably promotes the absorption of acetic acid on the surface of

ZnO nanoparticles, if compared to paper. Nevertheless, if the addition of nanoparticles helps to increase the bonding strength between the sponge and acetic acid, on the other hand, nanoparticles probably tend to aggregate during the uploading process in the sponge with a consequent decrease in the extension of the interface as we see from FE-SEM micrographs (Fig. 11).

Concerning SPEI-based systems, the absorption capacity of SPEI ($\text{AcOH}_{\text{ab}}\%:258\pm7\%$, $\text{AcOH}_{\text{eq}}\%:76\pm4\%$, $\text{AcOH}_{\text{sb}}\%:44\pm3\%$, Paragraph 4.3.4) is slightly higher than the one of the combined system SPEI+ZnO ($\text{AcOH}_{\text{ab}}\%:246\pm8\%$ and $\text{AcOH}_{\text{eq}}\%:65\pm4\%$, $\text{AcOH}_{\text{sb}}\%:32\pm2\%$). It is reasonable to hypothesize that, also in this case, the aggregation of nanoparticles occurs during the synthesis process, probably because of the instability of ZnO nanoparticles in water dispersions. In fact, also in this case, pure ZnO nanoparticles show a higher $\text{AcOH}_{\text{sb}}\%$ ($120\pm3\%$) than sponge system ($32\pm2\%$). Anyway, both the SPEI ($44\pm3\%$) and SPEI+ZnO ($33\pm2\%$) show a higher $\text{AcOH}_{\text{sb}}\%$ than the WP+ZnO ($14\pm1\%$), probably due to the intrinsic adsorption capacity of acetic acid of the pure SPEI system.

Comparing PVF+ZnO and SPEI+ZnO, the major amount of both $\text{AcOH}_{\text{sb}}\%$ and $\text{AcOH}_{\text{wb}}\%$ (Eq. 5.8) is detected for SPEI+ZnO, confirming that the SPEI sponge is probably the best system to use as acetic acid adsorber.

Tab. 3 Acetic acid absorbed percentage in weight calculated after the absorption test ($AcOH_{ab}\%$), after the equilibration period ($AcOH_{eq}\%$) and after the desorption test ($AcOH_{sb}\%$ and $AcOH_{wb}\%$) for PVF+ZnO, PVF, SPEI+ZnO, SPEI 4, WP+ZnO and ZnO nanoparticles.

Sample	$AcOH_{ab}\%$ *	$AcOH_{eq}\%$ #	$AcOH_{sb}\%$ °	$AcOH_{wb}\%$ §
PVF + ZnO	95±5	20±2	20±2	7±2
PVF	114±2	17±1	6±1	11±1
SPEI+ZnO	246±8	65±4	33±2	32±2
SPEI 4	258±7	76±4	44±3	34±3
WP+ZnO	17±1	17±1	14±1	2±1
ZnO nps	122±6	121±3	120±3	1±3

$$*Eq. 5.5: AcOH_{ab}\% = \left(\frac{W_{ab} - W_{dry}}{W_{dry}}\right) \cdot 100 \quad \#Eq. 5.6: AcOH_{eq}\% = \left(\frac{W_{eq} - W_{dry}}{W_{dry}}\right) \cdot 100$$

$$°Eq. 5.7: AcOH_{sb}\% = \left(\frac{W_{des} - W_{dry}}{W_{dry}}\right) \cdot 100 \quad §Eq. 5.8: AcOH_{wb}\% = AcOH_{eq}\% - AcOH_{sb}\%$$

In Fig. 13, FTIR-ATR spectra of PVF and SPEI-based systems are reported before and after the absorption test: in both PVF+ZnO_AcOH (A) and SPEI+ZnO_AcOH (B) spectra, typical peaks of the acetyl group at about 1550 cm^{-1} and 1400 cm^{-1} (C-O asymmetric and symmetric stretching) are evident.

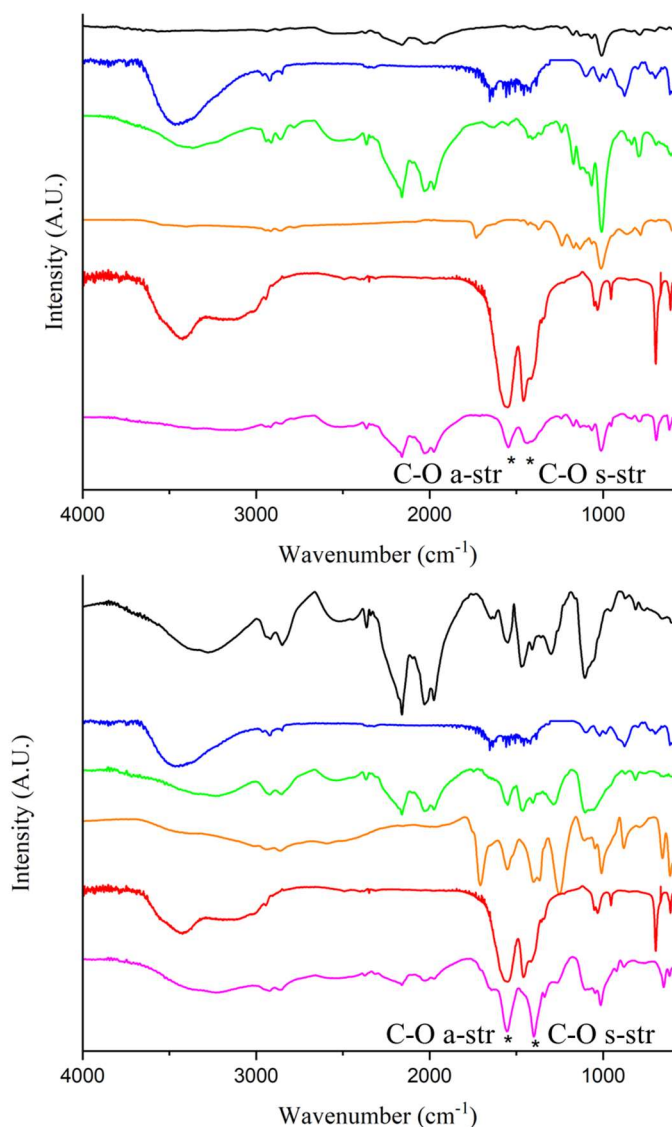


Fig. 13 FTIR-ATR spectra of (A) PVF-based systems: PVF sponge (black), ZnO nanoparticles (blue), PVF+ZnO (green), PVF_AcOH (after the absorption test, orange), ZnO_AcOH (after the absorption test, red), PVF+ZnO_AcOH (after the absorption test, pink); (B) SPEI-based systems: SPEI sponge (black), ZnO nanoparticles (blue), SPEI+ZnO (green), SPEI_AcOH (after the absorption test, orange), ZnO_AcOH (after the absorption test, red), SPEI+ZnO_AcOH (after the absorption test, pink). Peaks associated with the acetate group are labeled with “*”.

In TGA profile of PVF+ZnO (Fig. 14) a first weight loss of 13% between 25 and 250 °C is ascribable to the loss of moisture in the PVF network (i.e. bulk water and strongly bound water) and a second weight loss of 89% between 250 and 450 °C (that corresponds to the two peaks at 328 and 414 °C in the DTG curve), is associated

with the degradation of PVF (in pure PVF a weight loss of 91 wt% is detected in the same range, as indicated by the peak at 392 °C in the DTG curve). The presence of two peaks in the DTG profile of PVF+ZnO while in the DTG profile of PVF only one is detected is not clear. To better understand this point further SAXS and rheological analysis are needed. The thermal decomposition of ZnO is not detectable in this temperature range because its degradation temperature occurs above 500 °C. Concerning PVF+ZnO after the desorption test (PVF+ZnO_AcOH_{sb}), a weight loss of 63% between 150 and 350 °C (peak at 253 °C) could be ascribed to the presence of zinc acetate inside the sponge (the same weight loss of 63% is visible in ZnO_AcOH) and a second weight loss of 23% between 350 and 500 °C (peak at 415°C) can be due to the degradation of PVF sponge.

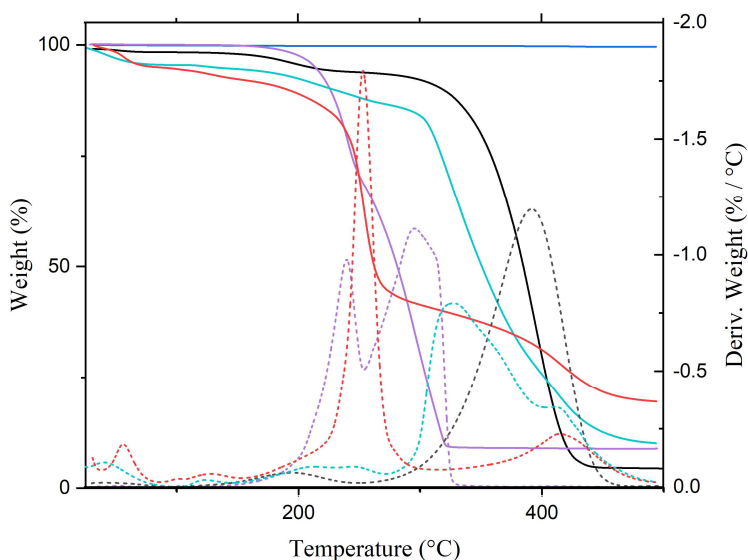


Fig. 14 TGA and DTG profiles of (A) PVF sponge (black), PVF+ZnO (green), PVF+ZnO_AcOH (after the absorption test, red), ZnO nanoparticles (blue), ZnO_AcOH (after the absorption test, purple).

For SPEI+ZnO (Fig. 15), a first weight loss of 10% between 25 and 150 °C could be associated with the moisture absorbed on the sponge; a second weight loss of 69% is detected between 210 and 420 °C, as indicated by the double peak at 300 and 336 °C in the DTG curve. This last peak appears at lower temperatures than in pure SPEI,

(range 210-420 °C, double peak at 357 and 372 °C) because the addition of ZnO nanoparticles probably affects the crosslinking of PEI with BDDE. Further tests are needed to clarify this point.

In the sample SPEI+ZnO_AcOH_{sb} obtained after the desorption of the acetic acid, a first weight loss of 39% due to moisture and the residual acetic acid adsorbed on the SPEI sponge is detected between 70 °C and 175 °C, peak at 119 °C (also in pure SPEI_AcOHdes this weigh loss is 39% and appears in the same range). In addition, a second weight loss of 42% is visible between 200 °C and 450 °C (peak at 283 and 331 °C), probably due to the pyrolysis of PEI. Because the weight loss associated with the degradation of zinc acetate appears in the same range as the one of PEI, detecting the presence of zinc acetate is difficult through TGA. The residual weight of SPEI+ZnO_AcOHdes is 19%, which is higher than the one of SPEI_AcOHdes (0.03%): this could indicate the presence of inorganic residues, probably ZnO, which degrades at higher temperatures than 500 °C.

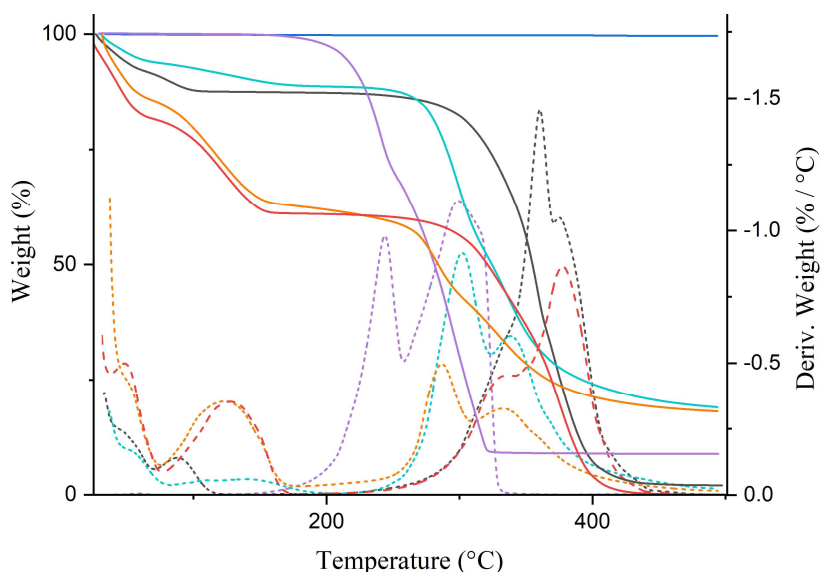


Fig. 15 (B) SPEI-based systems: SPEI sponge (black), SPEI_AcOHdes (after the absorption test, red), ZnO nanoparticles (blue), ZnO_AcOH (after the absorption test, purple), SPEI+ZnO (green), SPEI+ZnO_AcOH (after the absorption test, orange).

5.4 Conclusions

In this Chapter, the possibility of using nanoparticle-based systems for the inhibition of the “vinegar syndrome” has been evaluated.

First of all, we tested the gaseous acetic acid absorption capacity of different kinds of nanoparticles ($\text{Ca}(\text{OH})_2$, $\text{Mg}(\text{OH})_2$, CaCO_3 , ZnO , TiO_2 , Al_2O_3): the ones which give the better performance both in terms of total absorbed acetic acid ($\text{AcOH}_{\text{ab}}\%$, Eq. 5.5, and $\text{AcOH}_{\text{eq}}\%$, Eq. 5.6) and strongly bonded acetic acid ($\text{AcOH}_{\text{sb}}\%$, Eq. 5.7) were ZnO ($122\pm 6\%$ and $120\pm 6\%$), $\text{Mg}(\text{OH})_2$ ($125\pm 9\%$ and $110\pm 8\%$), $\text{Ca}(\text{OH})_2$ ($116\pm 3\%$ and $111\pm 4\%$) and CaCO_3 ($98\pm 9\%$ and $92\pm 10\%$). Concerning TiO_2 and Al_2O_3 further tests will be needed taking more into account their photocatalytic activity and their dimension, respectively. Some of the four better systems have been uploaded on different kinds of supports with different porosity: in particular, $\text{Ca}(\text{OH})_2$, $\text{Mg}(\text{OH})_2$ and ZnO of nanoparticles have been uploaded on WP disks and ZnO nanoparticles on two sponge-like systems based on PVF and SPEI.

Concerning both WP and sponge-based systems, they show lower absorption properties than pure nanoparticles (es. WP+ ZnO $\text{AcOH}_{\text{ab}}\%$: $17\pm 1\%$ and $\text{AcOH}_{\text{sb}}\%$: $14\pm 1\%$), probably because nanoparticles tend to aggregate during the synthesis/uploading process. WP systems show lower absorption capacity than sponges because the porous nature of the latest ones is able to promote acetic acid absorption.

SPEI+ ZnO showed the best performance in terms of both total absorbed acetic acid ($\text{AcOH}_{\text{ab}}\%$: $246\pm 8\%$ and $\text{AcOH}_{\text{eq}}\%$: $65\pm 4\%$) and strongly bonded acetic acid ($\text{AcOH}_{\text{sb}}\%$ $33\pm 2\%$), followed by PVF+ ZnO ($\text{AcOH}_{\text{ab}}\%$: $95\pm 5\%$, $\text{AcOH}_{\text{eq}}\%$: $20\pm 2\%$, $\text{AcOH}_{\text{sb}}\%$: $20\pm 2\%$). This is due to the fact that SPEI is able to neutralize acetic acid also on its own, thanks to the presence of amino groups inside the sponge network. In fact, pure SPEI ($\text{AcOH}_{\text{ab}}\%$: $258\pm 7\%$, $\text{AcOH}_{\text{eq}}\%$: $76\pm 4\%$, $\text{AcOH}_{\text{sb}}\%$: $44\pm 3\%$) shows an absorption capacity higher than SPEI+ ZnO . On the contrary, pure PVF is able only to weakly absorb acetic acid ($\text{AcOH}_{\text{ab}}\%$: $114\pm 2\%$, $\text{AcOH}_{\text{eq}}\%$: $17\pm 1\%$, $\text{AcOH}_{\text{sb}}\%$: $6\pm 1\%$), while the nanoparticles are the actual neutralization system.

On this basis, we decided to select some of these systems (in particular pure $\text{Ca}(\text{OH})_2$ and ZnO nanoparticles, SPEI 4 and composed system of nanoparticles and WP, SPEI 4 (SPEI+ZnO) and PVF (PVF+ZnO)) in order to test their efficacy in inhibiting the deacetylation process in motion picture films (i.e. the “vinegar syndrome”). These tests were performed on both CTA-based films and real motion picture films on which the deacetylation process has been artificially induced (as reported in Chapter III) and on real motion picture films naturally affected by the vinegar syndrome.

References

- [1] D. Baglioni, P.; Chelazzi, *Nanoscience for the conservation of works of art*. RSC Publishing, 2013.
- [2] R. Giorgi, L. Dei, M. Ceccato, C. Schettino, and P. Baglioni, “Nanotechnologies for conservation of cultural heritage: Paper and canvas deacidification,” *Langmuir*, vol. 18, no. 21, pp. 8198–8203, 2002, doi: 10.1021/la025964d.
- [3] R. Giorgi *et al.*, “Nanoparticles of calcium hydroxide for wood deacidification: Decreasing the emissions of organic acid vapors in church organ environments,” *J. Cult. Herit.*, vol. 10, no. 2, pp. 206–213, 2009, doi: 10.1016/j.culher.2008.06.012.
- [4] C. Baglioni, P.; Dei, L.; Giorgi, R.; Schettino, “Basic suspensions: their preparation and use in processes for paper deacidification. International patent pending.,” PCT/EP02/00319, 2002.
- [5] B. Salvadori and L. Dei, “Synthesis of Ca(OH)₂ nanoparticles from diols,” *Langmuir*, vol. 17, no. 8, pp. 2371–2374, 2001, doi: 10.1021/la0015967.
- [6] L. Nanni, A.; Dei, “Ca(OH)₂ nanoparticles from o/w microemulsion,” *Langmuir*, vol. 19, p. 993, 2003.
- [7] P. Poggi, G.; Giorgi, R.; Toccafondi, N.; Katur, V.; Baglioni, “Hydroxide Nanoparticles for Deacidification and Concomitant Inhibition of Iron-Gall Ink Corrosion of Paper.,” *Langmuir*, vol. 26, p. 19084, 2010.
- [8] R. Giorgi, C. Bozzi, L. Dei, C. Gabbiani, B. W. Ninham, and P. Baglioni, “Nanoparticles of Mg(OH)₂: Synthesis and application to paper conservation,” *Langmuir*, vol. 21, no. 18, pp. 8495–8501, 2005, doi: 10.1021/la050564m.
- [9] G. Poggi *et al.*, “Calcium hydroxide nanoparticles for the conservation of cultural heritage: New formulations for the deacidification of cellulose-based artifacts,” *Appl. Phys. A Mater. Sci. Process.*, vol. 114, no. 3, pp. 685–693, 2014, doi: 10.1007/s00339-013-8172-7.
- [10] P. Dillmann, L. Bellot-Gurlet, and I. Nenner, *Nanoscience and cultural heritage*. 2016.
- [11] E. J. Sequeira, S.; Casanova, C.; Cabrita, “Deacidification of paper using dispersions of Ca(OH)₂ nanoparticles in isopropanol. Study of efficiency,” *J Cult Herit*, vol. 7, pp. 264–272, 2006.

- [12] E. Tétreault, J.; Stamatopoulou, “Determination of concentrations of acetic acid emitted from wood coatings in enclosures.,” *Stud Conserv*, vol. 42, no. 3141–156, 1997.
- [13] E. David and V. C. Niculescu, “Volatile organic compounds (Vocs) as environmental pollutants: Occurrence and mitigation using nanomaterials,” *Int. J. Environ. Res. Public Health*, vol. 18, no. 24, 2021, doi: 10.3390/ijerph182413147.
- [14] Z. Rao *et al.*, “Photocatalytic oxidation mechanism of Gas-Phase VOCs: Unveiling the role of holes, $\bullet\text{OH}$ and $\bullet\text{O}_2^-$,” *Chem. Eng. J.*, vol. 430, no. P2, p. 132766, 2022, doi: 10.1016/j.cej.2021.132766.
- [15] S. Almaie, V. Vatanpour, M. H. Rasoulifard, and I. Koyuncu, “Volatile organic compounds (VOCs) removal by photocatalysts: A review,” *Chemosphere*, vol. 306, no. July, p. 135655, 2022, doi: 10.1016/j.chemosphere.2022.135655.
- [16] H. Honda, H. Takamatsu, and J. J. Wei, “直観像 : アルファ波と眼球運動© 1972 Nature Publishing Group,” *Nihon Kikai Gakkai Ronbunshu, B Hen/Transactions Japan Soc. Mech. Eng. Part B*, vol. 68, no. 672, pp. 2327–2332, 1972.
- [17] O. Carp, C. L. Huisman, and A. Reller, “Photoinduced reactivity of titanium dioxide,” *Prog. Solid State Chem.*, vol. 32, no. 1–2, pp. 33–177, 2004, doi: 10.1016/j.progsolidstchem.2004.08.001.
- [18] Y. Chen and Q. Yu, “Research progress on degradation of VOCs by metal ions doped titanium dioxide nanoparticles,” *J. Phys. Conf. Ser.*, vol. 2021, no. 1, 2021, doi: 10.1088/1742-6596/2021/1/012063.
- [19] U. Diebold, “<(Surf.Sci.Rep.)[2003]The surface science of titanium dioxide.pdf>,” *Surf. Sci. Rep.*, vol. 48, no. 1, pp. 53–229, 2002, [Online]. Available: <http://linkinghub.elsevier.com/retrieve/pii/S0167572902001000>.
- [20] A. Fujishima, X. Zhang, and D. A. Tryk, “TiO₂ photocatalysis and related surface phenomena,” *Surf. Sci. Rep.*, vol. 63, no. 12, pp. 515–582, 2008, doi: 10.1016/j.surfrep.2008.10.001.
- [21] M. Addamo, M. Bellardita, A. Di Paola, and L. Palmisano, “Preparation and photoactivity of nanostructured anatase, rutile and brookite TiO₂ thin films,” *Chem. Commun.*, no. 47, pp. 4943–4945, 2006, doi: 10.1039/b612172a.
- [22] H. Kominami, Y. Ishii, M. Kohno, S. Konishi, Y. Kera, and B. Ohtani,

- “Nanocrystalline brookite-type titanium(IV) oxide photocatalysts prepared by a solvothermal method: Correlation between their physical properties and photocatalytic activities,” *Catal. Letters*, vol. 91, no. 1–2, pp. 41–47, 2003, doi: 10.1023/B:CATL.0000006316.45620.30.
- [23] T. Guohui, F. Honggang, J. Liqiang, X. Baifu, and P. Kai, “Preparation and characterization of stable biphasic TiO₂ photocatalyst with high crystallinity, large surface area, and enhanced photoactivity,” *J. Phys. Chem. C*, vol. 112, no. 8, pp. 3083–3089, 2008, doi: 10.1021/jp710283p.
- [24] S. Ardizzone, C. L. Bianchi, G. Cappelletti, S. Gialanella, C. Pirola, and V. Ragaini, “Tailored anatase/brookite nanocrystalline TiO₂. the optimal particle features for liquid and gas-phase photocatalytic reactions,” *J. Phys. Chem. C*, vol. 111, no. 35, pp. 13222–13231, 2007, doi: 10.1021/jp0741096.
- [25] B. Kraeutler and A. J. Bard, “Heterogeneous Photocatalytic Decomposition of Saturated Carboxylic Acids on TiO₂ Powder. Decarboxylative Route to Alkanes,” *J. Am. Chem. Soc.*, vol. 100, no. 19, pp. 5985–5992, 1978, doi: 10.1021/ja00487a001.
- [26] J. M. Janusz and J. A. Berson, “Heterogeneous Photocatalytic Synthesis of Methane from Acetic Acid—New Kolbe Reaction Pathway,” *J. Am. Chem. Soc.*, vol. 100, no. 7, pp. 2239–2240, 1978, doi: 10.1021/ja00475a049.
- [27] L.-F. Liao, C.-F. Lien, and J.-L. Lin, “FTIR study of adsorption and photoreactions of acetic acid on TiO₂,” doi: 10.1039/b103419g.
- [28] A. Mattsson and L. Österlund, “Adsorption and photoinduced decomposition of acetone and acetic acid on anatase, brookite, and rutile TiO₂ nanoparticles,” *J. Phys. Chem. C*, vol. 114, no. 33, pp. 14121–14132, 2010, doi: 10.1021/jp103263n.
- [29] G. Capecchi, M. G. Faga, G. Martra, S. Coluccia, M. F. Iozzi, and M. Cossi, “Adsorption of CH₃COOH on TiO₂: IR and theoretical investigations,” *Res. Chem. Intermed.*, vol. 33, no. 3–5, pp. 269–284, 2007, doi: 10.1163/156856707779238748.
- [30] G. Mahmodi, S. Sharifnia, M. Madani, and V. Vatanpour, “Photoreduction of carbon dioxide in the presence of H₂, H₂O and CH₄ over TiO₂ and ZnO photocatalysts,” *Sol. Energy*, vol. 97, pp. 186–194, Nov. 2013, doi: 10.1016/J.SOLENER.2013.08.027.
- [31] A. Zuliani, D. Bandelli, D. Chelazzi, R. Giorgi, and P. Baglioni, “Environmentally friendly ZnO/Castor oil polyurethane composites for the gas-phase adsorption of

- acetic acid,” *J. Colloid Interface Sci.*, vol. 614, pp. 451–459, 2022, doi: 10.1016/j.jcis.2022.01.123.
- [32] A. Zuliani, D. Chelazzi, R. Mastrangelo, R. Giorgi, and P. Baglioni, “Adsorption kinetics of acetic acid into ZnO/castor oil-derived polyurethanes,” *J. Colloid Interface Sci.*, vol. 632, pp. 74–86, 2023, doi: 10.1016/j.jcis.2022.11.049.
- [33] S. R. Tong, L. Y. Wu, M. F. Ge, W. G. Wang, and Z. F. Pu, “Heterogeneous chemistry of monocarboxylic acids on α -Al₂O₃ at different relative humidities,” *Atmos. Chem. Phys.*, vol. 10, no. 16, pp. 7561–7574, 2010, doi: 10.5194/acp-10-7561-2010.
- [34] M. Tang, W. A. Larish, Y. Fang, A. Gankanda, and V. H. Grassian, “Heterogeneous Reactions of Acetic Acid with Oxide Surfaces: Effects of Mineralogy and Relative Humidity,” *J. Phys. Chem. A*, vol. 120, no. 28, pp. 5609–5616, 2016, doi: 10.1021/acs.jpca.6b05395.
- [35] M. Thongkam *et al.*, “Research Article Simple and Rapid Synthesis of Calcium Acetate from Scallop Shells to Reduce Environmental Issues,” 2021, doi: 10.1155/2021/6450289.
- [36] A. T. Pemberton, D. Brandon, and D. A. King, “Integrated TGA, FTIR, and Computational Laboratory Experiment,” 2018, doi: 10.1021/acs.jchemed.8b00607.
- [37] S. Seesanong *et al.*, “Bio-green synthesis of calcium acetate from oyster shell waste at low cost and reducing the emission of greenhouse gases,” *Sustain. Environ. Res.*, vol. 33, no. 1, pp. 1–22, 2023, doi: 10.1186/s42834-023-00187-6.
- [38] H. Yin and P. S. Casey, “ZnO nanorod composite with quenched photoactivity for UV protection application,” *Mater. Lett.*, vol. 121, pp. 8–11, 2014, doi: 10.1016/j.matlet.2014.01.103.
- [39] S. F. Pang, C. Q. Wu, Q. N. Zhang, and Y. H. Zhang, “The structural evolution of magnesium acetate complex in aerosols by FTIR-ATR spectra,” *J. Mol. Struct.*, vol. 1087, no. January, pp. 46–50, 2015, doi: 10.1016/j.molstruc.2015.01.034.
- [40] F. Laoutid, M. Lorgouilloux, L. Bonnaud, D. Lesueur, and P. Dubois, “Fire retardant behaviour of halogen-free calcium-based hydrated minerals,” *Polym. Degrad. Stab.*, vol. 136, pp. 89–97, 2017, doi: 10.1016/j.polymdegradstab.2016.12.013.
- [41] K. Isa and M. Nogawa, “Thermal decomposition of magnesium acetate tetrahydrate under self-generated atmosphere,” *Thermochim. Acta*, vol. 75, no. 1–2, pp. 197–206,

- Apr. 1984, doi: 10.1016/0040-6031(84)85020-0.
- [42] Y. Jiang, H. Chen, X. Mu, and Z. He, “Thermal decomposition of magnesium acetate in nitrogen,” *J. Phys. Conf. Ser.*, vol. 1653, no. 1, p. 12057, 2020, doi: 10.1088/1742-6596/1653/1/012057.
- [43] A. V. Ghule *et al.*, “In situ thermo-TOF-SIMS study of thermal decomposition of zinc acetate dihydrate,” *J. MASS Spectrom. J. Mass Spectrom.*, vol. 39, pp. 1202–1208, 2004, doi: 10.1002/jms.721.
- [44] C. C. Lin and Y. Y. Li, “Synthesis of ZnO nanowires by thermal decomposition of zinc acetate dihydrate,” *Mater. Chem. Phys.*, vol. 113, no. 1, pp. 334–337, Jan. 2009, doi: 10.1016/J.MATCHEMPHYS.2008.07.070.

Chapter VI

Evaluation of the efficacy of our systems in the inhibition of the “vinegar syndrome”

In this Chapter, the efficacy of some of the systems synthesized and characterized in Chapters IV and V in inhibiting the “vinegar syndrome” was tested.

CTA-based films and real motion picture films have been subjected to the degradation protocol reported in Paragraph 3.1.2.2 (ATM2.X): the evolution of the deacetylation process was monitored with the multi-analytical protocol proposed in Paragraph 3.1.3 on both treated and untreated samples in order to evaluate the performance of our inhibitors.

The efficacy of one of the treatments has been tested also on real motion picture films naturally affected by the vinegar syndrome kindly provided by “L’Immagine Ritrovata-Film Restoration and Conservation Institute”, Bologna, Italy.

6.1 Material and Methods

6.1.1 Chemicals and samples

For SPEI synthesis: branched polyethyleneimine (PEI) with an average molecular weight of 750 kDa at 50% solution in water, 1,4-butanedioldyglycidyl ether (BDDE) were purchased from Sigma Aldrich.

For PVF synthesis: polyvinyl alcohol was purchased from Kuraray (Kuraray Poval 10-98). Formaldehyde, Triton X100 were purchased from Sigma Aldrich. Sulfuric acid 96% was purchased from Carlo Erba Reagents.

Nanoparticles: Nanorestore Plus® of calcium hydroxide, $\text{Ca}(\text{OH})_2$, nanoparticles dispersed in ethanol (10 g/L) have been kindly provided by the CSGI consortium; zinc oxide, ZnO, nanopowder (<100 nm particle size) were purchased from Sigma Aldrich.

Whatman Paper (55 mm Ø, Cat. No. 1001-055).

Cellulose triacetate (CTA, 43.3-45 wt.% acetyl content), cellulose diacetate (CDA, 39.8 wt.% acetyl content), dichloromethane (DCM, purity \geq 99.8%) were purchased from Sigma Aldrich. Sodium Hydroxide (\geq 98.5% pellets, anhydrous) was purchased by Acros Organics. Hydrochloric acid (37%) and ethanol anhydrous denatured were purchased from Carlo Erba Reagents. Phenolphthalein was purchased from Merk reagents. All the products were used without further purification.

Water used for all the procedures was purified by a Millipore MilliQ Direct-Q® & Direct-Q UV water purification system (Water Resistivity: 18,2 M Ω at 25°C).

CTA-based films were obtained as reported in Paragraph 3.1.1.

Real motion picture films used for the evaluation of the performance of the treatments on samples on which the deacetylation process has been artificially induced are from the reel called “Vita di una Pianta” (Paragraph 3.1.1.).

To evaluate the efficacy of our treatments on real motion picture films on which the vinegar syndrome has naturally occurred, some fragments in an advanced state of degradation from the Cineteca di Bologna (Bologna, Italy) have been gently supplied by the restoration laboratory “L’Immagine Ritrovata” srl (Fig. 1). It is a 35 mm color motion picture film that emits a strong vinegar odor and appears wavy and slightly deformed. The frames appear yellowed and the fading of the image and the shifts in color balance are due to the spontaneous degradation processes involving the dyes in the emulsion layer [1]. Considering these symptoms and based on the analysis that will be reported below, it is plausible to affirm that the film is affected by the vinegar syndrome.



Fig. 1 Motion Picture film from the Cineteca di Bologna, gently provided by the restoration lab “L’Immagine Ritrovata” srl.

6.1.2 The inhibition of the artificially-induced deacetylation process

6.1.2.1 The protocol to artificially induce the deacetylation process

CTA-based films and real motion picture films have been subjected to the degradation protocol reported in Paragraph 3.1.2.2 (ATM2.X) which is characterized by three steps as follows:

- 1) first step: the deacetylation process was artificially induced by exposing the samples to an atmosphere saturated by HCl (9 days for motion picture films and 3 days for CTA-based films);
- 2) second step: the samples were put out of the chamber and left for 24 h under hood at 50 RH% and room temperature (25 ± 3 °C);
- 3) third step: the samples were stored again in hermetic chambers at 100 RH% and 25 ± 3 °C for 12, 24, 36, 48 for real motion picture films and 12, 24, 36, 48, 60 days for CTA-based films with or without a selected treatment.

In this way, it is possible to evaluate the evolution of the deacetylation process in sealed jars in the presence of the different inhibitors or not, obtaining rigorous information on their efficacy.

6.1.2.2 Treatments and their applications

Based on the results reported in Chapter V, we decided to make a first, preliminary attempt by evaluating the efficacy of $\text{Ca}(\text{OH})_2$ nanoparticles in the inhibition of the “*vinegar syndrome*” on both pure cellulose triacetate films properly prepared in the lab and on real motion picture films where the deacetylation process was artificially induced through the procedures ATM2.3 and ATM2.9, respectively. In these first tests, dispersions of nanoparticles in ethanol at different concentrations (1, 0.5 and 0.1 g/L) were applied directly onto the surface of these supports by spray. Unfortunately, even if their effect as inhibitors for the development, the propagation and the kinetic of the “*vinegar syndrome*” was positive, as indicated by the trend of the parameters investigated through the multi-analytical approach proposed in Chapter II (weight loss, free acidity, correct acetyl content via HSM, FTIR-ATR ratio, TGA and tensile tests), two important limitations emerged. The first one is the strong alteration of the optical properties of the treated supports, as indicated by the decrease of the transmittance of the visible light. The second one, on real motion picture film, is the potential degradation of the emulsion layer due to the high pH of the $\text{Ca}(\text{OH})_2$. It is worth pointing out that the evaluation of the alteration of the optical properties was conducted only on the support, not on the emulsion layer, because the gelatine is sensibly altered by the high moisture condition of the third phase of the degradation protocol (100% RH) independently from the application of the treatment and the development of the deacetylation process. At this stage of the work, the attention was focused on the effect of the CA-based support.

Then, in order to overcome these problems, some further tests were also carried out by using the same molar amount of both $\text{Ca}(\text{OH})_2$ and ZnO nanoparticles that were

placed into an open vial in the same sealed jar as the motion picture film samples, but not in direct contact with them. In this case, their efficacy strongly decreased as confirmed by the trend of the free acidity values that only slightly decreased during the degradation protocol and by the acetyl content and the ATR-FTIR ratio, which decreased with a rate quite equal to the one of the untreated samples. This behavior was mainly attributed to the aggregation of the nanoparticles and the consequent decrease of the available surface area for the interaction with the acetic acid produced.

On these bases, we decided to test the efficacy of the following systems:

- 1) $\text{Ca}(\text{OH})_2$, $\text{Mg}(\text{OH})_2$, ZnO nanoparticles uploaded on WP and not in direct contact with the samples (labels: $\text{WPCa}(\text{OH})_2$, $\text{WPMg}(\text{OH})_2$, WPZnO);
- 2) pure SPEI and PVF not in direct contact with the sample (labels: SPEI and PVF);
- 3) PVF and SPEI sponges uploaded with ZnO nanoparticles not in direct contact with the samples (labels: $\text{SPEI}+\text{ZnO}$, $\text{PVF}+\text{ZnO}$).

Synthesis and characterization of the above-mentioned systems are reported in Chapter IV for PVF (Paragraph 4.2.4.2) and SPEI (Paragraph 4.3.2) and Chapter V for pure nanoparticles (Paragraph 5.3.1) and nanoparticles uploaded in WP (Paragraph 5.2.3) and sponge-like systems (Paragraph 5.2.2).

1) A sheet of Whatman® paper (WP) soaked with 5 g/L dispersion in ethanol of $\text{Ca}(\text{OH})_2$, $\text{Mg}(\text{OH})_2$ and ZnO nanoparticles (Paragraph 5.2.3, total weight of the $\text{WP}+\text{nps}$ in the jar: ~0.5g, with a concentration of nanoparticles of 1.1, 0.9 and $1.05 \pm 0.3 \text{ mg}\cdot\text{cm}^{-2}$, respectively) were hung in between the motion picture films inside the jar, spaced out with glass marbles, to avoid direct contact with them. The distance between the film and the WP was about 2 mm (the thickness of the glass marble). The total amount of nanoparticles inside the jar is about 50 mg (Fig. 2A).

2-3) For the sponge-like systems (PVF, SPEI, SPEI+ZnO and PVF+ZnO) the sponge (a cylinder with a 2 cm diameter, 0.5 cm thickness and about 0.3 g) was put at the bottom of the chamber, at about 0.5 cm from the films, not in direct contact with them (Fig. 2B-C).

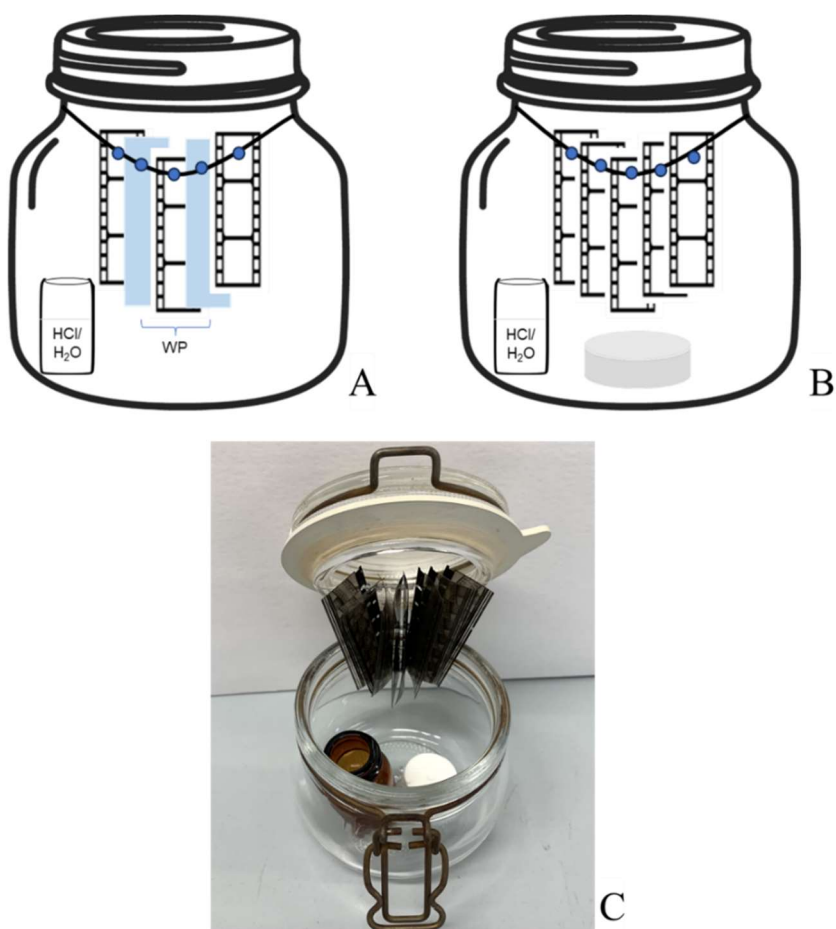


Fig. 2. Applications of different treatments on CTA-based films and real motion picture films and assets of the corresponding degradation tests: (A) use of fragments of Whatman Paper (WP) soaked with a dispersion 5 g/L in ethanol of nanoparticles (in light blue) and hung between the films spaced out with glass marbles (thickness: 2 mm); (B-C) sponge-like systems put at the bottom of the jar (distance from the bottom of motion picture films: 0.5 cm).

All the samples analyzed and discussed in this chapter are resumed in Tab. 1.

Tab. 1 Resume of all the samples used to evaluate the effect of our treatment to inhibit the artificially induced deacetylation process (see paragraph 6.1.2.1).

Sample	Material	Duration of the first degradation step (days)	Duration of the second degradation step (days)	Duration of the third degradation step (days)	Treatment
P9 HCl5M	RMPF**	9	1	/	/
P12 ATM2.9 NT	RMPF	9	1	12	/
P24 ATM2.9 NT	RMPF	9	1	24	/
P36 ATM2.9 NT	RMPF	9	1	36	/
P48 ATM2.9 NT	RMPF	9	1	48	/
P12 ATM2.9 WPCa(OH) ₂	RMPF	9	1	12	WP uploaded with Ca(OH) ₂ nps (total weight: 0.5 g)
P24 ATM2.9 WPCa(OH) ₂	RMPF	9	1	24	
P36 ATM2.9 WPCa(OH) ₂	RMPF	9	1	36	
P48 ATM2.9 WPCa(OH) ₂	RMPF	9	1	48	
P12 ATM2.9 WMg(OH) ₂	RMPF	9	1	12	WP uploaded with Mg(OH) ₂ nps (total weight: 0.5 g)
P24 ATM2.9 WPMg(OH) ₂	RMPF	9	1	24	
P36 ATM2.9 WPMg(OH) ₂	RMPF	9	1	36	
P48 ATM2.9 WPMg(OH) ₂	RMPF	9	1	48	
P12 ATM2.9 WPZnO	RMPF	9	1	12	WP uploaded with ZnO nps (total weight: 0.5 g)
P24 ATM2.9 WPZnO	RMPF	9	1	24	
P36 ATM2.9 WPZnO	RMPF	9	1	36	
P48 ATM2.9 WPZnO	RMPF	9	1	48	
P12 ATM2.9 SPEI	RMPF	9	1	12	SPEI 4 sponge at the bottom of the jar (0.3 g)
P24 ATM2.9 SPEI	RMPF	9	1	24	
P36 ATM2.9 SPEI	RMPF	9	1	36	
P48 ATM2.9 SPEI	RMPF	9	1	48	
P12 ATM2.9 PVF	RMPF	9	1	12	PVF sponge at the bottom of the jar (0.3 g)
P24 ATM2.9 PVF	RMPF	9	1	24	
P36 ATM2.9 PVF	RMPF	9	1	36	
P48 ATM2.9 PVF	RMPF	9	1	48	
P12 ATM2.9 SPEI+nps	RMPF	9	1	12	SPEI 4 sponge uploaded with ZnO nps at the bottom of the jar (0.3 g)
P24 ATM2.9 SPEI+nps	RMPF	9	1	24	
P36 ATM2.9 SPEI+nps	RMPF	9	1	36	
P48 ATM2.9 SPEI+nps	RMPF	9	1	48	
P12 ATM2.9 PVF+nps	RMPF	9	1	12	PVF sponge uploaded with ZnO nps at the bottom of the jar (0.3 g)
P24 ATM2.9 PVF+nps	RMPF	9	1	24	
P36 ATM2.9 PVF+nps	RMPF	9	1	36	
P48 ATM2.9 PVF+nps	RMPF	9	1	48	

**Real motion picture films (RMPF) from the reel "Vita di una Pianta".

6.1.3 The inhibition of the naturally induced deacetylation process

As a final step, we decided to perform a very preliminary test to evaluate the efficacy of the SPEI 4 sponge in the inhibition of the vinegar syndrome in a naturally degraded motion picture film. For this purpose, we used a film already affected by the syndrome and kindly gifted by the restoration laboratory "L'Immagine Ritrovata" srl in Bologna, Italy.

The film was cut into two fragments of 10x3.5 cm and put inside two sealed metal-foil bags (15x20x0.22 cm) internally coated with a layer of polyethylene. A SPEI 4 sponge of the same dimension as the films was placed between the two fragments, in contact with the support sides, as shown in Fig. 3 (PBO_SPEI_7M, Tab. 2).

In parallel, the same amount of film was put inside a bag without the treatment (PBO_NT_7M, Tab. 2). The samples were stored for 7 months (210 days) at room temperature and humidity (25 ± 3 °C and 50 ± 2 %) inside the bags in order to promote the deacetylation process and the consequent vinegar syndrome by the increase of acetic acid concentration in a closed and small environment. Treated and untreated samples were compared at the end of the period to evaluate the eventual effect of the inhibitor.

Samples are resumed in Tab. 2 where the sample PBO_0 is made by a motion picture film that was analyzed as received and not subjected to the test described in Fig. 3.

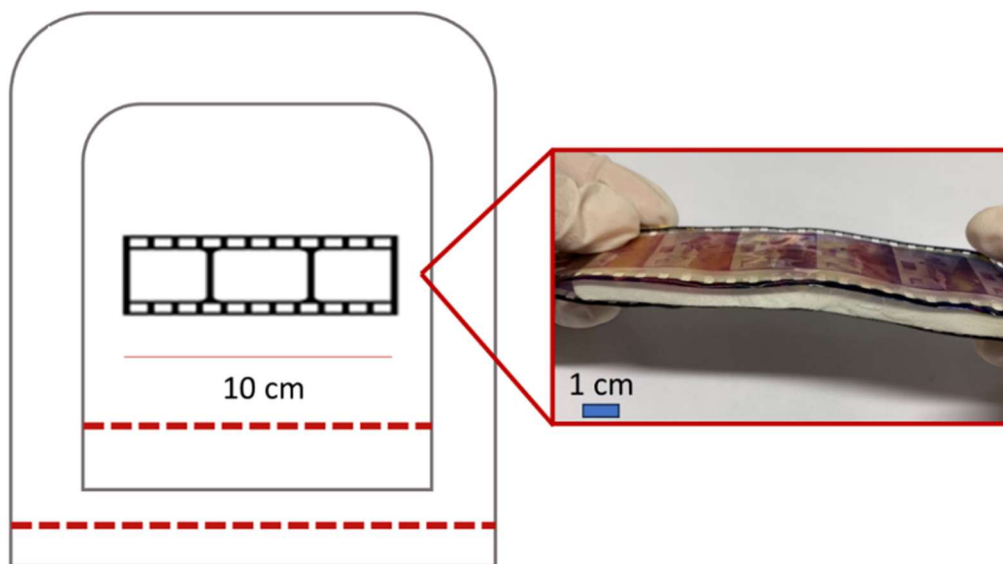


Fig. 3 Asset of the test to evaluate the efficacy of SPEI 4 on the inhibition of the deacetylation process on samples naturally affected by the vinegar syndrome.

Tab. 2 Resume of the samples used to evaluate the efficacy of SPEI 4 in the inhibition of the deacetylation process on samples naturally affected by the vinegar syndrome.

Sample	Material	Duration of the test (months)	Treatment
PBO_0	RMPF*	/	/

PBO_NT_7M	RMPF	7	/
PBO_SPEI_7M	RMPF	7	SPEI 4 in contact with the film

*Real motion picture films came from fragments kindly gifted by the “Cineteca di Bologna”.

6.1.4 The multi-analytical method to monitor the degradation process

To monitor the evolution of the degradation protocol on both treated and untreated samples the multi-analytical protocol proposed in Paragraph 3.1.3 was used.

In particular, the following analyses were performed.

Gravimetry test.

Free acidity.

Combined acetyl or acetic acid content calculation through Heterogeneous Saponification Method (HSM).

Acetyl content with FTIR-ATR Spectroscopy.

Thermogravimetric Analysis (TGA).

Tensile test.

Optical microscopy.

The last two tests were conducted only on the samples (both treated and untreated) degraded for 48 days.

For all the experiments the data reported for the gravimetry test, acetyl content and free acidity correspond to the average values obtained from the analyses carried out on three replicas of the same sample. For tensile tests, five replicas were considered. For the FTIR-ATR ratio, the data correspond to the average of the ratios obtained from five spectra collected from different areas of each sample. The errors correspond to the standard deviation.

6.2 Results and discussion

6.2.1 Ca(OH)₂, Mg(OH)₂ and ZnO nanoparticles uploaded on Whatman® Paper

In this test, we uploaded different kinds of nanoparticles (Ca(OH)₂, Mg(OH)₂ and ZnO) on WP. WP and film fragments were alternatively hung to a Teflon wire inside the hermetic chamber spaced out with small glass marbles. So the distance between a fragment of film and the WP sheet was equal to the thickness of a single marble (about 2 mm).

The samples were analyzed at different times during the third degradation step. The samples were degraded through the protocol ATM2.9 (see paragraph 3.1.2.2) and labeled as follows: PX_ATM2.9_NT (samples degraded through the protocol ATM2.9 in the absence of any inhibitor), PX_ATM2.9_ZnO (samples degraded through the protocol ATM2.9 in the presence of Whatman® paper loaded with ZnO nanoparticles), PX_ATM2.9_Ca(OH)₂ (samples degraded through the protocol ATM2.9 in the presence of Whatman® paper loaded with Ca(OH)₂ nanoparticles) and PX_ATM2.9_Mg(OH)₂ (samples degraded through the protocol ATM2.9 in the presence of Whatman® paper loaded with Mg(OH)₂ nanoparticles), where “X” indicates the duration of the third degradation step in days. ATM2.9 indicates the degradation protocol that was applied.

Gravimetry test. The gravimetry tests (Fig. 4A) indicate a slowdown in the weight decrease for all the samples degraded through the protocol ATM2.9 in the presence of Whatman® paper loaded with the three kinds of nanoparticles. In particular, Ca(OH)₂ nanoparticles seem to give the best performance as indicated by the stabilization of the weight of the motion picture film fragments that, for WPCa(OH)₂ samples, was registered after the 24th day (P24_ATM2.9_WPCa(OH)₂; weight decrease equal to $-4.1 \pm 0.2\%$). For the Whatman® paper loaded with the ZnO and Mg(OH)₂ nanoparticles, instead, the weight stabilization occurs only after the 36th day of the degradation protocol and a higher weight loss is observed (see samples

P36_ATM2.9_WPMg(OH)₂ and P36_ATM2.9_WPZnO with a weight loss of -7.4±0.4% and -7.1±0.35% respectively).

Free acidity. The trend of the free acidity reported in Fig. 4B shows very promising results: a decrease and a stabilization of this parameter were detected for samples degraded in the presence of Whatman® paper doped with all the nanoparticles and, already after 12 days, the free acidity decreases from 0.6±0.1% up to ca 0.2±0.1% (in detail its value is 0.16±0.01% for P12_ATM2.9_WPCa(OH)₂, 0.2±0.1% for P12_ATM2.9_WPMg(OH)₂ and 0.25±0.1% for P12_ATM2.9_WPZnO). This trend can be attributed both to the partial absorption of the free acetic acid produced by the support of the motion picture films by nanoparticles, and, as a consequence, to the partial inhibition of its autocatalytic effect which causes the decrease of further emission of acetic acid.

After the 12th day, the free acidity values for all the treated samples degraded in the presence of inhibitors, range between 0.3% and 0.1%, while, for NT samples, this parameter rises to ca. 1.8%, with an increase of almost 145% compared to the initial value.

Acetyl content via HSM. Also the trend of the acetyl content is strongly influenced by the presence of the Whatman® paper doped with all the nanoparticles that induce a stabilization of the acetyl content after 24 days of the degradation protocol at about 37% (Fig. 4C) (in detail, for samples P24_ATM2.9_WPCa(OH)₂, P24_ATM2.9_WPMg(OH)₂ and P24_ATM2.9_WPZnO the free acidity values are respectively 37.5±0.6%, 36.9±0.3% and 37.1±0.3%). Concerning the substitution degree, the acetyl content data indicate that all the samples degraded in the presence of the Whatman® paper loaded with all the nanoparticles maintain a degree of substitution close to 2 after the test; on the contrary, for the NT ones, after 48 days of degradation, the substitution degree decreases reaching a value typical of monoacetate (Tab. 4, Paragraph. 3.1.3).

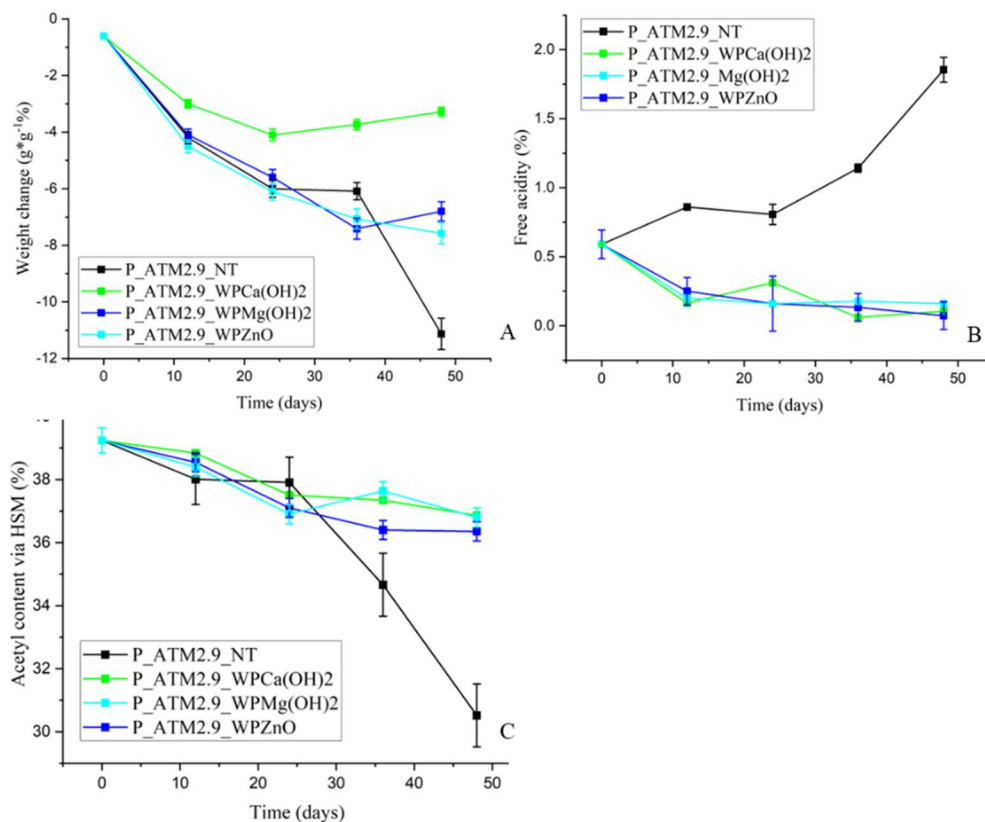


Fig. 4 (A) Weight loss (%), (B) free acidity (%), (C) correct acetyl content calculated via HSM (%) measured for untreated (P_ATM2.9_NT, black) and treated real motion picture films (P_ATM2.9_WPCa(OH)₂, green; P_ATM2.9_WPMg(OH)₂, cyan; P_ATM2.9_WPZnO, blue).

FTIR-ATR Spectroscopy. For all the motion picture films degraded in the presence of the different nanoparticles on WP sheets, the ATR-FTIR spectra (Fig. 5A-B) indicate that the decrease of the intensities of the peaks associated with the acetyl group (peaks at 1220, 1330 and 1730 cm⁻¹) is very low for samples P48_ATM2.9_WPMg(OH)₂ and P48_ATM2.9_WPZnO or zero for sample P48_ATM2.9_WPCa(OH)₂. Even for the intensity of the peak associated with the OH group, only a low increase is observed for all the treated samples after 48 days of the degradation protocol, probably due to the absorption of moisture. The trend of the ratio of the intensities of IR peaks at 1220 cm⁻¹ and at 1030 cm⁻¹ reported in Fig. 5C indicates that up to 24 days of degradation, the value of this

parameter is almost invariant (and equal to ca. 0.9). But in the following period, up to 48 days, for the NT sample, this ratio decreases up to ca. 0.4 while no significant variations are detected for all the samples degraded in the presence of the WP sheets containing the nanoparticles (the values are the following: P48_ATM2.9_WPCa(OH)₂: 0.86±0.02; P. P48_ATM2.9_WPMg(OH)₂: 0.89±0.01; P48_ATM2.9_WPZnO: 0.86±0.03).

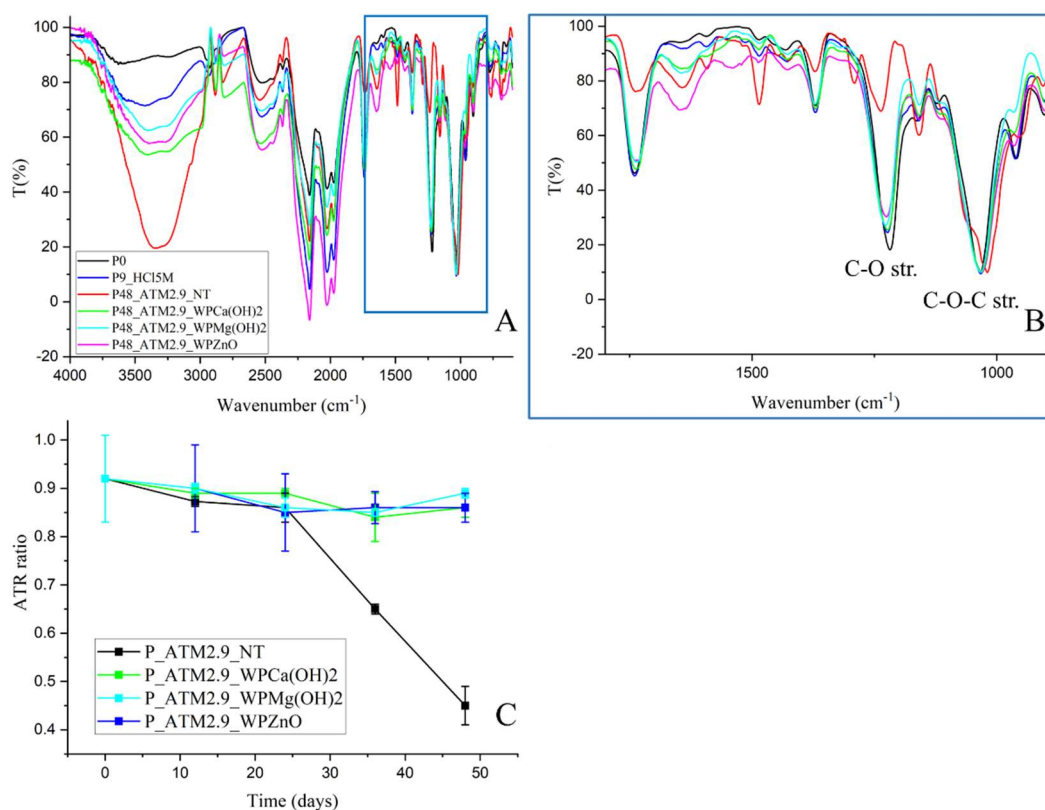


Fig. 5 FTIR-ATR spectra of P0 (black) and P9_HCl5M (blue) and P48_ATM2.9_NT (red) and P48_ATM2.9_WPCa(OH)₂ (green), WPMg(OH)₂ (cyan), WPZnO (pink) in the range 4000-600 cm⁻¹ (A) and 1800-900 cm⁻¹ (B); (C) FTIR-ATR ratio I₁₂₂₀/I₁₀₃₀ for untreated (P_ATM2.9_NT, black) and treated (P_ATM2.9_WPCa(OH)₂ green, WPMg(OH)₂ cyan, WPZnO blue).

All the results of the weight change, the free acidity, the acetyl content and the ATR-FTIR ratio of the samples treated with WP uploaded with nanoparticles are resumed in Tab. 3.

Tab. 3 Resume of the results associated with real motion picture films treated with WPCa(OH)_2 , WPMg(OH)_2 and WPZnO not in contact with the samples. Films were subjected to the ATM2.9 degradation protocol. Results of corresponding untreated samples are reported in Tab. 13, Paragraph 3.2.2.2.

Sample	Weight Loss (%)	Free acidity (%)	Correct Acetyl Content (%)	ATR-FTIR Ratio I_{1220}/I_{1030}
P0	0	0.02±0.1	41.7±0.7	0.91±0.04
P9_HCl5M	-0.60±0.03	0.6±0.09	39.2±0.4	0.92±0.08
P12_ATM2.9_WPCa(OH) ₂	-3.1±0.15	0.16±0.01	38.8±0.4	0.89±0.01
P24_ATM2.9_WPCa(OH) ₂	-4.1±0.2	0.31±0.09	37.5±0.6	0.89±0.01
P36_ATM2.9_WPCa(OH) ₂	-3.7±0.2	0.06±0.03	37.34±0.03	0.84±0.05
P48_ATM2.9_WPCa(OH) ₂	-3.3±0.2	0.10±0.03	36.86±0.09	0.86±0.02
P12_ATM2.9_WPMg(OH) ₂	-4.1±0.2	0.2±0.1	38.4±0.4	0.90±0.01
P24_ATM2.9_WPMg(OH) ₂	-5.6±0.3	0.2±0.2	36.9±0.3	0.86±0.02
P36_ATM2.9_WPMg(OH) ₂	-7.4±0.4	0.2±0.1	37.6±0.3	0.85±0.01
P48_ATM2.9_WPMg(OH) ₂	-6.8±0.3	0.2±0.1	36.7±0.3	0.89±0.01
P12_ATM2.9_WPZnO	-4.5±0.2	0.25±0.1	38.5±0.3	0.90±0.09
P24_ATM2.9_WPZnO	-6.1±0.3	0.2±0.2	37.1±0.3	0.85±0.08
P36_ATM2.9_WPZnO	-7.1±0.3	0.1±0.1	36.4±0.3	0.86±0.03
P48_ATM2.9_WPZnO	-7.6±0.4	0.1±0.1	36.3±0.3	0.86±0.03

Thermogravimetric analysis. In Fig. 6, the TGA and DTG profiles of the P0, P9_HCl5M, P48_ATM2.9_NT and the P48_ATM2.9_WPCa(OH)₂ are reported. There are no significant differences compared to the profile of the DTG curve of the sample P9_HCl5M (that, as indicated in paragraphs 3.1.2.2 and in Tab. 2, corresponds to the time 0 of the third degradation step) indicating that probably the depolymerization process of the support has been inhibited by the presence of the Ca(OH)₂ nanoparticles onto the WP sheet. On the contrary, for the P48_ATM2.9_NT sample, the profile of the DTG curve indicates a shift of the pyrolysis temperature (from ca. 365 °C for P9_HCl5M to 350 °C) toward lower values and the presence of a peak at ca 280 °C. This effect can be attributed to the partial depolymerization of the CTA support induced by the hydrolytic action of the acetic acid.

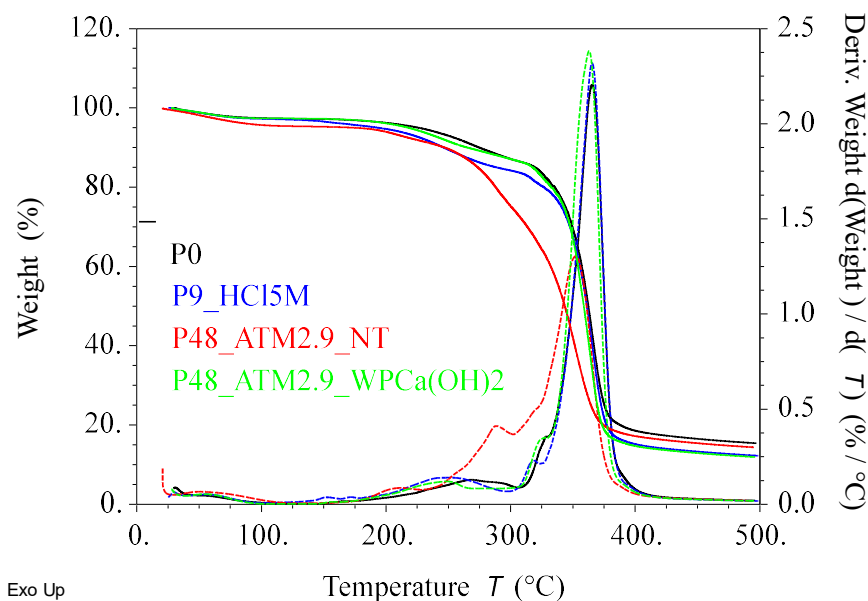


Fig. 6 TGA and DTG profiles for P0 (black), P9_HCl5M (blue) and P48_ATM2.9_NT (red) and P48_ATM2.9_WPCa(OH)₂ (green).

Tensile tests. On the other hand, the Young's Modulus measured for the same sample (P48_ATM2.9_WPCa(OH)₂) is equal to 11±2 MPa and, even if a small decrease was observed compared to the P9_HCl5M sample (14±1MPa). However, by comparing this value to the one for the P48_ATM2.9_NT (7.3±0.2 MPa), the sample degraded in the presence of Ca(OH)₂ nanoparticles shows a higher tensile strength. This indicates a higher mechanical resistance of the P48_ATM2.9_WPCa(OH)₂ sample due to a higher degree of polymerization. These results are in agreement with the TGA data.

In conclusion, the application of Ca(OH)₂, Mg(OH)₂ and ZnO nanoparticles on a WP support and their collocation into the same container of the film, but not in direct contact with it, seems to offer promising results. Probably the application of the treatments on WP improves the interaction between the acetic acid produced by the films affected by the induced “vinegar syndrome” and the nanoparticles. In addition, it is possible to suppose that the proximity of the treatment to the film also favors its

action. By using WP as support for the nanoparticles, the risk of altering the optical properties of the film is minimized if compared to applying directly the nanoparticles on the surface of the film. In addition, WP probably absorbs part of the moisture during the third step of the degradation process and consequently favors the slowdown of the deacetylation reaction. Further tests will be needed to evaluate in deep the effect of this procedure on the emulsion layer.

Comparing the three examined kinds of nanoparticles, no significant differences in terms of efficacy were detected as a function of their chemical nature.

6.2.2 SPEI and PVF

In this Paragraph, the efficacy of the two sponge-like systems PVF and SPEI (see paragraphs 4.2 and 4.3 respectively), for the inhibition of the deacetylation process that affects the CTA-based motion picture films will be also evaluated and the obtained results be compared.

As indicated in paragraph 4.3, while SPEI can neutralize the acetic acid due to the presence of amino groups in its structure, PVF could only weakly bond acetic acid inside its network, as we saw in Paragraph 4.2.6. Both systems were put at the bottom of the jar, not in direct contact with the samples, at about 0.5 cm from the films hung on top of the chamber.

As in previous experiments, also in this case, the samples were degraded through the protocol ATM2.9 (see paragraph 3.1.2.2) and labeled as follows: PX_ATM2.9_NT (samples degraded through the protocol ATM2.9 in the absence of any inhibitor), PX_ATM2.9_SPEI (samples degraded through the protocol ATM2.9 in the presence of SPEI systems) and PX_ATM2.9_PVF (samples degraded through the protocol ATM2.9 in the presence of PVF systems). As indicated before, “X” indicates the duration of the third degradation step in days.

Gravimetry test. The results of the gravimetry test reported in Fig. 7A show a trend in the weight of the films that is similar to the one registered for the sample degraded

in the absence of the other inhibitors. Nevertheless, even in the presence of PVF and SPEI, no significant variations in the trend of the weight decrease are observed. In particular, the weight decrease is $-11\pm 1\%$ for P48_ATM2.9_NT and $-8.8\pm 0.4\%$ and $-9.9\pm 0.5\%$ for P48_ATM2.9_SPEI and P48_ATM2.9_PVF, respectively.

Free acidity. On the other hand, free acidity results (Fig. 7B) are very promising for SPEI: a strong decrease (almost 40%) due to the alkaline character of the SPEI is observed in the first 12 days (this parameter decreases from 0.6 ± 0.1 for the sample P9_HCl5M up to 0.29 ± 0.07 for P12_ATM2.9_SPEI). Then, in the following 36 days, the rate of the process decreases (as indicated by the lower slope of the curve) and the value registered for the P48_ATM2.9_SPEI sample is $0.16\pm 0.04\%$. On the other hand, for samples degraded in the presence of PVF, higher free acidity values are detected for the entire duration of the degradation protocol, of ca. 0.8%, even if a sort of stabilization is observed around this value. An opposite trend is observed for all the samples degraded in the absence of inhibitors: in this case the free acidity value increases by almost 200% (from ca $0.6\pm 0.07\%$ for the sample P9_HCl5M up to $1.85\pm 0.09\%$ for the sample P48_ATM2.9_NT).

Acetyl content via HSM. A similar trend is observed also for the acetyl content (Fig. 7C) whose value remains almost equal to 39% for the entire duration of the third step of the degradation process for the samples degraded in the presence of SPEI systems. On the contrary after 36 days for the samples degraded in the presence of PVF and after 24 days for the samples degraded in the absence of inhibitors, a strong decrease in the acetyl content (almost 20%) is observed (from $39.2\pm 0.4\%$ of the P9_HCl5M sample up to the $31.5\pm 0.3\%$ of the P48_ATM2.9_PVF sample and to the $30.5\pm 0.4\%$ of the P48_ATM2.9_NT sample). While for the samples degraded in the absence of inhibitors and in the presence of PVF the acetyl content of the film decreased from a value that is typical of CDA to a value that corresponds to CMA, samples degraded in the presence of SPEI remained close to 2 (CDA).

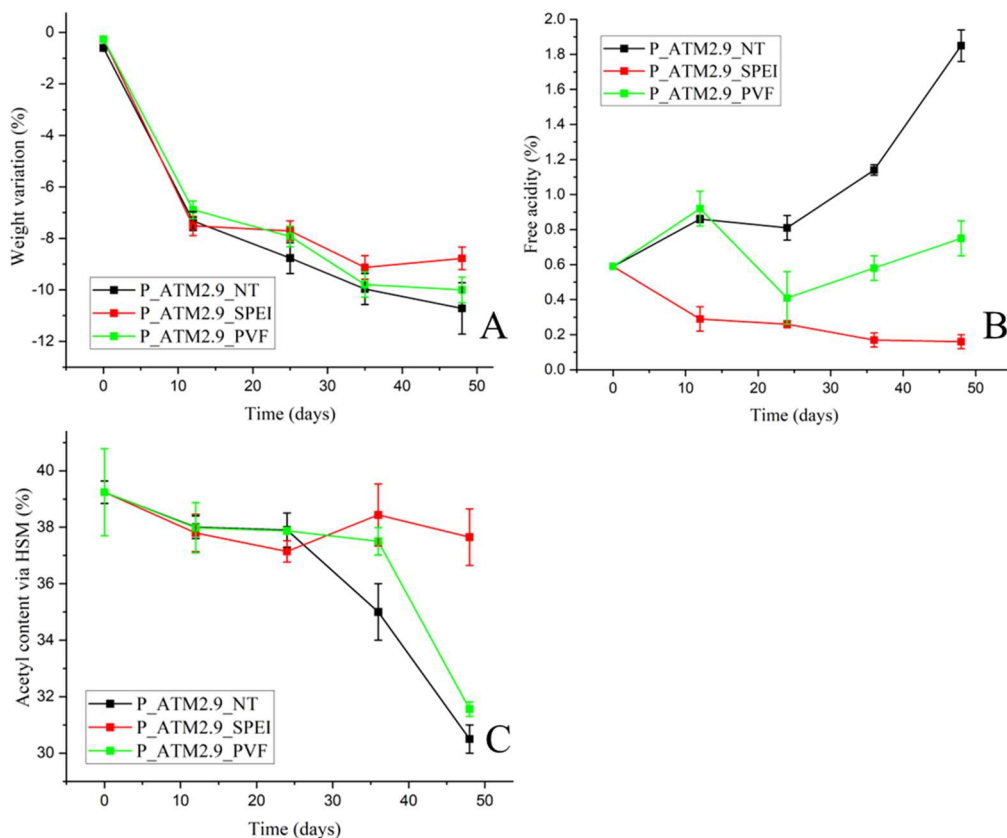


Fig. 7 (A) Weight loss (%), (B) free acidity (%), (C) correct acetyl content calculated via HSM (%) measured for untreated (P_ATM2.9_NT, black) and treated real motion picture films (P_ATM2.9_SPEI, red; P_ATM2.9_PVF, green)

FTIR-ATR Spectroscopy. Also the FTIR-ATR spectroscopy confirms the good performance of the SPEI systems. Indeed, the spectra reported in Fig. 8A-B show that the peaks associated with the acetyl group (at 1220, 1330 and 1730 cm^{-1}) in samples degraded in the presence of SPEI sponges show a little decrease in intensity if compared with the sample P9_HCl5M but not as pronounced as in the samples degraded in the presence of PVF and NT samples. Concerning the peak ascribed to the OH group, the trend for films degraded in the presence of SPEI is similar to the one observed for the other treatments (the increase of its intensity is always ascribable to the absorption of moisture, probably by the highly hydrophilic emulsion

layer). On the contrary, for films degraded in the presence of PVF, the trend is more similar to the NT samples.

Concerning the ratio between the intensities of the peaks at 1220 and 1030 cm^{-1} , for the samples degraded in the presence of SPEI, a low decrease is observed after the 12th day (from 0.9 ± 0.05 for P9_HCl5M up to 0.80 ± 0.04 for P12_ATM2.9_SPEI) with a subsequent stabilization from the 12th to the 48th day of the degradation process (the I_{1220}/I_{1030} ratio is 0.78 ± 0.02 for P48_ATM2.9_SPEI). On the contrary, for samples degraded in the presence of PVF, a strong decrease of this parameter is observed already after the 12th day, as indicated by the increase of the slope of the curve in Fig. 8C (the I_{1220}/I_{1030} ratio is 0.60 ± 0.03 for P48_ATM2.9_PVF). Also for films degraded in the absence of treatment, after the 24th day, the trend of this parameter confirms the strong increase in the rate of the degradation process (the I_{1220}/I_{1030} ratio is 0.45 ± 0.04 for P48_ATM2.9_NT).

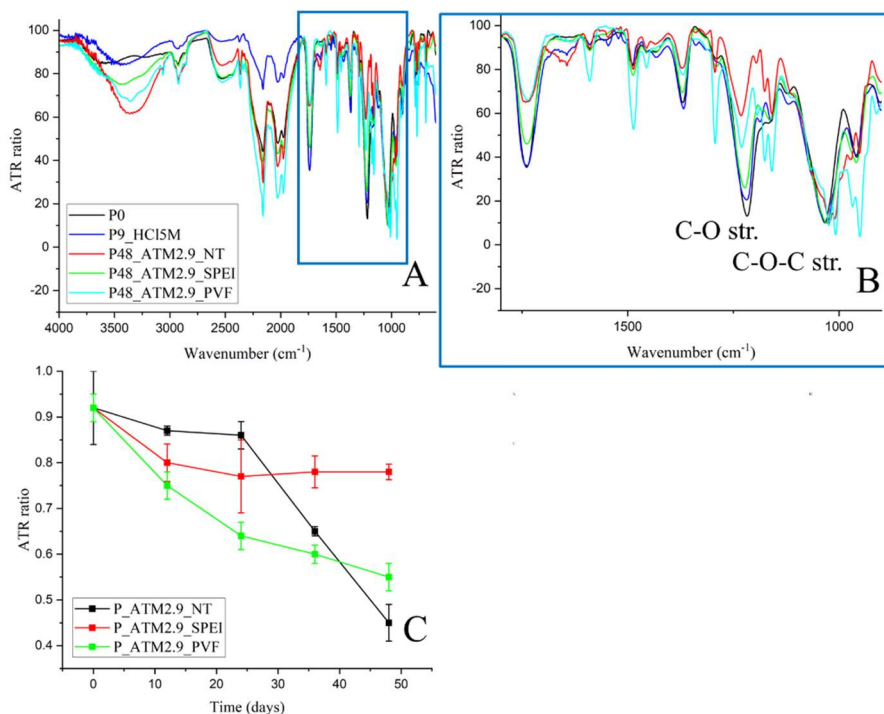


Fig. 8 FTIR-ATR spectra of P0 (black) and P9_HCl5M (blue) and P48_ATM2.9_NT (red) and P48_ATM2.9_SPEI (green), PVF (cyan) in the range 4000-600 (A) and 1800-900 (B); (C) FTIR-ATR ratio I_{1220}/I_{1030} for untreated (P_ATM2.9_NT, black) and treated (SPEI red, PVF green).

In Tab. 4 the results associated with real motion picture films treated with SPEI and PVF are resumed.

Tab. 4 Resume of the results associated with real motion picture films treated with SPEI and PVF not in contact with the samples. Films were subjected to the ATM2.9 degradation protocol. Results of corresponding untreated samples are reported in Tab. 13, Paragraph 3.2.2.2.

Sample	Weight Loss (%)	Free acidity (%)	Correct Acetyl Content (%)	ATR-FTIR Ratio I_{1220}/I_{1030}
P0	0	0.02±0.1	41.7±0.7	0.91±0.04
P9_HC15M	-0.60±0.03	0.6±0.09	39.2±0.4	0.92±0.08
P12_ATM2.9_SPEI	-7.3±0.4	0.29±0.07	37.8±0.7	0.80±0.04
P24_ATM2.9_SPEI	-8.8±0.6	0.26±0.02	37.1±0.4	0.77±0.08
P36_ATM2.9_SPEI	-10.0±0.6	0.17±0.04	38±1	0.78±0.04
P48_ATM2.9_SPEI	-11±1	0.16±0.04	38±1	0.78±0.02
P12_ATM2.9_PVF	-6.9±0.3	0.9±0.1	37.9±0.9	0.92±0.03
P24_ATM2.9_PVF	-7.9±0.4	0.75±0.1	37.87±0.1	0.75±0.03
P36_ATM2.9_PVF	-9.8±0.5	0.8±0.1	37.30±0.5	0.64±0.02
P48_ATM2.9_PVF	-9.9±0.5	0.8±0.1	31.5±0.3	0.60±0.03

Thermogravimetric analysis. In Fig. 9 the TGA and DTG profiles of the samples P0, P9_HC15M (the sample that corresponds to the starting point of the third degradation step, see paragraphs 3.1.2.2 and Tab.2), P48_ATM2.9_NT, P48_ATM2.9_SPEI and P48_ATM2.9_PVF are reported. From Fig. 9 is evident that there are no significant differences between the profiles of the DTG curves of the samples P0, P9_HC15M (the starting sample of the third degradation step) and P48_ATM2.9_SPEI. In the meanwhile, for the sample degraded in the presence of PVF (P48_ATM2.9_PVF) and in the absence of inhibitors (P48_ATM2.9_NT), the profile of the DTG curve indicates a shift of the pyrolysis temperature (from ca 365 °C for P9_HC15M to 360 °C and 340 °C for P48_ATM2.9_PVF and P48_ATM2.9_NT, respectively) and the presence of a shoulder at ca. 315 °C for P48_ATM2.9_PVF and of a second peak at ca. 280 °C for P48_ATM2.9_NT. This is a further confirmation that the presence of SPEI, unlike PVF, inhibits the depolymerization process of the support induced by the hydrolytic action of the acetic acid.

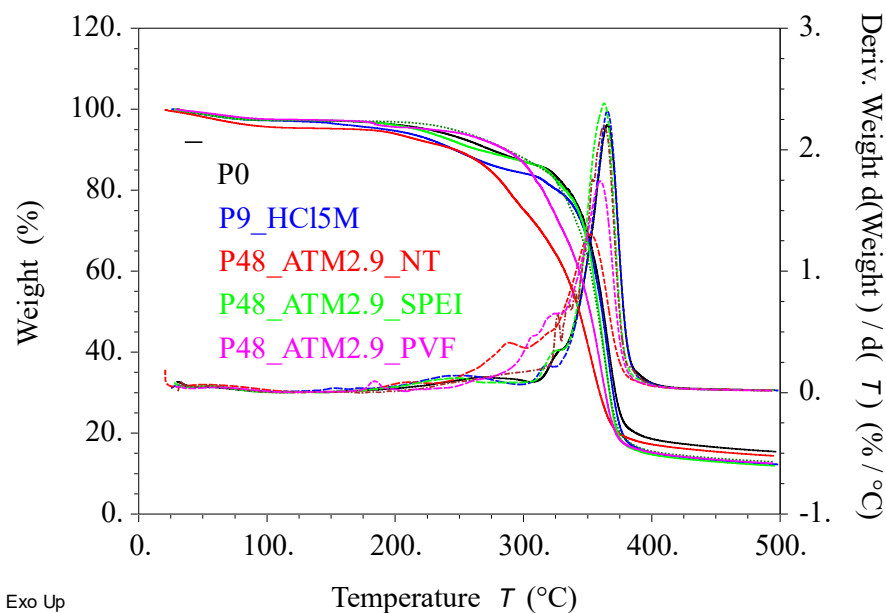


Fig. 9 TGA and DTG profiles for P0 (black), P9_HCl5M (blue) and P48_ATM2.9_NT (red), P48_ATM2.9_SPEI (green) and P48_ATM2.9_PVF (pink).

Tensile tests. From tensile tests, the Young's Modulus calculated for the film treated with SPEI (P48_ATM2.9_SPEI: 11 ± 2 MPa) is lower than the one measured for P9_HCl5M (14 ± 1 MPa) but higher than the one determined for the untreated sample (P48_ATM2.9_NT: 7.3 ± 0.2 MPa).

In conclusion, treatment with SPEI seems to offer a very effective option for the inhibition of the deacetylation process on real motion picture films: the stabilization of the free acidity and the acetyl content values is observed already in the first phase of the degradation process (12 days). In addition, this result has been achieved even if the inhibitor (i.e. the SPEI) was not in direct contact with the films, but at a distance of almost 0.5 cm. The simultaneous neutralization of the acetic acid (due to the alkaline character of the polymer) and the absorption of moisture carried out by this system, are synergistic and probably play an important role in determining the efficacy of the SPEI. This is a very important advantage in terms of both the usability of the inhibitor and the preservation of the optical properties of the films. On the

contrary, PVF seems to induce only a minor deceleration of the degradation processes (both deacetylation and depolymerization, as it is possible to see from the variation in the acetyl content, free acidity and TGA profiles). This is probably due to the high hydrophilicity of this system, which can absorb moisture and weakly absorb part of the free acidity. However, this capacity seems to be not enough to significantly inhibit the degradation process.

In any case, more investigations will be needed to further study the role of moisture retention on the performance of the systems and their effect on the optical properties of the emulsion layer.

6.2.3 SPEI and PVF uploaded with ZnO nanoparticles (SPEI+ZnO, PVF+ZnO)

In this last Paragraph, the performance in the inhibition of the deacetylation process of sponge-like systems SPEI and PVF uploaded with ZnO nanoparticles is evaluated. The procedures for the preparation of these mixed systems are reported in Paragraph 5.2.2. This test aims to study the following points:

- for PVF sponges (that form weak interactions with acetic acid, see paragraph 4.2.6), the efficacy of the ZnO nanoparticles uploaded into the system in slowing down the rate of the deacetylation process for CTA-based motion picture films;
- in the case of SPEI, which can interact much more strongly with acetic acid, the goal is to understand if the addition of ZnO nanoparticles inside the structure contributes to improving the performance of the pure sponge (see Paragraph 4.3.4).

Gravimetry test. The gravimetry tests (Fig. 10A) show a stabilization in the weight after the 12th day only for samples of films subjected to the degradation protocol in the presence of PVF+ZnO (P9_HCl5M: $-0.60 \pm 0.03\%$; P12_ATM2.9_PVF+ZnO: -

6.7±0.6%; P48_ATM2.9_PVF+ZnO: -5.0±0.6%). For other samples, both the ones degraded in the presence of SPEI+ZnO and the NT ones, the weight keeps decreasing during the entire duration of the degradation protocol up to -9.4±0.8% and -11±1% for P48_ATM2.9_SPEI+ZnO and P48_ATM2.9_NT respectively.

Free acidity. For samples subjected to the ATM2.9 degradation protocol in the presence of both SPEI+ZnO and PVF+ZnO, a decrease of the free acidity (Fig. 10B) is detected in the first 12 days (P9_HCl5M: 0.60±0.09%; P12_ATM2.9_SPEI+ZnO: 0.4±0.1%; P12_ATM2.9_PVF+ZnO: 0.2±0.1%) with a subsequent stabilization until the end of the test (P48_ATM2.9_SPEI+ZnO: 0.19±0.05%; P48_ATM2.9_PVF+ZnO: 0.2±0.1%). As already discussed in previous experiments (see paragraphs 6.2.1 and 6.2.2) this effect is probably due to the absorption by the inhibitors of a portion of the free acetic acid produced by the support, and to the partial inhibition of the autocatalytic process that slows down the emission of acetic acid. A confirmation of the good performance of the inhibitors is given by the increase in the free acidity detected for NT samples that reaches 1.85±0.09% for P48_ATM2.9_NT.

Acetyl content via HSM. A similar trend is observed also for the correct acetyl content (Fig. 10C): for real motion picture films degraded in the presence of both SPEI+ZnO and PVF+ZnO it remains almost constant for the entire duration of the degradation process (P9_HCl5M: 39.2±0.4%; P48_ATM2.9_SPEI+ZnO: 38±1%; P48_ATM2.9_PVF+ZnO: 38±1%) just as the degree of substitution remains also constant. On the other hand, for NT samples, a decrease in the degree of substitution from ca 2 to ca 1 occurs, according to Tab. 4 of Paragraph 3.1.3 as indicated by the acetyl content measured for P48_ATM2.9_NT, which is 30.5±0.4%.

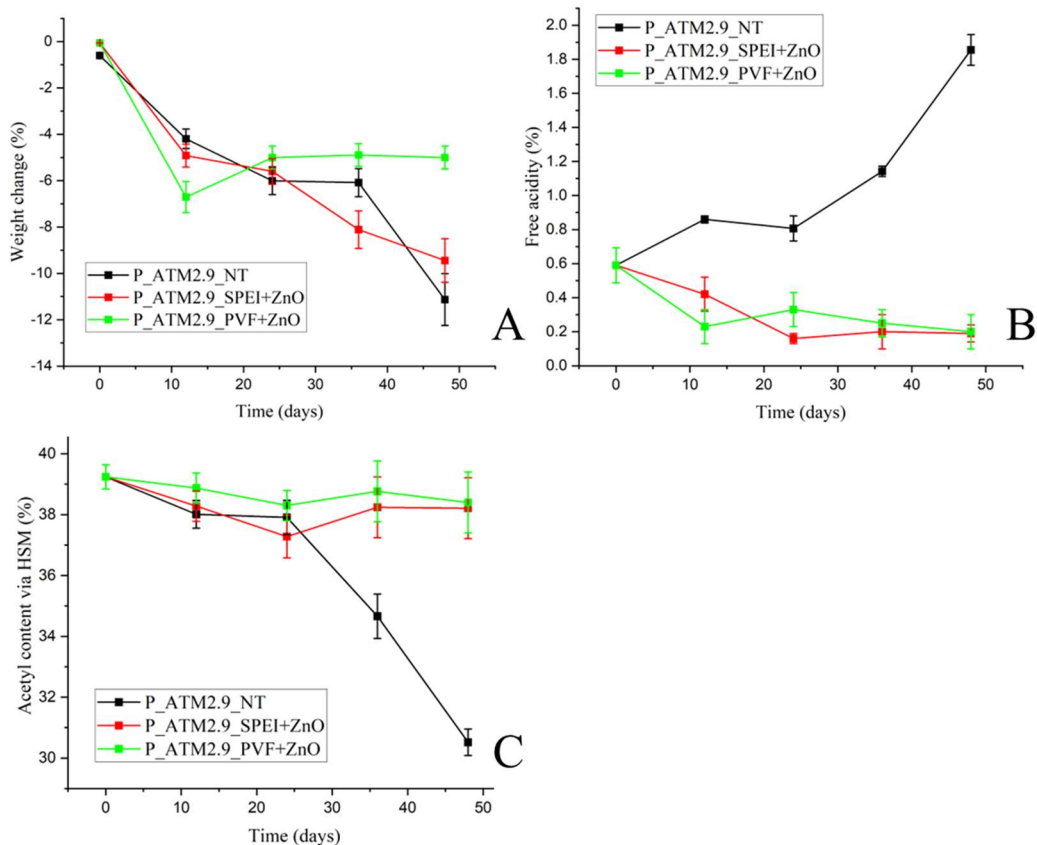


Fig. 10 Weight loss (%), (B) free acidity (%), (C) correct acetyl content calculated via HSM (%) measured for untreated (P_ATM2.9_NT, black) and treated real motion picture films (P_ATM2.9_SPEI+ZnO, red; P_ATM2.9_PVF+ZnO, green).

ATR-FTIR Spectroscopy. Results obtained from previous tests are confirmed through FTIR-ATR spectra (Fig. 11A-B): it is evident that the intensity of the peaks associated with the acetyl group (peaks at 1220, 1330 and 1730 cm^{-1}) in samples degraded in the presence of both SPEI+ZnO and PVF+ZnO sponges decreases if compared with the sample P9_HCl5M but much less than in the NT samples. For the peak ascribed to the OH group, the trend for films treated with SPEI+ZnO and PVF+ZnO is similar to the one observed for the other treatments (the increase of its intensity is always ascribable to the absorption of moisture, probably by the highly hydrophilic emulsion layer).

Examining the ratio between the intensities of the peaks at 1220 and 1030 cm^{-1} (Fig. 11C), for the samples degraded in the presence of both the sponge+nps systems, after 12 days a low decrease is observed (from 0.9 ± 0.05 for P9_HCl5M up to 0.79 ± 0.07 and 0.75 ± 0.03 for P12_ATM2.9_SPEI+ZnO and P12_ATM2.9_PVF+ZnO, respectively) with a subsequent stabilization from the 12th to the 48th day of the degradation process (the I_{1220}/I_{1030} ratio is 0.80 ± 0.02 for P48_ATM2.9_SPEI+ZnO and 0.72 ± 0.04 for P48_ATM2.9_PVF+ZnO). On the contrary, for films degraded in the absence of inhibitors, after the 24th day, the decrease of this parameter up to 0.45 ± 0.04 for P48_ATM2.9_NT confirms the strong increase of the rate of the degradation process.

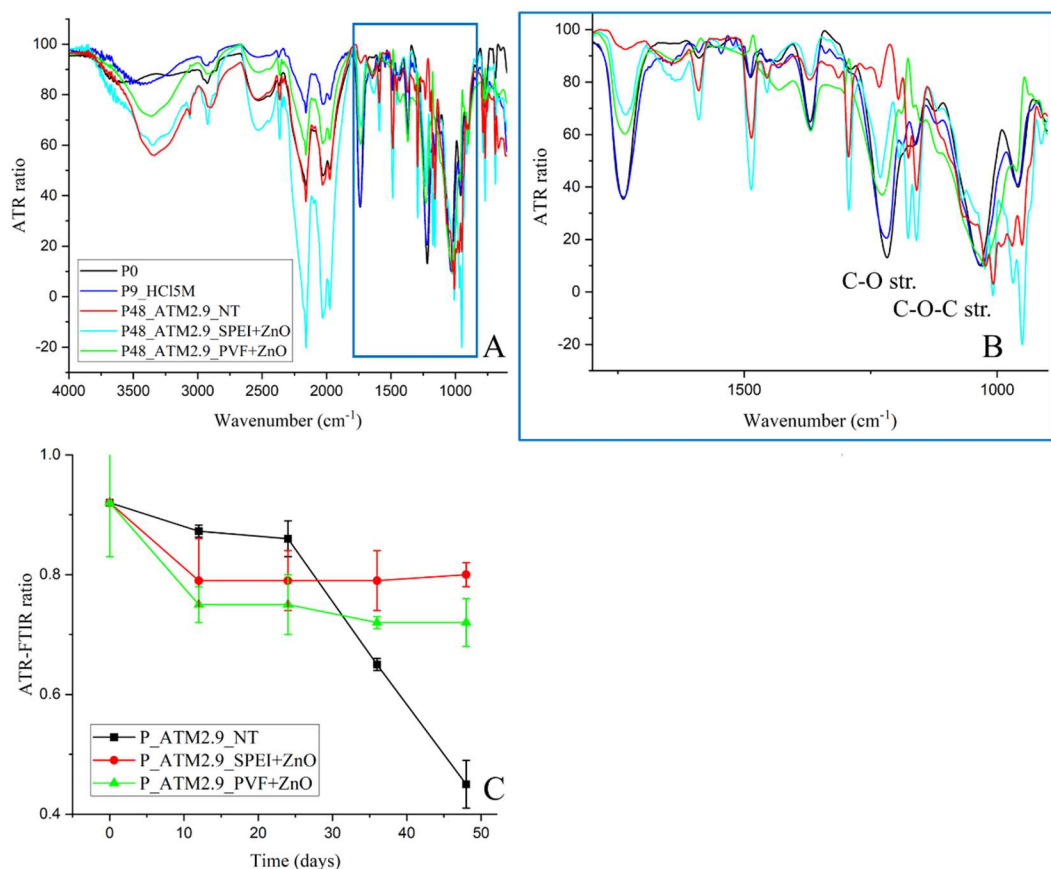


Fig. 11 FTIR-ATR spectra of P0 (black) and P9_HCl5M (blue) and P48_ATM2.9_NT (red) and P48_ATM2.9_SPEI+ZnO (cyan), PVF+ZnO (green) in the range 4000-600 (A) and 1800-900 (B); (C) FTIR-ATR ratio I_{1220}/I_{1030} for untreated (P_ATM2.9_NT, black) and treated (SPEI+ZnO, red, PVF+ZnO, green).

In Tab. 5, the results for films subjected to the ATM2.9 degradation protocol in the presence of SPEI+ZnO and PVF+ZnO are resumed.

Tab. 5 Resume of the results associated with real motion picture films treated with SPEI+ZnO and PVF+ZnO not in contact with the samples. Films were subjected to the ATM2.9 degradation protocol. Results of corresponding untreated samples are reported in Tab. 13, Paragraph 3.2.2.2.

Sample	Weight Loss (%)	Free acidity (%)	Correct Acetyl Content (%)	ATR-FTIR Ratio I_{1220}/I_{1030}
P0	0	0.02±0.1	41.7±0.7	0.91±0.04
P9_HCl5M	-0.60±0.03	0.6±0.09	39.2±0.4	0.92±0.08
P12_ATM2.9_SPEI+ZnO	-4.9±0.5	0.4±0.1	38.3±0.5	0.79±0.07
P24_ATM2.9_SPEI+ZnO	-5.6±0.6	0.16±0.030	37.3±0.7	0.79±0.05
P36_ATM2.9_SPEI+ZnO	-8.1±0.8	0.2±0.1	38 ±1	0.79±0.05
P48_ATM2.9_SPEI+ZnO	-9.4±0.8	0.19±0.05	38±1	0.8±0.02
P12_ATM2.9_PVF+ZnO	-6.7±0.6	0.2±0.1	38.9±0.5	0.75±0.03
P24_ATM2.9_PVF+ZnO	-5.0±0.5	0.3±0.1	38.3±0.5	0.75±0.05
P36_ATM2.9_PVF+ZnO	-4.8±0.5	0.25±0.08	39±1	0.72±0.01
P48_ATM2.9_PVF+ZnO	-5±0.6	0.2±0.1	38±1	0.72±0.04

Thermogravimetric analysis. From TGA (Fig. 12A) and DTG (Fig. 12B) profiles, no variation in the pyrolysis temperature is observed for P48_ATM2.9_SPEI+ZnO and P48_ATM2.9_PVF+ZnO if compared to P9_HCl5M and P0, indicating the persistence of the polymeric structure of the samples subjected to the ATM2.9 degradation protocol in the presence of both SPEI and PVF sponges containing ZnO nanoparticles. In the meanwhile, for the sample degraded in the absence of inhibitors (P48_ATM2.9_NT), the profile of the DTG curve indicates a shift of the pyrolysis temperature (from ca 365 °C for P0 to 350 °C for P48_ATM2.9_NT, respectively) and of a second peak at ca. 280 °C. This effect can be attributed to a decrease in the average molecular weight of the polymeric chains of the support due to the hydrolysis of the glycosidic bonds of the cellulosic backbone.

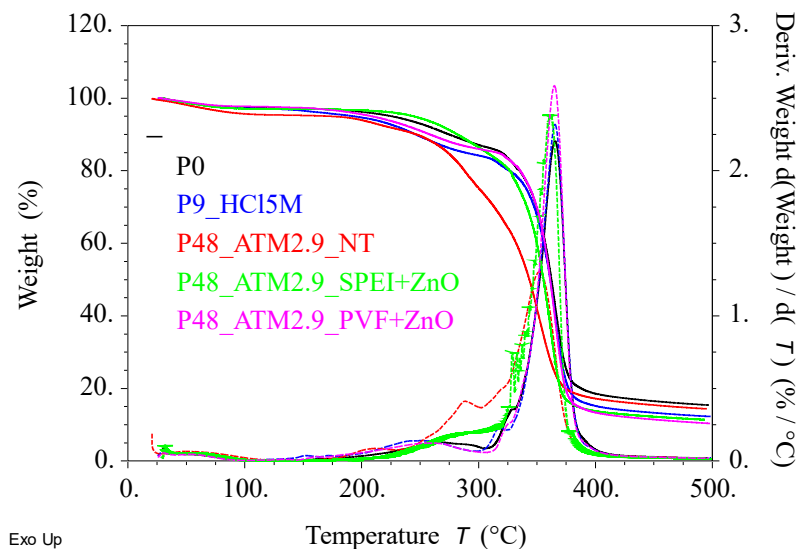


Fig. 12 TGA and DTG profiles for P0 (black), P9_HCl5M (blue) and P48_ATM2.9_NT (red) and P48_ATM2.9_SPEI+ZnO (green); P48_ATM2.9_PVF+ZnO (pink).

From the results reported above, is evident that the addition of ZnO nanoparticles to pure SPEI does not significantly increase the performance of the system in terms of inhibition of the artificially induced deacetylation of the support of the motion picture films carried out through the ATM2.9 protocol. Both the systems (pure SPEI and SPEI+ZnO), in fact, seem to have the same effect on the stabilization of the acetyl content and on the free acidity. On the other hand, the addition of ZnO nanoparticles to PVF seems to be very useful in improving the efficacy of the PVF system, which has a very mild action in the inhibition of the “*vinegar syndrome*” if used by itself. Probably, while the SPEI system, thanks to the presence of free NH groups inside its structure, is able to react with the acetic acid emitted by the films and also with the moisture of the environment, the action of pure PVF is only limited in the absorption of water. By adding ZnO nanoparticles to PVF, they can act as absorbers for the free acidity and consequently improve the efficacy of the composite system (PVF+ZnO).

6.2.4 Comparison between various treatments

As a further resume, macro- and micro-images of motion picture films before and after the degradation protocol, stored with and without various systems are reported in Fig. 14 and 15.

In Fig 14, an evident alteration in terms of emulsion loss, deformation and opacization of the support is observed for the motion picture film degraded for 48 days without any system (NT); on the other hand, films degraded in the presence of WP_ZnO, PVF+ZnO and SPEI show better conservation conditions. The slight alteration of the emulsion layer and consequently deformation of the support also in these latest three cases is due to the exposition to RH 100% for 48 days, which obviously alters the stability of the emulsion layer, independently from the presence of the inhibitors. More studies will be conducted in this sense, to consider how the inhibitors are able to influence the RH inside the storage environment.

In Fig. 15, micrographs of motion picture films at different steps of the degradation protocol with and without the inhibitors have been acquired.

In Fig. 15A (P0) apart from scratches due to the use and manipulation of the film, no alterations are visible; in Fig. 15B (motion picture films after the first step of the ATM2.9 degradation protocol), more irregularities are present on the surface of the film, maybe due to the initial insurgence of the deacetylation process. In Fig. 15C, a micrograph of the motion picture films degraded for 48 days without any system is reported: important signs of degradation are evident, such as the crystallization of plasticers on the surface.

P48_ATM2.9

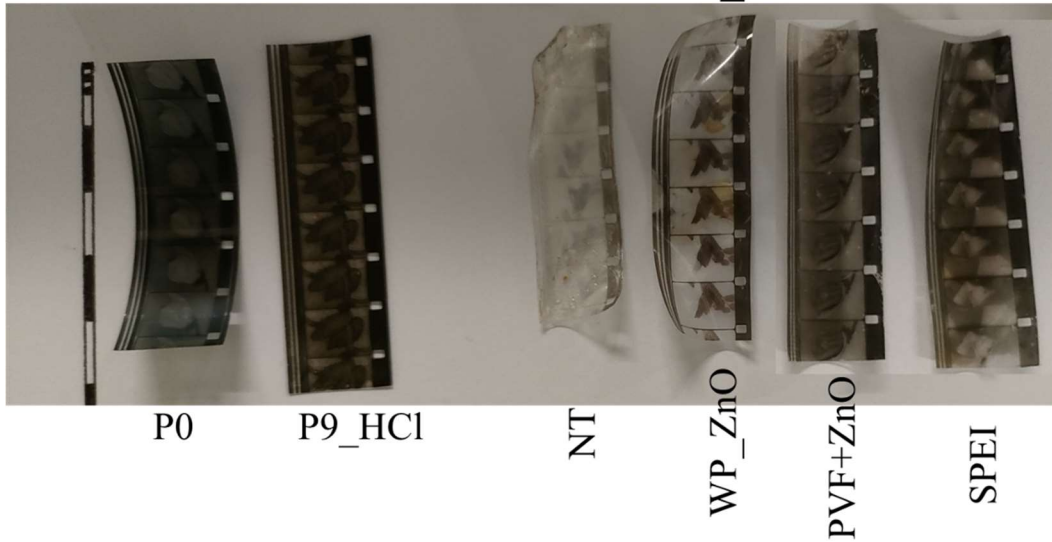


Fig. 14 (A) Not degraded motion picture film; motion picture film subjected to the first step of ATM2.9 degradation protocol (9 days of exposition to HCl 5M saturated atmosphere; motion picture films after 48 days of the third phase of the ATM2.9 degradation protocol (100%RH) without any system and in presence of WP_ZnO, PVF+ZnO and SPEI.

In Fig. 15D, E and F, which correspond to the micrographs acquired on samples degraded for 48 days, in the presence of WP_ZnO, PVF+ZnO and SPEI, respectively, no important differences are observed if compared with Fig. 15B, except for Fig. 15D, where more irregularities are visible.

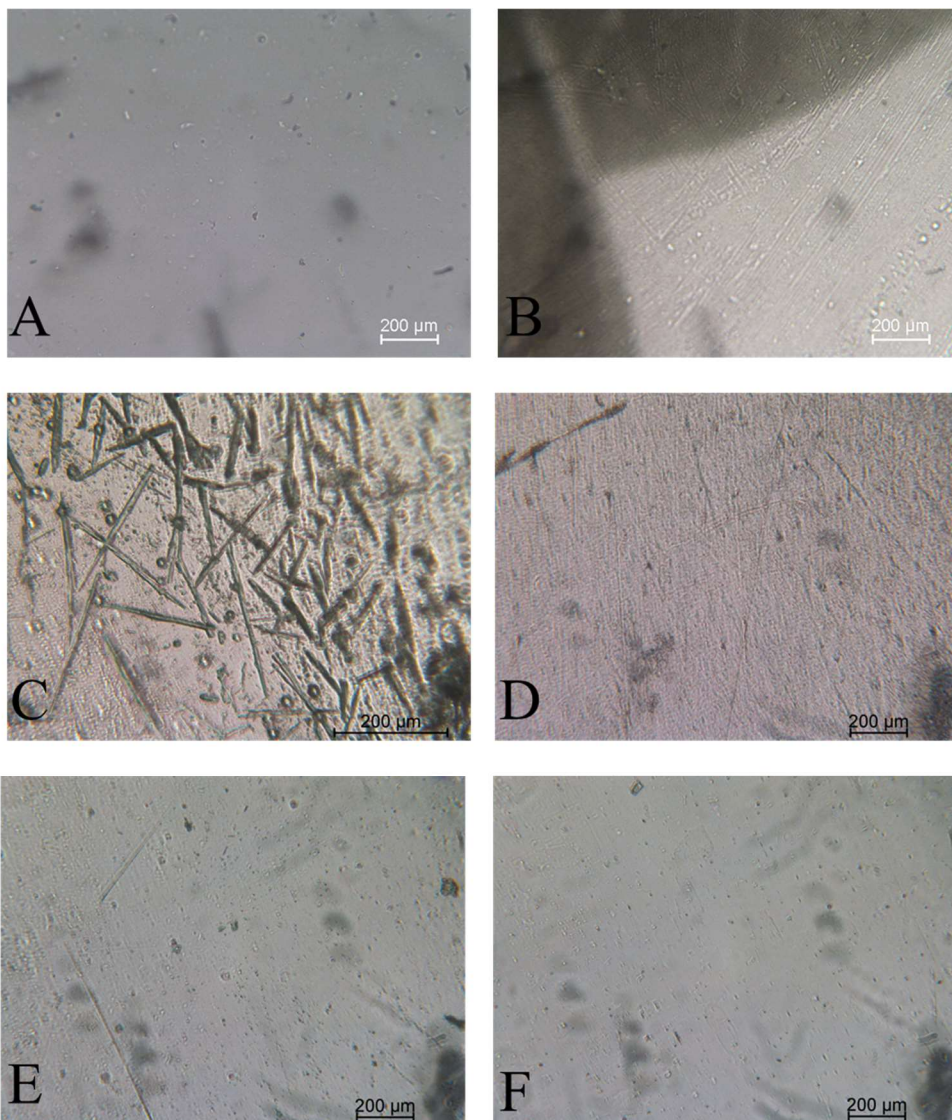


Fig. 15 Micrograph acquired with a magnification of 20x on (A) not degraded motion picture film; (B) motion picture film subjected to the first step of ATM2.9 degradation protocol (9 days of exposition to HCl 5M saturated atmosphere; motion picture films after 48 days of the third phase of the ATM2.9 degradation protocol (100%RH) (C) without any system and in presence of (D) WP_ZnO, (E) PVF+ZnO and (F) SPEI.

In addition, to further confirm the considerations expressed in the previous paragraphs about the performance of the different treatments proposed to inhibit the “vinegar syndrome” during the ATM2.9 degradation protocol on real motion picture film (WP soaked with different nanoparticles in Paragraph 6.2.1, SPEI and PVF

sponge in Paragraph 6.2.2 and SPEI and PVF sponges soaked with ZnO nanoparticles in Paragraph 6.2.3), a linear fitting has been performed for the correct acetyl content data in the range 24-48 days (the same range selected to comment on the untreated samples in Paragraph 3.4). These results are reported in Tab. 6 and Fig. 13.

As it is possible to see from Fig. 13A and Tab. 6, the slope of the linear fitting associated with degraded and untreated samples is -0.3, due to the decrease in the acetyl content during the degradation protocol, as previously observed and commented in Paragraph 3.4. On the other hand, for all the samples subjected to the degradation protocol in the presence of a treatment, the absolute value of the slope of the corresponding linear fitting is lower by one or two orders of magnitude and very near to 0. This could be considered a clear indication of the stabilization of the acetyl content during the degradation protocol due to the action of various treatments. The only exception is registered for samples degraded in the presence of PVF sponges (Fig. 13C); in this case, the slope of the curve is only slightly lower than for untreated samples (-0.25, Tab. 6). As we already commented in Paragraph 6.2.2, the action of only PVF seems to be not enough to inhibit the “vinegar syndrome”.

For samples treated with WP soaked with different nanoparticles (Fig. 13B), the slope of the curve is -0.04 and -0.03 for samples degraded in the presence of ZnO and Ca(OH)₂ nanoparticles, respectively, and -0.004 for samples degraded in the presence of Mg(OH)₂. In the last case, the R² is very low (0.01), due to the value associated with the 36th day of degradation. The acetyl content value ranges between the same value (37) between days 24 and 48. A slowdown in the decrease of the acetyl content is evident for all three tests.

For samples degraded in the presence of both SPEI (Fig. 13C) and SPEI+ZnO (Fig. 13D), the slope of the curve is 0.03 and 0.04, respectively, confirming the good performance of both treatments due, in particular, to the capacity of SPEI to

neutralize the free acidity produced by CA-based films and consequently stabilize the acetyl content (Paragraph 6.2.2 and 6.2.3).

For samples treated with PVF+ZnO (Fig. 13D), the slope of the linear fitting is 0.0035, much lower if compared to the one ascribed to only PVF: thanks to the addition of ZnO nanoparticles, the action of the composed system is not only limited to the weakly absorption of acetic acid and moisture of PVF but also to the neutralization of the free acidity produced by degraded CA-based films conducted by ZnO nanoparticles. Also in this case the R^2 is very low (0.05) due to the value associated with day 36 of the degradation protocol. The acetyl content value ranges between the same value (38) between days 24 and 48.

Tab. 6 Linear fitting curves calculated from the data obtained from real motion picture films subjected to ATM2.9 degradation method with and without treatments.

Test	Treatment	Range (days)	Linear fitting	R^2
P_ATM2.9_NT	/	24-48	$y=-0.3x+45.4$	0.99
P_ATM2.9_WPCa(OH) ₂	WP + Ca(OH) ₂ nps	24-48	$y=-0.04x+38.8$	0.99
P_ATM2.9_WPMg(OH) ₂	WP + Mg(OH) ₂ nps	24-48	$y=-0.004x+37.3$	0.01
P_ATM2.9_WPZnO	WP + ZnO nps	24-48	$y=-0.03x+37.7$	0.79
P_ATM2.9_SPEI	SPEI	24-48	$y=0.03x+36.4$	0.47
P_ATM2.9_PVF	PVF	24-48	$y=-0.25x+43.9$	0.95
P_ATM2.9_SPEI+ZnO	SPEI + ZnO nps	24-48	$y=0.04x+36.5$	0.8
P_ATM2.9_PVF+ZnO	PVF +ZnO nps	24-48	$y=0.0035x+38.6$	0.05

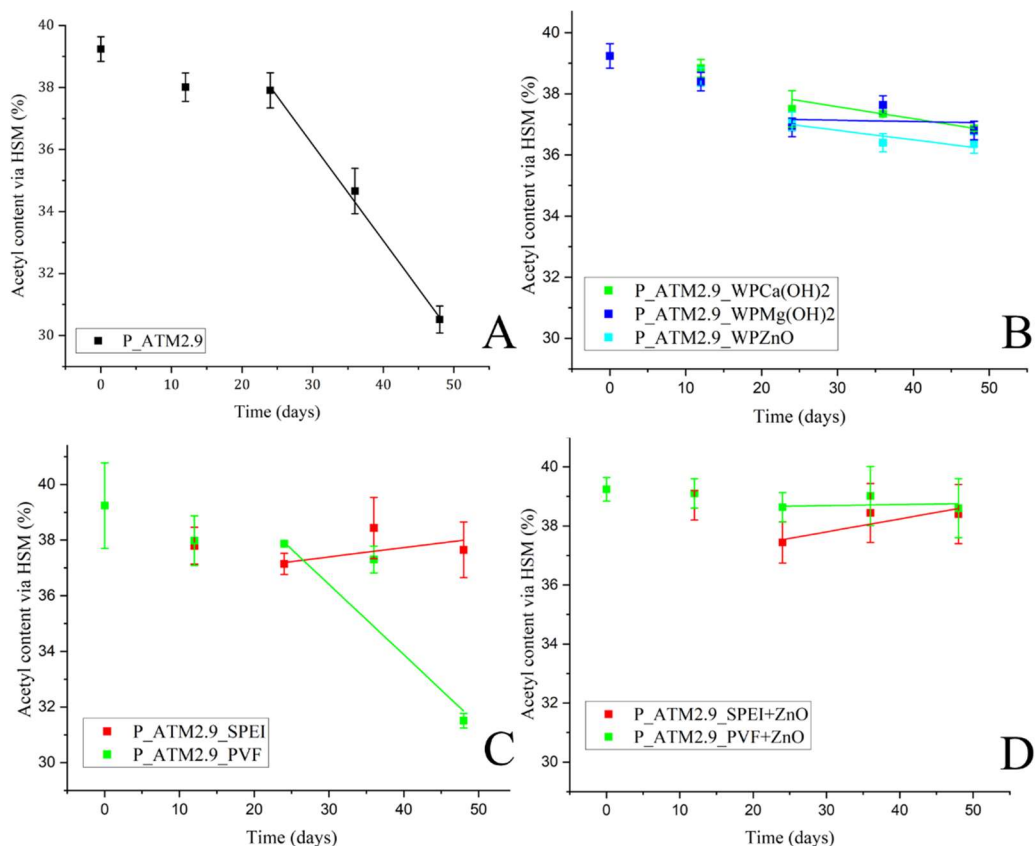


Fig. 13 Linear fitting calculated on the curves associated with the variation in the correct acetyl content for samples subjected to ATM2.9 degradation protocol with and without a treatment: (A) P_ATM2.9_NT (black), (B) P_ATM2.9_WPCa(OH)₂ (green), P_ATM2.9_WPMg(OH)₂ (blue), P_ATM2.9_WPZnO (cyan), (C) P_ATM2.9_SPEI (red), P_ATM2.9_PVF (green), (D) P_ATM2.9_SPEI+ZnO (red), P_ATM2.9_PVF+ZnO (green).

6.2.5 Evaluation of the efficacy of SPEI on real motion picture films naturally affected by the vinegar syndrome

In this Paragraph, we evaluated the performance of one of the systems set up in the frame of this work for the inhibition of the deacetylation process in real motion picture film naturally affected by the “*vinegar syndrome*”. We chose to test pure SPEI 4 because it is one of the inhibitors that provided better results in terms of the

capability to adsorb the gaseous acetic acid (Paragraph 4.3.4) and inhibit the artificially induced deacetylation process (Paragraph 6.2.2).

In this case, being the motion picture film naturally affected by the “*vinegar syndrome*”, they were not subjected to any artificial degradation process such as ATM2.3 or ATM2.9 as for the previous experiments described in this chapter. Motion picture films were put into two sealed aluminum bags and the SPEI 4 was maintained in direct contact with the samples at room temperature for 7 months. Further tests will be necessary to evaluate its action also at a certain distance.

The 4 samples that were analyzed in this Paragraph were labeled as follows:

1. P0 is a sample of a motion picture film that is not affected by any natural deacetylation process (it is the same film that has been used for the test described in the previous paragraph of this chapter). Based on the data reported in Tab. 7 and Tab. 4 of Chapter III, this motion picture film is in a very good state of conservation;
2. PBO_0 is a sample of the motion picture film naturally affected by the “*vinegar syndrome*” before its insertion inside the aluminum bag (time 0). Based on the data reported in Tab. 7 and Tab. 4 of Chapter III, the support of this motion picture film has a very low degree of acetylation (< 1) indicating that, in this case, the film is in an advanced state of degradation due to the “*vinegar syndrome*”.

For these two samples, both the free acidity and the acetyl content via HSM (Paragraph 3.1.3) were measured. PBO_0 shows a higher free acidity value than P0 (P0: $0.02 \pm 0.1\%$ vs PBO_NT_0: $0.25 \pm 0.1\%$), suggesting that a certain quantity of acetic acid is currently stored inside the support and that the deacetylation reaction is probably actually active [3]. Moreover, also the correct acetyl content measured for PBO_0 is $11.2 \pm 0.5\%$ which is sensibly lower than the one of P0 ($41.7 \pm 0.7\%$). According to Tab. 4 of Chapter III, this value could be ascribed to a “0”-CA. This point confirms that this motion

picture film is almost completely deacetylated and that it is affected (or was affected in the past) by the “*vinegar syndrome*”.

3. PBO_NT_7M is a sample of the motion picture film naturally affected by the “*vinegar syndrome*” after 7 months inside the aluminum bag at room temperature in the absence of any inhibitor;

4. PBO_SPEI_7M is a sample of the motion picture film naturally affected by the “*vinegar syndrome*” after 7 months inside the aluminum bag at room temperature in the presence of SPEI.

P0 has been used as reference material and it has been compared with the sample PBO_0 to analytically verify its status at the beginning of the test.

Tab. 7 Resume of the results associated with real motion picture films naturally affected by the vinegar syndrome and treated with SPEI in contact with the samples.

Sample	Weight Loss (%)	Free acidity (%)	Correct Acetyl Content (%)	ATR-FTIR Ratio I ₁₂₂₀ / I ₁₀₃₀
P0	/	0.02±0.1	41.7±0.7	0.91±0.04
PB_0	/	0.25±0.1	11.2±0.5	0.3±0.1
PB_NT_7M	-1.6±0.2	0.26±0.1	8.35±0.7	0.16±0.03
PB_SPEI_7M	-0.46±0.04	0.09±0.1	10.7±0.7	0.4±0.1

Gravimetry test. In comparison with the weight decrease measured in previous experiments, in this case the gravimetric data indicate that for both PBO_NT_7M and PBO_SPEI_7M the weight loss respect to the PBO_0 sample is much smaller, even if the value registered for PBO_NT_7M (-1.6±0.2%) is much higher than the one measured for PBO_SPEI_7M (-0.46±0.04%).

Free acidity. Comparing both the samples stored in an aluminum bag for seven months with (PB_SPEI_7M) and without the inhibitor (PB_NT_7M) to the sample at time 0 (PB_0), it is possible to note that, for the PB_NT_7M sample the free acidity is almost unchanged, if compared to the initial value (PB_0), while, for the

treated sample, a decrease in the free acidity of ca. 65% is observed (free acidity of PB_0: $0.25 \pm 0.1\%$; PB_NT_7M: $0.26 \pm 0.1\%$; PB_SPEI_7M: $0.09 \pm 0.08\%$, Tab. 7).

Acetyl content. Also the value of the acetyl content of the films stored in the presence or in the absence of the inhibitor is different: while the acetyl content of PB_SPEI_7M is almost unchanged from that of the sample at the beginning of the test (PB_0), for PB_NT_7M a significant decrease of ca. 25% was observed (Tab. 7).

ATR-FTIR Spectroscopy. From ATR-FTIR spectra (Fig. 16 A-B), first of all, is possible to confirm that the motion picture film PBO_0 is made by “0”-CA and that, already at the beginning of the test, it is in an advanced state of degradation as indicated by the value of the I_{1220}/I_{1030} ratio equal to 0.3 ± 0.1 (Tab. 7). The difference between PBO_NT_7M and PBO_SPEI_7M samples at the end of the test is evident by examining the intensity of the peaks ascribed to the acetyl group (Fig. 16 C-D): while for PBO_SPEI_7M the intensity of the peaks at 1220 , 1330 and 1730 cm^{-1} are almost equal to the ones of PBO_0, for PBO_NT_7M, it strongly decreases. Concerning the peak assigned to the OH stretching, the intensity does not vary significantly in the three examined samples. In fact, in this case, the conditioning of the sample was carried out at an RH value of around 80-85%. This is an indication that the increase of the peak at 3500 cm^{-1} observed in all the previous experiments, where the samples were maintained in a jar at an RH equal to 100%, was due to the absorption of moisture.

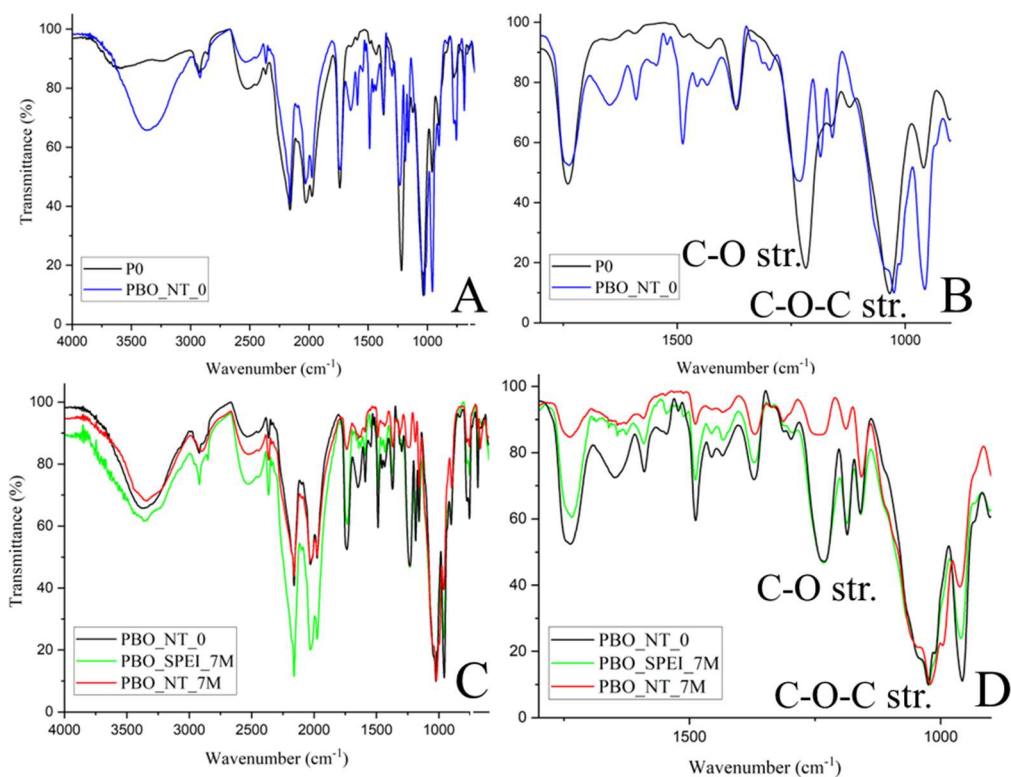


Fig. 16 FTIR-ATR spectra of P0 (black) and PBO_NT_0 (blue) in the range 4000-600 (A) and 1800-900 (B) cm^{-1} ; FTIR-ATR spectra of PBO_NT_0 (black), PBO_NT_7M (red) and PBO_S_SPEI (green) in the range 4000-600 (C) and 1800-900 (D) cm^{-1} .

Finally, the ratio between the intensities of the peaks at 1220 and at 1030 cm^{-1} is lower for PBO_NT_7M (0.4 ± 0.1) than PBO_0 (0.3 ± 0.1) while is quite unchanged for PBO_S_SPEI_7M: (0.4 ± 0.05). Even if the standard deviations are quite high (suggesting that deacetylation in real motion picture films occurred inhomogeneously on the surface of the film), the FTIR-ATR analysis is in agreement with the other data and clearly indicates that SPEI is effective in the inhibition of the progress of the deacetylation process in real motion picture films naturally affected by the “vinegar syndrome”.

Thermogravimetric analysis. From the TGA and DTG profiles (Fig. 17) it is evident that PB_0 has a lower pyrolysis temperature than P0 (a weight loss is registered between 230 and 300 $^{\circ}\text{C}$ ca., with a peak in DTG at 263 $^{\circ}\text{C}$ for PB_0, while for P0

the weight loss ascribed to the thermal degradation is registered between 300 and 400 °C ca., with a peak in DTG at 365 °C). This could be due to the advanced state of decay of the sample PB_0, for which the acidity emitted as a by-product of the deacetylation process and stored in the polymer induced the hydrolysis of the glycosidic bonds of the CA, promoting the depolymerization of the cellulosic backbone. Another possible explanation could be the use of CA with different degrees of polymerization for the manufacture of the two motion picture films (P0 and PB_0).

Observing the profiles of PB_0, PB_NT_7M and PB_SPEI_7M the differences are minimal, probably because 7 months of conditioning are not enough to appreciate a significant difference in the thermal behavior. However, comparing the DTG profile of PB_0 with the one of PB_NT_7M, a little shift of the peak ascribed to the pyrolysis temperature of the polymer is observed from 263 °C to 260 °C, while this peak is identical to the one PB_0 for PB_SPEI_7M.

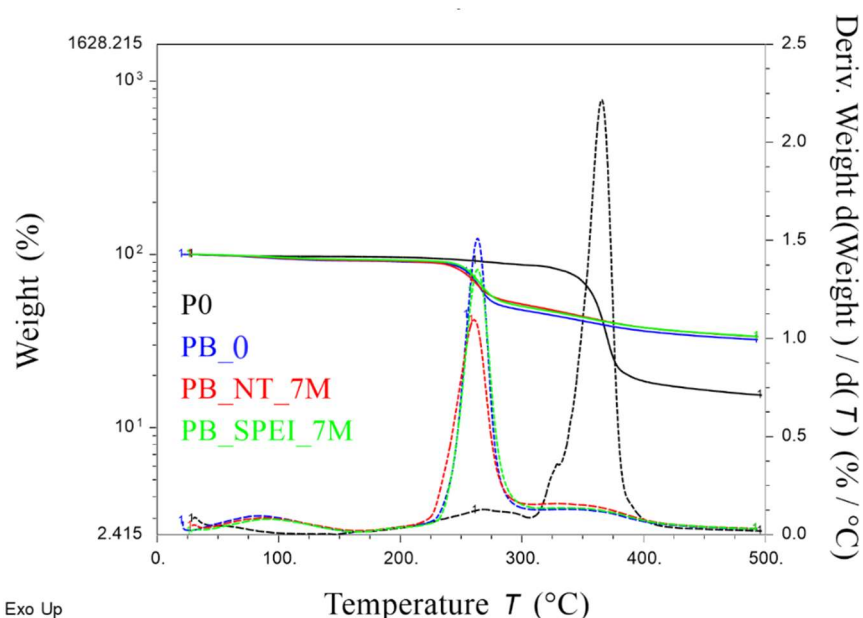


Fig. 17 TGA and DTG profiles for P0 (black), PB_0 (blue), PB_NT_7M (red) and PB_SPEI_7M (green).

The results discussed above indicate that SPEI can be a promising solution for the inhibition of the degradation processes in real motion picture films naturally affected by the “*vinegar syndrome*”. In fact, by storing two fragments of the same film affected by the syndrome in the same environmental conditions with or without the SPEI, it has been possible to appreciate two different behaviors: a decrease in the free acidity and a stabilization of the acetyl content for the sample stored in the presence of SPEI, while the free acidity of the NT sample remained similar to the initial value and its acetyl content slightly decreased. Further studies will be necessary to test the performance of SPEI on a wider range of case studies (i.e. on motion picture films affected by “*vinegar syndrome*” at different levels and, then, in different conservation statuses), to evaluate its performance for longer periods and also not in direct contact with the films.

6.3 Conclusions

In this Chapter, the efficacy of various systems properly set up for the inhibition of the deacetylation process (i.e. the “*vinegar syndrome*”) that affects motion picture films was evaluated on both artificially and naturally degraded motion picture films through a multi-analytical protocol that was previously discussed in Chapter III.

Concerning this analytical approach, it is possible to affirm that, in all the tests where the deacetylation process was artificially induced, the gravimetry test is strictly influenced by both the loss of the emulsion layer in both treated and untreated samples (as was already mentioned in Chapter III) and the content of moisture absorbed by the film (both emulsion layer and support). In fact, the loss in weight detected also for treated films could be due also to the capacity of the treatments (sponges and soaked WP) to absorb part of the moisture that, in untreated samples, is stored inside the film. Probably, for this reason, the trend of these data is not coherent with the results provided by the other techniques. On the other hand, a good accordance between free acidity, acetyl content via HSM and FTIR-ATR ratio was observed and, for this reason, these data will be taken mostly into account for the

evaluations reported below. Concerning the Young's Modulus, the data obtained through tensile stress measurements indicate that for all the films subjected to artificially induced deacetylation treatments for 48 days, this parameter always decreases by almost 20% for all the samples degraded in the presence of an inhibitor. While for the samples degraded without the presence of an inhibitor, the decrease of the Young Modulus was around 50%. In the evaluation of the meaning of these data, it is important to take into account that the value of the Young Modulus is strongly affected also by the moisture adsorbed by the emulsion layer. This effect should be studied in detail in the future through experiments specifically tailored.

Concerning tests performed on artificially degraded samples, various kinds of information were obtained comparing in particular acetyl content (calculated via HSM and ATR-FTIR ratio) and free acidity data:

- different kinds of nanoparticles (in particular ZnO, Ca(OH)₂ and Mg(OH)₂) gave good results in the inhibition of the artificially induced "*vinegar syndrome*", if uploaded on a sheet of Whatman® paper or into PVF sponges. In particular, the nanoparticles uploaded into a porous support such as a PVF sponge, seem to have a better performance in comparison to when they are applied onto a sheet of Whatman® paper;
- concerning the efficacy of the sponge-like systems obtained through the crosslinking of PolyEthyleneImine (SPEI), they contain many free aminic groups, available for the neutralization of acetic acid produced by the motion picture films affected by the "*vinegar syndrome*". The results obtained indicate SPEI is highly effective in the inhibition of the deacetylation process on both motion picture films where the "*vinegar syndrome*" was artificially induced and also on naturally degraded samples. On these bases, it is possible to affirm that the SPEI system seems to be a promising inhibitor of the "*vinegar syndrome*".

References

- [1] M.-P. M. Paul Read, *Restoration of Motion Picture Film*, Butterworth. Oxford, 2000.
- [2] G. Poggi *et al.*, “Calcium hydroxide nanoparticles for the conservation of cultural heritage: New formulations for the deacidification of cellulose-based artifacts,” *Appl. Phys. A Mater. Sci. Process.*, vol. 114, no. 3, pp. 685–693, 2014, doi: 10.1007/s00339-013-8172-7.
- [3] B. Knight, “Lack of evidence for an autocatalytic point in the degradation of cellulose acetate,” *Polym. Degrad. Stab.*, vol. 107, pp. 219–222, 2014, doi: 10.1016/j.polymdegradstab.2013.12.002.

VII. Conclusions

The present work was focused on the setup of innovative, cheap, easy-to-produce and handle and possibly reusable chemical inhibitors for the so-called “*vinegar syndrome*” that affects motion picture films whose support is made by cellulose triacetate (CTA). In order to evaluate the performance of our systems, an innovative degradation method to artificially induce the deacetylation reaction on motion picture films based on the exposition to a high acidity saturated atmosphere has been successfully set up. Another fundamental novelty of this work was the development of a multi-analytical protocol able to monitor the chemical alterations of the base supports connected with the occurrence and the evolution of the “*vinegar syndrome*”.

The artificial degradation method and the multi-analytical protocol

In order to evaluate the performance of our systems in the inhibition of the “*vinegar syndrome*” of CA-based motion picture films, several degradation methods to artificially induce the deacetylation reaction in motion picture films have been set up.

We found that the most promising degradation method has been the one in which the deacetylation process is first induced thanks to the exposition of the film to an acid atmosphere, using HCl as a catalyst. Afterward, the samples are maintained for 24 hours under hood to promote the removal of the HCl absorbed onto the film and then the samples are stored in sealed cells at 100% RH. Unlike other proposed degradation protocols, this procedure was able to artificially induce the deacetylation process and showed proper kinetics to be studied, compatible with laboratory timelines. In addition, no relevant physico-chemical alterations have been observed on inhibitors subjected to this degradation protocol.

Furthermore, a multi-analytical method able to monitor the chemical alterations of the base supports connected with the occurrence and the evolution of the “*vinegar*

syndrome” was developed. The multi-analytical method, based on the calculation of the acetyl content through HSM (corrected with free acidity) and through the calculation of the ratios between the intensities of some FTIR-ATR diagnostic peaks (in particular the I_{1220}/I_{1030} ratio) and on the free acidity, could be considered useful to follow the evolution of artificially induced deacetylation processes that artificially simulate the “*vinegar syndrome*” on both CA-based films and real motion picture films. In fact, the linear fittings of the normalized data collected from artificially degraded CA and motion picture films, that describe the correct acetyl content, the FTIR-ATR ratio and the free acidity, are coherent with each other. Then, the possible use of FTIR-ATR spectroscopy could be a great alternative to HSM because it is a non-invasive and non-destructive technique that allows to collect a large number of spectra onto a film sample. In addition, TGA and tensile tests gave precious informations about collateral degradation pathways which are promoted by deacetylation (i.e. variation in the molecular weight of CA chains and loss of plasticizers). This is a key point of this project, being that this degradation phenomenon, at today, has been mostly investigated by using single techniques that often do not give exhaustive information about all the aspects involved in the progress of the deacetylation process.

The inhibitors: synthesis and preliminary studies

The approach proposed in this work was the conversion of the acetic acid, which is a by-product of the degradation process of the CA-based motion picture films and the main catalyst of the deacetylation reaction, into an acetate salt in order to neutralize it through an acid/base reaction.

For this purpose, two different strategies have been followed:

1. the setup of sponges or gel-like systems composed of polyethyleneimine (PEI) and/or polyvinylalcohol (PVA). In particular, the systems proposed were a cryogel obtained by mixing PVA and PEI (PVA-PEI-CG), a PVA network

crosslinked with formaldehyde (PVF) in which PEI is incorporated, in order to obtain a sponge-like system (PVF-PEI-GA) and a sponge-like system indicated as SPEI, obtained through the chemical crosslinking of PEI with 1,4-butanedioldyglycidyl ether (BDDE);

2. the use of inorganic nanoparticles uploaded on different substrates, such as paper or the sponges previously described. In particular, the attention has been focused on different kinds of nanoparticles such as $\text{Ca}(\text{OH})_2$, $\text{Mg}(\text{OH})_2$, CaCO_3 , ZnO , TiO_2 and Al_2O_3 that have been uploaded on various supports (Whatmann Paper, PVF and SPEI sponges) and tested.

From preliminary gaseous acetic acid absorption tests, SPEI sponges showed a better performance in terms of gaseous acetic acid absorption in comparison to PVF-PEI-GA and PVA-PEI-CG, both in terms of weakly and strongly bonded acetic acid. This is probably due to the higher porosity of the SPEI system compared to the cryogel (PVA-PEI-CG) and to the fact that the crosslinking reaction efficacy between PEI and PVF in PVF-PEI-GA systems needs to be improved. In addition, SPEI systems appear reusable (at least 3 times) because of the possibility to easily regenerate them with a basic bath in 1M NaOH. On the contrary, the efficacy of both PVF-PEI-GA and PVA-PEI-CG drastically decreases after the regeneration treatment probably due to the loss of PEI and the rearrangement of the cryogel network, respectively.

Concerning SPEI sponges, it was seen that by increasing the molar ratio between PEI and BDDE from 1:1 to 3:1 and decreasing PEI concentration from 8% to 4%, it is possible to increase the amount of both total and strongly absorbed acetic acid. In fact, in this way, the grafting reaction is favored on the crosslinking one and the number of free amino groups (able to react with acetic acid) increases. On the other hand, on the basis of the rheological analyses, being that the mechanical strength of the systems strongly depends on the amount of PEI and the spatial density of crosslinking, in the view to reach a compromise between acetic acid absorption efficiency and mechanical properties, the system chosen for the further test and

studies was the one characterized by a PEI:BDDE ratio equal to 3:1 and a PEI concentration of 6 wt%.

Regarding nanoparticles-based systems, we chose to focus our attention on ZnO, Ca(OH)₂ and Mg(OH)₂ nanoparticles because, from the preliminary gaseous acetic acid absorption test, were the ones that give the best performance in terms of the amount of adsorbed acetic acid. Then, ZnO nanoparticles were uploaded on WP disks and two sponge-like systems based on PVF and SPEI. Concerning both WP and sponge-based systems, they show lower absorption capacity than pure nanoparticles, because, as indicated by the SEM analysis, during the synthesis/uploading process, nanoparticles tend to aggregate each other. However, sponge-like systems seem more efficient than WP thanks to their porous structure. Pure SPEI and the mixed systems SPEI+ZnO and PVF+ZnO showed the best performance in terms of both total absorbed acetic acid and strongly bonded acetic acid. In the case of SPEI, this is mainly due to the chemical nature of SPEI which can neutralize acetic acid also on its own, thanks to the presence of amino groups inside the sponge network. On the other hand, in the case of PVF, the pure PVF is not able to neutralize acetic acid by itself but, by adding ZnO nanoparticles, which act as the actual neutralization system, the performance of the composite inhibitor drastically improves.

The evaluation of the proposed systems in the inhibition of the “vinegar syndrome”

Some of the above-mentioned systems were selected in order to test their efficacy in inhibiting the deacetylation process in motion picture films. These tests were performed on real motion picture films on which the deacetylation process has been artificially induced and on films naturally affected by the vinegar syndrome. The different behaviors of untreated and treated films have been evaluated through the above-mentioned defined multi-analytical protocol.

First, we tried to apply nanoparticles by spraying directly onto the surface of the film. Even if this treatment seems to be effective in the inhibition of the deacetylation

process, their presence induces a strong alteration of the optical properties of the film that makes this approach not promising for extensive applications.

Different types of nanoparticles (in particular ZnO, Ca(OH)₂ and Mg(OH)₂) gave good results in the slowdown/inhibition of the artificially induced “*vinegar syndrome*”, if uploaded on a sheet of Whatman® paper or into PVF and SPEI sponges. In particular, the nanoparticles uploaded into porous supports (PVF+ZnO and SPEI+ZnO) seem to have a better performance in comparison to when they are applied onto a sheet of Whatman® paper.

Concerning the performance of the sponge-like systems obtained through the cross-linking of PEI (SPEI) with and without the addition of ZnO nanoparticles, the results obtained indicate that the two systems are highly effective in the inhibition of the deacetylation process on both motion picture films where the “*vinegar syndrome*” was artificially induced and also on naturally degraded samples.

On these bases, it is possible to affirm that both PVF downloaded with ZnO nanoparticles and the SPEI system (with and without nanoparticles) seem to be a promising inhibitor of the “*vinegar syndrome*”. Their easy and cheap synthesis routes and the possibility to easily adapt their shape make them a promising option to be used by conservators and archivists on a large scale. For future studies, it could be interesting to evaluate the use of these systems also for the conservation of different kinds of artifacts showing the same issues of motion picture films (it is well known that also wood or other plastics-based objects typically stored in a museum emit VOCs and in particular acetic acid).

Moreover, SPEI seems to be regenerable and reusable by simply washing it with a 1M NaOH solution. Further studies will be dedicated to the possibility of regenerating and reusing also PVF systems soaked with nanoparticles through both chemical (acid-basic reaction as for SPEI) and photocatalytic (for ZnO and TiO₂) routes. A more detailed characterization needs to be performed on pure sponge-like

systems and composite systems in terms of morphological analysis (through SAXS) and rheological analysis (for SPEI+ZnO and PVF+ZnO).

In addition, more tests on a wider panorama of real motion picture films of different compositions and in different conservation conditions are needed to further verify the efficacy of our systems. In particular, additional tests on the effect of our inhibitors on the optical properties of the emulsion layer will be performed and more in-depth studies will be conducted about their efficacy if they are put not in direct contact with the motion picture films.

Acknowledgments

First and foremost, I would like to express my sincere gratitude to my supervisor, Professor Emiliano Carretti, for allowing me to work with him on this fascinating and stimulating project. For guiding my path with his precious indications but, most of all, with his indefatigable attention, infinite patience and unwavering support. He has been an inspiration, not only from the academic point of view, due to his impeccable professionalism, but also and especially from a personal point of view, by being an example of Humanity in a field where this value is forgotten too often.

I would like to extend my sincere thanks also to my co-supervisor, Professor Luigi Dei, for his insightful comments and suggestions and for his availability to patiently listen to my doubts and proposals.

I am deeply grateful to all the undergraduate students who collaborated on this project, Alessia Maiano, Camilla Forcellini, Carlotta D'Aleo, Lorenzo Lisi, Fedora Olivadese and Emma Dini: without their enthusiasm and their brilliant ideas, this work would not have been possible. And my job would not have been as exciting.

I would like to offer my special thanks to Marianna De Sanctis and Maura Pischedda for welcoming me to the “Immagine Ritrovata” lab (Bologna, Italy) and for providing motion picture films affected by the “vinegar syndrome”.

I would like to thank also the Istituto Agrario ITAGR (Florence, Italy), for kindly gifted most of the motion picture films on which we conducted our studies.

I would like to thank Dr. Teresa Guaragnone and the CSGI for providing the dispersion of $\text{Ca}(\text{OH})_2$ nanoparticles and Kuraray for providing the polyvinyl alcohol used in this work.

I would like to extend my sincere thanks also to Dr. Giovanna Poggi for the tips and the help in the development of the tensile tests, Dr. Samuele Ciattini (CRIST) for the

assistance with μ -TOM and XRD measurements and Dr. Rita Gelli for her impressive helpfulness to follow me for FE-SEM measurements.

I would like to thank all my colleagues and mates of the lab. 181: Dr. Daniela Porcu, Dr. Chiara Cianci, Dr. Corinne Suraci, Dr. Damiano Bandelli, Dr. Vanessa Rosciardi, Dr. Andrea Casini, Dr. Rosangela Mastrangelo for their precious support and tips.

I am deeply grateful to Dr. Barbara Berrie and Dr. Teresa D. Duncan for giving me the amazing opportunity to work with them at the National Gallery of Art (Washington D.C.) on the development of the PDMS-based sponges.

Finally, I would like to thank my second academic family at Georgetown University (Washington D.C.), Dr. Shae London, Dr. Danielle Beaupre, Dr. Girishma Grover, for welcoming me, making me feel at home and helping me with laboratory workflows, microscopy and thermogravimetric analysis.

I would like to dedicate an important mention to Professor Richard G. Weiss, who has been my mentor at Georgetown University. His immense knowledge and plentiful experience have deeply inspired this work. I will never forget his precious teachings and suggestions, his capacity to be a strict and severe Professor but also a helpful and generous Person. It has been a real honor and privilege for me to know him and to work under his supervision.



OPEN

Performance of innovative nanomaterials for bone remains consolidation and effect on ^{14}C dating and on palaeogenetic analysis

Francesca Porpora¹, Valentina Zaro², Lucia Liccioli³, Alessandra Modi², Arianna Meoli¹, Giulia Marradi¹, Serena Barone³, Stefania Vai², Luigi Dei¹, David Caramelli², Mariaelena Fedi^{3✉}, Martina Lari^{2,4✉} & Emiliano Carretti^{1,4✉}

An innovative protocol for the consolidation of ancient bone remains based on the use of nanometric HydroxyAPatite (HAP) was set up and tested through a multidisciplinary approach. A new protocol for the synthesis of HAP nanoparticles was developed, and the composition of the obtained nanomaterial was investigated through Fourier Transform Infrared Spectroscopy (FTIR) and X-Ray Diffraction (XRD); sizes, shape and morphology of the synthesized particles were studied by Scanning Electron Microscopy (SEM). The consolidation performance was evaluated by testing the new nanomaterial on degraded ancient bone findings. An increase of the mineral density and of the micro-hardness of the bone were observed. The new consolidation method was also tested to assess possible effects on the palaeogenetic analysis and radiocarbon dating on the treated bones. The consolidation treatment does not introduce any contaminations that could affect radiocarbon dating and has no general detrimental impact on the genetic characterization of the skeletal remains. This consolidation procedure represents a more compatible conservation tool with respect to traditional procedures: it has been shown that the treatment is effective, easily-applicable and compatible with post-consolidation analysis.

In the field of cultural heritage conservation, bone remains from historical, archaeological and paleontological contexts are peculiar and precious finds. Particularly, human skeletal remains represent an enormous source of information about ancient humans in terms of their evolutionary and adaptation mechanisms, migratory flows and lifestyle (social and cultural behaviours, diet and diseases)^{1–7}. Similarly, animal skeletal remains can provide information on past environments and on the social and economic organization of the populations which they are associated with^{8–11}.

The chemical composition of bones is characterized by packed collagen fibres interconnected with a network of microcrystals of apatite with general formula $\text{Ca}_{10}(\text{PO}_4)_X$, where X usually indicates a hydroxyl group (HydroxyAPatite, HAP). While the stoichiometric hydroxyapatite shows a Ca:P ratio of 1.67, the value typically observed in the organisms is widely variable due to several ion substitutions present in the hydroxyapatite of biological origin¹².

Ancient bone remains are typically discovered in critical conservation conditions, mostly in direct contact with the soil. The physico-chemical characteristics of the external environment (pH of the soil, moisture, temperature, environmental redox potential), the prolonged interaction with micro- and macro-organisms, together with the intrinsic physico-chemical properties of the remains, such as porosity and crystallinity, can strongly

¹Department of Chemistry Ugo Schiff and CSGI Consortium, University of Florence, via della Lastruccia 3-13, 50019 Sesto Fiorentino, FI, Italy. ²Department of Biology, University of Florence, via del Proconsolo 12, 50122 Florence, FI, Italy. ³INFN (Istituto Nazionale Di Fisica Nucleare) Sezione Di Firenze, via G. Sansone 1, 50019 Sesto Fiorentino, FI, Italy. ⁴These authors contributed equally: Martina Lari and Emiliano Carretti. ✉email: fedi@fi.infn.it; martina.lari@unifi.it; emiliano.carretti@unifi.it

affect the preservation of the bones^{13–15}. Consequently, in view of future studies, analyses and exhibitions, the recovery and handling of these objects are often critical.

Since the beginning of the twentieth century, the products typically used for consolidation treatments and fixing of the fragments are realized by natural and synthetic organic polymers (i.e., vinyl and acrylic polymers and copolymers)¹⁶. Unfortunately, their scarce physico-chemical compatibility with the substrate and their low chemical stability, can lead to a rapid decrease of their performance, cause alterations of the bone matrix (yellowing and strong change of the porosity) and induce mechanical stresses due to the shrinking of these polymeric materials upon ageing. In addition, their degradation can seriously compromise their removal and the re-treatability of the object, besides hampering the analysis of biomolecules such as DNA and protein^{16,17}. Moreover, the application of organic polymers may significantly alter ¹⁴C radiocarbon dating analysis by introducing external carbon atoms, especially in the case of poor information about the previous treatments or severe degradation processes occurred to those polymers.

In the last few years, inorganic nanomaterials have been proposed as a useful alternative to organic polymers^{18,19} for the conservation of different classes of works of art (i.e., consolidation of wall paintings and carbonate stones, and deacidification of cellulosic materials such as canvas and papers). These materials have the great advantage of physicochemical compatibility with the materials constituting the works. As an example, Ca(OH)₂ nanoparticles dispersed in 2-propanol have been used for the consolidation of archaeological bones to promote, through carbonation induced by the atmospheric CO₂, the formation of aragonite, a metastable polymorph of CaCO₃ characterized by strong mechanical properties²⁰. Since aragonite is not the best conservation material for bones (mainly composed by HAP), the use of HAP for consolidation purposes of archaeological bones was evaluated in more recent studies. Indeed, HAP has also recently given promising results for restoring the mechanical integrity of degraded stones^{21–24}. Some studies have examined the possibility to induce the precipitation *in situ* of HAP: the first approach considered is the reaction between a solution of a phosphate precursor, such as Diammonium hydrogen Phosphate (DAP), with the calcium present in the bone²⁵. Unfortunately, the magnesium cation strongly affects the HAP crystallization processes²⁶, and, as in the case of many other ions that are naturally present inside the bone matrix, can influence/inhibit the formation of a crystalline network of HAP.

In recent studies^{27,28}, the possibility to induce the *in-situ* growth of HAP was evaluated by immersing the bone fragments in an aqueous solution of DAP and also adding a dispersion of Ca(OH)₂ nanoparticles in alcohol. Despite the promising results obtained in a recent study²⁸, three main aspects remained to be deeper investigated and possibly solved in the sense of improving performance: (i) no reliable data were achieved about the amount of neo-formed HAP and its possible relationship with the increase of sample compactness (as deduced from BET specific area, porosity, and micro-hardness), (ii) the negative side effect of pre-treating the bone samples by Ca(OH)₂ nanoparticles before DAP solution application, resulting in both reduced mechanical performance and structural compactness with respect to the treatment by only DAP, probably due to the occlusion of surface pores by the Ca(OH)₂, pre-treatment inhibiting the HAP successive formation inside the bulk bone samples, (iii) whereas palaeogenetic analysis was not compromised by this new treatment, no information about ¹⁴C radiocarbon analysis, that is another technique very sensitive to organic treatments, were known, and (iv) the development of a new application method to treat huge and extremely fragile samples, in order to avoid consolidation by soaking. The present paper aims to study these three aspects via a novel approach that follows three innovative research strategies for the four above mentioned points: (i) separately preparing HAP nanoparticles with smaller size than Ca(OH)₂ and applying directly them on the bone samples as the first step of the procedure, (ii) applying the Ca(OH)₂ as second step after the HAP nanoparticles, so that inner pores were already filled by the HAP particles before the DAP solution application that was selected as the last step, (iii) adding to palaeogenetic analysis also the ¹⁴C dating that is well known to be extremely sensitive to organic – traditional – consolidation treatments, and (iv) applying the consolidant system only by brushes to facilitate the treatment of bones even directly on the archeological site. Therefore, the approach was truly multi-disciplinary aimed to evaluate simultaneously the improvement of the nanotechnological approach with respect to the previous work²⁸, and to test the null impact on successive ¹⁴C dating and palaeogenetic analysis²⁹.

The efficacy of the consolidation was examined in terms of the impact of the treatment on the physico-chemical and mechanical properties of the treated bones. Their morphology – homogeneity and surface cohesion –, porosity and micro-hardness were assessed. To investigate the impact of the consolidation treatment on the retrieval of endogenous DNA, we applied biomolecular technologies typically used in the field of ancient DNA (aDNA) to recover the mitochondrial genome (mtDNA) from both treated and untreated fragments deriving from the same bone sample. The genetic results were then compared to spot any significant impact on the quality and reliability of the genetic data. As far as radiocarbon dating is concerned, once pre-screened that the bone samples contain collagene, tests were carried out to determine whether the consolidation treatment might introduce contamination that could not be eliminated by applying the typical procedures used to extract collagen and lately purify it from natural exogenous substances²⁹: to this purpose, both untreated and treated bone samples were dated.

Materials and methods

Chemicals. Calcium nitrate (Ca(NO₃)₂·4H₂O, 99%, Sigma Aldrich), diammonium hydrogen phosphate (NH₄)₂HPO₄, DAP, 98%, Sigma Aldrich), 2-propanol (99.9%, Carlo Erba Reagents) and ethanol (99.2%, Carlo Erba Reagents) were used as received. As HAP standard we use hydroxyapatite nanoparticles purchased from Sigma Aldrich. Highly pure water (having a resistivity of 18 MΩ cm) produced by a Millipore Milli-Q UV system was used during all the experiments.

Synthesis no	Temperature (°C)	pH	Ageing time (min)
1	25	9	60
2	50	9	60
3	25	11	60
4	25	11	30

Table 1. Experimental conditions for the synthesis by chemical precipitation from two aqueous solutions of $\text{Ca}(\text{NO}_3)_2 \cdot 4\text{H}_2\text{O}$ and $(\text{NH}_4)_2\text{HPO}_4$.

Skeletal Materials. The consolidation tests were performed on a set of human long bone fragments from two different archaeological sites (Table S11). Fragments of the same size (of about $4 \times 2 \times 0.5$ cm) were obtained from the diaphysis of each bone. The evaluation of the physico-chemical and mechanical properties, and the palaeogenetic analysis were performed on a set of femurs from Mušov, a Longobard necropolis located in the Czech Republic. From a first macroscopic observation, the bones appeared fragmented and prone to partially break apart when handled. The impact of the treatment on mineral density, porosity and micro-hardness was evaluated on sample Mušov66, while the palaeogenetic analysis was carried out on four different samples (Table S11).

The radiocarbon dating was performed on three femurs from Mušov and an additional humerus from *Porticus Octaviae*, an archaeological site in Rome (Italy) used as a common burial during the Middle Ages (Table S11). In particular, the bone from *Porticus Octaviae* was previously restored using Paraloid B72 as a glue to stick fragments together; the restoration of the skeletal materials from *Porticus Octaviae* was conducted between 2001–2015. This consolidant is well known to be a source of exogenous carbon in radiocarbon dating when the applied collagen extraction procedure just takes possible natural contaminations into account³⁰. In such a situation, to compare the impact of both Paraloid treatment and the consolidation protocol proposed in this study on radiocarbon dating, the analysis was also performed collecting a sample from the restored area.

Synthesis of HAP nanoparticles. The nanoparticles of hydroxyapatite were synthesised by chemical precipitation from two aqueous solutions of calcium nitrate [$[\text{Ca}(\text{NO}_3)_2 \cdot 4\text{H}_2\text{O}]$] and diammonium hydrogen phosphate [$(\text{NH}_4)_2\text{HPO}_4$, DAP], 1 M and 0.6 M, respectively³¹. The concentration was chosen to obtain a Ca:P ratio equal to 1.67^{32,33}, which is the atomic ratio of stoichiometric hydroxyapatite. For the synthesis of nanometric HAP, the DAP solution was put in an ultrasonic bath (Elmasonic S 30H, *Elma*) with a power of 80 W³⁴. Thereafter, the same volume of the $\text{Ca}(\text{NO}_3)_2 \cdot 4\text{H}_2\text{O}$ solution was added in a single quick step. The fast addition of the second precursor is fundamental to induce the formation of a huge number of nuclei at the same time and favour the production of a population of small particles with low polydispersity¹⁸. To study the effects of different experimental conditions on the resulting particles, several syntheses were performed changing step by step a single parameter while maintaining constant the others. The investigated parameters were the temperature (25 and 50 °C; the temperature was maintained constant by using a thermostatic bath), the pH (between 9 and 11), which was adjusted by dripping ammonium hydroxide 2 M in each precursor solution, and the ageing time (between 60 and 30 min). Finally, to avoid any interference of multi-ion doping during the HAP crystals formation, no ions different from that needed for making the HAP synthesis to occur were present. The experimental conditions of each synthesis are resumed in Table 1.

After the reaction, the precipitate was washed six times with ethanol and five times by water and, after each washing, it was separated by centrifugation at 5000 rpm for 5 min using a Centrifugette 4206 (*Thermo Electron Corporation, ALC*). Finally, the particles were dried overnight in an oven at 80 °C. The particles were applied as dispersions in 2-propanol (concentration 1 g/L). Before the application, the dispersions were sonicated in a digital sonifier (S-250D, *Branson*) with a power between 90 and 100 W (that corresponds to an amplitude value equal to 20%) for 1 min.

Bones consolidation. First, the surface of the bone fragments was cleaned by brush to remove dust and soil residues. For each bone, two samples of similar dimensions (of about $4 \times 2 \times 0.5$ cm) were cut from the diaphysis using diamond wheels mounted on a dental device (Marathon-Multi 600 Micromotor): one piece was left untreated (NT samples) and the other one was consolidated (T samples)²⁸, through consequential application by brush of the three following systems:

- a 1 g/L dispersion of HAP nanoparticles in 2-propanol (prior to apply the nanoparticles, the dispersion is sonicated again to flake off possible aggregates³⁵);
- a 0.05 g/L dispersion of $\text{Ca}(\text{OH})_2$ nanoparticles in 2-propanol;
- a 1 M deionized water solution of DAP.

The three above mentioned systems were applied by 10 (HAP), 2 ($\text{Ca}(\text{OH})_2$) and 10 (DAP) brushstrokes. The number of treatments corresponded to the maximum amount of brushstrokes that it was possible to apply without having perceptible color changes to human eye ($\Delta E < 2$); moreover, in order to maximize the physico-chemical compatibility of the consolidation treatment, the amount of applied $\text{Ca}(\text{OH})_2$ nanoparticles was minimized. Each application was carried out only after the complete evaporation of the previously applied solvent from the bone

fragment. After that, samples were maintained at room temperature for one week and then kept for two weeks in a dryer at RH = 75% before evaluation.

Analytical techniques. *Fourier Transform Infrared Spectroscopy Measurements.* Fourier Transform Infrared Spectroscopy (FTIR) spectra were collected to compare the molecular composition of products obtained by the various synthesis protocols. FTIR measurements were performed using a BioRad FTS-40 spectrometer in the range 4000–400 cm^{-1} . Spectra were averages of 64 scans recorded in absorbance mode with 2 cm^{-1} resolution. KBr pellets were prepared by finely grinding and mixing few milligrams of bone powder (1–5 mg) and 200 mg of pure KBr.

X-ray diffraction. Powder X-ray diffraction (XRD) analyses were carried out to define the mineralogical phases obtained by the synthesis. Few milligrams of bone powder were finely ground in a mortar and analysed at the CRIST Centre of the University of Florence (Italy). A Bruker D8 Advance diffractometer equipped with a Cu K α radiation, and a Lynx Eye detector was used operating in θ -2 θ Bragg–Brentano geometry at 40 kV and 40 mA, in the range of 10–60° with a step size of 0.035° and a count time of 0.3 s.

Scanning electron microscope. A FEG-SEM SIGMA (Carl Zeiss, Germany), equipped with a detector INCA X-act (Oxford Instruments) for EDX analysis, was used to collect micrographs of bone samples before and after the consolidation treatment using an acceleration potential of 10 kV and a working distance of 1.4 mm. In addition, dispersions 0.04 g/L of the obtained products in 2-propanol were first ultrasonicated by a digital sonifier at the amplitude of 20% (power between 90 and 100 W) for 1 min, then a droplet of each dispersion was deposited onto a stub and left to dry. Size data used for statistical analysis were extracted from SEM micrographs by using the Image J software.

Turbidimetry measurements. Turbidimetry measurements were performed with a UV–Vis Evolution 220 Spectrophotometer (Thermo Scientific) equipped with a Xenon lamp, measuring the absorbance of the sample at 640 nm as a function of time. At this wavelength, the hydroxyapatite does not show electronic transition phenomena and the absorbance is only due to turbidity phenomena. *Pseudo*-absorbance was assumed proportional to the system turbidity: the decrease of absorbance over time is due to particles sedimentation^{36,37}. The stability of two dispersions of the obtained particles in water and 2-propanol (2 g/L) was evaluated. Every system was sonicated at 20% (power between 90 and 100 W) of amplitude for 1 min and the analysis was performed at room temperature for 2400 s with an interval of 10 s between each measurement.

X-ray microtomography. X-ray microtomography (μ -CT) measurements, that permit to evaluate the penetration capacity of the consolidant and to define the consequent variation of mineral density and porosity of the bone, were carried out with a Skyscan 1172 high-resolution MicoCT system at CRIST Centre, University of Florence (Italy) on a sample of $\sim 10 \times 5 \times 5$ mm. This system has an X-ray tube with a 5 μm focal spot size. The X-rays tube equipped with a tungsten anode was operated at 100 kV and 100 μA . Placing the sample between the X-ray source and the CCD detector, 2D X-ray images were captured over 180-degree rotating sample with a slice-to-slice rotation angle of 0.3. Each 2D image represents one slice and has an acquisition time of approximately 3 s. The spatial resolution of the image was kept in a range of 5 μm in terms of pixel size.

The 3D image was reconstructed from the projections using the Nrecon software (Bruker μ -CT 1.6.10.2), which allows adjusting reconstruction parameters (smoothing, beam-hardening, ring artifact, misalignment compensation). After reconstruction, the image was analysed to obtain information on the bone structure through the CTAnalyser software (Bruker μ -CT 1.18.8.0). A 3D representation in false colour was realized by the CTVox software (Bruker μ -CT 3.3.0) to graphically identify regions with different densities.

Gas porosimetry. Pore size distribution measurements were performed via the N₂ adsorption method using a Beckman Coulter SA-3100 Surface Area analyser. With the 10 points fitting carried out in the linear region of the isotherm it was possible to obtain the specific surface area through Brunauer Emmet and Teller (BET) theory³⁸. The pore size distribution was calculated from the desorption branches of isotherms by means of the Barret, Joyner and Halenda (BJH) method³⁹. The bone samples (0.3–0.4 g of bone fragments of few millimetres) were outgassed before analysis in vacuum conditions at a temperature of 40 °C for 12 h.

Vickers Micro-hardness Measurements. The effect of the consolidation treatment on the mechanical properties of the bones was investigated through Vickers micro-hardness measurements. The measurements were carried out at room temperature through an HX-1000 TM (Remet, Italy) micro-hardness tester using a Vickers square-based diamond pyramid indenter and applying a load of 25 g for 15 s. The images were analysed using Autovickers® software. The data were obtained without any previous preparation of the sample, performing 10 measurements onto the surface, and calculating the corresponding average value and standard deviation.

Palaeogenetic analysis. Treated (T) and untreated (NT) bone fragments from the necropolis of Mušov were processed at the Molecular Anthropology and Palaeogenetics Laboratory of the University of Florence to test whether the consolidation treatment could in any way affect the outcomes of the palaeogenetic analysis.

After the consolidation procedure, both T and NT samples were superficially cleaned by removing ca. 1–2 mm of bone surface using disposable rotary tools mounted on the same dental device previously used to cut the bone fragments. Decontamination of the samples was performed under ultraviolet (UV) light at 254 nm before

proceeding with the collection of approximately 50 mg of bone powder from the inner part of the fragments. DNA was extracted from the bone powder following a protocol commonly used in the field of ancient DNA to optimise the retrieve of short molecules⁴⁰, 20 µL of each extract were converted in double stranded and dual indexed genomic libraries⁴¹. No UDG treatment was performed to preserve nucleotide misincorporation patterns. Libraries were subsequently enriched for mitochondrial genome by applying a capture protocol developed by Maricic and colleagues⁴². Blanks have been included in the experimental steps and processed alongside the samples to trace any possible contamination occurred during the laboratory procedures.

The captured libraries were pooled in equimolar amount and sequenced in paired-end mode on an Illumina MiSeq instrument (2 × 75 + 8 + 8 cycles) for a depth of ~ 1 million reads for sample. Raw reads generated from the sequencing were processed through the EAGER software (v 1.92.55), following a pipeline specifically developed for the analysis of aDNA⁴³. In particular, aDAPter sequences were removed and the merging of paired-end sequencing data with Clip&Merge was performed by retaining only read pairs with a minimum overlap of 10 bp. Moreover, DNA sequences shorter than 30 bp were discarded. After this filtering step, merged reads were mapped against the revised Cambridge Reference Sequence (rCRS [NC_012920.1]) using CircularMapper, a tool specifically designed for mapping against circular genomes. Only reads with a mapping quality > 30 were kept and clonal molecules were removed with DeDup. Afterwards, MapDamage 2.0⁴⁴ was used to check for the presence of typical aDNA damage patterns such as short length of the reads and deamination rates increasing at the ends of the fragments⁴⁵.

Mitochondrial DNA consensus sequence was reconstructed using samtools (v 1.7) in combination with bcftools (v 1.12)^{46,47} and applying a quality filter of at least 30 to retain only high confidence calls. The mtDNA haplogroup was assigned with Mitomaster⁴⁸ and the mitochondrial data was authenticated by estimating the proportion of human endogenous reads using ContamMix⁴⁹.

Furthermore, to prevent our observations from being influenced by potential bias associated with the different number of raw reads generated for each sample, the EAGER pipeline was run again after having down sampled the merged data using seqtk (<https://github.com/lh3/seqtk>). This analysis was carried out only on the two best preserved samples (Mušov66 and Mušov71) and the merged data were down sampled to the lowest number of merged reads observed among the NT and T fragments of the same bone before subsampling.

Radiocarbon dating. After collagen extraction, radiocarbon concentrations in the selected bone samples were measured by Accelerator Mass Spectrometry (AMS), using the dedicated beam line installed at the 3 MV Tandem accelerator in Florence⁵⁰. Collagen was collected from bone powder according to the following procedure, which is intended just to remove contamination due to the natural environment:

- demineralisation at room temperature in 1 M HCl aqueous solution for at least 24 h;
- purification of the extracted material in 0.1 M NaOH aqueous solution for 2 h and possibly in 1 M HCl for 2 h;
- gelatinisation of the residue at pH = 3 in oven at 80 °C.

Carbon was then extracted from the recovered collagen by combustion in a CHN elemental analyser Thermo Flash EA 1112 and lately converted to graphite by reaction with H₂ in presence of Fe as catalyst⁵¹.

¹⁴C/¹²C and ¹³C/¹²C were measured along the AMS beam line to correct for isotopic fractionation. NIST Oxalic Acid II (SRM 4990C) and IAEA C7 were used as primary and secondary standards, respectively. Blank samples, with nominally no ¹⁴C in, were also measured to correct for background counts.

Results and discussion

Characterisation of products. The first aim of this study was the synthesis of very small HAP nanoparticles, to be used as physico-chemically compatible consolidant for degraded bone remains. To maximise the penetration of the HAP nanocrystals into the porous matrix of the bones, it was mandatory to minimise the dimensions of the synthesised objects as much as possible. To optimise the synthesis procedure, the effects of the experimental conditions (such as temperature, pH and stirring procedure) on the composition and the particle size of the products were investigated.

To identify the mineral phase of the obtained products an XRD investigation was carried out (Fig. 1). In particular, the XRD patterns of syntheses 1 and 2 (that were carried out at T = 25 °C and 50 °C respectively and pH = 9 with an ageing time of 60 min, Table 1) indicated respectively the presence of monetite (CaHPO₄, JCPDS no. 9-0080) and brushite (CaHPO₄·2H₂O, JCPDS no. 9-0077) as the main phases. Nevertheless, the data indicate the formation of pure hydroxyapatite from syntheses 3 and 4 (JCPDS no. 9-0432), as it was evident also by comparing the corresponding XRD patterns with the one collected from a sample of standard HAP and as confirmed by the FTIR spectra (Figure S11 and Table S12). This result confirmed what recently found by other Authors⁵² that showed the strong effect of pH (above 11) in determining the formation of HAP; instead of other metastable phases. This result is in contrast with what found when applying DAP on marble, probably since in our case the reaction occurred in homogeneous solution obtaining results in agreement with the data in the literature³³, while in the case of marble the reaction proceeded by an epitaxial mechanism via solid-liquid interface and a too alkaline environment may alter the mutual stability of HAP against metastable phases³⁴. According to the literature^{32,34}, temperature and pH are parameters that strongly affect the mineral phase of the final synthesised product, while the ageing time does not seem to affect the mineral composition. It was interesting to notice that in this study pH = 11 at 25 °C promoted the formation of pure hydroxyapatite. On the contrary, working at pH = 9 at 50 °C and 25 °C induced the selective formation of brushite or monetite (also with the presence of some impurities) respectively, that, in this context, must be considered as undesired products. Nevertheless, these minerals

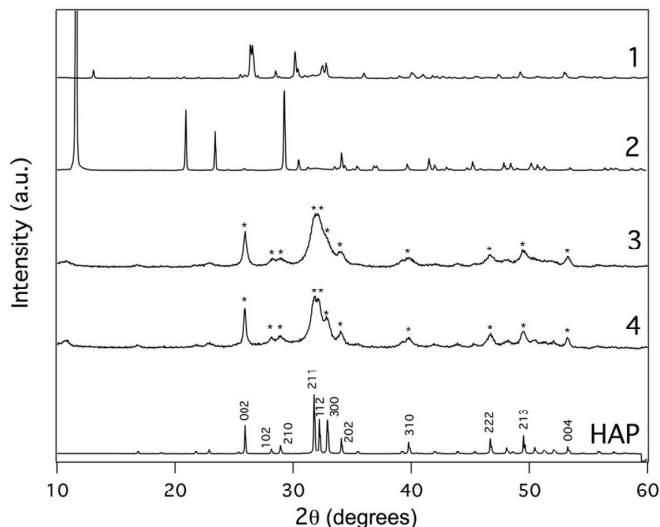


Figure 1. XRD patterns of the particles obtained from the syntheses 1, 2, 3 and 4 and a pattern of HAP standard purchased from Sigma Aldrich. The symbol “*” indicates the typical peaks of hydroxyapatite (JCPDS no. 9–0432).

are used in biomedicine for orthopedic and dental applications, such as bone regeneration, as well as for other biotechnological uses (drug delivery, cancer therapy and biosensing)^{55–57}. Therefore, the development of a new procedure for the synthesis of these nanoparticles based on the improvement of the present results could be an interesting subject for further studies.

To obtain information about the size and the shape of the synthesised HAP particles, SEM analysis was carried out on the products of syntheses 3 and 4 (Figure S12 and Fig. 2). Both the size distribution and the polydispersity (given by the width of the distribution) did not seem to sensibly vary with the ageing time. Moreover, in both cases, HAP particles appeared as pseudo-spherical crystals with dimensions centred at 65–75 nm and ranging in the order of few tens of nanometres. EDX analysis shows that the Ca:P ratio was 1.58 ± 0.05 that, in the limit of the experimental error, is very close to 1.67 (i.e. the stoichiometric HAP Ca:P ratio) suggesting the presence of HAP, as indicated by XRD (Fig. 1). For application purposes, HAP nanoparticles obtained through synthesis 4 were used due to the shorter ageing time. Additional tests suggested that the application of ultra-sonication during the synthesis process reduced both the dimensions of the HAP nanoparticles and their aggregation, since the acoustic cavitation phenomenon, induced during sonication, promoted the formation of a high number of disaggregated HAP nanocrystals (Fig. 2A and B, Figure S12 and S13).

The HAP nanoparticles were applied as dispersions in 2-propanol. The stability of this system was verified through turbidimetry measurements and compared to dispersions in a different solvent like water (Figure S14). This is a key point because the settling process is strictly related to the rate of aggregation of the nanocrystals: as faster is the sedimentation of the nanoparticles, as higher is the aggregation degree that inhibits their penetration into the porous matrix of the bone. The HAP nanoparticles dispersed in 2-propanol resulted stable up to 2500 s, while in water they sedimented after few minutes (Figure S14).

Evaluation of the impact of the consolidation treatment on the physico-chemical and mechanical properties of bone. To evaluate the effectiveness of the consolidation protocol, bone fragments from sample Mušov66 (Table S11) were analysed before (NT) and after (T) the consolidation treatment by using multiple techniques that give complementary information. SEM micrographs showed that before the consolidation the sample surface appeared inhomogeneous and with many cavities and fractures (Fig. 3A), while after the treatment surface morphology was more compact, with an apparent decrease of the fraction of the open pores (Fig. 3B and S15).

Microtomography analysis showed a decrease of less dense regions in favour of denser ones and more compact regions in all the volume of the sample after the consolidation (Fig. 4), thus demonstrating the capacity of this treatment to deeply penetrate the bone matrix. This was also confirmed by the three sections of the 3D reconstruction of the examined bone samples before and after the treatment (Figure S16): it was possible to appreciate an increase of the mineral density in the overall volume of the sample. Therefore, the penetration of the treatment resulted homogeneously distributed inside the bones without forming any crust at the surface layers. Consequently, the porosity decrease was homogeneously distributed over the entire sample volume, and not due to the formation of thick crusts that would be detrimental for treatment efficacy and durability. Moreover, comparing the observed porosity decrease (from 3.84 to 2.25%) with some data reported in the literature for some normal

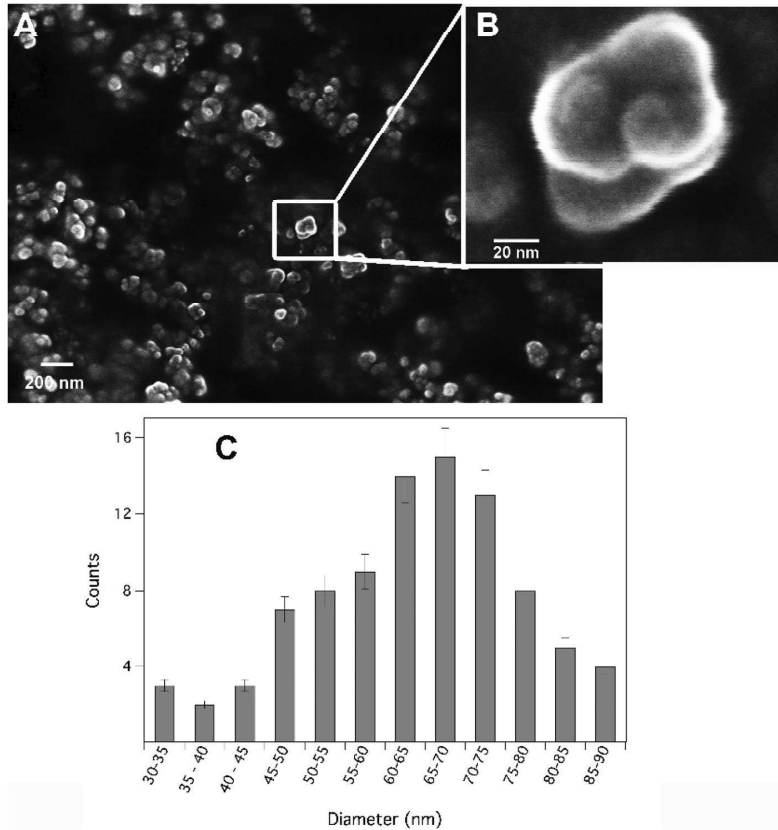


Figure 2. SEM micrographs of HAP nanoparticles obtained from synthesis 4 collected at different magnifications: 10^5 X (A) and 10^6 X (B); (C) size distributions of HAP nanoparticles from synthesis 4 dispersed in 2-propanol obtained by the SEM micrographs and elaborated through ImageJ.

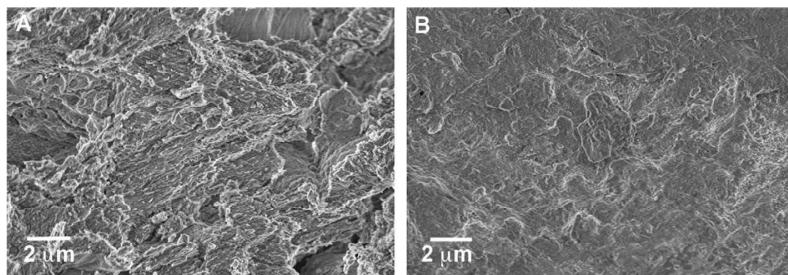


Figure 3. SEM micrographs registered at 10 kx of magnitude of two samples of bone from Mušov66 before (A) and after (B) the consolidation treatment.

bones allows to conclude that the porosity of the treated sample remained in the range of the desired values (1.11–7.01%)⁵⁸. These results confirmed that HAP nanoparticles followed by $\text{Ca}(\text{OH})_2$ nanoparticles and DAP aqueous solution treatment succeeded in being well integrated within the complex bone structure.

The tomography analysis also provides data about the porosity with a diameter over 5 μm (Table SI3), that is correlated to the material real density and to its compactness. After the treatment, a decrement of the total porosity (from 3.84% to 2.25%) and of the open porosity (from 3.48 to 1.31%) was measured in the overall volume of the examined sample, confirming the capacity of the treatment to deeply penetrate the bone matrix. Moreover, the observed increase of the closed porosity, from 0.38% up to 0.96%, cannot be univocally attributed to the conversion of open pores into closed pores. In fact, it was impossible to discriminate between the situation where

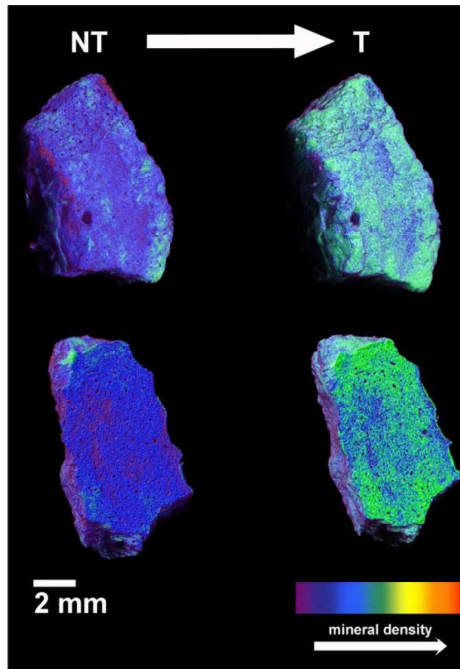


Figure 4. 3D reconstructions in false colour of a bone fragment from the archaeological site of Mušov (Mušov 66) before (left) and after (right) the consolidation treatment: less dense regions (in purple-blue) decrease after the consolidation in favour of a denser phase (in cyan-green). The images represent a side (top) and a section (down) of the sample.

biggest open pores are partially occluded generating new closed pores, or opened pores connected by channels below the detectability threshold. Additional information on the porosity variation detected by gas porosimetry are reported in the SI (Fig. SI7).

An increase in the average value of the Vickers micro-hardness of about 64% (from 56 ± 3 to 92 ± 3) was reported in the consolidated sample. From this standpoint, this datum indicated that the method described here represented an improvement of the procedure reported in a previous paper²⁸. This result can be interpreted in terms of an increase of the mineral density and a decrease of the total porosity of the bone induced by the proposed treatment (Table SI3).

It is worthwhile to underline that this was the first consolidation method for bone remains based on the application of HAP nanocrystals followed by a mixture of $\text{Ca}(\text{OH})_2$ nanoparticles and subsequent DAP aqueous solution. Since the observed results represented truly a significant improvement with respect to the previous approach²⁸ (increase of compactness as deduced from micro-hardness + 64% versus + 42% and + 56%, homogeneous distribution (from μ -CT) of the consolidant within the whole bone sample versus mainly surface consolidation, no negative effects due to pore occlusion by $\text{Ca}(\text{OH})_2$ nanoparticles), it could be interesting to further study why this sequence HAP nanoparticles application, followed by $\text{Ca}(\text{OH})_2$ treatment, and at the end by DAP solution, succeeded in giving such positive results solving the problems encountered in the previous work²⁸. A hypothesis that could be the starting point for a new study could be the following. The HAP nanoparticles act as fillers for the small cavities present within the degraded bone; the subsequent application of the larger $\text{Ca}(\text{OH})_2$ nanoparticles dispersed in 2-propanol followed by an aqueous solution of DAP, leads to the *in-situ* formation of a continuous matrix of HAP and perhaps CaCO_3 that, during crystallisation, both act as binders in a sort of mortar, where the inert phase is now consisted of the previously applied HAP nanoparticles.

Palaeogenetic analysis. To investigate the impact of the consolidation protocol on the yield of human aDNA, the results of the palaeogenetic analysis from treated and untreated fragments were compared. The reconstruction of the complete mitochondrial genome from both T and NT fragments was successful only for two out of four individuals (Mušov66 and Mušov71) due to lower DNA preservation in the remaining samples (Mušov65 and Mušov73b) (Table 2, Table SI4). Indeed, we found that Mušov65 exhibits a very low preservation of endogenous DNA and returned very low-quality data in both T and NT fragments that precludes meaningful comparison. With the exception of Mušov66, the percentage of endogenous DNA slightly decreased in the consolidated fragments with respect to the corresponding untreated ones. Mušov73b showed the largest decrease, with an amount of endogenous DNA of 5.84% in the untreated sample and of 1.20% in the treated one. The same trend was also detected when considering the mean coverage, which corresponds to the average number

Sample Name	Endogenous DNA (%)	Mean Coverage (X)	Coverage $\geq 1X$ (%)	Coverage $\geq 5X$ (%)	Missing position in the consensus sequence	DMG 1st base 3'	DMG 1st base 5'	Average fragment length (bp)	Proportion of authentic reads (%)—ContamMix	mtDNA haplogroup	# of variants
Mušov65-NT	1.49	1.21	65.08	2	5887	0.32	0.38	49.08	99.43	T2	17
Mušov65-T	0.66	0.42	31.35	0	11.461	0.43	0.25	45.56	96.69	–	1
Mušov66-NT	16.93	24.95	100	99.89	2	0.32	0.31	50.97	98.83	T2e	36
Mušov66-T	22.56	33.83	100	99.91	1	0.29	0.32	51.73	99.97	T2e	35
Mušov71-NT	5.13	11.21	100	95.30	3	0.34	0.35	49.45	99.29	H1c1	11
Mušov71-T	4.54	8.32	99.96	87.08	11	0.33	0.35	51.55	99.69	H1c1	12
Mušov73b-NT	5.84	6.08	99.50	67.31	103	0.38	0.36	49.79	99.81	H1c1	14
Mušov73b-T	1.20	0.43	34.79	0	10.850	0.36	0.29	46.20	98.40	–	3

Table 2. Results of the analysis performed on the mitochondrial DNA recovered from the untreated (NT) and treated (T) bone samples coming from the Longobard site of Mušov.

of unique DNA sequences covering each position of the reference genome. In Mušov66 the mean coverage was slightly higher in the consolidated fragment (33.83X) than in the untreated one (24.95X), while the depth of coverage decreased in the consolidated fragments of the other samples with Mušov73b showing the most detrimental impact (from 6.08X to 0.43X in consolidated and untreated fragments respectively).

These observations were also confirmed by the onefold and fivefold mitogenome coverage parameters, representing the percentage of mitochondrial genome positions covered by at least 1 and 5 reads, respectively. Over 99% of the mitochondrial genome of both Mušov66-T and Mušov66-NT was covered at least fivefold. At the same coverage good percentages were also observed for Mušov71-T (95.30%), Mušov71-NT (87.08%) and Mušov73b-NT (67.31%), while no data was available for the remaining analysed samples. On the contrary, the low percentages of mitochondrial genome covered at least onefold in Mušov73b-T (34.79%), as well as in Mušov65-NT (65.08%) and Mušov65-T (31.35%), indicated that a large portion of the mitochondrial genome is missing. Starting from the reconstructed consensus sequence, it was possible to determine the mitochondrial haplogroup from both T and NT fragments only in the case of Mušov66 and Mušov71. For each individual both fragments returned exactly the same mtDNA haplogroup and the same variants with respect to the reference sequence (rCRS) except a single position in a homopolymeric C-stretch, proving that the consolidation procedure did not affect the reliability of the results in the samples exhibiting a degree of DNA preservation suitable for palaeogenetic analysis. However, the accurate determination of the mitochondrial haplogroup from the consolidated samples Mušov65-T and Mušov73b-T was not possible due to the high number of missing positions in the consensus sequence (more than 10.000 missing positions out of a total mtDNA length of 16.569 bp). Instead, haplogroup identification was successfully performed from the untreated fragments despite the presence of several missing positions in the consensus sequence of Mušov65-NT. The full analyses repeated after performing the down sampling on the two best preserved samples Mušov66 and Mušov71 confirm the observations reported so far, excluding any possible bias in the interpretation of the results associated with the different number of raw reads generated by sequencing (Table S15).

For what concerns the assessment of the damage patterns, no relevant variation was detected between treated and untreated samples in terms of deamination rates (namely, proportion of damaged cytosine at both 5' and 3' ends of DNA molecules) and average fragment length, which were both in line with values expected for degraded ancient DNA samples. The results of the ContamMix test showed very similar proportion of authentic reads in both consolidated and untreated samples, demonstrating that no significant contamination with modern DNA was introduced by applying the treatment. The slight decrease in the percentage of authentic reads observed for Mušov65-T and of Mušov73b-T was likely to derive from the low amount of mtDNA retrieved from these samples, which surely represents a limiting factor for the analysis. In fact, the software was not able for these two samples, as well as for Mušov65-NT, to calculate a precise estimate of the percentage of authentic reads, as can be noticed considering the wide distribution obtained in a 95% confidence interval (Table S14).

Despite the high variability within the samples, the overall result may suggest that consolidation protocol does not significantly affect the quality of the genetic data in adequately well-preserved samples, where the same consensus sequences was obtained from both treated and untreated fragments. On the contrary, the consolidation treatment seems to potentially affect the yield of the palaeogenetic analysis when applied on specimens with particularly scarce DNA preservation. Additional bones with different conservation conditions need to be tested to confirm this hypothesis.

Radiocarbon analysis. Table 3 shows the AMS radiocarbon results: for each of the bones, the radiocarbon concentrations measured in the untreated (NT) and in the HAP treated (T) fractions are compared. In the case of the sample from *Porticus Octaviae* (P.O.us898), the radiocarbon concentration measured in a Paraloid-treated sample is also reported.

The comparison of the NT data with the T data showed that no contamination due to the HAP treatment was detected. Indeed, both T and NT fractions, as well as P.O.us898 Paraloid-treated sample, were prepared for the ^{14}C measurement following the aforementioned procedure based on HCl and NaOH solutions, that are meant

	NT	T	Paraloid-T
	¹⁴ C conc. (pMC)	¹⁴ C conc. (pMC)	¹⁴ C conc. (pMC)
Mušov65	83.74 ± 0.69	82.71 ± 0.44	
Mušov66	83.03 ± 0.35	82.81 ± 0.47	
Mušov73b	82.75 ± 0.34	82.58 ± 0.51	
P.O.us898	88.25 ± 0.40	88.42 ± 0.22	82.95 ± 0.54

Table 3. ¹⁴C-AMS results: radiocarbon concentrations measured in untreated (NT) and HAP treated (T) fractions. In the case of the sample from Porticus Octaviae (P.O.us898), the radiocarbon concentration measured in a Paraloid-treated sample is also reported.

to achieve the complete demineralisation of the bone and its purification from natural humic substances but are likely to have a poor effect on anthropogenic contaminations. The consolidation by HAP treatment thus appeared as a safe operation, which can assure good radiocarbon results also in those cases when no information about previous restorations has been given to the dating laboratory. In fact, the applied preparation procedure is basically the standard approach for any bone sample collected from an archaeological context before radiocarbon dating.

In the case of the P.O.us898 Paraloid-treated sample, a lower concentration than the one observed in the corresponding NT fraction was measured. This was somehow expected, since Paraloid is typically synthesised from low-¹⁴C materials (i.e., materials rich in fossil carbon whose radiocarbon concentration is well below the sensitivity limits of the measurement technique), and it cannot be removed by just applying the acidic and basic solutions used in the preparation procedure described above. However, some preparation strategies exploiting organic volatile solvents can be used to get rid of such a contamination, even though these procedures are more time consuming and challenging.

Conclusions

In this study, we set up an innovative and easily applicable protocol for the consolidation of ancient bones based on the use of inorganic nanostructured materials with high physico-chemical compatibility with the bone matrix. The goal was to recover mechanical properties lost due to the damages induced by interactions with the external that cause an increase of the porosity and a consequent decrease of density and mechanical resistance. We also aimed at defining a consolidation protocol that did not compromise the results of molecular analyses, such as ¹⁴C radiocarbon dating and palaeogenetic analysis, that can be carried out on archaeological and historical bone remains.

Our results suggest the availability of an easy and low-cost method that will be implemented for production on a large scale in further studies, also in the view of evaluating the use of these products for other applications (i.e. in the biomedical field).

From the physico-chemical standpoint, several analytic tests proved the effectiveness of the proposed consolidation protocol. SEM data indicated an increase of the homogeneity of the structure of the bone induced by the consolidation treatment. These data were confirmed by microtomography, which showed an increase of the density and a decrease of the total porosity of the treated bones, not only on the surface of the samples, but also in the bulk of the porous network of the bone, indicating a deep penetration of the treatment. In addition, the increment of the Vicker micro-hardness also confirmed the improvement of the physical-mechanical properties of the consolidated bones. All the results evidenced that the four main open points derived from a previous work²⁸ were cleared and the new methodology revealed itself original, novel, and improved.

One of the key features of this work is the evaluation of the impact of the proposed protocol on the results of two analyses typically performed on ancient bone remains, namely palaeogenetic analysis and radiocarbon dating. In agreement with the results of a previous study based on a similar approach²⁸, mitogenome reconstruction from both untreated and consolidated bone fragments have shown that the consolidation protocol does not significantly affect the quality of the genetic results in bones with adequate DNA preservation. However, we noticed that the treatment might have a negative impact on the endogenous DNA yield and on subsequent genetic results when applied on samples with a particularly poor amount of preserved genetic material (such as Mušov65 and Mušov73b). Although additional tests on a larger set of bones with different conservation conditions need to be carried out to better address this issue, we caution to apply the consolidation protocol here developed on bone fragments that could represent unique remains. It is worthwhile to specify that, at the state of the art, palaeogenetic analyses are preferably performed on the petrous part of the temporal bones rather than long bones because endogenous DNA is known to be much better preserved and protected from exogenous contamination in that skeletal element⁵⁹. Therefore, the evidence of a potential negative influence of the consolidant on extremely degraded long bones (that could benefit from this treatment) does not exclude the possibility of carrying on palaeogenetic analysis on other skeletal districts, such as the petrous bone, when available for study. The evaluation of the impact of consolidation on radiocarbon dating represents one of the most important novelty of this study. The results have shown that no contamination due to the HAP treatment is detected, thus avoiding the need for time-consuming decontamination protocols during sample preparation.

In conclusion, the protocol developed in this study offers a more compatible alternative to traditional consolidation based on organic polymers and to inorganic treatments reported in previous studies. Even if additional studies will be necessary to improve the applicative procedures, the treatment is easily-applicable and compatible with different molecular analyses. Such exhaustive and informative evaluation of the performance and the

effects of the proposed consolidation protocol was achieved integrating expertises from different scientific fields, showing the benefit of a multidisciplinary approach to face problems and individuate effective solutions in the field of cultural heritage conservation.

Received: 22 December 2021; Accepted: 12 April 2022

Published online: 28 April 2022

References

- Green, R. *et al.* A draft sequence of the Neandertal genome. *Science* **328**(5979), 710–722 (2010).
- Hublin, J. *et al.* Radiocarbon dates from the Grotte du Renne and Saint-Césaire support a Neandertal origin for the Châtelperronian. *PNAS* **109**(46), 18743–18748 (2012).
- Sankararaman, S. *et al.* The genomic landscape of Neanderthal ancestry in present-day humans. *Nature* **507**, 354–357 (2014).
- Fu, Q. *et al.* The genetic history of Ice Age Europe. *Nature* **543**, 200–205 (2016).
- Marciniak, S. & Perry, G. Harnessing ancient genomes to study the history of human adaptation. *Nat. Rev. Genet.* **18**, 659–674 (2017).
- Spyrou, M., Tukhbatova, R., Wang, C., Valtueña, A., Lankapalli, A., Kondrashin, V., Tsybin, V., Khokhlov, A., Kühnert, D., Herbig, A., Bos, K., & Krause, J. Analysis of 3800-year-old *Yersinia pestis* genomes suggests Bronze Age origin for bubonic plague. *Nature Communications*, vol. 9, no. 2234, (2018).
- Douka, K. *et al.* Age estimates for hominin fossils and the onset of the Upper Palaeolithic at Denisova Cave. *Nature* **565**, 640–644 (2019).
- Steele, T. The contributions of animal bones from archaeological sites: the past and future of zooarchaeology. *J. Archaeol. Sci.* **56**, 168–176 (2015).
- Frantz, L. *et al.* Genomic and archaeological evidence suggest a dual origin of domestic dogs. *Science* **352**(6290), 1228–1231 (2016).
- A. Caliebe, A. Nebel, C. Makarewicz, M. Krawczak and B. Krause-Kyora, “Insights into early pig domestication provided by ancient DNA analysis,” *Scientific Reports*, vol. 7, no. 44550, 2017.
- F. Boschini, F. Bernardini, E. Pilli, S. Vai, C. Zanolli, A. Tagliacozzo, R. Fico, M. Fedi, J. Corny, D. Dreossi, M. Lari, A. Modi, C. Vergata, C. Tuniz, A. Moroni and e. al., “The first evidence for Late Pleistocene dogs in Italy,” *Scientific Reports*, vol. 10, no. 13313, 2020.
- Figuciredo, M., Gamelas, J. & Martins, A. Characterization of bone and bone-based graft materials using FTIR spectroscopy. In *Infrared Spectroscopy - Life and Biomedical Science* (ed. Theophile, T.) 315–338 (IntechOpen, London, 2012).
- Nielsen-Marsh, C. & Hedges, R. Pattern of diagenesis in bone I: the effects of site environments. *J. Archaeol. Sci.* **27**, 1139–1150 (2000).
- Hedges, R. Bone Diagenesis: an overview of processes. *Archaeometry* **44**(3), 319–328 (2002).
- Kendall, C., Eriksen, A. M. H., Kontopoulos, I. & Collins, M. J. Diagenesis of archaeological bone and tooth. *Palaeogeogr. Palaeoclimatol. Palaeoecol.* **491**, 21–37 (2018).
- Johnson, J. Consolidation of archaeological bone: a conservation perspective. *J. Field Archaeol.* **21**(2), 221–233 (1994).
- López-Polin, L. Possible interferences of some conservation treatments with subsequent studies on fossil bones: a conservator’s overview. *Quat. Int.* **275**, 120–127 (2012).
- Baglioni, P. & Chelazzi, D. *Nanoscience for the conservation of works of art* (RSC Publishing, 2013).
- Baglioni, P., Chelazzi, D. & Giorgi, R. *Nanotechnologies in the Conservation of Cultural Heritage A compendium of materials and techniques* (Springer, Dordrecht, 2015).
- Natali, I. *et al.* Aragonite Crystals grown on bones by reaction of CO₂ with nanostructured Ca(OH)₂ in the Presence of Collagen. Implication in Archeology and Paleontology. *Langmuir* **30**(2), 660–668 (2014).
- Sassoni, E., Naidu, S. & Scherer, G. The use of hydroxyapatite as a new inorganic consolidant for damaged carbonated stones. *J. Cult. Herit.* **12**, 346–355 (2011).
- Matteini, M., Rescic, S., Fratini, F. & Botticelli, G. Ammonium phosphates as consolidating agents for carbonatic stone materials used in architecture and cultural heritage: preliminary research. *Int. J. Archit. Heritage* **5**(6), 717–736 (2011).
- Balonis, M., Ma, X. & Kakoulli, I. Preliminary Results on biomimetic methods based on soluble ammonium phosphate precursors for the consolidation of archaeological wall paintings. In *Archeological Chemistry VIII, vol. 1147, ACS Symposium Series*, 419–447 (Washington DC, American Chemical Society, 2013)
- Sassoni, E. Hydroxyapatite and other calcium phosphates for the conservation of cultural heritage: a review. *Materials* **11**, 557 (2018).
- North, A., Balonis, M. & Kakoulli, I. Biomimetic hydroxyapatite as a new consolidating agent for archaeological bone. *Stud. Conserv.* **61**(3), 146–161 (2016).
- Bigi, A. *et al.* Magnesium influence on hydroxyapatite crystallization. *J. Inorg. Biochem.* **49**, 69–78 (1993).
- Yang, F. *et al.* Conservation of bone relics using hydroxyapatite as protective material. *Appl. Phys. A* **122**, 479 (2016).
- Salvatore, A. *et al.* Evaluation of Diammonium hydrogen phosphate and Ca(OH)₂ nanoparticles for consolidation of ancient bones. *J. Cult. Herit.* **41**, 1–12 (2019).
- Longin, R. New method of collagen extraction for radiocarbon dating. *Nature* **230**, 241–242 (1971).
- Liccioli, L., Fedi, M., Carresi, L. & Mandò, P. Characterization of the chloroform-based pretreatment method for 14C dating of restored wooden samples. *Radiocarbon* **59**, 757–764 (2017).
- Subramanian, R., Sathish, S., Murugan, P., Mohamed Musthafa, A. & Elango, M. Effect of piperine on size, shape and morphology of hydroxyapatite nanoparticles synthesized by the chemical precipitation method. *J. King Saud Univ. Sci.* **31**, 667–673 (2019).
- Mansour, S., El-dek, S., Ahmed, M., Abd-Elwahab, S. & Ahmed, M. Effect of preparation conditions on the nanostructure of hydroxyapatite and brushite phases. *Appl. Nanosci. (Switzerland)* **6**(7), 991–1000 (2016).
- Cengiz, B., Gokce, Y., Yildiz, N., Aktas, Z. & Calimli, A. Synthesis and characterization of hydroxyapatite nanoparticles. *Colloids Surf. A* **332**(1–3), 29–33 (2008).
- Rouhani, P., Taghavinia, N. & Rouhani, S. Rapid growth of hydroxyapatite nanoparticles using ultrasonic irradiation. *Ultrason. Sonochem.* **17**(5), 853–856 (2010).
- Salvadori, B. D. L. Synthesis of Ca(OH)₂ nanoparticles from diols. *Langmuir* **17**(8), 2371–2374 (2001).
- Carretti, E. *et al.* Interactions between nanostructured calcium hydroxide and acrylate copolymers: implications in cultural heritage conservation. *Langmuir* **29**, 9881–9890 (2013).
- Giorgi, R., Luigi, D. & Baglioni, P. A new method for consolidating wall paintings based on dispersions of lime in alcohol. *Stud. Conserv.* **3**(45), 154–161 (2000).
- Brunauer, S., Emmett, P. & Teller, E. Adsorption of gases in multimolecular layers. *J. Am. Chem. Soc.* **60**(2), 309–319 (1938).
- Barrett, E., Joyner, L. & Halenda, P. The determination of pore volume and area distributions in porous substances. I. Computations from nitrogen isotherms. *J. Am. Chem. Soc.* **1**(73), 373–380 (1951).
- Dabney, J. *et al.* Complete mitochondrial genome sequence of a Middle Pleistocene cave bear reconstructed from ultrashort DNA fragments. *Proc. Natl. Acad. Sci.* **110**, 15758–15763 (2013).

41. Meyer, M. & Kircher, M. Illumina sequencing library preparation for highly multiplexed target capture and sequencing. *Cold Spring Harbor Protocols* 6, 2010.
42. Maricic, T., Whitten, M. & Paabo, S. Multiplexed DNA sequence capture of mitochondrial genomes using PCR products. *PLoS ONE* 5(11), e14004 (2010).
43. Peltzer, A. *et al.* EAGER: efficient ancient genome reconstruction. *Genome Biol.* 17, 60–74 (2016).
44. Jönsson, H., Ginolhac, A., Schubert, M., Johnson, P. & Orlando, L. Map-Damage2.0: fast approximate Bayesian estimates of ancient DNA damage parameters. *Bioinformatics* 29, 1682–1684 (2013).
45. Dabney, J. & Meyer, M. P. S. Ancient DNA damage. *Cold Spring Harb Perspect Biol.* 5, a012567 (2013).
46. Li, H., Handsaker, B., Wysoker, A. & Fennell, T. 1000 Genome project data processing subgroup. The sequence Alignment/Map format and SAMtools. *Bioinformatics* 25, 2078–2079 (2009).
47. Danecek, P., Bonfield, J., Liddle, J., Marshall, J., Ohan, V., Pollard, M., Whitwham, A., Keane, T., McCarthy, S., Davies, R. & Li, H. Twelve years of SAMtools and BCFtools. *GigaScience*, vol. 10(2), (2021).
48. Lott, M. T. *et al.* mtDNA variation and analysis using MITOMAP and MITOMASTER. *Curr. Protoc. Bioinform.* 44, 23–26 (2013).
49. Fu, Q. *et al.* A revised timescale for human evolution based on ancient mitochondrial genomes. *Curr. Biol.* 23, 553–559 (2013).
50. Fedi, M., Cartocci, A., Manetti, M., Taccetti, F. & Mandò, P. The ¹⁴C AMS facility at LABEC, Florence. *Nucl. Instrum. Methods Phys. Res. Sect. B* 259, 18–22 (2007).
51. Vogel, J., Southon, J., Nelson, D. & Brown, T. Performance of catalytically condensed carbon for use in accelerator mass spectrometry. *Nucl. Instrum. Methods Phys. Res. Sect. B* 5(2), 289–293 (1984).
52. Montes-Hernandez, G. & Renard, F. Nucleation of Brushite and Hydroxyapatite from amorphous calcium phosphate phases revealed by dynamic in situ raman spectroscopy. *J. Phys. Chem. C Am. Chem. Soc.* 28(124), 15302–15311 (2020).
53. Chuprunov, K., Yudin, A., Lysov, D., Kolesnikov, E., Kuznetsov, D., Leybo, D. The pH level influence on hydroxyapatite phase composition synthesized with hydrothermal method. In *OP Conf. Series: Materials Science and Engineering*, vol. 731, 012023 (2020).
54. Naidu, S. & Scherer, G. Nucleation, growth and evolution of calcium phosphate films on calcite. *J. Colloid Interface Sci.* 435, 128–137 (2014).
55. Tamimi, F., Sheikh, Z. & Barralet, J. Dicalcium phosphate cements: Brushite and monetite. *Acta Biomater.* 8(2), 474–487 (2012).
56. Motamenia, A., Alshemary, A. & Evis, Z. A review of synthesis methods, properties and use of monetite cements as filler for bone defects. *Ceram. Int.* 47(10), 13245–13256 (2021).
57. Nasrollahi, N., Dehkordi, A., Jamshidizad, A. & Chehelgerdi, M. Preparation of brushite cements with improved properties by adding graphene oxide. *Int. J. Nanomed.* 14, 3785–3797 (2019).
58. Renders, G., Mulder, L., van Ruijven, L. & van Eijden, T. Porosity of human mandibular condylar bone. *J. Anat.* 210(3), 239–248 (2007).
59. Pinhasi, R. *et al.* Optimal ancient DNA yields from the inner ear part of the human petrous bone. *PLoS ONE* 10(6), e0129102 (2015).

Acknowledgements

Thanks are due to Dr. Z. Loskotová who provided the human skeletal remains and archaeological information for the necropolis of Mušov, to Dr. P. Ciancio Rossetto (Soprintendenza ai Beni Culturali of Rome) and to Prof. J. Moggi Cecchi for facilitating access to the skeletal materials of the medieval cemetery in the area of *Porticus Octaviae*.

Author contributions

M.L. and E.C. conceived the study; F.P., V.Z., L.L., A.Me., G.M., S.B. and A.Mo. performed lab work; F.P., V.Z., L.L. and A.Mo. analyzed data; M.F., M.L. and E.C. supervised the study; S.V., L.D. and D.C. contributed tools, materials and reagents; F.P., V.Z., L.L., A. Mo., L.D., M.F., M.L. and E.C. wrote the paper with the input of all co-authors.

Funding

This work has been funded by University of Florence (“Bando di Ateneo per il finanziamento di progetti competitivi per Ricercatori a Tempo Determinato” of the University of Florence - Year 2016) and by the Italian Ministry of Education, University and Research (Project Dipartimenti di Eccellenza 2018–2022, PRIN2017 Grants No. 20177PJ9XF and 20174BTC4R).

Competing interests

The authors declare no competing interests.

Additional information

Supplementary Information The online version contains supplementary material available at <https://doi.org/10.1038/s41598-022-10798-5>.

Correspondence and requests for materials should be addressed to M.F., M.L. or E.C.

Reprints and permissions information is available at www.nature.com/reprints.

Publisher's note Springer Nature remains neutral with regard to jurisdictional claims in published maps and institutional affiliations.



Open Access This article is licensed under a Creative Commons Attribution 4.0 International License, which permits use, sharing, adaptation, distribution and reproduction in any medium or format, as long as you give appropriate credit to the original author(s) and the source, provide a link to the Creative Commons licence, and indicate if changes were made. The images or other third party material in this article are included in the article's Creative Commons licence, unless indicated otherwise in a credit line to the material. If material is not included in the article's Creative Commons licence and your intended use is not permitted by statutory regulation or exceeds the permitted use, you will need to obtain permission directly from the copyright holder. To view a copy of this licence, visit <http://creativecommons.org/licenses/by/4.0/>.

© The Author(s) 2022

SUPPORTING INFORMATION

Performance of innovative nanomaterials for bone remains consolidation and effect
on ¹⁴C dating and on palaeogenetic analysis

Francesca Porpora¹, Valentina Zaro², Lucia Liccioli³, Arianna Meoli¹, Giulia Marradi¹, Serena Barone³, Alessandra Modi², Stefania Vai², Luigi Dei¹, David Caramelli², Mariaelena Fedi³, Martina Lari², Emiliano Carretti¹

¹*Department of Chemistry “Ugo Schiff” and CSGI, University of Florence, Via della Lastruccia 3, 50019, Sesto Fiorentino, FI, Italy*

²*University of Florence, Department of Biology, via del Proconsolo 12, 50122 Firenze, Italy*

³*INFN (Istituto Nazionale di Fisica Nucleare) Sezione di Firenze, Via Sansone 1, 50019, Sesto Fiorentino, FI, Italy*

1. Skeletal materials

Table S11. Human bone remains selected for the evaluation of the consolidation treatment.

Sample code	Archeological site	Bone district	Analyses		
			Physico-chemical	Paleogenetical	Radiocarbon dating
Mušov65	Mušov (Czech Republic)	Femur		X	X
Mušov66	Mušov (Czech Republic)	Femur	X	X	X
Mušov71	Mušov (Czech Republic)	Femur		X	
Mušov73b	Mušov (Czech Republic)	Femur		X	X
P.O.us898	Porticus Octaviae (Italy) ¹	Humerus			X

2. Characterization of products

The chemical nature of the synthesized materials has been investigated also through FTIR that has been carried out on all the powders in transmittance mode in the range 4000-400 cm^{-1} (Fig. SIIA). In particular, a weak peak associated with the P-O symmetric stretching is visible at $\sim 996 \text{ cm}^{-1}$ and 982 cm^{-1} for samples obtained from syntheses 1 and 2 respectively, and at 962 cm^{-1} for syntheses 3 and 4. The position of this peak allows discriminating between the phases formed through the different syntheses procedures. In fact, as reported in literature, while the peak at 962 cm^{-1} is characteristic of hydroxyapatite, the band at $\sim 995 \text{ cm}^{-1}$ and at $\sim 985 \text{ cm}^{-1}$ are typical of monetite and brushite respectively [1] (Fig. SII B), preliminarily indicating that only through syntheses 3 and 4 hydroxyapatite is formed selectively. All the spectra show the typical bands of calcium phosphate, that are listed in Table SII with the corresponding attributions [2, 3, 4, 5].

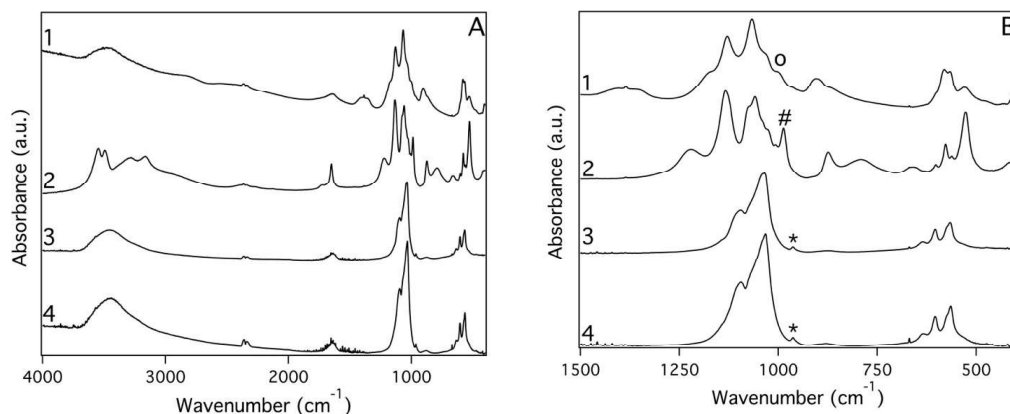


Figure SII. (A) FTIR spectra ($4000\text{-}400 \text{ cm}^{-1}$) of calcium phosphates obtained from syntheses indicated in Table 1. (B) FTIR spectra ($1500\text{-}400 \text{ cm}^{-1}$). The symbols indicate the peak associated with the P-O symmetric stretching at 960 and 964 cm^{-1} (*), which is typical for hydroxyapatite; when the peak is shifted to 996 cm^{-1} (°) and 982 cm^{-1} (#), it points to the presence of monetite and brushite, respectively.

ù

Table SI2. Wavenumbers for functional groups of the particles obtained from syntheses 1-4 (cm^{-1}).

Samples				Assignment
1	2	3	4	
Wavenumber (cm^{-1})				
	3542			ν OH
	3491			ν OH
3460		3566	3566	ν OH
	3285			ν OH
3209				ν OH
	3162			ν OH
2803				ν OH
	1724			δ OH ⁻
1641	1650	1641	1646	δ OH ⁻
1384			1456	ν_{as} CO ₃ ²⁻ / δ HPO ₄ ²⁻
1185	1222			δ HPO ₄ ²⁻
1128	1131			ν HPO ₄ ²⁻
1064	1060	1097	1093	ν_{as} PO ₄ ³⁻
1031	1027	1037	1031	ν_{as} PO ₄ ³⁻
	1004			ν PO ₄ ³⁻
996	982	960	964	ν PO ₄ ³⁻
900	872			δ CO ₃ ²⁻ / ν HPO ₄ ²⁻
	789			OH ⁻ (libration)
	660	660	668	CO ₂
		636	633	OH ⁻ (libration)
	602	602	602	δ PO ₄ ³⁻
580	576			δ PO ₄ ³⁻
564	564	564	564	δ PO ₄ ³⁻
527	523			δ PO ₄ ³⁻
404	408			δ PO ₄ ³⁻

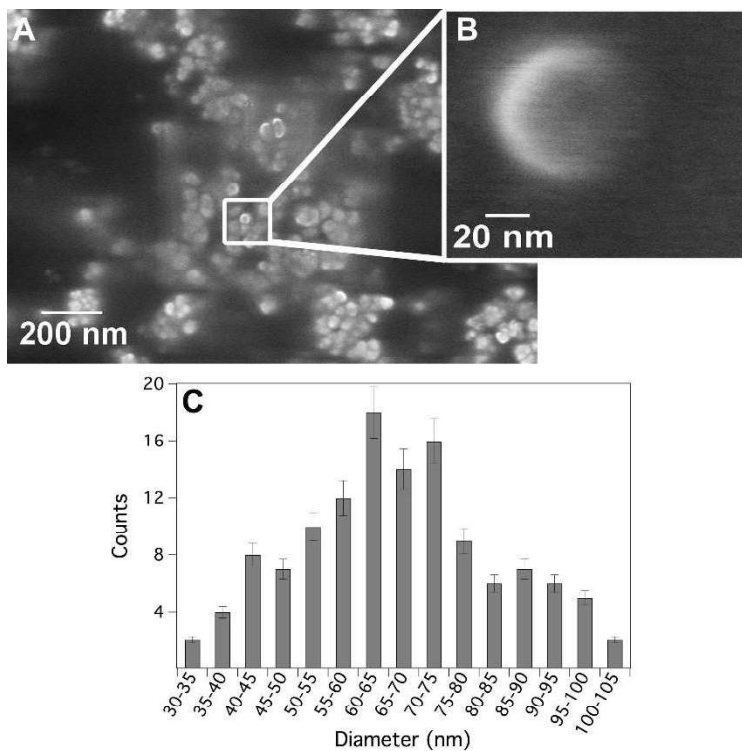


Figure SI2. SEM micrographs of HAP nanoparticles obtained from synthesis 3 collected at different magnifications: 10^5 X (A) and 10^6 X (B); (C) size distributions of HAP nanoparticles from synthesis 3 obtained by the SEM micrographs and elaborated through ImageJ.

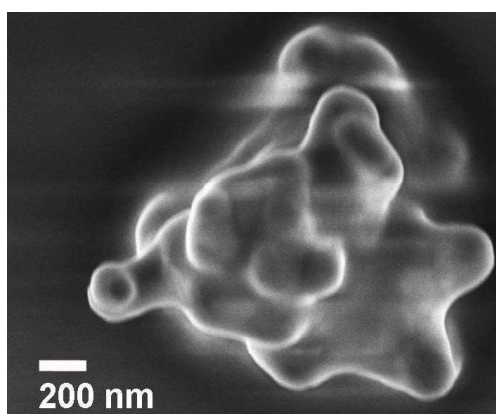


Figure SI3. SEM micrograph registered at 100 kx of magnitude of an agglomerate of HAP particles obtained under the same conditions of synthesis 4 (Table 1) but in the absence of the ultrasonic bath.

The stability of the dispersions of HAP nanoparticles in 2-propanol was evaluated through turbidimetry measurements (Figure SI4). Comparing them to dispersions in a different solvent like water. This is a key point because the settling process is strictly related to the rate of aggregation of the nanocrystals: as faster is the sedimentation of the nanoparticles, as higher is the aggregation degree that inhibits their penetration into the porous matrix of the bone. From Figure SI4A, it is evident that HAP nanoparticles dispersed in 2-propanol result stable up to 2500 s, while in water they sediment after few minutes.

From a qualitative observation of the two dispersions in water and in 2-propanol (Fig. SI4B), the one in 2-propanol seems to be still stable even after five hours indicating a low tendency to the aggregation of the HAP nanoparticles dispersed in this solvent. Because of similar polarity, this behavior is probably comparable to that shown by analogous dispersions of $\text{Ca}(\text{OH})_2$ nanoparticles [6]. The water molecules interact with the phosphate groups of the HAP nanoparticles and intercalate between them through the formation of hydrogen bonds, promoting their aggregation. On the contrary, in 2-propanol, hydroxyl groups are absorbed on the surface of the nanoparticles and the aggregation is inhibited thanks to the low interaction between the short aliphatic chains.

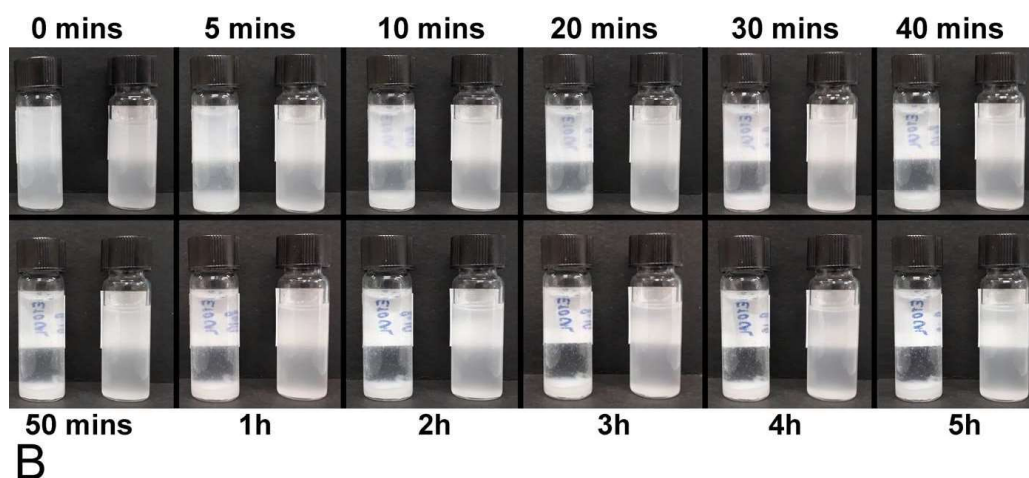
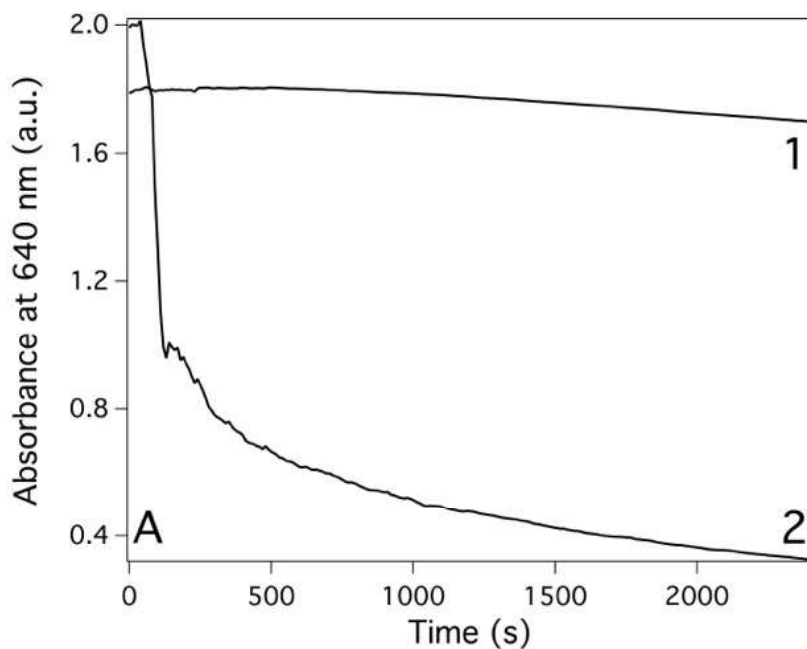


Figure SI4. (A) Absorbance at 640 nm as a function of time for HAP nanoparticles from synthesis 4 dispersed in 2-propanol (1) and water (2); (B) Stability of the HAP nanoparticles from synthesis 4 dispersed in water (left) and 2-propanol (right) between 0 and 5 hours. While nanoparticles dispersed in water start to sediment after few minutes, those dispersed in 2-propanol appear still stable even after five hours.

3. Evaluation of the impact of the consolidation treatment on the physico-chemical and mechanical properties of the bone

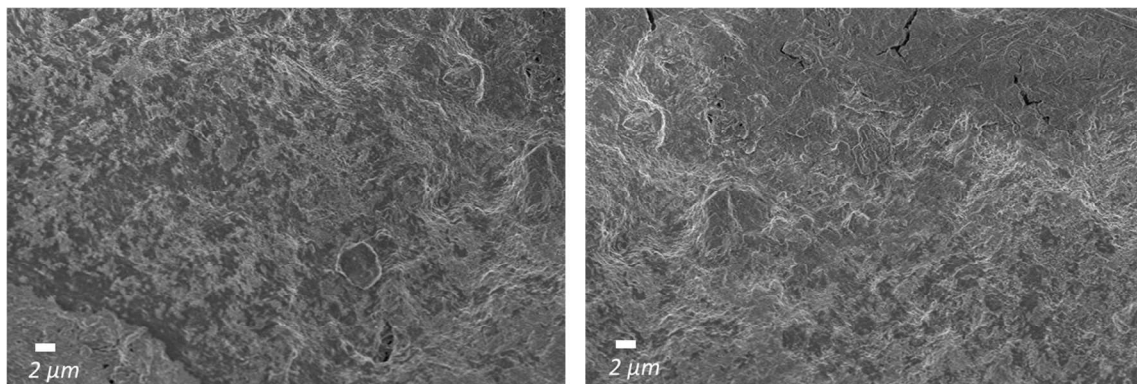


Figure SI5. SEM micrographs registered at 5 kx of magnitude of the sample from Mušov66 acquired after the treatment.

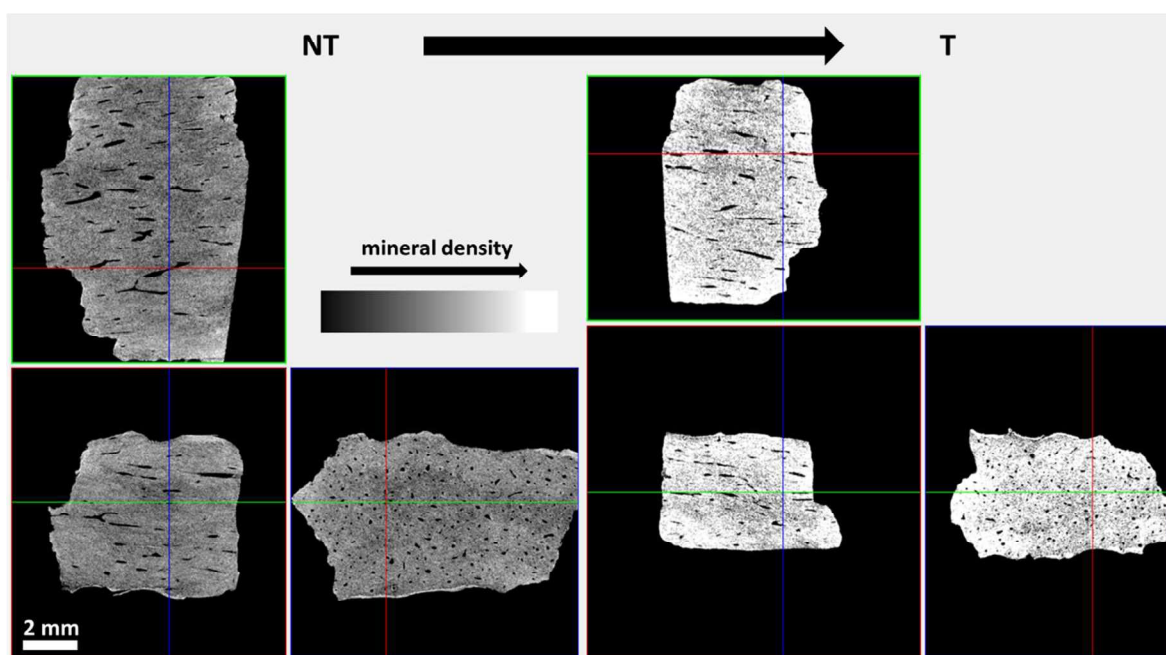


Figure SI6. Sections along three axes of a 3D reconstructions of a bone fragment from the archaeological site of Mušov (Mušov 66) before (left) and after (right) the consolidation treatment: it is possible to appreciate an increase in the mineral density in both the surface and the bulk of the sample.

Table SI3. Porosity data obtained from microtomography analysis performed on the untreated and the treated samples

	Sample name	
	NT	T
Total volume of pores (mm³)	4.28	1.46
Total Porosity (%)	3.84	2.25
Volume of closed pores (mm³)	0.40	0.61
Closed Porosity (%)	0.38	0.96
Volume of open pores (mm³)	3.87	0.85
Open Porosity (%)	3.48	1.31

The nitrogen adsorption-desorption isotherms (Fig. SI7A), recorded from bone fragments of 1-2 millimeters, give information about the pore size distribution in the range of 0.4 to 200 nm in diameter. According to IUPAC classification [7], all the bone samples exhibit a type IV(a) isotherm, characteristic of mesoporous materials with pores ranging from 2 to 50 nm in pore size and a type H3 hysteresis loop, given by non-rigid aggregates of plate-like particles. This kind of loop is typical of pores with irregular size and shape, suggesting the presence of slit-like pores [7, 8].

By comparing the profiles of the isotherms acquired from NT and T samples, the volume of absorbed gas is lower in the consolidated sample:

- at low partial pressures (up to 0.2), indicating the filling of the micropores;
- after the inflection point, suggesting the reduction of available area for multilayer adsorption due to the formation of a homogeneous coating.

In Fig. SI7B, the graph shows the size distribution of pores obtained from the desorption isotherm before and after the treatment: although the model applied [9] considers the presence of cylindrical pore, which is not our case, it is possible to appreciate a decrease of the differential volume for pores with diameter up to 50 nm. Moreover, Figure SI7B indicates that the trend of the differential pore volume as a function of the pore diameter doesn't change meaningfully after the consolidation treatment, suggesting a homogeneous distribution of the consolidant inside of the bone matrix.

In particular, on the basis of what we reported in a previous paper [8], the decrease of the differential pore volume in the range of micro- and mesopores, can be mainly attributed to the precipitation of phosphate salts deriving from the DAP solution in the narrowest pores.

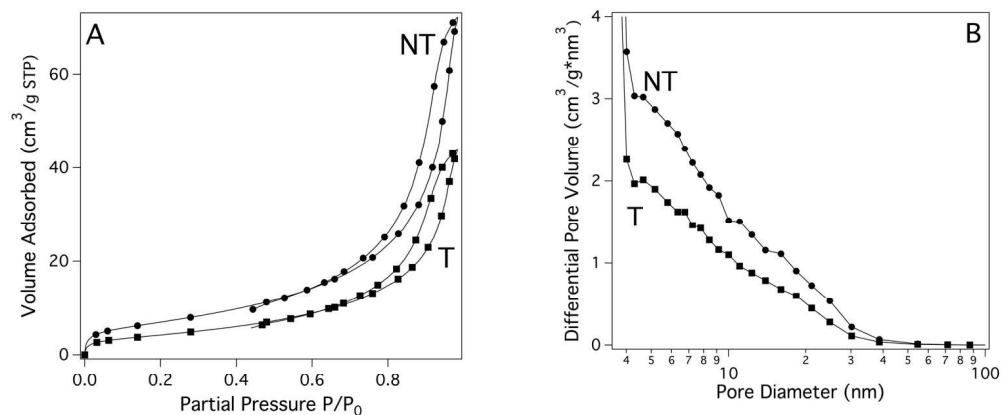


Figure SI7. (A) BET adsorption-desorption isotherms for bone samples from Mušov obtained before (NT) and after (T) the consolidation treatment; (B) Pore diameter distribution plots for bone samples from Mušov before (NT) and after (T) the consolidation treatment.

4. Paleogenetic analysis

Table SI4. Full sequencing and bioinformatic results of the mitochondrial genomes obtained from the untreated (NT) and treated (T) bone samples from Mušov.

Sample Name	Raw reads prior Clip&Merge	Merged reads	% Merged Reads	Mapped reads prior duplicates removal	Mapped Reads after duplicates removal	% Endogenous DNA	Cluster factor
Musov65-NT	1889070	562097	50,67	8391	410	1,49	20,47
Musov65-T	1482784	422262	47,84	2793	154	0,66	18,14
Musov66-NT	2766938	993235	67,71	168192	8111	16,93	20,74
Musov66-T	3466068	1277411	69,95	288125	10835	22,56	26,59
Musov71-NT	2863170	1059589	70,11	54365	3757	5,13	14,47
Musov71-T	1951798	633975	56,42	28775	2675	4,54	10,76
Musov73b-NT	2040470	619621	52,38	36167	2025	5,84	17,86
Musov73b-T	762148	203254	43,54	2447	153	1,20	15,99

Sample Name	Mean Coverage	Standard deviation coverage	Coverage ≥ 1X (%)	Coverage ≥ 2X (%)	Coverage ≥ 3X (%)	Coverage ≥ 4X (%)	Coverage ≥ 5X (%)
Mušov65-NT	1,21	1,25	65,08	33,99	14,04	5,54	2
Mušov65-T	0,42	0,73	31,35	8,49	1,91	0,59	0
Mušov66-NT	24,95	8,72	100	100	100	99,94	99,89
Mušov66-T	33,83	10,62	100	99,99	99,99	99,99	99,91
Mušov71-NT	11,21	4,27	100	99,80	99,31	98,09	95,30
Mušov71-T	8,32	3,49	99,96	99,65	98,47	94,39	87,08
Mušov73b-NT	6,08	2,89	99,50	96,68	90,13	79,87	67,31
Mušov73b-T	0,43	0,65	34,79	6,71	1,04	0,11	0

Sample Name	DMG 1st base 3'	DMG 1st base 5'	Average fragment length (bp)	Missing position in the consensus sequence	Proportion of authentic reads (%) - ContamMix	Proportion of authentic reads (%) CI (2.5%-97.5%) - ContamMix	mtDNA haplogroup
Mušov65-NT	0,32	0,38	49,08	5887	99,43	87,46-99,91	T2
Mušov65-T	0,43	0,25	45,56	11461	96,69	42,65-99,39	-
Mušov66-NT	0,32	0,31	50,97	2	98,83	96,24-99,79	T2e
Mušov66-T	0,29	0,32	51,73	1	99,97	99,20-99,99	T2e
Mušov71-NT	0,34	0,35	49,45	3	99,29	94,18-99,90	H1c1
Mušov71-T	0,33	0,35	51,55	11	99,69	95,06-99,94	H1c1
Mušov73b-NT	0,38	0,36	49,79	103	99,81	95,61-99,97	H1c1
Mušov73b-T	0,36	0,29	46,20	10850	98,40	69,06-99,71	-

Table S15. Results obtained from the EAGER pipeline after having downsampled the merged data of Mušov66-T and Mušov71-NT to a number of 993235 and 633975 reads respectively.

Sample Name	Reads prior mapping	Mapped reads prior duplicates removal	Mapped reads after duplicates removal	% Endogenous DNA	Mean Coverage	Coverage \geq 1X (%)	Coverage \geq 5X (%)
Mušov66-NT	993235	168192	8111	16,93	24,9508	100	99,89
Mušov66-T	993235	224249	10709	22,58	33,4548	100	99,82
Mušov71-NT	633975	32471	3606	5,12	10,7963	100	94,65
Mušov71-T	633975	28775	2675	4,54	8,3226	99,96	87,08

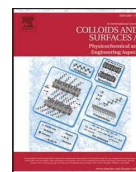
References

- [1] C. Drouet, «Apatite Formation: Why It May Not Work as Planned, and How to Conclusively Identify Apatite Compounds,» *BioMed Research International*, vol. 2013, pp. 1-12, 2013.
- [2] L. Berzina-Cimdina e N. Borodajenko, «Research of Calcium Phosphate Using Fourier Transform Infrared Spectroscopy,» in *Infrared Spectroscopy - Material Science, Engineering and Technology*, InTech, 2012.
- [3] S. Mansour, S. El-Dek, M. Ahmed, S. Abd-Elwahab e M. Ahmed, «Effect of preparation conditions on the nanostructure of hydroxyapatite and brushite phases,» *Applied Nanoscience (Switzerland)*, vol. 6, n. 7, pp. 991-1000, 2016.
- [4] N. Nga, N. Chau e P. Viet, «Facile synthesis of hydroxyapatite nanoparticles mimicking biological apatite from eggshells for bone-tissue engineering,» *Colloids and Surfaces B: Biointerfaces*, vol. 172, pp. 769-778, 2018.
- [5] B. Cengiz, Y. Gokce, N. Yildiz, Z. Aktas e A. Calimli, «Synthesis and characterization of hydroxyapatite nanoparticles,» *Colloids and Surfaces A: Physicochemical and Engineering Aspects*, n. 1-3, pp. 29-33, 2008.
- [6] E. Fratini, G. Page, R. Giorgi, H. Colfen, P. Baglioni e B. e. Z. T. Demé, «Competitive Surface Adsorption of Solvent Molecules and Compactness of Agglomeration in Calcium Hydroxide Nanoparticles,» *Langmuir*, vol. 23, n. 5, p. 2330–2338, 2007.
- [7] M. Thommes, K. Kaneko, A. Neimark, J. Olivier, F. Rodriguez-Reinoso, J. Rouquerol e K. Sing, «Physisorption of gases, with special reference to the evaluation of surface area and pore size distribution (IUPAC Technical Report),» *Pure and Applied Chemistry*, 2015.
- [8] A. Salvatore, S. Vai, S. Caporali, D. Caramelli, M. Lari e E. Carretti, «Evaluation of Diammonium hydrogen phosphate and Ca(OH)₂ nanoparticles for consolidation of ancient bones,» *Journal of Cultural Heritage*, vol. 41, n. 2019, pp. 1-12.
- [9] P. Ravikovitch e A. Neimark, «Calculations of pore size distributions in nanoporous materials from adsorption and desorption isotherms,» *Studies in Surface Science and Catalysis*, vol. 129, pp. 597-606, 2000.



Contents lists available at ScienceDirect

Colloids and Surfaces A: Physicochemical and Engineering Aspects

journal homepage: www.elsevier.com/locate/colsurfa

Nanostructured fluids confined into Highly Viscous Polymeric Dispersions as cleaning tools for artifacts: A rheological, SAXS, DSC and TOF-SIMS study

Emiliano Carretti^{a,b,*}, Giovanna Poggi^{a,b}, Elisa Ghelardi^{a,b,c}, Francesca Porpora^{a,b}, Agnese Magnani^{b,d}, Emiliano Fratini^{a,b}, Luigi Dei^{a,b}, Marco Consumi^{b,d}

^a Department of Chemistry "Ugo Schiff", University of Florence, via della Lastruccia, 3-13, Sesto Fiorentino, FI 50019, Italy

^b Center for Colloid and Surface Science (CSGI), via della Lastruccia 3, Sesto Fiorentino 50019, Italy

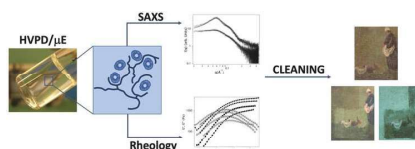
^c Department of Chemistry and Industrial Chemistry, University of Pisa, via Giuseppe Moruzzi 13, Pisa 56124, Italy

^d Department of Biotechnology Chemistry and Pharmacy, University of Siena, via A. Moro 2, Siena 53100, Italy

HIGHLIGHTS

- Retainment of the p-xylene in water microemulsion nanostructure in a gel matrix.
- The main relaxation process of the network follows a sticky reptation mechanism.
- The system is effective for cleaning painted surfaces of artistical interest.
- No residues were left onto the paint surface after the cleaning action.
- The cleaning action interests selectively only the foreign surface patina.

GRAPHICAL ABSTRACT



ARTICLE INFO

Keywords:
Chemical hydrogels
Microemulsions
SAXS
Rheology
Varnish removal

ABSTRACT

The development, and the structural and mechanical characterization of a new complex system composed by an oil-in-water microemulsion (μE) embedded in an aqueous 3D Highly Viscous Polymeric Dispersion (HVPD) of poly (vinyl alcohol) (PVA) cross-linked by borax, is here presented together with its possible implications in paintings conservation. The HVPD/ μE was characterized by Small Angle X-Rays Scattering (SAXS), Differential Scanning Calorimetric (DSC) and rheology to obtain information about the mutual effect of the μE and of the PVA network on both the nanostructure of the μE , and on the mechanical behavior of the system. Experimental data indicate that the nanostructure of the μE is retained even in the presence of the PVA/borax network whose mechanical properties are enhanced by the presence of the nanofluid. The effect of HVPD/ μE on organic molecules thin films of varnish coatings usually used on easel paintings, was studied by Attenuated Total Reflection Fourier Transform InfraRed spectroscopy (ATR-FTIR) and Time-of-Flight Secondary Ion Mass Spectrometry (TOF-SIMS). The results showed that an interaction occurred leading to the extraction of the organic molecules within the HVPD/ μE . The applicative consequence was that the HVPD/ μE complex fluid revealed itself to be a potential, very powerful and "green" tool for selective cleaning of easel paintings affected by artificial aged coatings, with very low environmental impact and leaving no residues onto the painting surface.

* Corresponding author at: Department of Chemistry "Ugo Schiff", University of Florence, via della Lastruccia, 3-13, Sesto Fiorentino, FI 50019, Italy.
E-mail address: emiliano.carretti@unifi.it (E. Carretti).

<https://doi.org/10.1016/j.colsurfa.2022.128968>

Received 24 February 2022; Received in revised form 6 April 2022; Accepted 10 April 2022

Available online 14 April 2022

0927-7757/© 2022 Elsevier B.V. All rights reserved.

1. Introduction

Poly(vinyl alcohol) (PVA) is one of the hydrophilic polymers most largely used to make three-dimensional networks [1–4], due to its excellent chemical versatility [5–7], biocompatibility [8,9], mechanical strength [10], flexibility [11], biodegradability [12], cheapness and low toxicity [13]. A further important feature of PVA is its ability to form thermodynamically stable and thermoreversible highly-viscous polymeric dispersions (HVPDs) through a esterification reaction between the vinyl hydroxyl groups and different anions like borate, vanadate or antimonite [14,15]. Moreover, due to the reversibility of that reaction, these covalent cross-links are dynamic and an equilibrium tridimensional density is established as a function of temperature [16]. Moreover, the structural features of the polymer network of these HVPDs, are strictly related to many other key factors such as the equilibrium between the electrostatic interactions, the excluded volume of the PVA chains, the spatial density of the cross-linking, and the charge-shielding effects [17,18]. From the applicative standpoint, a fundamental property of these systems is that they show the peculiar ability to load significant amounts of organic solvents with high and medium polarity. This is potentially a key-feature to use these HVPDs as cleaning tools for painted surfaces of historical and artistic interest, particularly easel paintings [15]. In this way, thanks to their high viscosity, the uncontrollable penetration of pure organic solvents into the paint layer, which represents the main drawback resulting from the use of unconfined fluids for cleaning operations, is avoided. Indeed, the penetration of free organic solvents, traditionally used for the cleaning of easel paintings, may cause some undesirable effects, the most important and common of which are the swelling and the leaching of the organic structural components [19] and/or the spreading of the solubilized materials into the porous matrix of the paint [20].

Other peculiar features of the PVA/borax-based HVPDs are connected to their structural dynamic and to their mechanical properties easily modulable by varying both the amount and the molecular weight of the polymer, and the nature and the amount of the solvent loaded into the system. In other terms, by changing the composition of the system, it is possible to obtain HVPDs having values of both the elastic modulus G' and $\tan\delta$ (G''/G'), which, after application, allow for an easy and complete removal through simple a peeling action [21]. This is the way to minimize the HVPD's residues on the paint surface and to avoid, at the same time, the mechanical action and the application of free solvents usually needed for the complete removal of traditional gel used for cleaning purposes [22].

In this work we demonstrate that the above mentioned PVA-based HVPDs, in addition to being able to load many solvents with different polarity, are also capable of loading a nanostructured complex fluid such as a oil-in-water (o/w) microemulsion (μE). It is well known that nanostructured fluids are highly effective in the swelling/solubilization of several hydrophobic materials from painted surfaces of historical and artistic interest and, in comparison to organic solvents, ensure a better control of the cleaning action [23–26]. Unfortunately, net of that, the application of these systems on water-sensitive porous artifacts (i.e. easel paintings, cellulosic materials etc) makes mandatory their confinement in a solid-like matrix (i.e. a physical or a chemical gel) [27].

Here we present the set-up of a thermodynamically and kinetically stable HVPD composed of PVA covalently crosslinked with $\text{Na}_2\text{B}_4\text{O}_7 \cdot 10\text{H}_2\text{O}$ containing a p-xylene-in-water microemulsion (HVPD/ μE), to exploit the advantages connected to the use of nanostructured fluids in combination to those typical of gel-like polymeric dispersion, improving the performances of systems that have already been successfully tested. [28].

The dynamic, the mechanical and the structural properties of the HVPD/ μE complex system were investigated through rheological and Small Angle X-rays Scattering (SAXS) measurements respectively. Rheological analysis paid attention on the effect of the serial addition of the components of the μE on the viscoelastic properties of the HVPD/ μE .

This is a crucial factor because both the cleaning performances and the possibility to safely and completely remove the HVPD/ μE from the paint surface after the cleaning, are influenced by the mechanical behavior of the system [29]. Moreover, SAXS curves were collected to characterize the μE structure at the nanoscale and to check whether it was retained once it is loaded inside the PVA/borax network and to understand if structural changes occurred in this nanofluid. Finally, the effect of HVPD/ μE on organic molecules thin film constituted by aged linseed oil and dammar varnish were studied by means of Attenuated Total Reflection Fourier Transform InfraRed spectroscopy (ATR-FTIR) and Time of Flight Secondary Ion Mass Spectrometry (ToF-SIMS). In particular, these two analytical techniques were used to verify the presence of the above-described organic molecules onto the surface of a 19th century egg-tempera canvas painting before and after the application of the HVPD/ μE . ToF-SIMS is a powerful surface-sensitive analytical method with the peculiar ability to determine the chemical composition (spatially-resolved) with ppm-ppb sensitivity of both inorganic and organic analytes and, therefore, represents the best analytical method to analyze the painting surface and evaluate the effect of our cleaning system on aged organic molecules [30–32]. It is worthwhile to recall the extremely high surface sensitivity of TOF-SIMS that allows highlighting traces of chemical compounds and their distribution onto the surfaces with lateral resolution less than $1\ \mu\text{m}$ [33,34]. ToF-SIMS associated with ATR-FTIR was here used to obtain information both about the occurred interaction of the organic aged molecules with HVPD/ μE , and on the cleaning performance. Moreover, for the first time, ToF-SIMS was also used to monitor the presence of residues of the cleaning system, i.e. HVPD/ μE , onto the painting surface after its application and removal, providing a solid proof-of-concept about the possible application of this analytical technique for the evaluation of new cleaning materials for the conservation of cultural heritage.

2. Materials and methods

2.1. Materials

1-pentanol (1PeOH, 99%, Sigma Aldrich, Germany), p-xylene (Merck, Germany), poly(vinyl alcohol) 80% hydrolysed (PVA, Kuraray, Japan), sodium tetraborate decahydrate (borax, 99.5% Sigma Aldrich, Germany) were used as received. Sodium dodecylsulfate (SDS, 99% Sigma Aldrich, Germany), was recrystallized from ethanol before the use [35]. Water was purified by means of a Millipore Elix3 system ($R \geq 15\ \text{M}\Omega\ \text{cm}$).

2.2. Methods

2.2.1. Preparation of the HVPD/ μE

SDS was first solubilized in water and 1PeOH was added dropwise to form a micellar solution; then 80PVA was added and completely dissolved at room temperature by stirring the system in a hermetically closed vial for 2 h. After the complete solubilization of the polymer, p-xylene and a 4 wt% aqueous solution of borax were added dropwise in sequence. The system was initially opalescent, but after 24 h at $25\ ^\circ\text{C}$, it became completely transparent.

2.3. HVPD/ μE characterization

2.3.1. Rheology

Rheological measurements in oscillatory regime were carried by using a Paar Physica UDS200 rheometer (the temperature was maintained at $25 \pm 0.1\ ^\circ\text{C}$ through a Peltier) with a cone-plate geometry (40 mm diameter and 1° cone angle; the gap was 0.5 mm). Once loaded, before the beginning of the measurements, the samples were equilibrated for at least 30 mins at $25\ ^\circ\text{C}$. The frequency sweep tests were carried out always in the linear viscoelastic regime (the oscillation strain was 1%), previously determined for each sample, through an amplitude

sweep test. The trend of both the storage (G') and loss (G'') moduli was measured in the frequency range between 0.01 and 100 Hz.

2.3.2. Small angle X- rays scattering

Small Angle X-Ray Scattering (SAXS) curves were collected by means of a Hecus X-Ray System GmbH Kratky camera equipped with two 1-D Position-Sensitive Detectors (Methane/Ar) mounted on a ID3003 generator (Seifert). $\text{CuK}\alpha$ radiation of wavelength ($\lambda = 1.54 \text{ \AA}$) was provided by an ultra-brilliant point micro-focus X-ray source (GENIX-Fox 3D, Xenocs, Grenoble), operating at a maximum power of 50 W (50 kV and 1 mA). The sample-to-detector distance was 281 mm. The space between the sample and the detector was kept under vacuum during the measurements to minimize scattering from the air. The Kratky camera was calibrated in the small angle region using silver behenate ($d = 58.34 \text{ \AA}$) [36]. Samples were placed in mark tubes (thickness = 1 mm). The temperature, 25 °C, was controlled by a Peltier element with a precision of 0.1 °C. All scattering curves were corrected for the empty cell/solvent contribution considering the relative transmission factor. The experimental SAXS curves of the liquid microemulsion (μE) and of the μE loaded into the PVA/borax-based HVPD (HVPD/ μE) were analyzed using a non-linear least-square fitting (statistically weighed) where the microemulsion was considered as composed by spheres with a core (hydrophobic)-shell (hydrophilic) structure. The polydispersity of the radii dimensions was described by the Schulz distribution. In the modeling of the nanodroplets, the external shell was considered composed by the polar heads and the first CH_2 of the hydrocarbon tails of the SDS and 1PeOH molecules, by the OH groups of the 1PeOH molecules, the hydration water, and some counterions. The hydrophobic core was considered as composed by p-xylene molecules and the hydrocarbon tails, $\text{C}_{11}\text{H}_{23}$ and C_4H_9 appertaining to SDS and 1PeOH, respectively. Further details on the scattering length densities calculation for core and shell regions can be found in SI.

On these bases, the dependence of the scattering intensity $I(Q)$ from the scattering vector Q is:

$$I(Q) = A\phi\tilde{P}(Q)\tilde{S}(Q) + I_{bkg} \quad (1)$$

where A is an instrumental factor, ϕ is volume fraction of the microemulsion, $\tilde{P}(Q)$ is the form factor (spherical particles), $\tilde{S}(Q)$ is the structure factor accounting of the inter-particle interactions, and I_{bkg} is the instrumental background [29]. Moreover,

$$Q = \frac{4\pi}{\lambda} \sin \frac{\theta}{2} \quad (2)$$

where θ is the scattering angle and λ is 0.1542 nm.

The SAXS curve of the HVPD/ μE system was obtained by scaling and subtracting the contribution of the PVA/borax network (Fig. S11).

2.3.3. Differential Scanning Calorimetry (DSC)

DSC measurements were carried out by means of a Q1000 TA Instruments calorimeter with sealed aluminum pans under nitrogen atmosphere (nitrogen flow: $50.0 \pm 0.5 \text{ cm}^3 \text{ min}^{-1}$). The temperature cycle was the following: from room temperature up to $-90 \text{ }^\circ\text{C}$ ($60 \text{ }^\circ\text{C min}^{-1}$), isotherm at $-90 \text{ }^\circ\text{C}$ for 8 min, from $-90 \text{ }^\circ\text{C}$ up to $30 \text{ }^\circ\text{C}$ at $1 \text{ }^\circ\text{C min}^{-1}$.

2.4. Application of HVPD/ μE

To study the interaction between the HVPD/ μE system and organic molecules thin films, with also the aim of discovering potential application in cultural heritage conservation, the HVPD/ μE was kept in contact with some thin film coatings present onto a 19th century Tuscan egg-tempera canvas painting. The HVPD/ μE was applied onto the painted surface by means of a spatula, at least 48 h after its preparation (application time: about 5 mins; the procedure was repeated twice). Afterwards, the system was peeled from the surface by means of a pincher, avoiding the use of any additional liquid after the peeling process.

Images of the paint before and after the application of the HVPD/ μE system were acquired under visible light and with UV-induced fluorescence using a Canon EOS 60D camera equipped with a 100 mm f/2.8 Macro lens.

2.5. Organic molecules thin films characterization

2.5.1. Fourier Transform InfraRed Spectroscopy (FTIR)

ATR-FTIR spectra of the organic thin films were collected with a Thermo Nicolet Nexus 870 (128 scans with 4 cm^{-1} of optical resolution) equipped with a Golden Gate diamond by using a Mercury- Cadmium-Telluride (MCT; the extension of the sampling area was 150 mm^2).

2.5.2. Time of flight secondary ion mass spectrometry measurements (ToF-SIMS)

ToF-SIMS measurements were carried out on a TRIFT III spectrometer (Physical Electronics, Chanhassen, MN, USA) equipped with a gold liquid-metal primary ion source. HVPD/ μE was analyzed following a procedure developed for the analysis of hydrogels [37,38]. All the samples were kept overnight in a conditioning pre-chamber with a vacuum value of 10^{-5} Pa and then moved to the analyzing chamber where the pressure was lower than 10^{-8} Pa . Positive and negative ions spectra were acquired with a pulsed, bunched 22 keV Au^+ primary ion beam, by rastering the ion beam over a sample area $100 \text{ }\mu\text{m}^2$ and maintaining static SIMS conditions (primary ion dose density $< 10^{12} \text{ ions/cm}^2$). Positive ion spectra were calibrated with CH_3^+ (15.023 m/z), C_2H_3^+ (27.023 m/z) C_3H_5^+ (41.039 m/z). The mass resolution ($m/\Delta m$) was 3000 at 27 m/z because of the roughness of the samples. Negative ions spectra were not reported because no additional can be obtained. Chemical images were acquired with a pulsed, unbunched 22 keV Au^+ primary ion beam, by rastering the ion beam over a $400 \text{ }\mu\text{m}^2$ sample area and maintaining static SIMS conditions. The lateral resolution was about $1 \text{ }\mu\text{m}$.

3. Results and discussion

3.1. Formulation and characterization of the HVPD/ μE system

In the following paragraphs, details about the formulation of a HVPD/ μE system, composed of a PVA covalently crosslinked by $\text{Na}_2\text{Ba}_4\text{O}_7 \cdot 10\text{H}_2\text{O}$ (HVPD) and a p-xylene-in-water microemulsion (μE), are reported. The system was formulated on the basis of the following considerations: (i) the ratio 1PeOH/SDS was kept at 1.84, as in case of a similar μE already successfully developed for applicative purposes in cultural heritage conservation [39]; (ii) on the basis of previous studies [15], a concentration of 80PVA equal to 4 wt% was used, which was deemed optimal in terms of cleaning effectiveness and complete removal of the HVPD after use. Several systems have been prepared by varying the composition of the μE . The corresponding phase diagram, obtained through visual inspection of the systems, is reported in Fig. 1. The aim was to maximize the amount of the organic solvents (p-xylene and 1-PeOH) included in the formulation within the monophasic region 1 Φ , where the system is homogeneous and stable both from the kinetic and the thermodynamic standpoint.

Following the approach detailed above, the composition of the system used for this study was the one reported in Table 1. With the aim of detailing the effect of the μE components on the mechanical behavior of the HVPD, the frequency sweeps of the HVPD progressively loaded with the components of the μE (SDS, 1PeOH and p-xylene) were carried out (Fig. 2).

Fig. 2 shows that the addition of 2.5 wt% SDS to the PVA/borax/ H_2O based HVPD caused a shift of the G' curve towards lower values. It is well known that the asymptotic value of G' at high frequencies corresponds to the intrinsic elastic modulus G^0 that is proportional to the density of the covalent cross-linking (μ_c) forming the PVA/borate network at a temperature T (Eq. 3) [40]:

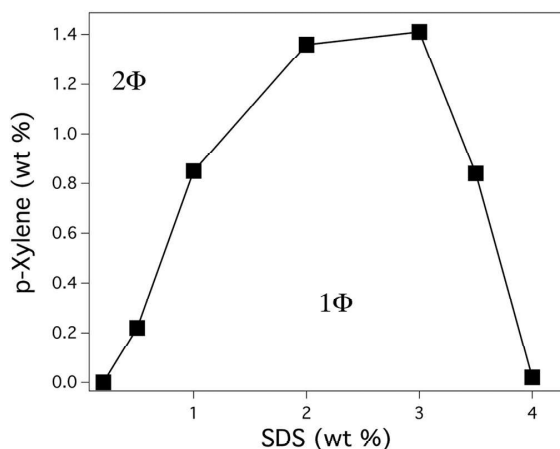


Fig. 1. Phase diagram of the HVPD/μE system. The amount of 80PVA is equal to 4 wt% and the ratio 1PeOH/SDS equal to 1.84. 1Φ indicates the monophasic region; 2Φ indicates the biphasic region.

Table 1

Composition (w/w %) of the HVPD/μE.

Components	w/w %
SDS	2.50
H ₂ O	86.60
1-PeOH	4.60
80PVA	4.00
p-xilene	1.30
Borax	1.00

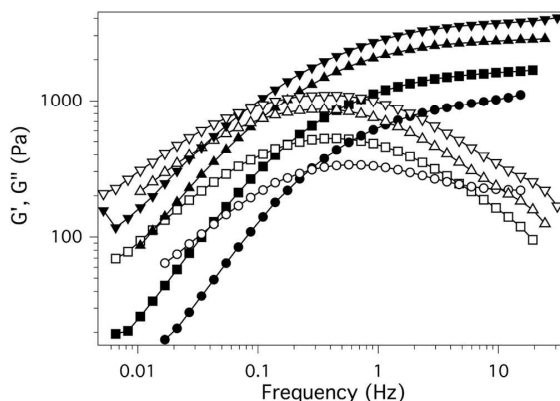


Fig. 2. Frequency sweep curves of PVA (4 wt%)/borax (1 wt%)/H₂O based HVPD (squares), PVA (4 wt%)/borax (1 wt%)/H₂O based HVPD containing 2.5 wt% of SDS (circles), PVA (4 wt%)/borax (1 wt%)/H₂O based HVPD containing 2.5 wt% of SDS and 4.6 wt% of 1PeOH (up triangles) and PVA (4 wt %)/borax (1 wt%)/H₂O based HVPD containing 2.5 wt% of SDS, 4.6 wt% of 1PeOH and 1.3 wt% of p-xylene (down triangles). Filled symbols indicate the elastic modulus G' and the empty symbols indicate the loss modulus G'' .

$$G^0 = \rho_e k_B T \quad (3)$$

(k_B is the Boltzman constant). The decrease of G^0 observed after the loading of SDS into the HVPD corresponds to a decrease of ρ_e due to a de-structuring effect of the anionic surfactant on the 3D polymeric network. This effect was due to the increase of the ionic strength of the system; in fact, as reported in Fig. S12, the frequency sweep curves of the SDS/

HVPD systems and of a system obtained by adding to the HVPD system an amount of NaCl equivalent to SDS, were superimposable. On the contrary, the addition of 1PeOH to the HVPD caused an increase of G^0 and then, of ρ_e (Fig. 2). The structuring effect of 1PeOH, already observed for HVPDs made by 99% hydrolyzed PVA [41], was attributed [42] the decrease of the dielectric constant of the continuous phase induced by this solvent, that causes an increase of the amount of borate ions interacting with PVA chains. Finally, the data reported in Fig. 2 also indicated that the addition of p-xylene to the SDS/1-pentanol/HVPD system induced a further increase of G^0 . In a previous paper [42], it has been demonstrated that the most important rheological parameter that affects the “peelability” of a HVPD from a surface is G^0 : for G^0 values higher than 400 Pa, the gel can be easily and completely removed by “peeling” it with tweezers without leaving any detectable residue onto the cleaned surface. In our case the HVPD/μE had a very high G^0 value (about 1000 Pa); on the contrary, traditional physical gels commonly used for cleaning purposes display G^0 values well below this threshold, making the peeling action not feasible [15].

Fig. S13 shows the frequency sweep of Fig. 2 normalized over the crossover coordinates of the G' and G'' curves. The superimposition of the curves means that the addition of the components of the microemulsion has a limited effect on the relaxation mechanism of the HVPDs even if the time scale of the relaxation processes changes.

To investigate both the effect of the PVA content on the mechanical behavior and the relaxation mechanism of the HVPD/μE system, frequency sweep tests were also carried out as a function of the PVA concentrations (see Fig. S14), and the continuous relaxation spectra $H(\tau)$ were obtained (Fig. 3A). The increase of the width of the $H(\tau)$ curves observed upon increasing PVA content indicated the progressive increase of the complexity of the relaxation dynamics. This was probably due to the increasing entanglements among the polymer chains, such as polymer–polymer interactions, as already observed for similar systems [16]. It is well known that usually the driving factor of the dynamic of solutions of interacting polymers in good solvents is the association of the entangled groups; this behavior can be explained considering a sticky reptation mechanism [43]. The corresponding relaxation (i.e. reptation) time is related to the concentration through a power law:

$$\tau_{\text{rep}} \sim C^a \quad (4)$$

The exponent a usually varies between 1.44 and 4.5 by varying the distance between the interaction points. Fig. 3B reports the trend of the main relaxation time τ_H , corresponding to the peak of $H(\tau)$ curves, as a function of the PVA content C (g/L):

$$\log(\tau_H) = a \log C + b \quad (5)$$

The linear fit of the plot $\log(\tau_H)$ vs $\log C$ reported in Fig. 3B indicates that for the HVPD/μE HVPD, the exponent a is equal to 2.01. Therefore, it could be concluded that water was a good solvent for the HVPD based network and that the mechanism that drove the main relaxation process was characterized by a sticky reptation [43].

The structure of the complex fluid HVPD/μE was investigated by SAXS measurements and the relative curves are reported in Fig. 4. To analyze the nanostructure of the μE in the HVPD system, the contributions to the scattering intensities coming from the HVPD network (in the absence of the o/w μE) and from the nanofluid were considered purely additive [29]. Therefore, the curve of the HVPD network (Fig. S1) was scaled and subtracted from the curve obtained from the HVPD/μE; in that way, the signal of the μE confined inside the HVPD network was isolated and plotted in Fig. 4 (open triangles) together with the one of the “free” μE (open circles). The SAXS curve for the microemulsion μE is characterised by a correlation peak due to the para-crystalline structure induced by the electrostatic interaction (repulsive) between the negatively charged nanodroplets constituting the system. The correlation peak was also present, even if less pronounced, in the μE confined in the HVPD network. This alteration can be attributed to a partial screening

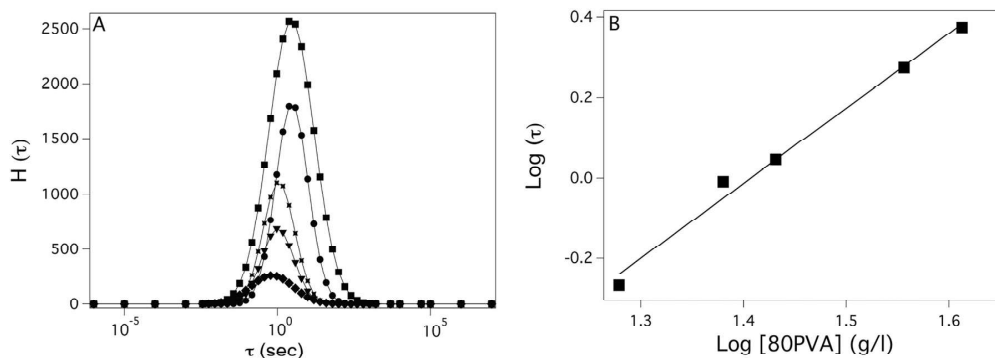


Fig. 3. A. Stress relaxation spectra $H(\tau)$ of HVPD/ μE containing 2 wt% (diamonds), 2.5 wt% (triangles), 3.0 wt% (stars), 3.5 wt% (circles) and 4.0 wt% (squares) of PVA. B. The mean relaxation times τ of the HVPD/ μE as a function of increasing concentration of PVA used to prepare the system. The straight line is the best linear fit of the experimental data ($R^2 = 0.95842$).

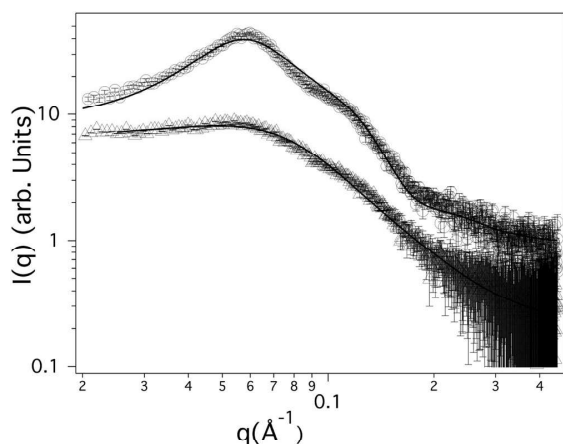


Fig. 4. Log-log SAXS curves of μE (\circ) and of the μE confined in the HVPD network (Δ). The μE in HVPD curve was obtained by scaling and subtracting the contribution of the PVA/borax network. The continuous lines are the best-fitting curves obtained using the model described in the Materials and Methods section.

effect of the polymer network on the charged droplets. Then, SAXS data confirm that the nanostructure of the microemulsion was retained even in the polymeric network, which is a fundamental topic for the subsequent study of the interaction between the HVPD/ μE and aged organic molecules. In fact, it is to be expected that such interaction should occur between the hydrophobic core of the nanodroplets and the aged thin films molecules. The parameters obtained from fitting of the SAXS curves according to the model reported in Section 2.2.2 of the Materials and Methods section are shown in Table 2. The data clearly showed that

Table 2
Structural parameters extracted from SAXS analysis of the microemulsion μE and of the μE confined in the HVPD network.

	μE	μE in HVPD
Volume Fraction	0.1 ± 0.1	0.12 ± 0.1
Core radius (nm)	2.4 ± 0.2	2.0 ± 0.2
Shell thickness (nm)	0.7 ± 0.2	0.9 ± 0.2
Polydispersity	0.19 ± 0.02	0.39 ± 0.02
$\text{SLD}_{\text{core}} (\text{\AA}^{-2}) \times 10^{-6}$	7.45 ± 0.1	7.29 ± 0.1
$\text{SLD}_{\text{shell}} (\text{\AA}^{-2}) \times 10^{-5}$	1.04 ± 0.1	0.97 ± 0.1
Charge (e)	40 ± 3	10 ± 2

the inclusion of the microemulsion into the HVPD network resulted in minimal changes in the size of the nanodroplets which mean size remains almost unchanged, in terms of core radius and shell thickness; the only difference concerning dimensions was a slight increase in the polydispersity. It was interesting to note that, however, the nanodroplets charge strongly decreased (about four times), as also indicated by the less evident peak at about 0.06\AA^{-1} in the SAXS curve of the confined μE . This effect can be mainly ascribed to the screening effect imparted by the ionic PVA/borax network on the charged nanodroplets [16], even though further steric constraints induced by the polymer network are not considered in the model.

DSC measurements gave a further confirmation that the nanostructure of the o/w microemulsion was retained inside the HVPD network. As shown in Fig. 6, the DSC curve of the μE was characterized by three endothermic peaks (labelled as μE_1 , μE_2 , μE_3) due to the melting of different populations of water molecules inside the system.

In particular, the strongest peak μE_3 is due to the melting of the so-called “freezable bulk water”, while the other peaks, i.e. μE_1 and μE_2 , are related to “confined water” where μE_1 and μE_2 correspond to the so-called “bound freezable water” [44,45] that fraction of water more or less bound to the oil droplets in the μE , that does not melt at 273 K, but at temperatures below 0°C . A similar behavior was observed for the o/w μE confined into the HVPD (the three endothermic peaks are labelled as $\mu\text{E}_1/\text{HVPD}$, $\mu\text{E}_2/\text{HVPD}$, $\mu\text{E}_3/\text{HVPD}$). Slight differences in the onset values and in the shape of DSC peaks of the confined μE were probably due to the interactions occurring between the polymeric network and the nanodroplets. Nevertheless, the presence of the three endothermic DSC peaks in the confined μE was a further confirmation of the retainment of the nanostructure of the nanofluid even when included in the HVPD, which, as shown in Fig. 3, shows only one DSC peak due to “freezable bulk water” (labeled as HVPD₁).

Fig. 6 shows that the endothermic peak for $\mu\text{E}_2/\text{HVPD}$ is much sharper than that of μE_2 , even though the polydispersity of the μE in HVPD was larger than that of pure μE (Table 2). This means that, once started at the surface, the ice (solid “bound freezable water”) melting proceeds very fast within the bulk of this kind of water. More than the polydispersity, the critical factor seems to be the interactions between this kind of water molecules (“bound”) and the μE droplets: the strong charge decrease of the droplets (see Table 2 and Fig. 5) in passing from free μE to the μE embedded in the HVPD matrix, states an important weakening of these molecular interactions (dipole-charge). This would result both in a strong decrease of the first endothermic peak μE_1 (stronger bounds that correspond to lower melting temperatures), and in a faster reaction for the second step, probably due to some cooperative effects for which, at present, the role of polydispersity is unknown.

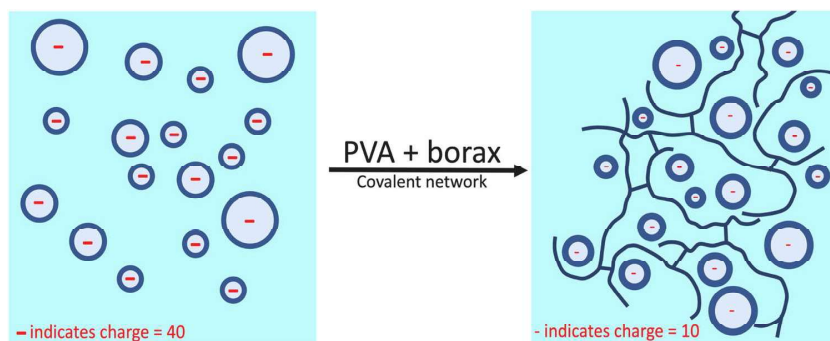


Fig. 5. Structural representation of the μE and of the $\mu\text{E}/\text{PVA}/\text{borax}$ systems revealed by the SAXS analysis.

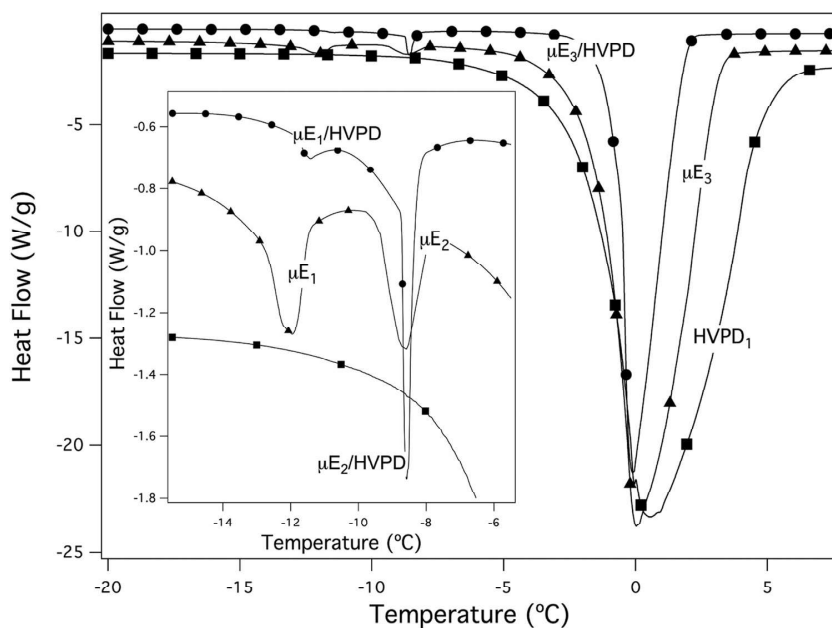


Fig. 6. DSC curves obtained for HVPD (■), μE (▲) and μE confined in HVPD (●). The inset shows the thermograms in the range between $-16\text{ }^{\circ}\text{C}$ and $-5\text{ }^{\circ}\text{C}$.

3.2. Application of HVPD/ μE system for cleaning of painted surfaces

The organic molecules constituting the thin films coating a 19th century egg-tempera canvas painting of a bucolic scene were selected due to their peculiarity of constituting a good test for applicative purposes. The interaction between the organic molecules constituting the painting coating and the HVPD/ μE system was monitored by ATR-FTIR and ToF-SIMS. Indeed, the two techniques were also employed to ascertain the chemical nature of such molecules. The ATR-FTIR spectrum collected onto the paint surface before cleaning (Fig. 7, black line) showed a strong band centered at 1703 cm^{-1} ($\text{C}=\text{O}$ str.), and absorptions at ca. 1633 cm^{-1} (shoulder, $\text{C}=\text{C}$ str.), 1456 cm^{-1} (CH_2 bend.), 1377 cm^{-1} ($\text{C}-\text{H}$ bend.), 1240 cm^{-1} ($\text{C}-\text{O}$ str., ester), 1162 cm^{-1} (shoulder $\text{C}-\text{O}$ str., acid), 1105 cm^{-1} ($\text{C}-\text{O}$ str., alcohol), and 920 cm^{-1} (shoulder $\text{C}-\text{H}$ bend.), which confirmed the presence of both a natural dammar resin, and possibly residues of siccative oil treatments [46,47]. It is not surprising such chemical nature, considering that mixtures of dammar resin and siccative oil have been often used as conservation materials in the past to “renew” the painting surfaces [48]. Analogously,

the brown and dark aspect of the coating (vide infra Fig. 8) was expected due to natural aging of these conservation materials [49,50]. The study of the interaction between these aged substances and the developed HVPD/ μE system was also representative of a challenge for checking the performance of an innovative, “green”, selective procedure for preventive conservation.

A preliminary experiment made on a very small portion of the painting sample showed that p-xylene was able to clean the surface and remove the brown, dark coating: this was the confirmation that this apolar solvent inside the nanodroplets was a good solvent for the aged dammar and linseed oil. The HVPD/ μE system was made interacting with the organic molecules thin films constituting the coating according to the procedure described in the paragraph 2.3 of the Materials and Methods section. Fig. 8A shows the aspect of the painting surface, where the dark, brown coating is well visible. Aged dammar and linseed oil originated, as known [51], strong UV-induced fluorescence, as documented by the B picture of Fig. 8. The interaction occurred between the applied HVPD/ μE and the organic molecules constituting the coating was strongly evident by the pictures C and D of Fig. 8: both the photos

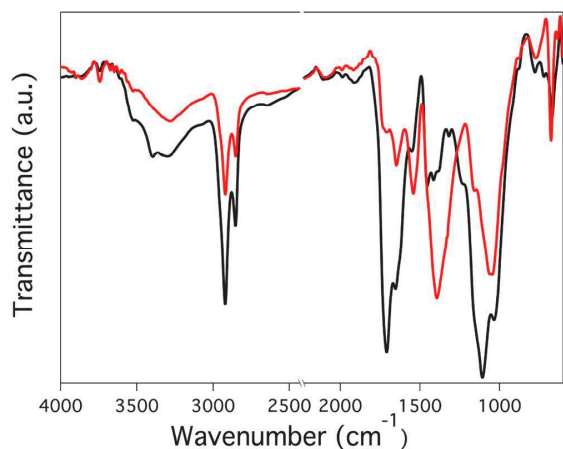


Fig. 7. ATR-FTIR spectrum of the paint surface collected before (black) and after the application of the HVPD/ μ E system (red).

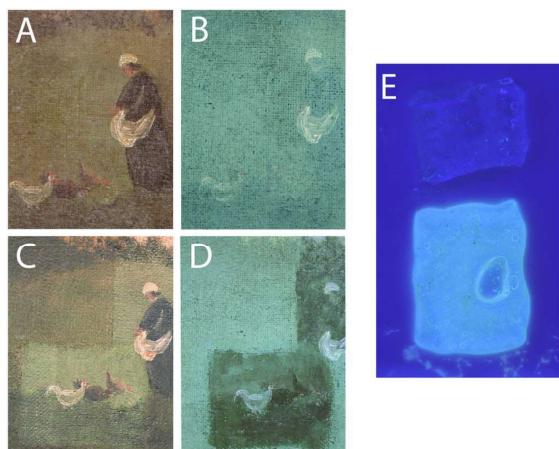


Fig. 8. Detailed pictures of the XVIII century Tuscan egg-tempera canvas painting before the cleaning test carried out through the HVPD/ μ E: visible light (A) and UV-induced visible fluorescence (B). The same area of the painting after cleaning procedures: visible light (C) and UV-induced visible fluorescence (D). Image E shows the UV-induced visible fluorescence pictures of the HVPD/ μ E before (top) and after (bottom) the cleaning test.

collected in visible light and UV-fluorescence showed that the aged organic molecules were completely removed by the HVPD/ μ E system that entrapped them within its structure, as documented by the picture E in the same Fig. 8. This was also confirmed by the results of the ATR-FTIR reported in Fig. 6 (red spectrum): the intensity of all the peaks associated with the aged organic molecules was strongly decreased. The fact that the peaks decreased their intensity, but not completely disappeared, should be considered as a positive feedback, since in preventive conservation a very soft approach according to the rule that it is better leaving some aged patinas, rather than making a strong, radical cleaning is highly desired [52]. Moreover, the ATR-FTIR spectrum in Fig. 7 (red) showed a strong increase of the intensity of the peaks at 1653 and 1540 cm^{-1} , which are related to the stretching of amide I and II respectively, and are due to the proteinaceous binding medium (i.e. egg) used for the realization of the tempera, confirming the unveiling of the original painting surface covered by the aged conservation past treatment layers.

ToF-SIMS was performed to deeper investigate the interaction of HVPD/ μ E with the aged organic molecules and to achieve analytical results with very great sensitivity, much higher with respect to ATR-FTIR. The purpose of this analysis in the present study was twofold: (i) evaluating the effective interaction, and (ii) detecting possible residues of the HVPD/ μ E system onto the painting surface. The positive ToF-SIMS spectra acquired on the same surface region before and after the interaction time were compared to the spectrum of the HVPD/ μ E system. Figs. 9 and 10 show the surface spectra of the painting sample before and after the interaction time, respectively. As shown in Fig. 9, the chemistry of the surface before the treatment is, as expected, very complex and characterized by many organic fragments, especially in the 0–100 amu range. The ToF-SIMS spectra indicated the presence of a siccativ oil in the surface coating: the peaks at m/z 279, 281, and 283 attributable to compounds having a generic formula $\text{C}_2\text{H}_3(\text{CH}_2)_x\text{COO}$ indicated the presence of several fatty acids such as linoleic, oleic and stearic acid respectively, as also confirmed by the peaks at m/z 263, 265 and 267, which belong to their acyl ions. Moreover, the group of peaks at m/z 431 and 447 are probably due to the same fatty acid conjugated with lead, as confirmed also by the isotopic ratio of the fragments and by the low intense signals at m/z 207. This composition suggests that a lead salt was added to the mixture used as varnish to speed up the drying process.

Ion peaks at $m/z = 65, 77, \text{ and } 91$, that are normally assigned to ion fragments C_5H_5^+ , C_6H_5^+ , and tropylium C_7H_7^+ , can be attributed to aromatic compounds that, together with the fragment at m/z 208, could be assigned to the fragmentation of lupane-type molecules, suggesting the presence of a natural dammar resin [53]. Moreover, this attribution is confirmed by the peaks in the range of 300–400 amu, due to natural terpenoid acids and their derivatives that often generate few fragments in this range. Indeed, these peaks can be also related to the presence of photo-oxidation products of aged natural resin, whose characteristic peaks are m/z 307, 317, and 325, and are due to abietic acid derivatives [54].

After the interaction time and the removal of the HVPD/ μ E from the surface the chemistry of the surface strongly changed, showing a strong reduction of the peaks due to both the fatty acids (m/z 279, 281, and 283) and to the natural resin (m/z 208) indicating that the interaction between the HVPD/ μ E enabled to segregate the most part of the aged organic molecules by the complex nanostructured fluid.

Moreover, the appearance of two intense peaks at m/z 63 and 65 due to copper (Fig. 10A) was a further indication of a strong thinning of the surface coating, that discovered the paint layers underneath.

The presence of copper confirmed that the green color in the area selected for the cleaning tests was due to inorganic copper-based pigment mixed with Sienna (a natural mixture of aluminosilicate of Ca and Fe oxides), as indicated by the peaks at m/z 27, 40 and 55 which can be attributed to Al, Ca and Fe, respectively.

ToF-SIMS results agreed with ATR-FTIR analyses. In particular, both analytical techniques showed that the interaction between the HVPD/ μ E system and the aged organic molecules constituting the dark and brown thin films coating onto the painting was strong enough to remove the coating, with successful recovery of the painting readability and simultaneously preserving the underneath layers, as documented by the remaining traces of the aged organic materials.

ToF-SIMS was also employed to ascertain down to ppb, for the first time as we know, the absence of residues coming from the HVPD/ μ E system after the interaction time. Fig. 11 shows the TOF-SIMS spectra before the interaction time (A), after interaction time and removal of HVPD/ μ E (B), and native HVPD/ μ E (C), used as a reference. The HVPD/ μ E spectra shows, as expected, many fragments. Among them, the characteristic and intense peak at $m/z = 165$, attributed to crosslinked polyvinyl alcohol (PVA), highlighted in Fig. 11C, falls in a spectral region where the painting surface has a peak (both before and after the interaction time, see Figs. 11A and 10B), but with very low intensity. Therefore, this peak was selected to detect the presence of HVPD/ μ E

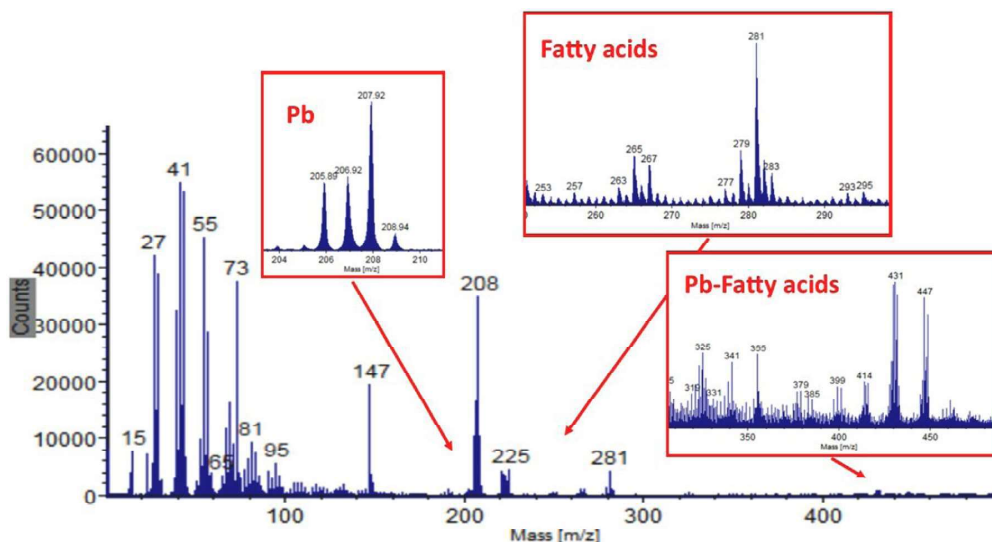


Fig. 9. Mass spectra of the painting surface before the test of interaction in the range 0–500 amu: the regions where fragments belonging to Pb, fatty acids and Pb-fatty acids conjugates are found, are highlighted.

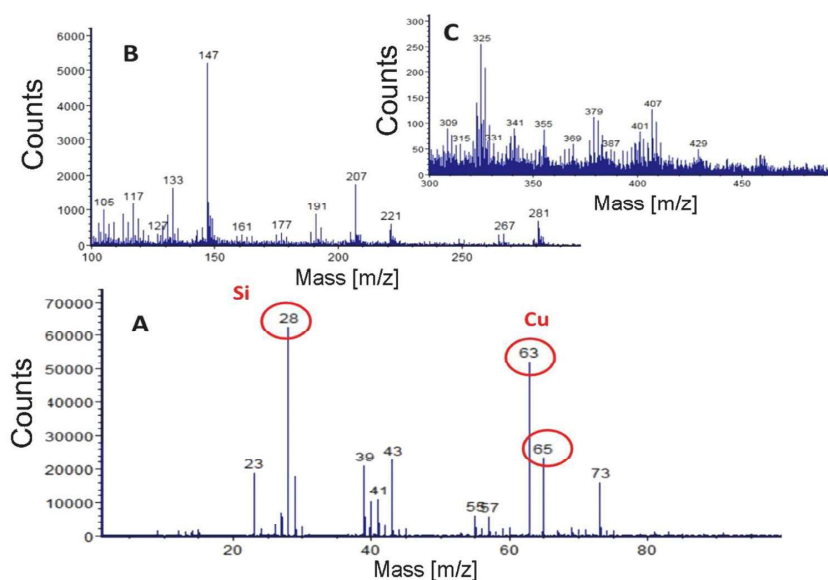


Fig. 10. Mass spectra of the painting surface after the test of interaction and removal of the HVPD/ μ E system in the range 0–500 amu divided in 3 parts: (A) Range 0–100 amu (B) 100–300 amu (C) 300–500 amu.

residues after cleaning procedures. Looking at the three spectra reported in Fig. 11 it was observed that the peak at m/z 165 presented this trend of intensity: $I_C >> I_A > I_B$. This could be interpreted in the following sense: the peak was due to both PVA and fragments associated to the aged organic molecules; the very strong intensity in C was due to the high content of PVA in the sample subjected to ToF-SIMS analysis, while the presence in A was due to a fragment – not the most important – of the organic aged molecules. The lowest intensity of this peak in B was due to the strong interaction between the aged organic molecules and the HVPD/ μ E system that led to the thinning of the coating.

Chemical images of the samples acquired in bunched mode before

and after the interaction time and removal of the HVPD/ μ E system over an area of about $400 \mu\text{m}^2$ with a lateral resolution of $\sim 1 \mu\text{m}$, are reported in Fig. S15. In the chemical map of the surface before the test of the interaction between HVPD/ μ E and organic aged molecules (Fig. S15A), the dominant signals were due to lead and various organic fragments. After the interaction time and the removal of HVPD/ μ E, the surface became more homogeneous from a chemical point of view and showed itself unveiled by the organic coating: in fact, the spots that were visible before the interaction disappeared and copper and silica became predominant. No fragment at m/z 165 were detected over the analyzed area, confirming the absence of residues left by the cleaning treatment.

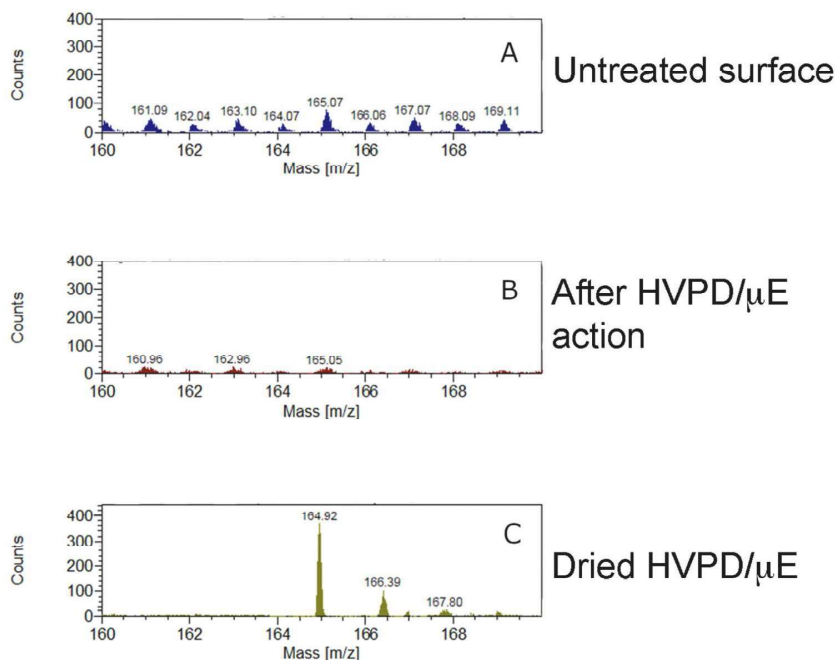


Fig. 11. TOF-SIMS spectra of untreated surface (A), of surface after the interaction time and removal of HVPD/ μ E (B), and of the HVPD/ μ E system (C) in the 160–170 m/z mass range.

4. Conclusions

A new complex, nanostructured fluid constituted of aqueous Highly Viscous Polymeric Dispersion (HVPD) composed by a 3D network of poly(vinyl alcohol) covalently crosslinked by borax and loaded with a o/w microemulsion (μ E) was developed and characterized from a structural and rheological point of view. The rheological analysis indicated that the loading of the o/w microemulsion into the HVPD network induced an increase of the stiffness of the system, as indicated by the growth of the elasticity of the HVPD/ μ E respect to the starting aqueous HVPD. It was interesting to notice that this effect resulted as the sum of two opposite causes: the de-structuring due to the SDS surfactant (lower) and the structuring one attributed to both the co-surfactant 1PeOH and the apolar solvent p-xylene. The retention of the strong elasticity of the HVPD/ μ E played a fundamental role in view of possible applications of this complex nanostructured fluid for cleaning purposes in cultural heritage conservation. The structural characterization carried out through SAXS indicated the persistence of the nanostructure of the μ E, even after its confinement inside the HVPD. The confinement of the liquid microemulsion into the HVPD induced some limited changes of the μ E nanodroplets structure: while their mean size remained almost unchanged, the polydispersity increased by a factor 2 and the particles charge decreased about four times due to the screening effect of the 3D PVA/borax network on the charged objects constituting the microemulsion. The retention of the μ E structure, apart from the changes evidenced by SAXS, was ascertained also by DSC measurements, that showed the persistence of the three water populations as in the pure μ E.

The interactions between the HVPD/ μ E system and organic molecules – siccativ oils and dammar varnish – constituting aged thin films coating the surface of a 19th century Tuscan egg-tempera canvas showed the high segregation of these molecules within the complex fluid acting as a “green”, selective cleaning agent. ATR-FTIR and TOF-SIMS analyses carried out onto the painting surface before and after the interaction time clearly highlighted the occurred strong interaction

leading to the removal of the dark, brown coating without leaving any traces of the HVPD/ μ E system and recovering the original painting layers. The possibility to completely remove the cleaning system simply by a peeling action without leaving any instrumentally detectable residue of it onto the cleaned area, especially avoiding both the use of free organic solvents and any mechanical action onto the paint surface, represents a fundamental upgrade compared to the traditional cleaning methods based on the use of gels [Stulik, D.; Dorge, V. Solvent gels for the cleaning of works of art: the residue question. *Getty Publications* 2004, Los Angeles]. Theoretically there are not limitations to the use of this system, even for the cleaning of paintings having different composition (i.e. oil paintings). Nevertheless, in this last case, the composition of the o/w microemulsion embedded into the PVA/borax network should be modulated by choosing as dispersed phase and cosurfactants, organic solvents able in the bulk solubilization of the patina to be removed.

CRedit authorship contribution statement

Emiliano Carretti: Conceptualization, Methodology, Data curation, Writing – review & editing, Supervision. **Giovanna Poggi:** Data curation, Writing – review & editing, Supervision. **Elisa Ghelardi:** Data curation, Writing – original draft. **Francesca Porpora:** Data curation, Writing – original draft. **Agnese Magnani:** Data curation. **Emiliano Fratini:** Data curation, Writing – original draft. **Luigi Dei:** Conceptualization, Writing – review & editing, Data curation. **Marco Consumi:** Conceptualization, Data curation, Writing – original draft.

Declaration of Competing Interest

The authors declare that they have no known competing financial interests or personal relationships that could have appeared to influence the work reported in this paper.

Acknowledgments

Center for Colloid and Surface Science (CSGI), University of Florence, is acknowledged for financial support.

Appendix A. Supporting information

Supplementary data associated with this article can be found in the online version at doi:10.1016/j.colsurfa.2022.128968.

References

- [1] D. Jeong, H. Lim, M.-S. Ko, W. Kim, Utilization of three-layered polyvinyl alcohol gel cubes for treating low-strength ammonium wastewater in a single-stage autotrophic nitrogen removal process, *J. Environ. Chem. Eng.* 10 (2022), 106934, <https://doi.org/10.1016/j.jece.2021.106934>.
- [2] H. Abiral, A. Atmajaya, M. Mahardika, F. Hafizulhaq, Kadriadi, D. Handayani, S. M. Sapuan, R.A. Ilyas, Effect of ultrasonication duration of polyvinyl alcohol (PVA) gel on characterizations of PVA film, *J. Mater. Res. Technol.* 9 (2020) 2477–2486, <https://doi.org/10.1016/j.jmrt.2019.12.078>.
- [3] R. Mastrangelo, D. Chelazzi, G. Poggi, E. Fratini, L. Pensabene Buemi, M. L. Petruzzellis, P. Baglioni, Twin-chain polymer hydrogels based on poly(vinyl alcohol) as new advanced tool for the cleaning of modern and contemporary art, *Proc. Natl. Acad. Sci.* 117 (2020) 7011–7020, <https://doi.org/10.1073/pnas.1911811117>.
- [4] N. Bonelli, G. Poggi, D. Chelazzi, R. Giorgi, P. Baglioni, Poly(vinyl alcohol)/poly(vinyl pyrrolidone) hydrogels for the cleaning of art, *J. Colloid Interface Sci.* 536 (2019) 339–348, <https://doi.org/10.1016/j.jcis.2018.10.025>.
- [5] E.F.D. Januário, T.B. Vidovix, M.A. Calsavara, R. Bergamasco, A.M.S. Vieira, Membrane surface functionalization by the deposition of polyvinyl alcohol and graphene oxide for dyes removal and treatment of a simulated wastewater, *Chem. Eng. Process. - Process. Intensif.* 170 (2022), 108725, <https://doi.org/10.1016/j.ccep.2021.108725>.
- [6] Y. Huo, K. Zhao, Z. Xu, F. Li, X. Zhao, Q. Meng, C. Tang, Y. Tang, Ultralight and superelastic polyvinyl alcohol/SiC nanofiber/reduced graphene oxide hybrid foams with excellent thermal insulation and microwave absorption properties, *Ceram. Int.* 47 (2021) 25986–25996, <https://doi.org/10.1016/j.ceramint.2021.06.004>.
- [7] M. Akter, N. Hirase, M.T. Sikder, M.M. Rahman, T. Hosokawa, T. Saito, M. Kurasaki, Pb (II) Remediation from aqueous environment using chitosan-activated carbon-polyvinyl alcohol composite beads, *Water Air Soil Pollut.* 232 (2021) 272, <https://doi.org/10.1007/s11270-021-05243-8>.
- [8] R. Rodríguez-Rodríguez, H. Espinosa-Andrews, C. Velasco-Quintero-Martínez, Z. Y. García-Carvajal, Composite hydrogels based on gelatin, chitosan and polyvinyl alcohol to biomedical applications: a review, *Int. J. Polym. Mater. Polym. Biomater.* 69 (2020) 1–20, <https://doi.org/10.1080/00914037.2019.1581780>.
- [9] M.I. Baker, S.P. Walsh, Z. Schwartz, B.D. Boyan, A review of polyvinyl alcohol and its uses in cartilage and orthopedic applications, *J. Biomed. Mater. Res. Part B Appl. Biomater.* 100B (2012) 1451–1457, <https://doi.org/10.1002/jbm.b.32694>.
- [10] Q. Ye, S. Chen, Y. Zhang, B. Ruan, Y. Zhang, X. Zhang, T. Jiang, X. Wang, N. Ma, F. Tsai, Chitosan/Polyvinyl Alcohol/Lauramidopropyl Betaine/2D-HOF mixed film with abundant hydrogen bonds acts as high mechanical strength artificial skin, *Macromol. Biosci.* 21 (2021), 2100317, <https://doi.org/10.1002/mabi.202100317>.
- [11] L. Cao, S. Huang, F. Lai, Z. Fang, J. Cui, X. Du, W. Li, Z. Lin, P. Zhang, Z. Huang, Sucrose in situ physically cross-linked of polyaniline and polyvinyl alcohol to prepare three-dimensional nanocomposite hydrogel with flexibility and high capacitance, *Ion. (Kiel.)* 27 (2021) 3431–3441, <https://doi.org/10.1007/s11581-021-04010-3>.
- [12] M.H. Azarian, P. Boochathum, M. Kongseema, Biocompatibility and biodegradability of filler encapsulated chloroacetylated natural rubber/polyvinyl alcohol nanofiber for wound dressing, *Mater. Sci. Eng. C* 103 (2019), 109829, <https://doi.org/10.1016/j.msec.2019.109829>.
- [13] O. Alonso-López, S. López-Ibáñez, R. Beiras, Assessment of toxicity and biodegradability of poly(vinyl alcohol)-based materials in marine water, *Polym. (Basel)* 13 (2021) 3742, <https://doi.org/10.3390/polym13213742>.
- [14] A.-L. Kjøniksen, B. Nystrom, Effects of polymer concentration and cross-linking density on rheology of chemically cross-linked poly(vinyl alcohol) near the gelation threshold, *Macromolecules* 29 (1996) 5215–5222, <https://doi.org/10.1021/ma960094q>.
- [15] L.V. Angelova, P. Terech, I. Natali, L. Dei, E. Carretti, R.G. Weiss, Cosolvent gel-like materials from partially hydrolyzed poly(vinyl acetate)s and Borax, *Langmuir* 27 (2011) 11671–11682, <https://doi.org/10.1021/la202179e>.
- [16] E. Carretti, C. Matarrese, E. Fratini, P. Baglioni, L. Dei, Physicochemical characterization of partially hydrolyzed poly(vinyl acetate)-borate aqueous dispersions, *Soft Matter* (2014), <https://doi.org/10.1039/C4SM00355A>.
- [17] K. Nakamura, T. Hatakeyama, H. Hatakeyama, Relationship between hydrogen bonding and bound water in polyhydroxystyrene derivatives, *Polym. (Guildf.)* 24 (1983) 871–876, [https://doi.org/10.1016/0032-3861\(83\)90206-9](https://doi.org/10.1016/0032-3861(83)90206-9).
- [18] Y. Sakai, S. Kuroki, M. Satoh, Water properties in the super-salt-resistive gel probed by NMR and DSC, *Langmuir* 24 (2008) 6981–6987, <https://doi.org/10.1021/la800397f>.
- [19] S. Michalski, A physical model of the cleaning of oil paint, *Stud. Conserv.* 35 (1990) 85–92, <https://doi.org/10.1179/sic.1990.35.s1.020>.
- [20] P. Baglioni, D. Chelazzi, Nanoscience for the Conservation of Works of Art, Royal Society of Chemistry, Cambridge, 2013, <https://doi.org/10.1039/9781849737630>.
- [21] P. Baglioni, D. Chelazzi, R. Giorgi, *Nanotechnologies in the Conservation of Cultural Heritage - A Compendium of Materials and Techniques*, Springer, Heidelberg New York London, 2015.
- [22] E. Carretti, I. Natali, C. Matarrese, P. Bracco, R.G. Weiss, P. Baglioni, A. Salvini, L. Dei, A new family of high viscosity polymeric dispersions for cleaning easel paintings, *J. Cult. Herit.* 11 (2010) 373–380, <https://doi.org/10.1016/j.culher.2010.04.002>.
- [23] M. Baglioni, D. Berti, J. Teixeira, R. Giorgi, P. Baglioni, Nanostructured surfactant-based systems for the removal of polymers from wall paintings: A small-angle neutron scattering study, *Langmuir* 28 (2012) 15193–15202, <https://doi.org/10.1021/la303463m>.
- [24] M. Baglioni, R. Giorgi, D. Berti, P. Baglioni, Smart cleaning of cultural heritage: a new challenge for soft nanoscience, *Nanoscale* 4 (2012) 42–53, <https://doi.org/10.1039/C1NR10911A>.
- [25] P. Baglioni, E. Carretti, D. Chelazzi, Nanomaterials in art conservation, *Nat. Publ. Gr.* 10 (2015) 287–290, <https://doi.org/10.1038/nnano.2015.38>.
- [26] E. Carretti, B. Salvadori, P. Baglioni, L. Dei, Microemulsions and micellar solutions for cleaning wall painting surfaces, *Stud. Conserv.* 50 (2005) 128–136, <https://doi.org/10.1179/sic.2005.50.2.128>.
- [27] M. Baglioni, J.A.L. Domingues, E. Carretti, E. Fratini, D. Chelazzi, R. Giorgi, P. Baglioni, Complex fluids confined into semi-interpenetrated chemical hydrogels for the cleaning of classic art: A rheological and SAXS study, *ACS Appl. Mater. Interfaces* 10 (2018) 19162–19172, <https://doi.org/10.1021/acsmi.8b01841>.
- [28] P. Baglioni, D. Berti, M. Bonini, E. Carretti, L. Dei, E. Fratini, R. Giorgi, Author's personal copy Micelle, microemulsions, and gels for the conservation of cultural heritage, (n.d.).
- [29] E. Carretti, E. Fratini, D. Berti, L. Dei, P. Baglioni, Nanoscience for art conservation: Oil-in-water microemulsions embedded in a polymeric network for the cleaning of works of art, *Angew. Chem. Int. Ed.* 48 (2009) 8966–8969, <https://doi.org/10.1002/anie.200904244>.
- [30] Y. Lee, J. Lee, Y. Kim, S. Choi, S.W. Ham, K.-J. Kim, Investigation of natural dyes and ancient textiles from Korea using TOF-SIMS, *Appl. Surf. Sci.* 255 (2008) 1033–1036, <https://doi.org/10.1016/j.apsusc.2008.05.097>.
- [31] A. Tognazzi, R. Lapucci, S. Martini, G. Leone, A. Magnani, C. Rossi, TOF-SIMS characterization of pigments and binders in 'the Martyrdom of St. Catherine', in Zejtun (Malta), *Surf. Interface Anal.* 43 (2011) 1152–1159, <https://doi.org/10.1002/sia.3272>.
- [32] G. Leone, A. De Vita, A. Magnani, C. Rossi, Characterization of archaeological mortars from Herculaneum, *Thermochim. Acta* 624 (2016) 86–94, <https://doi.org/10.1016/j.tca.2015.12.003>.
- [33] J.C. Vickerman, TOF-SIMS - an overview, in: J.C. Vickerman, D. Briggs (Eds.), *TOF-SIMS Surf. Anal. by Mass Spectrom., Surface Spectra and IM Publications*, Manchester and Chichester, UK, 2001, pp. 1–40.
- [34] G. Leone, M. Consumi, S. Lamponi, A. Magnani, Combination of static time of flight secondary ion mass spectrometry and infrared reflection-adsorption spectroscopy for the characterisation of a four steps built-up carbohydrate array, *Appl. Surf. Sci.* 258 (2012) 6302–6315, <https://doi.org/10.1016/j.apsusc.2012.03.027>.
- [35] P. Baglioni, E. Rivara-Mintin, L. Dei, E. Ferroni, ESR study of sodium dodecyl sulfate and dodecyltrimethylammonium bromide micellar solutions: effect of urea, *J. Phys. Chem.* 94 (1990) 8218–8222, <https://doi.org/10.1021/j100384a044>.
- [36] T.N. Blanton, M. Rajeswaran, P.W. Stephens, D.R. Whitcomb, S.T. Mixture, J. A. Kaduk, Crystal structure determination of the silver carboxylate dimer [Ag(O 2C 22H 43)] 2, silver behenate, using powder X-ray diffraction methods, *Powder Diffr.* 26 (2011) 313–320, <https://doi.org/10.1154/1.3661981>.
- [37] G. Leone, M. Consumi, S. Pepi, S. Lamponi, C. Bonechi, G. Tamasi, A. Donati, C. Rossi, A. Magnani, Alginate-gelatin formulation to modify lovastatin release profile from red yeast rice for hypercholesterolemia therapy, *Ther. Deliv.* 8 (2017) 843–854, <https://doi.org/10.4155/tde-2017-0025>.
- [38] G. Leone, M. Consumi, S. Lamponi, C. Bonechi, G. Tamasi, A. Donati, C. Rossi, A. Magnani, Thixotropic PVA hydrogel enclosing a hydrophilic PVP core as nucleus pulposus substitute, *Mater. Sci. Eng. C* 98 (2019) 696–704, <https://doi.org/10.1016/j.msec.2019.01.039>.
- [39] E. Carretti, L. Dei, P. Baglioni, Solubilization of acrylic and vinyl polymers in nanocontainer solutions. Application of microemulsions and micelles to cultural heritage conservation, *Langmuir* 19 (2003) 7867–7872, <https://doi.org/10.1021/la034757q>.
- [40] B. a Schubert, E.W. Kaler, N.J. Wagner, The microstructure and rheology of mixed cationic/ anionic wormlike micelles, *Langmuir* (2003) 4079–4089, <https://doi.org/10.1021/la202821c>.
- [41] E. Carretti, S. Grassi, M. Cossalter, I. Natali, G. Caminati, R.G.R.G. Weiss, P. Baglioni, L. Dei, Poly(vinyl alcohol)-borate hydro/cosolvent gels: Viscoelastic properties, solubilizing power, and application to art conservation, *Langmuir* 25 (2009) 8656–8662, <https://doi.org/10.1021/la804306v>.
- [42] I. Natali, E. Carretti, L. Angelova, P. Baglioni, R.G.R.G. Weiss, L. Dei, Structural and mechanical properties of "peelable" organoaqueous dispersions with partially hydrolyzed poly(vinyl acetate)-borate networks: applications to cleaning painted surfaces, *Langmuir* 27 (2011) 13226–13235, <https://doi.org/10.1021/la2015786>.
- [43] M. Rubinstein, A.N. Semenov, Dynamics of entangled solutions of associating polymers, *Macromolecules* 34 (2001) 1058–1068, <https://doi.org/10.1021/ma0013049>.

- [44] M. Shibukawa, K. Aoyagi, R. Sakamoto, K. Oguma, Liquid chromatography and differential scanning calorimetry studies on the states of water in hydrophilic polymer gel packings in relation to retention selectivity, *J. Chromatogr. A* 832 (1999) 17–27, [https://doi.org/10.1016/S0021-9673\(98\)00988-1](https://doi.org/10.1016/S0021-9673(98)00988-1).
- [45] H. Hauser, G. Haering, A. Pande, P.L. Luisi, Interaction of water with sodium bis(2-ethyl-1-hexyl) sulfosuccinate in reversed micelles, *J. Phys. Chem.* 93 (1989) 7869–7876, <https://doi.org/10.1021/j100360a029>.
- [46] M. Derrick, Fourier transform infrared spectral analysis of natural resins used in furniture finishes, *J. Am. Inst. Conserv.* 28 (1989) 43–56, <https://doi.org/10.1179/019713689806046264>.
- [47] M.R. Derrick, D. Stulik, J.M. Landry, *Infrared Spectroscopy in Conservation Science*, Getty Conservation Institute, Los Angeles, USA, 1999.
- [48] T. Poli, O. Chiantore, E. Diana, A. Piccirillo, Drying oil and natural varnishes in paintings: A competition in the metal soap formation, *Coatings* 11 (2021) 171, <https://doi.org/10.3390/coatings11020171>.
- [49] J. Malléol, J. Lemaire, J.-L. Gardette, Yellowing of oil-based paints, *Stud. Conserv.* 46 (2001) 121–131, <https://doi.org/10.1080/00393630.2001.12071699>.
- [50] E. Kirchner, I. van der Lans, F. Ligterink, E. Hendriks, J. Delaney, Digitally reconstructing Van Gogh's Field with Irises near Arles. Part I: Varnish, *Color Res. Appl.* 43 (2018) 150–157, <https://doi.org/10.1002/col.22162>.
- [51] E.R. de la Rie, Fluorescence of paint and varnish layers (Part II), *Stud. Conserv.* 27 (1982) 65–69, <https://doi.org/10.1179/sic.1982.27.2.65>.
- [52] R. Wolbers, *Cleaning Painted Surfaces: Aqueous Methods*, Archetype Books, London, 2000.
- [53] P. Biocca, P. Santopadre, G. Sidoti, G. Sotgiu, F. de Notaristefani, L. Tortora, ToF-SIMS study of gilding technique in the fresco Vela della Castità by Giotto's school, *Surf. Interface Anal.* 48 (2016) 404–408, <https://doi.org/10.1002/sia.5956>.
- [54] *Organic Mass Spectrometry*, in: M.P. Colombini, F. Modugno (Eds.), *Art and Archaeology*, Wiley, Chichester, West Sussex, UK, 2009.

Nanostructured Fluids Confined into Highly Viscous Polymeric Dispersions as cleaning tools for artifacts: A Rheological, SAXS, DSC and TOF-SIMS Study

Emiliano Carretti^{1,2,*}, Giovanna Poggi^{1,2}, Elisa Ghelardi^{1,2,3}, Francesca Porpora^{1,2},
Agnese Magnani^{2,4}, Emiliano Fratini^{1,2}, Luigi Dei^{1,2} and Marco Consumi^{2,4}

¹Department of Chemistry “Ugo Schiff”, University of Florence,
via della Lastruccia, 3-13 – 50019 Sesto Fiorentino (FI) – Italy

²Center for Colloid and Surface Science (CSGI), via della Lastruccia 3, 50019
Sesto Fiorentino, Italy

³Department of Chemistry and Industrial Chemistry, University of Pisa, via
Giuseppe Moruzzi 13 – 56124 Pisa, Italy

⁴Department of Biotechnology Chemistry and Pharmacy, University of Siena, via
A. Moro 2, 53100 Siena, Italy

*To whom correspondence should be addressed emiliano.carretti@unifi.it

Abstract

The development, and the structural and mechanical characterization of an new complex system composed by an oil-in-water microemulsion (μ E) embedded in a aqueous 3D Highly Viscous Polymeric Dispersion (HVPD) of poly(vinyl alcohol) (PVA) cross-linked by borax, is here presented together with its possible

implications in paintings conservation. The HVPD/ μ E was characterized by Small Angle X-Rays Scattering (SAXS), Differential Scanning Calorimetric (DSC) and rheology to obtain information about the mutual effect of the μ E and of the PVA network on both the nanostructure of the μ E, and on the mechanical behavior of the system. Experimental data indicate that the nanostructure of the μ E is retained even in the presence of the PVA/borax network whose mechanical properties are enhanced by the presence of the nanofluid. The effect of HVPD/ μ E on organic molecules thin films of varnish coatings usually used on easel paintings, was studied by Attenuated Total Reflection Fourier Transform InfraRed spectroscopy (ATR-FTIR) and Time-of-Flight Secondary Ion Mass Spectrometry (TOF-SIMS). The results showed that an interaction occurred leading to the extraction of the organic molecules within the HVPD/ μ E. The applicative consequence was that the HVPD/ μ E complex fluid revealed itself to be a potential, very powerful and “green” tool for selective cleaning of easel paintings affected by artificial aged coatings, with very low environmental impact and leaving no residues onto the painting surface.

Keywords: chemical hydrogels, microemulsions, SAXS, rheology, varnish removal

1. Introduction

Poly(vinyl alcohol) (PVA) is one of the hydrophilic polymers most largely used to make three-dimensional networks [1–4], due to its excellent chemical versatility [5–

7], biocompatibility [8,9], mechanical strength [10], flexibility [11], biodegradability [12], cheapness and low toxicity [13]. A further important feature of PVA is its ability to form thermodynamically stable and thermoreversible highly-viscous polymeric dispersions (HVPDs) through a esterification reaction between the vinyl hydroxyl groups and different anions like borate, vanadate or antimonite [14,15]. Moreover, due to the reversibility of that reaction, these covalent cross-links are dynamic and an equilibrium tridimensional density is established as a function of temperature [16]. Moreover, the structural features of the polymer network of these HVPDs, are strictly related to many other key factors such as the equilibrium between the electrostatic interactions, the excluded volume of the PVA chains, the spatial density of the cross-linking, and the charge-shielding effects [17,18]. From the applicative standpoint, a fundamental property of these systems is that they show the peculiar ability to load significant amounts of organic solvents with high and medium polarity. This is potentially a key-feature to use these HVPDs as cleaning tools for painted surfaces of historical and artistic interest, particularly easel paintings [15]. In this way, thanks to their high viscosity, the uncontrollable penetration of pure organic solvents into the paint layer, which represents the main drawback resulting from the use of unconfined fluids for cleaning operations, is avoided. Indeed, the penetration of free organic solvents, traditionally used for the cleaning of easel paintings, may cause some undesirable effects, the most important and common of which are the swelling and the leaching of the organic structural

components [19] and/or the spreading of the solubilized materials into the porous matrix of the paint [20].

Other peculiar features of the PVA/borax-based HVPDs are connected to their structural dynamic and to their mechanical properties easily modulable by varying both the amount and the molecular weight of the polymer, and the nature and the amount of the solvent loaded into the system. In other terms, by changing the composition of the system, it is possible to obtain HVPDs having values of both the elastic modulus G' and $\tan\delta$ (G''/G'), which, after application, allow for an easy and complete removal through simple a peeling action [21]. This is the way to minimize the HVPD's residues on the paint surface and to avoid, at the same time, the mechanical action and the application of free solvents usually needed for the complete removal of traditional gel used for cleaning purposes [22].

In this work we demonstrate that the above mentioned PVA-based HVPDs, in addition to being able to load many solvents with different polarity, are also capable of loading a nanostructured complex fluid such as a oil-in-water (o/w) microemulsion (μE). It is well known that nanostructured fluids are highly effective in the swelling/solubilization of several hydrophobic materials from painted surfaces of historical and artistical interest and, in comparison to organic solvents, ensure a better control of the cleaning action [23–26]. Unfortunately, net of that, the application of these systems on water-sensitive porous artifacts (i.e. easel paintings, cellulosic materials etc) makes mandatory their confinement in a solid-like matrix (i.e. a physical or a chemical gel) [27].

Here we present the set-up of a thermodynamically and kinetically stable HVPD composed of PVA covalently crosslinked by $\text{Na}_2\text{Ba}_4\text{O}_7 \cdot 10\text{H}_2\text{O}$ containing a p-xylene-in-water microemulsion (HVPD/ μE), to exploit the advantages connected to the use of nanostructured fluids in combination to those typical of gel-like polymeric dispersion, improving the performances of systems that have already been successfully tested. [28]

The dynamic, the mechanical and the structural properties of the HVPD/ μE complex system were investigated through rheological and Small Angle X-rays Scattering (SAXS) measurements respectively. Rheological analysis paid attention on the effect of the serial addition of the components of the μE on the viscoelastic properties of the HVPD/ μE . This is a crucial factor because both the cleaning performances and the possibility to safely and completely remove the HVPD/ μE from the paint surface after the cleaning, are influenced by the mechanical behavior of the system [29]. Moreover, SAXS curves were collected to characterize the μE structure at the nanoscale and to check whether it was retained once it is loaded inside the PVA/borax network and to understand if structural changes occurred in this nanofluid. Finally, the effect of HVPD/ μE on organic molecules thin film constituted by aged linseed oil and dammar varnish were studied by means of Attenuated Total Reflection Fourier Transform InfraRed spectroscopy (ATR-FTIR) and Time of Flight Secondary Ion Mass Spectrometry (ToF-SIMS). In particular, these two analytical techniques were used to verify the presence of the above-described organic

molecules onto the surface of a 19th century egg-tempera canvas painting before and after the application of the HVPD/ μ E. ToF-SIMS is a powerful surface-sensitive analytical method with the peculiar ability to determine the chemical composition (spatially-resolved) with ppm-ppb sensitivity of both inorganic and organic analytes and, therefore, represents the best analytical method to analyze the painting surface and evaluate the effect of our cleaning system on aged organic molecules [30–32]. It is worthwhile to recall the extremely high surface sensitivity of TOF-SIMS that allows highlighting traces of chemical compounds and their distribution onto the surfaces with lateral resolution less than 1 micron [33,34]. ToF-SIMS associated with ATR-FTIR was here used to obtain information both about the occurred interaction of the organic aged molecules with HVPD/ μ E, and on the cleaning performance. Moreover, for the first time, ToF-SIMS was also used to monitor the presence of residues of the cleaning system, i.e. HVPD/ μ E, onto the painting surface after its application and removal, providing a solid proof-of-concept about the possible application of this analytical technique for the evaluation of new cleaning materials for the conservation of cultural heritage.

2. Materials and Methods

2.1 Materials

1-pentanol (1PeOH, 99%, Sigma Aldrich, Germany), p-xylene (Merck, Germany), poly(vinyl alcohol) 80% hydrolysed (PVA, Kuraray, Japan), sodium tetraborate decahydrate (borax, 99.5% Sigma Aldrich, Germany) were used as received. Sodium

dodecylsulfate (SDS, 99% Sigma Aldrich, Germany), was recrystallized from ethanol before the use [35]. Water was purified by means of a Millipore Elix3 system ($R \geq 15 \text{ M}\Omega\text{cm}$).

2.2 Methods

2.2.1 Preparation of the HVPD/ μ E

SDS was first solubilized in water and 1PeOH was added dropwise to form a micellar solution; then 80PVA was added and completely dissolved at room temperature by stirring the system in a hermetically closed vial for 2 hours. After the complete solubilization of the polymer, p-xylene and a 4 wt% aqueous solution of borax were added dropwise in sequence. The system was initially opalescent, but after 24 hour at 25°C, it became completely transparent.

2.3 HVPD/ μ E characterization

2.3.1 Rheology

Rheological measurements in oscillatory regime were carried by using a Paar Physica UDS200 rheometer (the temperature was maintained at $25 \pm 0.1 \text{ }^\circ\text{C}$ through a Peltier) with a cone-plate geometry (40 mm diameter and 1° cone angle; the gap was 0.5 mm). Once loaded, before the beginning of the measurements, the samples were equilibrated for at least 30 mins at 25 °C. The frequency sweep tests were carried out always in the linear viscoelastic regime (the oscillation strain was 1%), previously determined for each sample, through an amplitude sweep test. The trend

of both the storage (G') and loss (G'') moduli was measured in the frequency range between 0.01 and 100 Hz.

2.3.2 Small Angle X- Rays Scattering

Small Angle X-Ray Scattering (SAXS) curves were collected by means of a Hecus X-Ray System GmbH Kratky camera equipped with two 1-D Position-Sensitive Detectors (Methane/Ar) mounted on a ID3003 generator (Seifert). The experimental SAXS curves of the liquid microemulsion (μE) and of the μE loaded into the PVA/borax-based HVPD (HVPD/ μE) were analyzed using a non-linear least-square fitting (statistically weighed) where the microemulsion was considered as composed by spheres with a core (hydrophobic)-shell (hydrophylic) structure. The polydispersity of the radii dimensions was described by the Schulz distribution. In the modeling of the nanodroplets, the external shell was considered composed by the polar heads and the first CH_2 of the hydrocarbon tails of the SDS and 1PeOH molecules, by the OH groups of the 1PeOH molecules, the hydration water, and some counterions. The hydrophobic core was considered as composed by p-xylene molecules and the hydrocarbon tails, $\text{C}_{11}\text{H}_{23}$ and C_4H_9 appertaining to SDS and 1PeOH, respectively.

On these bases, the dependence of the scattering intensity $I(Q)$ from the scattering vector Q is:

$$I(Q) = A\phi\tilde{P}(Q)\tilde{S}(Q) + I_{bkg} \quad (2)$$

where A is an instrumental factor, ϕ is volume fraction of the microemulsion, $\tilde{P}(Q)$ is the form factor (spherical particles), $\tilde{S}(Q)$ is the structure factor accounting of the inter-particle interactions, and I_{bkg} is the instrumental background [29]. Moreover, $Q = \frac{4\pi}{\lambda} \sin \frac{\theta}{2}$, where θ is the scattering angle and λ is 0.1542 nm.

The SAXS curve of the HVPD/ μ E system was obtained by scaling and subtracting the contribution of the PVA/borax network (Figure SI1).

2.3.3 Differential Scanning Calorimetry (DSC)

DSC measurements were carried out by means of a Q1000 TA Instruments calorimeter with sealed aluminum pans under nitrogen atmosphere (nitrogen flow: $50.0 \pm 0.5 \text{ cm}^3 \text{ min}^{-1}$). The temperature cycle was the following: from room temperature up to -90°C ($60^\circ\text{C min}^{-1}$), isotherm at -90°C for 8 min, from -90°C up to 30°C at 1°C min^{-1} .

2.4 Application of HVPD/ μ E

To study the interaction between the HVPD/ μ E system and organic molecules thin films, with also the aim of discovering potential application in cultural heritage conservation, the HVPD/ μ E was kept in contact with some thin film coatings present onto a 19th century Tuscan egg-tempera canvas painting. The HVPD/ μ E was applied onto the painted surface by means of a spatula, at least 48 hours after its preparation (application time: about 5 mins; the procedure was repeated twice). Afterwards, the system was peeled from the surface by means of a pincer, avoiding the use of any additional liquid after the peeling process.

Images of Figure 7 were acquired under visible light and with UV-induced fluorescence using a Canon EOS 60D camera equipped with a 100 mm f/2.8 Macro lens.

2.5 Organic molecules thin films characterization

2.5.1 Fourier Transform InfraRed Spectroscopy (FTIR)

ATR-FTIR spectra of the organic thin films were collected with a Thermo Nicolet Nexus 870 (128 scans with 4 cm^{-1} of optical resolution) equipped with a Golden Gate diamond by using a Mercury- Cadmium-Telluride (MCT; the extension of the sampling area was 150 mm^2).

2.5.2 Time of flight secondary ion mass spectrometry measurements (ToF-SIMS)

ToF-SIMS measurements were carried out on a TRIFT III spectrometer (Physical Electronics, Chanhassen, MN, USA) equipped with a gold liquid-metal primary ion source. HVPD/ μE was analyzed following a procedure developed for the analysis of hydrogels[36,37]. All the samples were kept overnight in a conditioning pre-chamber with a vacuum value of 10^{-5} Pa and then moved to the analyzing chamber where the pressure was lower than 10^{-8} Pa . Positive and negative ions spectra were acquired with a pulsed, bunched 22 keV Au^+ primary ion beam, by rastering the ion beam over a sample area $100\text{ }\mu\text{m}^2$ and maintaining static SIMS conditions (primary ion dose density $< 10^{12}\text{ ions/cm}^2$). Positive ion spectra were calibrated with CH_3^+ (15.023 m/z), C_2H_3^+ (27.023 m/z) C_3H_5^+ (41.039 m/z). The mass resolution ($m/\Delta m$) was 3000 at 27 m/z because of the roughness of the samples. Negative ions spectra were not reported because no additional can be obtained. Chemical images were acquired with

a pulsed, unbunched 22 keV Au⁺ primary ion beam, by rastering the ion beam over a 400 μm² sample area and maintaining static SIMS conditions. The lateral resolution was about 1 micron.

3. Results and discussion

3.1 Formulation and characterization of the HVPD/μE system

In the following paragraphs, details about the formulation of a HVPD/μE system, composed of a PVA covalently crosslinked by Na₂Ba₄O₇·10H₂O (HVPD) and a p-xylene-in-water microemulsion (μE), are reported. The system was formulated on the basis of the following considerations: (i) the ratio 1PeOH/SDS was kept at 1.84, as in case of a similar μE already successfully developed for applicative purposes in cultural heritage conservation [38]; (ii) on the basis of previous studies [15], a concentration of 80PVA equal to 4wt% was used, which was deemed optimal in terms of cleaning effectiveness and complete removal of the HVPD after use. Several systems have been prepared by varying the composition of the μE. The corresponding phase diagram, obtained through visual inspection of the systems, is reported in Figure 1. The aim was to maximize the amount of the organic solvents (p-xylene and 1-PeOH) included in the formulation within the monophasic region 1Φ, where the system is homogeneous and stable both from the kinetic and the thermodynamic standpoint.

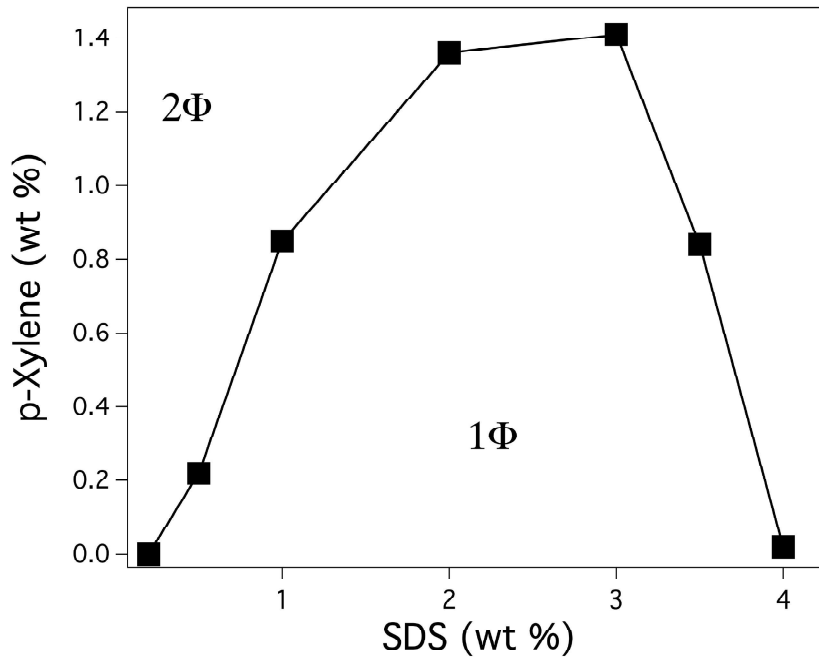


Figure 1. Phase diagram of the HVPD/ μ E system. The amount of 80PVA is equal to 4wt% and the ratio 1PeOH/SDS equal to 1.84. 1 Φ indicates the monophasic region; 2 Φ indicates the biphasic region.

Following the approach detailed above, the composition of the system used for this study was the one reported in Table 1. With the aim of detailing the effect of the μ E components on the mechanical behavior of the HVPD, the frequency sweeps of the HVPD progressively loaded with the components of the μ E (SDS, 1PeOH and p-xylene) were carried out (Figure 2).

Table 1. Composition (w/w %) of the HVPD/ μ E

Components	w/w %
SDS	2.50
H ₂ O	86.60
1-PeOH	4.60
80PVA	4.00
p-xilene	1.30
Borax	1.00

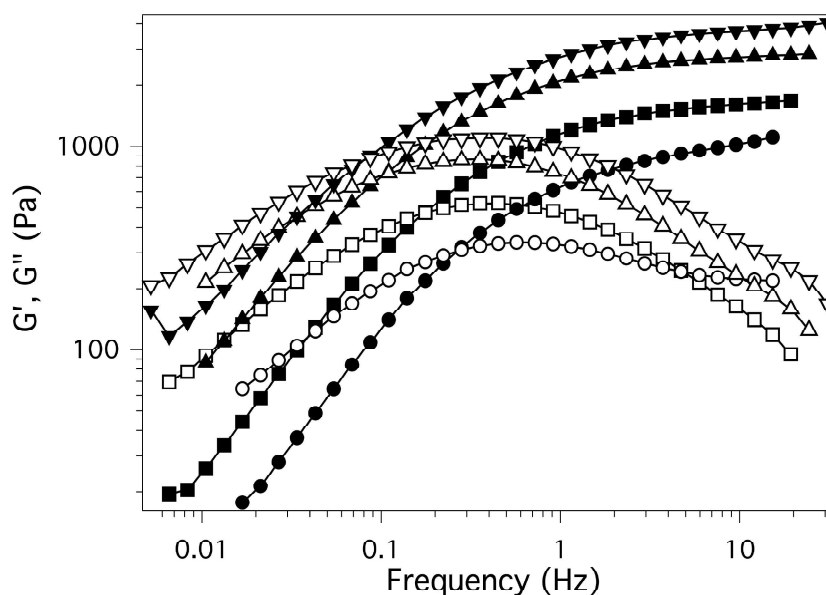


Figure 2. Frequency sweep curves of PVA (4wt%)/borax (1wt%)/H₂O based HVPD (squares), PVA (4wt%)/borax (1wt%)/H₂O based HVPD containing 2.5 wt% of SDS (circles), PVA (4wt%)/borax (1wt%)/H₂O based HVPD containing 2.5 wt% of SDS and 4.6 wt% of 1PeOH (up triangles) and PVA (4wt%)/borax (1wt%)/H₂O based HVPD containing 2.5 wt% of SDS, 4.6 wt% of 1PeOH and 1.3 wt%

of p-xylene (down triangles). Filled symbols indicate the elastic modulus G' and the empty symbols indicate the loss modulus G'' .

Figure 2 shows that the addition of 2.5 wt% SDS to the PVA/borax/H₂O based HVPD caused a shift of the G' curve towards lower values. It is well known that the asymptotic value of G' at high frequencies corresponds to the intrinsic elastic modulus G^0 that is proportional to the density of the covalent cross-linking (ρ_e) forming the PVA/borate network at a temperature T (eq. 3) [39]:

$$G^0 = \rho_e k_B T \quad (3)$$

(k_B is the Boltzmann constant). The decrease of G^0 observed after the loading of SDS into the HVPD corresponds to a decrease of ρ_e due to a de-structuring effect of the anionic surfactant on the 3D polymeric network. This effect was due to the increase of the ionic strength of the system; in fact, as reported in Figure SI2, the frequency sweep curves of the SDS/HVPD systems and of a system obtained by adding to the HVPD system an amount of NaCl equivalent to SDS, were superimposable. On the contrary, the addition of 1PeOH to the HVPD caused an increase of G^0 and then, of ρ_e (Figure 2). The structuring effect of 1PeOH, already observed for HVPDs made by 99% hydrolyzed PVA [40], was attributed [41] the decrease of the dielectric constant of the continuous phase induced by this solvent, that causes an increase of the amount of borate ions interacting with PVA chains. Finally, the data reported in Figure 2 also indicated that the addition of p-xylene to the SDS/1-pentanol/HVPD system induced a further increase of G^0 . In a previous paper [41], it has been

demonstrated that the most important rheological parameter that affects the “peelability” of a HVPD from a surface is G^0 : for G^0 values higher than 400 Pa, the gel can be easily and completely removed by “peeling” it with tweezers without leaving any detectable residue onto the cleaned surface. In our case the HVPD/ μ E had a very high G^0 value (about 1000 Pa); on the contrary, traditional physical gels commonly used for cleaning purposes display G^0 values well below this threshold, making the peeling action not feasible [15].

Figure SI3 shows the frequency sweep of Figure 2 normalized over the crossover coordinates of the G' and G'' curves. The superimposition of the curves means that the addition of the components of the microemulsion has a limited effect on the relaxation mechanism of the HVPDs even if the time scale of the relaxation processes changes.

To investigate both the effect of the PVA content on the mechanical behavior and the relaxation mechanism of the HVPD/ μ E system, frequency sweep tests were also carried out as a function of the PVA concentrations (see Figure SI4), and the continuous relaxation spectra $H(\tau)$ were obtained (Figure 3A). The increase of the width of the $H(\tau)$ curves observed upon increasing PVA content indicated the progressive increase of the complexity of the relaxation dynamics. This was probably due to the increasing entanglements among the polymer chains, such as polymer–polymer interactions, as already observed for similar systems [16]. It is well known that usually the driving factor of the dynamic of solutions of interacting polymers in good solvents is the association of the entangled groups; this behavior can be

explained considering a sticky reptation mechanism [42]. The corresponding relaxation (i.e. reptation) time is related to the concentration through a power law:

$$\tau_{\text{rep}} \sim C^a \quad (5)$$

The exponent a usually varies between 1.44 and 4.5 by varying the distance between the interaction points. Figure 3B reports the trend of the main relaxation time τ_H , corresponding to the peak of $H(\tau)$ curves, as a function of the PVA content C (g/L):

$$\log(\tau_H) = a \log C + b \quad (4)$$

The linear fit of the plot $\log(\tau_H)$ vs $\log C$ reported in Figure 3B indicates that for the HVPD/ μ E HVPD, the exponent a is equal to 2.01. Therefore, it could be concluded that water was a good solvent for the HVPD based network and that the mechanism that drove the main relaxation process was characterized by a sticky reptation [42].

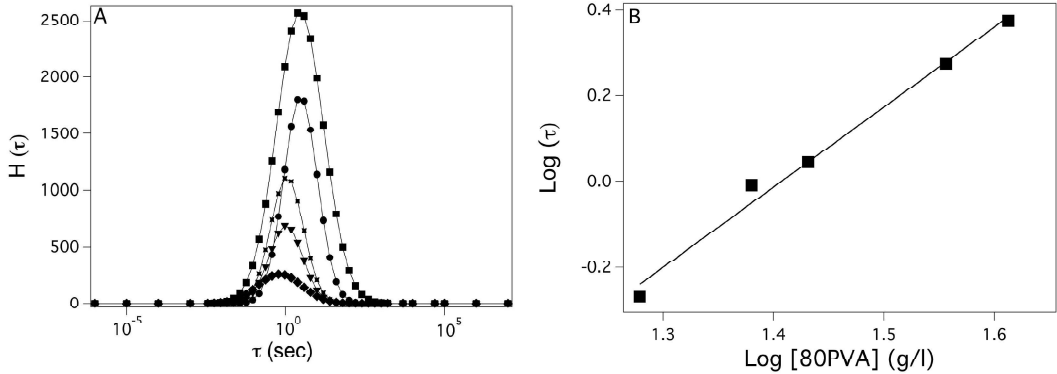


Figure 3. A. Stress relaxation spectra $H(\tau)$ of HVPD/ μ E containing 2 wt% (diamonds), 2.5 wt% (triangles), 3.0 wt% (stars), 3.5 wt% (circles) and 4.0 wt% (squares) of PVA. B. The mean relaxation times τ of the HVPD/ μ E as a function of increasing concentration of PVA used to prepare the system. The straight line is the best linear fit of the experimental data ($R^2 = 0.95842$).

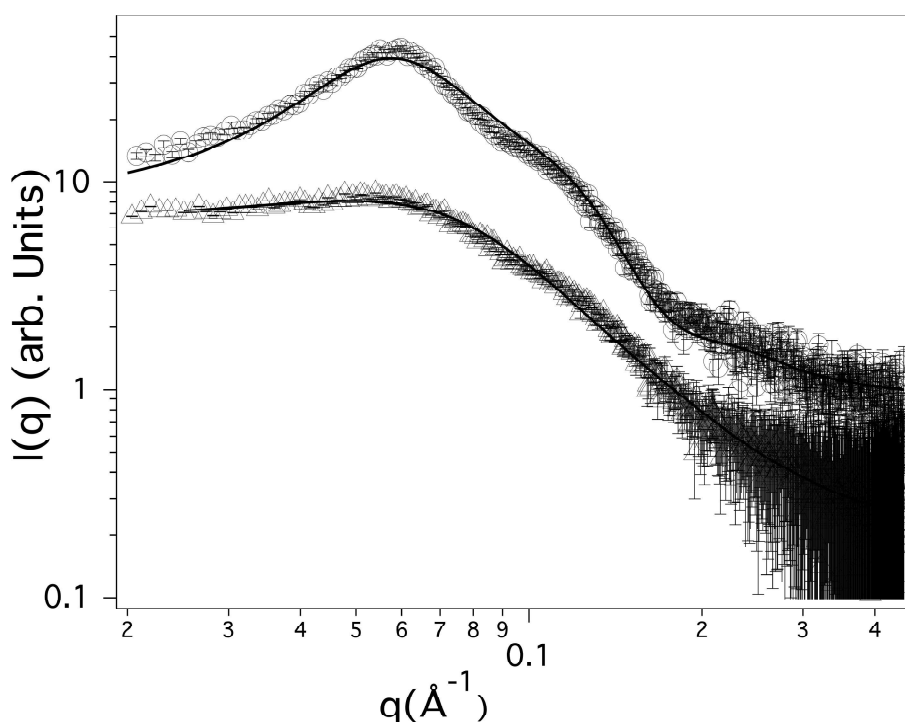


Figure 4. Log-log SAXS curves of μE (O) and of the μE confined in the HVPD network (Δ). The μE in HVPD curve was obtained by scaling and subtracting the contribution of the PVA/borax network. The continuous lines are the best-fitting curves obtained using the model described in the Materials and Methods section.

The structure of the complex fluid HVPD/ μE was investigated by SAXS measurements and the relative curves are reported in Figure 4. To analyze the nanostructure of the μE in the HVPD system, the contributions to the scattering intensities coming from the HVPD network (in the absence of the o/w μE) and from the nanofluid were considered purely additive [29]. Therefore, the curve of the HVPD network (Figure S1) was scaled and subtracted from the curve obtained from the HVPD/ μE ; in that way, the signal of the μE confined inside the HVPD network was isolated and plotted in Figure 4 (open triangles) together with the one of the

“free” μE (open circles). The SAXS curve for the microemulsion μE is characterised by a correlation peak due to the para-crystalline structure induced by the electrostatic interaction (repulsive) between the negatively charged nanodroplets constituting the system. The correlation peak was also present, even if less pronounced, in the μE confined in the HVPD network. This alteration can be attributed to a partial screening effect of the polymer network on the charged droplets. Then, SAXS data confirm that the nanostructure of the microemulsion was retained even in the polymeric network, which is a fundamental topic for the subsequent study of the interaction between the HVPD/ μE and aged organic molecules. In fact, it is to be expected that such interaction should occur between the hydrophobic core of the nanodroplets and the aged thin films molecules. The parameters obtained from fitting of the SAXS curves according to the model reported in Section 2.2.2 of the Materials and Methods section are shown in Table 2. The data clearly showed that the inclusion of the microemulsion into the HVPD network resulted in minimal changes in the size of the nanodroplets which mean size remains almost unchanged, in terms of core radius and shell thickness; the only difference concerning dimensions was a slight increase in the polydispersity. It was interesting to note that, however, the nanodroplets charge strongly decreased (about four times), this effect can be ascribed to the screening effect of the PVA/borax network on charged objects [16], as also indicated above to explain the less evident peak at about 0.06 \AA^{-1} in the SAXS curve of the confined μE .

Table 2. Structural parameters extracted from SAXS analysis of the microemulsion μE and of the μE confined in the HVPD network.

	μE	μE in HVPD
Core radius (nm)	2.4 ± 0.2	2.0 ± 0.2
Shell thickness (nm)	0.7 ± 0.2	0.9 ± 0.2
Polydispersity	0.19 ± 0.02	0.39 ± 0.02
Charge (e)	40 ± 3	10 ± 2

DSC measurements gave a further confirmation that the nanostructure of the o/w microemulsion was retained inside the HVPD network. As shown in Figure 5, the DSC curve of the μE was characterized by three endothermic peaks (labelled as μE_1 , μE_2 , μE_3) due to the melting of different populations of water molecules inside the system.

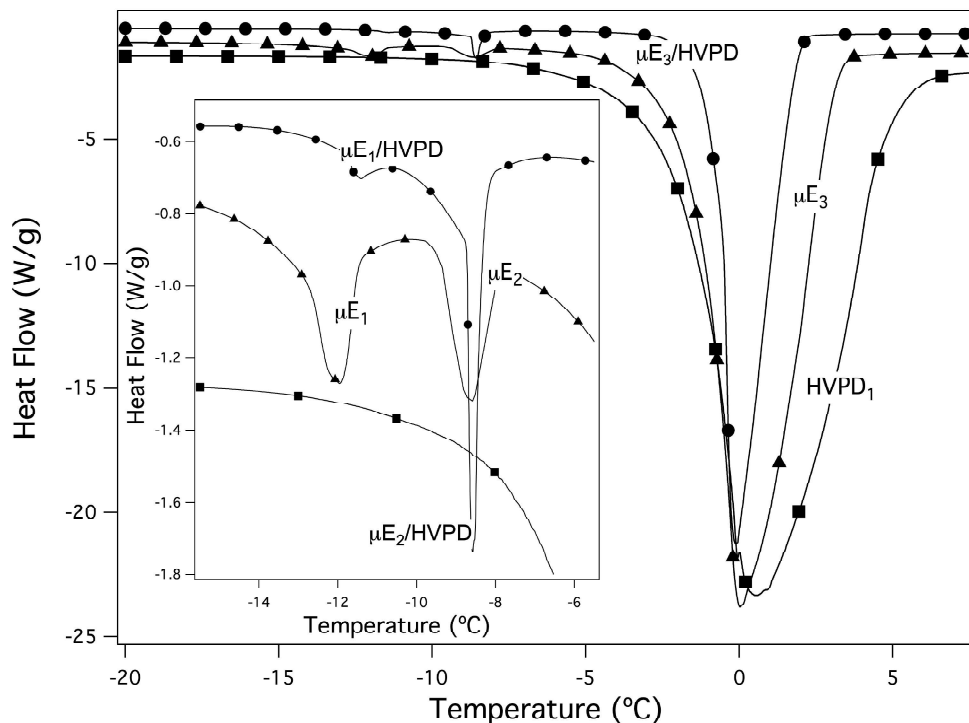


Figure 5. DSC curves obtained for HVPD (■), μE (▲) and μE confined in HVPD (●). The inset shows the thermograms in the range between -16°C and -5°C.

In particular, the strongest peak μE₃ is due to the melting of the so-called “freezable bulk water”, while the other peaks, i.e. μE₁ and μE₂, are related to “confined water” [43]. A similar behavior was observed for the o/w μE confined into the HVPD (the three endothermic peaks are labelled as μE₁/HVPD, μE₂/HVPD, μE₃/HVPD). Slight differences in the onset values and in the shape of DSC peaks of the confined μE were probably due to the interactions occurring between the polymeric network and the nanodroplets. Nevertheless, the presence of the three endothermic DSC peaks in the confined μE was a further confirmation of the retainment of the nanostructure of the nanofluid even when included in the HVDP, which, as shown in Figure 3, shows

only one DSC peak due to “freezable bulk water” (labeled as HVPD₁).

3.2 Application of HVPD/ μ E system for cleaning of painted surfaces

The organic molecules constituting the thin films coating a 19th century egg-tempera canvas painting of a bucolic scene were selected due to their peculiarity of constituting a good test for applicative purposes. The interaction between the organic molecules constituting the painting coating and the HVPD/ μ E system was monitored by ATR-FTIR and ToF-SIMS. Indeed, the two techniques were also employed to ascertain the chemical nature of such molecules. The ATR-FTIR spectrum collected onto the paint surface before cleaning (Figure 6, black line) showed a strong band centered at 1703 cm⁻¹ (C=O str.), and absorptions at ca. 1633 cm⁻¹ (shoulder, C=C str.), 1456 cm⁻¹ (CH₂ bend.), 1377 cm⁻¹ (-C-H bend.), 1240 cm⁻¹ (C-O str., ester), 1162 cm⁻¹ (shoulder C-O str., acid), 1105 cm⁻¹ (C-O str., alcohol), and 920 cm⁻¹ (shoulder =C-H bend.), which confirmed the presence of both a natural dammar resin, and possibly residues of siccative oil treatments [44,45]. It is not surprising such chemical nature, considering that mixtures of dammar resin and siccative oil have been often used as conservation materials in the past to “renew” the painting surfaces [46]. Analogously, the brown and dark aspect of the coating (*vide infra* Figure 7) was expected due to natural aging of these conservation materials [47,48]. The study of the interaction between these aged substances and the developed HVPD/ μ E system was also representative of a challenge for checking the performance of an innovative, “green”, selective procedure for preventive

conservation.

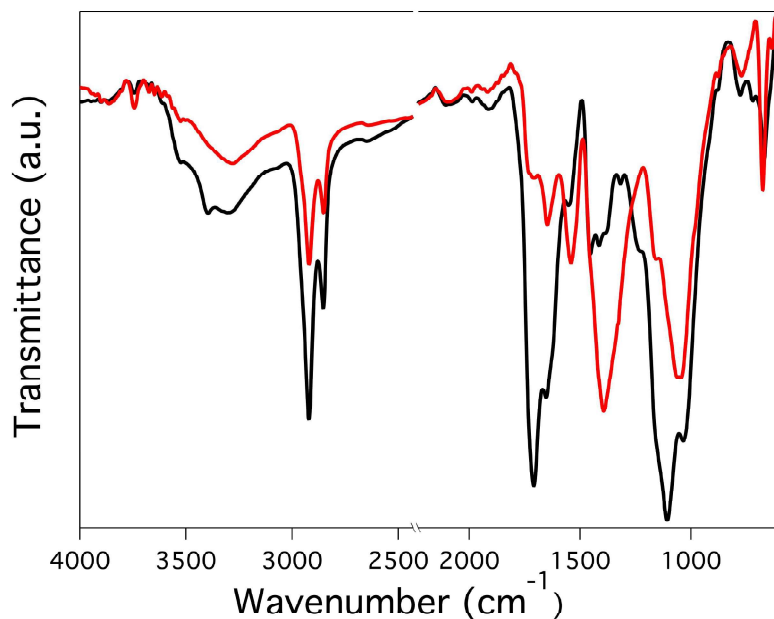


Figure 6. ATR-FTIR spectrum of the paint surface collected before (black) and after the application of the HVPD/ μ E system (red).

A preliminary experiment made on a very small portion of the painting sample showed that p-xylene was able to clean the surface and remove the brown, dark coating: this was the confirmation that this apolar solvent inside the nanodroplets was a good solvent for the aged dammar and linseed oil. The HVPD/ μ E system was made interacting with the organic molecules thin films constituting the coating according to the procedure described in the paragraph 2.3 of the Materials and Methods section. Figure 7A shows the aspect of the painting surface, where the dark, brown coating is well visible. Aged dammar and linseed oil originated, as known [49], strong UV-induced fluorescence, as documented by the B picture of Figure 7. The interaction occurred between the applied HVPD/ μ E and the organic molecules

constituting the coating was strongly evident by the pictures C and D of Figure 7: both the photos collected in visible light and UV-fluorescence showed that the aged organic molecules were completely removed by the HVPD/ μ E system that entrapped them within its structure, as documented by the picture E in the same Figure 7. This was also confirmed by the results of the ATR-FTIR reported in Figure 6 (red spectrum): the intensity of all the peaks associated with the aged organic molecules was strongly decreased. The fact that the peaks decreased their intensity, but not completely disappeared, should be considered as a positive feedback, since in preventive conservation a very soft approach according to the rule that it is better leaving some aged patinas, rather than making a strong, radical cleaning is highly desired [50]. Moreover, the ATR-FTIR spectrum in Figure 6 (red) showed a strong increase of the intensity of the peaks at 1653 and 1540 cm^{-1} , which are related to the stretching of amide I and II respectively, and are due to the proteinaceous binding medium (i.e. egg) used for the realization of the tempera, confirming the unveiling of the original painting surface covered by the aged conservation past treatment layers.

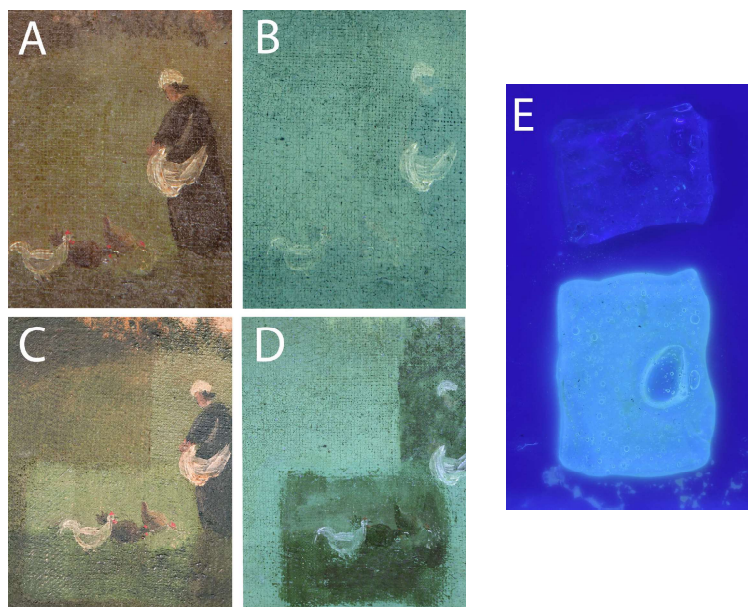


Figure 7. Detailed pictures of the XVIII century Tuscan egg-tempera canvas painting before the cleaning test carried out through the HVPD/ μ E: visible light (A) and UV-induced visible fluorescence (B). The same area of the painting after cleaning procedures: visible light (C) and UV-induced visible fluorescence (D). Image E shows the UV-induced visible fluorescence pictures of the HVPD/ μ E before (top) and after (bottom) the cleaning test.

ToF-SIMS was performed to deeper investigate the interaction of HVPD/ μ E with the aged organic molecules and to achieve analytical results with very great sensitivity, much higher with respect to ATR-FTIR. The purpose of this analysis in the present study was twofold: (i) evaluating the effective interaction, and (ii) detecting possible residues of the HVPD/ μ E system onto the painting surface. The positive ToF-SIMS spectra acquired on the same surface region before and after the interaction time were compared to the spectrum of the HVPD/ μ E system. Figures 8 and 9 show the surface spectra of the painting sample before and after the interaction time, respectively. As shown in Figure 8, the chemistry of the surface before the

treatment is, as expected, very complex and characterized by many organic fragments, especially in the 0-100 amu range. The ToF-SIMS spectra indicated the presence of a siccative oil in the surface coating: the peaks at m/z 279, 281, and 283 attributable to compounds having a generic formula $C_2H_3(CH_2)_xCOO$ indicated the presence of several fatty acids such as linoleic, oleic and stearic acid respectively, as also confirmed by the peaks at m/z 263, 265 and 267, which belong to their acyl ions. Moreover, the group of peaks at m/z 431 and 447 are probably due to the same fatty acid conjugated with lead, as confirmed also by the isotopic ratio of the fragments and by the low intense signals at m/z 207. This composition suggests that a lead salt was added to the mixture used as varnish to speed up the drying process.

Ion peaks at $m/z = 65, 77, \text{ and } 91$, that are normally assigned to ion fragments $C_5H_5^+$, $C_6H_5^+$, and tropylium $C_7H_7^+$, can be attributed to aromatic compounds that, together with the fragment at m/z 208, could be assigned to the fragmentation of lupane-type molecules, suggesting the presence of a natural dammar resin [51]. Moreover, this attribution is confirmed by the peaks in the range of 300-400 amu, due to natural terpenoid acids and their derivatives that often generate few fragments in this range. Indeed, these peaks can be also related to the presence of photo-oxidation products of aged natural resin, whose characteristic peaks are m/z 307, 317, and 325, and are due to abietic acid derivatives [52].

After the interaction time and the removal of the HVPD/ μ E from the surface the chemistry of the surface strongly changed, showing a strong reduction of the peaks due to both the fatty acids (m/z 279, 281, and 283) and to the natural resin (m/z 208)

indicating that the interaction between the HVPD/ μ E enabled to segregate the most part of the aged organic molecules by the complex nanostructured fluid.

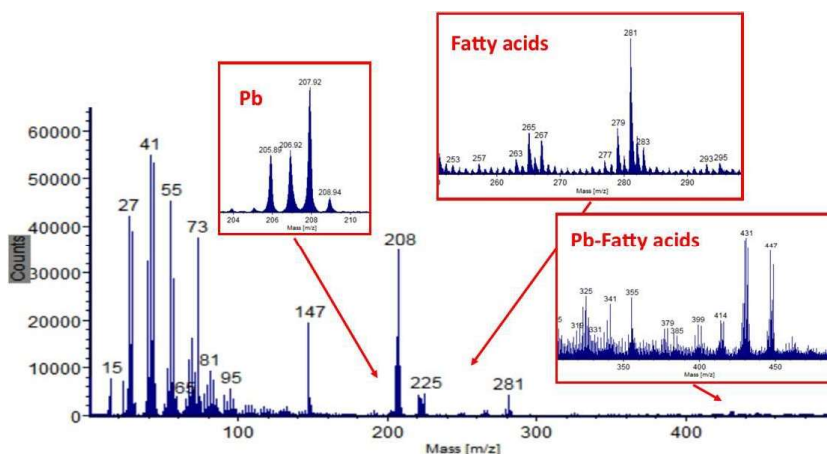


Figure 8. Mass spectra of the painting surface before the test of interaction in the range 0-500 amu: the regions where fragments belonging to Pb, fatty acids and Pb-fatty acids conjugates are found, are highlighted.

Moreover, the appearance of two intense peaks at m/z 63 and 65 due to copper (Figure 9A) was a further indication of a strong thinning of the surface coating, that discovered the paint layers underneath.

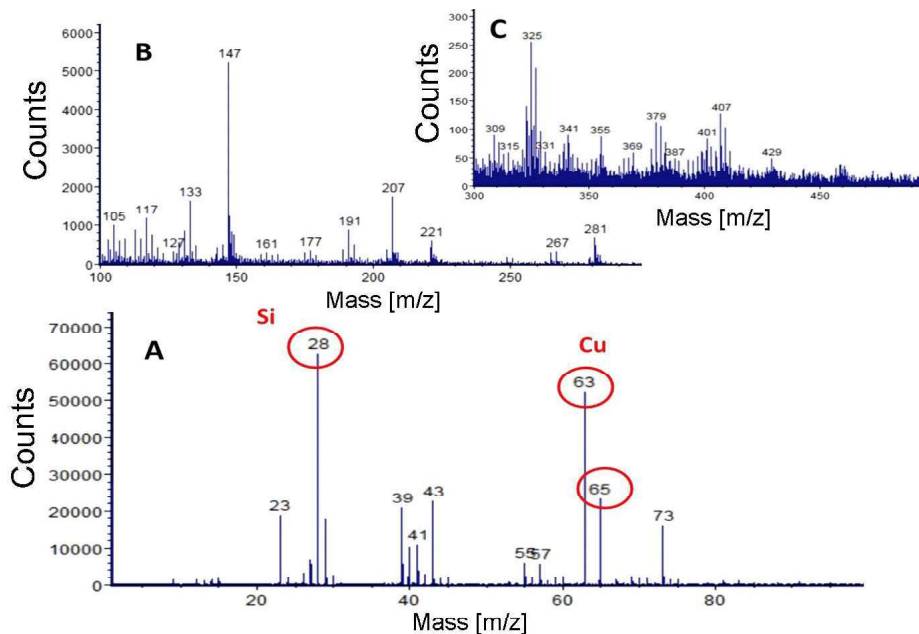


Figure 9. Mass spectra of the painting surface after the test of interaction and removal of the HVPD/ μ E system in the range 0-500 amu divided in 3 parts: (A) Range 0-100 amu (B) 100-300 amu (C) 300-500 amu.

The presence of copper confirmed that the green color in the area selected for the cleaning tests was due to inorganic copper-based pigment mixed with Sienna (a natural mixture of aluminosilicate of Ca and Fe oxides), as indicated by the peaks at m/z 27, 40 and 55 which can be attributed to Al, Ca and Fe, respectively.

ToF-SIMS results agreed with ATR-FTIR analyses. In particular, both analytical techniques showed that the interaction between the HVPD/ μ E system and the aged organic molecules constituting the dark and brown thin films coating onto the painting was strong enough to remove the coating, with successful recovery of the

painting readability and simultaneously preserving the underneath layers, as documented by the remaining traces of the aged organic materials.

ToF-SIMS was also employed to ascertain down to ppb, for the first time as we know, the absence of residues coming from the HVPD/ μ E system after the interaction time. Figure 10 shows the TOF-SIMS spectra before the interaction time (A), after interaction time and removal of HVPD/ μ E (B), and native HVPD/ μ E (C), used as a reference. The HVPD/ μ E spectra shows, as expected, many fragments. Among them, the characteristic and intense peak at $m/z = 165$, attributed to crosslinked polyvinyl alcohol (PVA), highlighted in Figure 10C, falls in a spectral region where the painting surface has a peak (both before and after the interaction time, see Figures 10A and 10B), but with very low intensity. Therefore, this peak was selected to detect the presence of HVPD/ μ E residues after cleaning procedures. Looking at the three spectra reported in Figure 10 it was observed that the peak at $m/z 165$ presented this trend of intensity: $I_C \gg I_A > I_B$. This could be interpreted in the following sense: the peak was due to both PVA and fragments associated to the aged organic molecules; the very strong intensity in C was due to the high content of PVA in the sample subjected to ToF-SIMS analysis, while the presence in A was due to a fragment – not the most important – of the organic aged molecules. The lowest intensity of this peak in B was due to the strong interaction between the aged organic molecules and the HVPD/ μ E system that led to the thinning of the coating.

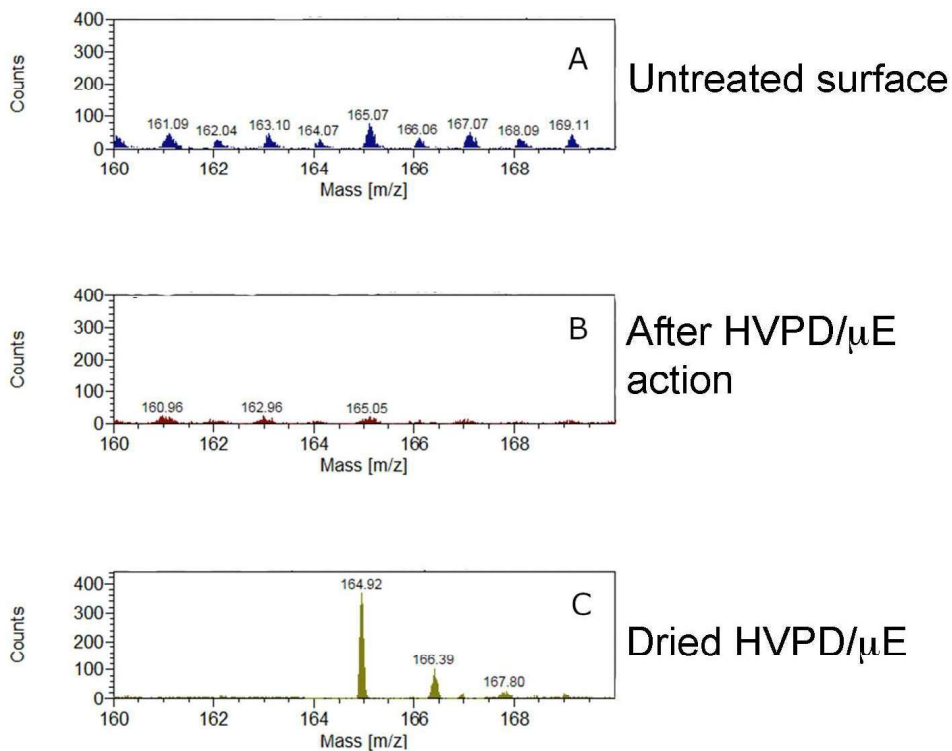


Figure 10. TOF-SIMS spectra of untreated surface (A), of surface after the interaction time and removal of HVPD/μE (B), and of the HVPD/μE system (C) in the 160-170 m/z mass range.

Chemical images of the samples acquired in bunched mode before and after the interaction time and removal of the HVPD/μE system over an area of about $400 \mu\text{m}^2$ with a lateral resolution of $\sim 1 \mu\text{m}$, are reported in Figure SI5. In the chemical map of the surface before the test of the interaction between HVPD/μE and organic aged molecules (Figure SI5A), the dominant signals were due to lead and various organic fragments. After the interaction time and the removal of HVPD/μE, the surface became more homogeneous from a chemical point of view and showed itself unveiled by the organic coating: in fact, the spots that were visible before the interaction disappeared and copper and silica became predominant. No fragment at

m/z 165 were detected over the analyzed area, confirming the absence of residues left by the cleaning treatment.

4. Conclusions

A new complex, nanostructured fluid constituted of aqueous Highly Viscous Polymeric Dispersion (HVPD) composed by a 3D network of poly(vinyl alcohol) covalently crosslinked by borax and loaded with a o/w microemulsion (μ E) was developed and characterized from a structural and rheological point of view. The rheological analysis indicated that the loading of the o/w microemulsion into the HVPD network induced an increase of the stiffness of the system, as indicated by the growth of the elasticity of the HVPD/ μ E respect to the starting aqueous HVPD. It was interesting to notice that this effect resulted as the sum of two opposite causes: the de-structuring due to the SDS surfactant (lower) and the structuring one attributed to both the co-surfactant 1PeOH and the apolar solvent p-xylene. The retention of the strong elasticity of the HVPD/ μ E played a fundamental role in view of possible applications of this complex nanostructured fluid for cleaning purposes in cultural heritage conservation. The structural characterization carried out through SAXS indicated the persistence of the nanostructure of the μ E, even after its confinement inside the HVPD. The confinement of the liquid microemulsion into the HVPD induced some limited changes of the μ E nanodroplets structure: while their mean size remained almost unchanged, the polydispersity increased by a factor 2 and the

particles charge decreased about four times due to the screening effect of the 3D PVA/borax network on the charged objects constituting the microemulsion. The retention of the μ E structure, apart from the changes evidenced by SAXS, was ascertained also by DSC measurements, that showed the persistence of the three water populations as in the pure μ E.

The interactions between the HVPD/ μ E system and organic molecules – siccativ oils and dammar varnish – constituting aged thin films coating the surface of a 19th century Tuscan egg-tempera canvas showed the high segregation of these molecules within the complex fluid acting as a “green”, selective cleaning agent. ATR-FTIR and TOF-SIMS analyses carried out onto the painting surface before and after the interaction time clearly highlighted the occurred strong interaction leading to the removal of the dark, brown coating without leaving any traces of the HVPD/ μ E system and recovering the original painting layers.

References

- [1] D. Jeong, H. Lim, M.-S. Ko, W. Kim, Utilization of three-layered polyvinyl alcohol gel cubes for treating low-strength ammonium wastewater in a single-stage autotrophic nitrogen removal process, *J. Environ. Chem. Eng.* 10 (2022) 106934. <https://doi.org/10.1016/j.jece.2021.106934>.
- [2] H. Abrial, A. Atmajaya, M. Mahardika, F. Hafizulhaq, Kadriadi, D. Handayani, S.M. Sapuan, R.A. Ilyas, Effect of ultrasonication duration of polyvinyl alcohol (PVA) gel on characterizations of PVA film, *J. Mater.*

- Res. Technol. 9 (2020) 2477–2486.
<https://doi.org/10.1016/j.jmrt.2019.12.078>.
- [3] R. Mastrangelo, D. Chelazzi, G. Poggi, E. Fratini, L. Pensabene Buemi, M.L. Petruzzellis, P. Baglioni, Twin-chain polymer hydrogels based on poly(vinyl alcohol) as new advanced tool for the cleaning of modern and contemporary art, *Proc. Natl. Acad. Sci.* 117 (2020) 7011–7020.
<https://doi.org/10.1073/pnas.1911811117>.
- [4] N. Bonelli, G. Poggi, D. Chelazzi, R. Giorgi, P. Baglioni, Poly(vinyl alcohol)/poly(vinyl pyrrolidone) hydrogels for the cleaning of art, *J. Colloid Interface Sci.* 536 (2019) 339–348.
<https://doi.org/10.1016/j.jcis.2018.10.025>.
- [5] E.F.D. Januário, T.B. Vidovix, M.A. Calsavara, R. Bergamasco, A.M.S. Vieira, Membrane surface functionalization by the deposition of polyvinyl alcohol and graphene oxide for dyes removal and treatment of a simulated wastewater, *Chem. Eng. Process. - Process Intensif.* 170 (2022) 108725.
<https://doi.org/10.1016/j.cep.2021.108725>.
- [6] Y. Huo, K. Zhao, Z. Xu, F. Li, X. Zhao, Q. Meng, C. Tang, Y. Tang, Ultralight and superelastic polyvinyl alcohol/SiC nanofiber/reduced graphene oxide hybrid foams with excellent thermal insulation and microwave absorption properties, *Ceram. Int.* 47 (2021) 25986–25996.
<https://doi.org/10.1016/j.ceramint.2021.06.004>.
- [7] M. Akter, N. Hirase, M.T. Sikder, M.M. Rahman, T. Hosokawa, T. Saito, M.

- Kurasaki, Pb (II) Remediation from Aqueous Environment Using Chitosan-Activated Carbon-Polyvinyl Alcohol Composite Beads, *Water, Air, Soil Pollut.* 232 (2021) 272. <https://doi.org/10.1007/s11270-021-05243-8>.
- [8] R. Rodríguez-Rodríguez, H. Espinosa-Andrews, C. Velasquillo-Martínez, Z.Y. García-Carvajal, Composite hydrogels based on gelatin, chitosan and polyvinyl alcohol to biomedical applications: a review, *Int. J. Polym. Mater. Polym. Biomater.* 69 (2020) 1–20. <https://doi.org/10.1080/00914037.2019.1581780>.
- [9] M.I. Baker, S.P. Walsh, Z. Schwartz, B.D. Boyan, A review of polyvinyl alcohol and its uses in cartilage and orthopedic applications, *J. Biomed. Mater. Res. Part B Appl. Biomater.* 100B (2012) 1451–1457. <https://doi.org/10.1002/jbm.b.32694>.
- [10] Q. Ye, S. Chen, Y. Zhang, B. Ruan, Y. Zhang, X. Zhang, T. Jiang, X. Wang, N. Ma, F. Tsai, Chitosan/Polyvinyl Alcohol/ Lauramidopropyl Betaine/2D-HOF Mixed Film with Abundant Hydrogen Bonds Acts as High Mechanical Strength Artificial Skin, *Macromol. Biosci.* 21 (2021) 2100317. <https://doi.org/10.1002/mabi.202100317>.
- [11] L. Cao, S. Huang, F. Lai, Z. Fang, J. Cui, X. Du, W. Li, Z. Lin, P. Zhang, Z. Huang, Sucrose in situ physically cross-linked of polyaniline and polyvinyl alcohol to prepare three-dimensional nanocomposite hydrogel with flexibility and high capacitance, *Ionics (Kiel)*. 27 (2021) 3431–3441. <https://doi.org/10.1007/s11581-021-04010-3>.

- [12] M.H. Azarian, P. Boochathum, M. Kongsema, Biocompatibility and biodegradability of filler encapsulated chloroacetated natural rubber/polyvinyl alcohol nanofiber for wound dressing, *Mater. Sci. Eng. C.* 103 (2019) 109829. <https://doi.org/10.1016/j.msec.2019.109829>.
- [13] O. Alonso-López, S. López-Ibáñez, R. Beiras, Assessment of Toxicity and Biodegradability of Poly(vinyl alcohol)-Based Materials in Marine Water, *Polymers (Basel)*. 13 (2021) 3742. <https://doi.org/10.3390/polym13213742>.
- [14] A.-L. Kjøniksen, B. Nyström, Effects of Polymer Concentration and Cross-Linking Density on Rheology of Chemically Cross-Linked Poly(vinyl alcohol) near the Gelation Threshold, *Macromolecules*. 29 (1996) 5215–5222. <https://doi.org/10.1021/ma960094q>.
- [15] L. V. Angelova, P. Terech, I. Natali, L. Dei, E. Carretti, R.G. Weiss, Cosolvent Gel-like Materials from Partially Hydrolyzed Poly(vinyl acetate)s and Borax, *Langmuir*. 27 (2011) 11671–11682. <https://doi.org/10.1021/la202179e>.
- [16] E. Carretti, C. Matarrese, E. Fratini, P. Baglioni, L. Dei, Physicochemical characterization of partially hydrolyzed poly(vinyl acetate)-borate aqueous dispersions, *Soft Matter*. (2014). <https://doi.org/10.1039/C4SM00355A>.
- [17] K. Nakamura, T. Hatakeyama, H. Hatakeyama, Relationship between hydrogen bonding and bound water in polyhydroxystyrene derivatives, *Polymer (Guildf)*. 24 (1983) 871–876. [https://doi.org/10.1016/0032-3861\(83\)90206-9](https://doi.org/10.1016/0032-3861(83)90206-9).

- [18] Y. Sakai, S. Kuroki, M. Satoh, Water Properties in the Super-Salt-Resistive Gel Probed by NMR and DSC, *Langmuir*. 24 (2008) 6981–6987.
<https://doi.org/10.1021/la800397f>.
- [19] S. Michalski, A physical model of the cleaning of oil paint, *Stud. Conserv.* 35 (1990) 85–92. <https://doi.org/10.1179/sic.1990.35.s1.020>.
- [20] P. Baglioni, D. Chelazzi, *Nanoscience for the Conservation of Works of Art*, Royal Society of Chemistry, Cambridge, 2013.
<https://doi.org/10.1039/9781849737630>.
- [21] P. Baglioni, D. Chelazzi, R. Giorgi, *Nanotechnologies in the Conservation of Cultural Heritage - A compendium of materials and techniques*, Springer, Heidelberg New York London, 2015.
- [22] E. Carretti, I. Natali, C. Matarrese, P. Bracco, R.G. Weiss, P. Baglioni, A. Salvini, L. Dei, A new family of high viscosity polymeric dispersions for cleaning easel paintings, *J. Cult. Herit.* 11 (2010) 373–380.
<https://doi.org/10.1016/j.culher.2010.04.002>.
- [23] M. Baglioni, D. Berti, J. Teixeira, R. Giorgi, P. Baglioni, Nanostructured Surfactant-Based Systems for the Removal of Polymers from Wall Paintings: A Small-Angle Neutron Scattering Study, *Langmuir*. 28 (2012) 15193–15202. <https://doi.org/10.1021/la303463m>.
- [24] M. Baglioni, R. Giorgi, D. Berti, P. Baglioni, Smart cleaning of cultural heritage: a new challenge for soft nanoscience, *Nanoscale*. 4 (2012) 42–53.
<https://doi.org/10.1039/C1NR10911A>.

- [25] P. Baglioni, E. Carretti, D. Chelazzi, Nanomaterials in art conservation, *Nat. Publ. Gr.* 10 (2015) 287–290. <https://doi.org/10.1038/nnano.2015.38>.
- [26] E. Carretti, B. Salvadori, P. Baglioni, L. Dei, Microemulsions and Micellar Solutions for Cleaning Wall Painting Surfaces, *Stud. Conserv.* 50 (2005) 128–136. <https://doi.org/10.1179/sic.2005.50.2.128>.
- [27] M. Baglioni, J.A.L. Domingues, E. Carretti, E. Fratini, D. Chelazzi, R. Giorgi, P. Baglioni, Complex Fluids Confined into Semi-interpenetrated Chemical Hydrogels for the Cleaning of Classic Art: A Rheological and SAXS Study, *ACS Appl. Mater. Interfaces.* 10 (2018) 19162–19172. <https://doi.org/10.1021/acsami.8b01841>.
- [28] P. Baglioni, D. Berti, M. Bonini, E. Carretti, L. Dei, E. Fratini, R. Giorgi, Author 's personal copy Micelle , microemulsions , and gels for the conservation of cultural heritage, (n.d.).
- [29] E. Carretti, E. Fratini, D. Berti, L. Dei, P. Baglioni, Nanoscience for Art Conservation: Oil-in-Water Microemulsions Embedded in a Polymeric Network for the Cleaning of Works of Art, *Angew. Chemie Int. Ed.* 48 (2009) 8966–8969. <https://doi.org/10.1002/anie.200904244>.
- [30] Y. Lee, J. Lee, Y. Kim, S. Choi, S.W. Ham, K.-J. Kim, Investigation of natural dyes and ancient textiles from korea using TOF-SIMS, *Appl. Surf. Sci.* 255 (2008) 1033–1036. <https://doi.org/10.1016/j.apsusc.2008.05.097>.
- [31] A. Tognazzi, R. Lapucci, S. Martini, G. Leone, A. Magnani, C. Rossi, TOF-SIMS characterization of pigments and binders in ‘the Martyrdom of St.

- Catherine', in Zejtun (Malta), *Surf. Interface Anal.* 43 (2011) 1152–1159.
<https://doi.org/10.1002/sia.3272>.
- [32] G. Leone, A. De Vita, A. Magnani, C. Rossi, Characterization of archaeological mortars from Herculaneum, *Thermochim. Acta.* 624 (2016) 86–94. <https://doi.org/10.1016/j.tca.2015.12.003>.
- [33] J.C. Vickerman, ToF-SIMS - an overview, in: J.C. Vickerman, D. Briggs (Eds.), *TOF-SIMS Surf. Anal. by Mass Spectrom., Surface Spectra and IM Publications*, Manchester and Chichester, UK, 2001: pp. 1–40.
- [34] G. Leone, M. Consumi, S. Lamponi, A. Magnani, Combination of static time of flight secondary ion mass spectrometry and infrared reflection–adsorption spectroscopy for the characterisation of a four steps built-up carbohydrate array, *Appl. Surf. Sci.* 258 (2012) 6302–6315.
<https://doi.org/10.1016/j.apsusc.2012.03.027>.
- [35] P. Baglioni, E. Rivara-Minten, L. Dei, E. Ferroni, ESR study of sodium dodecyl sulfate and dodecyltrimethylammonium bromide micellar solutions: effect of urea, *J. Phys. Chem.* 94 (1990) 8218–8222.
<https://doi.org/10.1021/j100384a044>.
- [36] G. Leone, M. Consumi, S. Pepi, S. Lamponi, C. Bonechi, G. Tamasi, A. Donati, C. Rossi, A. Magnani, Alginate–gelatin formulation to modify lovastatin release profile from red yeast rice for hypercholesterolemia therapy, *Ther. Deliv.* 8 (2017) 843–854. <https://doi.org/10.4155/tde-2017-0025>.

- [37] G. Leone, M. Consumi, S. Lamponi, C. Bonechi, G. Tamasi, A. Donati, C. Rossi, A. Magnani, Thixotropic PVA hydrogel enclosing a hydrophilic PVP core as nucleus pulposus substitute, *Mater. Sci. Eng. C*. 98 (2019) 696–704. <https://doi.org/10.1016/j.msec.2019.01.039>.
- [38] E. Carretti, L. Dei, P. Baglioni, Solubilization of Acrylic and Vinyl Polymers in Nanocontainer Solutions. Application of Microemulsions and Micelles to Cultural Heritage Conservation, *Langmuir*. 19 (2003) 7867–7872. <https://doi.org/10.1021/la034757q>.
- [39] B. a Schubert, E.W. Kaler, N.J. Wagner, The Microstructure and Rheology of Mixed Cationic/ Anionic Wormlike Micelles, *Langmuir*. (2003) 4079–4089. <https://doi.org/10.1021/la020821c>.
- [40] E. Carretti, S. Grassi, M. Cossalter, I. Natali, G. Caminati, R.G.R.G. Weiss, P. Baglioni, L. Dei, Poly(vinyl alcohol)–Borate Hydro/Cosolvent Gels: Viscoelastic Properties, Solubilizing Power, and Application to Art Conservation, *Langmuir*. 25 (2009) 8656–8662. <https://doi.org/10.1021/la804306w>.
- [41] I. Natali, E. Carretti, L. Angelova, P. Baglioni, R.G.R.G. Weiss, L. Dei, Structural and Mechanical Properties of “Peelable” Organoaqueous Dispersions with Partially Hydrolyzed Poly(vinyl acetate)-Borate Networks: Applications to Cleaning Painted Surfaces, *Langmuir*. 27 (2011) 13226–13235. <https://doi.org/10.1021/la2015786>.
- [42] M. Rubinstein, A.N. Semenov, Dynamics of Entangled Solutions of

- Associating Polymers, *Macromolecules*. 34 (2001) 1058–1068.
<https://doi.org/10.1021/ma0013049>.
- [43] M. Shibukawa, K. Aoyagi, R. Sakamoto, K. Oguma, Liquid chromatography and differential scanning calorimetry studies on the states of water in hydrophilic polymer gel packings in relation to retention selectivity, *J. Chromatogr. A*. 832 (1999) 17–27. [https://doi.org/10.1016/S0021-9673\(98\)00988-1](https://doi.org/10.1016/S0021-9673(98)00988-1).
- [44] M. Derrick, Fourier Transform Infrared Spectral Analysis of Natural Resins used in Furniture Finishes, *J. Am. Inst. Conserv.* 28 (1989) 43–56.
<https://doi.org/10.1179/019713689806046264>.
- [45] M.R. Derrick, D. Stulik, J.M. Landry, *Infrared Spectroscopy in Conservation Science*, Getty Conservation Institute, Los Angeles, USA, 1999.
- [46] T. Poli, O. Chiantore, E. Diana, A. Piccirillo, Drying Oil and Natural Varnishes in Paintings: A Competition in the Metal Soap Formation, *Coatings*. 11 (2021) 171. <https://doi.org/10.3390/coatings11020171>.
- [47] J. Mallégol, J. Lemaire, J.-L. Gardette, Yellowing of Oil-Based Paints, *Stud. Conserv.* 46 (2001) 121–131.
<https://doi.org/10.1080/00393630.2001.12071699>.
- [48] E. Kirchner, I. van der Lans, F. Ligterink, E. Hendriks, J. Delaney, Digitally reconstructing Van Gogh’s Field with Irises near Arles . Part 1: Varnish, *Color Res. Appl.* 43 (2018) 150–157. <https://doi.org/10.1002/col.22162>.
- [49] E.R. de la Rie, Fluorescence of paint and varnish layers (Part II), *Stud.*





- Conserv. 27 (1982) 65–69. <https://doi.org/10.1179/sic.1982.27.2.65>.
- [50] R. Wolbers, *Cleaning Painted Surfaces: Aqueous Methods*, Archetype Books, London, 2000.
- [51] P. Biocca, P. Santopadre, G. Sidoti, G. Sotgiu, F. de Notaristefani, L. Tortora, ToF-SIMS study of gilding technique in the fresco Vela della Castità by Giotto's school, *Surf. Interface Anal.* 48 (2016) 404–408. <https://doi.org/10.1002/sia.5956>.
- [52] M.P. Colombini, F. Modugno, eds., *Organic Mass Spectrometry in Art and Archaeology*, Wiley, Chichester, West Sussex, UK, 2009.

Acknowledgments

Consorzio interuniversitario per lo sviluppo dei sistemi a Grande Interfase (CSGI), University of Florence, is acknowledged for financial support

Article

Non-Aqueous Poly(dimethylsiloxane) Organogel Sponges for Controlled Solvent Release: Synthesis, Characterization, and Application in the Cleaning of Artworks

Francesca Porpora ¹, Luigi Dei ¹, Teresa T. Duncan ², Fedora Olivadese ¹, Shae London ³, Barbara H. Berrie ⁴, Richard G. Weiss ³ and Emiliano Carretti ^{1,5,*}

- ¹ Department of Chemistry “Ugo Schiff” & CSGI Consortium, University of Florence, Via della Lastruccia, 3-13, 50019 Sesto Fiorentino, Italy; francesca.porpora@unifi.it (F.P.); luigi.dei@unifi.it (L.D.); fedora.olivadese@stud.unifi.it (F.O.)
- ² Scientific Analysis of Fine Art, LLC, Berwyn, PA 19312, USA
- ³ Department of Chemistry and Institute for Soft Matter Synthesis and Metrology, Georgetown University, 37th and O Streets NW, Washington, DC 20057, USA; ssl63@georgetown.edu (S.L.); weissr@georgetown.edu (R.G.W.)
- ⁴ Department of Scientific Research, National Gallery of Art, 2000 South Club Drive, Landover, MD 20785, USA; b-berrie@nga.gov
- ⁵ National Research Council—National Institute of Optics (CNR-INO), Largo E. Fermi 6, 50125 Florence, Italy
- * Correspondence: emiliano.carretti@unifi.it; Tel.: +39-0554-573-046

Abstract: Polydimethylsiloxane (PDMS) organogel sponges were prepared and studied in order to understand the role of pore size in an elastomeric network on the ability to uptake and release organic solvents. PDMS organogel sponges have been produced according to sugar leaching techniques by adding two sugar templates of different forms and grain sizes (a sugar cube template and a powdered sugar template), in order to obtain materials differing in porosity, pore size distribution, and solvent absorption and liquid retention capability. These materials were compared to PDMS organogel slabs that do not contain pores. The sponges were characterized by Fourier-transform infrared spectroscopy with attenuated total reflectance (FTIR-ATR) and compared with PDMS slabs that do not contain pores. Scanning electron microscopy (SEM) provided information about their morphology. X-ray micro-tomography (XMT) allowed us to ascertain how the form of the sugar templating agent influences the porosity of the systems: when templated with sugar cubes, the porosity was 77% and the mean size of the pores was ca. 300 μm ; when templated with powdered sugar, the porosity decreased to ca. 10% and the mean pore size was reduced to ca. 75 μm . These materials, porous organic polymers (POPs), can absorb many solvents in different proportions as a function of their polarity. Absorption capacity, as measured by swelling with eight solvents covering a wide range of polarities, was investigated. Rheology data established that solvent absorption did not have an appreciable impact on the gel-like properties of the sponges, suggesting their potential for applications in cultural heritage conservation. Application tests were conducted on the surfaces of two different lab mock-ups that simulate real painted works of art. They demonstrated further that PDMS sponges are a potential innovative support for controlled and selective cleaning of works of art surfaces.

Keywords: Polydimethylsiloxane (PDMS) organogel sponges; template effects; viscoelastic properties; solvent swelling/de-swelling; cleaning works of art



Citation: Porpora, F.; Dei, L.; Duncan, T.T.; Olivadese, F.; London, S.; Berrie, B.H.; Weiss, R.G.; Carretti, E. Non-Aqueous Poly(dimethylsiloxane) Organogel Sponges for Controlled Solvent Release: Synthesis, Characterization, and Application in the Cleaning of Artworks. *Gels* **2023**, *9*, 985. <https://doi.org/10.3390/gels9120985>

Academic Editor: Shiyang Li

Received: 10 November 2023

Revised: 7 December 2023

Accepted: 11 December 2023

Published: 15 December 2023



Copyright: © 2023 by the authors. Licensee MDPI, Basel, Switzerland. This article is an open access article distributed under the terms and conditions of the Creative Commons Attribution (CC BY) license (<https://creativecommons.org/licenses/by/4.0/>).

1. Introduction

Recently, significant research has focused on the exploitation of the properties of some polymeric materials with porous structures (i.e., porous organic polymers, POPs) because they possess large surface areas and well-defined and tuneable pore size distributions [1,2]. The combination of these variable properties can provide synergic effects that

are suitable for many technological applications [3]. POPs can be synthesised according to several routes with many functionalisations and are easily processed. Thus, the significant attention that POPs have received during the last decades can be attributed to their fundamental scientific characteristics as well as the extremely broad range of their realized and potential applications (these include greenhouse gas adsorption, proton conduction, energy storage and conversion, sensing, separation, catalysis, drug delivery and release, and tissue engineering) [3–10]. Polydimethylsiloxane (PDMS) organogel sponges [11–27] are important examples of POPs due to their elasticity, hydrophobicity, low surface tension, controllable porosity, low-toxicity, low-flammability, high thermal and electrical resistance, low bulk density, mechanical robustness, and high transmittance and low absorption of UV radiation [28–33].

A preliminary goal of this paper has been the assessment of a suitable strategy for the synthesis of PDMS-based systems using sugar as a templating agent [3,22,34] and exploiting the possibility of producing a large number of PDMS porous systems (i.e., sponges) [16,34]. Two different synthetic routes based on this strategy were followed. In one, sugar cubes with an edge of ca. 1 cm and comprised of grains with dimensions of a few hundred microns were chosen as templating agents; in another the templating agent was made from powdered sugar with grains having dimensions in the order of tens of microns. In both cases, the chemical and physicochemical properties of PDMS slabs (i.e., pure PDMS cast without templating agents) and of the two sponges (obtained using sugar cubes and fine powdered sugar as the templating agents) were investigated. Chemical analyses were performed using Fourier-transform infrared spectroscopy in the attenuated total reflectance mode (FTIR-ATR). Physicochemical characterizations were carried out using scanning electron microscopy (SEM) to obtain information about the morphology, and X-ray micro-tomography (XMT) was employed for the determination of the 3D structures and calculations of the porosity and of the pore size distributions. Analyses of these data have been useful for designing these materials for specific applications. Another aim of this work has been to obtain PDMS based systems with different porosity and pore size distributions that would present different and controllable properties in terms of solvent swelling, retention, and release. A possible application for such materials is as physically “gentle” cleaning agents for painted surfaces of historical and artistic interest.

By exploiting (1) the ability to modulate the porosity of the PDMS systems by varying the granularity of the templating agent [3], and (2) the well-known compatibility of PDMS with a wide range of mid-to-low-polarity solvents [35], materials were produced with varying interactions between the systems explored and the organic solvents chosen here (many of which have been used for the cleaning of painted surfaces). These interactions were examined by measuring the amounts of the solvents absorbed [36] as a function of both solvent polarity and of the porosity of the PDMS). The rheology of the PDMS systems was investigated before and after loading solvents to obtain information about their effect on the viscoelastic properties, with particular attention to the elasticity and the complex viscosity of the systems. In fact, the ability to control these mechanical features is critical in determining two fundamental properties that a cleaning system tailored for painted surfaces of works of art should possess: (1) the retention of the solvents within the slabs/sponges and (2) adequate contact with the surface of the work-of-art.

Despite the large differences among distinct classes of physical and chemical gels that have been tailored for the selective removal of coating materials on surfaces of painted works of art [37–42], few organogels and sponge-like systems have been reported for cleaning of works of art. Among these, a new class of polyhydroxybutyrate-based physical organogels have been prepared and successfully employed for the selective cleaning of bronze and water-sensitive painted surfaces of historical and artistic interest [43–46]. These systems can be easily prepared and loaded with organic solvents at different polarities (i.e., lactones and alkyl carbonates). The introduction of solvent-swelled PDMS gels adds to the range of solvents that can be applied via gel to works of art; moreover, the ability to tune the porosity implements a strategy that could potentially be applied to a range of gelled

systems currently used in conservation. Thus, an aim of this research is a preliminary evaluation of the performance of PDMS-based water-free organogels. To investigate the use of these gels for conservation applications, cleaning tests were carried out on two lab mock-ups: a fresco and an easel painting that have naturally-aged, previously-applied surface coatings.

2. Results and Discussion

The chemical characterization of the PDMS slabs (PDMS systems obtained without the use of any templating agent, see Section 4.2) and PDMS_SC (PDMS systems obtained using a sugar cube as templating agent, see Section 4.2) and PDMS_PS sponges (PDMS systems obtained using powdered sugar as templating agent, see Section 4.2) using FTIR-ATR spectra are reported in Figure 1. All of the characteristic peaks of both the two components, the 'base' A and 'curing agent' B, and the cross-linked polymer are in agreement with the data reported in the literature [47,48]. Moreover, no meaningful differences in the profiles of the FTIR spectra of the three PDMS-based systems are observed, indicating that their chemical compositions are the same and that the templating agents have no influence on that. The absence of signals associated with sugar suggests that no detectable residues of the sugar templating agent are present. In addition, no glucose was detected by a Fehling [49] test carried out on the central portions of PDMS_SC and PDMS_PS fragments.

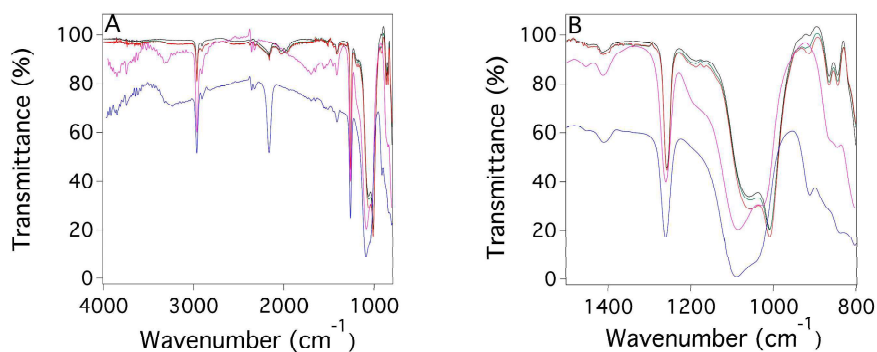


Figure 1. FTIR-ATR spectra of the A (magenta) and B (blue) components of the PDMS slab (ratio component A/component B = 20:1), the cross-linked polymer (black), and of the two different PDMS sponges (component ratio A/B = 10:1 for both systems); that with sugar cube as template (PDMS_SC red) and that with powdered sugar as template (PDMS_PS green). (A) reports the FTIR-ATR spectra in the range 4000–800 cm^{-1} ; (B) reports the FTIR-ATR spectra in the range 1500–800 cm^{-1} .

The morphology of the two porous sponges was investigated by SEM. Figure 2 shows the micrographs of the two PDMS sponges, PDMS_SC (A and B) and PDMS_PS (C and D).

The images in Figure 2 indicate that the two templating agents result in very different morphologies, with a porosity much higher for sponges synthesized using sugar cubes than for systems obtained using the powdered sugar template.

To obtain more detailed information about the porosity of the two systems, XMT measurements were carried out, and the 3D images obtained through the procedure described in Section 4.2 are displayed in Figure 3. These images confirm that the use of the two different templating agents produces sponges with different porosities [16,34]. By employing the procedure described in Section 4.3, it was possible to deduce the pore size distribution (for pores larger than 5 μm) for both sponges. These values are reported in Figure 4A,B for PDMS_SC and PDMS_PS, respectively. The results confirm that the pore size of the PDMS_SC (ca. 303 μm) is larger than that of PDMS_PS (ca. 76 μm). Table 1 summarizes the results from the porosity analysis performed on the two sponges.

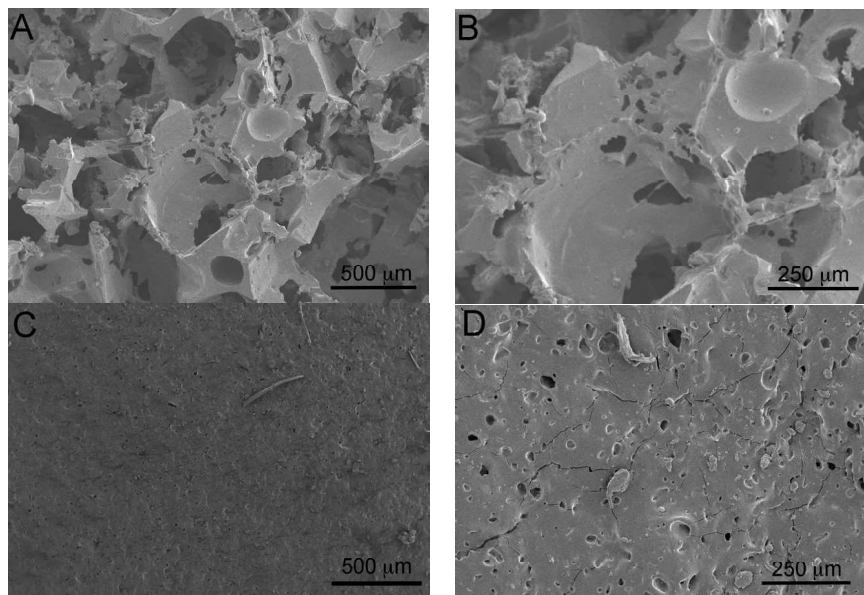


Figure 2. SEM micrographs of two different PDMS sponges: (A) PDMS_SC magnification 50×; (B) PDMS_SC magnification 100×; (C) PDMS_PS magnification 50×; (D) PDMS_PS magnification 100×. For both samples, the ratio of components A/B was 10:1.

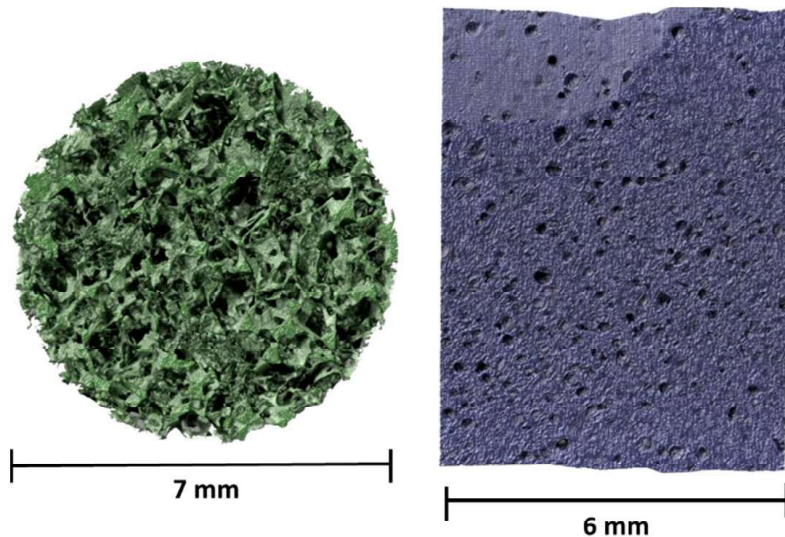


Figure 3. XMT 3D images for two different PDMS sponges in which the A/B component ratio was 10:1: (left) PDMS_SC; (right) PDMS_PS.

A fundamental aspect to investigate here, in view of a possible application of these systems as cleaning tools for painted surfaces, is a comparison of solvent absorption by the two sponges and that of the PDMS slab, focusing on both the swelling of the slab and on the capillary action of the porous PDMS sponges. This experiment is fundamental to understand the maximum amount of solvent that can be loaded into the three different systems in the view of a possible application as cleaning tools for painted surfaces; this is the reason why the absorption tests have been carried out over up to 25 h (Figure 5).

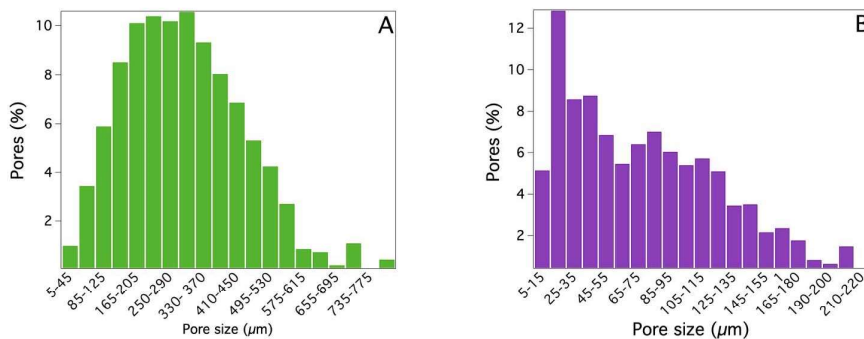


Figure 4. Histograms of the pore size distributions for two different PDMS sponges (10 × 5 × 5 mm) derived from XMT measurements: (A) PDMS_SC; (B) PDMS_PS. For both samples, the A/B component ratio was 10:1.

Table 1. Porosities and mean pore diameters (mm) of the pores of PDMS_SC and PDMS_PS sponges as calculated from the % of polymers.

Sample	Polymer (%)	Porosity (%)	Mean Pore Diameter (μm)
PDMS_SC	22.6 ± 0.7	77.4 ± 5.2	303 ± 15
PDMS_PS	90.2 ± 1.5	9.8 ± 0.38	76 ± 5

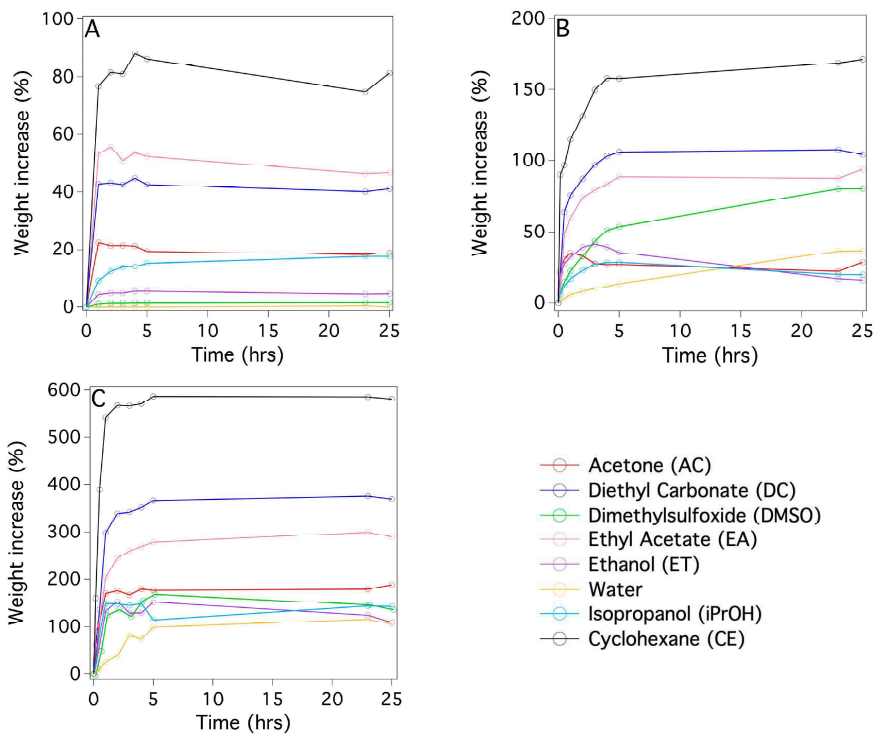


Figure 5. Kinetics curves for solvent absorption of the two different PDMS sponges and of the PDMS slab for various solvents (ratio component A/component B = 10:1): (A) PDMS slab, (B) PDMS_PS, (C) PDMS_SC.

In that regard, Figure 5 shows the kinetics of absorption by the three systems with various organic solvents, including some that are used for cleaning purposes in cultural heritage conservation. Figure 6A,B report the maximum amounts of the solvents absorbed by the PDMS-based systems and the initial absorption rates, respectively. From Figures 5 and 6A, the PDMS_SC, with the highest porosity and the larger pore size, absorbed up to four times the amount of solvent as absorbed by the PDMS_PS sponge with a higher rate (Figure 6B). This indicates that porosity is the key factor in determining the kinetics of solvent absorption. This is also confirmed by the lowest absorption amount is observed for the nonporous PDMS slabs (Figure 5A). Another result, that is in agreement with the literature data [35], is the strong dependence between the rates of the absorption and the magnitude of the dielectric constants ϵ of the solvents (Figure 6A,B). As expected, because PDMS is a low-polarity polymer, the maximum absorption amount and rate were observed for solvents with low ϵ values, such as cyclohexane; conversely, in polar solvents such as water, ethanol and DMSO, absorption was smaller and slower. This behavior is due to the large difference between the physico-chemical affinities of the solvents and the hydrophobic network of the PDMS matrix. Absorption tests have been carried out with cyclohexane and DMSO, solvents that should not be used in conservation due to health concerns, in these experiments to demonstrate that it is possible to load solvents having very different polarities into the PDMS based systems.

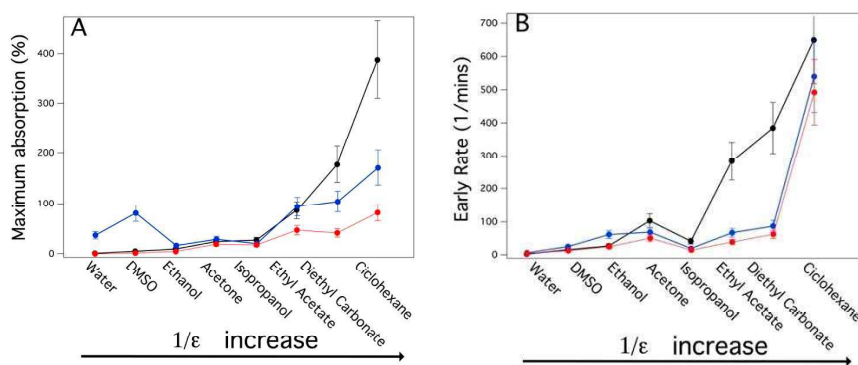


Figure 6. Maximum amount of organic solvent absorbed (A) and swelling rate (B) by PDMS slab (red dots), PDMS_PS (blue dots), PDMS_SC (black dots). The solvents on X axis are presented as a function of $1/\epsilon$, where ϵ is the dielectric constant of the solvents.

Rheological measurements were carried out to obtain information about the viscoelastic properties of the systems. These data indicate a solid-like rheological behavior for all the investigated samples ($G' \gg G''$ over the whole range of frequencies investigated; see Figure 7), and, according to the literature, [50] they can be mechanically classified as solid-like materials. Since one of the main goals of the study is the application of these systems as cleaning tools for works of art surfaces, it was crucial to ascertain how the viscoelastic properties could be affected by the presence of absorbed solvent in the swollen sponges. Therefore, frequency sweeps were carried out after the absorption of some organic solvents that were chosen among the ones used for cleaning purposes in cultural heritage conservation. Four solvents covering an extended range of polarities, were selected: ET, DMSO, DC, and EA (acetone was not used here due to its low boiling point). Figure 8, as an example, reports the trend of G' and G'' versus frequency sweep for the two sponges containing two solvents, among the four tested, at the extremes of the polarity scale, that are DC and DMSO. The other frequency sweep diagrams of PDMA_SC and PDMS_PS loaded with ET and EA are reported in Figure S1. These data clearly indicate that none of the four solvents tested alters the porosity or the gel-like nature of the two sponges independently (see Figure 7 and Figure S1).

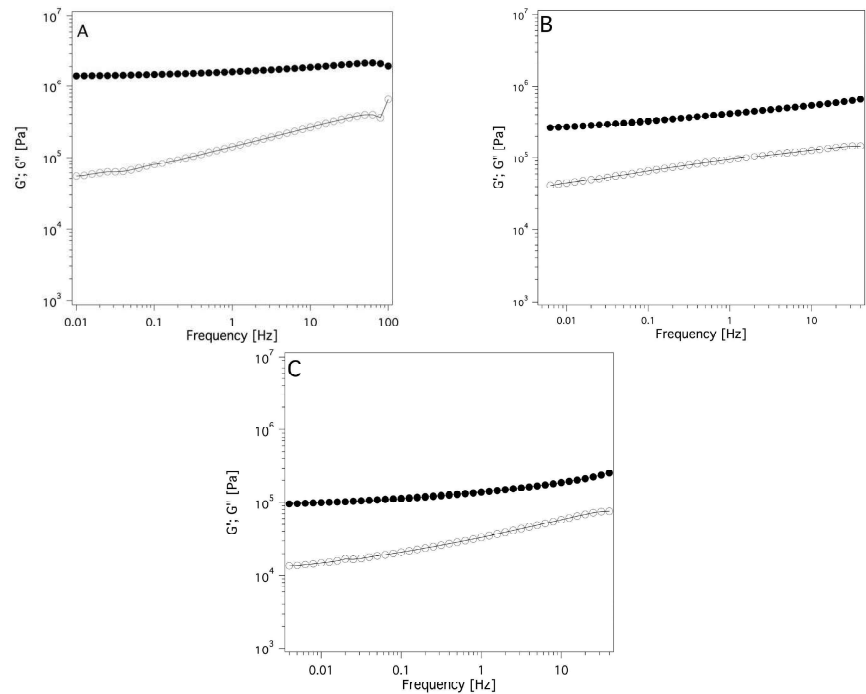


Figure 7. Frequency sweep diagrams of the (A) PDMS slab, (B) PDMS_PS, (C) PDMS_SC systems. Filled circles indicate G' ; open circles indicate G'' (component ratio A/B = 10:1).

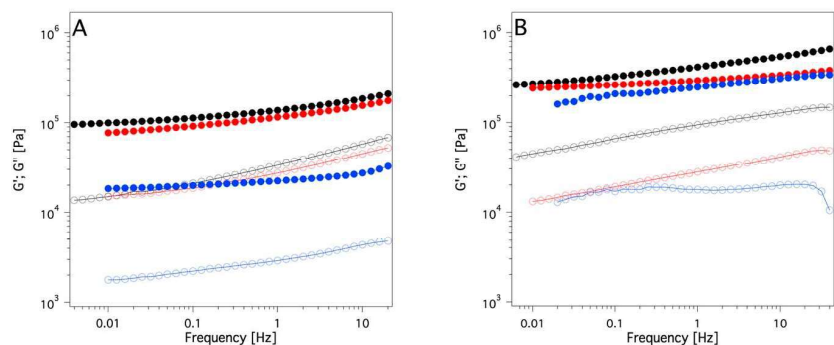


Figure 8. Frequency sweep diagram of the: (A) PDMS_SC sponge alone (black), with absorbed DC (blue), with absorbed DMSO (red); (B) PDMS_PS sponge alone (black), with absorbed DC (blue), and with absorbed DMSO (red). Absorption time: 24 h. Filled circles indicate G' ; open circles indicate G'' .

The main finding from the rheology measurements (Figure 8 and Figure S1) is a decrease of the G' value for both the investigated systems (PDMS_SC and PDMS_PS) after loading the four solvents. This effect is higher for DC than for DMSO and, with the same solvent this effect is more pronounced for the PDMS_SC. This is attributable to the higher porosity of the PDMS_SC system that allows the absorption of a larger amount of this solvent (Figure 5B,C). The trend of the complex viscosity η^* (see Figure 9A,B) for the pure sponges and the swollen sponges by the four solvents after 24 h of absorption confirms the findings of frequency sweep measurements: a pronounced decrease of η^* due to the presence of a purely viscous liquid phase within the pores is observed. Moreover, this effect

seems to be inversely proportional to the polarity of the confined solvents as indicated by the lowest η^* values of the DC and EA-based systems.

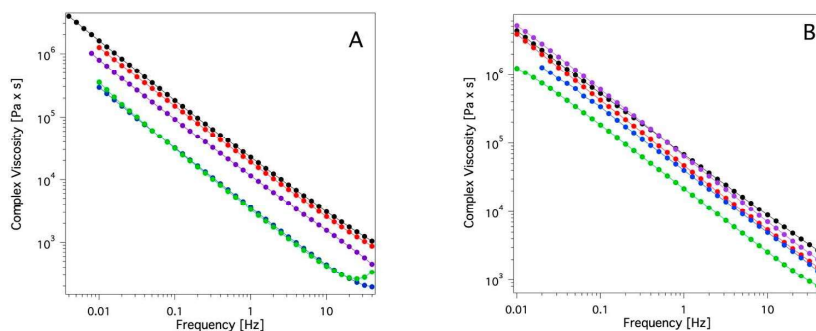


Figure 9. Complex viscosity of the PDMS_SC (A) and PDMS_PS (B) sponges alone (black) and with absorbed ethyl acetate (green), diethyl carbonate (blue), DMSO (red) and ethanol (purple).

From an application standpoint, one of the main advantages of using gels for cleaning surfaces of porous matrices of historical and artistic interest is linked to the high retention of the solvents confined within them. This allows control of the cleaning action which ideally remains limited to the contact area between the gel itself and the surface of the object to be cleaned. To obtain information for the PDMS-based systems investigated here, absorption tests of the solvents loaded inside them were carried out on sheets of Whatman® paper (which was chosen as a model porous system). The results are reported in Figure 10.

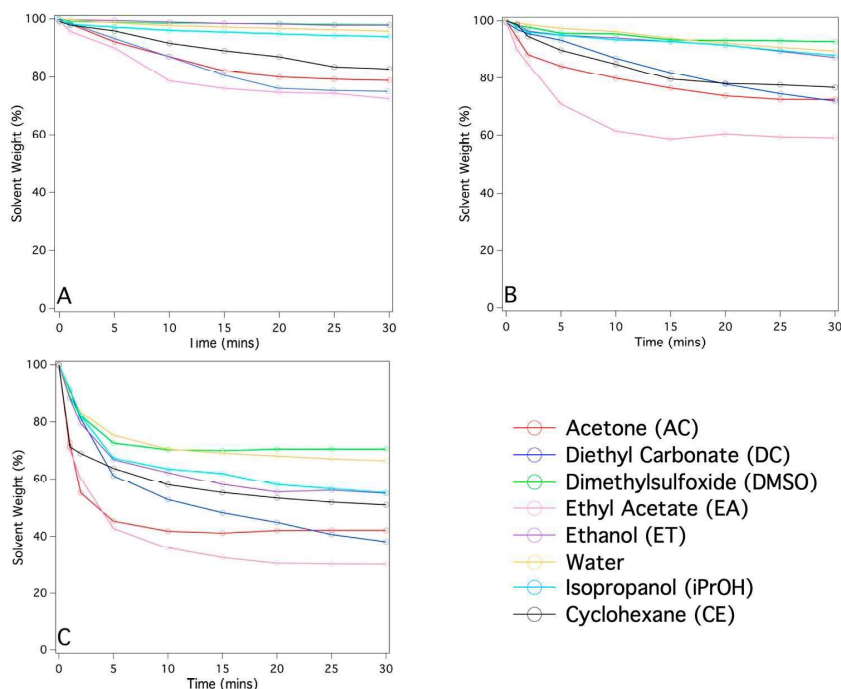


Figure 10. Kinetic curves describing the weight loss of the PDMS based systems soaked with organic solvents and placed in direct contact with a stack of Whatman® papers: (A) PDMS slab, (B) PDMS_PS, (C) PDMS_SC. The A/B component ratio is 10:1.

The data reported in Figure 10 clearly indicate that the extent of solvent release is proportional to the porosity of the PDMS-based networks and, therefore, to the maximum amount of solvent that can be loaded inside them. In fact, for the PDMS-SC system, release values ranging approximately between 30 and 65 wt% are observed, while for the PDMS slab and PDMS-PS, the values never exceeded 50 wt%.

The efficacy of the PDMS based systems as cleaning agents for painted surfaces was first tested on the surface of a fresco mock-up with a 20-year-old surface layer of poly(EMA/MA) 70:30. Figure 11A shows a region of the painting affected by this surface coating. Different tests were carried out by increasing the contact times up to 12 min. The grazing-light image on the right of Figure 11A, collected after the application of a PDMS_PS loaded with EA (ca. 10 wt%) for 12 min, shows the complete disappearance of the glossy effect typical of the copolymer film in the area of the cleaning test. This image indicates macroscopically that the cleaning system was effective for removing the aged coating. Figure 11B reports the FTIR spectra of the organic fraction extracted from mortar samples collected from areas of the fresco where the cleaning tests was carried out (for the detailed experimental procedure, see Section 4). In particular, the FTIR analysis of the cleaned surface (see Figure 11B) confirmed that the poly(EMA/MA) 70:30 layer was no longer detectable after a 12 min treatment with the PDMS_PS sponge, based on the absence of the peak at 1735 cm^{-1} , which is a marker of poly(EMA/MA) 70:30. Furthermore, Figure 11C shows the trend of the ratio between the intensity of the peaks at 1732 cm^{-1} and 2092 cm^{-1} (stretching of the $\text{C}\equiv\text{N}$ bond of the Prussian blue used as internal standard) as a function of the application time. The decrease in the value of this parameter indicates the progressive cleaning action of the PDMS_PS sponge by increasing the contact time with the fresco surface.

The surface morphology was investigated by scanning electron microscopy (SEM); it is typical of wall paintings affected on the surface by polymeric coatings that make the surface “smooth” (i.e., with very low roughness and open porosity (Figure S2A)). After application of the cleaning system, the texture of the surface appeared much rougher with a higher porosity that is typical of an original mortar (Figure S2B).

Another potential application for these systems is the removal of aged organic coatings from the surface of easel paintings, as shown in the case study involving the removal of a 25 year naturally aged polymeric ketone resin varnish from the surface of a canvas mock-up. Even in this case, the cleaning test was carried out by means of a PDMS_PS loaded with EA (ca. 10 wt%) with a contact time of 5 min. In fact, from the Teas diagrams [51] it can be deduced that EA is a good solvent for the removal of this class of varnishes. Figure 12A shows the area of the painting treated. The picture on the right, collected after the application of the PDMS_PS system, indicates the visual absence of the varnish layer in the area involved in the cleaning test. ATR-FTIR spectra of the artwork surface before and after cleaning are consistent with this conclusion: the cleaning (Figure 12B, black line) shows strong absorbances centered at 1716 cm^{-1} , 1454 cm^{-1} and 1070 cm^{-1} attributable to the ketone resin [52]; in the spectrum collected after the cleaning test (Figure 12B, red line), the intensity of these diagnostic peaks is strongly decreased, indicating the removal of the surface coating. Also, SEM analysis (Figure S3) of the treated area confirms qualitatively that the cleaning test was successful. Note that the morphology of the paint surface after the cleaning test (Figure S3C) is similar to that of the area of the mock-up where the surface coating was absent (Figure S3A) and that it appears less homogeneous and rougher than the region treated by the surface varnish layer before the application of the PDMS_PS system (Figure S3B).

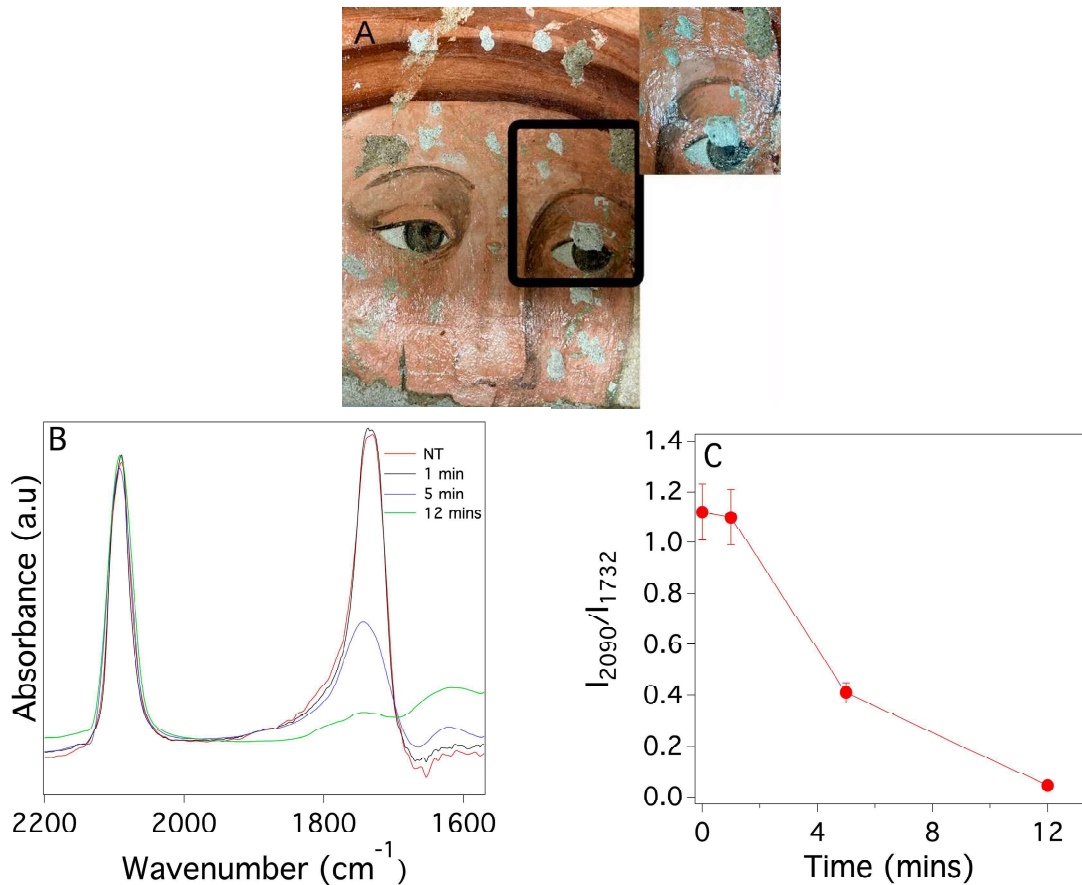


Figure 11. Results of the cleaning test carried out on a fresco mock-up coated with a surface layer of naturally aged poly(EMA/MA) 70:30 by means of a PDMS_PS sponge loaded with ca 10 wt% of EA: (A) image of the mock-up before (big picture) and after the cleaning (small picture showing a detail of the area where the 12 min test was carried out): (B) FTIR spectra of the resin extracted from mortar fragments collected in the area where the cleaning tests were carried out before (NT, red line) and after the PDMS_PS system application with different contact times: 1 min (black line), 5 min (blue line) and 12 min (green line). (C) ratio between the intensity of the peaks at 1732 cm⁻¹ and at 2092 cm⁻¹ as a function of the application time.

In both cases FTIR spectra did not indicate the presence of PDMS residues on the cleaned surfaces.

The first aspect to be discussed is the two synthetic routes selected to obtain the two POPs PDMS that have different total porosity and pore size distributions. Although the results are consistent with results already reported in the literature for using a sugar cube [34], the material prepared using powdered sugar was more compact with much lower porosity. The FTIR-ATR analysis reported in Figure 1 indicates that there is no meaningful difference in the composition of the PDMS sponges with respect to non-porous slabs (i.e., that no sugar residues were present).

Thus, for these three systems, the non-porous PDMS slab, porous PDMS_SC and PDMS_PS, we conclude that the chemical nature of the materials is the same and the templating agents did not leave any discernible residues.

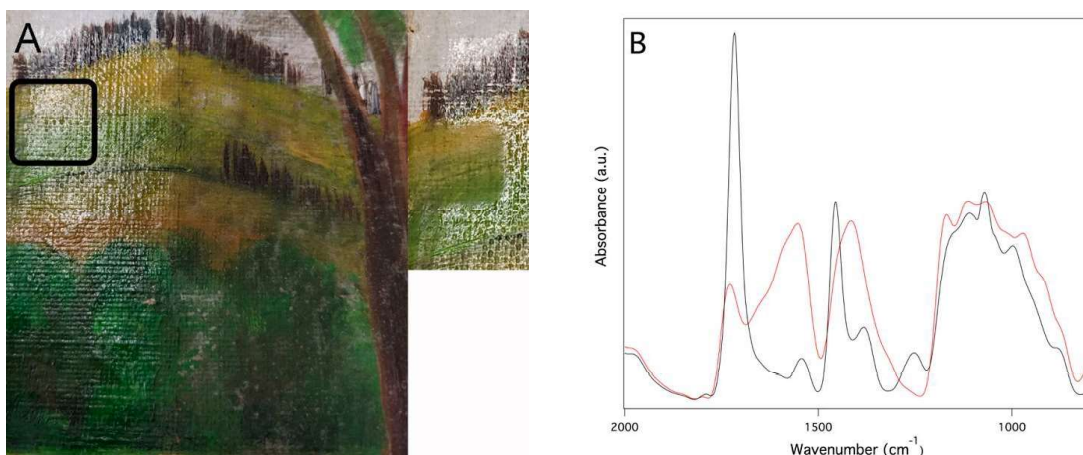


Figure 12. Cleaning of a canvas painting mock-up by means of a PDMS_PS system loaded with about 10 wt% of EA. (A) Image of the mock-up before and after the cleaning (small insert on the right) showing a detail of the area where the test was carried out; (B) ATR-FTIR collected in the cleaning test area before (black line) and after (red line) the application of the PDMS_PS system.

From a comparison of the morphology and porosity data reported in Table 1 and Figures 3 and 4, it is evident that the two sponges, although chemically the same, have different porosities: PDMS_SC has a much higher porosity than PDMS_PS derived from the large dimensions of the grains constituting the sugar cube (in the order of few hundreds of microns). Moreover, the mechanism of polymerization in the presence of the two templating agents (sugar cube or powdered sugar) differed. In the first case, the appropriately mixed A and B components of the polymerization were absorbed by the porous structure of the sugar cube, so that the polymerization occurred within the fixed macropores of the sugar cube. In the second case, the polymerization occurred at the random interstices among the fine sugar grains that were mixed with the A and B components. Both the different size of the crystal grains for cube and powdered sugar and the larger macropores present in the cube with respect to the smaller ones, consisting of interstices among fine powder grains, generated a large difference in the two PDMS sponges.

The swelling kinetics of the PDMS slab, PDMS_SC and PDMS_PS sponges was a clear indicator of the large difference in porosity among the three materials. Figure 5 shows that PDMS_SC has both the fastest kinetics of solvent absorption and the largest amount of swelling at the asymptotes. This was ascribed to its very high porosity with respect to PDMS_PS and to the non-porous PDMS. In this regard, we reiterate that solvent absorption by the polymer was due simply to swelling phenomena for the PDMS slab but, two synergistic effects were present (i.e., swelling of the polymer enhanced by capillary action mediated by the pores) for the POPs PDMS sponges. These results agree with observations from the literature [35] which show that the driving factor for solvent absorption by PDMS is the magnitude of the hydrophobic interaction which is largest for solvents with the lowest dielectric constants (Figure 5). This is a key point in view of a possible use of these systems as cleaning tools for surfaces of works of art. The swelling/absorption data indicate that these materials may be suitable as cleaning solvents which are able to be released in a controlled way which minimizes both their spreading into the work of art porous support, and any water contamination that is typical for most of the commonly used chemical hydrogels.

Another aspect investigated is their rheological properties (reported in Section 4 and in Supplementary File data). All the investigated systems are characterized by a solid-like behavior, so it is possible to classify them as chemical organogel sponges. As far as we know, these systems may be truly innovative tools for cleaning works of art, especially

where even the presence of traces of water during the cleaning procedure represents a possibility of serious damage for the surface. A further interesting finding was that the amount of solvent absorbed by the PDMS-based systems did not meaningfully change the viscoelastic behavior of the PDMS sponges and slabs. As a result, the application tests could open new perspectives for cultural heritage conservation in the field of selective cleaning.

In that regard, the action of the PDMS_PS system loaded with the 10 wt% of acetone, and two different polymeric coatings present on the surface of two lab mock-ups—poly(EMA/MA) 70:30 and a ketone resin on the surface of a fresco and of a canvas painting respectively—indicates the selective extraction of these molecules within the cleaning agent. FTIR analysis carried out on the painting surface before and after the application of the cleaning systems clearly highlights the removal of both the coatings and the recovery of the original morphology typical of uncoated paint layers. Moreover, once the cleaning action is carried out, the PDMS_PS systems have been completely removed, without leaving any instrumentally detectable traces on the cleaned area. This avoids both the use of free-flowing organic solvents and any mechanical action on the paint surface. This feature represents a fundamental improvement over many other the traditional cleaning methods that employ physical gels [53].

3. Conclusions

Synthetic routes have been employed to obtain two types of PDMS sponges with large differences in both their total porosity and mean pore size. These sponges show strong promise as systems to be tried in cleaning tests for the surfaces of works of art. They allow the roles of porosity and pore size in determining solvent/release retention, its spreading within the works of art support, and the solubilization ability against coatings to be removed.

Chemical characterization by FTIR-ATR permitted a comparison of the properties of PDMS slabs with the above-mentioned sponges and to ascertain that the chemical composition of the cross-linked polymer was the same for all the investigated systems. Moreover, no traces of the sugar templating agents used for the preparation of the sponges were present after polymerization. Physicochemical characterizations, carried out by means of SEM, XTM, and porosity determinations, showed that while the sponges obtained using sugar cubes as a templating agent have a porosity around 77% with a mean pore size ca. 300 μm (with a distribution of pore diameters ranging from a few microns to several hundred microns), the porosity of the sponges synthesized using powdered sugar decreased up to 10% with a mean pore size of ca. 75 μm . In this case the distribution of pore diameters ranges from a few microns up to 200 microns.

The very low polarity of PDMS is a key factor in determining the amount of absorbed solvent through polymer swelling and capillary action. They decrease as the dielectric constant of the liquid is increased.

The rheology data indicate that all the systems tested are characterized by a gel-like behavior. G' was larger than G'' over the measured frequency range. In materials with higher porosity, the large amount of bulk and free solvent entrapped within the large pores caused a decrease of G' compared to the dry sponge. This effect is strictly related to the polarity of the solvent according to the greater absorption of low polarity solvents within the pores due to the high hydrophobicity of the PDMS. At lower porosities, the mean sizes of the pores were strongly reduced, and the bulk and free solvent absorbed by the porous polymers were strongly decreased. As a result, the effect on the elastic behavior of the sponges was limited too.

Application of the two porous PDMS based systems containing a small amount of a solvent commonly used for the removal of foreign patinas from painted surfaces of historical and artistic interest (i.e., acetone) allowed selective removal of aged varnishes from the surfaces of two mock-ups that simulate artworks with different substrates (i.e., a fresco and a canvas), without negatively altering the original substrates and without leaving any discernible traces of the PDMS_PS system. These preliminary results/proofs of concept,

indicate that the PDMS systems loaded with different organic solvents presented in this paper should be explored further as selective cleaning tools for painted surfaces of historical and artistic interest, even for the cleaning of paintings having different compositions (i.e., modern and contemporary paintings).

The systems presented in this paper are complementary to other physical organogels presented in the literature [43–46]. In particular, due to their physicochemical properties, the PDMS-based organogels and sponges can be loaded with solvents (tunable by varying the contact time between the sponge and the solvent to be loaded, see Figure 5) having different dielectric constants (varying from 2 for cyclohexane to 47 for DMSO). Moreover, thanks to their strong cohesive internal forces (i.e., covalent bonds) they minimize residues left onto the painted surface as indicated by the FTIR data collected on the surfaces after cleaning.

Moreover, the PDMS-based organogels and sponges represent a potentially important alternative to the most used physical cleaning techniques, such as laser or micro-sandblasting, especially in those cases where the cleaning operation must have a high selectivity and a gentle mechanical action.

4. Materials and Methods

4.1. Materials

Polydimethylsiloxane, Sylgard 184[®] from Dow Corning Corporation (Wiesbaden, Germany), was composed of the base (component A) and a curing agent (component B). Commercial sugar cubes (1 × 1 × 0.7 cm, Diator Vantaggio[®]) were pure saccharose grains having average dimensions of about 200 μm and the powdered sugar (dimensions of the grains on the order of tens of microns) were supplied by Sperlari S.r.l., Cremona, Italy. Solvents were from Sigma-Aldrich c/o Merck Life Science S.r.l., Milano, Italy (purity > 99%) and used without further purification. Dow Sylgard[™] 184 was supplied by DOW Italy, Milan, Italy. Water was purified by a Millipore MilliQ Direct-Q[®] & Direct-Q UV water purification system (Water Resistivity: 18.2 MΩ at 25 °C) purchased from Merck-Millipore, Milano, Italy. Polyethyl methacrylate/methyl methacrylate 70/30 (ParaloidB72[®]) was purchased from Zecchi, Firenze, Italy. The ketone resin was purchased from Phase s.r.l., Firenze, Italy. Melinex[®] was purchased from Phase s.r.l., Firenze, Italy. Watman[®] paper was purchased from Cytiva, Little Chalfont, Kent, UK.

4.2. Synthesis Methods

The best ratio to obtain a sufficiently elastic material for applicative purposes was found to be 10:1 A/B by weight. The synthesis was performed as follows:

1. a total amount of 2 g of A and B were vigorously stirred in a Petri dish for approximately 2 min;
2. after homogenization, the Petri dish was placed in a dryer under vacuum at room temperature (ca. 20 °C) to eliminate air bubbles;
3. the polymerisation occurred at room temperature (ca. 20 °C) and soft filter paper was placed onto the Petri dish to avoid dust deposition;
4. after three days, the resulting material, transparent to the eye and elastic, was formed (see Figure S4).

The analogous procedure was performed inside an oven at 60–80 °C for 2 h instead of at room temperature for 3 days. The scheme of the reaction is reported in the literature [54–56].

The same procedure was used also for the synthesis of the porous sponges by using the sugar template method [34] with a further step (also for both the PDMS-based sponges, PDMS_SC and PDMS_PS, the A:B ratio was chosen as 10:1). For the sugar cube sponges (PDMS_SC), the synthesis procedure is reported below:

1. after air bubbles were eliminated, a sugar cube (1.4 g and 1 × 1.5 × 1 cm composed of grains having dimensions ranging in the order of 150–300 μm) was put onto the A/B mixture (A:B ratio was 10:1) at the center of the Petri dish;

2. the Petri dish containing the A/B mixture and the sugar cube was put into a dryer under vacuum for 30 min at room temperature (ca. 20 °C) and then kept under static vacuum for 2 h to allow complete infiltration of the A/B mixture within the porous structure of the sugar cube;
3. then, the Petri dish was put into an oven at 60 °C for 2 h. The curing time was determined by monitoring the trend of the value of the elastic modulus G' at 60 °C as a function of the time for 3 h at constant frequency (1 Hz) and amplitude strain (1%). Figure S5 shows that even after 1.5 h G' reached an asymptotic value indicating that the polymerization reaction was complete.
4. After this time, it was possible to put the sugar cube imbibed with PDMS into a vial filled in with MilliQ water at 40 °C to entirely solubilize the sugar and obtain only the porous PDMS_SC sponge (see Figure S6).

For sponges made using a powdered sugar as template (PDMS_PS), the synthesis procedure is reported below:

1. 2.8 g of powdered sugar (composed of grains having dimensions of a few tens of microns) was incorporated within the A/B mixture until it became a homogeneous system and was placed in a silicon mold ($1 \times 1.2 \times 1.5$ cm);
2. the mold was put inside a Petri dish and dried under vacuum for 30 min to eliminate any air bubbles;
3. thereafter, it was put into an oven at 60 °C for 2 h to complete the polymerization.
4. it was possible to remove the powdered sugar by keeping the sample (PDMS_PS cube) for 15 h at 90 °C in a beaker filled with MilliQ water to entirely solubilize the powdered sugar; this procedure left only the porous PDMS_PS sponge (see Figure S7).

After the preparations, all the systems were washed 3 times for 8 h in a mixture hexane:acetone 1:1 to completely remove any PDMS that was not polymerized. After the third wash, the FTIR spectra collected from the residues of the hexane/acetone mixtures indicated the absence of detectable PDMS residues.

In order to verify the absence of sugar residues the Fehling test was carried out onto 1 g of PDMS sponges fragments following the procedure reported in literature [49].

4.3. Physicochemical Characterization

FTIR spectra of the PDMS slabs and sponges were collected using a Shimadzu, Milan, Italy, IRAffinity-1S Fourier transform infrared spectrometer in transmittance mode (KBr pellets) for the liquid A and B components (Dow Sylgard™ 184) and using the MIRacle single reflection horizontal ATR accessory equipped with a diamond/ZnSe performance flat tip crystal plate. All spectra were then normalized for transmittance (%) intensity as a function of wavenumbers (cm^{-1}). The resolution was 4 cm^{-1} and the number of scans was 64 for both the spectra collected in transmittance (KBr) and ATR mode.

The SEM images were collected on a FEG-SEM SIGMA (Carl Zeiss, Jena, Germany) using an acceleration potential of 5 kV at a working distance of 5 mm. The metallization used gold vapor under vacuum; the magnifications were $50\times$ and $100\times$ for all the samples and there was no evidence of decomposition induced by the electron beam.

XMT analysis was carried out with a Skyscan 1172 high-resolution MicroCT system at CRIST Centre, University of Florence (Italy) on a sample of $\sim 10 \times 5 \times 5$ mm equipped with an X-ray tube having a focal spot size of $5 \mu\text{m}$. The X-rays tube was equipped with a tungsten anode operating at 100 kV and $100 \mu\text{A}$. 2D X-ray images (acquisition time is 3 s for each image) were captured over 180-degree on a rotating sample with a slice-to-slice rotation angle of 0.3 by placing the sample between the X-ray source and the CCD detector. The spatial resolution was ca. $5 \mu\text{m}$. The 3D images were reconstructed from the tomographic projections using Micro Photonics Nrecon® software version 1.6.10.4. Analysis of the obtained 3D images by means of the CTAn software v.1.18 allowed the pore size distribution of each sample subjected to XMT analysis to be obtained. Two different batches for each sample were considered and the error associated both to porosity and

to the mean pores diameter was calculated by averaging these two parameters over the volume of the two samples.

The kinetics of solvent absorption (swelling and capillary action) of PDMS slab, PDMS_SC and PDMS_PS sponges were monitored by the weight increase of the slab and sponges as a function of time. PDMS slabs and PDMS_SC or PDMS_PS sponges were cut appropriately to obtain samples of 0.35 g (the exact weights $W_{dry}(time=0)$ were determined on an analytical balance). The samples were kept immersed in 3 cm³ of each solvent in a capped vial and removed at appropriate time intervals. Then, the samples were softly and rapidly dabbed on a Whatman filter paper and immediately weighed ($W_{wet}(time=ti)$). ATR-FTIR spectra were collected on the paper after its contact with the PDMS-based systems to determine whether part of the PDMS was removed during this operation. However, no evidence of the presence of PDMS residues was observed. The value of Weight Increase in percent $(WI\%)_{time=ti}$ was calculated according to the formula

$$(WI\%)_{time=ti} = \frac{W_{wet}(time=ti) - W_{dry}(time=0)}{W_{dry}(time=0)} \times 100$$

This WI% was plotted as a function of time to obtain the kinetics curve of solvent absorption. The solvents tested were acetone (AC), ethanol (ET), isopropanol (PR), dimethylsulfoxide (DMSO), propylene carbonate (PC), water (W), diethyl carbonate (DC), cyclohexane (CH), ethyl acetate (EA). From these curves, the initial absorption rates were extracted as the slopes obtained by the linear fitting of the early-time absorption values, and the maximum amounts of the absorbed solvents were calculated from the asymptotic values of the curves reported.

The weight loss of the three classes of PDMS-based systems saturated with the solvents indicated above (the initial weight was $W_{wet}(time=0)$) and placed in contact with sheets of Whatman[®] paper, was monitored as a function of time. For these measurements, to minimize the evaporation of the solvents, the PDMS systems were covered with a polyester sheet (Melinex[®]). Evaporation of the solvent was monitored over time; even in this case, the PDMS systems were covered with a polyester sheet (Melinex[®]) and the evaporated solvent at time t_i was measured too.

Then, the amount of solvent absorbed by the Whatman[®] paper was calculated as follows:

$$\Delta W_{TOT}(time=ti) = \Delta W_{ABS}(time=ti) - \Delta W_{EVAP}(time=ti)$$

where:

$$\Delta W_{TOT}(time=ti) = 100 - \left(\frac{W_{wet}(time=0) - W'_{wet}(time=ti)}{W_{wet}(time=0)} \right) \times 100$$

$$\Delta W_{ABS}(time=ti) = 100 - \left(\frac{W_{wet}(time=0) - W''_{wet}(time=ti)}{W_{wet}(time=0)} \right) \times 100$$

$$\Delta W_{EVAP}(time=ti) = 100 - \left(\frac{W_{wet}(time=0) - W'''_{wet}(time=ti)}{W_{wet}(time=0)} \right) \times 100$$

Here $W'_{wet}(time=ti)$ is the total weight loss, $W''_{wet}(time=ti)$ is the weight loss due to the solvent absorption by the Whatman[®] paper and $W'''_{wet}(time=ti)$ is the weight loss due to solvent evaporation.

The rheology measurements were carried out using a TA Discovery HR-3 hybrid rheometer according to the following procedure. Frequency sweep measurements were performed in the linear viscoelastic range, to monitor the behavior of the two parameters G' (elastic modulus) and G'' (viscous modulus) as a function of the oscillation frequency at constant oscillation amplitude. The check of this range was determined through amplitude sweep measurements of G' and G'' at constant frequency sweep (1 Hz) as a function of the oscillation amplitude (Figure S8). The normal force was set equal to 0.5 N for all

measurements. The evaporation of the solvent was minimized by using a solvent trap system provided by TA Instruments (New Castle, DE, USA). All the measurements were repeated at least three times in order to verify the reproducibility.

4.4. Application Tests

In order to determine the efficacy of this methodology, two different cleaning tests were carried out using a PDMS_PS sponge soaked with acetone onto the surface of a fresco mock-up coated with a 20 years old layer of poly(EMA/MA) 70:30 and a canvas painting mock-up coated with a ketone resin. Two different cleaning procedures were followed: for the fresco, three applications on three different areas were carried out on the fresco surface with the following contact times: 1 min, 5 min and 12 min (a small sample of the cleaned area was collected of the uncleaned area and after each application), while a single application was carried out on the canvas sample with a contact time of 12 min.

FTIR spectra of samples from the fresco mock-up were collected in transmittance mode using the following procedure: four small (few mg) fragments of fresco, collected before the cleaning and after each application of the PDMS_PS sponge soaked with acetone, were immersed in chloroform for 24 h in order to selectively extract the poly(EMA/MA) 70:30 film residues. Then, 25 drops of the resulting solutions were placed into an agate mortar and the solvent allowed to evaporate. The spectrum of the obtained solid residue was recorded using a pellet made from 200 mg of KBr containing 0.0125 wt% of the residue and Prussian blue as internal standard. The Prussian blue was added in order to normalize the intensity of the peak at 1732 cm^{-1} (that is a marker of the poly(EMA/MA) 70:30) with the Prussian blue signal at 2092 cm^{-1} . This allowed a semiquantitative comparison among the different samples [57]. Spectra are the average of 64 scans recorded in the absorbance mode using a BioRad (Milan, Italy) model FTS-40 spectrometer with a resolution of 4 cm^{-1} .

The FTIR spectra of the area of interest on canvas in the cleaning tests with the PDMS_PS sponge soaked with acetone were collected in ATR mode through the procedure described above.

Supplementary Materials: The following supporting information can be downloaded at: <https://www.mdpi.com/article/10.3390/gels9120985/s1>. Figure S1: Frequency sweep diagram of the PDMS sponges; Figure S2: Scanning Electron Microscopy (SEM) images collected before and after the application of PDMS_PS sponge loaded with ca. 10 wt% of EA onto the surface of a fresco mock-up; Figure S3: Scanning Electron Microscopy (SEM) images collected in a region of the canvas painting mock-up where the coating was absent and in a region affected by the surface coating before and after the application of PDMS_PS sponge loaded with ca. 10 wt% of EA; Figure S4: Photographs of the obtained PDMS slab; Figure S5: Trend of the elastic modulus G' for a mixture composed by the base and by the curing agent of the Sylgard 184[®] kit as a function of time; Figure S6: Photograph of the obtained PDMS_SC sponge; Figure S7: Photograph of the obtained PDMS_PS sponge; Figure S8: Amplitude sweep diagram of the PDMS based systems.

Author Contributions: Conceptualization, E.C., R.G.W., L.D., T.T.D. and F.P.; methodology, E.C., R.G.W., L.D., T.T.D., B.H.B., F.O. and F.P.; validation, F.P., F.O., S.L., T.T.D. and E.C.; resources, E.C., R.G.W. and B.H.B.; data curation, E.C., R.G.W., F.P. and L.D.; writing—original draft preparation, L.D., E.C., F.P. and R.G.W.; writing—review and editing, L.D., E.C., F.P. and R.G.W.; visualization, L.D., E.C., F.P. and R.G.W.; supervision, E.C., L.D., F.P., T.T.D., B.H.B. and R.G.W.; project administration, E.C., L.D., F.P., T.T.D. and R.G.W.; funding acquisition, E.C., L.D. and R.G.W. All authors have read and agreed to the published version of the manuscript.

Funding: This research was funded by University of Florence, the CSGI Consortium and by Italian Ministry of University and Research (MUR) PRIN-2022 2022XX8BRT “Reversible adsorbent smart materials for molecular archaeology to disclose palaeolithic stone tools as bio-archives-SMarT4BioArCH”, CUP Master & CUP B53DZ3014020006.

Informed Consent Statement: Informed consent was obtained from all subjects involved in the study.

Data Availability Statement: The data presented in this study are openly available in article.

Acknowledgments: Emma Dini is acknowledged for her help in the preparation of the PDMS based systems.

Conflicts of Interest: The authors declare no conflict of interest. Author Teresa T. Duncan was employed by the company Scientific Analysis of Fine Art, LLC. The remaining authors declare that the research was conducted in the absence of any commercial or financial relationships that could be construed as a potential conflict of interest.

References

1. Yang, X.-Y.; Chen, L.-H.; Li, Y.; Rooke, J.C.; Sanchez, C.; Su, B.-L. Hierarchically Porous Materials: Synthesis Strategies and Structure Design. *Chem. Soc. Rev.* **2017**, *46*, 481–558. [[CrossRef](#)]
2. Das, S.; Heasman, P.; Ben, T.; Qiu, S. Porous Organic Materials: Strategic Design and Structure–Function Correlation. *Chem. Rev.* **2017**, *117*, 1515–1563. [[CrossRef](#)] [[PubMed](#)]
3. Zhu, D.; Handschuh-Wang, S.; Zhou, X. Recent Progress in Fabrication and Application of Polydimethylsiloxane Sponges. *J. Mater. Chem. A* **2017**, *5*, 16467–16497. [[CrossRef](#)]
4. Ding, S.-Y.; Wang, W. Covalent Organic Frameworks (COFs): From Design to Applications. *Chem. Soc. Rev.* **2013**, *42*, 548–568. [[CrossRef](#)] [[PubMed](#)]
5. Kaur, P.; Hupp, J.T.; Nguyen, S.T. Porous Organic Polymers in Catalysis: Opportunities and Challenges. *ACS Catal.* **2011**, *1*, 819–835. [[CrossRef](#)]
6. Kim, S.; Lee, Y.M. Rigid and Microporous Polymers for Gas Separation Membranes. *Prog. Polym. Sci.* **2015**, *43*, 1–32. [[CrossRef](#)]
7. Sun, J.-K.; Xu, Q. Functional Materials Derived from Open Framework Templates/Precursors: Synthesis and Applications. *Energy Environ. Sci.* **2014**, *7*, 2071. [[CrossRef](#)]
8. Sun, L.-B.; Liu, X.-Q.; Zhou, H.-C. Design and Fabrication of Mesoporous Heterogeneous Basic Catalysts. *Chem. Soc. Rev.* **2015**, *44*, 5092–5147. [[CrossRef](#)]
9. Wang, W.; Zhou, M.; Yuan, D. Carbon Dioxide Capture in Amorphous Porous Organic Polymers. *J. Mater. Chem. A* **2017**, *5*, 1334–1347. [[CrossRef](#)]
10. Xiang, Z.; Cao, D. Porous Covalent–Organic Materials: Synthesis, Clean Energy Application and Design. *J. Mater. Chem. A* **2013**, *1*, 2691–2718. [[CrossRef](#)]
11. Choi, S.-J.; Kwon, T.-H.; Im, H.; Moon, D.-I.; Baek, D.J.; Seol, M.-L.; Duarte, J.P.; Choi, Y.-K. A Polydimethylsiloxane (PDMS) Sponge for the Selective Absorption of Oil from Water. *ACS Appl. Mater. Interfaces* **2011**, *3*, 4552–4556. [[CrossRef](#)] [[PubMed](#)]
12. McCall, W.R.; Kim, K.; Heath, C.; La Pierre, G.; Sirbully, D.J. Piezoelectric Nanoparticle–Polymer Composite Foams. *ACS Appl. Mater. Interfaces* **2014**, *6*, 19504–19509. [[CrossRef](#)] [[PubMed](#)]
13. Yuen, P.K.; Su, H.; Goral, V.N.; Fink, K.A. Three-Dimensional Interconnected Microporous Poly(Dimethylsiloxane) Microfluidic Devices. *Lab. Chip.* **2011**, *11*, 1541. [[CrossRef](#)] [[PubMed](#)]
14. Zheng, Q.; Zhang, H.; Mi, H.; Cai, Z.; Ma, Z.; Gong, S. High-Performance Flexible Piezoelectric Nanogenerators Consisting of Porous Cellulose Nanofibril (CNF)/Poly(Dimethylsiloxane) (PDMS) Aerogel Films. *Nano Energy* **2016**, *26*, 504–512. [[CrossRef](#)]
15. Park, J.; Wang, S.; Li, M.; Ahn, C.; Hyun, J.K.; Kim, D.S.; Kim, D.K.; Rogers, J.A.; Huang, Y.; Jeon, S. Three-Dimensional Nanonetworks for Giant Stretchability in Dielectrics and Conductors. *Nat. Commun.* **2012**, *3*, 916. [[CrossRef](#)] [[PubMed](#)]
16. Wang, J.; Guo, J.; Si, P.; Cai, W.; Wang, Y.; Wu, G. Polydopamine-Based Synthesis of an In(OH) 3 –PDMS Sponge for Ammonia Detection by Switching Surface Wettability. *RSC Adv.* **2016**, *6*, 4329–4334. [[CrossRef](#)]
17. Kim, D.H.; Jung, M.C.; Cho, S.-H.; Kim, S.H.; Kim, H.-Y.; Lee, H.J.; Oh, K.H.; Moon, M.-W. UV-Responsive Nano-Sponge for Oil Absorption and Desorption. *Sci. Rep.* **2015**, *5*, 12908. [[CrossRef](#)]
18. Yu, C.; Yu, C.; Cui, L.; Song, Z.; Zhao, X.; Ma, Y.; Jiang, L. Facile Preparation of the Porous PDMS Oil-Absorbent for Oil/Water Separation. *Adv. Mater. Interfaces* **2017**, *4*, 1600862. [[CrossRef](#)]
19. Li, Q.; Duan, T.; Shao, J.; Yu, H. Fabrication Method for Structured Porous Polydimethylsiloxane (PDMS). *J. Mater. Sci.* **2018**, *53*, 11873–11882. [[CrossRef](#)]
20. Jung, S.; Kim, J.H.; Kim, J.; Choi, S.; Lee, J.; Park, I.; Hyeon, T.; Kim, D.-H. Reverse-Micelle-Induced Porous Pressure-Sensitive Rubber for Wearable Human–Machine Interfaces. *Adv. Mater.* **2014**, *26*, 4825–4830. [[CrossRef](#)]
21. Liu, W.; Chen, Z.; Zhou, G.; Sun, Y.; Lee, H.R.; Liu, C.; Yao, H.; Bao, Z.; Cui, Y. 3D Porous Sponge-Inspired Electrode for Stretchable Lithium-Ion Batteries. *Adv. Mater.* **2016**, *28*, 3578–3583. [[CrossRef](#)] [[PubMed](#)]
22. Liang, S.; Li, Y.; Yang, J.; Zhang, J.; He, C.; Liu, Y.; Zhou, X. 3D Stretchable, Compressible, and Highly Conductive Metal-Coated Polydimethylsiloxane Sponges. *Adv. Mater. Technol.* **2016**, *1*, 1600117. [[CrossRef](#)]
23. Han, J.-W.; Kim, B.; Li, J.; Meyyappan, M. Flexible, Compressible, Hydrophobic, Floatable, and Conductive Carbon Nanotube–Polymer Sponge. *Appl. Phys. Lett.* **2013**, *102*, 051903. [[CrossRef](#)]
24. Pedraza, E.; Brady, A.-C.; Fraker, C.A.; Molano, R.D.; Sukert, S.; Berman, D.M.; Kenyon, N.S.; Pileggi, A.; Ricordi, C.; Stabler, C.L. Macroporous Three-Dimensional PDMS Scaffolds for Extrahepatic Islet Transplantation. *Cell Transplant.* **2013**, *22*, 1123–1135. [[CrossRef](#)]
25. Zhao, X.; Li, L.; Li, B.; Zhang, J.; Wang, A. Durable Superhydrophobic/Superoleophilic PDMS Sponges and Their Applications in Selective Oil Absorption and in Plugging Oil Leakages. *J. Mater. Chem. A* **2014**, *2*, 18281–18287. [[CrossRef](#)]

26. Shi, J.; Zhang, H.; Jackson, J.; Shademani, A.; Chiao, M. A Robust and Refillable Magnetic Sponge Capsule for Remotely Triggered Drug Release. *J. Mater. Chem. B* **2016**, *4*, 7415–7422. [[CrossRef](#)]
27. Liang, S.; Li, Y.; Chen, Y.; Yang, J.; Zhu, T.; Zhu, D.; He, C.; Liu, Y.; Handschuh-Wang, S.; Zhou, X. Liquid Metal Sponges for Mechanically Durable, All-Soft, Electrical Conductors. *J. Mater. Chem. C* **2017**, *5*, 1586–1590. [[CrossRef](#)]
28. Bélanger, M.-C.; Marois, Y. Hemocompatibility, Biocompatibility, Inflammatory and in Vivo Studies of Primary Reference Materials Low-Density Polyethylene and Polydimethylsiloxane: A Review. *J. Biomed. Mater. Res.* **2001**, *58*, 467–477. [[CrossRef](#)]
29. Lötters, J.C.; Olthuis, W.; Veltink, P.H.; Bergveld, P. The Mechanical Properties of the Rubber Elastic Polymer Polydimethylsiloxane for Sensor Applications. *J. Micromech. Microeng.* **1997**, *7*, 145–147. [[CrossRef](#)]
30. Mata, A.; Fleischman, A.J.; Roy, S. Characterization of Polydimethylsiloxane (PDMS) Properties for Biomedical Micro/Nanosystems. *Biomed. Microdevices* **2005**, *7*, 281–293. [[CrossRef](#)]
31. Dong, C.-H.; He, L.; Xiao, Y.-F.; Gaddam, V.R.; Ozdemir, S.K.; Han, Z.-F.; Guo, G.-C.; Yang, L. Fabrication of High-Q Polydimethylsiloxane Optical Microspheres for Thermal Sensing. *Appl. Phys. Lett.* **2009**, *94*, 231119. [[CrossRef](#)]
32. Piruska, A.; Nikcevic, I.; Lee, S.H.; Ahn, C.; Heineman, W.R.; Limbach, P.A.; Seliskar, C.J. The Autofluorescence of Plastic Materials and Chips Measured under Laser Irradiation. *Lab. Chip.* **2005**, *5*, 1348. [[CrossRef](#)] [[PubMed](#)]
33. Yilgör, E.; Yilgör, I. Silicone Containing Copolymers: Synthesis, Properties and Applications. *Prog. Polym. Sci.* **2014**, *39*, 1165–1195. [[CrossRef](#)]
34. González-Rivera, J.; Iglío, R.; Barillaro, G.; Duce, C.; Tinè, M. Structural and Thermoanalytical Characterization of 3D Porous PDMS Foam Materials: The Effect of Impurities Derived from a Sugar Templating Process. *Polymers* **2018**, *10*, 616. [[CrossRef](#)] [[PubMed](#)]
35. Lee, J.N.; Park, C.; Whitesides, G.M. Solvent Compatibility of Poly(Dimethylsiloxane)-Based Microfluidic Devices. *Anal. Chem.* **2003**, *75*, 6544–6554. [[CrossRef](#)]
36. Phenix, A. The Swelling of Artists' Paints in Organic Solvents. Part 2, Comparative Swelling Powers of Selected Organic Solvents and Solvent Mixtures. *J. Am. Inst. Conserv.* **2002**, *41*, 61–90. [[CrossRef](#)]
37. Duncan, T.T.; Chan, E.P.; Beers, K.L. Quantifying the 'Press and Peel' Removal of Particulates Using Elastomers and Gels. *J. Cult. Herit.* **2021**, *48*, 236–243. [[CrossRef](#)]
38. Duncan, T.T.; Berrie, B.H.; Weiss, R.G. Soft, Peelable Organogels from Partially Hydrolyzed Poly(Vinyl Acetate) and Benzene-1,4-Diboronic Acid: Applications to Clean Works of Art. *ACS Appl. Mater. Interfaces* **2017**, *9*, 28069–28078. [[CrossRef](#)]
39. Duncan, T.T.; Vicenzi, E.P.; Lam, T.; Brogdon-Grantham, S.A. A Comparison of Materials for Dry Surface Cleaning Soot-Coated Papers of Varying Roughness: Assessing Efficacy, Physical Surface Changes, and Residue. *J. Am. Inst. Conserv.* **2023**, *62*, 152–167. [[CrossRef](#)]
40. Duncan, T.T.; Chan, E.P.; Beers, K.L. Maximizing Contact of Supersoft Bottlebrush Networks with Rough Surfaces To Promote Particulate Removal. *ACS Appl. Mater. Interfaces* **2019**, *11*, 45310–45318. [[CrossRef](#)]
41. Carretti, E.; Dei, L.; Macherelli, A.; Weiss, R.G. Rheoreversible Polymeric Organogels: The Art of Science for Art Conservation. *Langmuir* **2004**, *20*, 8414–8418. [[CrossRef](#)]
42. Carretti, E.; Dei, L.; Weiss, R.G.; Baglioni, P. A New Class of Gels for the Conservation of Painted Surfaces. *J. Cult. Herit.* **2008**, *9*, 386–393. [[CrossRef](#)]
43. Samorì, C.; Galletti, P.; Giorgini, L.; Mazzeo, R.; Mazzocchetti, L.; Prati, S.; Scitutto, G.; Volpi, F.; Tagliavini, E. The Green Attitude in Art Conservation: Polyhydroxybutyrate-Based Gels for the Cleaning of Oil Paintings. *ChemistrySelect* **2016**, *1*, 4502–4508. [[CrossRef](#)]
44. Yiming, J.; Scitutto, G.; Prati, S.; Catelli, E.; Galeotti, M.; Porcinai, S.; Mazzocchetti, L.; Samorì, C.; Galletti, P.; Giorgini, L.; et al. A New Bio-Based Organogel for the Removal of Wax Coating from Indoor Bronze Surfaces. *Herit. Sci.* **2019**, *7*, 34. [[CrossRef](#)]
45. Prati, S.; Volpi, F.; Fontana, R.; Galletti, P.; Giorgini, L.; Mazzeo, R.; Mazzocchetti, L.; Samorì, C.; Scitutto, G.; Tagliavini, E. Sustainability in Art Conservation: A Novel Bio-Based Organogel for the Cleaning of Water Sensitive Works of Art. *Pure Appl. Chem.* **2018**, *90*, 239–251. [[CrossRef](#)]
46. Çakmak, Y.; Çakmakçi, E.; Apohan, N.K.; Karadag, R. Isosorbide, Pyrogallol, and Limonene-Containing Thiol-Ene Photocured Bio-Based Organogels for the Cleaning of Artworks. *J. Cult. Herit.* **2022**, *55*, 391–398. [[CrossRef](#)]
47. Johnson, L.M.; Gao, L.; Shields IV, C.W.; Smith, M.; Efimenko, K.; Cushing, K.; Genzer, J.; López, G.P. Elastomeric Microparticles for Acoustic Mediated Bioseparations. *J. Nanobiotechnol.* **2013**, *11*, 22. [[CrossRef](#)] [[PubMed](#)]
48. Zhang, A.; Cheng, L.; Hong, S.; Yang, C.; Lin, Y. Preparation of Anti-Fouling Silicone Elastomers by Covalent Immobilization of Carboxybetaine. *RSC Adv.* **2015**, *5*, 88456–88463. [[CrossRef](#)]
49. Hörner, T.G.; Klüfers, P. The Species of Fehling's Solution. *Eur. J. Inorg. Chem.* **2016**, *2016*, 1798–1807. [[CrossRef](#)]
50. Almdal, K.; Dyre, J.; Hvidt, S.; Kramer, O. Towards a Phenomenological Definition of the Term 'Gel'. *Polym. Gels Netw.* **1993**, *1*, 5–17. [[CrossRef](#)]
51. Horie, V.C. *Materials for Conservation*, 1st ed.; Architectural Press: Oxford, UK, 1998.
52. Sandu, I.C.A.; Candeias, A.; van den Berg, K.J.; Sandbakken, E.G.; Tveit, E.S.; van Keulen, H. Multi Technique and Multiscale Approaches to the Study of Ancient and Modern Art Objects on Wooden and Canvas Support. *Phys. Sci. Rev.* **2019**, *4*, 20180016. [[CrossRef](#)]
53. Stulik, D.; Miller, D.; Khanjian, H.; Khandekar, N.; Richard, W.; Carlson, J.; Petersen, W.C. *Solvent Gels for the Cleaning of Works of Art: The Residue Question*; Dorge, V., Ed.; Getty Publications: Los Angeles, CA, USA, 2004.

54. Gupta, N.S.; Lee, K.-S.; Labouriau, A. Tuning Thermal and Mechanical Properties of Polydimethylsiloxane with Carbon Fibers. *Polymers* **2021**, *13*, 1141. [[CrossRef](#)] [[PubMed](#)]
55. Xia, Y.; Whitesides, G.M. Soft lithography. *Annu. Rev. Mater. Sci.* **1998**, *28*, 153–184. [[CrossRef](#)]
56. Lisensky, G.C.; Campbell, D.J.; Beckman, K.J.; Calderon, C.E.; Doolan, P.W.; Ottosen, R.M.; Ellis, A.B. Replication and Compression of Surface Structures with Polydimethylsiloxane Elastomer. *J. Chem. Educ.* **1999**, *76*, 537. [[CrossRef](#)]
57. Salvadori, B.; Errico, V.; Mauro, M.; Melnik, E.; Dei, L. Evaluation of Gypsum and Calcium Oxalates in Deteriorated Mural Paintings by Quantitative FTIR Spectroscopy. *Spectrosc. Lett.* **2003**, *36*, 501–513. [[CrossRef](#)]

Disclaimer/Publisher’s Note: The statements, opinions and data contained in all publications are solely those of the individual author(s) and contributor(s) and not of MDPI and/or the editor(s). MDPI and/or the editor(s) disclaim responsibility for any injury to people or property resulting from any ideas, methods, instructions or products referred to in the content.

Non-aqueous poly(dimethylsiloxane) organogel sponges for controlled solvent release: synthesis, characterization, and application in the cleaning of artworks

Francesca Porpora,¹ Luigi Dei,¹ Teresa Duncan,³ Fedora Olivadese,¹ Shae London,⁴ Barbara H. Berrie,² Richard G. Weiss,⁴ and Emiliano Carretti^{1,5*}

¹Department of Chemistry "Ugo Schiff" & CSGI Consortium, University of Florence, via della Lastruccia, 3-13 I-50019 Sesto Fiorentino (FI) – Italy.

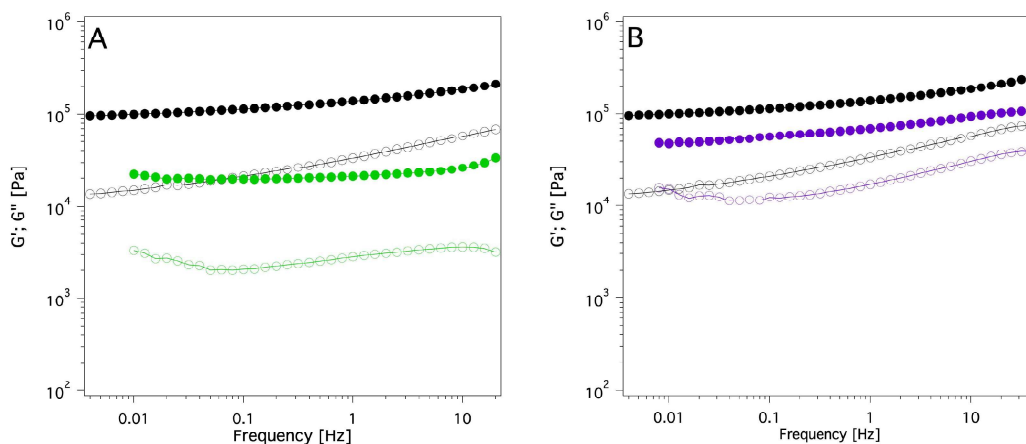
²National Gallery of Art, Department of Scientific Research, 2000 South Club Drive, Landover, Maryland 20785 – USA.

³Scientific Analysis of Fine Art, LLC, Berwyn, PA 19312 – USA.

⁴Department of Chemistry and Institute for Soft Matter Synthesis and Metrology, Georgetown University, 37th and O Streets NW, Washington, DC 20057 – USA.

⁵National Research Council—National Institute of Optics (CNR-INO), Largo E. Fermi 6, 50125 Florence, FI, Italy

* Correspondence: emiliano.carretti@unifi.it; +390554573046



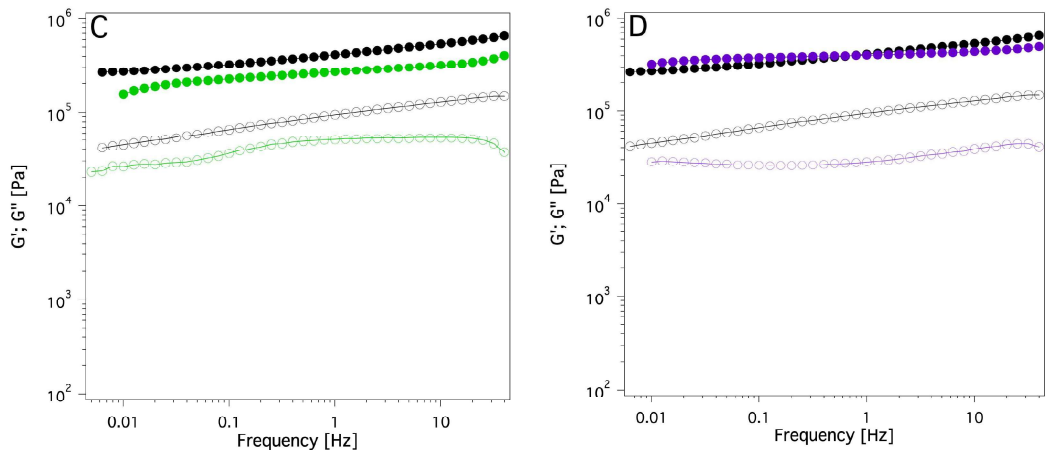


Figure SI_1. Frequency sweep diagram of the: A PDMS_SC sponge alone (black), with absorbed Ethyl acetate (green); B PDMS_SC sponge alone (black), with absorbed Ethanol (purple); C PDMS_PS sponge alone (black), with absorbed Ethyl acetate (red); D PDMS_PS sponge alone (black), with absorbed Ethanol (purple). Absorption time 24 hours. Filled circles indicate G' ; open circles indicate G'' .

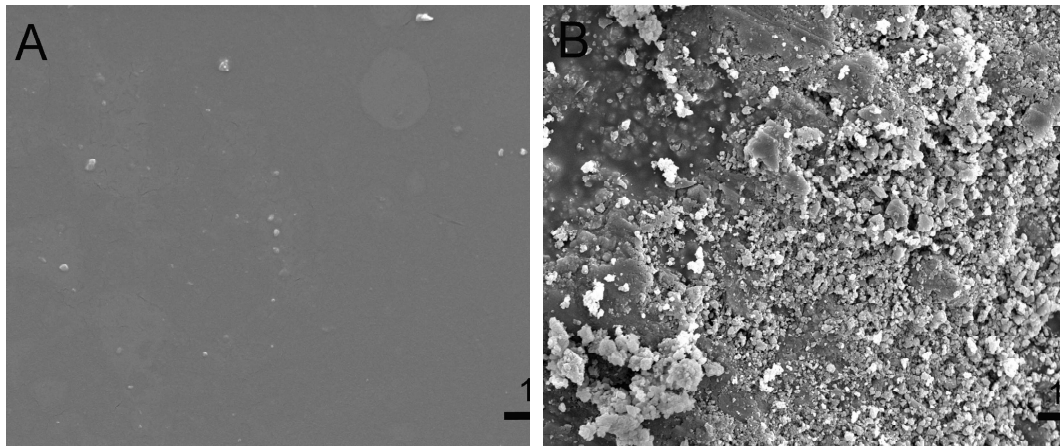


Figure SI_2. Scanning Electron Microscopy (SEM) images collected before (A) and after (B) the application of PDMS_SP sponge loaded with 10wt% ca of EA onto the surface of a fresco mockup.

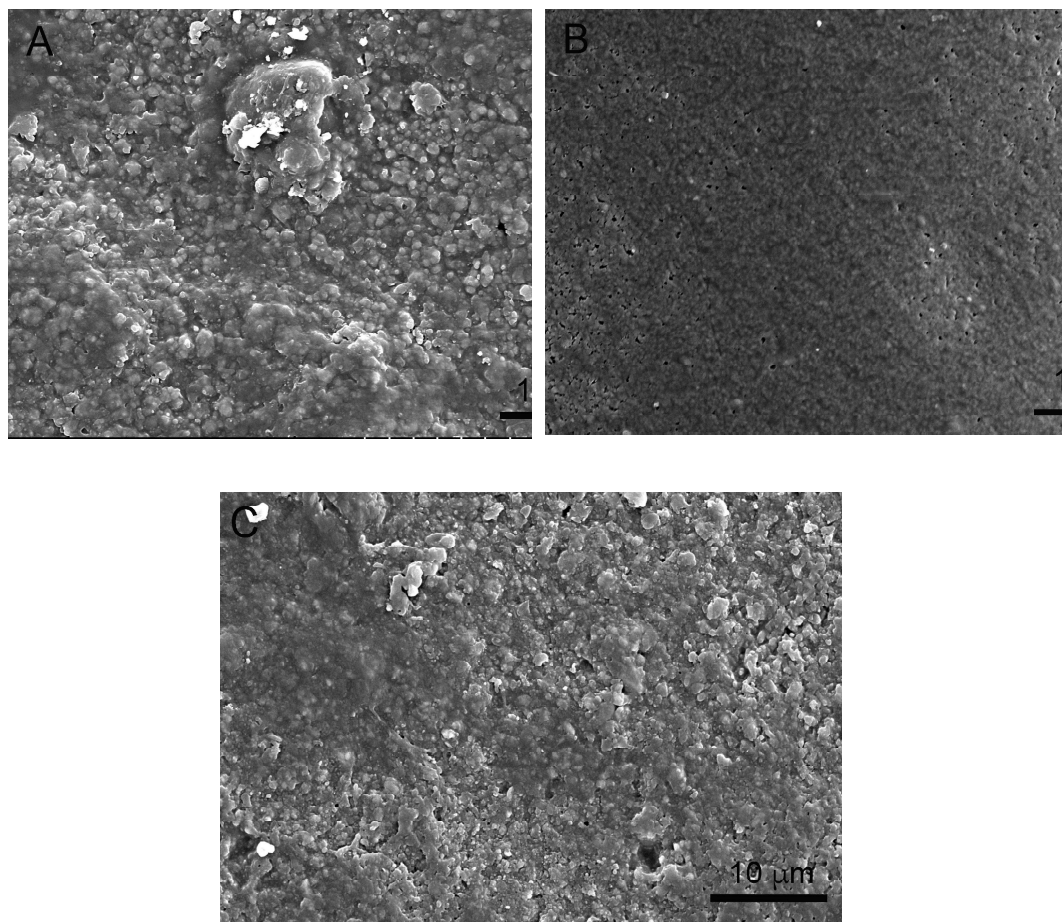


Figure SI_3. Scanning Electron Microscopy (SEM) images collected in a region of the canvas painting mockup where the coating was absent (A) and in a region affected by the surface coating before (B) and after (C) the application of PDMS_SP sponge loaded with 10wt% ca of EA.

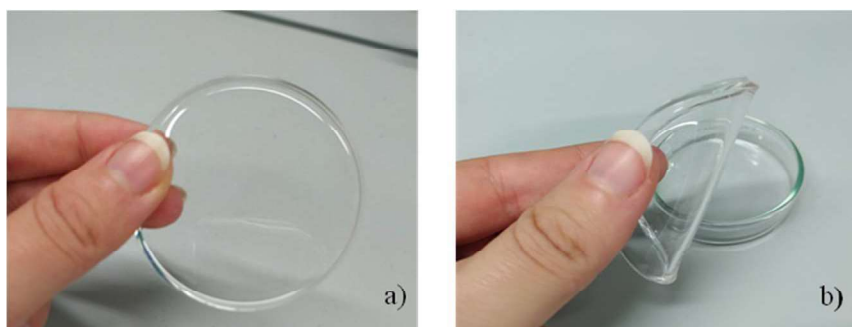


Figure SI_4. Photographs of the obtained PDMS slab showing both transparency (left) and elasticity (right).

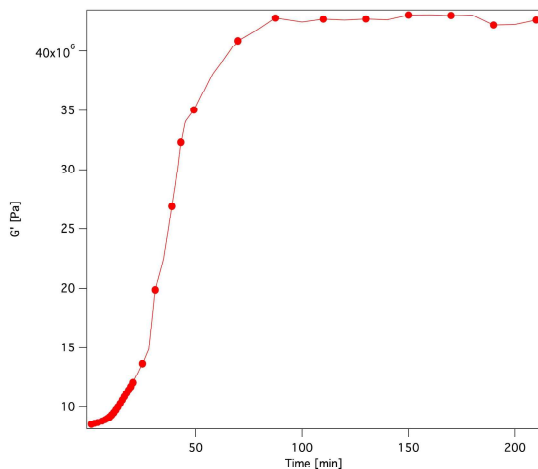


Figure SI_5. Trend of the elastic modulus G' for a mixture composed by the base and by the curing agent of the Sylgard 184® kit (ratio component A/component B = 20:1) as a function of time at constant frequency (1Hz), amplitude strain (1%) and temperature (60°C).



Figure SI_6. Photograph of the obtained PDMS_SC sponge (left) compared with the pure sugar cube (right).



Figure SI_7. Photograph of the obtained PDMS_PS sponge-

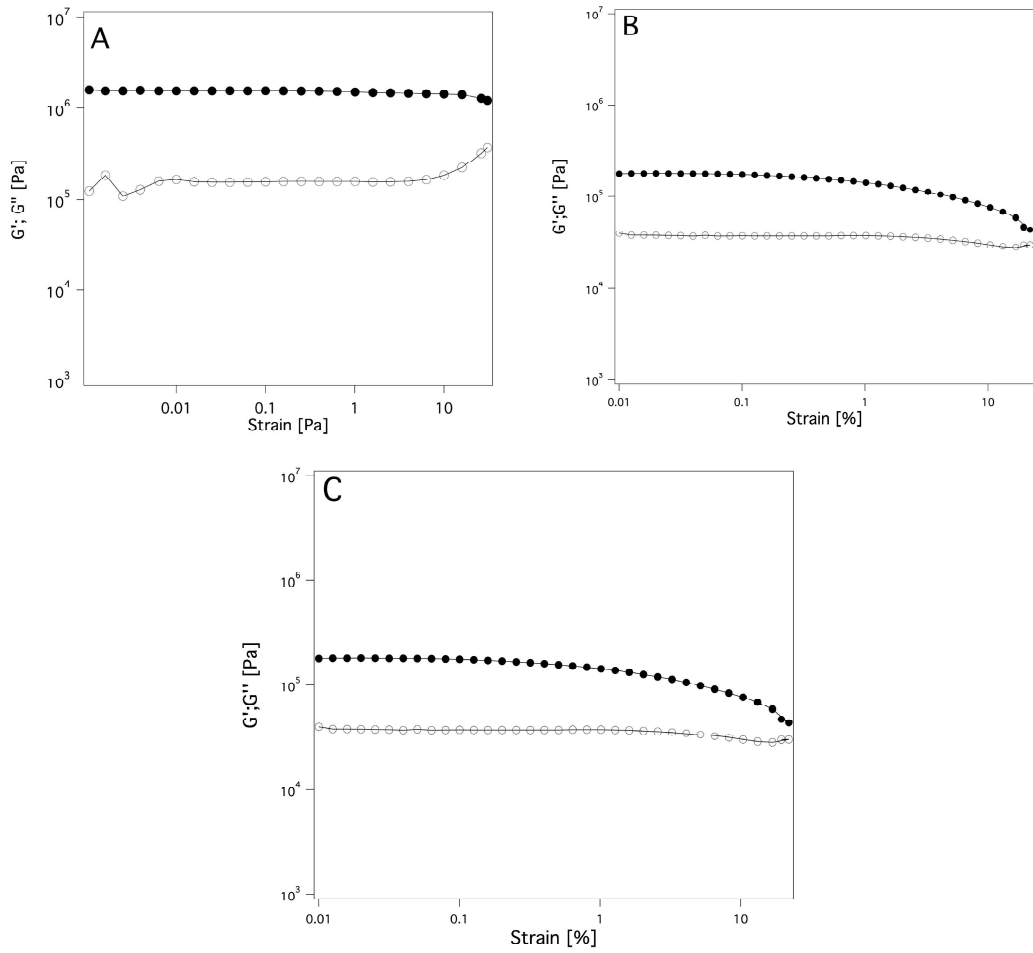


Figure SI_8. Amplitude sweep diagram of the: A PDMS slab 10:1; B PDMS_SC sponge (ratio component A/component B = 10:1); C PDMS_SP sponge (ratio component A/component B = 10:1). Filled circles indicate G' ; open circles indicate G'' .